



The
University
Of
Sheffield.

Spatial and physical organisation of the mammalian nucleus

Ália dos Santos

A thesis submitted in fulfilment of the requirements for the degree of
Doctor of Philosophy

December 2021

The University of Sheffield

Faculty of Medicine, Dentistry Health

Department of Oncology and Metabolism

Supervisor: Dr Christopher Toseland

“One never notices what has been done; one can only see what remains to be done.”

Marie Curie

I. Declaration

This thesis incorporates seven manuscripts. Each manuscript was part of a collaborative effort between multiple authors. For five of these manuscripts, I am a primary contributor and listed as first or co-first author.

My detailed contributions to each manuscript are outlined at the beginning of each chapter.

The text for the introductory chapter of this thesis (Chapter 1) has been adapted from a published review article written by me, with the title “Regulation of Nuclear Mechanics and the Impact on DNA Damage” (dos Santos and Toseland, 2021).

No part of this thesis has been submitted in support of an application for any degree or qualification at the University of Sheffield or any other University or institute of learning.

Ália dos Santos

A handwritten signature in black ink that reads "Ália dos Santos". The signature is written in a cursive style with a large initial 'A' and a long horizontal stroke at the end.

December 2021

II. Acknowledgements

First and foremost, I would like to thank my supervisor, Chris, for this wonderful opportunity. I could have not wished for a better, more rich PhD experience and a better mentor. Thank you for so carefully looking after my wellbeing, for believing in me - more than I do myself - and for investing so much in me. It has been an extremely rewarding time and I will miss working with you.

I would also like to thank all my lab mates, past and present, who shared with me the rewards and difficulties of the academic life. A special thanks to Yukti, who taught me so much over the years, Alex for always seeing the funny side of things and to Rosie, my good friend, who has shared so much with me over these last few years. I am also grateful to Chloe, for her continuous friendship over the years. To Natali, Aneira and Thalia, thank you for your kindness and for so generously hosting me on so many occasions - it has been incredibly fun and entertaining to spend time with you.

Over the years I had the opportunity to work with amazing collaborators. I would like to thank Florian, for hosting me in his lab in Germany and for always welcoming scientific discussions. I would also like to thank Iwan and Michael, for introducing me to AFM and for their endless enthusiasm for science. To the staff members at Harwell Research Campus, Lin, Sarah and Marisa, thank you for all your help during these last six years. I would also like to mention Kevin Howland who helped me with my many hours of mass spectrometry experiments.

A special thanks to all my siblings, who have shaped me into the person I am today. To Titi, who has always helped my academic success and kept the bar high. To my mum for her love and for always taking care of me and to Soraya, for understanding me. I would also to thank Jackie and Charlie, for taking me in and for being there for me every time.

To Ed, who has been my unwavering support throughout my PhD and who has never doubted me – this would have not been possible without you. I am incredibly grateful to you for being a constant presence in my life, in good times and bad times.

Lastly, this thesis is especially dedicated in memory of my father, who, I know, would have been tremendously proud today. Thank you for always encouraging my scientific mind, for my first microscope (and the second); thank you for always believing in me and for all the sacrifices you had to make in order for me to be where I am and who I am today.

III. Table of Contents

I. Declaration	3
II. Acknowledgements	4
IV. Table of Non-Manuscript Figures	8
V. List of Manuscripts	9
VI. Non-Manuscript Abbreviations	11
Abstract	13
1. Introduction - Nuclear mechanics and the spatial organisation of nuclear processes	15
1.1. Contributing Factors to Nuclear Mechanics	18
1.1.1. Cytoskeletal Forces in Nuclear Mechanics	18
1.1.2. The Nuclear Lamina	21
1.1.3. Chromatin is a key component of nuclear mechanics	23
1.2. Regulation of Chromatin structure	26
1.2.1. Epigenetic Modifications of Chromatin	27
1.2.2. Changes in chromatin structure through ATP-dependent chromatin remodellers	28
1.2.3. Chromatin Crosslinking	29
1.3. The Relationship between Nuclear Mechanics and Nuclear Processes	31
1.3.1. DNA damage	31
1.3.2. RNA Polymerase II Transcription	36
1.4. The spatial organisation RNA Polymerase II transcription	37
1.4.1. Transcription factors and coactivators of transcription in the nanoscale organisation of gene expression	43
1.4.2. CoCoA and NDP52 - gene paralogs in transcription regulation and autophagy	47
1.5. Actin and Myosin motors in chromatin regulation and transcription	53
1.5.1. Myosin VI – a Unique Molecular Motor	57
1.6 Methodological Approaches to Study Nuclear Architecture and Organisation	60
1.6.1. Atomic Force Microscopy	61
1.6.2. Stochastic Optical Reconstruction Microscopy	64
1.6.3. 3D Single-Molecule Tracking in Live Cells	67
1.6.4. Data Fitting and Statistics	72
2. Aims	73
3. Structural contributors to Nuclear Mechanics in DNA damage	75
3.1. Context of Research and Contributions	75
3.2. Manuscripts	78
3.2.1. Manuscript 1 - Atomic Force Microscopy micro-rheology reveals large structural inhomogeneities in single cell-nuclei.	78
3.2.1.1. Supplementary Material for Manuscript 1	92
3.2.2. Manuscript 2 - DNA damage alters nuclear mechanics through chromatin reorganisation	100
3.2.2.1. Supplementary Material for Manuscript 2	115

4. Activation of nuclear Myosin VI function	120
4.1. Context of Research and Contributions	120
4.2. Manuscripts	122
4.2.1. Manuscript 3 - NDP52 activates nuclear myosin VI to enhance RNA polymerase II transcription.	123
4.2.1.1. Supplementary Material for Manuscript 3	139
4.2.2. Manuscript 4 - Competition between two high-and low-affinity protein-binding sites in myosin VI controls its cellular function.	160
4.2.2.1. Supplementary Material for Manuscript 4	172
4.2.3. Manuscript 5 – Binding Partners Regulate Unfolding of Myosin VI to Activate the Molecular Motor	179
4.2.3.1. Supplementary Material for Manuscript 5	213
5. Myosin VI regulates the spatial organization of mammalian transcription	216
5.1. Context of Research and Contributions	216
5.2. Manuscript	217
5.2.1. Manuscript 6 - Myosin VI regulates the spatial organization of mammalian transcription	218
5.2.1.1. Supplementary Material for Manuscript 6	241
6. Autophagy receptor NDP52 modulates RNA Polymerase II transcription	249
6.1. Context of Research and Contributions	249
6.2. Manuscript	251
6.2.1. Manuscript 7 - Autophagy receptor NDP52 modulates RNA Polymerase II transcription	251
6.2.1.1. Supplementary Material for Manuscript 7	291
7. Discussion and Future Perspectives	315
7.1. Contribution of chromatin to nuclear mechanics and impact of DNA damage and repair on nuclear stiffness	315
7.2. Activation of Myosin VI by binding partners in transcription	320
7.3. Myosin VI regulates the spatial organisation of RNA Polymerase II clusters during transcription initiation	323
7.4. Autophagy receptor NDP52 modulates RNA Polymerase II transcription	327
8. Non-Manuscript References	331

IV. Table of Non-Manuscript Figures

Figure 1 - Schematic representation of the interconnectivity between cytoskeleton, nuclear envelope and chromatin.....	16
Figure 2 - Major contributors to nuclear morphology and mechanics.....	17
Figure 3 – Chromatin accessibility for transcription.....	26
Figure 4 - Role of chromatin decondensation following DNA damage.....	34
Figure 5 – Transcriptional condensate formation.	40
Figure 6 – Mechano-active transcriptional condensates.	42
Figure 7 – Major transcription factor families and their DNA binding motifs.	45
Figure 8 – Transcription factor and coactivator assembly and clustering to activate transcription	49
Figure 9 – Coactivator activity of CoCoA.....	50
Figure 11 – CALCOCO family domains.	52
Figure 12 – MVI domains and alternative splicing isoforms.....	59
Figure 13 – Diagram of AFM measurement.	62
Figure 14 – Example of mechanical measurements in live-cell nuclei.....	63
Figure 15 – Nuclear softening following MVI inhibition.....	326
Figure 16 – Chromatin decondensation by nuclear overexpression of NDP52.....	329

V. List of Manuscripts

Chapter 3: Structural Contributors to Nuclear Mechanics in DNA Damage

Manuscript 1 _____

Lherbette M*, **dos Santos Á***, Hari-Gupta Y, Fili N, Toseland CP, Schaap IAT; Atomic Force Microscopy micro-rheology reveals large structural inhomogeneities in single cell-nuclei. (*equal contribution) **Scientific Reports, 2017. 7:8116**

Manuscript 2 _____

dos Santos Á, Cook A, Gough RE, Schilling M, Olszok NA, Brown I, Wang L, Aaron J, Martin-Fernandez ML, Rehfeldt F, Toseland CP; DNA damage alters nuclear mechanics through chromatin reorganisation. **Nucleic Acids Research, 2021. 49(1):340-353**

Chapter 4: Activation of Nuclear Myosin VI Function

Manuscript 3 _____

Fili N, Hari-Gupta Y, **dos Santos Á**, Cook A, Poland S, Ameer-Beg SM, Parsons M, Toseland CP, NDP52 activates nuclear myosin VI to enhance RNA polymerase II transcription. **Nature Communications 8 1871 (2017)**

Manuscript 4 _____

Fili N*, Hari-Gupta Y*, Aston B, **dos Santos Á**, Gough RE, Alamad B, Wang L, Martin-Fernandez ML, Toseland CP, Competition between two high-and low-affinity protein-binding sites in myosin VI controls its cellular function. (*equal contribution) **Journal of Biological Chemistry 295(2): 337-347(2019)**

Manuscript 5

dos Santos Á*, Fili N*, Hari-Gupta Y, Gough RE, Wang L, Martin-Fernandez M, Aaron J, Chew TL, Toseland CP; Binding partners regulate unfolding of myosin VI to activate the molecular motor.

(*equal contribution) **BioRxiv (2020)** - <https://doi.org/10.1101/2020.05.10.079236> - Submitted to PNAS -

Chapter 5: Nuclear Myosin VI Regulates the Spatial Organisation of Mammalian Transcription Initiation

Manuscript 6

Hari-Gupta Y*, Fili N*, **dos Santos Á***, Cook AW, Gough RE, Reed HCW, Wang L, Aaron J, Venit T, Wait E, Grosse-Berkenbusch A, Gebhardt JCM, Percipalle P, Chew TL, Martin-Fernandez M, Toseland CP; Nuclear myosin VI regulates the spatial organization of mammalian transcription initiation.

(*equal contribution) **BioRxiv (2020)** <https://doi.org/10.1101/2020.04.21.053124> - Accepted **Nature Communications**

Chapter 6: Autophagy Receptor NDP52 Modulates RNA Polymerase II Transcription

Manuscript 7

dos Santos Á, Rollins DE, Hari-Gupta Y, Reed HCW, Ru SYZ, Pidllisna K, Stranger A, Lorgat F, Brown I, Howland K, Aaron J, Wang L, Ellis PJI, Chew TL, Pyne ALB, Martin-Fernandez ML, Toseland CP; Autophagy receptor NDP52 modulates RNA Polymerase II transcription. – **BioRxiv (2021)** <https://doi.org/10.1101/2022.02.01.478690> - In Revision - **Nature Communications**

VI. Non-Manuscript Abbreviations

In addition to these, additional abbreviations are listed within each publication.

acMFM	Aberration-corrected Multifocal Microscopy
AFM	Atomic Force Microscopy
ATM	Ataxia-Talangiectasia Mutated
ATR	ATM and RAD3-related
AR	Androgen Receptor
DDR	DNA Damage Response
DSB	Double-strand break
dsDNA	Double-stranded DNA
CALCOCO	Calcium-binding and Coiled-coil Containing
CBD	Cargo Binding Domain
CoCoA	Coiled-coil Coactivator
CTD	C-terminal Domain
Dab2	Disabled-2
ER	Oestrogen Receptor
ERE	Oestrogen Responsive Elements
HP1	Heterochromatin Protein 1
HR	Homologous Recombination
KMD	Histone Lysine Demethylases
KMT	Histone Lysine Methyltransferases
LAD	Lamina Associated Domain
LatB	Latrunculin B
LEM	Lap2, Emerin and Man1
LI	Long Insert
LINC	Linker of Nucleoskeleton and Cytoskeleton
LLPS	Liquid-Liquid Phase Separation
MVI	Myosin VI
NDP52	Nuclear Dot Protein 52
NE	Nuclear Envelope

NHEJ	Non-Homologous End-Joining
NI	Non- Insert
NLS	Nuclear Localisation Sequence
NM1	Nuclear Myosin 1
NR	Nuclear Receptor
PIKK	Phosphatidyl Inositol-3-Kinase
P-TEFb	Positive Transcription Elongation Factor b
RNAPII	RNA Polymerase II
RNAPII-Ser2P	RNA Polymerase II – Serine 2 Phosphorylated
RNAPII-Ser5P	RNA Polymerase II – Serine 5 Phosphorylated
ROS	Reactive Oxygen Species
SI	Small Insert
SKICH	Skeletal Muscle and Kidney Enriched Inositol Phosphatase (SKIP) Carboxyl Homology
STORM	Stochastic Optical Reconstruction Microscopy
TAD	Topologically Associated Domain
TAZ	Transcriptional Coactivator with a PDZ-binding motif
TIP	2,4,6-Triiodophenol
YAP	Yes-Associated Protein
ZF	Zing Finger

Abstract

The nucleus is a dynamic and highly adaptable structure, essential for eukaryotic cell survival and function. As the largest and stiffest organelle in the cell, the nucleus is especially sensitive to mechanical input. As a result, it is becoming increasingly evident that in addition to housing and protecting genomic material, the nucleus is capable of not only sensing but adapting and responding to its physical and biochemical environments. Considerable effort has been made in the past years to understand how mechanical cues can affect nuclear structure and nuclear processes. However, less is known regarding how the activation of cellular pathways and nanoscale organisation of nuclear proteins can affect local and overall nuclear mechanics and mechanotransduction. A link between nuclear activity and the mechanical properties of the nucleus also becomes more evident as chromatin arises as a major contributor to cell stiffness. The work presented in this thesis employed a multidisciplinary approach to study nuclear architecture and function – from large-scale nuclear adaptation to external stimuli and signalling pathways, to the nanoscale organisation of nuclear activity. As this thesis was written in manuscript format – as a collection of peer-reviewed publications or pre-print manuscripts submitted to different journals - my work is shown alongside that of others. For this reason, throughout the thesis, I use ‘we’ instead of ‘I’ when describing findings. For clarification on my individual contributions, I have detailed the work I performed for each manuscript at the beginning of each results chapter.

In a first instance, this thesis describes how chromatin is a major contributor to the viscoelastic response of the nucleus to mechanical strains. An important outcome of the work shown here was the understanding that chromatin mechanics are not homogeneous throughout the organelle. The work led by Lherbette and myself proposes that chromatin crosslinking, possibly by regulatory DNA-binding proteins, is important in defining the material properties and the mechanical response of the nucleus (Lherbette et al., 2017). This suggests that nuclear activity can directly impact the mechanical state of the organelle. To test this, I then investigated how DNA damage and activation of DNA repair signalling pathways affects nuclear stiffness. My work shows that, following cisplatin treatment, ATM kinase-dependent large-scale chromatin decondensation causes nuclear softening (dos Santos et al., 2021). This further supports our hypothesis, showing a clear link between biochemical processes and mechanical changes to the organelle. Furthermore, it highlights the importance of proteins that modulate nuclear processes, such as DNA repair factors, transcription regulators and proteins that regulate chromatin architecture.

An example of a protein with important roles in transcription regulation and chromatin architecture is Myosin VI. This molecular motor is mostly known for cytoplasmic functions in cargo transport, endocytosis and cell adhesions. Interestingly, recent work has linked it to gene pairing events and RNA Polymerase II regulation. However, at the time of the work presented here, it was not yet clear how Myosin VI nuclear activation occurs or the molecular mechanism through which the protein performs its regulatory role in transcription. Here, we investigated how nuclear Myosin VI is activated and how this activity impacts RNA Polymerase II organisation and dynamics (Hari-Gupta et al., 2020). We defined a general activation model for Myosin VI, whereby interactions with binding partners, such as the nuclear dot protein 52 (NDP52) or Disabled-2 (Dab2) release the protein from its auto-inhibited state and allow its dimerization and motor processivity (dos Santos et al., 2020; Fili et al., 2017). This motor activity of Myosin VI is essential for RNA Polymerase II clustering at transcriptional sites. In particular, the work presented here proposes that molecular anchoring of nuclear Myosin VI on actin filaments could be essential for increased RNA Polymerase II binding times at transcription initiation sites, leading to higher transcription efficiency.

As in Fili *et al.*, we explored Myosin VI nuclear activity, we also uncovered novel nuclear roles for its binding partner NDP52 (Fili *et al.*, 2017). NDP52 has been previously described in a cytoplasmic context, where, through interactions with Myosin VI and other autophagy adapters, it participates in the recognition and clearance of pathogens and damaged organelles. However, although NDP52 was first identified in the nucleus and shares high homology with a transcription coactivator (the Coiled-coil coactivator, CoCoA), until the study presented in this thesis, no clear functions had been attributed to the protein. My work indicates that NDP52 is involved in RNA Polymerase II transcription, through two possible mechanisms: either through direct interactions with transcription machinery and co-regulators, or through direct/indirect changes to chromatin structure (dos Santos et al., 2022).

Overall, this thesis describes different aspects of nuclear architecture, from overall organelle structure to the spatial distribution of enzymatic nuclear activity.

1. Introduction - Nuclear mechanics and the spatial organisation of nuclear processes

The nucleus houses the genetic information necessary for the activity and survival of the cell, but the nucleus is more than just a compartment to house DNA. Although the nucleus is the largest and stiffest cellular organelle, it is also a highly dynamic organelle that can sense the external environment and rapidly adapt (Heo et al., 2018; Kirby and Lammerding, 2018; Maniotis et al., 1997). The nuclear envelope comprises a double membrane—the outer nuclear membrane and the inner nuclear membrane—associated with various distinct transmembrane proteins, such as nuclear pore complexes and LEM (Lap2, emerin, and Man1)-domain proteins (Yang et al., 2017). This is followed by an assembly of lamin filaments at the nuclear interior that provides structural stability to the organelle and tethers chromatin to the nuclear envelope. From the outside, the nucleus is linked to the cytoskeleton through the Linker of Nucleoskeleton and Cytoskeleton (LINC) complex, which also binds to the nuclear lamina (Crisp et al., 2005). This nuclear connectivity allows external signals to modulate nuclear functions, such as transcription (Alam et al., 2016; Mammoto et al., 2012) and DNA replication (Leno, 1992; Wang et al., 2018). Moreover, it may allow communication in the opposite direction (Figure 1).

Within the nucleus, DNA associates to histone cores to form nucleosomes, the building blocks of chromatin. Through epigenetic regulation, chromatin can be packaged into different conformations and higher-order structures, which determine the accessibility (Klemm et al., 2019) of DNA to replication (Bellush and Whitehouse, 2017; Hayashi and Masukata, 2011), transcription (Dong and Weng, 2013; Miyamoto et al., 2018), and repair machinery (Hauer and Gasser, 2017; House et al., 2014). In this way, chromatin conformation and epigenetic marks are important for the spatial organisation of enzymatic processes within the nucleus and their efficiency. Higher-order compact chromatin structures, known as heterochromatin, are largely inaccessible and are usually associated with genomic regions of low transcriptional activity at the nuclear periphery (Pickersgill et al., 2006; Saksouk et al., 2015; van Steensel and Belmont, 2017). Meanwhile, more open conformations of chromatin, also known as euchromatin, are easily accessible and represent areas of active gene expression (Solovei et al., 2016; Stevens et al., 2017).

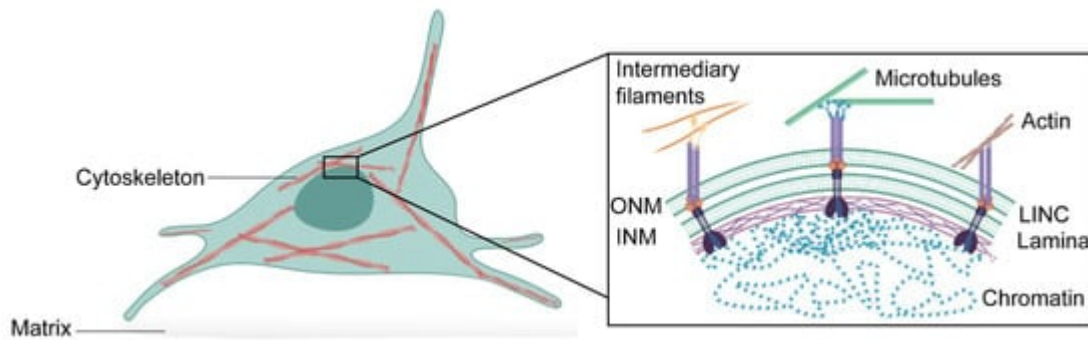


Figure 1 - Schematic representation of the interconnectivity between cytoskeleton, nuclear envelope and chromatin. The cytoskeleton is physically connected to the nuclear envelope consisting of the outer nuclear membrane (ONM) and the inner nuclear membrane (INM) through the LINC complex. The LINC complex is formed of trimers of SUN-domain proteins that bind different KASH-domain proteins at the nuclear membrane. LINC complexes can indirectly associate with intermediary filaments and microtubules through cyto-linker proteins or motor proteins, respectively, or directly interact with actin filaments. At the nuclear interior, the nuclear lamina tethers chromatin domains—lamina-associated domains—to the nuclear envelope. This allows effective mechanotransduction in the cell.

Variations to the biochemical components of the nucleus and their spatial organisation result in changes to the physical properties of the organelle and its morphology. The nuclear mechanical properties, comprising the viscoelastic behaviour and plasticity of the organelle, are tightly linked to cellular function and vary between cell stages and types (Pajerowski et al., 2007). Therefore, the physical properties of the nucleus and its mechanosensing capabilities largely influence the regulation of nuclear enzymatic processes.

There are four major contributors to nuclear shape and the mechanical properties of the nucleus: the magnitude of cytoskeletal forces exerted on the organelle, the composition and thickness of the nuclear lamina, the level of chromatin compaction within the nucleus, and the activity of proteins that modulate DNA structure (Figure 2).

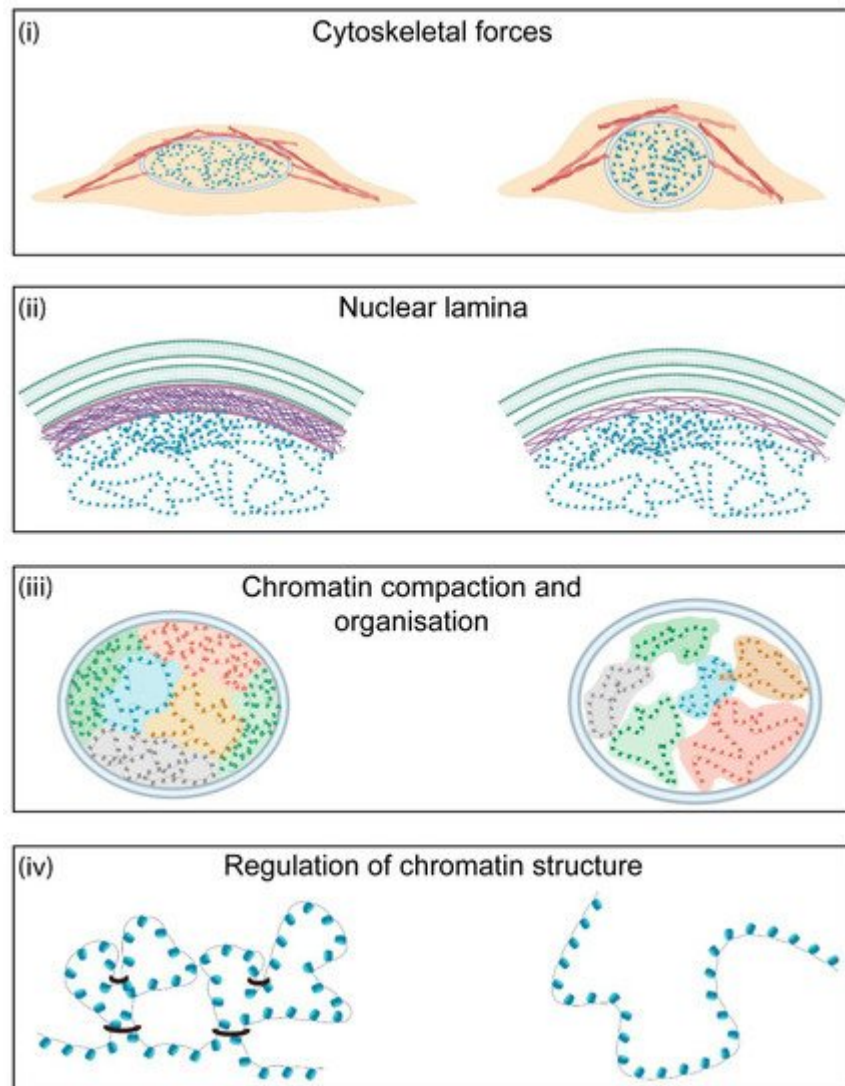


Figure 2 - Major contributors to nuclear morphology and mechanics. There are four major contributors to nuclear mechanics in the cell. (i) Cytoskeletal forces determine nuclear shape and morphology. Increased actin polymerisation leads to higher nuclear tension. (ii) The nuclear lamina is one of the major contributors to nuclear stiffness. This meshwork of intermediary filaments at the nuclear periphery is important for nuclear stability and chromatin organisation. Higher levels of lamin A/C or a thicker nuclear lamina lead to increased nuclear stiffness. (iii) Chromatin behaves as a crosslinked polymer gel. As a result, changes in chromatin organisation and levels of heterochromatin and euchromatin directly affect nuclear shape and mechanics. (iv) Regulation of chromatin architecture is dependent on the activity of several factors, such as cohesins, that allow crosslinking of chromatin and the formation of higher-order structures. The activity of these proteins can affect local and global chromatin conformation and, hence, is important for nuclear mechanics.

Altered nuclear morphology and mechanics are usually accompanied by changes in gene expression, sensitivity to DNA damage and cell function (Brandt et al., 2006; Dahl et al., 2008; Nader et al., 2021; Wang et al., 2016; Webster et al., 2009). Changes in the shape and size of the nucleus have been reported for different diseases, and in some

cases, this can also be used to help diagnosis. For example, abnormally shaped nuclei can be found in cardiomyopathies, progeria and in cancer. In particular, nuclei of cervical cancer cells present herniations or blebbing, and this constitutes part of the Pap smear test diagnosis (Papanicolaou and Traut, 1941); in breast cancer, nuclear pleomorphisms (altered nuclear morphology) are used for tumour grading and this correlates with patient outcome (Dunne and Going, 2001). It is therefore essential to understand how these changes in nuclear morphology arise, how they reflect altered mechanical properties of the nucleus and how this affects overall cellular function, mechanosensing and force transduction.

This work discusses how structural components of the nucleus contribute to the physical properties of the organelle, paying special attention to the newly emerging data on the importance of chromatin architecture and dynamics to nuclear morphology and stability. We also discuss how nuclear processes such as DNA repair and transcriptional activity might be interlinked with chromatin organisation and nuclear mechanics. In particular, we highlight the importance of proteins that regulate the nanoscale organisation of enzymatic processes in the nucleus and their potential impact on the mechanical environment of the nucleus.

1.1. Contributing Factors to Nuclear Mechanics

1.1.1. Cytoskeletal Forces in Nuclear Mechanics

Mechanotransduction refers to the process by which cells respond to external mechanical cues through the activation of biochemical pathways, changes in structure, and activation or repression of specific genes. This is a key mechanism for sensing and adapting to the extracellular microenvironment. The nucleus is the largest and the most mechanically prominent organelle in the cell, and so it would be expected to play a dominant role in cellular mechanics. It is, therefore, not surprising that it has been receiving increasing attention in the field of cell mechanics over the last decade.

Extracellular forces propagate into the nucleus through the LINC complex, located on the nuclear envelope. The LINC complex physically connects the nucleus to the cytoskeleton and, therefore, to cellular adhesions that can sense the mechanical microenvironment. Disruption of the LINC complex results in defective force transduction from the cytoplasm to the nucleus and is shown to disrupt the expression of mechanosensitive genes (Banerjee et al., 2014; Lombardi et al., 2011). This occurs, at least in part, because cytoskeletal forces can directly affect the localisation and nuclear

import of mechanosensitive transcription regulators. One functional example is the Yes-associated protein (YAP) and its transcriptional coactivator with PDZ-binding motif (TAZ). The mechanical regulation of YAP/TAZ requires cytoskeletal integrity and a functional LINC complex (Elosegui-Artola *et al.*, 2017). As a result, translocation of YAP/TAZ to the nucleus and consequent activation of YAP-dependent genes varies according to extracellular matrix rigidity (Calvo *et al.*, 2013; Chaudhuri *et al.*, 2016), cytoskeletal formation (Das *et al.*, 2016), LINC complex integrity (Driscoll *et al.*, 2015), and nuclear stiffness (Elosegui-Artola *et al.*, 2017; Koushki *et al.*, 2020).

Cytoskeletal forces also contribute to the regulation of nuclear movement, shape, orientation and morphology. In extreme cases, the accumulation of aberrant actin fibres around the nucleus can induce actin-dependent nuclear deformation through increased nuclear tension and lead to blebbing, herniation and even rupture of the nuclear envelope (Wesolowska *et al.*, 2020). Equally, chemical or genetic perturbation of the cytoskeleton results in deficient force transmission to the nucleus.

The tissue microenvironment is an important factor in cytoskeletal formation and structure, and hence it is a key determinant of the mechanical forces transmitted to the nucleus. The discovery of focal adhesions – multiprotein complexes that enable mechanical transduction from the outside of the cell to the inside - in the 1970s started shedding light on how the extracellular matrix impacts cellular functions (Abercrombie *et al.*, 1971; Curtis, 1964; Izzard and Lochner, 1976). We now know that the actomyosin cytoskeleton is attached to focal adhesions and, therefore, also in contact with the extracellular environment (Chen *et al.*, 1997; Wang *et al.*, 1993). This allows the cell to sense substrate rigidity and respond accordingly. One consequence of stiffer extracellular matrix microenvironments is the strengthening of cytoskeletal links to focal adhesions (Choquet *et al.*, 1997). The cytoskeletal response to biophysical cues of the extracellular environment has been shown to impact cell migration (Hynes and Lander, 1992; Lauffenburger and Horwitz, 1996; Mitchison and Cramer, 1996) cellular differentiation (Flaim *et al.*, 2005; Smith *et al.*, 2018b), as well as cell cycle and division (Théry *et al.*, 2005). As the nucleus is interconnected to the cytoskeleton, the mechanical environment of the cell is rapidly transmitted to the nucleus. This is particularly important when studying cancer biology and therapeutic approaches to disease. We are beginning to have insight into the mechanical consequences of different microenvironments and how they affect nuclear processes such as DNA repair, transcription and chromatin regulation.

However, studying the effects of cytoskeletal forces on nuclear processes comes with specific challenges. Many studies use drugs to disrupt cytoskeletal forces (Doss Bryant et al., 2020; Liu et al., 2010b; Rotsch and Radmacher, 2000; Streppa et al., 2018; Weihs et al., 2007; Würtemberger et al., 2020), and it is unclear how these may directly affect nuclear events, such as transcription or chromatin organisation. In the work presented in this thesis, for example, Latrunculin B is shown not only to disrupt cytoskeletal formation, through inhibition of actin polymerisation, but also nuclear actin and myosin functions, directly affecting transcription levels and the spatial organisation of RNA Polymerase II (RNAPII) (Hari-Gupta *et al.*, 2020). Methods such as micropatterning (Bautista et al., 2019; Théry, 2010) or the use of gels as substrates for cells (Charrier et al., 2018; Rehfeldt et al., 2012b; Vertelov et al., 2016) are becoming increasingly common to change the stresses exerted upon the cytoskeleton. Although these do not allow complete disruption of the cytoskeleton, they can mimic different tissue microenvironments and permit the fine-tuning of cytoskeletal forces. The data are both easier to interpret and, in some cases, can be a good alternative to chemical disruption of the cytoskeleton.

Accumulating evidence shows that actomyosin contractility around the nucleus has not only important repercussions to the deformability of the organelle, and therefore to cell migration and nuclear integrity, but it can also directly affect lamina structure and chromatin organisation. For example, using micropatterned substrates, Makhija and colleagues observed that cells lacking long stress fibres had reduced levels of lamin A/C expression, resulting in softer, more deformable nuclei. Interestingly, these cells also displayed increased chromatin and telomere dynamics, suggesting a direct relationship between geometric cell constraints and genome organisation (Makhija et al., 2016). Similarly, in rod photoreceptor cells, actomyosin deformation of the nucleus results in chromocenter clustering (condensed centromere heterochromatin regions) and inverted chromatin architecture, with euchromatin regions being redistributed to the nuclear periphery (Seirin-Lee et al., 2019).

Although the molecular mechanisms that link cytoskeletal forces to chromatin regulation are still largely unexplored, spatial redistribution and misregulation of nuclear transport of transcription factors and chromatin regulators, such as transcription coactivator MKL1 (Hu et al., 2019) or histone deacetylase HDAC3 (Jain et al., 2013), have been observed and could account, at least in part, for chromatin architectural changes.

A challenge often encountered in the study of nuclear mechanics—especially when performing measurements on adhered cells—is the masking effect that the stiff

cytoskeletal fibres around the nucleus have on measurements. Indeed, small changes in nuclear mechanics can be imperceptible if measured under a fully-formed cytoskeleton. Because of this, many studies resort to the use of isolated nuclei, removing the cytoskeletal impact entirely (Dahl et al., 2005; Guilluy et al., 2014; Herráez-Aguilar et al., 2020; Newberg et al., 2020; Rowat et al., 2006). This has proven useful when comparing nuclei across different cell types, as shown in this thesis (Lherbette *et al.*, 2017), or to study how the expression of nuclear envelope components affects nuclear stiffness (Ferrera et al., 2014), or how the nucleus itself—and independently of cytosolic intervention—adapts and responds to external forces (Guilluy *et al.*, 2014). The clear trade-off is the loss of physiological environment and understanding how nuclei in live-cells respond to matrix stiffness, drug treatments, radiation or other challenges. The work here described attempts to overcome these limitations, through the use of atomic force microscopy (AFM), in live cells, but at initially adhered stages. In this case, cells are allowed sufficient time to attach to their surface but, with their cytoskeleton not yet fully formed, as shown through actin staining, the nucleus occupies most of the cell volume and is the most important contributor to cell mechanics (dos Santos *et al.*, 2021). This has allowed the detection of mechanical changes that would have otherwise not been observed (dos Santos *et al.*, 2021).

Overall, there is a complex interplay of interactions between the nucleus and cytoskeletal components that contribute to the mechanics of the organelle, and much work is needed to understand how changes in cytoskeletal forces directly affect nuclear organisation and nuclear processes.

1.1.2. The Nuclear Lamina

The nuclear lamina is located between the INM and the chromatin. This is a dense, complex meshwork of proteins with a thickness up to 100 nm. It provides major structural support to the nucleus as well as support for a variety of nuclear functions, such as transcription, replication, DNA repair, and genome organisation. Lamina proteins fall into two separate classes, A-type and B type—lamin A and C, which are splice-isoforms of the LMNA gene—belong to the former and lamin B1 and B2, encoded by LMNB1 and LMNB2, respectively, belong to the latter (Dittmer and Misteli, 2011).

Lamins belong to a class of proteins called intermediate filaments, which contain rod domains that are critical to the formation of the meshwork (Aebi et al., 1986). Post-translational modifications of lamin proteins allow the regulation of this peripheral meshwork. One important post-translational modification is the farnesylation of both

lamin A and B at their C-terminal domains, which is thought to be important for the localisation and retention of these proteins at the nuclear envelope. Whilst lamin B is permanently farnesylated, lamin A is further processed by proteolytic cleavage, which includes removal of this group (Adam et al., 2013; Dittmer and Misteli, 2011; Sinensky et al., 1994).

Whilst B-type lamins are expressed throughout development and in all nucleated cells, the levels of type-A lamins are reduced or not present at early embryonic stages. Expression of lamin A onset is highly varied in different tissues during development and, in some cases, such as for stem cells or cells of the hemopoietic system, lamin A is never expressed (Rober et al., 1990).

The nuclear lamina is crucial for maintaining nuclear envelope integrity. Depletion or mutation of lamin components leads to severe nuclear instability, morphological defects in the nucleus and gives rise to disease, as in the case of laminopathies. For instance, in mice, loss of either lamin B1 or B2 leads to neuronal defects and perinatal death (Chen et al., 2019; Coffinier et al., 2011). Similarly, in humans, mutations in lamin A are associated with premature ageing and muscular malfunction, as observed in Hutchinson–Gilford progeria, muscular dystrophy, and cardiomyopathies (Schreiber and Kennedy, 2013).

The morphological defects observed in the nucleus of cells with lamina defects are also indicative of the important role of these proteins in nuclear mechanics. This is not surprising, as expression levels of lamin proteins, but in particular of lamin A/C, scale with nuclear stiffness. Depletion of lamin A/C makes the nucleus softer and more deformable, whilst expression of a shorter and permanently farnesylated mutant version, progerin, confers higher stiffness to the nucleus. In both cases, the expression of mechano-responsive genes is severely disrupted (Lammerding et al., 2004; Pajerowski *et al.*, 2007). Importantly, in these cells, nuclear processes such as chromatin structure regulation, DNA replication, DNA repair and gene expression are also invariably misregulated.

The nuclear envelope is not mechanically isolated. Instead, it is physically connected to the cytoskeleton on one side, through the LINC complex, and to the chromatin, through lamina-associated domains (LADs) on the other. This means that mechanical changes to one of these components will have large structural implications for the others. For example, Swift et al. described how matrix and cytoskeletal stiffness could directly influence lamin A expression and turnover (Swift et al., 2013). In stiffer matrices, phosphorylation of lamin A, which promotes disassembly, is reduced, and this increases

total amounts of lamin A at the nuclear envelope, which in turn increases nuclear stiffness (Buxboim et al., 2014; Swift *et al.*, 2013). Similarly, progerin-expressing cells, such as those from Hutchinson–Gilford progeria patients, display increased Filamentous-actin (F-actin) polymerisation and cytoskeletal stiffness, as well as reduced levels of heterochromatin (Mu et al., 2020). In these cells, destabilisation of microtubules to reduce cytoskeletal tension may be a promising therapeutic approach. It has been shown to restore nuclear morphology and alleviate premature ageing in progeria in mice (Larrieu et al., 2014). Conversely, a separate study also described how inhibition of histone demethylation, which directly leads to increased heterochromatin levels, also rescues morphological defects in progerin-expressing cells (Stephens et al., 2018).

Chromatin function is highly dependent on its conformation. This includes correct tethering to LADs at the nuclear periphery. Loss of lamin A function, for example, leads to higher chromatin dynamics and more diffuse genomic loci, representative of higher levels of decondensed chromatin. Complete lamin loss results in detachment of LADs and disruption of global 3D chromatin-chromatin interactions (Zheng et al., 2018). Similarly, lamin B1 also has an important role in maintaining chromatin structure and distribution, especially at the nuclear periphery (Chang et al., 2020). As a result, lamin regulation and chromatin structure are tightly linked as key components of nuclear mechanics. Future insights into how changes to nuclear envelope components affect the mechanical properties of the nucleus will be especially important in the study of ageing and cancer, where a defective lamina is often found (Bell and Lammerding, 2016; Cenni et al., 2020; Martins et al., 2020; Robin and Magdinier, 2016; Scaffidi and Misteli, 2006; Smith et al., 2018a). As nuclear integrity and nuclear mechanics are closely related (*i.e.*, nuclear envelope rupture becomes more likely if the mechanical properties of the nucleus are compromised) (Agrawal and Lele, 2019; Xie et al., 2020), mutation or organisation defects on structural components of the nucleus is a major driver of genomic instability (Lim et al., 2016; Shah et al., 2017). In addition to lamin proteins, other NE components, such as emerin, which is not discussed here in detail, might also contribute to the overall organisation of the NE and to nuclear mechanics (Fernandez et al., 2022; Liddane and Holaska, 2021).

1.1.3. Chromatin is a key component of nuclear mechanics

Chromatin organisation is highly regulated through epigenetic histone modifications that determine local and global levels of DNA compaction (Bannister and Kouzarides, 2011). The degree of chromatin condensation and the nuclear content of hetero *versus* euchromatin affects not only nuclear size and morphology but also determines DNA

accessibility to transcription machinery and all forms of DNA processing (Jovtchev *et al.*, 2006; Klemm *et al.*, 2019). In conventional nuclei, the highly compacted heterochromatin is spatially segregated from active, decondensed euchromatin, with the former usually occupying regions in the nuclear periphery and the latter in the nuclear core. Developments in genome-wide chromosome conformation capture (Hi-C) have shown that in addition to LAD formation, chromatin can also associate with itself to form sub-compartments called topologically associated domains (TADs) (Dixon *et al.*, 2012; Nora *et al.*, 2012).

We now know that chromatin is also a major contributor to nuclear stiffness and morphology. Historically, research has focused on the more clear-cut structural contributions of lamins, in particular, lamin A. Early experiments using micropipetting showed that the lamina dominates the mechanics of swollen nuclei, whilst chromatin is the main contributor to the mechanics of shrunken nuclei. Although this suggested two different types of mechanical contribution in the nucleus, chromatin is often regarded as a minor viscous component that flows upon applied force (Dahl *et al.*, 2005; Mazumder *et al.*, 2008; Pajeroski *et al.*, 2007). This view of chromatin as a secondary mechanical component, less important than the lamina, has started to change, and some recent studies have now shed light on how chromatin architecture can affect nuclear stiffness. A recent report by Strickfaden *et al.* highlights this by showing that self-associated condensed chromatin behaves as a solid or elastic gel instead of a liquid. This indicates that the intrinsic mechanical properties of chromatin have an impact on overall nuclear mechanics and its response to external force stimuli (Strickfaden *et al.*, 2020).

In line with this, experiments by Chalut *et al.*, using an optical stretching technique, show how nuclear deformability is directly related to the degree of chromatin condensation (Chalut *et al.*, 2012). Furthermore, experiments using MNase, for chromatin digestion also show that its structure determines nuclear morphology and governs nuclear responses to short-extension strains (<30%) (Stephens *et al.*, 2017). We now know that changes in nuclear mechanics and shape, including the occurrence of nuclear blebbing, can occur independently of lamina perturbation due to changes in the levels in euchromatin and heterochromatin. Overexpression of nucleosome binding protein HMG5 leads to chromatin decondensation, increased nuclear area, morphological aberrations to the nuclear envelope and nuclear softening. In mice, this leads to premature death as a result of cardiac defects (Furusawa *et al.*, 2015). Similarly, treatment with deacetylase inhibitor trichostatin A, which alters histone modifications and leads to chromatin decondensation, also results in nuclear softening and blebbing (dos Santos *et al.*, 2021; Shimamoto *et al.*, 2017; Stephens *et al.*, 2018).

Trying to resolve individual mechanical contributions from the lamina and chromatin is a major challenge for the field of nuclear mechanics. Their physical linkage means that force measurements provide a composite value for the contribution of both components. New methodologies in force measurements could prove particularly useful. For instance, a combined AFM-side-view light-sheet fluorescence microscope developed by Nelsen et al. allowed the 3D (x/z cross-section) visualisation of live-cells whilst performing force measurements with high spatio-temporal resolution (Nelsen et al., 2020). In fact, Hobson et al. recently used this approach to propose a two-regime nucleus, where lamina and chromatin respond differently to volume deformation and nuclear-area stretching (Hobson et al., 2020). Using 3D fluorescent imaging of the nucleus combined with mechanical measurements could be a powerful tool not only to probe the mechanical behaviour of different nuclear components but also to look at force transduction from the cytoskeleton, or how nuclear processes, such as transcription and DNA repair, affect cell mechanics. For example, this correlative approach could enable visualisation, in live-cells, of the structural response of NE components to load; how the spatial organisation of NE proteins affects local and global nuclear mechanics; or allow activation and studying of signalling events as a response to mechanical stress (e.g., recruitment of proteins such as ATM kinase, 53BP1 to sites of damage or translocation of YAP/TAZ. transcription factors).

Whilst mechanical differences between the lamina and chromatin are readily intuitive, differences within the chromatin itself at the nuclear interior are less so. Chromatin architecture is not homogeneous; its organisation is highly regulated, with different domains occupying different regions. This means that the nuclear interior is mechanically non-uniform. In the work presented here, we were able to detect mechanical variations within the nucleus, representative of a largely inhomogeneous chromatin interior. Two different mechanical regions within the nucleus could be observed, independently of the nuclear lamina — a more viscous periphery and a stiffer and predominantly elastic nuclear core (Lherbette *et al.*, 2017). A new methodology that allows a more in-depth study of chromatin environments could be important to understand how changes to chromatin organisation influence the mechanical behaviour of the nucleus.

1.2. Regulation of Chromatin structure

To understand the role of chromatin in nuclear mechanics, it is important to understand how chromatin is regulated in the nucleus. Nucleosomes, histone octamers (composed of H2A, H2B, H3 and H4 histones) wrapped in 147bp of DNA, are distributed throughout the genome, including at the promoter and enhancer regions of genes (Kornberg, 1977; Richmond and Davey, 2003; Segal et al., 2006). Nucleosome occupancy is highly variable and dynamic across the genome, creating a range of levels of chromatin accessibility: from closed high-order heterochromatin structures, to permissive chromatin or to highly dynamic and accessible DNA conformations (Figure 3) (Mieczkowski et al., 2016). Closed chromatin structures are usually associated with repressive states, whilst permissive chromatin is sufficiently accessible to binding of proteins, such as transcription factors, to target DNA-sequences (Figure 3), but it requires further modifications by chromatin remodellers, before processes such as transcription can occur (Klemm *et al.*, 2019; Tsompana and Buck, 2014).

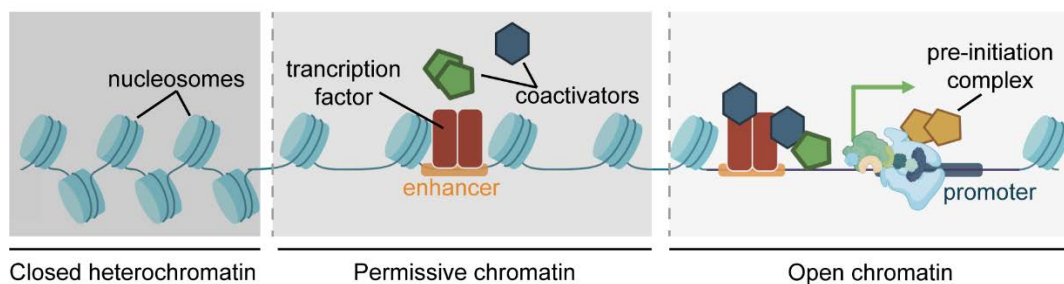


Figure 3 – Chromatin accessibility for transcription. In the nucleus, chromatin can adopt a range of conformations – from closed and tightly packed chromatin to more permissive conformations or open and highly dynamic chromatin. Transcription factors can bind to permissive chromatin states and, through the recruitment of coactivators with chromatin remodelling activity, alter chromatin conformation to more open states that permit transcription to occur.

Many different types of enzymes participate in chromatin organisation – the most prominent being DNA methyltransferases; covalent histone modifiers and ATP-dependent chromatin remodellers.

1.2.1. Epigenetic Modifications of Chromatin

DNA methyltransferases directly modify DNA to recruit gene repressors or inhibit binding of transcription factors (Moore et al., 2013). DNA methylation marks are much more stable than post-translational modifications of histones, and provide cell to daughter-cell gene silencing (Klose and Bird, 2006). Therefore, this process is more common in the regulation of lineage-specific genes that help shape organism development (Klose and Bird, 2006). On the other hand, histone modifications provide a versatile and dynamic mechanism for the regulation of nuclear processes, such as gene expression. In addition, they also act as recognisable marks for the recruitment of enzymes and co-factors to chromatin, to regulate such processes. Histone acetyltransferases and methyltransferases are the most well-studied histone modifiers, but many other covalent modifications have been described (e.g. ubiquitylation, sumoylation, citrullination, phosphorylation) (Bannister and Kouzarides, 2011).

Histone acetylation is commonly associated with open states of chromatin and active regions of transcription. During transcription, histone acetyltransferases (HATs), such as p300/CBP, are commonly recruited to regulatory elements coactivators of transcription (Bowers et al., 2010; Kim et al., 2006). They enable the addition of an acetyl group to a histone tail, which reduces the positive charge of the lysine residue where this modification occurs. This, in turn, weakens the interaction between nucleosomes and DNA resulting in more accessible chromatin (Bannister and Kouzarides, 2011). Conversely, Histone Deacetylases (HDACs) have the opposite function through their ability to remove acetyl groups from lysine residues, and often act as transcription repressors (Seto and Yoshida, 2014). Histone acetylation can occur on all core histones; however, H3K9ac and H3K27ac are the most commonly used marks to assess gene expression levels in cells – high levels of these marks being indicative of high transcriptional activity (Calo and Wysocka, 2013; Creyghton et al., 2010).

Histone lysine methyltransferases (KMTs) and demethylases (KMDs) are another group of histone-modifying enzymes. There are three lysine methylation states – mono-, di- and tri- (me, me₂ and me₃, respectively). Unlike other types of histone modifications, which generally represent either repressed or active chromatin, for histone methylation this is highly dependent on the position and number of methyl groups attached (Black et al., 2012). Generally, H3K9 and H3K27 methylation is largely related to heterochromatin structure and repressive transcription states, whilst H3K4 and H3K36 methylation usually occurs at active genes. Transcription factors and coactivators are known to recruit H3K4 methyltransferases, to target genes (Narayanan et al., 2007; Tang et al.,

2013; Yokoyama et al., 2004). Enhancers are usually found with H3K4me marks, whilst active promoters are enriched for H3K4me₃, and H3K4me₂ can be found at the 5' end of transcribing genes (Heintzman et al., 2007; Kim and Buratowski, 2009; Santos-Rosa et al., 2002).

Epigenetic changes are not uniquely linked to transcription regulation. For example, histone modifications have a major role in the DNA Damage Response (DDR). Following double-strand break (DSB) detection, caused by the ionising radiation or exposure to cytotoxic agents, histones H2AX in the vicinity of the lesion (2Mbp region adjacent to the break) are phosphorylated at Ser 139 (γ H2AX). Phosphorylation of H2AX occurs through the activity of phosphatidylinositol-3-kinase (PIKK) family members, which includes the ataxia telangiectasia mutated (ATM) kinase, DNA-PKcs and ATM- and RAD3-related (ATR) kinase (Burma et al., 2001; Fernandez-Capetillo et al., 2002; Lees-Miller et al., 1992). The γ H2AX epigenetic mark helps the creation of repair centres, known as repair foci, which act as signalling hubs for the rapid recruitment and accumulation of repair factors. Moreover, through the recruitment of additional factors to these regions, local chromatin conformation is known to change as a result of γ H2AX formation (Paull et al., 2000; Sedelnikova et al., 2003).

1.2.2. Changes in chromatin structure through ATP-dependent chromatin remodellers

Although covalent modifications on histones can be sufficient to induce small changes in chromatin conformation (*e.g.*, histone acetylation loosening of nucleosomal DNA), they often act in concert with additional DNA-binding proteins that are capable of recognising the histone code to cause larger-scale changes in chromatin architecture. These include ATP-dependent chromatin remodellers; heterochromatin modulators, such as Heterochromatin Protein 1 (HP1); NE tethering proteins that allow chromatin domains to form at the nuclear periphery; cohesins; and general transcription factors and coactivators (Lauberth et al., 2013; Vermeulen et al., 2007). These interactions are crucial for the global organisation of chromatin in the nucleus, as they can determine chromosome positioning, gene expression activity, repair efficiency and cell cycle progression.

Chromatin remodellers with ATPase activity, range from single small subunits, such as CHD1, to large multi-protein complexes (*e.g.* INO80 and SWI/SNF complexes) (Clapier and Cairns, 2009). These complexes can utilise the energy released by ATP hydrolysis to remodel nucleosome structure and change chromatin accessibility. Their activity includes exchanging canonical core histones (for example, the substitution of H2A/H2B

dimers for H2AZ/H2B at promoters) (Eberharter and Becker, 2004; Luk et al., 2010), nucleosome sliding (Willhoft et al., 2017) nucleosome eviction (Dechassa et al., 2010) and intra-chromatin folding to bring together regulatory elements of the same gene (Stadhouders et al., 2018). In the regulation of transcription, one of the main functions of ATP-dependent chromatin remodellers is nucleosome rearrangement at promoters. This is essential for transcription to occur, as regions of low nucleosome density are necessary to allow binding of transcription initiation factors (Imbalzano et al., 1994) and the activity of ATP-dependent chromatin remodellers is required for nucleosome eviction to enable the progression of elongating RNAPII through the gene body (Brown and Kingston, 1997; Schwabish and Struhl, 2007). Similarly, chromatin accessibility changes caused by remodelling complexes such as SWI/SNF and INO80 occur following DNA damage. This allows binding of repair factors and is important for repair efficiency (Bennett and Peterson, 2015; Cairns, 2004; Lans et al., 2012; Osley et al., 2007).

1.2.3. Chromatin Crosslinking

The highly targeted activity of different chromatin modulators means that chromatin conformation and mobility are irregular throughout the nucleus. Furthermore, many of these proteins alter the levels of chromatin crosslinking and, therefore, their interactions with DNA largely determine the levels of chromatin crosslinking. For example, lamins allow crosslinking of the chromatin to the nuclear periphery through interactions between heterochromatin and lamina-associated proteins and this is important in the regulation of global chromatin structure (Naetar et al., 2017; Ranade et al., 2019). Using liquid chromatin Hi-C, Belaghzal and colleagues recently showed that chromatin loci dynamics and association are largely determined by chromatin-associated factors, such as cohesins and lamins (Belaghzal et al., 2021). The authors found that chromatin behaves as a crosslinked polymer gel that, even upon digestion (within 10–25 kb), maintains its structural and mechanical connections. Furthermore, chromatin digestion at this scale did not affect nuclear stiffness, measured by micropipetting. Interestingly, after extensive chromatin digestion (<6 kb), loss of chromosome compartmentalisation was achieved, together with loss of chromatin-associated cohesins, which resulted in a 75% decrease in nuclear stiffness (Belaghzal *et al.*, 2021). This indicates that compartmental segregation of chromosomes and nuclear mechanics are highly dependent on the crosslinking capabilities of proteins that modulate DNA structure.

Cohesins are highly conserved protein complexes that can loop chromatin through their ring domain to create bundles that restrict chromatin movement (Ashwin et al., 2020; Nozaki et al., 2017). Together with the chromatin insulator CTCF, cohesin function is the

driver behind TAD formation and hence crucial for chromatin 3D organisation (Vietri Rudan and Hadjur, 2015; Wendt et al., 2008). CTCF/cohesin anchoring of chromatin has been shown to be important at different genomic length-scales, allowing the formation of long-range TAD compartments (megabase-sized), as well as intermediate (100 kb–1 Mb) and small-range (<100 kb) sub-compartments (Phillips-Cremins et al., 2013; Sofueva et al., 2013). Heterochromatin protein 1 (HP1) is another protein that is known for its role in chromatin organisation. HP1 binds to H3K9me3-rich areas, which represent constitutive heterochromatin regions (Bannister and Kouzarides, 2011), and is capable of bridging nucleosomes (Canzio et al., 2011). This crosslinking effect of HP1 is thought to stabilise compacted chromatin states and to be essential in heterochromatin phase separation (Larson et al., 2017; Strom et al., 2017) through the formation of membrane-less condensates. A recent report by Strom et al. also showed that HP1 chromatin crosslinking capabilities are important for nuclear shape maintenance, and its degradation leads to decreased chromatin stiffness and nuclear rigidity (Strom et al., 2020).

Chromatin crosslinking also occurs at active chromatin regions. For example, the transcriptional coactivator BRD4 can create condensates at active super-enhancer regions (Sabari et al., 2018). Similarly, during transcription, RNAPII forms large molecular clusters with transcription factors, as it will be discussed later in more detail. These networks have not only been associated with phase separation events but also with the formation of transient chromatin bridges (Cisse et al., 2013). Interestingly, whilst active chromatin regions are usually associated with open and dynamic conformations, recent reports challenge this view by showing that the bridging effect of RNAPII and associated transcription machinery can, in fact, increase chromatin constraints, reduce chromatin mobility and possibly alter local stiffness (Ashwin *et al.*, 2020; Nagashima et al., 2019).

As chromatin becomes more prominent in the field of nuclear mechanics, it becomes obvious that processes and proteins that regulate DNA structure and conformation have a large impact on the mechanical properties of the nucleus. Chromatin landscape is tightly regulated throughout the cell cycle and can undergo global changes, depending on the transcriptional activity of cells. In fact, in order for RNA Polymerase II (RNAPII) to perform its function in gene expression, the activity of several chromatin modulators is necessary. However, how this may affect nuclear mechanics, both locally and globally, is not yet clear. Furthermore, DNA damage, occurring either through ionising radiation or genotoxic agents, such as chemotherapy drugs, can result in global relaxation of the chromatin and mechanical softening of the nuclear envelope (dos Santos *et al.*, 2021).

Our knowledge of how these processes affect nuclear mechanics is still limited but may be of crucial importance.

1.3. The Relationship between Nuclear Mechanics and Nuclear Processes

1.3.1. DNA damage

Having described the contributing factors to nuclear mechanics, we will now exemplify how this can impact cellular processes using DNA damage. DNA damage events continuously occur throughout the life cycle of a cell. Following DNA damage, the cell activates the DDR to ensure appropriate repair of lesions and their survival. Failure of these mechanisms leads to apoptosis or drives genomic instability leading to diseases such as cancer (Jackson and Bartek, 2009). Both DNA damage and the DDR lead to large nuclear reorganisation and to activation of different biochemical pathways that may result in changes to the mechanical properties of the nucleus.

DNA damage can arise endogenously as a result of replication errors (Loeb and Monnat, 2008; Viguera et al., 2001), topoisomerase activity (Deweese and Osheroff, 2009) or reactive oxygen species (ROS) (Cadet and Wagner, 2013). Conversely, external insults to the cell, such as ionising radiation or chemotherapy drugs, also cause significant DNA damage and genomic instability. Types of damage range from base-mismatches, adducts and crosslinks introduced into the DNA helix, single-strand DNA breaks or, the more deleterious and toxic, double-strand breaks (DSBs). In order to allow efficient repair and prevent the propagation of mutations to daughter cells, once a lesion is detected, DDR is activated, cell cycle progression is halted, and transcriptional activity becomes markedly reduced (d'Adda di Fagagna, 2008). This is accompanied by changes to the 3D organisation of chromatin (Mehta et al., 2013).

Two key DDR components in mammalian cells are the Ataxia Telangiectasia-mutated (ATM) and the ATM Rad3-related protein (ATR) kinases. These early responders are recruited to sites of damage to initiate DNA damage checkpoints and are responsible for the phosphorylation of additional DNA repair factors that recruit and regulate repair machinery (Maréchal and Zou, 2013).

DNA damage and repair are not independent of the chromatin architecture. Two very early studies highlighted this relationship by showing that more accessible, open structures of chromatin are more susceptible to nuclease digestion (Cleaver, 1977;

Smerdon and Lieberman, 1978). We now know that local chromatin dynamics change following DNA damage and how this may be important for DDR (Adam et al., 2015). For example, Hauer et al. describe how induction of a single DSB in yeast increases damaged chromatin flexibility and motility as a result of chromatin decondensation and histone eviction (Hauer and Gasser, 2017). This was dependent on the activity of ATP-dependent chromatin remodelling complex INO80. Similarly, work in both yeast and mammalian cells show the recruitment of different remodelling complexes, such as SWI/SNF family members, and changes to overall chromatin structure during DDR (Kruhlak et al., 2006; Lou et al., 2019; Lu et al., 2019; Murga et al., 2007; Strickfaden et al., 2016; Ziv et al., 2006). Chromatin relaxation is now considered to be an important part of DDR that improves repair efficiency.

The chromatin context and nuclear positioning of the DNA lesion are also crucial determinants for DDR pathway selection (Clouaire et al., 2018; Kalousi and Soutoglou, 2016; Scully et al., 2019). Lesions occurring in active transcription regions of euchromatin, associated with histone mark H3K36me3, are preferentially repaired by the error-free Homologous Recombination (HR) (Aymard et al., 2014; Pfister et al., 2014). For these regions, the major determinant in pathway selection appears to be chromatin accessibility and not transcriptional activity (Jha and Strahl, 2014; Lemaître et al., 2014; Pai et al., 2014). Paradoxically, DNA breaks in heterochromatin, which packages inactive transcription sites, can also preferentially undergo HR (Alagoz et al., 2015; Baldeyron et al., 2011; Lee et al., 2013; Sun et al., 2009). However, for this to occur, DNA lesions need to be relocated to more permissive environments. Chiolo et al. described that, in *Drosophila*, following a DSB, the heterochromatin domain where the break occurs expands, and the lesion is relocated to the periphery or to the exterior of this domain (Chiolo et al., 2011). This movement of DNA lesions to euchromatin regions allows access to repair machinery and enables HR (Chiolo *et al.*, 2011; Ryu et al., 2015). Similar dynamics of double-strand breaks have also been observed in yeast (Horigome et al., 2014; Khadaroo et al., 2009; Oza et al., 2009). However, this is not always the case, and there is a large variability between the repair of lesions in different heterochromatin environments. For DNA breaks at LADs, HR is restricted, and error-prone DNA repair pathway non-homologous end-joining (NHEJ) is favoured instead. In this case, lesions do not migrate to euchromatin regions (Lemaître *et al.*, 2014). Similarly, differences between repair in centromeric and pericentric heterochromatin have also been reported, suggesting other factors might also influence repair strategies (Tsouroula et al., 2016). Although chromatin relaxation and reorganisation following DNA damage has been well documented, very little is known about how this impacts

nuclear structure and mechanics. The work presented here tries to shed light on this question, using AFM to probe the mechanical properties of the nucleus in cisplatin-treated cells. My work shows that DNA damage leads to significant softening of the nucleus, and this was the direct result of global chromatin decondensation (dos Santos *et al.*, 2021). Reduction in nuclear stiffness appears to correlate with the levels of damage and to be ATM-dependent, suggesting that DDR activation is necessary. In line with previous work (Hauer and Gasser, 2017; Hauer *et al.*, 2017), the chromatin decondensation observed leads to higher molecular dynamics in the nucleus, which could, in turn, lead to higher accessibility of repair factors and improve repair efficiency (Figure 4). Following detection of DNA damage, lesion repair often relies on the recruitment and clustering of bulky repair complexes (Hashiguchi *et al.*, 2007; Meister *et al.*, 2003). Furthermore, following DNA damage long chromosome repositioning has also been reported to occur, to facilitate repair (Kulashreshtha *et al.*, 2016; Mehta *et al.*, 2013; Oza *et al.*, 2009). Intuitively, it makes sense that open conformations of chromatin would enable these processes. However, chromatin compaction, following DNA damage, has also been reported as essential for DNA repair (Burgess *et al.*, 2014; Luijsterburg *et al.*, 2009). This is usually thought to occur following an initial decondensation process, possibly to restore chromatin to its original architecture (Burgess *et al.*, 2014; Strickfaden *et al.*, 2016). Following my findings presented in this thesis and published in dos Santos *et al.* (dos Santos *et al.*, 2021), a study by Fortuny *et al.*, showed that following UV damage, heterochromatic regions undergo large decondensation events through linker histone displacement (Fortuny *et al.*, 2021). Whilst it is possible that these would affect nuclear mechanics in a similar way to those reported here, this was not tested. Interestingly, a recent study also revealed a role for the ATR kinase in nuclear mechanics. Kidiyoor *et al.* showed that ATR ensures coupling of the nuclear envelope to the cytoskeleton, and its depletion leads to changes in chromatin organisation, nuclear softening and reduction in nuclear circularity (Kidiyoor *et al.*, 2020).

The consequences of DDR-induced nuclear softening on mechanotransduction are still unclear. However, it is likely that mechanical changes to the organelle during repair will have repercussions for cell migration, force transduction to the cytoplasm and transcription regulation.

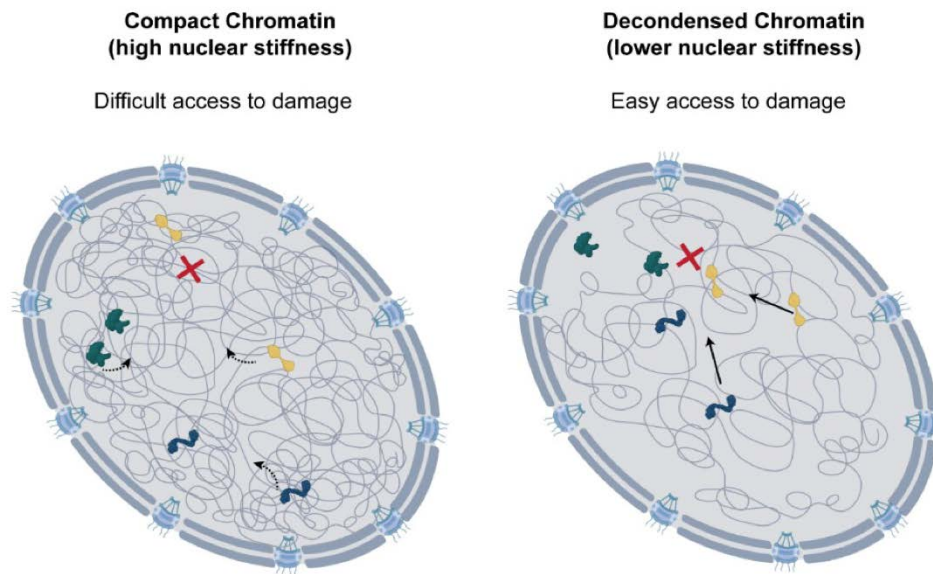


Figure 4 - Role of chromatin decondensation following DNA damage. Chromatin decondensation leads to higher nuclear diffusion, which could be important for rapid access of repair factors to DNA lesions. This could support the efficient repair of DNA damage.

The mechanical properties of the cell and the nucleus prior to the damage, are also known to influence the extent of DNA damage that the cell suffers, as well as the outcome and efficiency of repair. Increased cytoskeletal stiffness can lead to higher levels of DNA damage in the cell (Hatch and Hetzer, 2016), and this could be particularly important during confined migration. When cells migrate, especially through spaces smaller than their cross-sectional area, substantial compression forces are exerted on the nucleus. The nuclear deformation caused by these forces can in itself cause DNA damage, but it can also lead to rupture of the nuclear envelope, which, by exposing the nuclear contents to cytoplasmic factors, can cause severe genomic instability (Denais et al., 2016; Raab et al., 2016). Furthermore, during migration, the deformation of the nuclear envelope, as well as its rupture, can cause local loss of repair factors and other mobile proteins and have severe implications to the efficiency of DDR pathways (Irianto et al., 2016).

Both the cytoskeletal forces exerted on the nucleus, and nuclear stiffness, are important in determining nuclear deformability and the propensity of the nuclear envelope for rupture (Chen et al., 2018; Denais *et al.*, 2016; Hatch and Hetzer, 2016; Streppa *et al.*, 2018; Wesolowska *et al.*, 2020). As a result, the mechanical properties of the nucleus are tightly linked to the levels of DNA damage caused by migration and the outcome of DDR. Softer nuclei, with reduced levels of lamin A/C, require less pressure for nuclear envelope rupture to occur during migration and, therefore, display increased levels of

DNA damage (Chen *et al.*, 2018; Denais *et al.*, 2016; Irianto *et al.*, 2016). Similarly, in experiments using trichostatin A, nuclear softening caused by chromatin decompaction increased the likelihood of nuclear envelope rupture after shear stress application via syringe passes (Stephens *et al.*, 2018). Although this work from Stephens *et al.* appears to suggest that stiffer nuclei could be more protected from rupture, cells expressing progerin, which increases nuclear stiffness, display higher levels of DNA damage (Larrieu *et al.*, 2014). The mechanisms through which this occurs are not entirely clear, especially as progerin-expressing cells appear to require higher forces for nuclear envelope rupture (Dahl *et al.*, 2006). However, this reinforces the idea of a link between altered nuclear mechanics and the incidence of DNA damage in the cell.

Interestingly, cells treated with cisplatin display different levels of DNA damage, depending on the stiffness of their substrate. In the work presented in this thesis, we show that on softer surfaces, where the nuclear tension is lower due to reduced cytoskeletal forces (*e.g.*, polyacrylamide gels of different stiffness), cells have lower levels of DNA damage marker γ H2AX following cisplatin treatment. This is also true for cells treated with blebbistatin prior to DNA damage induction (dos Santos *et al.*, 2021). The reasons for this are not yet clear, and much work is still needed in order to understand how the mechanical state of the nucleus relates to the propensity of the cells for DNA damage. Furthermore, how the pre-existing mechanical state of the nucleus might influence the DDR pathway choice is also not clear. As we discussed, changes in cytoskeletal forces and lamina composition affect nuclear stiffness and are also likely to affect chromatin organisation. Similarly, dysregulation of chromatin compaction due to, for example, mutations in chromatin remodelling complexes are often observed in cancer, but there are no data on how this may affect overall nuclear mechanics. It is perhaps possible that, as nuclear mechanics is reflective of the chromatin environment, nuclear stiffness might influence DDR pathway choice and, as a result, genomic stability. Understanding this relationship is important, particularly in therapeutics, since the mechanical properties of the cells and of the nucleus are often altered in disease (Zwerger *et al.*, 2011), and a mechanically compromised nucleus could mean a different outcome in terms of drug efficacy.

1.3.2. RNA Polymerase II Transcription

Another nuclear process that is heavily impacted by mechanotransduction is transcription. This has mainly been shown for changes in cytoplasmic forces or for when cells are subjected to extreme mechanical stresses during migration (Shivashankar, 2011). Under these conditions, a number of transcriptional pathways can be activated upon mechanical cues (Shivashankar, 2011), these include the previously mentioned YAP/TAZ, which is activated and translocated into the nucleus upon mechanical stress (Elosegui-Artola *et al.*, 2017) and NF- κ B, whose activation has also been shown to occur through mechanical signals (Xu *et al.*, 1998). Moreover, nuclear membrane stretching has been shown to regulate the nuclear translocation of transcription factors, likely through changes to nuclear pore structure (Lam and Dean, 2008), whose configuration can dynamically adapt depending on the surrounding mechanical conditions of the NE (Schuller *et al.*, 2021; Zimmerli *et al.*, 2021). Our knowledge of how external forces to the nucleus affect gene expression has improved; however, how nuclear stiffness, specifically, impacts transcriptional activity is still unclear. As chromatin structure is a major determinant in both nuclear mechanics and transcriptional activity, it is likely that these are tightly interlinked. Furthermore, this is an important consideration because altered gene expression is consistently reported when NE structure is compromised (Osmanagic-Myers and Foisner, 2019; Stein *et al.*, 2000). Similarly, our knowledge of how changes in transcriptional activity directly affect local and global nuclear mechanics, is also limited. (Shivashankar, 2011)

As mentioned earlier, structural changes in chromatin occur for and during transcription through the activity of histone modifiers or ATP-dependent chromatin remodelling enzymes. These changes in chromatin organisation could potentially affect overall chromatin and nuclear stiffness, especially in cases where concerted gene expression is activated/repressed. Additionally, enzymatic processes in the nucleus, including transcription, have been linked to the formation of high-density clusters. Recent studies now point to these assemblies as being 'mechano-active' - capable of sensing their surroundings and of exerting mechanical forces in the neighbouring environment (Bracha *et al.*, 2018; Shin *et al.*, 2018; Welsh *et al.*, 2018). Therefore, in order to understand how nuclear processes, such as transcription, might impact the overall mechanical properties of the nucleus, it is important that we study their nanoscale spatial organisation and dynamic behaviour. In the next sections, the regulation of 3D organisation of gene expression how this may impact nuclear mechanics will be discussed.

1.4. The spatial organisation RNA Polymerase II transcription

Eukaryotic transcription is carried out by three distinct RNA Polymerases (RNAP): RNAPI, RNAPII and RNAPIII. RNAPI is responsible for the transcription of pre-ribosomal RNA (rRNA), which, following processing, will constitute the structural and catalytic components of ribosomes (Moore and Steitz, 2002). RNAPIII transcribes non-coding RNAs, such as transfer RNA (tRNA), which is necessary for translating mRNA into amino acid sequences (White, 2008). In contrast, RNAPII is responsible for the most well-known type of transcription – transcription of protein-coding genes to produce mRNAs.

RNAPII comprises 12 different enzymatic subunits, the largest of which is Rbp1. At the C-terminal domain (CTD) of Rbp1, a long, repetitive and unstructured region allows the regulation of transcription. Whilst this region is not required for the catalytic activity of RNAPII, its presence is conserved between species and is essential for life (Bartolomei et al., 1988; Meininghaus et al., 2000; West and Corden, 1995). The CTD of Rbp1 consists of a complex sequence of multiple tandem heptad repeats, with a consensus motif (Tyr1-Ser2-Pro3-Thr4-Ser5-Pro6-Ser7) (Corden et al., 1985). The number of repeats varies between organisms; for example, Rbp1 CTD in *Saccharomyces cerevisiae* has 26 repeats, whilst in mammalian cells, the consensus sequence is repeated 52 times (Liu et al., 2010a). In vertebrates, 21 of the 52 heptad repeats match the consensus sequence, whilst the remaining repeats display some variation (Hsin and Manley, 2012). Importantly, all amino acid residues within these repeats are possible targets for post-translational modifications, thus creating a complex regulatory code (Buratowski, 2003). These modifications include phosphorylation (Buratowski, 2009); ubiquitylation (Li et al., 2007); methylation (Sims et al., 2011) and glycosylation (Kelly et al., 1993). This allows fine tuning of the dynamic activity of RNAPII in gene expression, from enhancing transcriptional activity in cells; regulation of the transcription cycle, to eviction and degradation of transcription machinery (Egloff and Murphy, 2008; Hsin and Manley, 2012; Tufegdžić Vidaković et al., 2020). In addition, the CTD of Rbp1 also acts as a platform for the association of additional transcriptional regulators. Overall, through different post-translational modification patterns, the CTD can not only direct transcription but also modulate events such as mRNA capping, and promote the recruitment of histone modifiers and ATP-dependent chromatin remodellers that allow progression of transcription machinery (Brookes and Pombo, 2009; Komarnitsky et al., 2000; Phatnani and Greenleaf, 2006).

The transcription of a gene can be subdivided into three different stages – i) transcription initiation, ii) elongation and iii) termination. Phosphorylation of serines (Ser) 5 and 2 at multiple repeats of the CTD of Rbp1, indicate an initiating RNAPII or an elongating complex, respectively. Regulation of the transcription cycle from initiation to termination is extremely complex. Initiation requires the association of unphosphorylated RNAPII with general transcription factors TFIIB, D, E, F and H on target promoter DNA regions to form the pre-initiation complex (Roeder, 1996). Following this, Ser 5 of CTD repeats are phosphorylated by TFIIH-associated kinase CDK7 at the promoter, thus marking the beginning of the transcriptional cycle (Komarnitsky et al., 2000). Subsequently, RNA synthesis begins and, between 20-120 transcribed nucleotides, the RNAPII initiation complex pauses (Krumm et al., 1995). Its release into elongation occurs following activity of positive transcription elongation factor b (P-TEFb) or CDK9, which phosphorylates Ser 2 at the CTD of Rbp1. Concomitantly, phosphorylation at Ser 5 is gradually removed during elongation through the activity of phosphatases (Hsin and Manley, 2012). During transcription of the gene body, elongating RNAPII interacts with additional elongating factors that allow chromatin landscape changes and RNA processing. At the end of the gene, transcription is then terminated through eviction of RNAPII from chromatin (Mischo and Proudfoot, 2013; Pearson and Moore, 2013). Termination requires the recognition of the polyadenylation site (PAS) at the 3'-end of nascent mRNA transcripts by the cleavage and polyadenylation (CPA) complex (Connelly and Manley, 1988; Proudfoot, 2016). Other key termination factors are also known to interact with the CTD of Rbp1 to promote the end of the transcription cycle (Proudfoot, 2016).

Recent advances in super-resolution microscopy have provided a better understanding of the spatial organisation of transcriptional activity in the nucleus. We now know that during transcription, RNAPII forms localised high density clusters, also known as transcription factories or condensates (Boehning et al., 2018; Cho et al., 2016a; Cho et al., 2016b; Cho et al., 2018; Cisse *et al.*, 2013; Sabari *et al.*, 2018). These regions form during transcription initiation at promoters and can coordinate multiple enhancers (super-enhancer regions) to boost and synchronise the expression of proximal genes (Sabari *et al.*, 2018; Whyte et al., 2013). Nuclear concentrations of RNAPII are estimated to be approximately 1 μM ; however, at these clusters, concentrations of transcriptional machinery can increase by several orders of magnitude (Cook, 1999; Darzacq et al., 2007). Considering the estimate that only 1 in 90 RNAPII initiating complexes proceed into elongation (Darzacq *et al.*, 2007) these higher local concentrations substantially increase transcriptional efficiency. It is, therefore, not surprising that their formation and

density directly correlate with transcription levels (Cho *et al.*, 2016a). In fact, at these regions, concentrations of transcriptional factors and machinery reach such high levels that membraneless compartments are thought to form through liquid-liquid phase separation (LLPS) (A and Weber, 2019; Alberti *et al.*, 2019).

Phase separation is defined as a process through which macromolecules condense into a liquid-like phase - separated from the surrounding, more dilute, environment (Banani *et al.*, 2017). A large variety of biological processes, both in the nucleus and cytoplasm, have been linked to LLPS (Banjade and Rosen, 2014; Laflamme and Mekhail, 2020; Wang *et al.*, 2021a). These include transcription, as mentioned above, but also DNA repair (Levone *et al.*, 2021; Oshidari *et al.*, 2020), PML bodies (Lallemand-Breitenbach and de Thé, 2010), nuclear speckles (Kim *et al.*, 2019; Liu *et al.*, 2021), nucleoli (Lafontaine *et al.*, 2021), cytoplasmic stress granules and processing bodies (Decker and Parker, 2012; Yang *et al.*, 2020). RNA, DNA and proteins are the main drivers in the formation of these membraneless compartments. In particular, proteins with low-complexity domains or intrinsically disordered regions are often found to be important for the formation of liquid-like droplets in cells (Lin *et al.*, 2017). These protein regions do not adopt stable 3D structures and often display high promiscuity in their interaction profiles (Tompa *et al.*, 2015), which allows them to act as scaffolds in LLPS.

In the case of transcription, the largely disordered structure of the CTD of Rbp1 is thought to be essential for the formation of transcription condensates. During initiation, RNAPII condensates are enriched with Ser5 phosphorylated CTDs; however, condensate formation was also observed during elongation. In this case, elongation factors, splicing factors and P-TEFb form high-density clusters with elongating RNAPII (Ser2 phosphorylated). In addition to these factors, the phosphorylation state of the CTD is essential in determining the partitioning behaviour of RNAPII - between initiating and elongating condensates (Guo *et al.*, 2019; Lu *et al.*, 2018) (Figure 5). Here, I will refer to clusters, as assemblies of molecules, independently of their partitioning state relative to the environment, and refer to droplets or condensates, as those assemblies that have undergone LLPS and are considered to be membraneless compartments.

Interestingly, a recent study by Pancholi *et al.*, using zebrafish embryos, showed that RNAPII clusters are not morphologically uniform. These clusters form through surface condensation and present different shapes and sizes that correlate with the phosphorylation profiles of the CTD, as well as the amount of available chromatin as a condensation surface. The authors observed that i) small transcriptional clusters ($<0.1 \mu\text{m}^2$) presented low levels of both initiating and elongating RNAPII, ii) large and dense assemblies ($>0.85 \mu\text{m}^2$, high solidity) displayed the largest amount of initiating RNAPII and high amounts of RNAPII-Ser2P, and iii) large but disperse clusters ($>0.85 \mu\text{m}^2$, low solidity) presented higher levels of elongating RNAPII with intermediate levels of RNAPII-Ser5P. Furthermore, in large and dense transcriptional condensates RNAPII-Ser2P was found almost exclusively at the edges, where these clusters appear to unfold

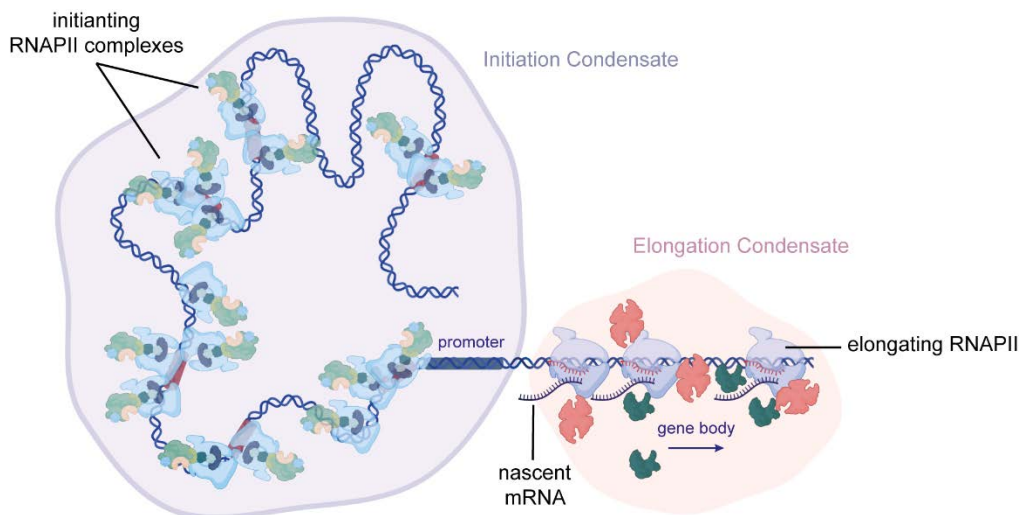


Figure 5 – Transcriptional condensate formation. RNAPII complexes, transcription factors and co-activators of transcription form condensates around promoter and enhancer regions to enzymatically enhance transcription initiation. Following escape of initiating RNAPII into the gene body for elongation, elongation condensates can also form in complex with splicing factors, elongation factors and mRNA.

and exclusion elongating RNAPII from condensates (Pancholi *et al.*, 2021). This subdivision of clusters points to a highly regulated nanoscale organisation of gene expression and suggests that the physical properties of RNAPII *foci* might align with their transcriptional activity. For example, RNAPII clusters are not exclusively found at

actively transcribing regions, but also present at the enhancers of silent genes and in Polycomb-repressed chromatin (Chopra et al., 2009; Dellino et al., 2004; Stock et al., 2007; Szutorisz et al., 2005). Based on the evidence discussed, it is expected that poised RNAPII clusters will have different morphologies, shapes and solidities, compared to RNAPII clusters where active elongation of genes is occurring (Lee et al., 2010; Stock et al., 2007).

Number, morphology, size and density of RNAPII clusters are, therefore, parameters of particular interest for understanding not only overall transcriptional activity in the cell, but also how gene expression might affect the physical properties of the surrounding environment and of the nucleus. The physicochemical properties of LLPS are still poorly understood, mostly due to the limitations of the available biophysical methods to study the material properties of small droplet-size volumes. However, by definition, phase separation is a change in the physical states of concentrated molecules (Banani et al., 2017) and, therefore, this will undoubtedly change the mechanical properties of the region. There is now growing evidence that, *in vitro*, LLPS condensates behave as viscoelastic materials and that their properties are highly dependent on physical crosslinks and electrostatic forces within the assembly (Choi et al., 2020; Jawerth et al., 2018). Recently, a study by Alshareedah and colleagues has also shown that, in the case of protein-RNA condensates, both protein and RNA sequences are deterministic of the physical properties of LLPS (Alshareedah et al., 2021). With this, it is likely that phase transition occurring, not only in transcription but in other nuclear processes, will have repercussions for the surrounding areas, related to changes in surface tension and viscoelastic behaviour (Wang et al., 2021b). In line with this, recent work used optogenetics to show that transcription regulators containing intrinsically disordered regions, such as BRD4, FUS and TAF15, associate into condensates that can both sense and change their mechanical microenvironment. Sizes and growth dynamics of transcriptional droplets were dependent on the stiffness of the condensation surface (chromatin), whereby large droplets were more likely to form in softer, low-density genomic regions (euchromatin) (Shin et al., 2018). Conversely, as they nucleate and grow, the surface tension of these condensates was also capable of deforming and physically excluding chromatin (Shin et al., 2018). This clearly suggests a link between nuclear mechanobiology and the 3D organisation of gene expression (Figure 6).

RNAPII clusters have also been proposed to have a role in promoting enhancer-promoter interactions, by allowing distal regions of the genome to come together (Hnisz et al., 2017). Shin and colleagues recently showed this through droplet seeding at distal genomic regions. Surface tension created by droplet formation at specific distal *loci* was

sufficient to induce chromatin displacement that led to the physical proximity of these regions and fusion of condensates (Shin *et al.*, 2018). Overall, transcriptional clusters appear to have a profound impact in the surrounding chromatin structure. How this affects global nuclear mechanics remains unclear.

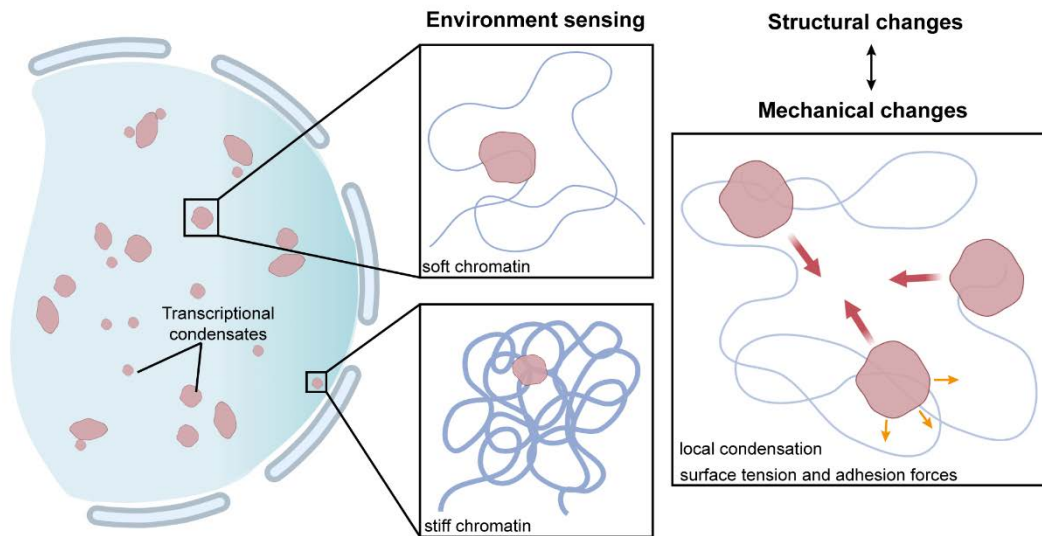


Figure 6 – Mechano-active transcriptional condensates. (left) Transcriptional condensates adapt to their mechanical environment. Size and morphology of condensates changes depending on substrate stiffness – softer euchromatin surfaces promote growth of transcriptional clusters. (right) Condensates can also induce mechanical changes to their microenvironment, through local changes to chromatin architecture – different degrees of crosslinking of the surrounding chromatin will change mechanical properties of the region.

The residence lifetime and dynamics of transcriptional clusters can vary, and kinetic estimations of RNAPII binding times depend on the methodological approach used – for example, Chromatin Immunoprecipitation (ChIP), Hi-C, Fluorescence *in situ* hybridization (FISH) or imaging in fixed *versus* live-cells (Cisse *et al.*, 2013; Darzacq *et al.*, 2007; Jackson *et al.*, 1993; Kimura *et al.*, 2002; Lieberman-Aiden *et al.*, 2009; Mitchell and Fraser, 2008; Tennyson *et al.*, 1995; wa Maina *et al.*, 2014). Although under normal conditions transcriptional assemblies are relatively stable for long periods of time (>10min) (Pancholi *et al.*, 2021), RNAPII clusters are also required to quickly respond to external stimuli and reorganise during mitosis (Zhang *et al.*, 2021). Single-particle tracking and Fluorescence Recovery After Photobleaching (FRAP) measurements have shown that RNAPII bound states in the nucleus are dependent on CTD length. Longer CTDs, such as the one present in mammalian cells with 52 repeats, correlate with not only higher probability of clustering, but also with slower molecular diffusion of Rbp1 and a higher percentage of molecules in the bound state (Boehning *et al.*, 2018). Importantly,

the residence time of RNAPII clusters directly and predictively correlates with the number of nascent mRNA molecules synthesized (Cho *et al.*, 2016a).

Although we now possess some level of understanding on the function, spatial organisation and molecular dynamics of these transcriptional clusters, our knowledge of how they are assembled and maintained during transcription or how their spatial organisation is regulated in response to external stimuli is still limited. A number of factors are thought to be essential in the formation of transcriptional condensates, including transcription factors, coactivators/corepressors, chromatin regulators and proteins with motor activity (Baarlink *et al.*, 2017; Rosin *et al.*, 2018; Ryu *et al.*, 2021; Saintillan *et al.*, 2018; Wei *et al.*, 2020). The work shown here explores this, with particular focus on the role of molecular motor Myosin VI (MVI) in the spatial organisation of transcription initiation and the description of a novel transcriptional regulator – the nuclear dot protein 52 (NDP52).

The next section will focus on these regulators of transcription, with the Coiled-coil Coactivator (CoCoA) as an example of a transcription coactivator, and our hypothesis that its close family member NDP52 might have similar nuclear functions. Following this, I will discuss the arising role of nuclear myosins and nuclear actin in the regulation of transcription.

1.4.1. Transcription factors and coactivators of transcription in the nanoscale organisation of gene expression

In addition to the intrinsic ability of RNAPII to cluster through interactions sustained by the CTD domain of Rbp1 (Boehning *et al.*, 2018), transcriptional activity and recruitment of RNAPII is also modulated by many additional regulatory proteins. The activity of these proteins ensures the temporal regulation of specific genes, according to developmental requirements, cell cycle stages and environmental cues. In particular, transcription factors, which recognise and bind to specific DNA sequences at enhancer regions, are crucial for initiating transcriptional signals that lead to the recruitment of transcription machinery. Due to their specificity, transcription factors are key to the control of specific pathways (*e.g.*, immune response), developmental patterning or cell differentiation (Iwafuchi-Doi and Zaret, 2016; Nakajima, 2011; Spitz and Furlong, 2012).

The major families of transcription factors are: i) Nuclear Receptors (NRs), which include the well-known oestrogen receptor (ER) and androgen receptor (AR); ii) C2H2 zinc finger (ZF), the largest transcription factor family, characterised by multiple tandemly arranged ZFs; iii) Homeodomain proteins, which recognise homeobox sequences; iv)

basic Helix-Loop-Helix (bHLH) and v) basic leucine zipper (bZIP) (Figure 7) (Adcock and Caramori, 2009). Transcription factors often bind to target DNA cooperatively, in the form of homodimers (*e.g.*, nuclear receptors) (Sever and Glass, 2013), trimers (*e.g.*, heat shock transcription factors) (Bonner et al., 1994) or even higher oligomeric forms (Hinde et al., 2016), thus increasing their binding affinity to specific DNA sequences.

Transcription factor activity is carefully modulated. Their expression at gene level can be induced or repressed, and they can be activated or deactivated through enzymatic activity (*e.g.*, kinase/phosphatase activity) or ligand binding (*e.g.*, hormone-dependent NRs) (Katzenellenbogen and Katzenellenbogen, 1996; Oeckinghaus and Ghosh, 2009; Primon et al., 2019). Once activated, transcription factors bind to their target DNA sequences at enhancers and promoter regions with high affinity (Figure 8A). For example, ER α is activated in the cytoplasm through hormone binding (oestradiol) and then translocated into the nucleus, where it interacts with oestrogen responsive elements (ERE) at target genes (Yaşar et al., 2016). Similarly, following activation of inflammatory signalling pathways in the cytoplasm, NF- κ B, which is generally sequestered by a family of inhibitory proteins, is released and translocates into the nucleus to regulate the expression of genes involved in innate immune responses (Lawrence, 2009).

Following binding to their target DNA, transcription factors recruit numerous coactivator proteins that help modulate the chromatin landscape and initiate the recruitment of RNAPII and other factors required for transcription initiation (Figure 8A). Unlike transcription factors, coactivators do not bind specifically to DNA, even though they can also interact with it. Transcriptional coactivators fall mostly under two categories, although some functional overlap often occurs: i) factors that promote the recruitment of other coactivators and of basal transcription machinery through protein-protein interactions and ii) chromatin-directed coactivators that act as chromatin modifying/remodelling enzymes (for example, through ATPase, kinase and or methyl/acetyltransferase activities) (Krasnov et al., 2016).

An example of the first category of coactivator is the mediator complex, the largest transcriptional coactivator known (a 33 multi-subunit complex composed of MED1-31, CDK8 and Cyclin C). The mediator complex is recruited by transcription factors to genes and provides a structural platform for the assembly of the pre-initiation complex (Kornberg, 2005). Alternatively, recruitment of methyl and acetyltransferases, such as the p300/CBP complex results in enzymatic activity of these complexes on histones,

leading to changes in chromatin accessibility that allow transcription to initiate (Figure 8A).

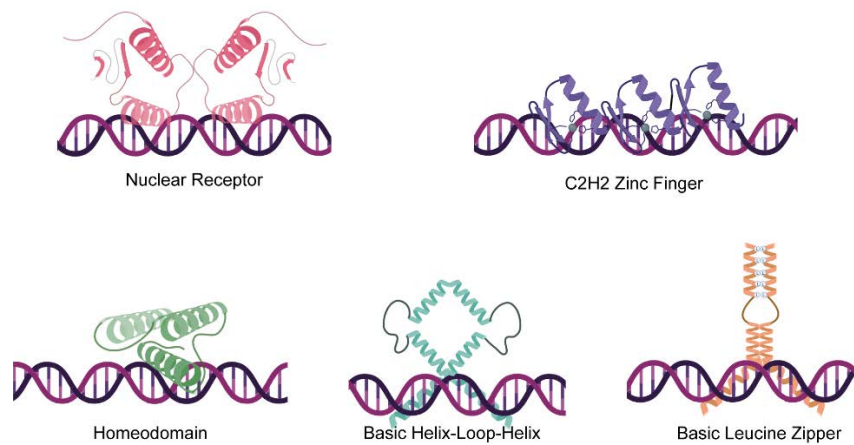


Figure 7 – Major transcription factor families and their DNA binding motifs.

Overall, coactivators enhance transcription by ensuring that promoter regions are cleared of nucleosomes for RNAPII loading and assembly of the pre-initiation complex (Vicent et al., 2011).

ChIP-Seq is commonly used for whole-genome mapping of transcription factor binding sites across the genome and provides important information regarding the activity of activators and coactivators of transcription at specific genes. However, the spatiotemporal resolution of these methods is limited, and they provide little information on kinetics and spatial organisation of transcription factors and their coactivators. As transcription is a highly dynamic process, it is essential to account for these properties.

The development of single-molecule microscopy techniques has substantially improved our spatiotemporal understanding of transcription. For example, reflected light-sheet microscopy developed by Gebhardt *et al.*, has allowed direct visualization of individual transcription factor dynamics and kinetic measurements of DNA binding in live-cells (Gebhardt et al., 2013). Using this technique, the authors were able to differentiate between monomeric, dimeric and indirect binding (through other transcription factors) of nuclear receptors to DNA, to measure differences in molecule residence times (Gebhardt *et al.*, 2013). Similarly, development of aberration-corrected Multifocal Microscopy (acMFM) by Abrahamsson *et al.* has also helped to shed light on the dynamic 3D behaviour of individual RNAPII molecules in the nucleus (Abrahamsson et al., 2013). Moreover, real-time imaging of nascent mRNA production in single cells has also described how transcription factor availability is an important determinant of

transcription frequency of target genes (Larson et al., 2013). Employing techniques such as these, alongside molecular biology and genome-wide characterisations, is essential to understand the highly dynamic process of transcription.

Much like RNAPII at initiation and elongation sites, transcription factors and coactivators do not appear to function as individual molecules, but organise into clusters (Figure 8B). Recently, a study by Wollman *et al.* in *Saccharomyces cerevisiae* showed that both a coactivator (Msn2) and a corepressor (Mig1) of transcription for genes involved in glucose metabolism, form clusters (Wollman et al., 2017). Using millisecond Slimfield microscopy, the authors found that both the coactivator and corepressor could bind to target genes as oligomeric clusters. Subsequent particle-tracking of these *foci* showed that the dynamics of these associated clusters were highly dependent on glucose state and, therefore, on the transcriptional activity of their target genes – cluster dynamics varied from a uniform population with highly dynamic behaviour (measured diffusion constants $D = 1\text{-}2 \mu\text{m}^2\cdot\text{s}^{-1}$) to a mixed population of immobile and mobile molecules (Leake, 2018; Wollman *et al.*, 2017).

Since then, similar observations have been reported for the organisation of other transcription factors and coactivators. For example, the aforementioned p300/CBP complex has also been observed at discrete nuclear *foci* (Ma et al., 2021). p300/CBP clusters are thought to be induced through their association with transcription factors at promoter regions. This clustering behaviour enhances the stability of the assembly between coactivator and transcription factor on DNA and enhances p300 acetyltransferase activity (Ma *et al.*, 2021). This, in turn, is thought to contribute to faster transcription initiation, longer duration of transcriptional bursts and leads to higher levels of expression of target genes (Ma *et al.*, 2021). In both cases, intrinsically disordered states of the proteins are thought to promote association of these clusters into condensates that enhance the individual activity of these molecules. Other examples of clustered transcription factors/coactivators include the mediator complex, ER, p53, Myc, GATA2 (Boija et al., 2018) and the glucocorticoid receptor (Frank et al., 2021) – all seen associated into highly condensed nuclear regions.

The observations discussed above highlight the importance of the spatial organisation, local concentrations and dynamics of transcription factors and their associated coactivators. The direct correlation observed between the spatial clustering of multiple transcription factors bound to their regulators and increased transcriptional efficiency strongly indicates a common strategy for these proteins to control gene expression at enhancers and super-enhancer regions (Figure 8B). It also underscores the importance

of understanding cluster formation and dynamics, as well as the mechanisms behind how these high-density regions are maintained for the duration of transcriptional activity.

Importantly, many of these proteins function by directly or indirectly inducing chromatin conformational changes. As we have previously discussed, changes to chromatin states will have a noticeable impact on the local and global mechanical properties of the nucleus. Hence, transcription factor and coactivator assemblies could potentially change the mechanical micro-environment, not only due to changes in surface tension associated to droplet formation through LLPS, but also by modulating chromatin compaction and gene positioning. This might be especially true during the coordinated activation of specific transcriptional pathways (e.g., in response to external stimuli or at different stages of development), as several genes would require simultaneous activation/repression, leading to chromatin structure change in a larger scale (Wegel and Shaw, 2005). In support of this, both the activation of ER and NF- κ B pathways have been linked to downstream large-scale chromatin decondensation and nuclear re-organisation events (Funsten et al., 2020; Nye et al., 2002; Rafique et al., 2015). Similarly, activation of DNA-lesion associated transcription pathways, such as p53, have also been shown to induce chromatin relaxation (Rubbi and Milner, 2003). Overall, the interlink between transcriptional activity and regulation of chromatin structure strongly suggest that gene expression could affect the mechanical properties of the nucleus.

Whilst not discussed here in detail, transcription corepressors also appear to follow the same preference for spatial clustering (Frank *et al.*, 2021; Wollman *et al.*, 2017). Corepressors, as the name suggests, have opposite functions to coactivators. Interestingly, some coactivators of transcription can also act as corepressors for different gene subsets and *vice-versa*, indicating that coactivator/corepressor activity is highly dependent on the biological context (Peterson et al., 2007; Rogatsky et al., 2001; Tagami et al., 1997; Weiss et al., 1999; Yang et al., 1999). It is, therefore, not surprising that their intrinsic properties result in similar organisational patterns across the nucleus.

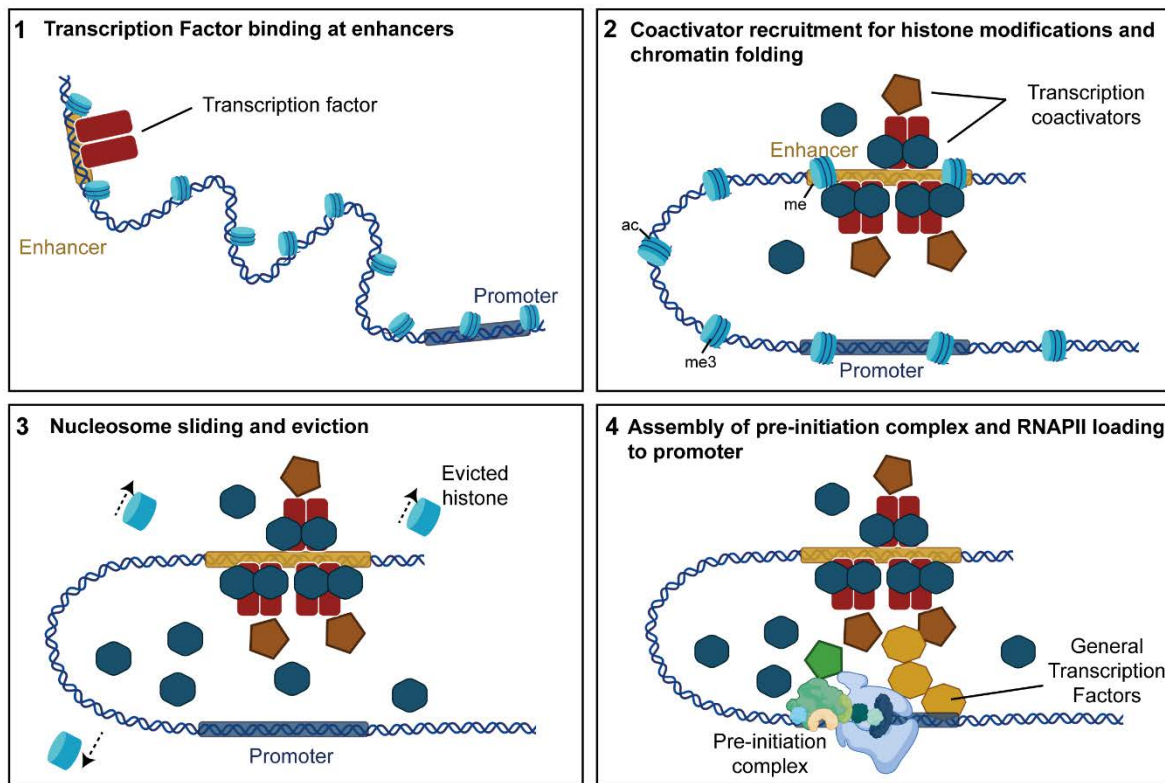
1.4.2. CoCoA and NDP52 - gene paralogs in transcription regulation and autophagy

An example of a coactivator of transcription is the Coiled-Coil Coactivator (CoCoA). CoCoA also known as CALCOCO1 belongs to the Calcium-binding and coiled coil-containing protein (CALCOCO) family. The other two members of this family are NDP52, also known as CALCOCO2 and TAX1BP1 (CALCOCO3) – two autophagy receptors (Morriswood et al., 2007).

In the nucleus, CoCoA is recruited to the regulatory region of genes to potentiate transcriptional activity. There, CoCoA can act as a primary coactivator for the aryl-hydrocarbon receptor (AHR) and AHR-translocator (ARNT) (Kim *et al.*, 2006) or as a secondary coactivator for nuclear receptors, including ER and AR, and for the Wnt/ β -catenin pathway, which regulates cell development and axis formation (Kim *et al.*, 2003; Yang *et al.*, 2006a; Yang *et al.*, 2006b). As a secondary coactivator, CoCoA is thought to be recruited by the coactivator p160, in preparation for RNAPII loading to DNA. Through this interaction, or independently as a primary coactivator, CoCoA cooperates synergistically with other coactivators – acetyltransferase p300/CBP, GRIP1 and with methyltransferase CARM1 – to promote chromatin remodelling at promoter regions (Figure 9). ChIP-qPCR experiments have shown CoCoA at promoter regions of target genes for the above-mentioned transcription factors and depletion of CoCoA leads to a reduction in the expression of these genes through faulty recruitment of chromatin modifying enzymes to these regions (Kim *et al.*, 2003; Kim *et al.*, 2006; Yang *et al.*, 2006b).

Conversely, NDP52 and TAX1BP1 have well described roles autophagy. Autophagy is the cellular process through which invading pathogens and cellular components, such as protein aggregates and damaged organelles (*e.g.*, depolarised mitochondria), are degraded and recycled. During this process, NDP52 simultaneously interacts with ubiquitylated cargo and other autophagy adaptors, including microtubule-associated protein 1 light chain 3 (LC3) and Atg8, to enable the formation of double-membraned structures in the cytoplasm – autophagosomes. Following this, through interactions with its binding partner MVI, NDP52 promotes autophagosome fusion with lysosomes (autophagosome maturation), which then allows the degradation of the enclosed macromolecules by hydrolases. Additionally, NDP52 has been linked to cell migration, adhesion (Kim *et al.*, 2013b; Morriswood *et al.*, 2007; Mostowy *et al.*, 2011; Thurston *et al.*, 2009; Verlhac *et al.*, 2015) and in the modulation of NF- κ B signalling through unknown mechanisms (Ellinghaus *et al.*, 2013).

A



B

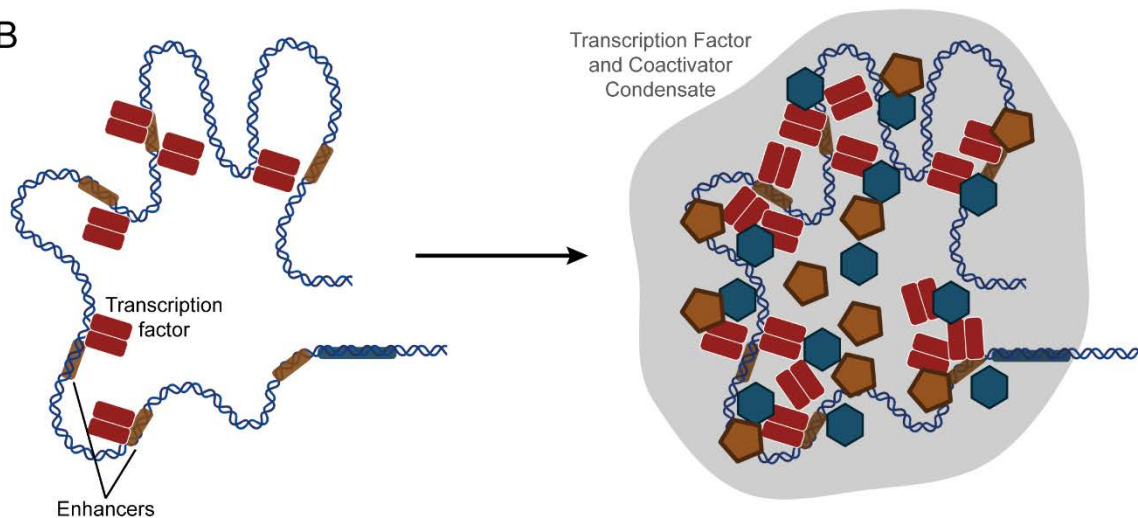


Figure 8 – Transcription factor and coactivator assembly and clustering to activate transcription. (A) Once activated, transcription factors bind specifically to DNA sequences at enhancers and promoter regions of target genes (1). Following this, they recruit many other coactivators of transcription (2) that cause changes to chromatin accessibility (3) and recruit basal transcription machinery, thus allowing the assembly of the pre-initiation complex and, subsequently, transcription to occur (4). (B) Association of multiple transcription factors at enhancers and super-enhancers leads to high concentrations of transcription coactivators and to the formation of clusters that enhance transcriptional activity.

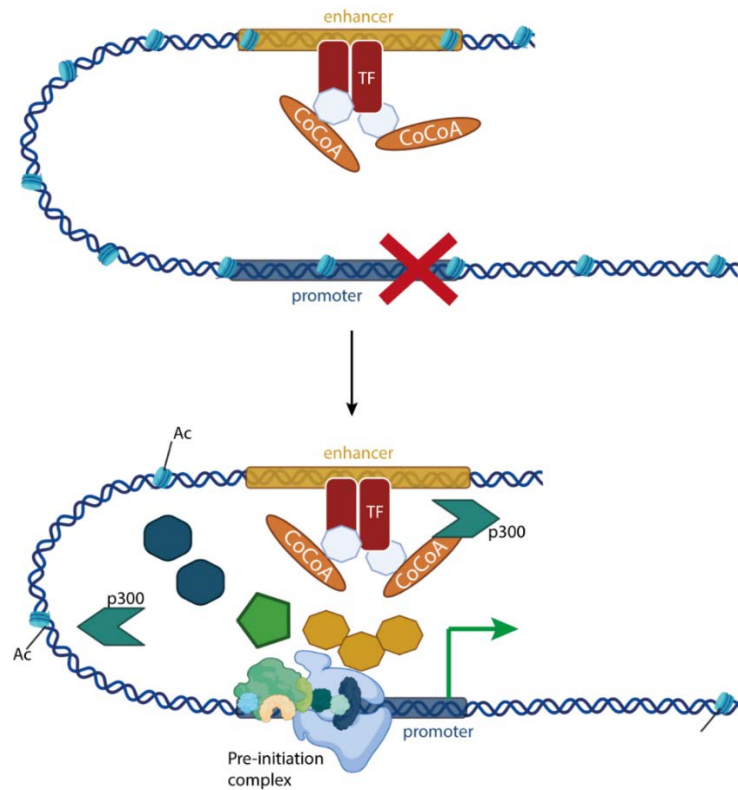


Figure 9 – Coactivator activity of CoCoA. CoCoA is recruited to regulatory elements by nuclear receptors or transcription factors such as LEF1. Following this, CoCoA recruits additional coactivators, including histone acetyltransferase p300. This leads to histone acetylation and subsequent chromatin remodelling that allows recruitment and loading of transcriptional machinery to the promoter region, to initiate gene expression.

Interestingly, CoCoA and its family members share high sequence homology and similar domain arrangements (Figure 10 and Figure 11A). All three proteins possess a Skeletal Muscle and Kidney Enriched Inositol Phosphatase (SKIP) Carboxyl Homology (SKICH) domain at their N-terminal (Figure 10, Figure 11A and B). For NDP52, the SKICH domain is thought to regulate its activity in autophagy, by mediating interactions with adaptor proteins and by facilitating its localisation to membranes (Fu et al., 2018; Gurung et al., 2003; Morriswood *et al.*, 2007). Conversely, for CoCoA, this domain is important for transcription coactivator activity and for the recruitment of acetyltransferase p300 to regulatory elements (Yang *et al.*, 2006b).

In all CALCOCO family members, the SKICH domain is followed by a coiled-coil region of variable length (Figure 11A). Coiled-coils often facilitate protein oligomerisation (Ciani et al., 2010), and this is thought to be true for NDP52, with some studies showing that the protein is capable of forming homodimers (Fu *et al.*, 2018; Kim et al., 2017). Within the coiled-coil regions of NDP52 and CoCoA, but not of TAX1BP1, one or three leucine



Figure 10 – Sequence alignment for CALCOCO family members NDP52, CoCoA and TAX1BP1. NDP52 domains – SKICH, Coiled-coil (CC), leucine zipper (LZ), ZF1 and ZF2 are shown. Common amino acid residues between the three proteins or between NDP52 and CoCoA are highlighted in green. Amino acid residues in blue show conservation between groups of strongly similar properties and in grey of weakly similar properties. C2H2 amino acid residues for ZF2 of NDP52 conserved in all three proteins highlighted in yellow.

zipper domains are also present, respectively (Figure 7A). At the C-terminal, all three proteins present one (CoCoA) or two zinc finger domains (NDP52 and TAX1BP1). The zinc finger domain common to all three proteins – ZF2 for NDP52 and TAX1BP1 - is a canonical C2H2 zinc finger and is well conserved between all family members (Figure 10 and Figure 11C). For NDP52, ZF2 sustains interactions with ubiquitin (Figure 11D) during autophagy (von Muhlinen et al., 2012; Xie et al., 2015), as well as interactions with binding partner MVI (Morriswood *et al.*, 2007; Xie *et al.*, 2015). Conversely, interactions between the C-terminal of CoCoA and MVI have never been explored and, instead, we know that CoCoA interacts with transcription coactivators, such as β -catenin, through this region. Although zinc finger domains are common motifs in transcription factors and coactivators, and often mediate protein-DNA interactions, this has never been explored for these proteins.

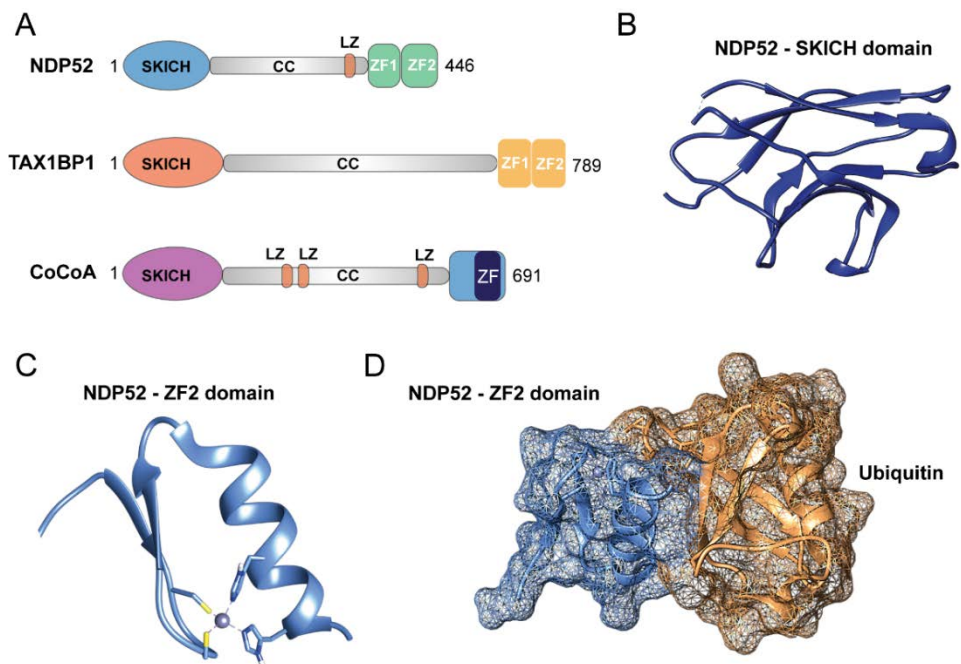


Figure 11 – CALCOCO family domains. (A) Domain arrangement for NDP52, TAX1BP1 and CoCoA. All three proteins contain SKICH domains at the N-terminal, followed by long coiled coil regions (CC), which in the case of CoCoA and NDP52 the coiled-coil region includes one or more predicted leucine zipper domain. At the C-terminal all proteins have a highly conserved zinc finger domain and, in the case of NDP52 and TAX1BP1, this is preceded by an additional zinc finger. (B) Crystal structure of the SKICH domain of NDP52 – PDB: 3VVV. (C) Crystal structure of the ZF2 domain of NDP52, which is highly conserved in all three members of the CALCOCO family, showing Zn^{2+} coordination. PDB: 4XKL (D) Crystal structure of ZF2 of NDP52 in complex with monoubiquitin. PDB: 4XKL.

The high sequence homology and domain similarity between CALCOCO family members suggests possible overlapping functions. This is, in fact, the case between NDP52 and TAX1BP1 - both involved in autophagy, with shared interacting partners (Fu *et al.*, 2018; Morriswood *et al.*, 2007). There is also now evidence that CoCoA, in addition to its transcriptional role, is involved in autophagy through the recruitment of endoplasmic reticulum and Golgi fragments to autophagosomes. This activity is mediated through interactions with adaptor proteins, such as members of the LC3 family and Atg8, during specific cell states (Nthiga *et al.*, 2020; Nthiga *et al.*, 2021). However, of all three proteins, CoCoA is the only one, so far, to be linked to roles in transcription regulation. This is particularly noteworthy, considering that the cellular localisation of CoCoA is identical to that of NDP52 - ubiquitously expressed across the cell, with higher cytoplasmic levels (Stefely *et al.*, 2020; Sternsdorf *et al.*, 1997; Yang *et al.*, 2006b). Furthermore, NDP52 was first characterised as a nuclear protein (Korioth *et al.*, 1995), with later work showing that the protein is distributed throughout the cell (Sternsdorf *et al.*, 1997).

The work presented here investigates a novel nuclear function for NDP52, by exploring its biochemical properties, nuclear organisation, interactome and effect on RNAPII-dependent transcription.

1.5. Actin and Myosin motors in chromatin regulation and transcription

In addition to the above-described roles of DNA-binding proteins and transcription coactivators, the arising field of nuclear actin and myosins also provides an interesting new perspective in chromatin mechanics and the dynamic regulation of nuclear processes.

Actin and myosins, in the cytoplasm, are usually associated with structural and mechanical roles. Whilst actin is one of the most abundant cytoplasmic proteins; its nuclear levels are comparatively low and tightly regulated - actin is actively transported in and out of the nucleus by importin-9 and exportin-6 (Dopie *et al.*, 2012; Stüven *et al.*, 2003). However, the presence of nuclear actin is essential for processes such as transcription (Dopie *et al.*, 2012; Wei *et al.*, 2020), mitosis (Baarlink *et al.*, 2017), DNA replication (Lamm *et al.*, 2020), DNA repair (Caridi *et al.*, 2019) and chromatin regulation (Kapoor and Shen, 2014).

Actin can be found in both monomeric (globular) and filamentous forms (G-actin and F-actin, respectively). In the cytoplasm, G-actin polymerises into long filamentous structures, which can subsequently arrange into higher-order 3D bundles, which are easily observed in the cytoplasm (Castaneda et al., 2021; Chandrasekaran et al., 2019; Fritzsche et al., 2017; Johnson et al., 2015). F-actin structures are important in the structural support and migration of the cell, as well as in intracellular transport and mechanosensing (Kim et al., 2012; Puleo et al., 2019; Sun et al., 2020). In the nucleus, due to the low concentrations of actin and the highly dynamic and transient nature of nuclear actin filaments, visualisation of these structures is particularly challenging, and much debate still surrounds them (Melak et al., 2017; Plessner and Grosse, 2019).

Notably, nuclear actin and actin-related proteins (Arps) are important components of ATP-dependent chromatin remodellers, such as the INO80 complex (Knoll et al., 2018) or members of the SWI/SNF family (Han et al., 2020). Two studies by Xie *et al.*, described how absence of β -actin disrupts binding of BRG1 - the catalytic subunit of SWI/SNF chromatin remodelling complex (Brahma-associated Factor) BAF – to chromatin. This resulted in global changes in heterochromatin levels, changes in gene expression profiles and abnormalities during neuronal cell reprogramming (Xie et al., 2018a; Xie et al., 2018b).

Nuclear actin has also been shown to physically interact with all three RNA polymerase complexes (Fomproix and Percipalle, 2004; Hofmann et al., 2004; Hu et al., 2004; Kukalev et al., 2005; Percipalle et al., 2003; Philimonenko et al., 2004). In the particular case of RNAPII, actin interacts with a hyperphosphorylated CTD domain of Rbp1 and is important for both transcription initiation and, through the recruitment of P-TEFb, to elongation (Hofmann *et al.*, 2004; Kukalev *et al.*, 2005; Qi et al., 2011). Furthermore, actin, specifically F-actin, is important for the enhancement of RNAPII clustering following serum stimulation (Wei *et al.*, 2020). The importance of actin to nuclear processes is further supported by a recent proteomics screen that showed its association to proteins involved in the transcription pre-initiation complex, pre-mRNA processing and elongation of RNAPII (Viita et al., 2019). Conversely, Serebryanny *et al.* show that stable and persistent dense actin filaments in the nucleus have a repressive effect on transcription. Upon the formation of these structures, RNAPII dynamics and nuclear localisation were altered (Serebryanny et al., 2016). This highlights the importance of a tight regulation of actin filament formation in the nucleus and might explain why such structures are rarely observed unless cells are under considerable stress. For examples, nuclear F-actin filament formation has been observed following DDR activation, caused by telomere uncapping, treatment with genotoxic drugs or UV

radiation. Following DNA damage, F-actin is recruited to sites of damage, and the formation of polymeric actin structures appears to be necessary for repair factors to cluster at DNA lesions (Andrin et al., 2012; Belin et al., 2013; Belin et al., 2015; Schrank et al., 2018).

Recent developments might help shed light on the role of actin in nuclear processes. For example, the use of actin chromobodies fused to Nuclear Localisation Sequences (NLS) has allowed live-cell visualisation of nuclear actin filament dynamics, without signal interference from the abundant cytoplasmic actin filaments (Baarlink *et al.*, 2017; Melak *et al.*, 2017). Additionally, Baarlink and co-workers developed a phalloidin-based assay and used STORM super-resolution imaging to visualise F-actin polymers in the nucleus. By using both these tools, the authors observed that these structures are necessary for reshaping nuclei following mitosis. Depletion of nuclear F-actin, either by overexpression of exportin-6 or a polymerisation-deficient mutant of nuclear actin (NLS-actin R62D), prevented the usual chromatin decondensation and nuclear expansion that occurs following cell division. In addition, this also led to impaired transcription and, in the case of mouse embryos, impaired development (Baarlink *et al.*, 2017).

Budding yeast experiments support the idea of a role for nuclear F-actin in chromatin organisation. In this case, inhibition of actin polymerisation was shown to reduce telomere and chromosome dynamics, and, interestingly, it also reduced the efficiency of DNA repair by HR (Spichal et al., 2016).

It seems very likely that mechanical changes to the nucleus would occur upon the formation of nuclear F-actin, as, in the cytoplasm, the extent of actin fibre formation scales with cellular stiffness (Palmer et al., 1998). However, it is still unclear how nuclear actin filament formation affects nuclear mechanics and nuclear mechanosensing. Nuclear actin may induce direct changes to local mechanics or alternatively through altered chromatin compaction and dynamics.

In the cytoplasm, the role of actin filaments is tightly linked to the function of myosins. These molecular motors use ATP hydrolysis to generate force and movement, and thus, are essential in several cellular processes such as cell migration (Vicente-Manzanares et al., 2009), intracellular transport (Fili and Toseland, 2019; Titus, 2018) and membrane regulation (Nambiar et al., 2009). Similar to F-actin, these proteins are also present in the nucleus. However, there are still many unanswered questions regarding their nuclear functions.

The first myosin to be found in the nucleus was Nuclear Myosin I (NM1), which was shown to colocalise with RNAPII (Nowak et al., 1997). NM1 is an isoform of the

cytoplasmic Myosin 1c, with the addition of an extra 16 amino acid residues at the N-terminal. Since then, NM1 has been linked to a plethora of nuclear processes, including chromatin organisation, transcription and DNA repair (Cook et al., 2020; Cook and Toseland, 2021). We now know that NMI acts cooperatively with actin, as a component of the chromatin remodelling complex B-WICH, to allow chromosomal rearrangements in RNAPI-related transcription (Percipalle et al., 2006; Sarshad et al., 2013). Moreover, ChIP-Seq data has identified the presence of NMI across the whole genome, with occupancy profiles correlated to the presence of RNAPII and active marks of transcription (Almuzzaini et al., 2015; Venit et al., 2020). In support of this, Venit *et al.* recently showed that knockout (KO) of NM1 in mouse embryonic fibroblasts leads to increased levels of heterochromatin and lower levels of active chromatin marks such as H3K9ac (Venit *et al.*, 2020). This caused dysregulation of DNA damage and cell cycle genes, causing KO cells to exhibit higher levels of DNA damage, cell proliferation and apoptosis. In a further link to DNA repair, NM1 has also been shown to facilitate chromosome territory relocation in an ATM and γ H2AX-dependent manner, following cisplatin treatment. Importantly, chromosome territory relocation by NM1, upon DNA damage, transcriptional activation or other stimuli, appears to be dependent on its motor activity (Cook and Toseland, 2021; Kulashreshtha *et al.*, 2016).

Another example of a myosin with nuclear functions is MVI. MVI was first attributed a nuclear role by Vreugde *et al.*, who observed high levels of the molecular motor at transcriptionally active *foci* in the nucleus (Vreugde et al., 2006). The authors found that MVI localised as 'punctate dot-like structures' that colocalised with RNAPII and newly transcribed mRNA, possibly at transcription factories, and that this localisation was lost following transcription inhibition. MVI was also found at the promoters of different genes and this correlated with their transcriptional activity (Vreugde *et al.*, 2006). Since this study, other observations of MVI nuclear clustering have been reported and additional nuclear roles have been attributed to the protein (Große-Berkenbusch et al., 2020; Majewski et al., 2018; Zorca et al., 2015).

Following transcription stimulation of particular gene subsets, long-range chromatin movements (1-5 μ m) have been reported (Chuang et al., 2006). This movement is thought to be essential in gene pairing, gene clustering and in the configuration of transcription factories, as it would allow different genes to localise at shared nuclear sub compartments for their co-regulation by common transcription factors and coactivators (e.g., genes co-regulated by ER) (Chakalova and Fraser, 2010; Osborne et al., 2004; Sutherland and Bickmore, 2009). MVI, in particular, is thought to play a role in chromosome reorganisation for gene pairing upon transcription stimulation of specific

genes, and this is thought to enhance transcription efficiency (Zorca *et al.*, 2015). MVI is thought to have the ability to reorganise and move chromatin across long nuclear distances and also to crosslink chromatin to allow gene proximity during transcription (Zorca *et al.*, 2015). In support of this finding, a recent report by Große-Berkenbusch and colleagues described how MVI can move on highly dynamic and transient nuclear actin filaments, to coordinate large-scale chromatin movement during transcription stimulation (Große-Berkenbusch *et al.*, 2020). This movement was observed across several micrometres, resembling the cytoplasmic motility of this molecular motor. The authors also reported ATPase-dependent movement of MVI on chromatin *in vitro* and described how this could have an important function in chromatin organisation by regulating long-range chromatin movement. Furthermore, MVI depletion has also been shown to cause defects in the release of paused RNAPII into elongation, suggesting that MVI might have different roles at different stages of transcription (Zorca *et al.*, 2015).

It is not yet clear how myosins and actin perform their various nuclear roles. However, interactions between myosins and ATP-dependent chromatin remodellers have been reported (Percipalle *et al.*, 2006). This, in conjunction with their ability to generate force/motion, and their activity in long-range chromatin movement (Wang *et al.*, 2020), suggests a role in the spatial organisation of transcription and other nuclear events.

The work described here aims to better understand the role of molecular motors, specifically of MVI in the regulation of transcription. We show how through its force sensing ability and interactions with nuclear actin, MVI is important for the regulation of the spatial organisation of initiating RNAPII (Hari-Gupta *et al.*, 2020).

As we investigate the mechanisms by which MVI modulates RNAPII transcription, it is also important to understand the biochemical regulation of the activity of this molecular motor. A brief description of our current biochemical knowledge of MVI activity is presented in the next section.

1.5.1. Myosin VI – a Unique Molecular Motor

During actin polymerisation, G-actin monomers face the same direction (Holmes *et al.*, 1990). This creates different polarities at either end of the filament – called ‘plus-’ and ‘minus-ends’. Actin filament polarity is particularly important in establishing directionality of myosin movement in the cell (Wells *et al.*, 1999). Of all myosins, MVI is the only myosin with the unique ability to travel towards the minus-end of actin filaments (Cramer, 2000; Wells *et al.*, 1999). This characteristic confers unique roles for MVI in endocytosis, as, generally, the plus-end of actin filaments grows towards the plasma membrane and

the minus-end towards the cell interior, to the nuclear periphery (Cramer, 2000; Granger et al., 2014; Qualmann et al., 2000).

MVI is a large molecular motor, comprising **i)** an N-terminal ATP-dependent motor domain, where actin binding occurs; followed by **ii)** a long neck region, with a unique insert that confers MVI its reverse directionality (Park et al., 2007), and an IQ domain capable of binding to calmodulin; **iii)** a tail region, encompassing three different structural domains - a three-helix-bundle, a single-alpha-helix and a short coiled-coil - and **iv)** a globular cargo binding domain (CBD) at the C-terminal of MVI tail (Figure 12).

MVI is a processive motor (Park et al., 2006), capable of acting as a load-dependent actin anchor (Altman et al., 2007). Processive movement – the ability to coordinate enzymatic states of catalytic domains to move on actin filaments without premature detachment - is a characteristic of some molecular motors (*e.g.*, Myosin V and Kinesin). Generally, this depends on the ability of these proteins to oligomerise, in order to coordinate their activity. Hence, surprisingly, the oligomeric state of MVI was the cause of debate for many years, with some reports supporting a monomeric form for the protein and others showing its dimerisation (Altman *et al.*, 2007; Park *et al.*, 2006; Spink et al., 2008; Spudich et al., 2007). We now know that MVI in its monomeric form, is in a folded, inactive state (non-processive activity), whereby the protein folds onto itself and the CBD interacts with the motor domain (Yu et al., 2009). Upon interactions different cargoes, MVI unfolds, and this is thought to allow dimerisation of the protein and activation of its motor activity (Mukherjea et al., 2009; Park *et al.*, 2006; Phichith et al., 2009). However, at the start of this work, there was still some uncertainty on whether this dimerisation is an intrinsic ability of MVI or if it occurs through dimerisation of its binding partners, as many of them are capable of dimerising.

Within the CBD of MVI, two different motifs - the RRL and WWY motifs - modulate interactions with binding partners (Figure 12) (Fili and Toseland, 2019; Morriswood *et al.*, 2007; Spudich *et al.*, 2007). Mutation of these motifs impairs the localisation and function of MVI, highlighting the regulatory importance of binding partners (Arden et al., 2016; Masters and Buss, 2017; Sobczak et al., 2016). Interestingly, alternative splicing of MVI can also drive binding partner selectivity. Splice isoforms of the protein result from either a 31 amino acid residue insertion (large-insert, LI) close to the CBD, and/or an 8 amino acid residue insertion (small-insert, SI) within the CBD (Figure 5A) (Buss et al., 2001). This generates four different possible isoforms: no-insert (NI), SI, LI and SI+LI, each with distinct cellular distributions and functions (Au et al., 2007; Buss *et al.*, 2001). In the LI isoform, the additional 31 amino acid residues encode an α -helix that

occludes the RRL motif, thus disrupting binding partner interactions through this region (Wollscheid *et al.*, 2016). Conversely, in the NI isoform, both motifs are available for binding and, therefore, other unknown factors may play a role in determining binding partner selectivity.

Many different partners with a wide range of functions have been identified for MVI. For example, in the cytoplasm, disabled-2 (Dab2) interacts with MVI through the WWY motif to target the molecular motor to clathrin-coated vesicles during early endocytosis (Spudich *et al.*, 2007). On the other hand, interactions with the NDP52 occur through the RRL motif to regulate autophagosome maturation during autophagy, as well as cell adhesion and cytokine signalling (Morriswood *et al.*, 2007; Tumbarello *et al.*, 2012; Verlhac *et al.*, 2015). MVI is also important for the organisation of cortical actin networks (Frank *et al.*, 2004) and, through interactions with binding partner optineurin, MVI also regulates Golgi complex organisation (Buss *et al.*, 1998; Sahlender *et al.*, 2005).

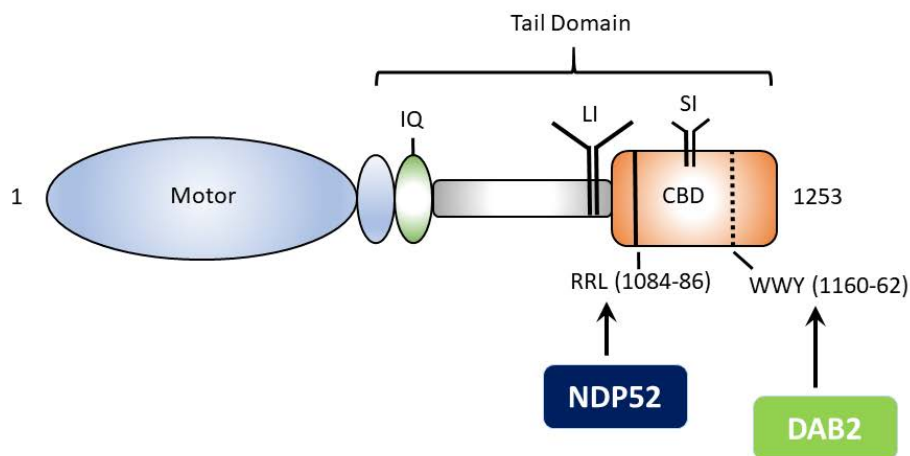


Figure 12 – MVI domains and alternative splicing isoforms. MVI comprises a motor domain with ATPase activity, where actin binding occurs. This is followed by an IQ domain that binds to calmodulin and by a long tail domain. At the C-terminal, a globular cargo-binding domain (CBD) has two motifs – RRL and WWY – that coordinate binding to different binding partners, such as NDP52 and Dab2. Due to alternative splicing, there are four MVI isoforms: NI, SI, LI, SI+LI, depending on the absence/presence of one or both possible inserts.

As these proteins are well-known for their role in force transduction in the cytoplasm, they may have a similar role in the nucleus (Cook *et al.*, 2020; Cook and Toseland, 2021). Future studies are necessary to shed light on the response of nuclear F-actin and nuclear myosins to external mechanical cues.

Given the variety of cellular roles highlighted above, it is not surprising that mutations or misregulation of MVI lead to disease. MVI mutation is associated with deafness (Arden *et al.*, 2016), hypertrophic cardiomyopathy (Buss *et al.*, 2004) and its overexpression is linked to cancer (Yoshida *et al.*, 2004). However, whilst misregulation of its many cytoplasmic functions is thought to lead to disease, we are now starting to consider how its newly described roles in transcription and chromatin regulation might also play a role in disease.

In part, this thesis aims to shed light on the nuclear role of MVI. We do not yet fully understand to what extent MVI nuclear function depends on its motor activity, or ability to interact with actin. For example, MVI function in chromosome reorganisation and gene pairing, could be linked to its ability to generate movement. Alternatively, its load-dependent anchoring capabilities might also provide stability for chromatin or transcription machinery during gene expression. Furthermore, initial observations of MVI in the nucleus have described it as part of transcriptionally active clusters. Does MVI contribute to cluster formation during transcription? Furthermore, it is important to understand how MVI activation occurs within a nuclear context. The work presented here addresses these questions, to expand our limited knowledge of how MVI is recruited into the nucleus of cells; which binding partners modulate its nuclear functions and how MVI regulates RNAPII-dependent transcription.

1.6. Methodological Approaches to Study Nuclear Architecture and Organisation

In order to study the regulation of nuclear architecture - from global nuclear structure and mechanics to the molecular organisation of nuclear processes - I used a multidisciplinary approach. This approach aims to provide a comprehensive view of the nucleus and the relationships between its physical status and function. Although I employed several different methods during this work (transcriptomics, biochemical methods, proteomics etc.), three different methodological approaches were essential for my results and were recurrently used by me: i) Atomic Force Microscopy (AFM); ii) Stochastic Optical Reconstruction Microscopy (STORM) with Cluster Analysis; and iii) Single-Molecule Tracking. In the next three sections, I will briefly discuss some of key aspects of these techniques and reasons for using them.

1.6.1. Atomic Force Microscopy

AFM is an extremely versatile technique that can provide detailed information on both cellular and single-molecule scales. This technique has often been used to provide high-resolution imaging of both cellular topography and of single-molecules, including of DNA and DNA-binding proteins (Pyne and Hoogenboom, 2016; Pyne et al., 2021; Tanigawa et al., 2000) as it is used in Chapter 6 to image NDP52 shape and binding to DNA. Additionally, AFM is also ideally suited to probe the mechanical properties of different materials, including cellular compartments such as the nucleus of mammalian cells (Engler et al., 2007; Rehfeldt et al., 2012a; Rehfeldt and Schmidt, 2017; Swift *et al.*, 2013; Zemel et al., 2010), as we use in Chapter 3 of this thesis.

First developed by Binnig *et al.* in 1986, the AFM is capable of exerting forces in the range of nN and pN on cells, single-molecules and other materials, with very high precision (Binnig et al., 1986). The technique relies on surface scanning by a physical probe – usually a thin tip at the end of a flexible cantilever. Samples, on a flat surface (*e.g.*, glass, mica or polyacrylamide gels) are probed, as the tip is lowered and contacts the material. Laser light, focused on the cantilever is reflected onto a four-quadrant-photodiode that allows detection of deflection (Figure 13) (Rehfeldt and Schmidt, 2017). This measurement of deflection can then be translated into values of applied Force, through Hooke's law, if the spring constant of the cantilever is known (**Equation 1**, where F is force, k is the spring constant of the cantilever and Δd is the cantilever deflection) (Hutter and Bechhoefer, 1993). Furthermore, deflection also allows us to measure indentation of the tip into the sample, through careful determination of the point of contact between the tip and the sample (Figure 14). The relationship between indentation and applied force can then provide detailed information on the mechanical properties of the sample, in the form of Young's Modulus (Burnham and Colton, 1989).

$$\text{(Equation 1)} \quad F = k\Delta d$$

Depending on probe geometry, different mathematical models can be used to calculate the mechanical properties of the material in question (Rehfeldt and Schmidt, 2017). In the case of pyramidal tips, such as the one used in the second publication of Chapter 3 (dos Santos *et al.*, 2021), the Hertz model is commonly applied, as it generally produces good and reproducible values for conically shaped tips (**Equation 2**, where ν is the Poisson's ratio – usually 0.45 in cells -, α is the opening angle of the pyramidal tip and F the applied force) (Hertz, 1882; Rehfeldt and Schmidt, 2017). Some limitations, however, arise from the use of the Hertz model (Kontomaris and Malamou, 2020). For

example, it assumes that contact between the cantilever and the sample is free of adhesion, which, especially in the case of cells, is not true. However, if the approach curve is used for calculating the Young's Modulus, instead of the retraction curve, this can be a valid assumption (Rehfeldt and Schmidt, 2017). The Hertz model also assumes that samples are homogeneous and isotropic. This, again is not the case, especially when considering complex cellular components and compartments such as the nucleus. In this case, when using the Hertz model to calculate the mechanical properties of the sample, we should refer to the fitted Young's modulus as the 'effective Young's modulus' (E^*) (Rehfeldt and Schmidt, 2017).

(Equation 2)
$$E = \frac{\pi F(1-\nu^2)}{\delta^2 \tan \alpha}$$

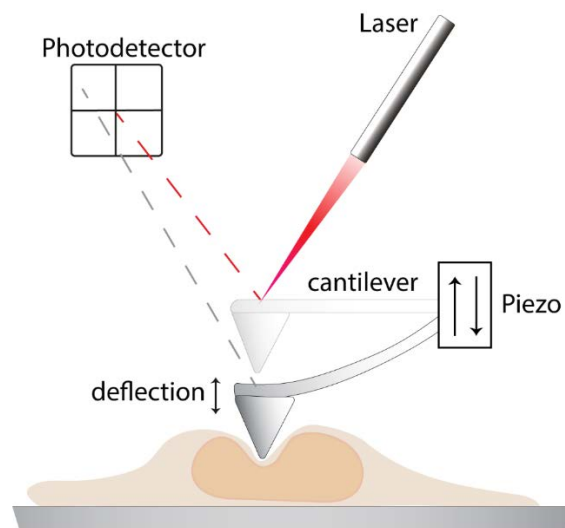


Figure 13 – Diagram of AFM measurement. A pyramidal tip at the end of a flexible cantilever indents the sample, in this case, the nucleus of a mammalian cell. Deflection of the cantilever is measured through the reflection of a focused laser beam onto a photodiode. Analysis of tip indentation *versus* applied force permits the calculation of effective Young's modulus E^* of our sample, which is a measure of stiffness. *From* (dos Santos et al., In press).

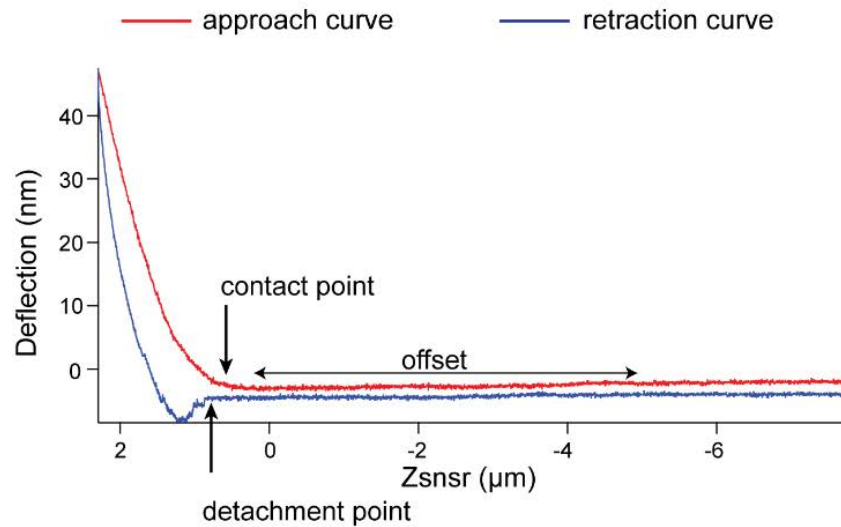


Figure 14 – Example of mechanical measurements in live-cell nuclei. (A) Force distance curve of the nucleus showing approach (red) and retraction (blue) curves. Contact point and detachment points are indicated and a flat offset in the curves is visible. *Adapted from (dos Santos et al., In press).*

The Young's Modulus is a combined measurement of the viscoelastic contributions of the material – between the loss modulus, which accounts for the viscous behaviour of the sample, and the storage or elastic modulus, a measurement of sample elasticity. In general, through traditional indentation curves using the AFM, it is not possible to deconvolve these two different components (Rehfeldt and Schmidt, 2017). However, it is possible to extract the viscoelastic properties of materials, if we account for the fact that they may respond differently depending on measurement time-scales (Rehfeldt and Schmidt, 2017). In other words, for some materials, their mechanical properties vary, depending on the frequency of the applied stress. Whilst this could appear to be a limitation of the method, AFM measurements at a range of different frequencies can provide extremely valuable insights into the structure and composition of complex materials. This can be achieved by applying sinusoidal stress to the sample, similarly to more traditional rheology methods (Mahaffy et al., 2004; Mahaffy et al., 2000). This approach has been used previously, for example, to probe differences between benign and malign cancer cells (Rother et al., 2014). Here, in the first part of Chapter 3, in a study led by Michael Lherbette and myself, we take advantage of this (Lherbette et al., 2017). By using different time- and length-scales, we were able to investigate the homogeneity of the nucleus interior.

Overall, AFM is an extremely sensitive and powerful technique to determine the mechanical properties of cells and subcellular compartments.

1.6.2. Stochastic Optical Reconstruction Microscopy

The development of different super-resolution microscopy approaches has enabled high-resolution visualisation of subcellular structures and localisation of single-molecules within cells in last few years (Fornasiero and Opazo, 2015; Hell Stefan, 2007; Huang et al., 2009; Toomre and Bewersdorf, 2010; van de Linde et al., 2012). In microscopy, resolution refers to the ability to separate two distinct points, close together, such as two fluorescently labelled molecules.

In 1873, Abbe described how optical resolution is limited by the diffraction of light (Abbe, 1873). This limitation is shown in **(Equation 3)** and arises due to the physical impossibility of the focal spot size in xy (d) to be smaller than the wavelength (λ) of light, divided by the NA the numerical aperture of the imaging objective - the opening angle of an objective lens (Abbe, 1873; Born and Wolf, 2013). The intensity profile of this optical spot corresponds to the Point Spread Function (PSF) of the microscope, and determines its resolution. Hence, if the distance between two objects is smaller than the PSF width, their signal will be overlapping and, therefore they are not resolved (Abbe, 1873; Born and Wolf, 2013). A major barrier to achieving high resolution images is that, in widefield (epifluorescence) or confocal microscopy, all fluorophores within the illuminated spot are simultaneously excited and, therefore, they also all emit quasi-simultaneously. With this, in crowded spaces, such as within a cellular context, separation between two molecules almost impossible.

As modern objectives can generally reach a NA of 1.4-1.6, this means that, for visible light, the minimum resolved distance achievable, under conventional methods and according to Abbe's law, is approximately >250nm - well above the size of individual proteins or protein complexes.

$$\text{(Equation 3)} \quad d = \frac{\lambda}{2NA}$$

Amongst the most common super-resolution techniques are: Stimulated Emission Depletion Microscopy (STED) (Hell et al., 2009); Structured Illumination Microscopy (SIM) (Heintzmann and Gustafsson, 2009); and Single-Molecule Localisation Microscopy (SMLM), which includes (Fluorescence) Photoactivated Localisation Microscopy ((F)PALM) (Betzig et al., 2006; Hess et al., 2006) and Stochastic Optical Reconstruction Microscopy (STORM) (Bates et al., 2013b). Here, I will focus on the latter approach, STORM, which relies on the detection of single-molecules.

Although the lateral image of a single fluorophore is limited by the diffraction limit to approximately 200-300 nm, its position can be precisely determined (in non-crowded environments), depending on the number of photons emitted (Thompson et al., 2002). This is achieved by calculating the centroid positions of emitting fluorophores and localisation accuracies as low as 1.5 nm have been achieved through this method (Yildiz et al., 2003). However, this still does not improve the resolution of an image in highly dense molecular environments, where PSFs of many fluorophores overlap.

STORM circumvents this problem by taking advantage of photo-switchable fluorophores that allow sequential localisation of individual molecules (Bates et al., 2008; Bates et al., 2013a; Bates *et al.*, 2013b). The photo-switchable nature of fluorophores allows molecules to be turned ON, into a 'bright state', at different time windows, whilst the remaining molecules populate a 'dark' state. With this, the position of 'ON' fluorophores can be easily determined by finding their centroids over many imaging frames. This allows not only high localisation precision for the different molecules detected, but also high image resolution (Bates *et al.*, 2008; Bates *et al.*, 2013b; Thomson et al., 2004). Using this technique, image resolution is no longer limited by the wavelength of light, but by the precision of each localisation, which, in turn, depends on the brightness of the fluorophore, background fluorescence, labelling efficiency, size of fluorescent label and the rate of transition of molecules from the dark to the bright state (Zhuang, 2009).

Several photo-switchable fluorophores can be used in STORM, including organic dyes, such as Alexa Fluor dyes (van de Linde et al., 2011b; Xu et al., 2017; Zhuang, 2009), and fluorescent protein tags, such as GFP (Betzig *et al.*, 2006; Hess *et al.*, 2006).

Briefly, a high-excitation power density (over 5kW/cm²) is used to excite photo-switchable fluorophores such as Alexa488 and Alexa647, which, in the presence of thiol-containing buffers (*e.g.*, β -mercaptoethanol) enter a long-lived dark state. Fluorophores spontaneously exit this dark state and return to the non-excited state, through emission of light. Repetition of this process over many frames enables reconstruction of high resolution images (Bates *et al.*, 2013a).

Importantly, especially for a large part of my work in this thesis, STORM not only allows a reduction in the minimum resolvable distance between individual fluorescent molecules, but also allows quantitative analysis of the image generated. Questions such as i) how many molecules populate a certain cellular region; ii) how are these molecules organised; iii) to what degree do they colocalise with other molecules of interest and iv) how these variables are affected by internal or external stimuli, can now be answered through image processing. Software packages, such as the one developed by Pajeon

et al., (Pageon *et al.*, 2016) which I often use in the work presented in this thesis, has also enabled statistical analysis of molecular behaviour in their cellular environment.

As I mentioned earlier in this chapter, molecular clustering is often associated to cellular function. A major aim of this thesis was to understand nuclear organisation of enzymatic processes, such as transcription. This includes investigating how the distribution of proteins thought to be involved in such processes (*e.g.*, MVI, transcription coactivators, etc.) relates to their nuclear function and impacts overall nuclear activity. In order to study protein clustering, it is necessary to obtain single-molecule localisation details on these proteins. STORM imaging permits this, allowing for high-resolution co-localisation studies with proteins of interest, quantitative analysis on number of molecules in regions of interest, as well as statistical analysis regarding clustering behaviour.

I will now briefly describe the principles behind cluster analysis, in particular the ones relevant to the analysis I have used in this thesis. Following STORM acquisition, a table of xy positions is generated with localisations of individual molecules (Endesfelder and Heilemann, 2015). For a general overview of point pattern data distribution, the Ripley K function can be used. The Ripley K function applies spatial statistics to provide information on whether points within a certain region are randomly distributed, aggregated or segregated (Owen *et al.*, 2010; Perry, 2004; Ripley, 1979). Clusters are defined as regions of higher density, that would not be expected to occur if the same number of molecules was randomly distributed. The Ripley K function is calculated over a range of distances (in the case of the single molecule data used in this thesis this is usually between 500 and 1000 nm) to determine how point pattern distributions change with distance – for example, molecules might have a tendency to cluster at shorter distances which disappears with longer distances or vice-versa (Owen *et al.*, 2010; Perry, 2004; Ripley, 1979). In the software developed by Pageon *et al.*, which I use here, a linearised form of the Ripley K function ($L(r)-r$) is integrated into the analysis. As a result, plots of $L(r)-r$ in function of r (r being the radius of search) can be generated and provide information on the likelihood of molecules to cluster. Positive function values indicate clustering, whilst values close to zero mean random distribution and negative values segregation. Examples of these plots are shown in Chapters 4, 5 and 6. Another important value generated by the Ripley K function is the maximum $L(r)-r$ radius value – the value at which clustering probability is the highest (Pageon *et al.*, 2016). This value can be used as a good estimate of the average size of clusters for a particular molecule and is a good starting point when applying further clustering statistical analysis to the single-molecule data set.

If the Ripley K function indicates that the molecules within the region of interest are clustered, further characterisation of their clustering behaviour is possible through Density-Based Spatial Clustering of Applications with Noise (DBSCAN) (Ester *et al.*, 1996). DBSCAN provides detailed information on individual clusters, including size, shape, density and the number of molecules in each cluster. For this, an arbitrary point is selected within the region of interest. The point is considered as being part of a cluster if a minimum number of points (MinPts - user defined) is in close proximity (distance must be lower than a user defined radius – usually the localisation precision of single molecule data acquisition) (Ester *et al.*, 1996; Pigeon *et al.*, 2016). The user defined MinPts value for cluster size calculation can vary depending on the type of data and biological system/process being studied. Pigeon *et al.* used MinPts = 3 as a starting point for analysis of cluster (Pigeon *et al.*, 2016). In this thesis I have used MinPts = 5, which means that only clusters where 5 or more neighbours are found in close proximity may be considered clusters. This allowed us to detect different types of clusters – relatively small clusters, as well as very large clusters. By having information on clusters of different sizes, it is also possible to infer on how biological function and activity in these regions may differ and to study how perturbations may affect a specific population of cluster.

In this thesis, I use this combined SMLM and cluster analysis approach to investigate i) activation of MVI through clustering with associated binding partners in cells; ii) spatial organisation of RNAPII and its dependency on MVI function and iii) NDP52 nuclear distribution relative to transcription in cells.

1.6.3. 3D Single-Molecule Tracking in Live Cells

When studying nuclear organisation and architecture another important consideration is molecular dynamics. In STORM, the long acquisition times combined with the high laser-power required to produce the photo-physical effects needed for single-molecule detection, translate into high levels of cytotoxicity (Henriques *et al.*, 2011; Tosheva *et al.*, 2020; van de Linde *et al.*, 2011a; Wäldchen *et al.*, 2015). Hence, this technique is most commonly used in fixed cells and not routinely used to observe dynamic cellular processes, in real-time.

Several imaging techniques allow measurement of molecular dynamics of fluorescently labelled proteins in live-cells. Fluorescence Recovery After Photobleaching (FRAP), for example, is often used to measure diffusion of molecules within the cellular context (Axelrod *et al.*, 1976; Kitamura and Kinjo, 2018; Pincet *et al.*, 2016; Wachsmuth, 2014).

However, this only provides information on the bulk behaviour of molecules and cannot distinguish subpopulations (*i.e.*, ratio of diffusive molecules versus static or confined molecules). Furthermore, as FRAP does not allow single-molecule observation, and events, such as binding or processive movement, are also indistinguishable. Conversely, single-molecule tracking in live-cells provides real-time, quantitative data regarding molecule dynamics, localisation and kinetics in the native environment of the particles of study (Lionnet and Wu, 2021; Liu et al., 2014; Miné-Hattab et al., 2021; Sako et al., 2000; Yang et al., 2004). As a result, single-molecule tracking has become a popular approach in the study of cellular processes.

Important considerations when designing single-molecule tracking experiments are i) the choice of fluorophores; ii) the spatiotemporal resolution and detection of fluorescent signal by optical setup and iii) phototoxicity (Liu et al., 2015). Arguably, selection of fluorophore is the most important choice for good live-cell single-molecule tracking data. Both the photobleaching rate of fluorophores, due to permanent electron loss as a consequence of photodamage (Ha and Tinnefeld, 2012; Hoogenboom et al., 2005) and their quantum yield – fraction of photons absorbed that are re-emitted as fluorescence by the fluorophore – heavily impact the quality of single-molecule data (Aaron et al., 2019). Low photon emission by fluorophores can lead to high signal-to-noise ratios when tracking molecules in the crowded cellular environment and, indirectly, to higher sample phototoxicity, as they will generally require higher illumination power and/or higher exposure times for detection (Aaron *et al.*, 2019). Genetically encoded fluorescent protein tags are an ideal tool to label and track molecules in their native environment. However, unlike organic dyes, regularly used fluorescent protein tags, such as GFP, have severe downsides for single-molecule tracking experiments due to their high photobleaching rate, low photostability and low brightness (Xia et al., 2013). To circumvent this, a combination of fluorescently labelled proteins with the photophysical benefits of organic dyes is possible using Halo and SNAP tags. These tags are, in themselves, not fluorescent, but are capable of forming irreversible covalent bonds with small ligands (Halo and DNAP ligands, respectively), with very high specificity under normal physiological conditions (Bosch et al., 2014; Keppler et al., 2003; Los et al., 2008). These ligands can have organic fluorescent dyes attached, which then allows their visualisation. Several dyes are available for this system, but of particular prominence are the Janelia Fluor dyes developed by the Lavis lab (Grimm et al., 2015). These dyes are available at a range of wavelengths and present fast labelling kinetics, high brightness, high cell permeability, high photostability and improved photon yield (Grimm *et al.*, 2015). Furthermore, these properties also allow lower illumination power

to be used during imaging, thus reducing overall phototoxicity. For the single-molecule work presented in this thesis, I used SNAP- and Halo-labelled proteins (*e.g.*, Halo-Rbp1, Halo-NDP52) to investigate their dynamic behaviour in the nucleus of cells.

As previously mentioned, another important consideration is the microscope setup for imaging. Most imaging setups can be used for single-molecule tracking – from wide-field or confocal microscopy (Martin *et al.*, 2013; Milenkovic *et al.*, 2015; Stehbens *et al.*, 2012), Total Internal Reflection Fluorescence Microscopy (TIRF) (Cai *et al.*, 2009; Harada *et al.*, 1999), Lattice Light-sheet Microscopy (Chen *et al.*, 2014) and even in some cases super-resolution techniques adapted to live cells (Cisse *et al.*, 2013; Manley *et al.*, 2008). High sensitivity and fast acquisition times (fast frame rates and low exposure times – approx. 30 ms) that provide a large number of quasi-uninterrupted trajectories points for each molecule are a necessity for good single-molecule tracking data, although in some cases very high frame rates can be counterproductive and introduce high signal-to-noise ratios (Aaron *et al.*, 2019; Abrahamsson *et al.*, 2013). Although this can be easily achieved with current technological developments, this temporal resolution requirement is a large limitation of 3D single-molecule tracking in cells.

Particles move in 3D and, therefore, three-dimensional tracking is important to fully understand molecular behaviour in cells. In 2D tracking, molecules often move out of the focal plane, leading to complete loss of signal and incomplete tracks (Aaron *et al.*, 2019). Conventional wide-field, confocal, spinning disk and light-sheet microscopes collect data from 2D focal planes. Consecutive 2D z-stacks obtained from confocal or spinning disk microscopes, can be compiled to generate 3D reconstructions, but this reduces the temporal resolution of acquisition, as the focal plane needs to change (Abrahamsson *et al.*, 2013). Out-of-focus fluorophores can be easily photobleached during 2D acquisitions and many photons will be unnecessarily rejected by the confocal pinholes, which results in loss of information (Aaron *et al.*, 2019; Abrahamsson *et al.*, 2013). Furthermore, it has been reported that sample refocusing during 3D single-molecule data acquisition (through z-stacks) can mechanically disturb the sample (Botcherby *et al.*, 2007).

To overcome these problems in 3D single-molecule tracking, Abrahamson developed a microscope – acMFM (as I have mentioned earlier in this chapter, in the context of transcription kinetics) - that allows simultaneous imaging of 9 z-planes (Abrahamsson *et al.*, 2013). My single-particle tracking work, presented in this thesis, across different projects and publications, heavily relied on the use of this technique. Briefly,

Abrahamson's approach uses a diffractive grating that automatically produces instant z-stacks of 2D projections in a single camera, following aberrant-free refocusing (Abrahamsson *et al.*, 2013). The optical system of the acMFM uses a wide-field epifluorescence microscope, a diffractive multifocal grating, to generate the multifocal image and a chromatic correction grating and prism for refocusing (Abrahamsson *et al.*, 2013). Using this system, I was able to track molecules through a depth of 4 μ m in z and 20x20 μ m in xy, which is approximately the size of the mammalian nucleus in adhered cells (dos Santos *et al.*, 2021; dos Santos *et al.*, 2020; dos Santos *et al.*, 2022; Hari-Gupta *et al.*, 2020).

Following image acquisition, especially for 3D single-particle analysis, powerful computational tools have to be applied, in order to calculate the dynamic behaviour of molecules. acMFM single-molecule tracking analysis requires a calibration procedure that i) accounts for the spacing between z-planes introduced by the physical multifocal grating (approximately 400nm spacing between each of the 9 z-planes), ii) aligns the xy planes relative to each other and iii) measures variations in detection of light for each z-plane (Aaron *et al.*, 2019; Abrahamsson *et al.*, 2013). Following this procedure, 3D tracks of particles can be reconstructed and diffusion constants of particles calculated, through mean square displacement (MSD) analysis, assuming an anomalous diffusion model (Aaron *et al.*, 2019). For the single-molecule tracking data acquired by me during the work presented in this thesis, the image processing and track analysis just described, was performed using the expertise and Matlab software packages developed by the Advanced Imaging Center team at HHMI Janelia Research Campus. I will, however, briefly describe some principles of MSD analysis and molecular diffusion.

MSD curves extracted from single-molecule data, describe the displacement of a particle at different time intervals. For a particle that is freely diffusive and moves randomly in an isotropic environment, Chandrasekhar showed that the MSD is linear over time and dependent on the diffusion coefficient (D), the time interval (Δt) and the number of spatial dimensions through which the particle can diffuse (γ) (*e.g.*, 2 for 2D, 3 for 3D) (**Equation 4**) (Chandrasekhar, 1943). Calculating the slope of MSD vs Δt curves for molecules, using a least squares regression, will allow the calculation of Diffusion coefficients.

$$\text{(Equation 4)} \quad MSD = 2\gamma D \Delta t$$

In crowded and complex environments, such as the cell, most molecules will not, however, diffuse freely. Molecules may be confined in one or more dimensions of space by membranes or through binding activity to complexes and cellular compartments or structures (Dietrich *et al.*, 2002; Kusumi *et al.*, 1993; Smith *et al.*, 1999). Alternatively,

molecules might be undergoing directed motion, as is the case of molecular motors that use ATP as a source of energy for movement (Saxton, 1994). In this case, particles undergo anomalous diffusion, as they are not equally likely to move in all directions, as expected in Brownian motion. The MSD over Δt relationship also loses linearity. This happens because, for example, at a shorter time scale a molecule might diffuse freely but later on encounter a cellular structure or other interacting molecules that will restrict its diffuse behaviour. This is called sub-diffusion and results in a decrease in the slope of the MSD curve at larger Δt . Conversely, for molecules undergoing directed motion, also called super-diffusion, the MSD slope will increase at larger Δt , as their displacement is larger than what would be expected of molecules diffusing freely (Metzler et al., 2014; Metzler and Klafter, 2000). For an anomalous diffusion model, Equation 4 can be modified to account for a component of anomalous diffusion (α), as described in **(Equation 5)**.

$$\text{(Equation 5)} \quad MSD = 2\gamma D \Delta t^\alpha$$

For the single-molecule data I obtained, analysis was performed assuming anomalous diffusion. The anomalous diffusion constant α , to which I refer in my analysis of acMFM data in the later chapters of this thesis, provides information on the type of diffusion of molecules – $\alpha=1$ signifies free diffusion (linear slope for MSD vs Δt curve), $\alpha<1$ describes sub-diffusive molecules and $\alpha>1$ super-diffusive particles (Aaron *et al.*, 2019; Metzler *et al.*, 2014; Metzler and Klafter, 2000; Saxton, 1994).

Importantly, having this detailed information on the behaviour of single-molecules within their cellular environment, also allows us to have insights into their cellular function and regulation. For example, we can investigate how the dynamic behaviour of RNAPII molecules is impacted by changes in activity of MVI; how interactions between MVI and binding partners affects MVI motion in cells; or how inhibition of transcription affects NDP52 nuclear diffusion (dos Santos *et al.*, 2020; dos Santos *et al.*, 2022; Hari-Gupta *et al.*, 2020). Furthermore, we can also interrogate the local physical environment of molecules by determining changes in the diffusive behaviour of reporter molecules (dos Santos *et al.*, 2021).

Throughout my single-molecule tracking data analysis, I sub-divide molecules into different categories: static ($D < 0.1 \mu\text{m}^2/\text{s}$), and diffusing ($0.1 \mu\text{m}^2/\text{s} > D > 5 \mu\text{m}^2/\text{s}$), or occasionally, static ($D < 0.1 \mu\text{m}^2/\text{s}$), 'slow' diffusing ($0.1 \mu\text{m}^2/\text{s} > D > 1 \mu\text{m}^2/\text{s}$) and 'fast' diffusing ($D > 2 \mu\text{m}^2/\text{s}$). These values were arbitrarily but consistently selected to represent the different populations of molecules and to measure how external stimuli affect changes to each population of molecules. Furthermore, data are truncated at 0

for diffusion coefficients values, as MSD (squared displacements) values are always positive and, therefore, it follows that D values will also be positive (Equation 5) (Aaron *et al.*, 2019).

1.6.4. Data Fitting and Statistics

In this thesis, I recurrently use similar statistical approaches to analyse my data. Briefly, I use an initial F-test to test whether groups demonstrated unequal variance. Secondly, as changes in measured values could feasibly result in mean differences that are either smaller or greater than zero, I employ a two-tailed statistical test, to allow for this possibility. In cases where analysis is performed on independent groups, testing using ANOVA, with post-hoc tests such as the Bonferroni-Holm, could also have been employed. However, I was not always able to satisfy this important condition of independence between groups, and hence I used individual t-tests as described above. An alternative and robust approach would be to also correct for the increased probability of false positive results, arising from multiple comparisons, using the Benjamini-Hochberg procedure (Benjamini and Hochberg, 1995). This has the additional advantage of allowing the false discovery rate (*e.g.*, 5%) to be specified. ANOVA post-hoc tests are sometimes considered overly conservative as post-hoc procedures attempt to limit the family-wise error rate (FWER) to less than one occurrence per test at the cost of reduced power (ability to detect true positive results) (Eichstaedt *et al.*, 2013; Krzywinski and Altman, 2014). Controlling for the proportion of false positives, using the Benjamini-Hochberg procedure, would increase the power to detect true positives.

To represent many of my quantitative data in this thesis (*e.g.*, AFM, single-particle tracking, cluster analysis), I use violin plots. I found this representation to be the most visually informative, as it provides additional information on the distribution of the data. Violin plots are a combination between box plots and kernel density plots – a non-parametric estimate of the probability function of the data. Violin plots can provide additional useful information on whether data are multimodal or on the uniformity of the data (Weissgerber *et al.*, 2019). Additionally, I always refer to mean values \pm standard error (unless otherwise clearly stated), when referring to my measurements. Whilst standard deviation can provide information on how varied and scattered a particular sample is, the standard error from the mean is far more informative, since it gives an estimate of how uncertain the mean value of a sample is, as it depends on both the standard deviation and the sample size (Altman and Bland, 2005).

2. Aims

The overarching aim of this thesis is to explore nuclear architecture and the physical organisation of the nucleus. In order to understand nuclear function, it is important to study different aspects of nuclear architecture – from the large structural characteristics of the organelle, to the smaller molecular detail, in the organisation and dynamics of the enzymatic processes that occur within its boundaries. My approach to study nuclear organisation, presented here, starts with how the organelle mechanically adapts to external and internal cues and extends into how enzymatic processes, in particular transcription, are organised at a nanoscale level. With this, I aimed to provide a global overview of nuclear function and provide insight into how nanoscale processes and their spatial organisation can impact global nuclear structure. To achieve this goal, the work performed here is subdivided into four aims, described below:

1. *To understand how different structural components of the nucleus contribute to its viscoelastic behaviour across different mammalian cell lines and how external stimuli and nuclear processes may affect nuclear mechanics.*

This aim strongly relied on the characterisation of the material properties of the nucleus using AFM, with a particular focus on the contributions of chromatin organisation to overall mechanics. Using a micro-rheology AFM method, we first compared the response of nuclei of different mammalian cells to mechanical input. Following this, we set out to explore the impact of cisplatin-induced DNA damage and DDR activation on nuclear organisation and overall mechanics.

2. *To explore the nuclear functions of MVI and investigate the molecular mechanisms of MVI activation. To understand the role of binding partners in MVI function.*

This aim utilised biochemical and cell biology approaches to explore how nuclear MVI undergoes activation - from an inactive backfolded conformation into an active unfolded dimeric motor. Several aspects of MVI were investigated during this study, including the impact of isoform splicing in the cellular distribution of MVI; binding partner selectivity and the importance of MVI motor activity in transcription.

3. *To explore how MVI activity contributes to the spatial organisation of RNAPII during initiation.*

Having explored the activation of MVI through interactions with binding partners and the potential roles of MVI in RNAPII transcription in aim 2, we then set out to investigate the role of this molecular motor in the nanoscale organisation of transcription factories. We used a multidisciplinary approach to investigate the overall impact of MVI in gene expression, cell proliferation, chromatin organisation and assembly of RNAPII clusters. This work also aimed to provide insight into the requirement for motor and anchoring activity of MVI in transcription.

4. *To provide insights into novel roles for NDP52 in the regulation of transcription.*

In aim 2, NDP52 was recurrently used as a binding partner of MVI to study the how the activity of this motor protein is regulated. Due to the high homology between NDP52 and its family member CoCoA, as mentioned in Chapter 1, in this aim, we set out to explore novel nuclear functions for NDP52, independently of MVI. We used a multidisciplinary approach to study the biochemical properties of the protein, its cellular distribution and a possible role in transcription.

3. Structural contributors to Nuclear Mechanics in DNA damage

3.1. Context of Research and Contributions

The work presented in this chapter explores the mechanical properties of the nucleus. For this, we try to answer the following questions:

- i) How do the mechanical properties of the nucleus vary spatially across the organelle and between cell types? How do lamina and chromatin contribute to the viscoelastic behaviour of the nucleus?*
- ii) How does DNA damage and activation of DDR impact nuclear mechanics? How does the mechanical state of the nucleus affect DNA damage incidence?*

This chapter comprises two different published works, as listed below. Contributions of individual authors are also detailed below.

- i) **Atomic Force Microscopy micro-rheology reveals large structural inhomogeneities in single cell-nuclei.** The first section of this chapter is described in:

Lherbette M*, [dos Santos Á*](#), Hari-Gupta Y, Fili N, Toseland CP, Schaap IAT; Atomic Force Microscopy micro-rheology reveals large structural inhomogeneities in single cell-nuclei. ([*equal contribution](#)) **Scientific Reports, 2017. 7:8116**

The mechanical properties of whole-cells have been the object of study for many years. We now know that cells behave as viscoelastic materials and actin filaments are considered one of the major contributors to overall cell stiffness. Many mechanotransduction studies have also been able to describe how changes in extracellular matrix composition/stiffness, or how cytoskeletal forces may affect transduction to the nucleus. However, less is known regarding how force transduction occurs within the nucleus. Furthermore, nuclei of different cell types have varied sizes and morphologies, but little is known how consistent their response to force and their mechanical properties are. At this first stage of the work, we set out to answer how the nuclear response to force varies between nuclei of different cell lines and at different time and length deformation scales. We determined that, qualitatively, nuclei responded similarly to force inputs, although quantitatively, the magnitude of this response varied accordingly the size of nuclei and, possibly, the degree of chromatin

confinement. We also shed light on the inhomogeneous nature of the nuclear interior, which highlighted the importance of chromatin organisation for the overall material properties of the nucleus and its viscoelastic behaviour.

Contributions

This first work was a collaborative effort between myself and Dr Christopher Toseland with Michael Lherbette and Dr Iwan Schaap at the Herriot-Watt University. Following scientific discussions with our collaborators, we agreed on using a micro-rheology approach to extract viscoelastic measurements for isolated nuclei. I performed nuclear extractions from all different cell lines for immunofluorescence experiments and for all AFM measurements. Dr Yukti Hari-Gupta and Dr Natalia Fili helped with nuclear isolation protocols. Dr Iwan Schaap and Michael Lherbette conceived micro-rheology experiments and analysis. I made several trips to Herriot-Watt University to perform AFM measurements in parallel with Michael Lherbette on both frozen and isolated nuclei and to provide guidance on experimental conditions, such as buffers, as well as sample quality. I designed swollen and shrunk nuclei experiments (supplementary information), performed all immunofluorescence imaging of nuclei and performed immunoblotting experiments to measure levels of LB1 on different cell lines. Michael Lherbette performed Finite Element Analysis (FEA) and modelling from micro-rheology data. The paper was drafted in collaboration between Dr Christopher Toseland, myself, Michael Lherbette and Dr Iwan Schaap.

- ii) **DNA damage alters nuclear mechanics through chromatin reorganisation.** The second part of this chapter is described in:

dos Santos Á, Cook A, Gough RE, Schilling M, Olszok NA, Brown I, Wang L, Aaron J, Martin-Fernandez ML, Rehfeldt F, Toseland CP; DNA damage alters nuclear mechanics through chromatin reorganisation. **Nucleic Acids Research**, 2021. **49(1):340-353**

Following this initial work, and the understanding that chromatin crosslinking and compaction are important contributors to nuclear stiffness, we decided to investigate how changes occurring within chromatin might impact nuclear mechanics. Nuclear activity, including transcription stimulation and DNA damage/DDR, leads to changes in chromatin organisation. Hence, targeting these processes would help us shed light on these questions. Here, we chose induced-DNA breaks and subsequent activation of DDR as an approach. Choosing DNA damage over stimulation of transcription, using for example serum stimulation, has several benefits. For example, time-scales

for DNA damage drug treatments are relatively short and well-defined, whilst transcription stimulation requires prior serum starvation, which leads to long experimental times. Furthermore, incidence of DNA lesions, such as DSBs, can be easily checked and quantified, through the use of DNA damage marks such as γ H2AX. DSBs are major drivers of genomic instability and cancer development; however, it is not yet clear how DNA damage itself, or downstream activation of repair pathways that induce changes to nuclear architecture, may affect the mechanical state of the nucleus. This is particularly important in a cancer and cancer-therapy context, as the mechanism of action of many chemotherapy drugs, such as cisplatin, rely on inflicting such lesions to DNA, in order to induce apoptosis. Furthermore, it is increasingly clear that there is a link between tissue and cell mechanics, cancer development, aggressiveness, metastatic behaviour and therapy-resistance.

Contributions

This work started following discussions between myself, Dr Christopher Toseland and Dr Florian Rehfeldt, our collaborator for this project, at the University of Göttingen, on the effects of DNA damage on nuclear mechanics. I led the project and coordinated the collaboration between the laboratories in Sheffield and Göttingen. For this, I designed the experiments, prepared samples and performed all AFM measurements and analysis in fully-adhered cells, initially-adhered cells and isolated nuclei, with and without drugs, whilst being hosted in the lab of Dr Florian Rehfeldt. During this time, two MSc students, Martin Schilling and Nora Olszok shadowed my work and contributed to general lab work and assisted with AFM experiments. I performed high-content screening experiments and analysis. I prepared samples for both STORM and acMFM experiments and, shared equally STORM and single-particle tracking data acquisition with Dr Christopher Toseland at Harwell Research Campus and HHMI Janelia Research Campus, respectively. Dr Christopher Toseland and I used software packages developed by Dr Jesse Aaron and the Advanced Imaging Centre at HHMI Janelia Research Campus (U.S.) for initial acMFM data analysis. During STORM data acquisition, Dr Lin Wang and Prof Marisa Martin-Fernandez and Research Complex at Harwell (U.K.) imaging facilities provided support. I provided Ian Brown at the University of Kent with cell samples for electron microscopy experiments. Ian Brown generated microtome slices of cells for electron microscopy and prepared negative stain samples. Both Ian Brown and I acquired electron microscopy images in parallel, which I then analysed. Experiments involving cells growing on polyacrylamide gels

were performed by Dr Alex Cook and Dr Rosemarie Gough. I produced a first draft of the manuscript with guidance from Dr Christopher Toseland and Dr Florian Rehfeldt, which then incorporated additional comments from all other authors.

3.2. Manuscripts

(see below)

3.2.1. Manuscript 1 - Atomic Force Microscopy micro-rheology reveals large structural inhomogeneities in single cell-nuclei.

SCIENTIFIC REPORTS

OPEN

Atomic Force Microscopy micro-rheology reveals large structural inhomogeneities in single cell-nuclei

Received: 19 April 2017
Accepted: 12 July 2017
Published online: 14 August 2017

Michael Lherbette¹, Ália dos Santos², Yukti Hari-Gupta², Natalia Fili², Christopher P. Toseland^{1,2} & Iwan A. T. Schaap^{1,2,3}

During growth, differentiation and migration of cells, the nucleus changes size and shape, while encountering forces generated by the cell itself and its environment. Although there is increasing evidence that such mechanical signals are employed to control gene expression, it remains unclear how mechanical forces are transduced through the nucleus. To this end, we have measured the compliance of nuclei by applying oscillatory strains between 1 and 700 Hz to individual nuclei of multiple mammalian cell-lines that were compressed between two plates. The quantitative response varied with more than one order of magnitude and scaled with the size of the nucleus. Surprisingly, the qualitative behaviour was conserved among different cell-lines: all nuclei showed a softer and more viscous response towards the periphery, suggesting a reduced degree of crosslinking of the chromatin. This may be an important feature to regulate transcription via mechano-transduction in this most active and dynamic region of the nucleus.

In eukaryotic cells, the nucleus houses the genomic material and transcription machinery that allows the cell to develop and perform its role. In different cell types, nuclei show diverse morphology and diameters that can range from 5 to 20 μm . The densely packed nucleus is the largest organelle and it is relatively rigid compared to the rest of the cell body. Therefore, its properties are a dominating feature in whole cell mechanics, not to mention a limiting factor in processes such as cell migration¹. For example, the migration of melanoma cells was shown to be reduced by artificially stiffening their nuclei². Overall, the mechanical properties of the nucleus, such as its deformability under external forces, play a key role in enabling the morphological dynamics of cells.

The mechanics of the nucleus are defined by its architecture: the exterior lamina and interior chromatin. The nuclear lamina is important in controlling the shape of the nucleus^{3,4}. Directly under the nuclear envelope, it consists of a filamentous network, several tens of nanometres thick, made up of type A (A and C) and B (B1 and B2) lamin proteins. Diseases, such as cancer, are associated with changes in the lamina composition and introduce large-scale morphological alterations to the nucleus⁵. The resulting variations in nuclei stiffness have been related to increased motility and metastatic potential². A more pliable nucleus would help to squeeze through tissues during invasion, although it remains unclear if their stiffness is systematically reduced to enhance their invasive properties.

The nucleus' interior is largely occupied by chromatin, which is comprised of DNA wrapped by histone complexes. Transcription is not uniformly distributed within the nucleus, despite the presence of the machinery throughout the organelle. It has been shown that transcription activity mostly occurs in the outer half of the nucleus, approximately from half to three-quarters of the nucleus radius⁶. Re-localisation of genes from the periphery into the nucleus interior is hypothesised to be a mechanism to activate expression⁷. The chromatin organisation within these regions is not yet completely understood but appears to rely on well-defined spatial positioning of genes and chromosome territories⁸. Historically, the chromatin is organized in heterochromatin

¹Institute of Biological Chemistry, Biophysics and Bioengineering, School of Engineering and Physical Sciences, Heriot-Watt University, Edinburgh, EH14 4AS, UK. ²School of Biosciences, University of Kent, Canterbury, CT2 7NJ, UK. ³Present address: SmarAct GmbH, D26135, Oldenburg, Germany. Michael Lherbette and Ália dos Santos contributed equally to this work. Correspondence and requests for materials should be addressed to C.P.T. (email: c.toseland@kent.ac.uk) or I.A.T.S. (email: schaap@smaract.com)

and euchromatin, regions. Heterochromatin is most abundant at the periphery, closely associated with the nuclear lamina⁹. It was initially associated with regions of no transcription due to its high packaging density. However, it has been shown that transcription can take place in heterochromatin but is repressed by RNAi¹⁰. The majority of the chromatin is in the form of transcriptionally active euchromatin. However, there are still ambiguities as to how well all these regions are defined, regulated and how they change through cell signalling or stress pathways. Functional differences within the chromatin are likely a consequence of different organization details that enhance or inhibit transcription. Interestingly, because chromatin is such a closely packed polymer, any variation that affects its crosslinking will also have a large effect on its mechanical response¹¹.

Forces within the cell can mechanically perturb the nucleus^{12,13}, which in turn affects gene expression^{14,15}. Here, the nucleus functions as a mechano-sensor. However, how forces are converted into deformation of the nucleus and how this leads to changes in transcription is not clear. Because lamins, whose localization is not restricted to the nuclear lamina³, can bind DNA, this could provide a direct mechanism for the modulation of gene expression^{16,17}. In addition, force-induced rearrangements of the chromatin¹⁸ itself could act as a mechanism to regulate transcription. However, as cells constantly exert forces upon the nucleus¹⁹, there must be significant control of this process. In other words, the nucleus must have the ability to differentiate force signals to prevent continuous aberrant changes in gene expression. One way to achieve this is a mechanical response that is sensitive to the time- and length scales of the induced deformations.

The mechanical properties of single cells and nuclei have been intensely studied. Whole cells have been shown to behave as a non-homogeneous material with a complex viscoelastic response. Cells respond stiffer when deformed at higher frequencies and it is widely agreed that their stiffness k obeys a weak power law: $k(f) = Af^\alpha$, where f is the frequency, A a scaling factor and α the exponent^{20–22}. The value of the α lies in the range 0.1–0.35, and depends on how much the cell is deformed²³. At deformation frequencies above ~100 Hz, the value of α increases to 0.75 and above^{24–26}. This increase of α in a cell-like fashion can be reproduced with cross-linked networks of actin filaments^{27,28}. Modelling of such semi-flexible polymer networks identified a frequency dependence of the effective stiffness of individual polymers; because the longitudinal bending modes of single filaments need a certain time to relax, this leads to a higher effective stiffness on short time scales which results in $\alpha = 0.75$ ²⁹. In combination with cross-linking of the filaments, this can lead to the existence of various power law regimes³⁰.

For the nucleus, such a consensus picture is still missing, partly because of its smaller size and also because it is difficult to separate its response from the rest of the cell, in whole-cell measurements. Nevertheless, it has become clear that both the nuclear lamina^{31,32} and the chromatin contribute^{33–35}. At different deformation length-scales, the response can be either dominated by the chromatin or lamina³⁶. Measurements on nuclei lacking lamins showed that the chromatin responds nearly elastically to small (0.1 μm) deformations induced with optical tweezers¹⁹. At much larger deformations, induced with micropipettes, the chromatin showed a more pronounced viscous response and even plastic deformations³⁷.

To quantify the visco-elastic response of isolated nuclei at a large bandwidth of length- and time-scales, we adapted an atomic force microscopy (AFM) micro-rheology method, previously developed to measure the dynamic response of whole cells^{38,39}. Individual nuclei were compressed between two plates and subjected to small oscillations at frequencies between 1 and 700 Hz. The advantage of this approach is that a single measurement can reveal the response at different time scales and that both the elastic and viscous contribution can be separated. To probe the different regions of the nucleus, the measurements were repeated at different deformation length-scales that were mapped to different nuclear regions with finite element analysis (FEA). To identify conserved features of the mechanics of nuclei, measurements were performed on four common mammalian cell lines. The insight gained in the mechanical response of the nucleus at different time- and length-scales will be helpful to interpret deformations that are observed in nuclei of migrating and differentiating cells. In addition, we have identified spatial differences of the mechanics within the nucleus and possibly in the chromatin structure, shedding light on the relation between mechanics and transcription.

Results

Measuring nucleus mechanics under compression between two plates. We used nuclei isolated from the HeLa mammalian cell line as our model system. During the measurements, single nuclei were compressed between the supporting glass coverslip on one side and the tip-less cantilever on the other. To convert the measured stiffness into a Young's modulus that describes the intrinsic elastic properties of the nucleus, we first needed to know the contact conditions between the nucleus and both surfaces. Figure 1a,b show the microscopic top- and side-view of the nucleus, respectively, before and during the compression experiment. This was used to understand the contact boundary conditions and thus allowed us to choose which mechanical model to apply. If the nucleus behaves like a sphere compressed between planar surfaces, Hertzian contact mechanics can be used to extract the Young's modulus. However, this commonly used approach ignores two aspects of the experimental conditions that can be seen in the microscopic images: i) the nuclei showed an initial deformation; the bottom part is flattened because of adhesion of the nucleus to the supporting surface (Fig. 1b left), and ii) the AFM cantilever is tilted 10° with respect to the supporting surface (Fig. 1b right). Both aspects are missing in the Hertz theory, but would potentially affect the calculated values.

Adhesive contact. We visualized the shape of five adhered nuclei, using our previously described fluorescence microscope combined with AFM⁴⁰. The nuclear membrane was labelled and a stack of images at different focal planes was recorded with fluorescence microscopy, which allowed us to generate a 3D representation of the nucleus (Fig. 1b; see methods). This was used to measure the adhesive contact radius between the nucleus and the supporting surface. Figure 1c shows the adhesive contact radii for the five nuclei: the measured radius depends on the size of the nucleus and ranges between 3 and 6 μm . Due to the small vibrations caused by the re-focussing to record at different focal planes this method could not be applied during the mechanical measurements.

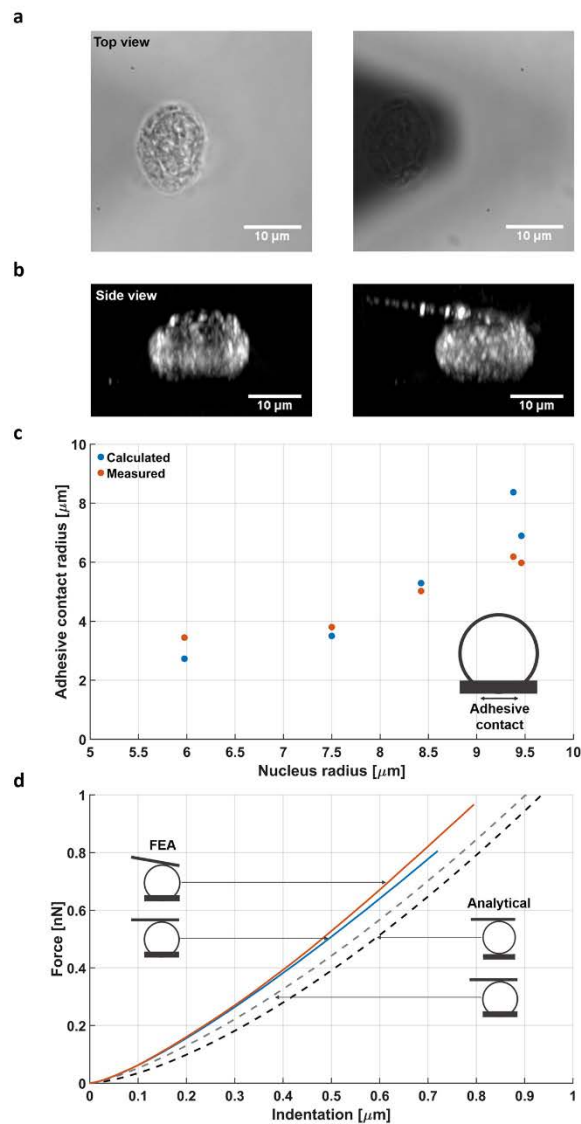


Figure 1. Defining contact conditions during compression of the nucleus. (a) Left: top-view microscopy image of the adhered nucleus. Right: the tip-less cantilever is brought down to compress the nucleus. (b) Left: side-view projection reconstructed from a stack of fluorescent microscopy images. The adhesive contact between nucleus and supporting surface is clearly visible. Right: the same nucleus under compression after the cantilever has been brought down. (c) The measured adhesive contact radii of five nuclei of different sizes (red). The calculated radii based on the height/width ratio agree within $\sim 15\%$ (blue). (d) Force versus indentation plots for comparing the calculated compression of a sphere with $E = 2$ kPa, assuming different contact conditions. Shown are two analytical solutions: the Hertzian contact (black dash line) and an extension of this model that includes the adhesive contact⁴² (grey dash line). The other two curves are from FEA and show the compression of a sphere with adhesive contact with a parallel (blue solid line) and tilted cantilever (red/orange solid line).

	HeLa	HeLa (fresh)	IMR5	HEK	MCF7
Height [μm]	10.91 \pm 0.59	16.20 \pm 0.48	6.19 \pm 0.35	8.31 \pm 0.26	15.95 \pm 0.66
Width [μm]	12.73 \pm 0.54	17.18 \pm 0.39	8.32 \pm 0.16	10.06 \pm 0.18	17.99 \pm 0.51
Height/Width	0.86 \pm 0.03	0.95 \pm 0.03	0.77 \pm 0.02	0.83 \pm 0.03	0.88 \pm 0.03
n	23	21	21	29	20

Table 1. Dimensions of all measured nuclei. All values are mean \pm s.e.m. The height was obtained with AFM. The width was obtained optical microscopy by taking the mean of the short and long axes.

Furthermore, the fluorescent labelling might affect the mechanical properties. So we tested an alternative method to obtain the adhesive contact. As shown in Fig. 1b, adhesion of the nuclei on the surface results in a decrease in height, from which in principle the adhesive contact radius can be extracted. To obtain the height reduction of each of the nuclei we combined optical microscopy for the measurement of the lateral dimensions and AFM for measuring the height. The ratio of the height and width was then used to calculate the contact radius (see methods). Figure 1c shows that the calculated adhesion radii for the five nuclei are in good agreement with the experimental values obtained from the reconstructed fluorescent cross-sections. For subsequent analysis of all nuclei (Table 1), we used the ratio of the height and width of each individual nucleus to obtain its adhesion contact radius.

Tilt of the cantilever. The second surface contact point of the nucleus occurs at its interface with the cantilever. Because this contact occurs upon initiation of the experiment, we assumed this contact radius to increase from zero according Hertzian contact mechanics. We initially attempted to visualise this, using the reconstructed fluorescent side-view projections at different forces. However, our results were not clear because the cantilever was poorly defined and it was difficult to maintain a constant force during image acquisition (data not shown). Because the cantilever has a 10° angle with respect to the supporting surface, there will be a horizontal force component that will affect the measured stiffness. To assess the consequences, we performed FEA of the experimental geometry using a parallel or a 10° tilted cantilever (see methods). Figure 1d shows that the difference between the two cantilever geometries is relatively small ($\approx 10\%$) in the simulated force versus indentation curves. This is consistent with previous experiments on whole cells in which wedged cantilevers (to achieve a 0° angle) were compared with tilted cantilevers⁴¹.

We compared the FEA, taking into account the adhesive contacts with the standard Hertz model. Although, this model ignores the aforementioned adhesive contact and the 10° angle of the cantilever, we found that the differences are relatively small. Recently, an analytical correction for the Hertz contact mechanics model was presented to include the adhesive contact area on spherical particles⁴², which is also plotted in Fig. 1d. Although this model still predicts a slightly softer response ($\approx 25\%$) than the FEA, we chose, for the sake of reproducibility, to use this modified Hertz contact model to quantify the Young's modulus of the following experiments. Hereafter, we will refer to the modulus as the complex Young's modulus (E^*) to indicate that this can contain both elastic (E') and viscous (E'') components.

The elastic modulus of the nucleus at small and large deformations. After establishing the experimental contact conditions and the relation between indentation and E^* , we performed AFM micro-rheology to measure the nucleus stiffness over a wide range of frequencies (see methods). The inset in Fig. 2a shows that, after the cantilever was brought down to compress the nucleus, it was then driven at a constant 25 nm amplitude at a frequency that increased from 1 to 700 Hz. Due to the compliance of the nucleus, the actual deflection at the end of the cantilever (Fig. 2a) will be less than the drive amplitude. The deformation and stiffness of the nucleus was calculated from the cantilever deflection (see methods), after which the aforementioned modified Hertz contact model was used to convert stiffness into E^* .

First, we focused on E^* at low frequency (1 Hz), which is comparable to the speed of conventional AFM indentation experiments. Compared to a whole cell, the nucleus would be expected to have a more homogeneous structure. As a consequence, the mechanical properties of an isolated nucleus would be expected to be more constant over different length scales. In the case of whole cells, which have a very inhomogeneous structure, we previously found E^* to increase two-fold when the indentation increased from 0.2 to 1 μm ²³. To test this for the nuclei, we measured their mechanical response at different deformations by varying the force from 1 to 15 nN. This led to deformations between 0.5 and 2.8 μm , which corresponds to deformations between 8 and 44% of the radius, when an average nucleus radius of 6.4 μm (Table 1) is taken into account. Interestingly, as Fig. 2b shows, E^* is not constant, but increases threefold at higher deformations, from 2 kPa at 0.5 μm deformation to 6.5 kPa at 2.6 μm deformation. The dependence of E^* on the deformation length-scale indicates substantial spatial differences in the organization of the nucleus interior.

The dynamic response of the nucleus between 1 and 700 Hz. The stiffness and E^* of the nuclei increase as a function of the frequency (Fig. 2b). Interestingly, the mode of increase depended on the deformation length-scale. At low deformation, the slope of the curve is non-constant but increases with the frequency. At high deformation, the slope is nearly constant. Because the curves are plotted on a double logarithmic scale, a constant slope means that the curve follows a power law with a constant exponent: $E^*(f) = Af^\alpha$, where f is the frequency, A the modulus at 1 Hz and α the exponent. At high deformation, α increases from 0.24 at frequencies below 100 Hz to 0.38 at higher frequencies. Previous micropipette aspiration measurements, where chromatin was subjected

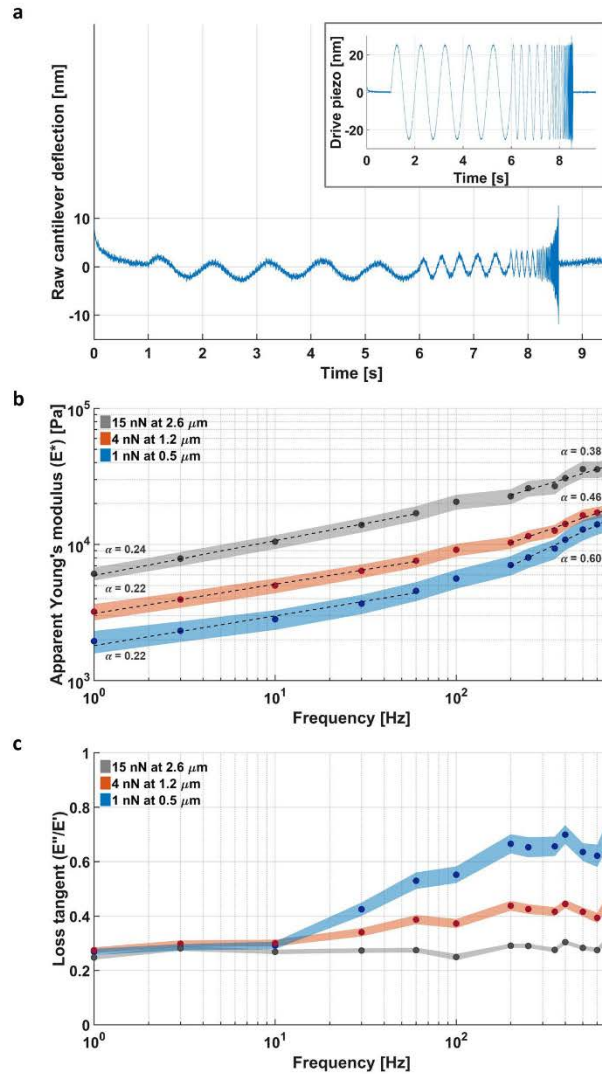


Figure 2. Measuring the response of the nucleus at different deformation length- and time-scales. (a) Inset shows the motion of the piezo-element that moves the base of the cantilever with increasing frequencies at a constant amplitude of 25 nm. The main panel shows the cantilever bending at its free end. Higher bending means more resistance, which can be induced by the compliance of the nucleus but also by the drag of the surrounding buffer. The latter is corrected for in the analysis. (b) At low deformation rates of 1 Hz, E^* is not constant but increases threefold when the indentation depth is increased from 0.5 to 2.6 μm . At higher deformation rates up to 700 Hz, the dependency on the indentation remains. In addition, the modulus increases multi-fold with frequency. E^* below and above the estimated threshold of 100 Hz had been fitted with a power law (dashed black line). The slope at low and high frequency are 0.22 and 0.60 at 1 nN, 0.22 and 0.46 at 4 nN and 0.24 and 0.38 at 15 nN. (c) The complex Young's modulus can be decomposed in its viscous (E'') and elastic (E') components. The ratio E''/E' (loss tangent), shows that the viscous contribution is small at high deformations and low frequencies. Only at small deformations and higher frequencies does the viscosity contribution becomes more pronounced. The data is shown as the mean \pm standard error of the mean of the log transformed data (shaded area).

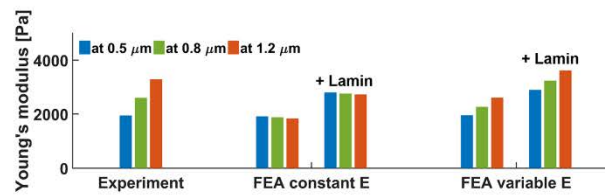


Figure 3. Modelling the spatial variation of the nucleus stiffness. Left: The experimental values, show a rise of E^* at increasing deformation (the response at 15 nN is not shown because the resulting high deformation proved to be very difficult to simulate numerically). Middle: When the nucleus is modelled with FEA as a sphere with a constant Young's modulus, the calculated values after analysis are nearly constant. Adding a stiff external layer, representing the nuclear lamina increases the absolute stiffness but does not introduce the deformation length-scale dependency. Right: Here, the modelled nucleus has a Young's modulus that linearly decreased from the centre to the periphery (from 10 to 0.3 kPa). The analysed values for E now increase with the deformation length-scale, similar as the experimental values. This is independent of the nuclear lamina.

to large multi-micrometer deformations, have shown that this chromatin power law rheology extends to much longer time-scales (100s of seconds) with $\alpha \approx 0.3^{33}$. At low deformation, we found the increase of α to be larger, up to 0.6 at high frequencies. A larger α corresponds to a steeper curve, therefore the higher value of α shows that at low deformations the nucleus is more sensitive to changes in the deformation rate.

To assess the contribution of viscosity, the complex Young's modulus was decomposed into its elastic E' and viscous components E'' (see methods and Supplementary Fig. S1). Figure 2c shows the ratio between viscosity and elasticity, namely the loss tangent. At high deformation, the contribution of the viscosity is small (ratio of 0.3) and constant along the entire frequency range. However, at low deformation, the viscous contribution increases up to a ratio of 0.7 at higher frequencies. The differences observed in slopes and the viscous contributions measured at different deformations, further support the presence of spatial differences in the organization of the nucleus as a whole, and potentially within the chromatin.

Modelling the spatial variation of stiffness for the nucleus. For small deformations, which would be limited to the outer region of the nucleus, E^* is low, while at higher deformations, reaching to the interior of the nucleus, E^* is much larger. To understand how the organization of the nucleus would have to vary to explain the observed response, we formulated a FEA model where E' is varied as a function of the distance to the nucleus centre. Viscosity is not considered in the model. Figure 3 shows that when E' is kept constant at 2 kPa, the calculated values for E' (obtained by analysing the simulated stiffness curves) remain nearly identical. When E' is linearly increased towards the centre, the calculated values for E' increase at larger deformations. Although it is clear that the Young's modulus increases towards the centre, a linear increase is a simple assumption and the real distribution of stiffness is likely more complicated. The presence of a stiff nuclear lamina does not affect the qualitative findings. By compressing the nucleus between two plates, we avoid localized bending of the nuclear lamina which reduces its mechanical influence in our experimental geometry. Simulations in which we included the nuclear lamina using reported elasticity values^{31,45} show that, although the absolute stiffness increases, the dependence on the interior composition remains (Fig. 3). Remarkably, the required increase of E' in the model to reproduce the experimental values is more than one order of magnitude, which is a strong indicator that chromatin, as the main component of the interior, is differently organized towards the periphery of the nucleus. The looser organization of the chromatin at the outer region results in a lower Young's modulus and a higher viscous contribution.

Comparing nuclei of different cell lines. So far we have used HeLa nuclei as our model system, however, nuclei from different cell types have diverse morphologies, which may have a large effect on their mechanical properties. Earlier work showed that all major lamin subtypes play roles in maintaining nuclear shape^{4,44}. We compared nuclei from HeLa, IMR5, HEK293T and MCF7 cells using immunofluorescence against lamin B (see methods) as a marker for the lamina. Nuclei are shown in Figure 4a and their respective size are displayed in Fig. 4b. Figure 4a shows that the smaller nucleus, IMR5, has a better-defined lamina than the largest one, MCF7. The thickness, measured from the fluorescent images, was almost double (1.0 vs. 0.65 μm ; Fig. 4c). For an accurate determination of the lamina quantity, we quantified the relative expression levels by western-blot. Figure 4d essentially shows identical protein content. These observations are consistent and showed that the amount of lamin B per nucleus is almost constant but organized as a thicker layer for smaller nuclei. A thicker lamina may enable greater compression of the chromatin to generate a higher packing density, as would be required in smaller nuclei, assuming the same chromatin content between small and large nuclei. An outlier to this conclusion is the HEK293T nuclei which displayed thicker lamina than expected. However, there are likely to be cell-to-cell and cell-type variations to fit with a general trend.

Despite the difference in nuclear size, the quantity of chromatin inside, at least based on karyotype, will be approximately identical in the different mammalian cell lines tested here. Therefore, the larger MCF7 nuclei will have their chromatin less densely packed which should result in a lower Young's modulus. To test this, we compared the stiffness of nuclei obtained from four different cell lines. Figure 4e shows that the main determinant for E^* is the size of the nuclei, small nuclei are much stiffer than large nuclei. Although the packing density of

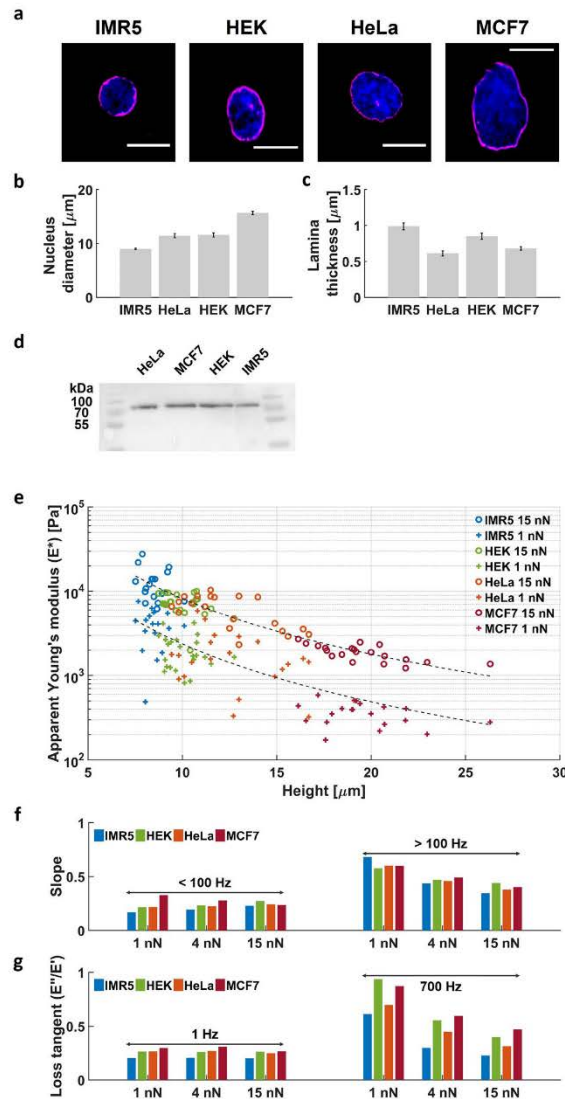


Figure 4. Comparing nuclei of different cell lines. (a) Example images from immunofluorescence staining against Lamin B with Hoechst staining for DNA in isolated IMR5, HEK293T, HeLa and MCF7 nuclei. Scale bar = 10 μm . (b) Diameter of the isolated nuclei determined from the immunofluorescence staining, 8.9 ± 0.2 (n = 33), 11.4 ± 0.4 μm (n = 18), 11.6 ± 0.4 μm (n = 20) and 15.6 ± 0.3 μm (n = 20), IMR5, HeLa, HEK293T and MCF7 respectively. Error bars are s.e.m. (c) The thickness of lamin B layer, estimated from the deconvoluted images, 0.99 ± 0.05 (n = 18), 0.62 ± 0.04 (n = 33), 0.85 ± 0.04 (n = 20) and 0.68 ± 0.02 (n = 20), IMR5, HeLa, HEK293T and MCF7 respectively. Error bars are s.e.m. (d) Western blot against lamin B in the nuclear extract from the cell lines used in the study. Samples were normalised to total protein content in the nuclear extract. (e) E^* scales with the inverse of the nucleus size as shown by the fit ($E^* = r^{-\alpha}$ with $\alpha = -2.21$ and -2.16 at 1 nN and 15 nN respectively). Nuclei appear always softer when subjected to smaller deformations. Individual responses can be found in Supplementary Figure S1. The number of nuclei investigated per cell line is indicated in Table 1. (f) All nuclei show a slope α of the modulus vs. frequency response that only increased when probed at small deformations at high frequency. (g) All nuclei show a loss-tangent that only increased when probed at small deformations at high frequency.

chromatin has a very large effect (order of magnitude) on the absolute Young's modulus, the difference between low and high deformations remained. This indicates that the softening towards the outside, as observed for HeLa nuclei, is preserved among all tested species and does not depend on the packing density.

This raises the question of whether the other qualitative features that we observed for HeLa nuclei are also conserved, namely the mode of increase of E^* (quantified by α in Fig. 2b) and the increased viscous contribution at the outer region. Figure 4f shows the slopes (α) of the E^* versus frequency plots of all different nuclei was nearly identical and unrelated to their size, with α always being highest at small deformation and high frequency. Also, the viscous properties are comparable for all nuclei, with viscosity always being most pronounced at small deformations (Fig. 4g). Although the isolated nuclei, that were stored at -80°C are susceptible to buffer composition and experimental conditions, their qualitative response is remarkably conserved (Figure S2). Despite the large differences in size and absolute stiffness, all tested nuclei exhibit a comparable qualitative response, which indicates conserved features in their structural organization.

Discussion

We have measured the visco-elastic properties of isolated mammalian nuclei by using AFM micro-rheology. By varying both the deformation length- and time-scales in combination with FEA, we could identify large spatial inhomogeneities in the structure of the nucleus. Our findings indicate there are spatial variations in the organization of the chromatin itself, rather than a homogeneous chromatin interior enveloped in a stiff lamina, which contribute to the overall mechanical properties.

All nuclei, small and large, showed a similar qualitative response. The outer region, several microns thick, is softer, more viscous and shows the strongest dependency of E^* on the rate of deformation. The core of the nucleus is always stiffer and predominantly elastic. What is the cause and consequence of these two zones within the nucleus? Crosslinking has a large effect upon the mechanical response of a polymer. An increasing number of cross-links will increase the stiffness of a polymer suspension and reduce the proportional contribution of viscosity^{41, 45}, which is fully consistent with our measurements. With respect to chromatin, crosslinking is achieved through condensation by condensin protein complexes and therefore, our data suggest that various levels of DNA condensation exist.

It is tempting to link crosslinking to the transcriptional activity inside the nucleus. Regions of high transcription activity have been localized in the outer half of the nucleus⁴, while also the regulation of transcription by gene repositioning takes place in the outer region⁴⁶. Thus, the mechanically looser organization of this part of the nucleus may be required to facilitate chromatin dynamics. In the nuclear core, transcription and its regulation may be inhibited by a high degree of cross-linking, which additionally also offers an increased resistance against mechanical perturbations. The reduced stiffness of the outer region of the nucleus also provides a higher sensitivity for mechanical stimuli to facilitate mechano-sensing. Furthermore, we found the outer region to have higher sensitivity for the deformation rate: low frequencies are more easily transmitted than high frequencies. This time-scale dependent force transduction may help the nucleus to separate short-lived perturbations from consistent mechanical signals which would protect against sporadic changes in gene expression.

The absolute stiffness of the nuclei varies by an order of magnitude when compared between different cell-lines. Thus, the chromatin density, likely controlled by the nuclear lamina, appears much less critical for its proper functioning. An interesting consequence is that, as long as the nucleus maintains the aforementioned gradient of crosslinking, this may equip the cells with a mechanism to tune the size and correlated stiffness of their nuclei to match cellular function.

While isolated nuclei provide a means to precisely determine their intrinsic mechanical properties, the experimental environment is very different to the cell. However, our observation of two mechanical zones within the nucleus was independent to shrinking and swelling (Figure S2) suggesting this property is maintained. The densely packed cytoplasm exerts forces upon nuclei which may perturb both their shape and size, which would in turn change the mechanical properties. However, this is cell line dependent whereby HEK293T cells display no change in size⁴⁷. Conversely HeLa cell nuclei have an elongated morphology of $10\text{--}20\ \mu\text{m}$ with a height as long as $4\ \mu\text{m}$ when grown in 2-dimensional culture. In the case of HeLa cells, the compression of the nucleus may reduce the inhomogeneity between the inner nucleus and periphery due to the reduction in volume. Intriguingly, nuclei within cells grown in 3-dimensional culture to mimic tissue grown adopt the spherical shape, as observed in the isolated nuclei. Therefore, the consistent visco-elastic properties of the several mammalian nuclei which we have observed here are likely to be conserved within the tissue microenvironment.

Methods

Chemicals and Reagents. Unless stated, all reagents were from Sigma Aldrich, UK.

Nuclei isolation. HeLa, MCF-7, IMR-5 and HEK293T Cell lines were cultured at 37°C and 5% CO_2 , in Gibco MEM Alpha medium with GlutaMAX (no nucleosides), supplemented with 10% heat-inactivated Fetal Bovine Serum (Gibco), 100 units/ml penicillin and 100 $\mu\text{g}/\text{ml}$ streptomycin (Gibco).

The nuclei isolation protocol was adapted from the Collas Lab protocol⁴⁸. Cells, plated at 90% confluency, were trypsinized in 0.05% trypsin/EDTA (Invitrogen) and harvested by centrifugation at $415 \times g$, at 4°C . Cells were washed once with ice-cold phosphate-buffered saline (PBS), re-suspended in ice-cold Hypotonic Buffer (10 mM HEPES pH 7.5, 2 mM MgCl_2 , 25 mM KCl supplemented with 1 mM phenylmethylsulfonyl fluoride (PMSF), 1 mM dithiothreitol (DTT) and 1x Halt Protease Inhibitor Cocktail (Thermo Fisher Scientific)) and harvested by centrifugation at $415 g$, at 4°C . Cells were then re-suspended in ice-cold hypotonic buffer and incubated for 1 hr on ice. Cells were then homogenized on ice with a glass Dounce homogeniser (Wheaton) by performing 100–150 strokes, until 90% lysis was achieved. Cell lysis was assessed on the TC20 Automated Cell Counter (Bio-Rad). Cell lysate was supplemented with 125 μl of 2M sucrose solution per ml of lysate and mixed well by inversion. The

lysate was centrifuged for at 4 °C at 184 g using a swinging bucket rotor. The pellet, which corresponded to isolated nuclei, was further cleaned by re-suspension in ice-cold Hypotonic Buffer plus 250 mM sucrose and further centrifugation at 4 °C at 184 g. The nuclei pellet was re-suspended in freezing medium (Hypotonic Buffer plus 70% glycerol) before storage at −80 °C. All measurements were performed on nuclei that were stored at −80 °C. As control we also performed measurements on nuclei that were freshly prepared. This data, included in Figure S2, shows that although the process of freezing induces shrinkage of the nuclei, the mechanical properties are fully consistent.

AFM sample preparation. The sample was thawed and diluted 100x in Hypotonic Buffer. 100 μ l was pipetted onto a 25 mm round coverslip that was mounted in the AFM coverslip holder, and left 5 minutes to adhere before the sample was washed with 500 μ l Hypotonic Buffer (to remove any unfixed nuclei).

For the experiments in which the nuclear membranes were fluorescently labelled, 1 μ l of a $10^4\times$ diluted BODIPY[®] 500/510 C4, C9 stock suspension (ThermoFisher; 2 mM in dimethyl sulfoxide) was added to the diluted nuclei.

Optical microscopy. Each nucleus was imaged with the integrated inverted optical microscope. Brightfield imaging was performed to measure the lateral dimensions of the nuclei with an oil immersion objective (Nikon; $100\times$ 1.49 NA). Fluorescence imaging was performed with a water immersion (Nikon; $60\times$ 1.27 NA) to achieve a constant focus quality throughout the sample which is important to obtain an accurate 3D reconstruction. The images were recorded with an EM-CCD camera (Luca S-659, Andor technology, UK). The magnifications were calibrated with a calibration grid: 97.5 nm/px for brightfield and 166 nm/px for fluorescence.

3D image reconstruction from fluorescence microscopy images. To measure the adhesive contact radius and initial deformation of the nucleus we performed z-stacks through adhered HeLa nuclei that were fluorescently labelled. The sample was excited with a 488 nm laser and a stack of 150 images spaced by 166 nm was recorded for each nucleus. A custom written routine in LabVIEW (National Instruments, TX, USA) was used to control the objective scanner (PIFOC, Physik Instrumente, Germany) and to trigger frame acquisition on the camera (50 ms exposure time).

The z-stacks were post-processed using *ImageJ* and the *DeconvolutionLab* plugin⁴⁹ to perform a 3D deconvolution. The point spread function was calculated using the Born and Wolf model⁵⁰. For the figures we used side-view projections through deconvolved z-stacks using the maximum intensity values.

The adhesion contact radius was quantified by manually plotting a circle around the nucleus to get the intersection with the supporting surface.

Immunofluorescence and imaging. Purified defrosted nuclei were immobilised on Poly-D-lysine (MW 70,000–150,000, Sigma) coated 13 mm glass coverslips (ThermoFisher). Immobilised nuclei were stained for 10 min at 37 °C with 1 μ g/ml Hoechst 33342 (ThermoFisher) in Hypotonic Buffer. Stained nuclei were fixed in 4% (w/v) paraformaldehyde (PFA) and residual PFA was quenched with 50 mM ammonium chloride. Nuclei were permeabilised and simultaneously blocked with 0.1% (v/v) Triton X-100 and 2% (w/v) BSA in Tris-buffered saline (TBS). Nuclei were then immunostained against the endogenous lamin B with the rabbit anti-Lamin B1 polyclonal antibody (Abcam) and subsequently the donkey anti-rabbit Alexa Fluor 555-conjugated antibody (1:500, Abcam), both diluted in 2% (w/v) BSA in TBS. Coverslips were mounted on microscope slides with Mowiol (10% (w/v) Mowiol 4–88, 25% (w/v) glycerol, 0.2 M Tris-HCl, pH 8.5), supplemented with 2.5% (w/v) of the anti-fading reagent DABCO (Sigma).

Nuclei were visualised using Olympus IX71 microscope with PlanApo 100xOTIRFM-SP 1.49 NA objective mounted on a PIFOC z-axis focus drive (Physik Instrumente, Karlsruhe, Germany), and illuminated with an automated 300W Xenon light source (Sutter, Novato, CA) with appropriate filters (Chroma, Bellows Falls, VT). Images were acquired using a QuantEM (Photometrics) EMCCD camera, controlled by the Metamorph software (Molecular Devices). The whole volume of the nuclei was imaged by acquiring z-sections with a spacing of 200 nm. Images presented here correspond to a middle section of the nucleus. Images were deconvolved with the Autoquant X software applying blind deconvolution and analysed by *ImageJ*. The nuclei diameter and lamina thickness was calculated by plotting *x* and *y* intensity profiles across the nuclei. Point-to-point distances were then measured across the peaks and nuclear body. The quoted values were calculated from the average of the *x* and *y* values.

Immunoblot analysis. Nuclei lysates were prepared by direct lysis of 4×10^6 freshly defrosted nuclei in NuPAGE sample buffer, followed by 5 minutes sonication. The total protein concentration of the nuclei fraction was determined by Bradford Assay (Sigma) following the manufacturer's instructions. Nuclei were heat-denatured and resolved by SDS-PAGE on an 8% acrylamide gel. Proteins were transferred to 0.45 μ m PVDF membrane using semi dry Power Blot Cassette (Thermo scientific). The membrane was blocked for 2 hours at room temperature with 5% (w/v) skimmed dried milk, 0.1% (v/v) TWEEN-20 in TBS and then probed against lamin B by incubation with the rabbit anti-Lamin B1 polyclonal antibody (Abcam) and subsequently a goat anti-rabbit antibody coupled to horseradish peroxidase (Abcam). The bands were visualised using the ECL Western Blotting Detection Reagents (Invitrogen) and the images were taken using Syngene GBox system. Images were processed in *ImageJ*.

Contact mechanics model. For a sphere that gets compressed between two planes, the indentation (δ) as function of the force (F) is given by the double contact Hertz model in eq. 1⁴². R_n is radius of the nucleus, E the Young's modulus and ν the Poisson ratio which was set at 0.4.

$$\delta(F) = 2 \left(\frac{3F(1 - \nu^2)}{4E\sqrt{R_n}} \right)^{\frac{2}{3}} \quad (1)$$

To include the adhesive contact radius between the nucleus and the supporting surface as seen in the experiments we used a modified Hertz contact model as derived by Glaubitz *et al.*⁴². Eq. 2 includes the surface adhesion energy γ , which is a function of the adhesive contact radius (R_c ; eq. 3).

$$\delta(F) = \left(\frac{3F(1 - \nu^2)}{4E\sqrt{R_n}} \right)^{\frac{2}{3}} + \left(\frac{3(1 - \nu^2)(F + 6\gamma\pi R_n + \sqrt{12\gamma\pi R_n F + (6\gamma\pi R_n)^2})}{(4E\sqrt{R_n})} \right)^{\frac{2}{3}} - \left(\frac{9\gamma\pi(1 - \nu^2)}{E} \right)^{\frac{2}{3}} R_n^{\frac{1}{3}} \quad (2)$$

$$\gamma(R_c) = \frac{R_c^3 E}{R_n^2 \pi 9(1 - \nu^2)} \quad (3)$$

The adhesive contact radius can be calculated according to Hertzian contact mechanics via eq. 4. R_n is defined as half the diameter as measured in the optical microscopy image of the nucleus. b is the initial deformation induced by adhesion, defined as $b = 2R_n - \text{height}$, where the height of the nucleus was measured with AFM as described in the next section.

$$R_c(b) = \sqrt{R_n b} \quad (4)$$

Atomic force microscopy. All experiments were performed on an MFP-3D AFM (Asylum Research, CA, USA) that was mounted on a custom made inverted optical microscope which is described in detail in ref. 40. For all measurements we used tip-less MLCT-O10 cantilevers (Bruker, CA, USA) that have a triangular geometry of 170 μm long, a width of 22 μm width per arm and a resonance frequency around 22 kHz. The spring constant of each cantilever was calibrated with the built-in calibration routine based on the thermal noise spectrum and the equipartition theorem. The average spring constant was $k = 0.069 \pm 0.003$ N/m ($n = 11$).

AFM micro-rheology. Prior to each mechanical measurement, the dimensions of the selected nucleus were measured. First, a bright field image was recorded and the length of long and short axes were averaged to get the mean width. To obtain the height we used the AFM. By performing a force curve on top of the nucleus and one next to it on the substrate, we could extract the difference in piezo extension that was required to establish contact which gives the (undeformed) height of the nucleus.

For the measurement, the cantilever was brought down onto the nucleus at a pre-set force to achieve the desired indentation. 1 second after contact, the cantilever was oscillated at 25 nm drive amplitude at its basis, at a frequency that increased from 1 to 700 Hz in the course of 7.5 s, after which the cantilever was retracted. Because the response of the Asylum MFP3D z-scanner is only linear up to ~100 Hz the amplitude of the drive signal was gradually increased at higher frequencies to maintain a constant oscillation amplitude over the whole bandwidth.

For the analysis, the recorded cantilever deflection curves must be converted into the stiffness of the nucleus at each frequency. This stiffness, which depends on both the visco-elastic properties and the contact mechanics of the nucleus, is eventually used with eqs 2 and 3 to extract E^* . However, the drag of the surrounding liquid leads an additional increase of the measured cantilever deflection when it is moved. This is especially pronounced at high frequencies and needs to be corrected for in the calibration procedure.

In order to exclude that the response at higher frequencies is biased by changes to the material induced by the preceding measurements at lower frequencies, we performed successive control experiments at identical measurement conditions on the same nucleus. Supplementary Figure S3 shows that there is no systematic change between the measured responses, which confirms that the dynamic oscillations during the first measurement do not bias the results of the second measurement.

Stiffness of the nucleus. Basically, the stiffness of the nuclei follows the ratio between the applied force and the sample deformation. Although we perform cyclic deformation experiments, this method is conceptually the same as performing nano indentation experiments on the sample. The stiffness of the nucleus is obtained by dividing the force amplitude of the oscillation signal by the deformation amplitude of the nucleus (eq. 5). The force amplitude is obtained by multiplying the cantilever deflection signal (d) with the cantilever spring constant k . The deformation amplitude is obtained from subtracting the cantilever deflection from the piezo drive signal (z).

All analysis was performed with MATLAB (Mathworks, MA, USA). The data was analysed in frequency domain by applying a rectangular-windowing discrete Fourier analysis that allows us to extract the amplitude

and phase of each signal and calculate the apparent stiffness (K) of the nucleus. f_i and the absolute values of $d(f_i)$ and $z(f_i)$ are the frequency and amplitudes of oscillation, respectively.

$$K(f_i) = \frac{k|d(f_i)|}{|z(f_i)| - |d(f_i)|} \quad (5)$$

In addition, the phase shift (P_s) between the piezo drive signal and the cantilever deflection was calculated (eq. 6), which is used to separate the elastic and viscous components of the measured response. P is the phase. The argument (\arg), denotes the phase of each signal.

$$P_s(f_i) = \arg(d(f_i)) - \arg(z(f_i)) \quad (6)$$

Cantilever drag correction. The calculated stiffness need first to be corrected for the viscous drag of the buffer that acts on the cantilever. We followed the procedure described by Alcaraz (equation 4 in ref. 51) to subtract the dynamic response of the environment and isolate the one of the nucleus. Briefly, the experiments were repeated at known distances away from the substrate. The measured cantilever deflection and phase shift will now only result from the hydrodynamic drag and the instrument response and can be parametrized at each frequency with respect to the distance from the substrate. When a measurement is performed on a nucleus, these values are subtracted from the cantilever deflection signal taking the actual height of the cantilever above the substrate into account. Values of the drag coefficients as function of the distance between the tip-less cantilever and substrate are shown in Supplementary Figure S4.

Calculating E^* , E' and E'' . The nucleus stiffness includes both the viscous and elastic response in an unknown ratio (the additional drag on the cantilever from the surrounding liquid is calibrated and subtracted). Via a contact mechanics model first the apparent Young's modulus (E^*) is calculated. Assuming the contact area to remain constant at the small oscillation amplitude, we can use the stiffness of the nucleus to calculate its viscoelastic properties. First, the contact radius is calculated based on the diameter and indentation of the nucleus with eq. 4. Then, after applying the cantilever drag correction, we obtain the nucleus' force and indentation amplitudes during the oscillatory stimuli. Finally, E^* is calculated incorporating eq. 3 into eq. 2, which is numerically solved. E^* will still be composed of a viscous and elastic contribution in an unknown ratio. To separate E^* in its elastic (E') and viscous components (E'') we use the phase shift (P_s) between the drive and response signal. If the signals are in phase the response is purely elastic, if they are out of phase by $\frac{1}{2}\pi$, the response is purely viscous. E^* can thus be decomposed by $E'(f_i) = E^*(f_i)\cos(P_s(f_i))$ and $E''(f_i) = E^*(f_i)\sin(P_s(f_i))$. Finally, the loss tangent is defined as the ratio between viscous and elastic component, (eq. 7).

$$\text{Loss Tangent}(f_i) = \frac{E''(f_i)}{E'(f_i)} = \tan(P_{\text{corrected}}(f_i)) \quad (7)$$

Fitting of E^* with a power law. We fitted E^* below 100 Hz and above 100 Hz, using a power law of the form $E^*(f) = Af^\alpha$, where A is a scaling factor, α is the exponent and f the frequency. These coefficients are estimated using a non-linear regression method. In cell mechanics a transition around 100 Hz is often reported^{24,25} and also in our data the transition is most pronounced at this frequency. Fitting with a double power law did not allow us to clearly separate the low frequency response from the high frequency response, which is due to our still rather limited bandwidth and the fact that in some case the difference between the exponents of the power law is very small which makes that the transition region is less well defined²².

Finite element analysis of nucleus deformation. All models were built with Comsol Multiphysic 5.2a (Comsol, Sweden) The nucleus was described as a sphere with a radius of 5.5 μm resting on a planar surface. The Young's modulus was set to 2 kPa to best match our experiments and the Poisson ratio was set to 0.4.

To mimic the adhesion and initial deformation, a boundary force over the lower boundary of the sphere was applied to pull the sphere closer to the substrate. This force was adjusted to reach an initial contact radius of 1.75 μm , consistent with the one measured from optical microscopy results. Finally, the tip-less cantilever, described by a plate tilted by 10° with respect to the substrate, was lowered to indent the sphere. Contacts between the substrate, sphere and nucleus, were described with contact pairs and the contact-penalty methods according to the manufacturer's instructions.

We used a 3D model to investigate the effect of the tilted cantilever on the forces measured. For the measurements in which we varied the Young's modulus in the sphere we used a 2D axisymmetric model to reduce the computation time. In these models the cantilever was not tilted but parallel to the substrate.

The 2D model was also used to investigate the effect of a non-constant Young's modulus. For these models the initial deformation was not included. The Young's modulus was described by a linear decrease of the Young's modulus from 10 kPa at the centre to 0.3 kPa at the periphery. This is the simplest assumption which can explain the experimental behaviour seen at different indentation depth. The lamin layer was described a 100 nm thick layer with a Young's modulus of 200 kPa which results in an elastic area compressibility modulus of 24 mN/m, similar to value reported by Dahl *et al.*³¹. Because the thickness of the actual lamina is very thin with respect to the nucleus radius its response will be dominated by in-plane stretching and not by bending. Thus, the used thickness (t) of the layer in our model is not critical as long as the elastic area compressibility modulus (a product of E and t) is correct.

References

- Friedl, P., Wolf, K. & Lammerding, J. Nuclear mechanics during cell migration. *Curr Opin Cell Biol* **23**, 55–64, doi:10.1016/j.cob.2010.10.015 (2011).
- Ribeiro, A. J., Khanna, P., Sukumar, A., Dong, C. & Dahl, K. N. Nuclear stiffening inhibits migration of invasive melanoma cells. *Cell Mol Bioeng* **7**, 544–551, doi:10.1007/s12195-014-0358-3 (2014).
- Goldman, R. D., Gruenbaum, Y., Moir, R. D., Shumaker, D. K. & Spann, T. P. Nuclear lamins: building blocks of nuclear architecture. *Genes Dev* **16**, 533–547, doi:10.1101/gad.960502 (2002).
- Lammerding, J. et al. Lamins A and C but not lamin B1 regulate nuclear mechanics. *J Biol Chem* **281**, 25768–25780, doi:10.1074/jbc.M513511200 (2006).
- Zink, D., Fischer, A. H. & Nickerson, I. A. Nuclear structure in cancer cells. *Nat Rev Cancer* **4**, 677–687, doi:10.1038/nrc1430 (2004).
- Levsky, J. M. et al. The spatial order of transcription in mammalian cells. *J Cell Biochem* **102**, 609–617, doi:10.1002/jcb.21495 (2007).
- Egecioglu, D. & Brickner, J. H. Gene positioning and expression. *Curr Opin Cell Biol* **23**, 338–345, doi:10.1016/j.cob.2011.01.001 (2011).
- Cremer, T. & Cremer, M. Chromosome territories. *Cold Spring Harb Perspect Biol* **2**, a003889, doi:10.1101/cshperspect.a003889 (2010).
- Denlaud, E. & Bickmore, W. A. Transcription and the nuclear periphery: edge of darkness? *Curr Opin Genet Dev* **19**, 187–191, doi:10.1016/j.gde.2009.01.005 (2009).
- Volpe, T. A. et al. Regulation of heterochromatic silencing and histone H3 lysine-9 methylation by RNAi. *Science* **297**, 1833–1837, doi:10.1126/science.1074973 (2002).
- Gardel, M. L. et al. Elastic Behavior of cross-linked and bundled actin networks. *Science* **304**, 1301–1305 (2004).
- Dahl, K. N., Ribeiro, A. J. & Lammerding, J. Nuclear shape, mechanics, and mechanotransduction. *Circ Res* **102**, 1307–1318, doi:10.1161/CIRCRESAHA.108.173989 (2008).
- Versaevl, M., Grevesse, T. & Gabriele, S. Spatial coordination between cell and nuclear shape within micropatterned endothelial cells. *Nat Commun* **3**, 671, doi:10.1038/ncomms1668 (2012).
- Engler, A. J., Sen, S., Sweeney, H. L. & Discher, D. E. Matrix elasticity directs stem cell lineage specification. *Cell* **126**, 677–689 (2006).
- Jain, N., Iyer, K. V., Kumar, A. & Shivashankar, G. V. Cell geometric constraints induce modular gene-expression patterns via redistribution of HDAC3 regulated by actomyosin contractility. *Proc Natl Acad Sci USA* **110**, 11349–11354, doi:10.1073/pnas.1300801110 (2013).
- Dechat, T. et al. Nuclear lamins: major factors in the structural organization and function of the nucleus and chromatin. *Genes Dev* **22**, 832–853, doi:10.1101/gad.1652798 (2008).
- Sterle, V. et al. The carboxyl-terminal region common to lamins A and C contains a DNA binding domain. *Biochemistry* **42**, 4819–4828, doi:10.1021/bi020704g (2003).
- Iyer, K. V., Pulford, S., Mogilner, A. & Shivashankar, G. V. Mechanical activation of cells induces chromatin remodeling preceding MKL nuclear transport. *Biophys J* **103**, 1416–1428, doi:10.1016/j.bpj.2012.08.041 (2012).
- Schreiner, S. M., Koo, P. K., Zhao, Y., Mochrie, S. G. & King, M. C. The tethering of chromatin to the nuclear envelope supports nuclear mechanics. *Nat Commun* **6**, 7159, doi:10.1038/ncomms8159 (2015).
- Balland, M. et al. Power laws in microrheology experiments on living cells: Comparative analysis and modeling. *Physical review. E, Statistical, nonlinear, and soft matter physics* **74**, 021911, doi:10.1103/PhysRevE.74.021911 (2006).
- Fabry, B. et al. Scaling the microrheology of living cells. *Phys Rev Lett* **87**, 148102, doi:10.1103/PhysRevLett.87.148102 (2001).
- Hoffman, B. D. & Crocker, J. C. Cell mechanics: dissecting the physical responses of cells to force. *Annual review of biomedical engineering* **11**, 259–288 (2009).
- Nawaz, S. et al. Cell Visco-Elasticity Measured with AFM and Optical Trapping at Sub-Micrometer Deformations. *PLoS one* **7**, e45297 (2012).
- Deng, L. et al. Fast and slow dynamics of the cytoskeleton. *Nature materials* **5**, 636–640, doi:10.1038/nmat1685 (2006).
- Hoffman, B. D., Massiera, G., Van Citters, K. M. & Crocker, J. C. The consensus mechanics of cultured mammalian cells. *Proc Natl Acad Sci USA* **103**, 10259–10264, doi:10.1073/pnas.0510348103 (2006).
- Rico, F., Rigato, A. & Scheuring, S. High Frequency Microrheology of Living Cells. *Biophysical Journal* **110**, 132a–132a (2016).
- Koenderink, G. H., Atakhorrami, M., MacKintosh, F. C. & Schmidt, C. F. High-frequency stress relaxation in semiflexible polymer solutions and networks. *Phys. Rev. Lett.* **96**, doi:10.1103/PhysRevLett.96.138307 (2006).
- Palmer, A., Xu, J. Y. & Wirtz, D. High-frequency viscoelasticity of crosslinked actin filament networks measured by diffusing wave spectroscopy. *Rheol Acta* **37**, 97–106, doi:10.1007/s003970050095 (1998).
- Gittes, E. & MacKintosh, F. C. Dynamic shear modulus of a semiflexible polymer network. *Phys Rev E* **58**, R1241–R1244, doi:10.1103/PhysRevE.58.R1241 (1998).
- Broedersz, C. P. & MacKintosh, F. C. Modeling semiflexible polymer networks. *Rev Mod Phys* **86**, 995–1036, doi:10.1103/RevModPhys.86.995 (2014).
- Dahl, K. N., Kahn, S. M., Wilson, K. L. & Discher, D. E. The nuclear envelope lamina network has elasticity and a compressibility limit suggestive of a molecular shock absorber. *J Cell Sci* **117**, 4779–4786, doi:10.1242/jcs.01357 (2004).
- Lammerding, J. et al. Lamin A/C deficiency causes defective nuclear mechanics and mechanotransduction. *J Clin Invest* **113**, 370–378, doi:10.1172/JCI19670 (2004).
- Dahl, K. N., Engler, A. J., Pajerowski, J. D. & Discher, D. E. Power-law rheology of isolated nuclei with deformation mapping of nuclear substructures. *Biophys J* **89**, 2855–2864 (2005).
- Gerlitz, G. & Bustin, M. The role of chromatin structure in cell migration. *Trends Cell Biol* **21**, 6–11, doi:10.1016/j.tcb.2010.09.002 (2011).
- Mazumder, A., Roopa, T., Basu, A., Mahadevan, L. & Shivashankar, G. V. Dynamics of chromatin decondensation reveals the structural integrity of a mechanically prestressed nucleus. *Biophys J* **95**, 3028–3035, doi:10.1529/biophysj.108.132274 (2008).
- Stephens, A. D., Banigan, E. J., Adam, S. A., Goldman, R. D. & Marko, J. F. Chromatin and lamin A determine two different mechanical response regimes of the cell nucleus. *Mol Biol Cell*, doi:10.1091/mbc.E16-09-0653 (2017).
- Pajerowski, J. D., Dahl, K. N., Zhong, E. L., Sannak, P. J. & Discher, D. E. Physical plasticity of the nucleus in stem cell differentiation. *Proc Natl Acad Sci USA* **104**, 15619–15624, doi:10.1073/pnas.0702576104 (2007).
- Mahaffy, R. E., Park, S., Gerde, E., Kas, I. & Shih, C. K. Quantitative analysis of the viscoelastic properties of thin regions of fibroblasts using atomic force microscopy. *Biophys J* **86**, 1777–1793 (2004).
- Mahaffy, R. E., Shih, C. K., MacKintosh, F. C. & Kas, I. Scanning probe-based frequency-dependent microrheology of polymer gels and biological cells. *Phys. Rev. Lett.* **85**, 880–883 (2000).
- Ortega-Esteban, A. et al. Fluorescence Tracking of Genome Release during Mechanical Unpacking of Single Viruses. *ACS nano* **9**, 10571–10579, doi:10.1021/acsnano.5b03020 (2015).
- Stewart, M. P. et al. Wedged AFM-cantilevers for parallel plate cell mechanics. *Methods* **60**, 186–194, doi:10.1016/j.ymeth.2013.02.015 (2013).
- Glaubit, M. et al. A novel contact model for AFM indentation experiments on soft spherical cell-like particles. *Soft Matter* **10**, 6732–6741, doi:10.1039/c4sm00788c (2014).
- Vaziri, A. & Mofrad, M. R. Mechanics and deformation of the nucleus in micropipette aspiration experiment. *J Biomech* **40**, 2053–2062, doi:10.1016/j.jbiomech.2006.09.023 (2007).

44. Coffinier, C. *et al.* Deficiencies in lamin B1 and lamin B2 cause neurodevelopmental defects and distinct nuclear shape abnormalities in neurons. *Mol Biol Cell* **22**, 4683–4693, doi:10.1091/mbc.E11-06-0504 (2011).
45. Winter, H. H. Can the Gel Point of a Cross-Linking Polymer Be Detected by the $G' - G''$ Crossover. *Polym Eng Sci* **27**, 1698–1702, doi:10.1002/pen.760272209 (1987).
46. Meister, P., Towbin, B. D., Pike, B. L., Ponti, A. & Gasser, S. M. The spatial dynamics of tissue-specific promoters during *C. elegans* development. *Genes Dev* **24**, 766–782, doi:10.1101/gad.559610 (2010).
47. Wei, F. L. E., Liu, B. & Li, G. Poroelectricity of cell nuclei revealed through atomic force microscopy characterization. *Applied Physics Letters* **109**, 213701, doi:10.1063/1.4968191 (2016).
48. Hakelien, A. M., Gaustad, K. G. & Collas, P. Modulation of cell fate using nuclear and cytoplasmic extracts. *Methods in molecular biology* **325**, 99–114, doi:10.1385/1-59745-005-7-99 (2006).
49. Sage, D. *et al.* DeconvolutionLab2: An open-source software for deconvolution microscopy. *Methods*, doi:10.1016/j.ymeth.2016.12.015 (2017).
50. Born, M. & Wolf, E. In *Principles of Optics* (Cambridge University Press, 2003).
51. Alcaraz, J. *et al.* Correction of microrheological measurements of soft samples with atomic force microscopy for the hydrodynamic drag on the cantilever. *Langmuir* **18**, 716–721, doi:10.1021/la0110850 (2002).

Acknowledgements

M.L. thanks Pierre Montebault for his assistance with the complex Fourier analysis procedures and Amy Davies for her valuable support regarding the fluorescence microscopy experiments. I.A.T.S. thanks Florian Rehfeldt for insightful discussions about cell and nucleus mechanics. C.P.T. thanks the MRC (MR/M020606/1) and Royal Society (RG150801) for funding. N.F. was supported by Royal Society Newton International Fellowship (NF151167).

Author Contributions


M.L., A.D.S., C.P.T. and I.A.T.S. conceived, designed and performed the experiments. Y.H.-G. and N.F. optimised and performed nuclei isolation. M.L., A.D.S., C.P.T. and I.A.T.S. wrote the paper.

Additional Information

Supplementary information accompanies this paper at doi:10.1038/s41598-017-08517-6

Competing Interests: The authors declare that they have no competing interests.

Publisher's note: Springer Nature remains neutral with regard to jurisdictional claims in published maps and institutional affiliations.

 **Open Access** This article is licensed under a Creative Commons Attribution 4.0 International License, which permits use, sharing, adaptation, distribution and reproduction in any medium or format, as long as you give appropriate credit to the original author(s) and the source, provide a link to the Creative Commons license, and indicate if changes were made. The images or other third party material in this article are included in the article's Creative Commons license, unless indicated otherwise in a credit line to the material. If material is not included in the article's Creative Commons license and your intended use is not permitted by statutory regulation or exceeds the permitted use, you will need to obtain permission directly from the copyright holder. To view a copy of this license, visit <http://creativecommons.org/licenses/by/4.0/>.

© The Author(s) 2017

3.2.1.1. Supplementary Material for Manuscript 1

Supplementary Information

Atomic Force Microscopy micro-rheology reveals large structural inhomogeneities in single cell-nuclei

Michael Lherbette^{1#}, Ália dos Santos^{2#}, Yukti Hari-Gupta², Natalia Fili², Christopher P. Toseland^{2§*}, Iwan A.T. Schaap^{1§}

¹ Institute of Biological Chemistry, Biophysics and Bioengineering
School of Engineering and Physical Sciences
Heriot-Watt University
Edinburgh EH14 4AS, UK

² School of Biosciences,
University of Kent,
Canterbury CT2 7NJ, UK

Equal contribution

§ Joint corresponding author

* Address correspondence to: c.toseland@kent.ac.uk

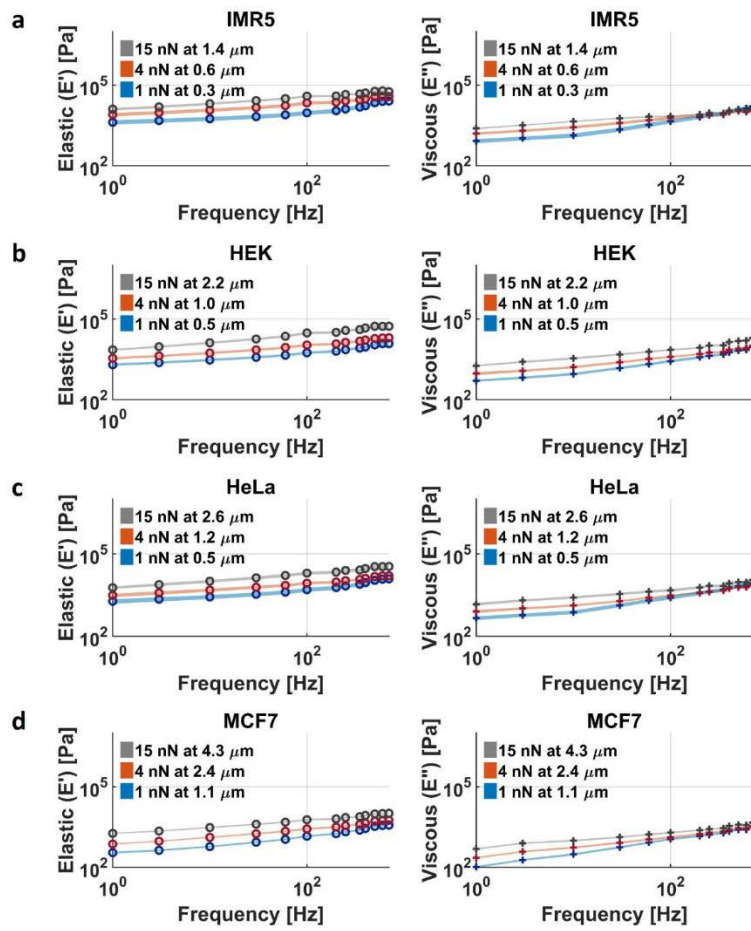


Figure S1. The elastic (E') and viscous (E'') response of the nuclei from different cell lines. The graphs are sorted by the average size of the nuclei, from small to large. a) IMR5, b) HEK, c) HeLa, and d) MCF7.

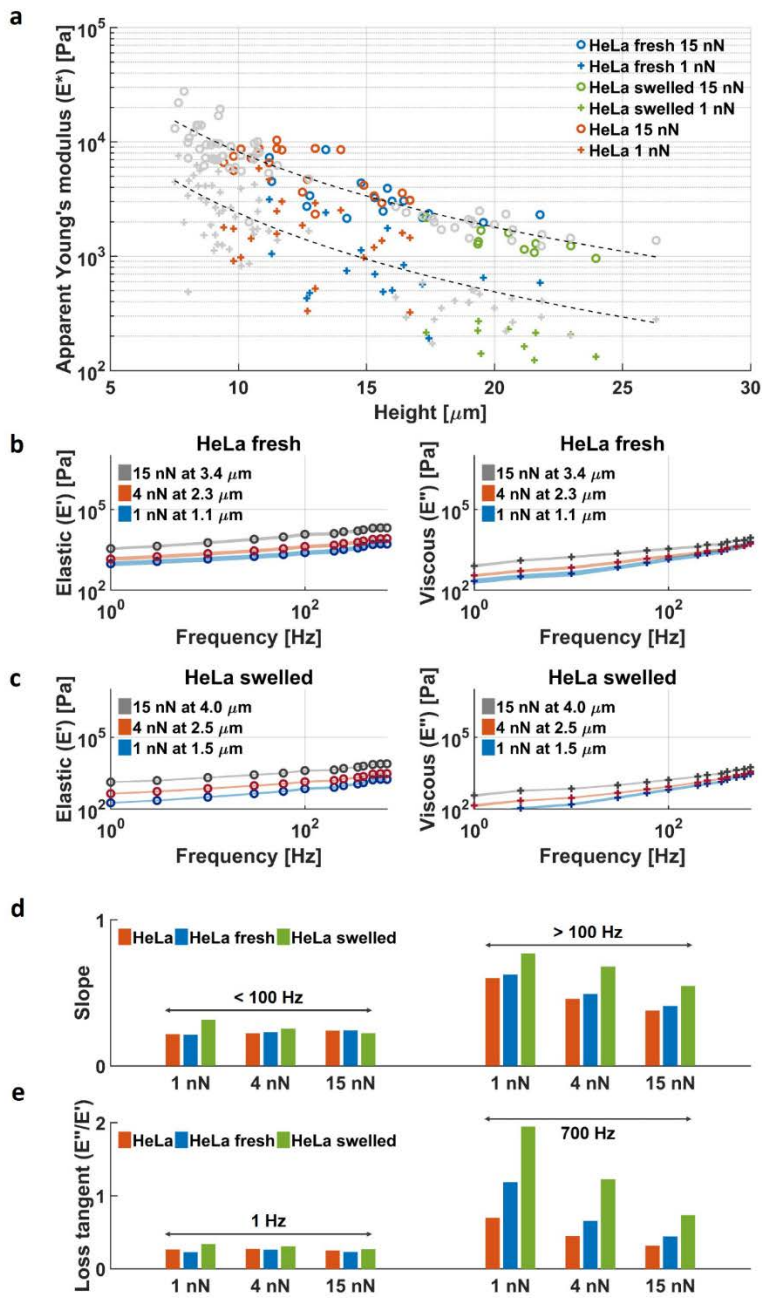


Figure S2. Effect of the storage conditions and the artificial swelling of HeLa nuclei. 'HeLa' nuclei are the ones presented in the main paper and have been stored at -80°C after isolation. 'HeLa fresh' nuclei were directly investigated after isolation to avoid storage at -80°C . 'HeLa swelled' were HeLa nuclei, previously stored at -80°C , which were subjected to hypotonic condition to induce osmotic swelling a) The response of 'HeLa' (orange), 'HeLa fresh' (blue) and 'HeLa swelled' (in green) reveal a size-dependent behavior similar to that of the nuclei of the different cell lines, the larger, the softer. To facilitate the comparison, the results from the IMR5, HEK and MCF7 nuclei are added in grey. The 'HeLa fresh' nuclei are larger than the 'HeLa' nuclei ($17.2 \pm 0.39 \mu\text{m}$ ($n = 16$) vs. $12.73 \pm 0.54 \mu\text{m}$ ($n = 23$)), whereas, the swelled nuclei were even larger ($20.7 \pm 0.61 \mu\text{m}$ ($n = 10$)). b) Frequency dependent E^* response of the 'HeLa fresh' nuclei and c) 'HeLa swelled' nuclei at different indentation depth. D) Values of the slope below and above 100 Hz are shown in. At low frequencies, the difference between differently treated HeLa samples is very small. However, at high frequencies, the swelled nuclei have the highest slope e) Differences between the loss tangent are noticeable at high frequencies. Notably, the response of the 'HeLa swelled' is clearly dominated by viscosity,

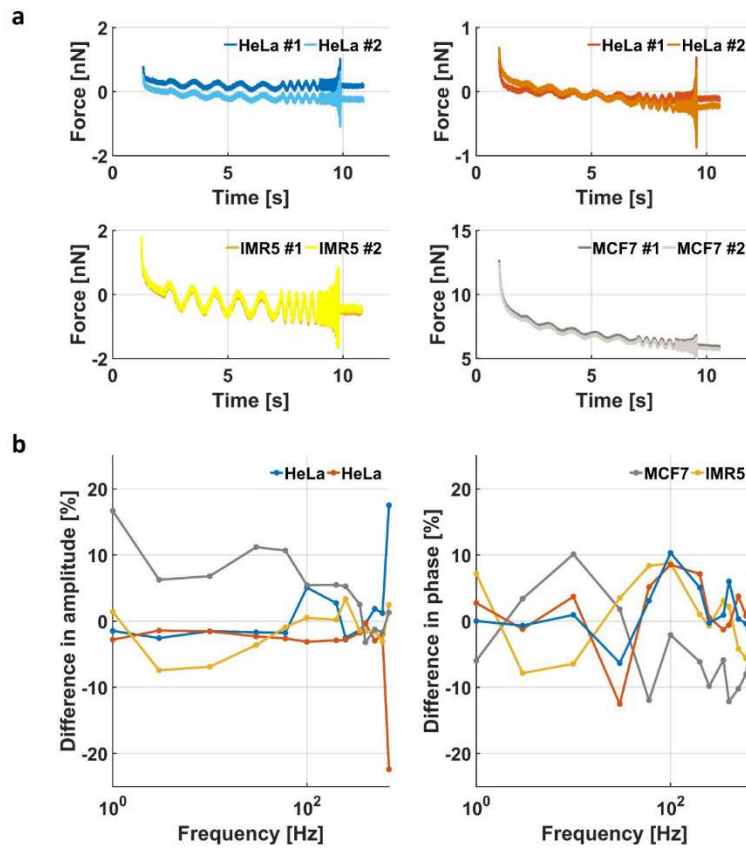


Figure S3. Repetitive experiments performed on the same nucleus show an identical response. a) Raw data curves for 4 different nuclei from three different cell lines, HeLa (blue and red), IMR5 (yellow) and MCF7 (grey). The dark curves represent the first frequency sequence and the light curves the second. The slight differences in force originate from the thermal drift that is present during the AFM measurements. b) The differences between the successive experiments of the amplitude and of the phase with respect to the drive signal. The differences are mostly below 10 % and do not show a systematic trend. This confirms that the first oscillation experiment does not bias the outcome of the second oscillation experiment.

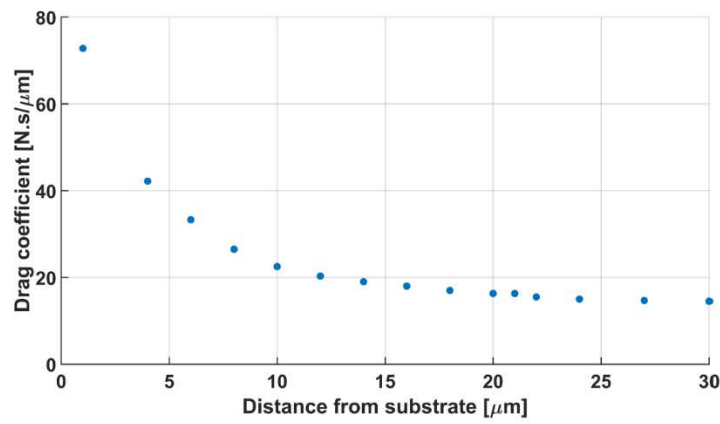


Figure S4. Drag coefficient of the cantilever as function of the cantilever-substrate separation. Drag coefficients were obtained by performing the oscillation experiment at increasing cantilever-substrate separations. Measurements were performed in the buffer used for the nuclei experiments. The drag coefficient decreases when the cantilever is further from the substrate. During the actual experiments on nuclei the cantilever-substrate separation is dictated by the height of the nuclei, typically between 10 and 20 μm .



Figure S5. Full size blot from Figure 4d.

3.2.2. Manuscript 2 - DNA damage alters nuclear mechanics through chromatin reorganisation

DNA damage alters nuclear mechanics through chromatin reorganization

Ália dos Santos¹, Alexander W. Cook¹, Rosemarie E. Gough¹, Martin Schilling²,
Nora A. Olszok², Ian Brown³, Lin Wang⁴, Jesse Aaron⁵, Marisa L. Martin-Fernandez⁴,
Florian Rehfeldt^{2,6,*} and Christopher P. Toseland^{1,*}

¹Department of Oncology and Metabolism, University of Sheffield, Sheffield S10 2RX, UK, ²University of Göttingen, 3rd Institute of Physics—Biophysics, Göttingen 37077, Germany, ³School of Biosciences, University of Kent, Canterbury CT2 7NJ, UK, ⁴Central Laser Facility, Research Complex at Harwell, Science and Technology Facilities Council, Rutherford Appleton Laboratory, Harwell, Didcot, Oxford OX11 0QX, UK, ⁵Advanced Imaging Center, HHMI Janelia Research Campus, Ashburn, VA 20147, USA and ⁶University of Bayreuth, Experimental Physics 1, Bayreuth, 95440, Germany

Received August 28, 2020; Revised November 13, 2020; Editorial Decision November 24, 2020; Accepted November 25, 2020

ABSTRACT

DNA double-strand breaks drive genomic instability. However, it remains unknown how these processes may affect the biomechanical properties of the nucleus and what role nuclear mechanics play in DNA damage and repair efficiency. Here, we have used Atomic Force Microscopy to investigate nuclear mechanical changes, arising from externally induced DNA damage. We found that nuclear stiffness is significantly reduced after cisplatin treatment, as a consequence of DNA damage signalling. This softening was linked to global chromatin decondensation, which improves molecular diffusion within the organelle. We propose that this can increase recruitment for repair factors. Interestingly, we also found that reduction of nuclear tension, through cytoskeletal relaxation, has a protective role to the cell and reduces accumulation of DNA damage. Overall, these changes protect against further genomic instability and promote DNA repair. We propose that these processes may underpin the development of drug resistance.

INTRODUCTION

Cells are known to respond to external stimuli through changes to their biomechanical properties, such as cellular stiffness. Some studies have previously related chemotherapy treatments to changes in the stiffness of cells and tissues (1,2). Chemotherapy agents such as cisplatin induce DNA damage, and therefore their main mechanism of action occurs within a nuclear context. However, little is known

about the biomechanical changes that might occur in the organelle following DNA damage.

Cisplatin, specifically, creates adducts within the double helix, which then lead to double-strand breaks (DSBs) in the DNA during replication, through replication-fork collapse (3).

DSBs can result in large genomic aberrations and are, therefore, the most deleterious to the cell. In the event of a DNA break, the cell activates DNA damage response (DDR) pathways that allow detection and repair of this lesion. Failure to repair damage leads to cell death through apoptosis, or to the propagation of mutations that drive genomic instability and cancer development (4–6).

It is well known that the ataxia-telangiectasia-mutated (ATM) kinase localizes to regions of damage, where it phosphorylates histone H2AX, producing γ H2AX. This, in turn, promotes the recruitment of multiple repair factors to foci of damage (7,8). However, it is not yet known if DNA damage, or DDR itself, could lead to alterations in nuclear mechanics.

It is established that chromatin and the lamina are major determinants of nuclear mechanics (9), and we have previously shown that a thicker nuclear lamina correlate with higher nuclear stiffness (10). It is also well reported that cancer cells change their stiffness compared to normal cell (11), where these parameters may be perturbed. In the context of DDR, local changes to the condensation state of the chromatin occur (12), which are associated to the efficiency of DNA repair and chromatin remodelling factors are known to be recruited to foci of damage (13,14). Interestingly, chromatin stiffness can be modified by nucleosome epigenetics (15) and protein complexes (16). Moreover, cytoskeletal proteins are also present within the nucleus and contribute to repair (17). As with DNA damage, it is still

*To whom correspondence should be addressed. Tel: +44 114 215 9080; Email: c.toseland@sheffield.ac.uk
Correspondence may also be addressed to Florian Rehfeldt. Tel: +49 921 55 2504; Email: florian.rehfeldt@uni-bayreuth.de

© The Author(s) 2020. Published by Oxford University Press on behalf of Nucleic Acids Research.
This is an Open Access article distributed under the terms of the Creative Commons Attribution License (<http://creativecommons.org/licenses/by/4.0/>), which permits unrestricted reuse, distribution, and reproduction in any medium, provided the original work is properly cited.

unknown how these alterations impact the physical properties of the nucleus.

Here, we investigated the relationship between DNA damage and nuclear mechanics. We used Atomic Force Microscopy (AFM) to probe mechanics of the nucleus of mammalian cells and monitor changes that occur after treatment with cisplatin. We found that, following DNA damage, large-scale mechanical alterations to the nucleus arise, caused by global decondensation of chromatin. This is dependent on DDR activation and increases molecular diffusion in the nucleus, potentially resulting in higher accessibility for repair factors. Surprisingly, we also found that mechanical relaxation of the nucleus, independently of chromatin, protects against genomic instability. Collectively, our data reveal how changes to chromatin architecture following DNA damage both suppress further genomic instability and provide an environment to promote repair. These findings may be harnessed to promote therapeutic approaches (e.g. resistance within a tumour environment).

MATERIALS AND METHODS

Drug treatments

Cisplatin [*cis*-diammineplatinum(II) dichloride] (Sigma) was resuspended in a 0.9% NaCl solution to a concentration of 3.3 mM, following manufacturer's instructions and used at a concentration of 25 μ M. Trichostatin A (TSA) (Sigma) was resuspended to 6.6 mM in DMSO and used at 400 nM in culturing medium, for 24 h. ATM inhibitor, KU55933 (Sigma), was resuspended in DMSO to 12.6 mM and used at a concentration of 20 μ M, 30 min prior treatment and then for the whole duration of cisplatin treatment in culturing medium. Blebbistatin (Sigma) was resuspended to 50 mM in DMSO and used at a concentration of 50 μ M for 1–2 h before AFM measurements and for 30 min, prior treatment and then the whole duration of cisplatin treatment for imaging. Latrunculin B (Sigma) was resuspended in DMSO to a concentration of 12.6 mM and used at 1 μ M for 1 h before AFM measurements.

Cell culture and transfection

HeLa cells (ECACC 93021013) were cultured at 37°C and 5% CO₂ in MEM Alpha medium with GlutaMAX, supplemented with 10% fetal bovine serum (Gibco) and 1% penicillin/streptomycin (Gibco). HeLa cells were transfected with 0.5 μ g pSNAP-C1 plasmid (Addgene 58186) using Lipofectamine 2000 (Invitrogen) and following manufacturer's instructions.

Nuclear isolation

Nuclei were prepared based on protocols in (10,18) HeLa cells and bone-marrow mesenchymal stem cells were washed with cold phosphate buffered saline (PBS), then washed in cold Hypotonic Buffer N—10 mM Hepes pH 7.5, 2 mM MgCl₂, 25 mM KCl, 1 mM PMSF, 1 mM DTT and Protease Inhibitor Cocktail (Thermo Fisher Scientific). Cells were then re-suspended in cold hypotonic buffer N and incubated for 1 h on ice. Cells were homogenized on

ice, using a glass Dounce homogenizer (Wheaton). Sucrose was added to the cell lysate to a final concentration of 220 mM and mixed well by inversion before centrifugation. The pellet, corresponding to isolated nuclei, was washed in cold Buffer N—10 mM Hepes pH 7.5, 2 mM MgCl₂, 25 mM KCl, 250 mM sucrose, 1 mM PMSF, 1 mM DTT Protease Inhibitor Cocktail. The nuclei pellet was re-suspended in PBS and used immediately for AFM measurements.

Immunofluorescence

HeLa cells grown on glass coverslips were incubated for 10 min at 37°C and 5% CO₂ with 1 μ g ml⁻¹ Hoechst 33342 in growth medium. Stained cells were fixed in 4% (m/V) paraformaldehyde (PFA). Residual PFA was quenched with 50 mM ammonium chloride for 15 min at room temperature. Cells were then permeabilized and blocked for 15 min with 0.1% (V/V) Triton X-100 and 2% (m/V) bovine serum albumin (BSA) in Tris-Buffered Saline (TBS). Antibodies were used as follows: mouse-Phospho-H2AX (Merck 05–636) at 1:500 dilution, rabbit-Lamin B1 (Abcam ab16048) at a dilution of 1:200, donkey anti-mouse Alexa Fluor 488-conjugated (Abcam Ab181289) at 1:500 and donkey anti-rabbit Alexa Fluor-488-conjugated (Abcam, Ab181346) at 1:500 dilution. For actin staining, fixed and permeabilized cells were stained prior to immunofluorescence with 165 nM Rhodamine-Phalloidin (ThermoFisher) for 20 min. Coverslips were mounted on microscope slides with 10% (m/V) Mowiol, 25% (m/V) glycerol, 0.2 M Tris-HCl, pH 8.5, supplemented with 2.5% (m/V) of DABCO (Sigma).

Fluorescence imaging

Cells were visualized using Wide-field microscope Olympus IX71, or Confocal microscope LSM 880. For confocal microscopy, a Plan-Apochromat 63 \times 1.4 NA oil immersion lens (Carl Zeiss, 420782–9900-000) was used. Three laser lines: 405, 488 and 561 nm, were used to excite Hoechst, Alexa 488 and Alexa 647 fluorophores, respectively. Built-in dichroic mirrors (Carl Zeiss, MBS-405, MBS-488 and MBS-561) were used to reflect the excitation laser beams onto cell samples. For fluorescence collection, the used emission spectral bands were: 410–524 nm (Hoechst), 493–578 nm (Alexa 488) and 564–697 nm (Alexa 647). The green channel (Alexa 488) was imaged using a 1 gallium arsenide phosphide (GaAsP) detector, while the blue (Hoechst) and red (Alexa 647) channels were imaged using two multi-anode photomultiplier tubes (MA-PMTs). For imaging acquisition and rendering, ZEN software was used. Confocal Images were deconvolved using the Zeiss Zen2.3 Blue software, using the regularized inverse filter method.

For Wide-field microscopy, a PlanApo 100 \times OTIRFM-SP 1.49 NA lens mounted on a PIFOC z-axis focus drive (Physik Instrumente, Karlsruhe, Germany) was used, with an automated 300W Xenon light source (Sutter, Novato, CA, USA) with appropriate filters (Chroma, Bellows Falls, VT, USA). QuantEM (Photometrics) EMCCD camera, controlled by the Metamorph software (Molecular Devices) was used for image acquisition. All images were then analysed by ImageJ.

STORM imaging

Cells were seeded on pre-cleaned No 1.5, 25-mm round glass coverslips, placed in 6-well cell culture dishes. Glass coverslips were cleaned by incubating them for 3 h, in etch solution, made of 5:1:1 ratio of H₂O: H₂O₂ (50 wt. % in H₂O, stabilized, Fisher Scientific): NH₄OH (ACS reagent, 28–30% NH₃ basis, Sigma), placed in a 70°C water bath. Cleaned coverslips were repeatedly washed in filtered water and then ethanol, dried and used for cell seeding. Transfected or non-transfected cells were incubated with 1 µg ml⁻¹ Hoechst 33342 in growth medium for 15 min at 37°C, 5% CO₂. Following this, cells were washed with PBS and fixed in pre-warmed 4% (w/v) PFA in PBS and residual PFA was quenched for 15 min with 50 mM ammonium chloride in PBS. Immunofluorescence (IF) was performed in filtered sterilized PBS, unless when anti-phospho antibodies were used. Then, IF was performed in filtered sterilized TBS. Cells were permeabilized and simultaneously blocked for 30 min with 3% (w/v) BSA in PBS or TBS, supplemented with 0.1% (v/v) Triton X-100. Permeabilized cells were incubated for 1 h with the primary antibody and subsequently the appropriate fluorophore-conjugated secondary antibody, at the desired dilution in 3% (w/v) BSA, 0.1% (v/v) Triton X-100 in PBS or TBS. The antibody dilutions used were the same as for the normal IF protocol (see above), except from the secondary antibodies which were used at 1:250 dilution. Following incubation with both primary and secondary antibodies, cells were washed three times, for 10 min per wash, with 0.2% (w/v) BSA, 0.05% (v/v) Triton X-100 in PBS or TBS. Cells were further washed in PBS and fixed for a second time with pre-warmed 4% (w/v) PFA in PBS for 10 min. Cells were washed in PBS and stored at 4°C, in the dark, in 0.02% NaN₃ in PBS, before proceeding to STORM imaging.

Before imaging, coverslips were assembled into the Attofluor[®] cell chambers (Invitrogen). Imaging was performed in freshly made STORM buffer consisting of 10% (w/v) glucose, 10 mM NaCl, 50 mM Tris-pH 8.0, supplemented with 0.1% (v/v) 2-mercaptoethanol and 0.1% (v/v) pre-made GLOX solution which was stored at 4°C for up to a week (5.6% (w/v) glucose oxidase and 3.4 mg/ml catalase in 50 mM NaCl, 10 mM Tris-pH 8.0). All chemicals were purchased from Sigma.

Imaging was undertaken using the Zeiss Elyra PS.1 system. Illumination was from a HR Diode 642 nm (150 mW) and HR Diode 488 nm (100 mW) lasers where power density on the sample was 7–14 kW/cm² and 7–12 kW/cm², respectively.

Imaging was performed under highly inclined and laminated optical (HILO) illumination to reduce the background fluorescence with a 100× NA 1.46 oil immersion objective lens (Zeiss alpha Plan-Apochromat) with a BP 420–480/BP495–550/LP 650 filter. The final image was projected on an Andor iXon EMCCD camera with 25 msec exposure for 20000 frames for γH2AX and 60 msec for 60000 frames for Hoechst imaging.

Image processing was performed using the Zeiss Zen software. Where required, two channel images were aligned following a calibration using pre-mounted MultiSpec bead sample (Carl Zeiss, 2076–515). The channel alignment was

then performed in the Zeiss Zen software using the Affine method to account for lateral, tilting and stretching between the channels. The calibration was performed during each day of measurements.

The images were then processed through our STORM analysis pipeline using the Zen software. Single molecule detection and localization was performed using a 9-pixel mask with a signal to noise ratio of 6 in the 'Peak finder' settings while applying the 'Account for overlap' function. This function allows multi-object fitting to localize molecules within a dense environment. Molecules were then localized by fitting to a 2D Gaussian.

The render was then subjected to model-based cross-correlation drift correction. The final render was then generated at 10 nm/pixel and displayed in Gauss mode where each localization is presented as a 2D gaussian with a standard deviation based on its precision.

High-content screening

HeLa cells were seeded in clear-bottom, black-walled 96-well plates at 10 000 cells/well in culturing medium and incubated overnight at 37°C, 5% CO₂. For Blebbistatin pre-treated cells, 50 µM Blebbistatin was added prior to 4-h incubation with 50 µM Blebbistatin and 25 µM cisplatin. For cisplatin-treated cells, only cisplatin was added at 25 µM for 4 h. Cells were then incubated for 15 min with Hoechst dye, at 37°C, 5% CO₂ and fixed using 4% (m/v) PFA. Cells were stained with 165 nM Rhodamine-Phalloidin (ThermoFisher) for 20 min and 1:500 dilution of mouse-Phospho-H2AX (Merck 05–636) antibody for 1 h, following the immunofluorescence protocol. High-content imaging was undertaken using a Cell Discoverer 7 (Zeiss), using a Plan-Apochromat 20 × 0.7 NA objective. Hoechst, Alexa 488 and Rhodamine fluorophores were excited using LED light at wavelengths 385, 470 and 567 nm, respectively. ZEN software was used for image acquisition and images were analysed using Zeiss Zen2.3 Blue software.

Multi-focal imaging and particle tracking analysis

Cells were transfected for 24 h with 0.5 µg of pSNAP_T-C1 (Addgene 58186) construct with Lipofectamine 2000 (Invitrogen), according to manufacturer's instructions. Following this, cells were treated with 25 µM cisplatin or 400 nM TSA in growth medium for 24 h.

Cells transiently expressing pSNAP_T-C1 construct were labelled for 15 min with 10 nM SNAP-tag-JF549 ligand, in cell culture medium at 37°C, 5% CO₂. Cells were washed for three times with warm cell culture medium and then incubated for further 30 min at 37°C, 5% CO₂. Cells were then washed three times in pre-warmed FluoroBrite Dulbecco's-modified Eagle's medium (ThermoFisher Scientific), before proceeding to imaging.

Single molecule imaging was performed using an aberration-corrected multifocal microscope (acMFM), as described by Abrahamsson et al. (19). Briefly, samples were imaged using 561 nm laser excitation, with typical irradiance of 4–6 kW/cm² at the back aperture of a Nikon 100 × 1.4 NA objective. Images were relayed through a custom optical system appended to the detection path of a Nikon Ti

microscope with focus stabilization. The acMFM detection path includes a diffractive multifocal grating in a conjugate pupil plane, a chromatic correction grating to reverse the effects of spectral dispersion, and a nine-faceted prism, followed by a final imaging lens.

The acMFM produces nine simultaneous, separated images, each representing successive focal planes in the sample, with ca. 20 μm field of view and nominal axial separation of ca. 400 nm between them. The nine-image array is digitized via an electron multiplying charge coupled device (EMCCD) camera (iXon Du897, Andor) at up to 32 ms temporal resolution, with typical durations of 30 s.

3D+t images of single molecules were reconstructed via a calibration procedure, implemented in Matlab (MathWorks), that calculates and accounts for (i) the inter-plane spacing, (ii) affine transformation to correctly align each focal plane in the xy plane with respect to each other and (iii) slight variations in detection efficiency in each plane, typically less than ± 5 –15% from the mean.

Reconstructed data were then subject to pre-processing, including background subtraction, mild deconvolution (3–5 Richardson-Lucy iterations) and/or Gaussian de-noising prior to 3D particle tracking using the MOSAIC software suite (20). Parameters were set where maximum particle displacement was 400 nm and a minimum of 10 frames was required. Tracks were reconstructed, and diffusion constants were extracted via MSD analysis (21) using custom Matlab software assuming an anomalous diffusion model.

Atomic force microscopy

AFM measurements were performed with an MFP 3D BIO (Asylum Research, Oxford Instruments, Santa Barbara, USA) on top of an inverted fluorescence microscope (IX71, Nikon Instruments, Japan). The combined instrument is mounted on a Halcyonics vibration isolation table (Accurion GmbH, Göttingen, Germany) inside an acoustic enclosure (Asylum Research) to minimize noise. Force-indentation curves were executed in contact mode using the longer triangular cantilever of a TR 400 PB chip that has a pyramidal tip with an opening angle of 35°. The spring constant was determined with the built-in macro based on the thermal method and was in the range (28–31 pN nm⁻¹) and therefore slightly stiffer than the nominal stiffness of 0.02 N m⁻¹. The nucleus was probed on several locations using the ForceMap macro with a maximum indentation force of 1.5 nN and the resulting force-indentation curves were analysed using a modified Hertz model within a self-written IGOR macro as described earlier (22,23).

Polyacrylamide gels

Elastic polyacrylamide (PA) gels were prepared as described earlier (23,24). In brief, mixtures for the desired elasticities were prepared using solutions of 40% acrylamide (#161-0140, Bio-Rad, Munich, Germany) and 2% bis-acrylamide (#161-0142, Bio-Rad, Munich, Germany) in PBS that are stored at 4°C for a maximum time of 2 months. These mixtures were polymerized through addition of 1% (v/v) ammoniumpersulfate and 0.1% (v/v) N,N,N,N-tetramethylethylenediamine onto

freshly plasma-cleaned cover slips that were treated with 3-aminopropyltriethoxysilane (Sigma, Munich, Germany, A3648) and subsequently with a 0.05% glutaraldehyde solution (Sigma, Munich, Germany, G7651) for firm attachment of the gels. For 25 mm coverslips, 35 μl of the PA gel solution was dispensed and covered with a square superhydrophobic cover glass to equally distribute the solution. Gels were polymerized for 60 min using a plastic box to keep them in a saturated water atmosphere to avoid evaporation. For quality control the Young's elastic modulus E was regularly measured with a bulk rheometer (MCR-501, Anton Paar, Austria) using a 2° cone and plate geometry. To facilitate cell attachment, the gels were functionalized with rat tail Collagen type I (0.2 mg/ml Corning, New York, NY, #354236) overnight at 4°C using the heterobifunctional crosslinker Sulfo-SANPAH (Thermo Scientific, Waltham, MA, USA 22,589; 0.4 mM in 50 mM HEPES buffer at pH 8) active with UV light ($\lambda = 365$ nm) for 10 min.

Electron microscopy

Cells attached to Aclar membrane (Agar Scientific) were fixed for 2 h in 2.5% glutaraldehyde (w/v) in 100 mM sodium cacodylate (CAB) buffer pH 7.2. Samples were washed twice for 10 min in 100 mM CAB and then post-fixed in 1% osmium tetroxide (w/v) in 100 mM CAB for 1 h before being dehydrated using an ethanol series of 50%, 70%, 90% (v/v) and three times with 100% ethanol for 10 min per step. The samples were then placed into propylene oxide, for (2 \times)10 min, and following this into a 1:1 mixture of propylene oxide and Agar LV resin (Agar Scientific) for 30 min. Following this, samples were embedded in freshly prepared Agar LV resin twice for 2 h before being placed in shallow aluminium moulds with the cells facing up and were polymerized at 60°C for 24 h before being examined with a dissecting microscope to identify areas confluent with cells. These areas were cut out with a jig saw and attached to polymerized resin blocks with superglue, and once attached, the Aclar membrane was peeled off, exposing a monolayer of cells in the block face. Sections of 70 nm were cut on a Leica EM UC7 ultramicrotome using a diamond knife (Diatome) and were collected on 400 mesh copper grids. Sections were counterstained in 4.5% uranyl acetate (w/v) in 1% acetic acid (v/v) for 45 min and in Reynolds' lead citrate for 7 min. Samples were viewed in a Jeol 1230 transmission electron microscope and images were captured with a Gatan One View 16mp camera.

RESULTS

Whilst the biochemical responses to DNA damage are well investigated (4,25,26), their effects on the biophysical properties of the nucleus are still poorly understood. To investigate this, we used cisplatin, a chemotherapy drug that crosslinks DNA, thereby inducing DSBs within DNA and AFM to measure mechanical changes in nucleus.

Cisplatin treatment reduces nuclear stiffness

Before AFM measurements, fully adhered cells on glass were treated with 25 μM cisplatin for 4 h, or 24 h, which

induced DNA damage, recorded as fluorescent foci of γ H2AX (Figure 1A). AFM measurements were performed at a central point above the nucleus of a selected cell, up to a maximal force of 10 nN (Figure 1B and C). Force-distance curves were then fitted using the Hertz model, to determine the effective Young's elastic moduli E . Figure 1D shows representative experimental curves of deflection versus probe-sample separation and, in the insets, the fitted curves.

We found that long treatment with cisplatin (24 h), but not short treatment (4 h), significantly reduced cellular stiffness (Figure 1E). Young's modulus values changed from 4.4 ± 0.6 kPa (mean \pm SEM) in non-treated cells to 3.2 ± 0.4 kPa after cisplatin 4-h and 1.9 ± 0.2 kPa in cells, following 24-h cisplatin treatment. These results suggest that the observed mechanical change is temporally separated from the DNA damage itself. Therefore, breaks in DNA do not directly change the mechanical properties of the nucleus, but rather trigger events that further downstream affect the nuclear stability.

Although these measurements were taken at a central point above the nucleus, the complex actin cytoskeleton extends throughout the whole cell and exerts large amounts of force on the nucleus through compression, thus altering its physical properties and potentially masking mechanical changes. As a result, it is difficult to understand what the individual contributions of the nucleus and the cytoskeleton are to whole-cell mechanics.

To understand if the mechanical changes observed were a result of alterations to the cytoskeleton, we labelled cells with phalloidin after cisplatin treatment (Supplementary Figure S1). Our data show that there is no actin cytoskeleton impairment, indicating that the observed mechanical effect is not a result of the dissociation of actin filaments in the cell. We therefore postulated that the change in stiffness could be the result of altered biophysical properties in the nucleus.

To understand the individual contribution of the nucleus to global mechanics, we decided to perform measurements on cells at initial adhesion stages, isolated nuclei (Figure 2A and Supplementary Figure S2) and cells treated with two different cytoskeletal destabilizing drugs—Blebbistatin and Latrunculin B (Supplementary Figure S1).

At initial adhesion stages, the nucleus is the largest contributor to whole-cell mechanics. In this case, the cells are given enough time to adhere to the surface (2–3 h for HeLa cells) but the cytoskeleton and in particular stress fibres, are not fully established (Supplementary Figure S1). As a result, AFM measurements taken above the nucleus only reflect the mechanical properties of the organelle. Alternatively, Blebbistatin, a Myosin II inhibitor, and Latrunculin B, an actin depolymerizing drug, relax the cytoskeleton (27–29), and therefore measurements in these cells are mainly directed at the nucleus, without a contribution from the cytoskeleton.

Our AFM data show that, as expected, fully-adhered cells (4.4 ± 0.7 kPa) are stiffer than Latrunculin B and Blebbistatin treated cells (2.6 ± 1.2 kPa and 2.1 ± 0.8 kPa, respectively), initially adhered cells (2.9 ± 0.3 kPa) and isolated nuclei (2.6 ± 0.4 kPa), whilst there is no significant difference between these four latter conditions (Figure 2B).

From these data we confirmed that nuclear measurements performed in initially-adhered cells are relatively free of cytoskeletal contributions and that the nucleus remains as the only large structural variable. Therefore, we decided to use this approach to investigate changes to nuclear mechanics, as this allows for the physical properties of nucleus to be probed whilst maintaining the organelle in its physiological environment and without the use of drugs that may have unknown effects in our study.

To investigate effects of DNA damage in nuclear mechanics, we used 25 μ M cisplatin treatments for 4 and 24 h on initially adhered HeLa cells, which were seeded on glass slides 2 h before AFM measurements. This revealed that the Young's moduli of nuclei were significantly reduced after both 4 h (1.6 ± 0.2 kPa, $P < 0.001$) and 24 h (1.2 ± 0.3 kPa, $P < 0.001$) of cisplatin treatment (Figure 2C). Surprisingly, we could observe mechanical changes after short cisplatin treatment in initially adhered cells (Figure 2C), whilst this was not possible in fully adhered (Figure 1C). This suggests that cytoskeletal contributions, present in fully adhered cells may be masking smaller nuclear mechanical changes occurring in shorter treatments.

To confirm that the observed effect is intrinsic to the nucleus, we also performed these measurements on isolated nuclei (Figure 2A), following 4-h cisplatin treatment. Immunofluorescence images of isolated nuclei with membrane dye DiD show that the nuclear membrane in isolated nuclei is intact (Supplementary Figure S2). As expected, there is a large decrease in Young's moduli values from non-treated nuclei (2.6 ± 0.4 kPa) to cisplatin-treated (0.9 ± 0.2 kPa, $P < 0.0001$), confirming these changes occur are intrinsic to the nucleus (Figure 2D).

The mechanical response to DNA damage may be specific to the tumorigenic state of the cells because we did not observe the DNA damage-induced decrease in stiffness with bone-marrow mesenchymal stem cells, or isolated nuclei. (Supplementary Figure S3).

DNA damage signalling is required for mechanical changes to the nucleus

As cisplatin treatment causes severe DNA damage, we wondered if these mechanical changes were dependent on DDR signalling. Following DSBs, ATM kinase is recruited to sites of damage, where it phosphorylates histone H2AX (30). This results in the recruitment of repair factors to DSBs and biochemical changes that determine the cell's fate (7,31–33).

To investigate this, we inhibited the ATM kinase, using inhibitor KU55933 (iATM) by pre-treating cells with iATM for 30 min before 4-h treatment with 25 μ M cisplatin (also in the presence of iATM). Immunofluorescence shows that treatment with iATM impairs the formation of γ H2AX foci (Figure 3A). AFM measurements on initially adhered cells (Figure 3B) show no difference between nuclei of non-treated cells (2.9 ± 0.3 kPa) and nuclei of cells treated with cisplatin after pre-incubation with iATM (2.7 ± 0.3 kPa). Surprisingly, these data suggest that mechanical changes to the nucleus occur after DDR signalling is activated and appears to be dependent on ATM kinase. This confirms that mechanical changes do not arise directly from the induction of the DSBs.

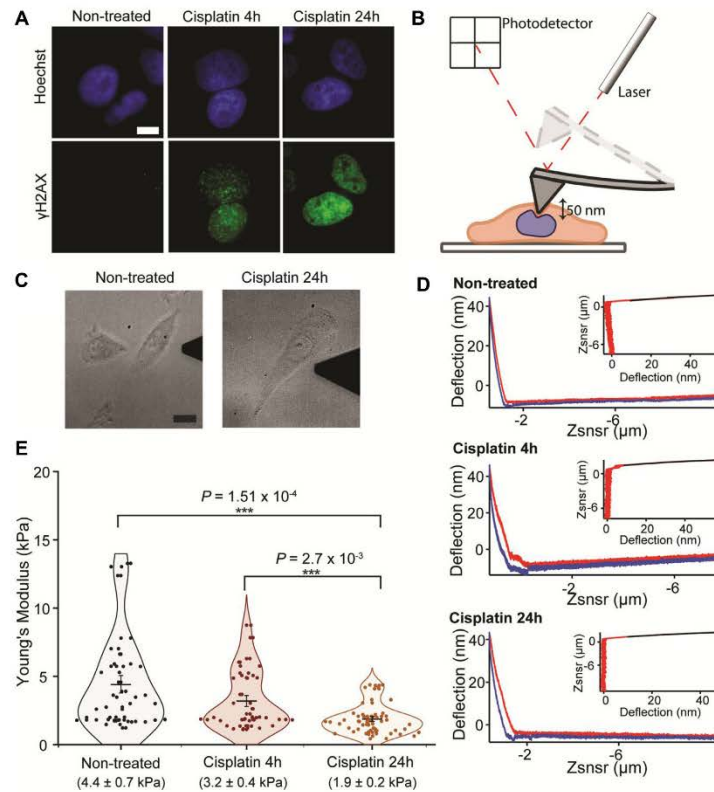


Figure 1. AFM measurement of cisplatin treated cells. (A) Wide-field immunofluorescence imaging of γ H2AX (green) in HeLa cells (scale bar = 10 μ m). (B) Cartoon depicting AFM measurement. Cells are attached on glass, and a cantilever with a pyramidal tip is used to probe cellular mechanics at a central point above the nucleus. (C) Transmitted light sample images from wide-field microscope coupled to AFM, showing non-treated cells and cells after long cisplatin treatment (24 h). Scale bar 20 μ m. (D) Representative distance (Znsnr) versus deflection AFM curves for all three conditions tested are shown, with approach and retraction curves in red and blue, respectively. Curve fitting, shown above curves, was performed using the Hertz model, as described in methods. (E) Young's moduli values for non-treated ($n = 29$), cisplatin 4 h ($n = 29$) and cisplatin 24 h ($n = 34$) treatments. Each point corresponds to the average value for a cell, calculated from 10 measurements. Mean \pm SE are represented in the plot and values are shown below each condition. P -values were calculated by a two-tailed t -test, assuming equal variance; *** $P < 0.001$.

Mechanical changes of the nucleus after DNA damage are caused by chromatin decondensation

The nuclear lamina is a major structural component of the nucleus. We therefore tested if cisplatin treatment changed lamina integrity, thus changing nuclear mechanics. Our results show that for non-treated and cisplatin-treated cells there are no changes in thickness of the nuclear lamina (Supplementary Figure S4A and B). Negative-stain electron microscopy (EM) data support this observation and show that nuclear membrane integrity is not compromised following cisplatin treatments (Supplementary Figure S4C). This suggests that the reduction of the Young's modulus of the nucleus is not a result of a structural compromise to the nuclear lamina.

Together with the lamina, chromatin compaction is one of the other major contributors for nuclear mechanics, and previous studies have suggested that the state of chromatin condensation can change following DSBs (14, 34–36). If this is the case, global changes to chromatin compaction could result in significant alterations to nuclear mechanics.

To investigate this hypothesis, we used EM to image both non-treated and cisplatin-treated cells and compared it to TSA, a deacetylase inhibitor that leads to decondensation of chromatin. Dense regions of staining corresponding to condensed chromatin are clearly visible in the non-treated cells. This contrasts with both cisplatin and TSA-treated cells (Figure 4A). Quantification of chromatin compaction from EM images, based on intensity of staining, shows

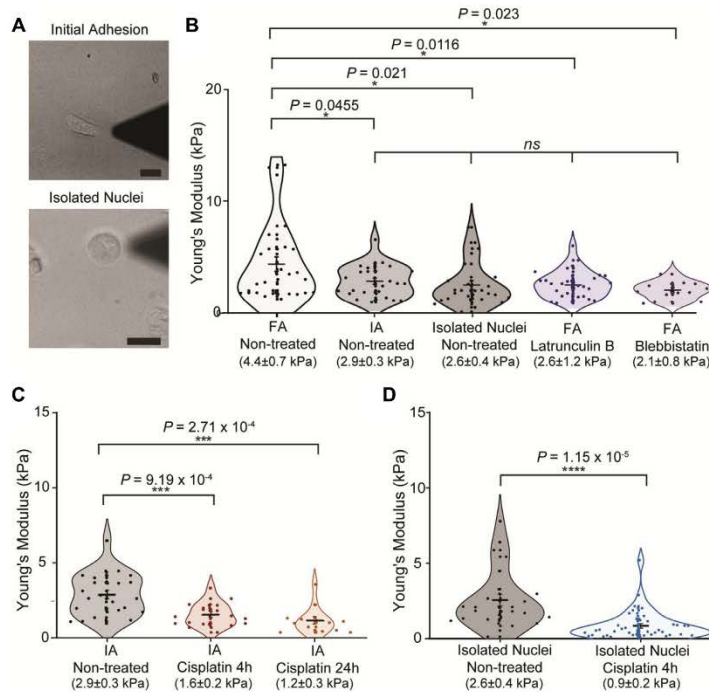


Figure 2. Initially adhered and isolated nuclei measurements in HeLa cells after DNA damage. (A) Representative transmitted light images from wide-field microscope coupled to AFM, showing initially adhered cells and isolated nuclei. (Scale bar 20 μm) (B) Young's moduli values for comparison between fully adhered cells ($n = 26$), initially-adhered cells ($n = 26$), isolated nuclei ($n = 32$) and after cytoskeleton disruption with drugs LatB ($n = 28$) and Blebbistatin ($n = 13$). (C) Young's moduli of initially adhered cells after 4 h ($n = 17$) and 24-h ($n = 13$) cisplatin treatments. (D) Values for AFM measurements of non-treated isolated nuclei and nuclei isolated after 4-h cisplatin treatment ($n = 40$). Mean values \pm SE are represented in the plot. P -values were calculated by two-tailed t -test, assuming equal variance; $ns > 0.05$ * $P < 0.05$; ** $P < 0.01$; *** $P < 0.001$; **** $P < 0.0001$.

that cells treated with cisplatin have higher levels of decondensed chromatin, similarly to TSA-treated cells, whilst non-treated cells have higher amounts of condensed chromatin (Figure 4B).

To test if chromatin decondensation, following TSA treatment, had a similar effect to cisplatin on nuclear stiffness, we measured the Young's modulus in nuclei of initially adhered cells. Our AFM data show (Figure 4C) that nuclei in TSA-treated cells (1.0 ± 0.1 kPa) are significantly softer than in non-treated cells (2.9 ± 0.3) and display similar mechanics to long-term cisplatin-treated cells (1.2 ± 0.3).

To complement EM data and confirm the observed effects of cisplatin on chromatin, we used super-resolution STORM imaging. Standard antibody staining was used to image γ H2AX, whilst we took advantage of the photophysical properties of the Hoechst DNA dye to visualize chromatin (Figure 5A and B). Qualitatively, our results confirm that chromatin decondensation occurs after cisplatin treatment (Figure 5A) compared to the non-treated sample, and similarly to TSA-treated cells (Figure 5B). In the non-treated sample, clearly defined chromatin bundles are

present within the nuclear periphery and interior. However, upon cisplatin treatment there are a few islands of condensed DNA but there is loss of the extensive network. The extent of chromatin relaxation in this case is comparative to TSA treatment. Taken together, these results strongly suggest that chromatin decondensation is a determining factor for changes in nuclear mechanics after DNA damage.

A possible benefit that arises from chromatin decondensation is that it may allow for higher protein diffusion in the nucleus, thus enabling repair factors to reach areas of damage more easily. To test this, we used Multifocal Microscopy (MFM) (19) and 3D single-particle tracking to measure the diffusion constants of a fluorescently labelled SNAP tag (37,38), expressed in HeLa cells, in treated and non-treated conditions. MFM allows us to do live-cell, single-molecule imaging across nine simultaneous z planes (Figure 5C) (19), hence creating a comprehensive 3D model of molecular diffusion in nucleus. The SNAP tag was used as a reporter of free diffusion within the nucleus. Figure 5D shows a representative 3D map for single-particle tracking using MFM.

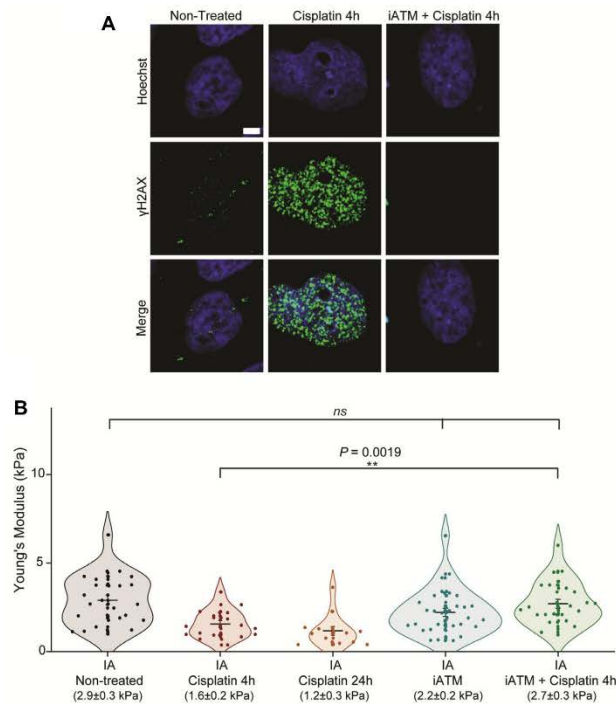


Figure 3. ATM inhibition impairs nuclear mechanical response to DNA damage. (A) Confocal immunofluorescence imaging of γ H2AX (green), with nuclear stain Hoechst, after cisplatin treatment in the presence or absence of ATM inhibitor (Scale bar = 10 μ m). (B) Young's moduli values after short and long cisplatin treatments, and in cells treated with both ATM inhibitor and cisplatin ($n = 24$). Cells treated with only iATM are also shown ($n = 31$). Plot shows mean values \pm SE. P -values from two-tailed t -test, assuming equal variance between conditions are also shown ($ns > 0.05$; $*P < 0.05$; $**P < 0.01$).

Our data show that the diffusion constant of the SNAP-tag in the nucleus of cells treated with cisplatin ($1.2 \pm 0.04 \mu\text{m}^2/\text{s}$) is significantly higher than in non-treated cells ($0.8 \pm 0.03 \mu\text{m}^2/\text{s}$), but similar to TSA-treated ($1.3 \pm 0.04 \mu\text{m}^2/\text{s}$) (Figure 5E). This supports the idea that chromatin decondensation following damage allows proteins to diffuse more rapidly within the nucleus.

Mechanical relaxation of the nucleus protects cells from damage

Recently, studies have linked the occurrence of DNA damage to external forces exerted on the nucleus (39,40). Similarly, there is some evidence that increased forces on the nucleus exacerbate the extent of DNA damage (41,42). It is possible that, after DNA damage, a softer nucleus, also leads to a loss of tension on the nucleus which prevents further genomic instability.

To investigate how forces exerted on the nucleus influence DNA damage, we decided to pre-treat cells with Blebbistatin for 30 min before 4-h treatment with cisplatin (also in

the presence of Blebbistatin). This allowed us to minimize cytoskeletal forces on the nucleus prior to the occurrence of damage. We used γ H2AX as a marker for damage. High-content screening revealed a large decrease in the percentage of damaged cells when they pre-incubated with Blebbistatin. In non-treated cells, only $5.1 \pm 0.2\%$ of the population showed γ H2AX signalling, as expected. $37.4 \pm 0.9\%$ of cisplatin-treated cells (short treatment) displayed signs of damage, whilst this value dropped to $21.2 \pm 0.6\%$ for cells that were pre-incubated with Blebbistatin (Figure 6A and B). This suggests that a decrease in forces acting on the nucleus has a protective effect towards DNA damage.

Matrix stiffness is tightly related to cell spread, adhesion formation and cytoskeletal force (24,43,44). As a result, a stiffer surface will create higher forces in the cytoskeleton, which would then translate into higher mechanical constraints to the nucleus (45–47). To further explore this relationship between stiffness and the extent of DNA damage, we used polyacrylamide gels of different stiffness (2, 11 and 30 kPa) as surfaces for cells (Figure 7A). The ability of the cells to respond to the gel stiffness is confirmed when we

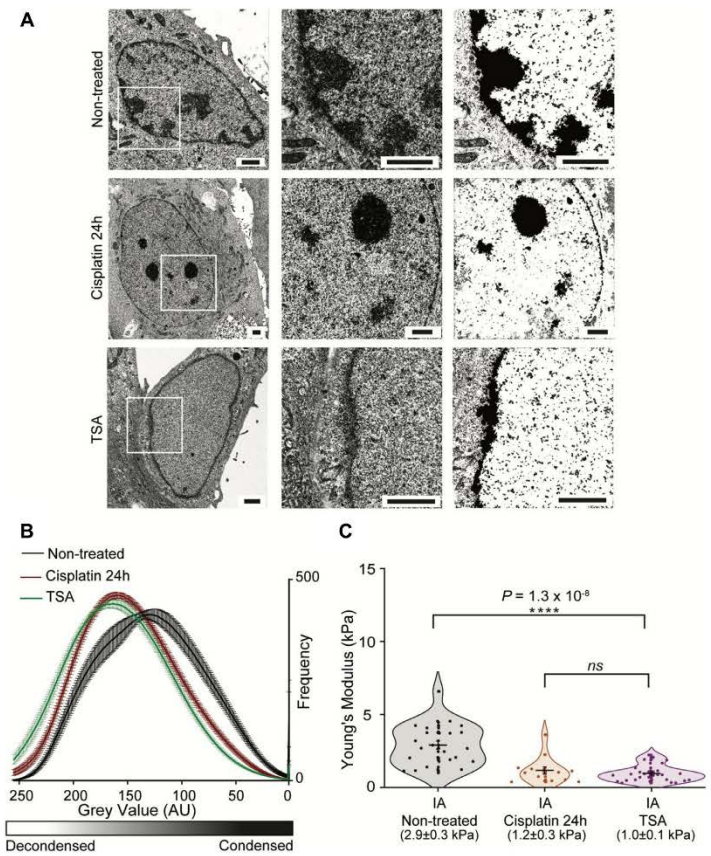


Figure 4. Electron Microscopy for quantification of chromatin condensation levels. (A) Electron microscopy of HeLa cells after long cisplatin treatment and treatment with deacetylase inhibitor TSA. White squares on left panel represent area selected for detail on middle panel. Threshold images are shown on the right panel (Scale bars = 2 μm). (B) Quantification of dark and light pixels from electron microscopy images inside the nucleus, representing condensed and decondensed chromatin. Values for non-treated cells are in black ($n = 21$), long cisplatin treatment in red ($n = 26$) and TSA ($n = 26$). (C) Young's moduli values of initially adhered cells, comparing non-treated and 24-h cisplatin treatment with TSA ($n = 28$). For all experiments, the mean values \pm SE are plotted. Statistical differences were calculated using two-tailed t -test, assuming equal variance between conditions and P -values are shown ($ns > 0.05$; $*P < 0.05$; $**P < 0.01$; $***P < 0.001$; $****P < 0.0001$).

measure the cross-sectional area of the nucleus. Here, the greater tension exerted by the stiffer gel matrix leads to an increase in nuclear area from $291.0 \pm 8.5 \mu\text{m}^2$ to $456.0 \pm 10.8 \mu\text{m}^2$ (Figure 7B), in line with earlier findings (48).

If we expect lower force to have a protective effect, lower surface stiffness should decrease the amount of damage in cells, in a similar way to Blebbistatin treatment. As expected, our data reveal that cells treated in stiffer gels, 30 kPa, have 65% higher levels of γH2AX levels compared to 2 kPa gels and 30% higher than 11 kPa gels (Figure 7C). Overall, less tension across the nucleus leads to less damage.

DISCUSSION

Our work reveals a direct link between DNA damage, chromatin condensation and nuclear mechanics. It has been shown that treatment with cisplatin and other chemotherapy drugs changes whole-cell mechanics (49,50). However, since most studies focus on cytoskeletal contributions, until now it remained unclear how these DNA damage-causing drugs alter the biomechanical properties of the nucleus. Here, by performing AFM measurements in initially adhered cells, we were able to probe the mechanical properties of the nucleus within its cellular environment. Our work shows that cisplatin treatment causes significant alterations

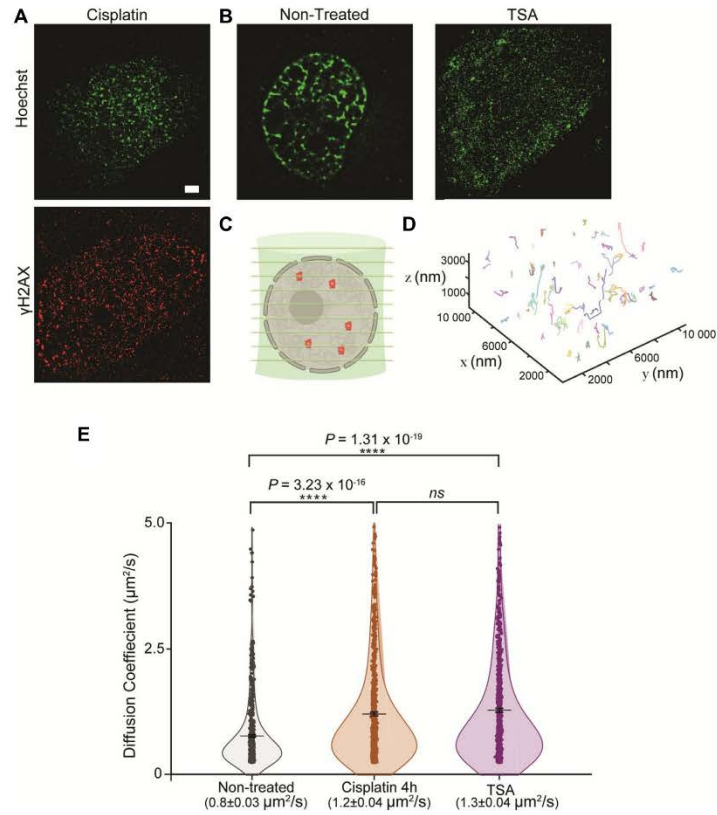


Figure 5. Impact of DNA damage on chromatin organization and molecular diffusion in the nucleus. (A) Representative STORM images of chromatin labelled with Hoechst of HeLa cells after cisplatin treatment, with immunolabelling of γ H2AX (red). Scale bar = 2 μ m. (B) STORM images of chromatin in non-treated and TSA treated HeLa cells. (C) Cartoon depicting simultaneous acquisition of nine focal planes using multifocal microscopy for 3D single-molecule tracking of a reporter SNAP-tag. (D) Example of 3D molecule trajectories under normal conditions. (E) Diffusion Coefficients calculated from 3D single-molecule tracking after fitting trajectories assuming an anomalous diffusion model. Plot shows mean values \pm SE. *P*-values were calculated with a two-tailed *t*-test, assuming equal variance (*ns* > 0.05; **P* < 0.05; ***P* < 0.01; ****P* < 0.001; *****P* < 0.0001).

to the state of chromatin condensation, which in turn results in a reduction of nuclear stiffness. This response may be specific to the tumorigenic background. However, a wider study of more cell lines is required to specifically address this point.

Mechanical changes to the nucleus do not arise spontaneously from breaks in the chromatin fibre, but are a result of downstream large-scale chromatin decondensation. The ATM kinase is activated by DNA damage, and its absence or inactivity can lead to a proportion of unrepaired DSBs in the cell (51,52). Interestingly, the mechanical softening of the nucleus also appears to be coupled to the activity of the ATM kinase, suggesting that chromatin decondensation occurs as a result of the DDR. Several studies have reported localized chromatin decondensation around areas of dam-

age and this is thought to lead to higher repair efficiency (34,35,53). Our data largely agree with this observation, but we cannot exclude that there are patches of condensed DNA around the damage sites. Moreover, we show that chromatin decondensation, following DNA damage, increases molecular diffusion within the nucleus. By creating greater exposure to DNA binding sites and enabling repair factors to readily reach sites of damage, chromatin decondensation could act as a major determinant for the outcome of repair events.

Interestingly, we found that alterations to biomechanics also appear to protect the cell from genomic instability. In addition to the intrinsic mechanical properties of the nucleus, the cytoskeleton also has a large impact on overall nuclear mechanics. Relaxation of the cytoskeleton results in

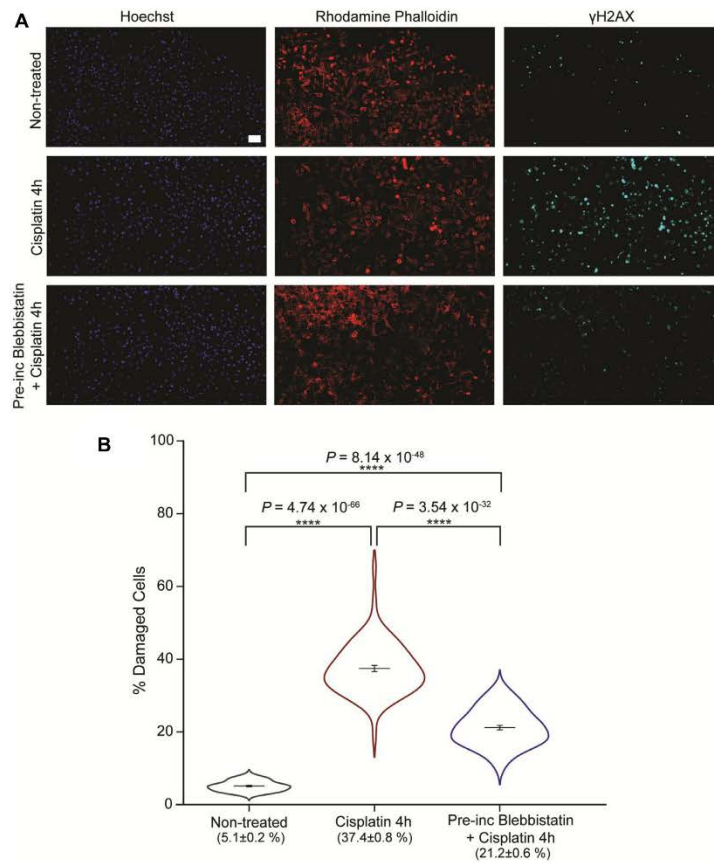


Figure 6. Impact of Blebbistatin on γ H2AX signalling in HeLa cells. (A) Representative images from high-content screening of HeLa cells treated with cisplatin in the presence or absence of Blebbistatin. Nuclear staining with Hoechst and Actin labelling with Rhodamine phalloidin are shown in addition to immunofluorescent labelling of γ H2AX. Scale bar = 100 μ m. (B) Levels of damage in HeLa cells from high-content screening, calculated as percentage of nuclei displaying γ H2AX signalling. *P*-values are shown between non-treated cells ($n = 58$, representing 51 233 cells), 4-h cisplatin treatment ($n = 70$, representing 63 422 cells) and combined Blebbistatin and cisplatin treatment ($n = 68$, representing 57 274 cells). For all conditions, mean values \pm SE are plotted. Two-tailed *t*-test, assuming equal variance, was used for *P*-value calculation (*ns* > 0.05; **P* < 0.05; ***P* < 0.01; ****P* < 0.001; *****P* < 0.0001).

reduced nuclear tension and, here, we show that this has a protective effect in DNA damage. It has been shown that reduction in matrix stiffness, a major determining factor for cytoskeletal organization, correlates with inhibition of replication (54–56). Cisplatin-induced DSBs require active DNA replication. It is, therefore, possible that the lower levels of DSBs detected in nuclei under lower mechanical tension are a result of altered DNA replication levels. We suggest that a decrease in nuclear stiffness would also destabilize cytoskeleton-nuclear linkage which could result in a change in nuclear tension. Our findings agree with the recent findings of Nava *et al.*, which showed that nuclear soft-

ening protects against mechanically induced DNA damage (41). Moreover, our observations build upon findings from Kumar *et al.* (57), which revealed how the ATR kinase modulates the nuclear membrane and chromatin in response to mechanical stress. Overall, it appears that the nucleus has an innate ability to protect against different agents.

Deformations to the nuclear envelope, as well as mechanical forces acting on the organelle are important for the regulation of cell-cycle progression (58) and transcription activity (59). Interestingly, DNA damage leads to cell cycle arrest and transcriptional repression to promote repair. Therefore, DNA damage-induced changes to the

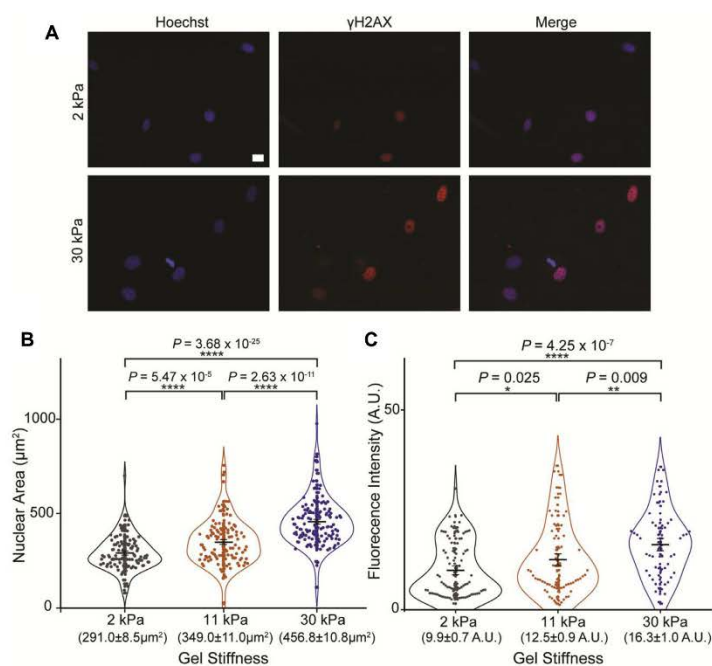


Figure 7. Impact of nuclear relaxation on γ H2AX signalling in HeLa cells. (A) Representative Wide-field images of HeLa cells growing on gels of different stiffness—2 and 30 kPa—after cisplatin treatment. Immunofluorescent labelling of γ H2AX is shown in red, with nuclear stain Hoechst in blue. (Scale bar = 20 μ m). (B) Nuclear area of cells on different surfaces—2 kPa ($n = 111$), 11 kPa ($n = 121$) and 30 kPa ($n = 139$). P -values are shown. (C) Fluorescence intensity of red channel (γ H2AX) within the nucleus of cells grown on surfaces of different stiffness—2 kPa ($n = 90$), 11 kPa ($n = 79$) and 30 kPa ($n = 61$). In all cases, mean values \pm SE are shown. Two-tailed t -test, assuming equal variance, was used for statistical calculations and P -values are shown ($ns > 0.05$; * $P < 0.05$; ** $P < 0.01$; *** $P < 0.001$; **** $P < 0.0001$).

mechanosensing properties of the nucleus could contribute to the regulation of these processes. In terms of cell cancer, during migration and invasion, altered nuclear mechanics may be an important factor. For example, whilst travelling through confined spaces, cells with softer nuclei could migrate more easily and with less DNA damage, induced by rupture events resulting from nuclear compression. In this case, a softer nucleus would, once again, protect from further damage.

There is growing evidence that tumorigenesis and resistance to chemotherapy agents correlate with changes in cellular and nuclear mechanics (60). Depending on the cell types and type of treatment, drug resistance has been associated with an increase or decrease in cell stiffness (60,61). Interestingly, there are also possible differences between *in vitro* cell lines and patient-derived primary samples, where the latter are more deformable. Our data fit with these scenarios, whereby decreased nuclear stiffness promotes repair and prevents further damage, which could subsequently drive drug resistance.

In summary, here, we describe how nuclear mechanics change due to induced DNA damage through chromatin remodelling events, as part of DDR. Furthermore, we show

that nuclear envelope relaxation protects against further damage. It will be of interest, in the future, to determine the molecular mechanisms through which nuclear mechanics directly influence DNA damage levels as these pathways may directly influence therapeutic resistance.

DATA AVAILABILITY

The data supporting the findings of this study are available from the corresponding author on request.

SUPPLEMENTARY DATA

Supplementary Data are available at NAR Online.

ACKNOWLEDGEMENTS

Aberration-corrected multi-focal microscopy was performed in collaboration with the Advanced Imaging Center at Janelia Research Campus, a facility jointly supported by the Howard Hughes Medical Institute and the Gordon and Betty Moore Foundation. We also thank Satya Khuon (Janelia Research Campus) for assisting with cell culture

and Thomas Helleday for sharing equipment. The JF549 dye was kindly provided by Luke Lavis (Janelia Research Campus).

Author Contributions: C.P.T. and F.R. conceived the study. A.d.S., F.R. and C.P.T. designed experiments. A.d.S. performed AFM measurements with support from M.S. and N.A.O., A.W.C. and R.E.G. performed experiments using the acrylamide gels. I.B. prepared and collected electron microscopy data. A.d.S. and C.P.T. performed single molecule imaging experiments. Imaging was supported by L.W., M.L.M.-F. and J.A. L.W., J.A., A.d.S. and C.P.T. contributed to single molecule data analysis. C.P.T. and F.R. supervised the study. A.d.S., C.P.T. and F.R. wrote the manuscript with comments from all authors.

FUNDING

Royal Society [IE170270 to C.P.T.]; Howard Hughes Medical Institute; Gordon and Betty Moore Foundation; Medical Research Council [MR/M020606/1 to C.P.T.]; Science and Technology Facilities Council [19130001 to C.P.T.]. Funding for open access charge: University of Sheffield UKRI.

Conflict of interest statement. None declared.

REFERENCES

- Lam, W.A., Rosenbluth, M.J. and Fletcher, D.A. (2006) Chemotherapy exposure increases leukemia cell stiffness. *Blood*, **109**, 3505–3508.
- Sharma, S., Santiskulvong, C., Bentolila, L.A., Rao, J., Dorigo, O. and Gimzewski, J.K. (2012) Correlative nanomechanical profiling with super-resolution F-actin imaging reveals novel insights into mechanisms of cisplatin resistance in ovarian cancer cells. *Nanomedicine*, **8**, 757–766.
- Frankenberg-Schwager, M., Kirchnermeier, D., Greif, G., Baer, K., Becker, M. and Frankenberg, D. (2005) Cisplatin-mediated DNA double-strand breaks in replicating but not in quiescent cells of the yeast *Saccharomyces cerevisiae*. *Toxicology*, **212**, 175–184.
- Jackson, S.P. and Bartek, J. (2009) The DNA-damage response in human biology and disease. *Nature*, **461**, 1071–1078.
- Shrova, O. and Zhivotovskiy, B. (2013) Various modes of cell death induced by DNA damage. *Oncogene*, **32**, 3789–3797.
- Torgovnick, A. and Schumacher, B. (2015) DNA repair mechanisms in cancer development and therapy. *Front. Genet.*, **6**, 157.
- Paull, T.T., Rogakou, E.P., Yamazaki, V., Kirchgessner, C.U., Gellert, M. and Bonner, W.M. (2000) A critical role for histone H2AX in recruitment of repair factors to nuclear foci after DNA damage. *Curr. Biol.*, **10**, 886–895.
- Polo, S.E. and Jackson, S.P. (2011) Dynamics of DNA damage response proteins at DNA breaks: a focus on protein modifications. *Genes Dev.*, **25**, 409–433.
- Stephens, A.D., Banigan, E.J., Adam, S.A., Goldman, R.D. and Marko, J.F. (2017) Chromatin and lamin A determine two different mechanical response regimes of the cell nucleus. *Mol. Biol. Cell*, **28**, 1984–1996.
- Lherbette, M., dos Santos, A., Hari-Gupta, Y., Fili, N., Toseland, C.P. and Schaap, J.A.T. (2017) Atomic Force Microscopy micro-rheology reveals large structural inhomogeneities in single cell-nuclei. *Sci. Rep.*, **7**, 8116.
- Fuhrmann, A., Staunton, J.R., Nandakumar, V., Banyai, N., Davies, P.C. and Ros, R. (2011) AFM stiffness nanotomography of normal, metaplastic and dysplastic human esophageal cells. *Phys. Biol.*, **8**, 015007.
- Yasui, L.S., Higashikubo, R. and Warters, R.L. (1987) The effect of chromatin decondensation on DNA damage and repair. *Radiat. Res.*, **112**, 318–330.
- Chai, B., Huang, J., Cairns, B.R. and Laurent, B.C. (2005) Distinct roles for the RSC and Swi/Suf ATP-dependent chromatin remodelers in DNA double-strand break repair. *Genes Dev.*, **19**, 1656–1661.
- Ziv, Y., Bielopolski, D., Galanty, Y., Lukas, C., Taya, Y., Schultz, D.C., Lukas, J., Bekker-Jensen, S., Bartek, J. and Shiloh, Y. (2006) Chromatin relaxation in response to DNA double-strand breaks is modulated by a novel ATM- and KAP-1 dependent pathway. *Nat. Cell Biol.*, **8**, 870–876.
- Melters, D.P., Pitman, M., Rakshit, T., Dimitriadis, E.K., Bui, M., Papoian, G.A. and Dalal, Y. (2019) Intrinsic elasticity of nucleosomes is encoded by histone variants and calibrated by their binding partners. *PNAS*, **116**, 24066–24074.
- Rakshit, T., Melters, D.P., Dimitriadis, E.K. and Dalal, Y. (2020) Mechanical properties of nucleoprotein complexes determined by nanoindentation spectroscopy. *Nucleus*, **11**, 264–282.
- Cook, A.W. and Toseland, C.P. (2020) The roles of nuclear myosin in the DNA damage response. *J. Biochem.*, doi:10.1093/jb/mvaa113.
- Fili, N., Hari-Gupta, Y., dos Santos, A., Cook, A., Poland, S., Ameer-Beg, S.M., Parsons, M. and Toseland, C.P. (2017) NDP52 activates nuclear myosin VI to enhance RNA polymerase II transcription. *Nat. Commun.*, **8**, 1871.
- Abrahamsson, S., Chen, J., Haji, B., Stallings, S., Katsov, A.Y., Wisniewski, J., Mizuguchi, G., Soule, P., Mueller, F., Darzacq, C.D. et al. (2013) Fast multicolor 3D imaging using aberration-corrected multifocus microscopy. *Nat. Methods*, **10**, 60–63.
- Sbalzarini, I.F. and Koumoutsakos, P. (2005) Feature point tracking and trajectory analysis for video imaging in cell biology. *J. Struct. Biol.*, **151**, 182–195.
- Aaron, J., Wait, E., DeSantis, M. and Chew, T.L. (2019) Practical considerations in particle and object tracking and analysis. *Curr. Protoc. Cell Biol.*, **83**, e88.
- Engler, A.J., Rehfeldt, F., Sen, S. and Discher, D.E. (2007) Microtissue elasticity: measurements by atomic force microscopy and its influence on cell differentiation. In: Wang, Y.-L. and Discher, D. (eds) *Methods in Cell Biology*. Academic Press, Cambridge, Vol. **83**, pp. 521–545.
- Kalman, S., Jayachandran, C., Rehfeldt, F. and Smith, A.S. (2014) Novel growth regime of MDCK II model tissues on soft substrates. *Biophys. J.*, **106**, L25–L28.
- Zemel, A., Rehfeldt, F., Brown, A.E., Discher, D.E. and Safran, S.A. (2010) Optimal matrix rigidity for stress fiber polarization in stem cells. *Nat. Phys.*, **6**, 468–473.
- Turgeon, M.-O., Perry, N.J.S. and Pouligianis, G. (2018) DNA damage, repair, and cancer metabolism. *Front. Oncol.*, **8**, 15.
- Scully, R., Panday, A., Elango, R. and Willis, N.A. (2019) DNA double-strand break repair-pathway choice in somatic mammalian cells. *Nat. Rev. Mol. Cell Biol.*, **20**, 698–714.
- Kovács, M., Tóth, J., Hetényi, C., Málnási-Csizmadia, A. and Sellers, J.R. (2004) Mechanism of Blebbistatin Inhibition of Myosin II. *J. Biol. Chem.*, **279**, 35557–35563.
- Wakatsuki, T., Schwab, B., Thompson, N.C. and Elson, E.L. (2001) Effects of cytochalasin D and latrunculin B on mechanical properties of cells. *J. Cell Sci.*, **114**, 1025–1036.
- Spector, I., Shochet, N.R., Blasberger, D. and Kashman, Y. (1989) Latrunculin—novel marine macrolides that disrupt microfilament organization and affect cell growth: I. Comparison with cytochalasin D. *Cell Motil. Cytoskeleton*, **13**, 127–144.
- Burma, S., Chen, B.P., Murphy, M., Kurimasa, A. and Chen, D.J. (2001) ATM phosphorylates histone H2AX in response to DNA double-strand breaks. *J. Biol. Chem.*, **276**, 42462–42467.
- Fragkos, M., Jurvasu, J. and Beard, P. (2009) H2AX is required for cell cycle arrest via the p53/p21 pathway. *Mol. Cell Biol.*, **29**, 2828–2840.
- Nakamura, A.J., Rao, V.A., Pommier, Y. and Bonner, W.M. (2010) The complexity of phosphorylated H2AX foci formation and DNA repair assembly at DNA double-strand breaks. *Cell Cycle*, **9**, 389–397.
- Strucki, M., Clapperton, J.A., Mohammad, D., Yaffe, M.B., Smerdon, S.J. and Jackson, S.P. (2005) MDC1 directly binds phosphorylated histone H2AX to regulate cellular responses to DNA double-strand breaks. *Cell*, **123**, 1213–1226.
- Lou, J., Scipioni, L., Wright, B.K., Bartolsc, T.K., Zhang, J., Masamsetti, V.P., Gaus, K., Gratton, E., Cesare, A.J. and Hinde, E. (2019) Phasor histone FLIM-FRET microscopy quantifies spatiotemporal rearrangement of chromatin architecture during the DNA damage response. *Proc. Natl. Acad. Sci. U.S.A.*, **116**, 7323–7332.
- Lu, H., Saha, J., Beckmann, P.J., Hendrickson, E.A. and Davis, A.J. (2019) DNA-PKcs promotes chromatin decondensation to facilitate

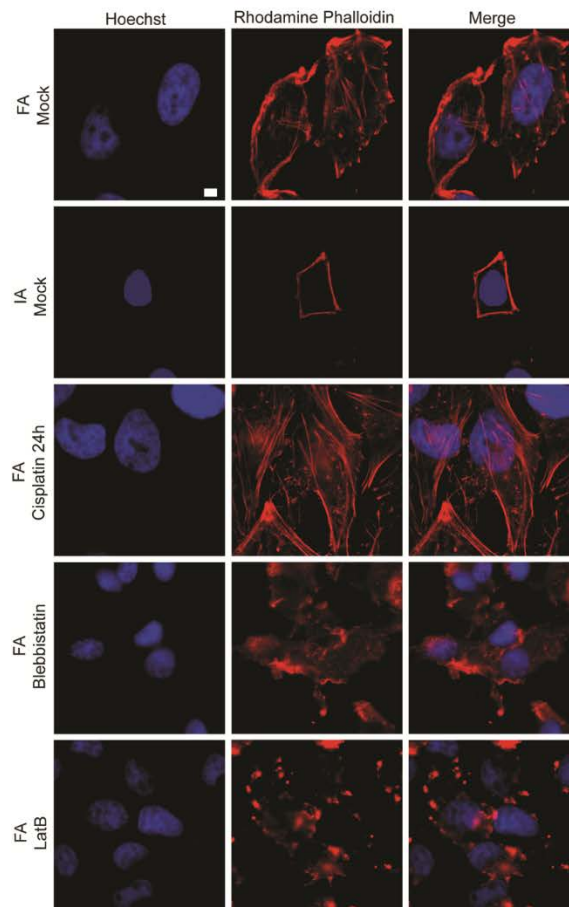
- initiation of the DNA damage response. *Nucleic Acids Res.*, **47**, 9467–9479.
36. Hauer, M.H. and Gasser, S.M. (2017) Chromatin and nucleosome dynamics in DNA damage and repair. *Genes Dev.*, **31**, 2204–2221.
 37. Sun, X., Zhang, A., Baker, B., Sun, L., Howard, A., Buswell, J., Maurel, D., Masharina, A., Johnsson, K., Noren, C.J. *et al.* (2011) Development of SNAP-tag fluorogenic probes for wash-free fluorescence imaging. *ChemBiochem*, **12**, 2217–2226.
 38. Toseland, C.P. (2013) Fluorescent labeling and modification of proteins. *J. Chem. Biol.*, **6**, 85–95.
 39. Pfeifer, C.R., Xia, Y., Zhu, K., Liu, D., Irianto, J., Garcia, V.M.M., Millán, L.M.S., Niese, B., Harding, S., Deviri, D. *et al.* (2018) Constricted migration increases DNA damage and independently represses cell cycle. *Mol. Biol. Cell*, **29**, 1948–1962.
 40. Cho, S., Vashisth, M., Abbas, A., Majkut, S., Vogel, K., Xia, Y., Ivanovska, I.L., Irianto, J., Tewari, M., Zhu, K. *et al.* (2019) Mechanosensing by the lamina protects against nuclear rupture, dna damage, and cell-cycle arrest. *Dev. Cell*, **49**, 920–935.
 41. Nava, M.M., Miroshnikova, Y.A., Biggs, L.C., Whitefield, D.B., Metge, F., Boncas, J., Vihinen, H., Jokitalo, E., Li, X., Garcia Arcos, J.M. *et al.* (2020) Heterochromatin-driven nuclear softening protects the genome against mechanical stress-induced damage. *Cell*, **181**, 800–817.
 42. Xia, Y., Ivanovska, I.L., Zhu, K., Smith, L., Irianto, J., Pfeifer, C.R., Alvey, C.M., Ji, J., Liu, D., Cho, S. *et al.* (2018) Nuclear rupture at sites of high curvature compromises retention of DNA repair factors. *J. Cell Biol.*, **217**, 3796–3808.
 43. Discher, D.E., Janmey, P. and Wang, Y.-I. (2005) Tissue cells feel and respond to the stiffness of their substrate. *Science*, **310**, 1139–1143.
 44. Rehfeldt, F., Engler, A.J., Eckhardt, A., Ahmed, F. and Discher, D.E. (2007) Cell responses to the mechanochemical microenvironment—implications for regenerative medicine and drug delivery. *Adv. Drug. Deliv. Rev.*, **59**, 1329–1339.
 45. Neelam, S., Chancellor, T.J., Li, Y., Nickerson, J.A., Roux, K.J., Dickinson, R.B. and Lele, T.P. (2015) Direct force probe reveals the mechanics of nuclear homeostasis in the mammalian cell. *Proc. Natl. Acad. Sci. U.S.A.*, **112**, 5720–5725.
 46. Wang, X., Liu, H., Zhu, M., Cao, C., Xu, Z., Tsatskis, Y., Lau, K., Kuok, C., Filleter, T., McNeill, H. *et al.* (2018) Mechanical stability of the cell nucleus—roles played by the cytoskeleton in nuclear deformation and strain recovery. *J. Cell Sci.*, **131**, jcs209627.
 47. Alisafaei, F., Jokhun, D.S., Shivashankar, G.V. and Shenoy, V.B. (2019) Regulation of nuclear architecture, mechanics, and nucleocytoplasmic shuttling of epigenetic factors by cell geometric constraints. *Proc. Natl. Acad. Sci. U.S.A.*, **116**, 13200–13209.
 48. Swift, J., Ivanovska, I.L., Buxboim, A., Harada, T., Dingal, P.C.D.P., Pinter, J., Pajewski, J.D., Spinler, K.R., Shin, J.-W., Tewari, M. *et al.* (2013) Nuclear Lamin-A scales with tissue stiffness and enhances matrix-directed differentiation. *Science*, **341**, 1240104.
 49. Sharma, S., Santiskulvong, C., Rao, J., Gimzewski, J.K. and Dorigo, O. (2014) The role of Rho GTPase in cell stiffness and cisplatin resistance in ovarian cancer cells. *Integr. Biol.*, **6**, 611–617.
 50. Raudenska, M., Kratochvilova, M., Vicar, T., Gumloc, J., Balvan, J., Polanska, H., Pribyl, J. and Masarik, M. (2019) Cisplatin enhances cell stiffness and decreases invasiveness rate in prostate cancer cells by actin accumulation. *Sci. Rep.*, **9**, 1660.
 51. Kühne, M., Riballo, E., Rief, N., Rothkamm, K., Jeggo, P.A. and Löbrich, M. (2004) A double-strand break repair defect in ATM-Deficient cells contributes to radiosensitivity. *Cancer Res.*, **64**, 500–508.
 52. Riballo, E., Kühne, M., Rief, N., Doherty, A., Smith, G.C.M., Recio, M.a.-J., Reis, C., Dahm, K., Fricke, A., Krempler, A. *et al.* (2004) A pathway of double-strand break rejoining dependent upon ATM, artemis, and proteins locating to γ -H2AX foci. *Mol. Cell*, **16**, 715–724.
 53. Murga, M., Jaco, I., Fan, Y., Soria, R., Martinez-Pastor, B., Cuadrado, M., Yang, S.-M., Blasco, M.A., Skoultschi, A.I. and Fernandez-Capetillo, O. (2007) Global chromatin compaction limits the strength of the DNA damage response. *J. Cell Biol.*, **178**, 1101–1108.
 54. Kocgozlu, L., Lavalle, P., Koenig, G., Senger, B., Haikel, Y., Schaa, P., Voegel, J.-C., Tenenbaum, H. and Vantier, D. (2010) Selective and uncoupled role of substrate elasticity in the regulation of replication and transcription in epithelial cells. *J. Cell Sci.*, **123**, 29–39.
 55. Klein, E.A., Yin, L., Kothapalli, D., Castagnino, P., Byfield, F.J., Xu, T., Levental, I., Hawthorne, E., Janney, P.A. and Assoian, R.K. (2009) Cell-cycle control by physiological matrix elasticity and in vivo tissue stiffening. *Curr. Biol.*, **19**, 1511–1518.
 56. Mih, J.D., Marinkovic, A., Liu, F., Sharif, A.S. and Tschumperlin, D.J. (2012) Matrix stiffness reverses the effect of actomyosin tension on cell proliferation. *J. Cell Sci.*, **125**, 5974–5983.
 57. Kumar, A., Mazzanti, M., Mistrik, M., Kosar, M., Bezoussenko, G.V., Mironov, A.A., Garre, M., Parazzoli, D., Shivashankar, G.V., Scita, G. *et al.* (2014) ATR mediates a checkpoint at the nuclear envelope in response to mechanical stress. *Cell*, **158**, 633–646.
 58. Aureille, J., Buffière-Ribot, V., Harvey, B.E., Boyault, C., Pernet, L., Andersen, T., Bacola, G., Balland, M., Fraboulet, S., Van Landeghem, L. *et al.* (2019) Nuclear envelope deformation controls cell cycle progression in response to mechanical force. *EMBO Rep.*, **20**, e48084.
 59. Tajik, A., Zhang, Y., Wei, F., Sun, J., Jia, Q., Zhou, W., Singh, R., Khanna, N., Belmont, A.S. and Wang, N. (2016) Transcription upregulation via force-induced direct stretching of chromatin. *Nat. Mater.*, **15**, 1287–1296.
 60. Park, S. (2018) Mechanical alteration associated with chemotherapeutic resistance of breast cancer cells. *J. Cancer Prevent.*, **23**, 87–92.
 61. Liu, H.-C., Gang, E.J., Kim, H.N., Lim, H.G., Jung, H., Chen, R., Abdel-Azim, H., Shung, K.K. and Kim, Y.-M. (2018) Characterizing deformability of drug resistant patient-derived acute lymphoblastic leukemia (ALL) cells using acoustic tweezers. *Sci. Rep.*, **8**, 15708.

3.2.2.1. Supplementary Material for Manuscript 2

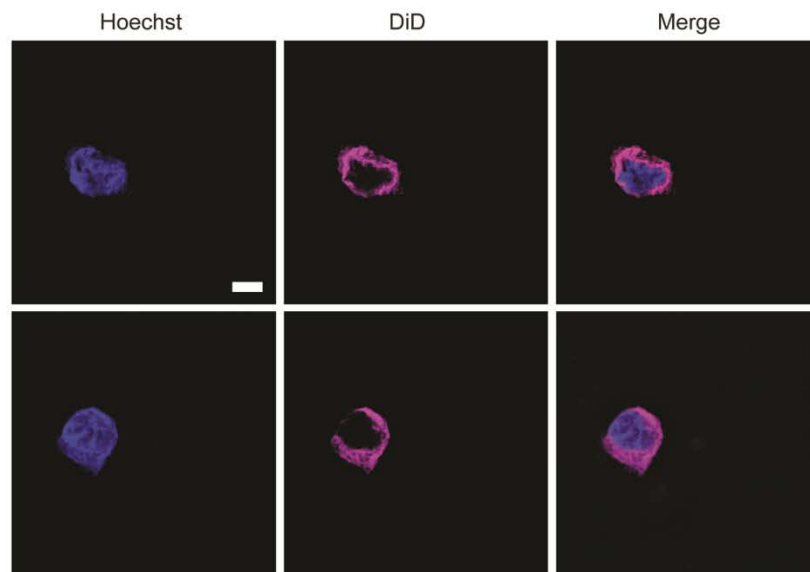
DNA damage alters nuclear mechanics through chromatin reorganisation

Ália dos Santos¹, Alexander W. Cook¹, Rosemarie E Gough¹, Martin Schilling², Nora Aleida Olszok², Ian Brown³, Lin Wang⁴, Jesse Aaron⁵, Marisa L. Martin-Fernandez⁴, Florian Rehfeldt^{2,6*} and Christopher P. Toseland^{1*}

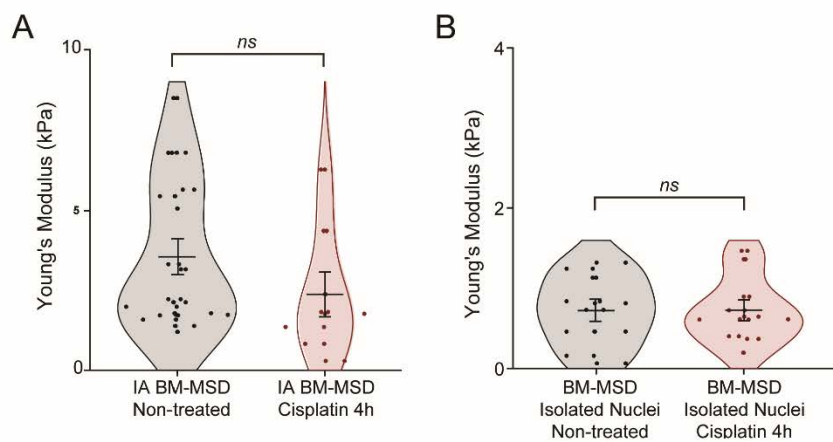
Supplementary Figures



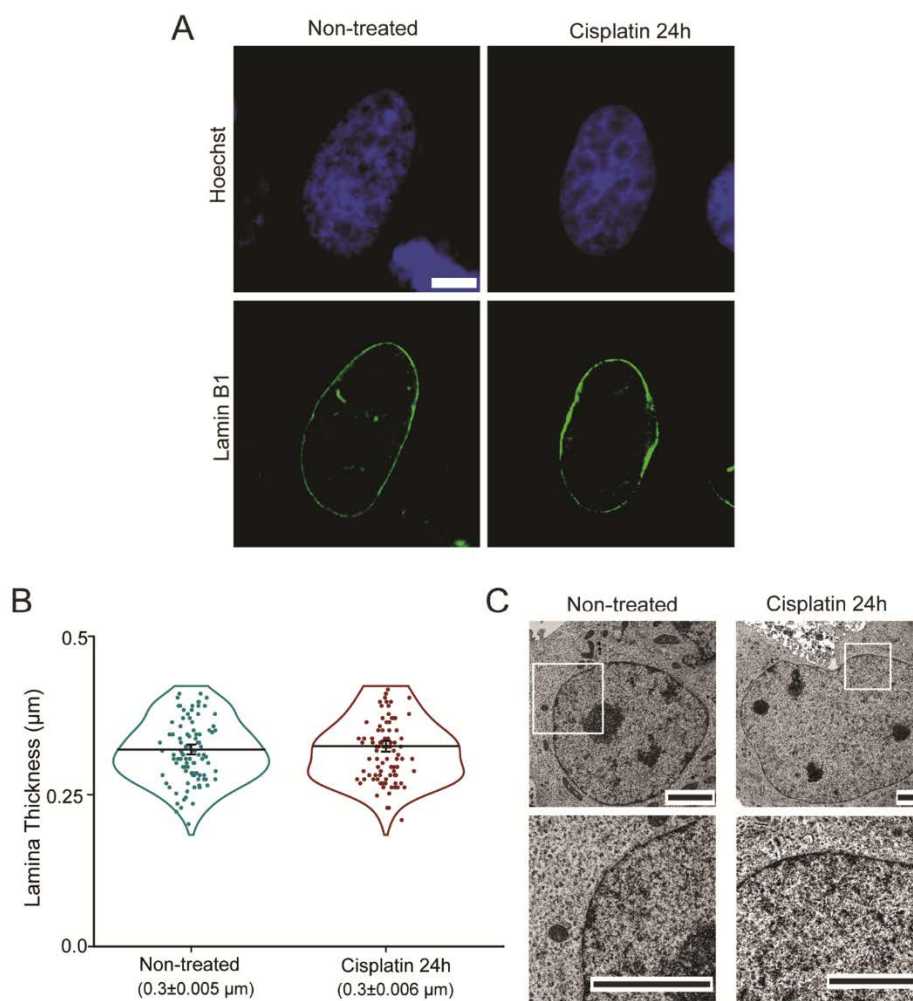
Supplementary Figure 1 – Actin labelling of HeLa cells under different conditions. Wide-field microscopy of actin labelled with Rhodamine Phalloidin, shown in red, and nuclear stain Hoechst, in blue, under stated conditions. (Scale bar = 5µm).



Supplementary Figure 2 – Membrane integrity in isolated nuclei. Wide-Field image of isolated nuclei with Hoechst DNA labelling and membrane staining using DiD. (Scale bar = 5 μ m).



Supplementary Figure 3 – Mechanics of Bone-marrow Mesenchymal stem cells (BM-MSD). (A) Young's modulus values for initially adhered BM-MSD cells before and after 4h cisplatin treatment. Non-treated: n = 17, mean +/- SE = 3.5 +/- 0.6. Cisplatin 4h: n = 8, mean +/- SE = 2.4 +/- 0.7. p = 0.23. (B) Young's modulus values for BM-MSD nuclei from non-treated cells and following 4h cisplatin treatment. Non-treated: n = 10, mean +/- SE = 0.7 +/- 0.1. Cisplatin 4h: n = 10, mean +/- SE = 0.7 +/- 0.1. p = 0.97. (B)



Supplementary Figure 4 – Nuclear envelope integrity in HeLa cells after cisplatin treatment. (A) Wide-field immunofluorescent images of Lamin B1 in non-treated and cisplatin-treated cells (green). (Scale bar = $5\mu\text{m}$). **(B)** Measurements of nuclear lamina thickness, using Lamin B1 as a marker. Each point represents the average of 5 measurements at different regions in the nucleus of non-treated ($n = 101$) and long cisplatin treatment ($n = 100$) $p > 0.05$, calculated using a two-tailed t-test and assuming equal variance. Mean \pm SE values are plotted. **(C)** Electron microscopy images showing membrane integrity in nuclei of both conditions. Lower panel shows zoomed in region in white square. (Scale bar = $2\mu\text{m}$).

4. Activation of nuclear Myosin VI function

4.1. Context of Research and Contributions

In order to study nuclear architecture and organisation, it is important not only to investigate the overall physical properties of the nucleus, but also to understand how enzymatic processes that occur within the organelle are regulated. In the previous chapter, our work makes a clear connection between nuclear mechanics and activation of DDR, by showing that changes to global chromatin conformation following ATM kinase activation directly affect nuclear stiffness. Here, we investigate another important nuclear process – RNAPII transcription.

A major aim of this thesis is to explore the role of nuclear MVI in the regulation of RNAPII transcription. However, in order to do this, we first need to understand how the biochemical functions of MVI are regulated, to assign a nuclear role to the protein. In this chapter, we investigated the activation of nuclear MVI by trying to answer the following questions:

- i) *Which specific splice-isoforms of MVI are recruited into the nucleus? How is MVI-RNAPII binding mediated and what biochemical properties of MVI are involved in the regulation of gene expression? How does competition between binding sites determine MVI cellular function?*
- ii) *How do interactions with binding partners regulate backfolding, dimerization and activation of MVI motor function?*

We shed light on these questions in three different publications (two publications that mainly address questions posed in i and one for ii), as listed below. Contributions are also stated below.

- i) **Activation of nuclear MVI for RNA Polymerase II transcription.** The first part of this chapter is described in the following two publications:

Fili N, Hari-Gupta Y, dos Santos Á, Cook A, Poland S, Ameer-Beg SM, Parsons M, Toseland CP, NDP52 activates nuclear myosin VI to enhance RNA polymerase II transcription. **Nature Communications 8 1871 (2017)**

Fili N*, Hari-Gupta Y*, Aston B, **dos Santos Á**, Gough RE, Alamad B, Wang L, Martin-Fernandez ML, Toseland CP, Competition between two high-and low-affinity protein-binding sites in myosin VI controls its cellular function. (*equal contribution) **Journal of Biological Chemistry 295(2): 337-347(2019)**

Over the last decade, the role of nuclear actin and myosins has gained increasing interest. So far, myosins have been reported in the context of chromatin remodelling, transcription regulation and DNA repair. The ability of myosins to generate force through ATP hydrolysis makes these proteins particularly interesting subjects in the study of nuclear organisation. Whilst previous work has linked MVI to RNAPII-dependent transcription and gene pairing events through chromatin reorganisation, at the time of the work presented in this chapter, the exact molecular mechanisms through which MVI performs these functions were largely unknown. In the first part of this of this chapter, we show that MVI regulates gene expression by nuclear receptors and that interactions with RNAPII are dependent on the ability of the molecular motor to bind DNA. Furthermore, we show that MVI motor activity is essential for its role in transcription. We thus propose a model for the activation of MVI and another for the possible molecular mechanism of MVI regulatory role in transcription.

Contributions

For the two publications listed in this sub-aim I was not a main contributor. My specific contributions were as follows: I performed nuclear extractions, recombinant protein expression and purification as well as DNA titration assays specifically for NDP52 and tDab2. I designed and performed cell proliferation experiments. I analysed cell proliferation assay data. All other experiments were led by Dr Fili (Fili *et al.*, 2017) or Dr Fili and Dr Hari-Gupta (Fili *et al.*, 2020) and contributions from additional authors are specified within the manuscript.

- ii) **Binding partners regulate unfolding of myosin VI to activate the molecular motor.** The following manuscript describes the second part of the work presented in this chapter:

dos Santos Á*, Fili N*, Hari-Gupta Y, Gough RE, Wang L, Martin-Fernandez M, Aaron J, Chew TL, Toseland CP; Binding partners regulate unfolding of myosin VI to activate the molecular motor. (*equal contribution) **BioRxiv (2020)**

<https://doi.org/10.1101/2020.05.10.079236>

This work further characterises the properties of MVI, in particular its ability to form molecular clusters, a property frequently found in the context of nuclear processes. Following the work performed in **i**), we decided to follow up on the activation of MVI motor activity by binding partners. In Fili *et al.* (Fili *et al.*, 2017), in addition to our findings relative to MVI function in transcription, we also propose a model of activation for the nuclear isoform of MVI (NI-MVI). In this model, activation of MVI required interactions between monomeric, backfolded, NI-MVI and binding partner NDP52. This interaction triggers unfolding of this auto-inhibited conformation, followed by subsequent dimerization and activity of MVI as a processive motor. From this earlier model, some questions were left unanswered. For example: are all isoforms of MVI similarly regulated through binding partner interactions at different binding motifs? Do binding partners induce unfolding of auto-inhibited MVI or simply stabilise this configuration? Is dimerization an intrinsic property of MVI or does it rely on oligomerisation of regulating partners? How relevant are these interactions in a cellular context for the regulation of MVI activity? In the second part of this chapter, we explore these questions.

Contributions

I prepared samples for STORM and acMFM and shared equally with Dr Christopher Toseland acquisition of single-molecule imaging experiments - STORM and acMFM. Both Dr Christopher Toseland and myself used analysis tools developed by Dr Jesse Aaron at HHMI Janelia Research Campus (U.S.) to analyse acMFM data. Additionally, I established a cluster analysis protocol to process STORM data using the tools published by Pagoon *et al.* (Pagoon *et al.*, 2016). This allowed quantification of MVI clustering to understand its spatial organisation of proteins. I also expressed and produced recombinant NDP52 and performed SEC-MALS experiments with this protein. Dr Natalia Fili performed all molecular biology work. All kinetic experiments and kinetic data analysis was performed by Dr Christopher Toseland.

4.2. Manuscripts

(see below)

4.2.1. Manuscript 3 - NDP52 activates nuclear myosin VI to enhance RNA polymerase II transcription.

ARTICLE

DOI: 10.1038/s41467-017-02050-w

OPEN

NDP52 activates nuclear myosin VI to enhance RNA polymerase II transcription

Natalia Fili¹, Yukti Hari-Gupta¹, Ália dos Santos¹, Alexander Cook¹, Simon Poland², Simon M. Ameer-Beg^{1,2}, Maddy Parsons² & Christopher P. Toseland¹

Myosin VI (MVI) has been found to be overexpressed in ovarian, breast and prostate cancers. Moreover, it has been shown to play a role in regulating cell proliferation and migration, and to interact with RNA Polymerase II (RNAPII). Here, we find that backfolding of MVI regulates its ability to bind DNA and that a putative transcription co-activator NDP52 relieves the auto-inhibition of MVI to enable DNA binding. Additionally, we show that the MVI-NDP52 complex binds RNAPII, which is critical for transcription, and that depletion of NDP52 or MVI reduces steady-state mRNA levels. Lastly, we demonstrate that MVI directly interacts with nuclear receptors to drive expression of target genes, thereby suggesting a link to cell proliferation and migration. Overall, we suggest MVI may function as an auxiliary motor to drive transcription.

¹School of Biosciences, University of Kent, Canterbury CT2 7NJ, UK. ²Randall Division of Cell and Molecular Biophysics, King's College London, Guys Campus, London SE1 1UL, UK. Correspondence and requests for materials should be addressed to C.P.T. (email: c.toseland@kent.ac.uk)

M yosins are molecular motors that perform vital roles in a plethora of cellular processes. Myosin VI (MVI) is a unique member of the myosin family with the ability to move towards the minus end of actin filaments¹. This property enables MVI to be involved in cell migration, endocytosis, exocytosis and transcription^{2, 3}. The functional diversity of MVI relies on its tightly regulated association with various binding partners. Given its multi-potent nature, malfunction of MVI leads to various diseases including cardiomyopathy, deafness and cancer^{4–7}.

MVI comprises a motor domain, followed by a neck region consisting of a unique insert, which confers the reverse directionality, and an IQ domain (Fig. 1a). The N-terminal tail domain (N_{MVI}TAIL) contains two structural domains a three-helix-bundle (amino acids 835–916)⁸ (3HB) and a single-alpha-helix (amino acids 942–978) (SAH)⁹. The C-terminal tail domain contains the globular cargo binding domain (CBD). In addition, two regions within the tail can be alternatively spliced resulting in a 31-residue insertion (large insert, LI) before the CBD, and/or an 8-residue insertion in the CBD (small insert, SI). This leads to four splice isoforms, the non-insert (NI), SI, LI and LI + SI¹⁰.

The CBD confers specificity for cargo through its ability to bind partners, such as Dab2, GIPC and NDP52, at two motifs WWY and RRL^{11–13}. NDP52 was initially identified in the nucleus^{14, 15} but has been better characterised in cell adhesion and autophagy^{11, 16}. Intriguingly, NDP52 shares 70% sequence identity to its family member CoCoA, a known transcription co-activator, which suggests a potential role in transcription¹⁷.

MVI is overexpressed in aggressive cancers including ovarian, breast and prostate^{5, 7, 18}, and depletion of MVI leads to decreased cell motility and/or proliferation^{18–20}. As MVI is known to have roles in gene expression^{3, 21}, it is possible that this is linked to the nuclear role of MVI.

To shed light upon this hypothesis, here we have explored the potential functions of nuclear MVI. The association of MVI with RNAPII is dependent upon its DNA binding, which is in turn regulated by co-activator NDP52. This alters the MVI oligomeric and mechanical properties. Moreover, MVI interacts with nuclear receptors for specific gene targeting. We suggest MVI is an auxiliary motor for RNAPII to drive gene expression.

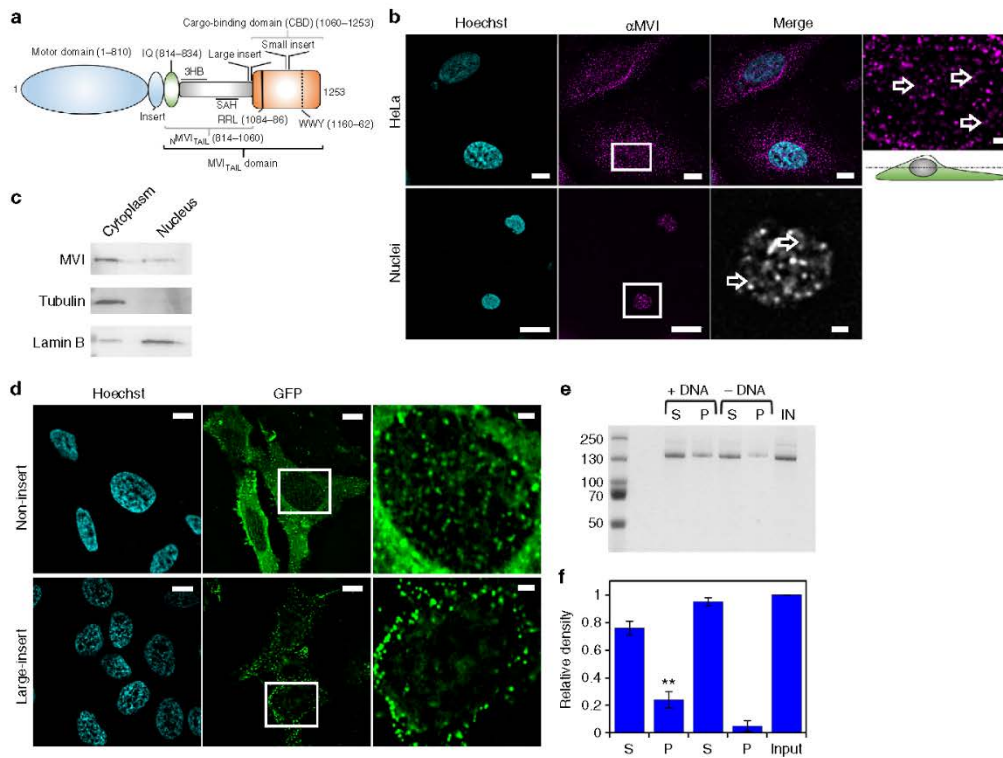


Fig. 1 Myosin VI is distributed throughout the nucleus. **a** Cartoon depiction of the MVI domains and key features discussed in the text. **b** Immunofluorescence staining against MVI (magenta) and DNA (cyan) in HeLa cells and isolated nuclei (see Supplementary Fig. 1 for nuclei images). Arrows highlight filamentous structures within the nucleus. Images were acquired at the mid-point of the nucleus. Scale bar 10 μ m for whole images and 1 μ m for inserts. **c** Western blot against MVI following HeLa cell fractionation. Tubulin and lamin B are used as cytoplasmic and nuclear markers, respectively. **d** Representative images of transiently expressed NI- and LI-GFP-MVI in HeLa cells combined with DNA staining (cyan) (Supplementary Fig. 3). Images acquired as in B. **e** Pull-down of recombinant MVI using a 500 bp DNA substrate. **f** Plot of band intensities normalised to the input sample (5 μ M). Errors bars represent SEM from three independent preparations. (**p < 0.001 by two-tailed t-test between presence and absence of DNA)

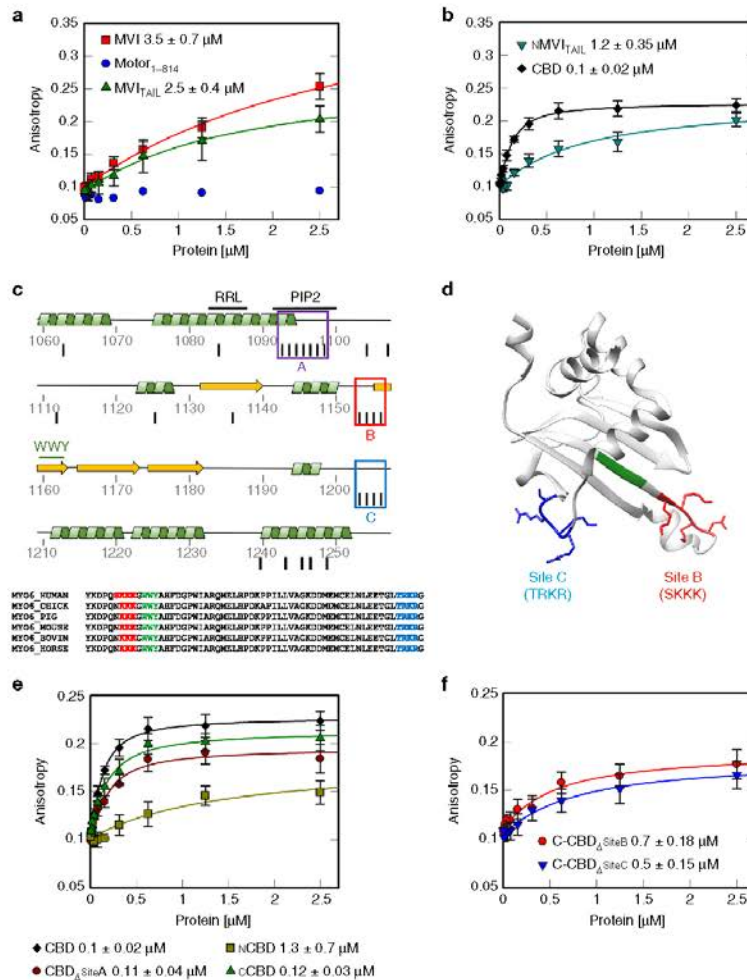


Fig. 2 DNA binding by myosin VI. **a, b** Fluorescence anisotropy titrations of MVI domains against a 40 bp fluorescein amidite (FAM)-DNA (50 nM). Data fitting was performed as described in Methods ($K_d \pm$ SEM $n = 3$ independent experiments). Due to the low binding affinity, Mot₁₋₈₁₄ could not be fitted using the model. **c** Cartoon depicting the secondary structure within the CBD. Binding partner motifs and known lipid binding sites are highlighted along with three predicted clusters of DNA binding. Black lines represent residues predicted to be involved in DNA binding. Sequence alignment shows the conservation of sites B and C. **d** Structure of cCBD with site B (red), C (blue) and WWVY motif (green) (PDB:2KIA⁵⁴). **e, f** Fluorescence anisotropy titrations of CBD constructs, as performed in **a**

Results

Myosin VI non-insert isoform is recruited to the nucleus. Before exploring the nuclear role of MVI, we first assessed its distribution. Immunofluorescence on both HeLa cells, and isolated nuclei, and cell fractionation confirmed an endogenous nuclear population (Fig. 1b, c and Supplementary Movies 1–5), consistent with previous reports⁵. MVI was distributed throughout the nucleus, although occluded from the nucleoli. MVI decorated punctate and filamentous structures, which occasionally interconnected forming small networks (Fig. 1b, Supplementary Movies 1 and 2). To explore the nature of these

structures, we tested the possibility of MVI localising on nuclear actin filaments. Dense nuclear actin cables were absent in whole cells (Supplementary Fig. 2a and Supplementary Movie 6), but a sparse actin network may be present. However, the lack of staining in the isolated nuclei (Supplementary Fig. 2a) suggested that MVI structures are not actin-based but may represent MVI bound to chromatin.

Recently, it was shown that several cancers only express the NI isoform²², as is the case in HeLa cells. Yet, it has not been shown if the isoform selection and nuclear localisation are functionally linked. To address whether such a relationship exists, we

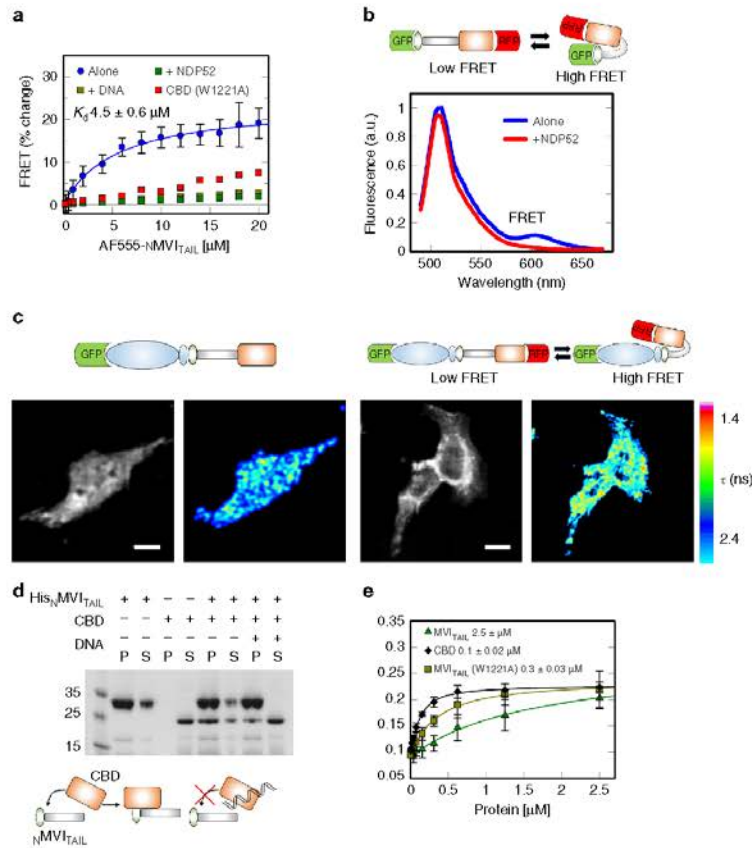


Fig. 3 Regulation of myosin VI backfolding. **a** FRET titration of $\text{NMVI}_{\text{TAIL}}$ against CBD (1 μM) or CBD(W1221A) in the presence of DNA, or NDP52, at 10 μM . Data fitting was performed as described in Methods. NDP52 and CBD(W1221A) data are plotted as disconnected points due to low signal change. See Supplementary Fig. 4a–c for raw intensity data. **b** Representative fluorescence spectra of 2 μM GFP-MVI_{TAIL}-RFP \pm 15 μM NDP52. **c** FLIM measurements of in vivo MVI conformational dynamics. Above, schematic showing the constructs. Left, GFP intensity and lifetime images. Right, intensity and lifetime images of the biosensor. Lifetime (τ) is represented by a pseudocolor scale. Scale bar is 20 μm . **d** Pull-down of CBD by His₆-tagged $\text{NMVI}_{\text{TAIL}}$ both at 10 μM \pm 20 μM 40 bp DNA. P and S represent pellet and supernatant fractions. **e** Fluorescence anisotropy titrations of MVI domains against a 40 bp FAM DNA, as performed in Fig. 2a

compared the intracellular distribution of transiently expressed EGFP-NI- and LI-MVI. EGFP-NI-MVI had a similar distribution to the endogenous protein (Fig. 1d). Strikingly, EGFP-LI-MVI localisation was restricted to the cell periphery (Fig. 1d and Supplementary Fig. 3a, b).

The LI has been recently shown to encode an alpha-helix that blocks the RRL-motif, establishing an isoform-specific regulation for the interactions with binding partners²². A point-mutation within the LI, namely M1062Q, disrupts this process. As expected, EGFP-LI-MVI(M1062Q) had a similar cellular distribution to the NI isoform (Supplementary Fig. 3c). Taken together, these data demonstrate that splicing regulates the recruitment of MVI into the nucleus, likely by controlling access to the RRL-motif.

Myosin VI binds DNA through its CBD. The presence of MVI throughout the nucleus and its known association with RNAPII

leads to the intriguing possibility that this myosin might bind to chromatin. BindN²³ predicted sites for interaction with DNA are highlighted throughout MVI, with higher frequency within its tail (Supplementary Table 1 and Fig. 2b). To establish if MVI can interact with DNA, we used a DNA pull-down assay. Recombinant NI-MVI was isolated in complex with the linear DNA (Fig. 1e).

To further explore this interaction in a quantitative manner, we utilised fluorescence anisotropy. MVI was titrated against DNA revealing a relatively weak binding (Fig. 2a and Supplementary Table 2). To identify the regions within MVI that mediate DNA binding, the titrations were also performed using isolated domains. Our results demonstrate that the DNA-binding ability is restricted to the MVI_{TAIL} (Fig. 2a). Intriguingly, the isolated CBD displayed a 25-fold higher affinity for DNA (Fig. 2b). The CBD bound promiscuously to single-stranded and double-stranded DNA of varying composition, although weaker for

substrates <20 bases (Supplementary Fig. 2c). The N-terminal MVI_{TAIL} (N_{MVI}TAIL814-1060) also bound DNA, but not as strongly as the CBD (Fig. 2b). A summary of the kinetic parameters is presented in Supplementary Table 2.

To understand the DNA-binding mechanism, we used pre-steady-state measurements. Here, the CBD had a four-fold higher association rate constant than full-length (FL) protein, while the dissociation rate constant was essentially unchanged (Supplementary Fig. 2d and Supplementary Table 3). This indicated that once binding is achieved, the stability of the bound state is the same in both constructs. Therefore, we conclude that MVI binds DNA through its CBD and this binding is impeded in the FL-MVI, possibly due to the adopted conformation.

DNA binding occurs through two adjacent loops in the CBD.

We decided to identify the sites conferring the DNA-binding ability. Based on predictions, we distinguished three clusters—sites A–C (Fig. 2c) in the MVI_{TAIL}. We generated various MVI_{TAIL} mutants and truncations, and assessed their DNA-binding potential. Mutagenesis of site A, which corresponds to a known PIP₂ lipid-binding site¹³, perturbed lipid binding (Supplementary Fig. 2e), but only partially affected DNA interactions (Fig. 2e). This suggested that binding occurs through sites B and C. This was further reinforced when we tested two truncations of CBD, N_{CBD}1060-1120 (containing Site A) and C_{CBD}1121-1253 (containing sites B and C) (Fig. 2e). N_{CBD} displayed a considerably reduced DNA binding, while the C_{CBD} was indistinguishable from the entire CBD domain. Sites B and C are located on two highly conserved adjacent loops which likely form a single binding surface in close proximity to the WWY motif (Fig. 2d). Alanine mutagenesis of either site reduced DNA binding (Fig. 2f), indicating that both sites are required for efficient interaction with the DNA. Mutagenesis of both sites destabilised the domain thereby preventing the measurements.

Backfolding of myosin VI regulates its ability to bind DNA.

As shown above, although the CBD binds DNA efficiently, the binding ability of the FL protein is impeded. This suggests that DNA binding is regulated. MVI is suggested to regulate its activity through backfolding^{24–26}. We therefore explored if such a mechanism regulates DNA association. Having already established that the MVI_{TAIL} displayed similar DNA binding behaviour as FL-MVI (Fig. 2a), we hypothesised that, if backfolding occurs, the tail should fold upon itself. Hence, we assessed whether the CBD and the N_{MVI}TAIL can form an interaction. To this end, a FRET-based assay was employed by titrating Alexa555-N_{MVI}TAIL to FITC-CBD. A significant change in FRET was detected, indicating that the two domains are in close proximity (Fig. 3a, dissociation constants are summarised in Supplementary Table 4). A fluorescence anisotropy assay confirmed this interaction (Supplementary Fig. 4d). To further confirm the ability of the MVI_{TAIL} to backfold, we used a dual-labelled construct, GFP-MVI_{TAIL}-RFP. Here, FRET would report upon the folded state. Indeed, a small FRET signal was observed (Fig. 3b), indicating a degree of backfolding.

While we have explored how backfolding occurs *in vitro*, it is unknown if this occurs *in vivo*. To explore the *in vivo* conformation dynamics, we used fluorescence lifetime imaging (Fig. 3c). A GFP-MVI-RFP construct was used as a conformation reporter in HeLa cells. Indeed, two populations were observed in a high and low FRET state, indicating that backfolding does occur *in vivo*.

The N_{MVI}TAIL-CBD complex represents the folded form, where we propose the DNA-binding sites are occluded. To test whether backfolding and DNA binding are mutually exclusive, we

performed the *in vitro* FRET measurements with a pre-formed CBD–DNA complex. There was a lack of interaction between the N_{MVI}TAIL and CBD–DNA complex, suggesting that the presence of DNA prevented backfolding (Fig. 3a). To further confirm our results, all the above interactions were also assessed using pull-down assays (Fig. 3d). The CBD co-purified with N_{MVI}TAIL whereas the presence of DNA sequestered the CBD. Taken together, these data demonstrate that DNA binding is regulated through intra-molecular backfolding.

Calcium does not regulate myosin VI backfolding.

A mechanism controlling the open/closed state of the tail could be regulated by cofactors such as ATP, actin and Ca²⁺. However, DNA binding by MVI was not enhanced in their presence (Supplementary Fig. 4f), even though Ca²⁺-Calmodulin was recently reported to regulate the backfolding of MVI²⁴. Pull-down assays in the presence of CBD, with and without calcium were performed using two truncations Motor₁₋₈₁₄ and Motor₁₋₁₀₆₀, containing 1 or 2 calmodulin binding sites, respectively. All constructs containing the motor domain were co-expressed with calmodulin. Supplementary Fig. 4g shows that both constructs associated with the CBD. Whilst expected for the Motor₁₋₁₀₆₀ binding to Motor₁₋₈₁₄ suggested the CBD also forms extensive contacts with the motor domain, which is consistent with SAXS data by Spink²⁶. However, Ca²⁺ had no discernible impact upon these interactions, in contrast to Batters²⁴. This discrepancy could be attributed to the fact that, in their work, the pull-down experiments, which were assessing the ability of the tail to backfold, were only performed in the absence of Ca²⁺. Instead, only far-dot western blots were performed in the presence of Ca²⁺. However, those experiments were addressing the effect of Ca²⁺ on the interaction of the tail with calmodulin, rather than the backfolding of the tail itself.

Interaction with NDP52 regulates myosin VI backfolding.

Having established that ATP, actin and Ca²⁺ do not regulate MVI backfolding, we explored the possibility that a binding partner could be an alternative regulator. The adaptor binding site, the RRL-motif, is situated away from sites B to C and, therefore, it is unlikely to perturb DNA binding. One such protein, which binds this motif, is NDP52. To address whether NDP52 is an MVI regulator, the FRET assay between the N_{MVI}TAIL and the CBD was repeated following pre-incubation of the CBD with NDP52. Similar to DNA, NDP52 sequestered the CBD preventing the interaction between the two domains (Fig. 3a). Moreover, addition of excess of NDP52 in our GFP-MVI_{TAIL}-RFP reporter resulted in the loss of the FRET signal (Fig. 3b), indicating the tail's unfolding.

For NDP52 to elicit unfolding of MVI, it would need to disrupt sites within the protein that form a stable interaction, such as the recently proposed W1221²⁷. Mutagenesis lead to an increase in actin binding, which was attributed to unfolding of MVI. Using the FRET assay, we observed that CBD(W1221A) failed to bind to N_{MVI}TAIL (Fig. 3a), confirming that the mutation likely leads to the unfolding of the protein. Interestingly, the MVI_{TAIL}(W1221A) was able to bind DNA, similar to the CBD (Fig. 3e), indicating that the adopted conformation enhances the ability of MVI to bind DNA. Taken together, our data suggest a model, whereby NDP52 triggers a conformational change of MVI leading to an unfolded state with enhanced DNA binding ability.

NDP52 is a nuclear binding partner of myosin VI. While calcium and ATP are important regulators that fine-tune motor function, we show that NDP52 can trigger unfolding of MVI by relieving the autoinhibition between the CBD and the N-terminal

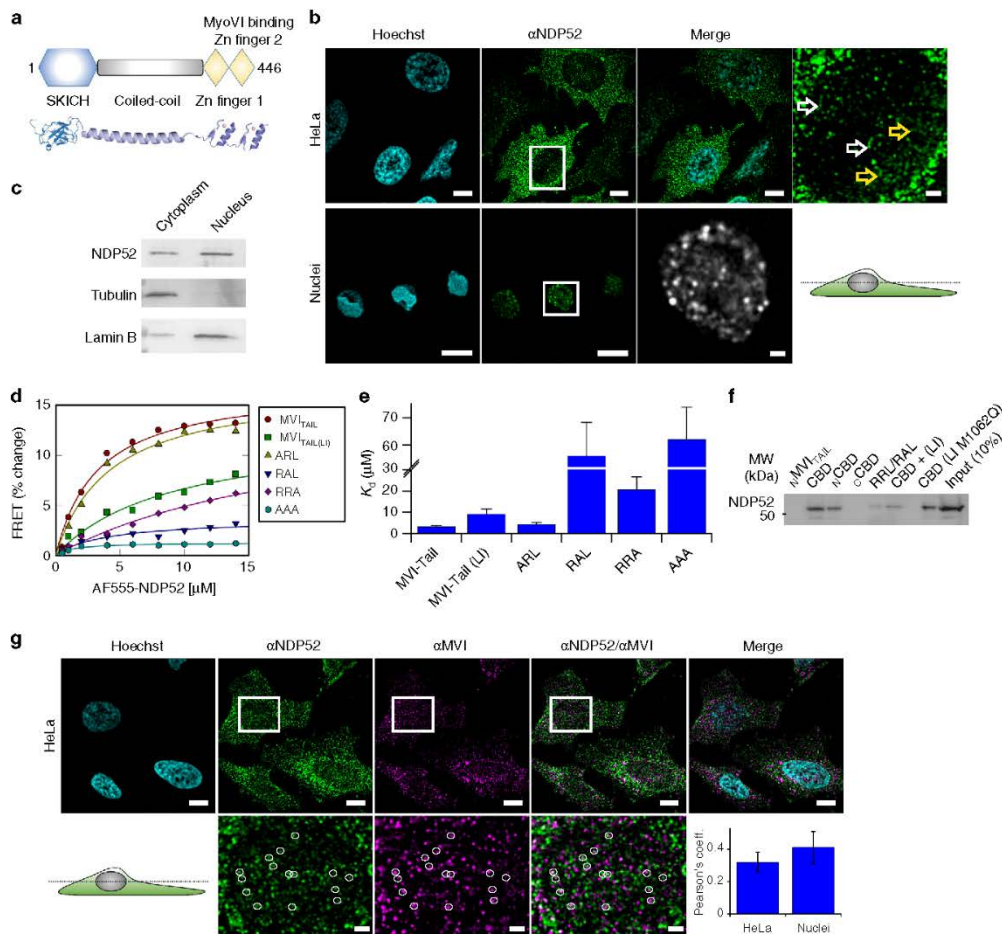


Fig. 4 NDP52 is a nuclear myosin VI binding partner. **a** Cartoon and structural model depicting NDP52 domains as mentioned in the text. **b** Immunofluorescence staining against NDP52 (green) and DNA (cyan) in HeLa cells and isolated nuclei, as performed in Fig. 1b. Arrows highlight filamentous structures. Scale bar 10 μm for whole images and 1 μm for inserts. **c** Western blot against NDP52 following HeLa cell fractionation. Tubulin and lamin B were used as cytoplasmic and nuclear markers, respectively. **d** FRET titration of MVI_{TAIL} constructs against NDP52 (1 μM). Data fitting was performed as described in Methods giving a K_d as plotted in **e** (error bars represent SEM from three independent experiments). **f** Western blot against NDP52 following isolation from nuclear extracts by MVI_{TAIL} constructs. Loading controls for the recombinant proteins is shown in Supplementary Fig. 9. **g** Immunofluorescence staining against NDP52 (green), MVI (magenta) and DNA (cyan), as performed in Fig. 1b. Insert depicts co-localising foci. Scale bar 10 μm for whole images and 1 μm for inserts. Pearson's coefficient is shown for HeLa and nuclei (Supplementary Fig. 5b). Error bars represent SEM from 10 images

tail/motor domain. In order to unravel the physiological relevance of our *in vitro* findings and explore the role of NDP52, we decided to characterise NDP52 and its interaction with MVI.

NDP52 consists of a SKICH domain followed by a long coiled-coil and two Zinc finger domains that may confer the ability to bind DNA (Fig. 4a). Indeed, we observed that NDP52 can bind DNA (Supplementary Fig. 5a) with high affinity. This binding precluded the use of this protein in our DNA-binding assays because the contribution by MVI would be masked by that of NDP52. However, together with MVI's ability to bind DNA and its nuclear distribution, this finding pointed towards the direction

of a potential partnership between NDP52 and MVI in the nucleus.

We observed the distribution of NDP52 in HeLa cells using immunofluorescence and cell fractionation. Endogenous NDP52 was distributed throughout the cytoplasm as well as into the nucleus, similar to MVI (Fig. 4b, c). The nuclear pool of NDP52 decorated punctate structures, which were, in places, interconnected into small ring-like networks (Supplementary Movie 7). Similar distribution was also observed in isolated HeLa nuclei, suggesting that these structures are stable (Fig. 4b and

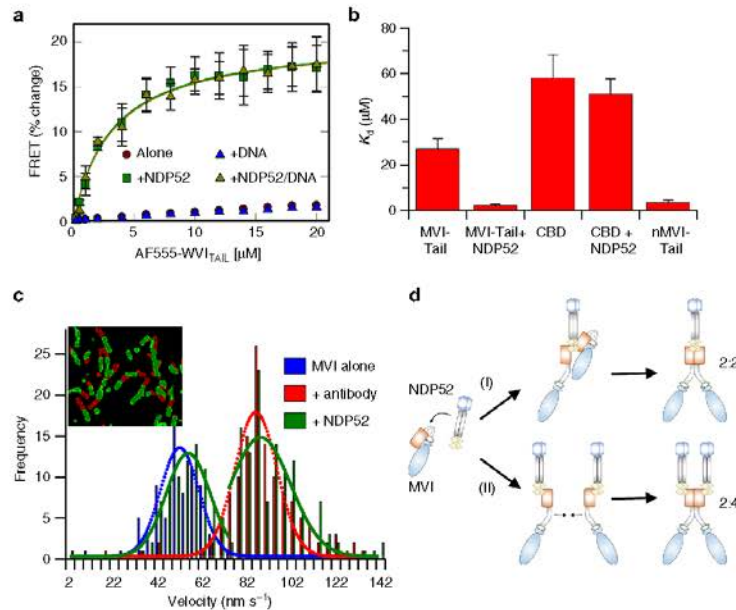


Fig. 5 NDP52-dependent dimerisation of myosin VI. **a** FRET titration of FITC-MVI_{TAIL} against 1 μ M AF555-MVI_{TAIL} \pm DNA (20 μ M) and NDP52 (20 μ M). Data fitting was performed as described in Methods giving a K_d as plotted in **b**. See Supplementary Fig. 7a–c for raw intensity data. **b** Plot of K_d from titrations in **a** and Supplementary Fig. 7d–g (error bars represent SEM from three independent experiments). **c** Velocity histogram from sliding filament assay with MVI immobilised alone (blue), through antibody (red) and NDP52 (green). Insert shows first frame (red) and after 60 s (green). **d** Two routes of NDP52-dependent dimerisation with different stoichiometry. (i) NDP52 unfolds MVI then directly recruits a second molecule. (ii) Each MVI is unfolded by an individual NDP52

Supplementary Movie 8). As with MVI, this may represent binding to chromatin.

To characterise the interaction between MVI and NDP52, we initially performed an in vitro FRET assay using FITC-MVI_{TAIL} and Alexa555-NDP52. NDP52 was titrated against MVI_{TAIL} containing various mutants of the RRL-site, as well as a LI-MVI_{TAIL} (Fig. 4d, e and Supplementary Table 4). Wild-type MVI_{TAIL} had a low micromolar affinity for NDP52. When we mutated the first arginine (ARL), there was essentially no effect upon NDP52 binding. Conversely, mutation of the second arginine (RAL) abolished the interaction, whereas removal of the leucine (RRA) led to a 10-fold decrease in affinity. Finally, the presence of the LI reduced binding by 4-fold.

This was complemented by pull-down assays using recombinant fragments of CBD as bait to search nuclear extracts for interactions with native nuclear NDP52 (Fig. 4f). As expected, binding occurred within the RRL-containing _NCBD. In addition, whereas the presence of the LI compromised the binding to NDP52, this effect was rescued by the MI062Q mutant. Overall, these data suggest that MVI can associate with the nuclear pool of NDP52. Indeed, when we immuno-stained HeLa cells (Fig. 4g) against the endogenous MVI and NDP52, we observed that the two proteins partially colocalised within the nucleus: they occasionally localised on the same punctate and filamentous structures, sometimes as part of the same local networks. This partial co-localisation is consistent with the micromolar dissociation constant, and is indicative of a dynamic interaction. The co-localisation was also dependent upon the MVI isoform whereby the LI displayed the lowest colocalisation (Supplementary Fig. 5c,

d). Therefore, taking all data together, we conclude that NDP52 is a nuclear partner of MVI.

Interaction with NDP52 mediates myosin VI dimerisation. We have revealed how NDP52 and MVI interact in the nucleus to bring about unfolding of MVI, enabling DNA binding. However, this may not be the only consequence of this interaction. The oligomeric state of MVI has long been a controversial subject, along with the possible roles of partners^{25, 28}. MVI contains a potential dimerisation site through a predicted coiled-coil²⁹, just before the CBD. It is probable that this motif is also masked in the folded conformation, in a similar manner to the DNA-binding site. Therefore, the NDP52-induced unfolding of MVI could enable dimerisation, forming a highly processive motor.

To explore this hypothesis, we firstly assessed the ability of MVI to dimerise, using an actin pull-down assay. Here, MVI pellets when bound to actin, causing co-sedimentation of proteins that MVI is in complex with. Therefore, if the MVI_{TAIL} is incubated with FL-MVI and a heterodimer is formed, the MVI_{TAIL} will pellet with the MVI-actin complex. Indeed, MVI_{TAIL} was observed in the pellet (Supplementary Fig. 6a, b). The bound molar concentration of MVI_{TAIL} was limited by the sub-stoichiometry concentration of MVI. When performed with higher MVI concentrations, a greater amount of MVI_{TAIL} co-sedimented. Overall these data show that MVI can dimerise, albeit inefficiently.

To quantify this process, we performed a FRET assay, whereby two pools of MVI_{TAIL} were labelled, one with FITC and the other

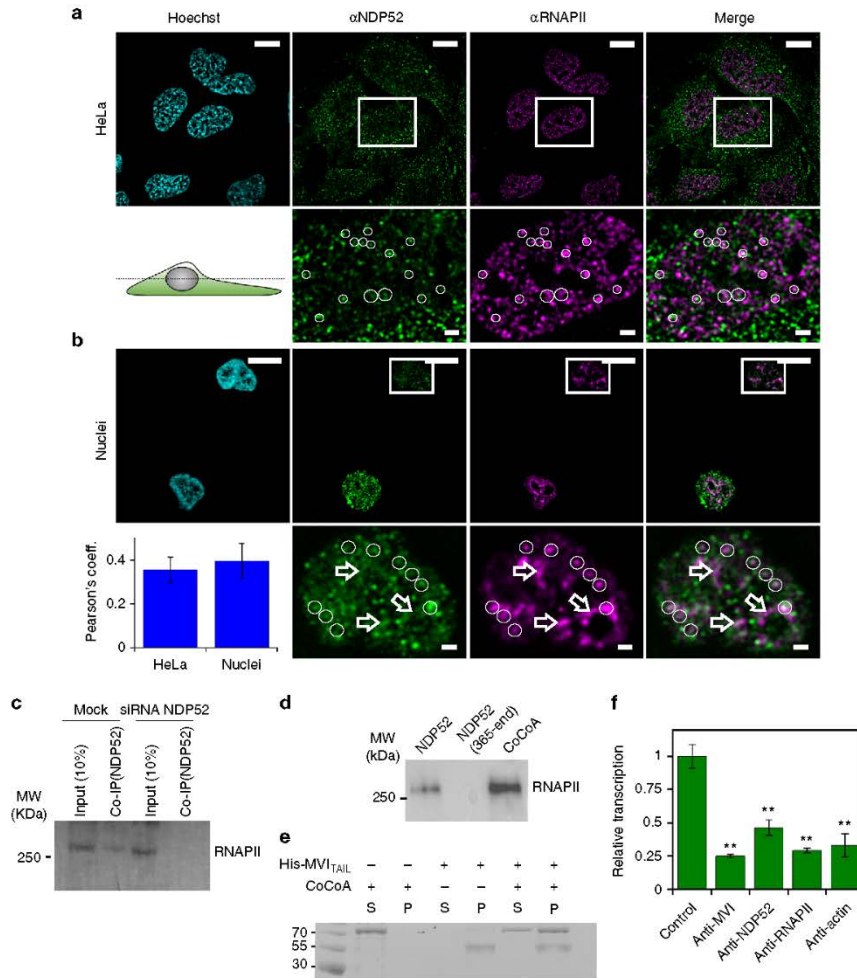


Fig. 6 NDP52 transcription regulation. **a** Immunofluorescence staining against NDP52 (green), RNAPII (magenta) and DNA (cyan), as performed in Fig. 1b. Insert depicts colocalising foci. Scale bar 10 μ m for whole images and 1 μ m for inserts. **b** Immunofluorescence on HeLa nuclei as in (a) with Pearson's coefficient (error bars represent SEM from 10 images). **c** Co-immunoprecipitation of NDP52 and RNAPII, using an antibody against NDP52 to immunoprecipitate RNAPII from HeLa cells. Immunoprecipitation does not occur in HeLa cells subjected to siRNA knockdown of NDP52. **d** Western blot against RNAPII following isolation from nuclear extracts by NDP52 constructs and CoCoA. Loading controls for the recombinant proteins is shown in Supplementary Fig. 9. **e** Pull-down of CoCoA by His-tagged $NMVI_{TAIL}$ both at 5 μ M. P and S represent pellet and supernatant fractions. **f** In vitro transcription by HeLaScribe extracts following antibody depletion as described in Methods. Samples were normalised to a non-depleted control reaction (error bars represent SEM ** $p < 0.001$ by two-tailed t -test) from 5 independent experiments (Supplementary Fig. 8a, b)

with Alexa555. Titrations revealed a weak association (Fig. 5a, b and Supplementary Fig. 7d), consistent with our pull-down results. Interestingly, upon addition of excess NDP52, a large change in FRET was observed, indicating the formation of a stable dimer. Moreover, while the presence of DNA could not yield dimerisation, it did not prevent it from occurring in the presence of NDP52. This observation highlights an important distinction between DNA and NDP52; while both can sequester the CBD, only NDP52 can disrupt the interaction with the rest of the tail and promote unfolding.

Dimerisation is an intrinsic property of the myosin VI. To determine whether dimerisation is driven by the coiled-coil domain located in the $NMVI_{TAIL}$, the FRET assay was repeated using $NMVI_{TAIL}$ and the CBD. A significant FRET change was observed for $NMVI_{TAIL}$, which was independent of its ability to bind NDP52 (Fig. 5b and Supplementary Fig. 7f). This confirmed the innate ability of MVI to dimerise within this region. The CBD did not dimerise, irrespective of NDP52 (Fig. 5b and Supplementary Fig. 7e, g). NDP52, and many other partners, are likely dimers themselves, and therefore, it has long been thought that

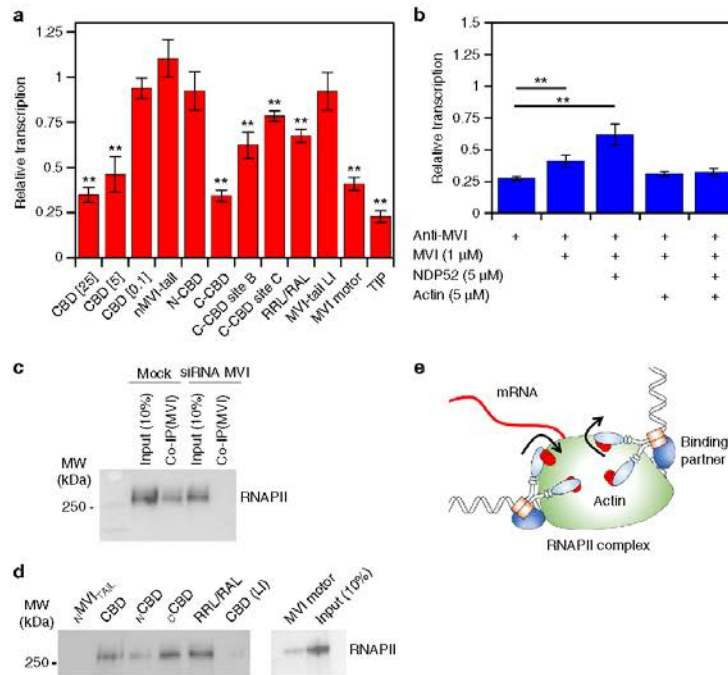


Fig. 7 Coupling myosin VI to the RNAPII complex. **a** In vitro transcription by HeLaScribe extracts in the presence of competitor MVI domains at 25 μ M, unless stated otherwise. Sites B and C refer to c CBD $_{\Delta$ SiteB and c CBD $_{\Delta$ SiteC, respectively. TIP refers to the control reaction performed in the presence of 25 μ M of the MVI inhibitor (TIP). Samples were normalised to the control sample in Fig. 6f (error bars represent SEM from five independent experiments $^{**}p < 0.001$ by two-tailed *t*-test). See Supplementary Fig. 8c for control experiments. **b** In vitro transcription following antibody depletion and rescue using recombinant MVI (1 μ M), NDP52 (5 μ M) and F-actin (5 μ M), as described in Methods (error bars represent SEM from five independent experiments $^{**}p < 0.001$ by two-tailed *t*-test). **c** Co-immunoprecipitation of MVI and RNAPII, using an antibody against MVI to immunoprecipitate RNAPII from HeLa cells. Immunoprecipitation does not occur in HeLa cells subjected to siRNA knockdown of MVI. **d** Western blot against RNAPII following isolation from nuclear extracts by MVI constructs. Loading controls for the recombinant proteins is shown in Supplementary Fig. 9. **e** Working model of MVI in transcription elongation. MVI is bound to partner and/or DNA at the C terminus and RNAPII through actin at the N terminus.

MVI dimerisation is driven through its partner, rather than being innate to itself. When sub-stoichiometric amounts of NDP52 were used, upon saturation of NDP52 with CBD, a FRET change was observed (Supplementary Fig. 7g). This is likely to be due to the binding of two CBD monomers to each subunit of NDP52. This indirect dimerisation was not observed with the MVI $_{TAIL}$ because NDP52 was in excess (Fig. 5a). However, when sub-stoichiometry NDP52 was used, a breakpoint in the titration was observed at a concentration equal to that of NDP52 (Supplementary Fig. 7h). This was followed by a linear increase in FRET, which is indicative of further binding, but in a different manner to the one observed in excess of NDP52. Therefore, our data suggest that both dimerisation mechanisms are possible (Fig. 5d), opening the intriguing possibility that localised partner concentration could regulate different complex formats, each with a potentially different role.

Partner induced dimerisation regulates myosin VI motility. Dimerisation can alter the mechanical properties of the protein, which translates into changes in the motor behaviour. The steady-state ATPase kinetics of MVI revealed a 50% reduction in the rate constant following addition of NDP52 (Supplementary Fig. 6c), but no change in the presence of DNA. This is typical of

molecular gating, whereby each head of the dimer alternates ATP hydrolysis³⁰. Moreover, the rate constant for FL-MVI in the presence of NDP52 was essentially identical to that of the MVI truncation without CBD (Motor $_{1-1060}$). We propose this construct would fail to backfold but could dimerise through the coiled-coil.

To explore the mechanical consequences of MVI dimerisation, sliding filament motility assays were performed (Fig. 5c). Antibodies to the MVI $_{TAIL}$ are used to immobilise MVI in the correct orientation, in order to enable translocation of actin filaments. This approach resulted in an increased velocity from 40–50 to 90 nm s^{-1} . However, antibodies were not required if MVI was pre-incubated with NDP52. Here, two populations were observed with velocities at 50–60 and 90 nm s^{-1} , which was dependent upon the NDP52 concentration (Supplementary Fig. 6d). We suggest this corresponds to apo- and NDP52-bound MVI, respectively. As we have shown, MVI exists in a folded conformation, where it would be unlikely to generate efficient motility, as revealed by the low velocity population. However, NDP52 unfolds MVI, inducing the mechanical activation of the motor.

Taking all our data together, we propose the following model (Fig. 5d): NDP52 initially associates with MVI in its folded state. This triggers unfolding of the protein and subsequent recruitment

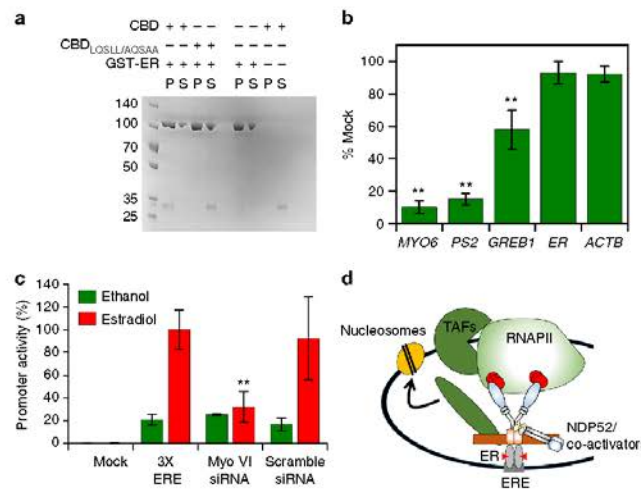


Fig. 8 Myosin VI is linked to oestrogen signalling. **a** Pull-down of 2 μ M CBD by 10 μ M GST-ER. P and S represent pellet and supernatant fractions. **b** Expression of ER gene targets following siRNA knockdown of MVI in MCF-7 cells. Expression is plotted as a percentage of expression in mock cells. ER (ESR) and β -actin were used to reflect global changes in transcription. **c** Luciferase reporter assay driven by the ERE promoter in MCF-7 cells. Estradiol led to a 5-fold increase in promoter activity. siRNA knockdown of MVI led to a 3-fold reduction in activity. Ethanol was used as a carrier control for the experiments (error bars represent SEM from three independent experiments ** $p < 0.001$ by two-tailed *t*-test). **d** Working model of MVI recruitment by the ER. MVI binds to the ER and then gets activated by NDP52 (or CoCoA), which enables binding to RNAPII through actin. Association with NDP52, or CoCoA, ties MVI with the general transcription co-activators to initiate recruitment of RNAPII

of a second myosin. Dimerisation could occur through two mechanisms: dimerisation of two MVI monomers around a single partner dimer, or dimerisation of two myosin molecules, each bound to a different partner molecule.

The nuclear role of NDP52 as a transcription regulator. Based upon its similarity to transcription co-activator CoCoA and its binding to MVI, we explored if NDP52 partners MVI in transcription. The distribution of the NDP52 in relation to RNAPII was examined using immunofluorescence (Fig. 6a, b). NDP52 partially colocalised with RNAPII on punctate structures. Moreover, using recombinant NDP52 as bait in nuclear extracts, we confirmed that FL-NDP52 formed a complex with RNAPII. This was further supported by co-immunoprecipitation of RNAPII by NDP52 from HeLa extracts (Fig. 6c, d).

The MVI-binding site is conserved between NDP52 and CoCoA, and a pull-down between recombinant proteins revealed the two form a stable interaction (Fig. 6e).

To further explore the role of NDP52 in transcription, we performed *in vitro* transcription assays using the HeLaScribe extracts. To assess the role of various proteins in transcription, we used antibody depletion to sequester selected proteins from the extracts, before performing the transcription assays (Fig. 6f and Supplementary Fig. 8a, b). As expected, depleting a pool of RNAPII led to a decrease in transcription. Moreover, depletion of actin which is known to be bound to the RNAPII complex^{31, 32}, also decreased transcription. Consistent with previous findings under the same conditions³, transcription was decreased to about 25% upon depletion of MVI. Interestingly, a 50% decrease was observed when NDP52 was depleted, suggesting that this protein is indeed involved in transcription.

Myosin VI's interaction with RNA polymerase II. MVI has previously been associated with sites of active transcription³.

Here, we have illustrated that MVI regulator NDP52 also colocalised with RNAPII and enhanced transcription.

Building upon our knowledge of which MVI domains bind DNA, we explored how these domains correspond to coupling MVI to the RNAPII complex. We employed a competition assay to displace the native protein using individual recombinant domains and then performed *in vitro* transcription. The CBD alone was able to displace MVI, leading to a decrease in transcription in a CBD concentration dependent manner (Fig. 7a). This effect was specific to the CBD and required the DNA binding ability within the domain to fully perturb the reaction. In addition, mutation of the RRL-motif revealed that successful competition is likely to be driven by partner association at this location. This was further supported by the lack of inhibition by the LI-CBD.

Our observation of the CBD competing off the MVI, leading to a decrease in transcription, indicated that the FL-MVI, is required for transcription. We tested whether the isolated MVI motor domain can function as a competitor. Indeed, the motor is a competitor (Fig. 7a), suggesting that MVI forms a bi-polar interaction with the RNAPII complex, which is vital for transcription. The importance of the motor domain was further confirmed when we used the MVI inhibitor 2,4,6-triiodophenol (TIP)³³ to inhibit the MVI motor activity. This treatment resulted in a transcription level equivalent to depleting MVI.

We explored how the conformation of MVI, its motor activity and, more specifically, actin binding can affect transcription. To further reinforce our results, we performed rescue assays on antibody depleted extracts, by adding recombinant proteins. The addition of FL-MVI led to a slight rescue in transcription (Fig. 7b). However, when in combination with NDP52, there was a two-fold increase in transcript production. This observation highlights that it is an active unfolded state of MVI that participates in transcription. When we incubated both samples with F-actin, we observed no increase in transcription. In this

case, while interactions through the CBD could occur, the motor was prevented from coupling to RNAPII because it was bound to F-actin. Therefore, we concluded that the actin binding site of MVI is required in transcription, possibly by coupling it to the complex through RNAPII-bound nuclear actin^{31,32}.

MVI can co-immunoprecipitate RNAPII from HeLa extracts, as shown previously³ (Fig. 7c). Subsequently, the recombinant MVI truncations were also tested for their ability to act as bait for RNAPII in nuclear extracts (Fig. 7c, d). Indeed, their ability to bind RNAPII was consistent to their ability to inhibit transcription. The _CCBD showed high RNAPII binding potential, whereas the _NCBD was weak. This suggests that the main coupling factor to the RNAPII complex is the DNA binding sites of the _CCBD, rather than the RRL motif. However, the LI did not bind to RNAPII, confirming that the RRL is still required for the interaction. Moreover, DNA binding is only possible once MVI is unfolded which is driven by binding partner at the RRL motif.

Overall, we propose a model whereby MVI is coupled to RNAPII through both motor-actin as well as interactions of the CBD with binding partners and/or DNA. This bipartite association to the complex in an active unfolded state enables MVI to utilise its mechanical ability during transcription to help drive or anchor the complex (Fig. 7e).

Myosin VI is coupled to gene expression by nuclear receptors.

Here we have shown that MVI and NDP52 have a role in transcription. Given the overexpression of MVI in breast, ovarian and prostate cancer^{5, 7, 18}, our findings indicated a possible link between MVI and the expression of genes under the regulation of hormone receptors. There is evidence of coupling MVI to the androgen receptor³⁴. However, this has not been explored for other hormone receptors, nor has the consequence upon gene expression been investigated.

To address such an intriguing possibility, we inspected the C terminus of MVI and identified an LxxLL nuclear receptor binding motif. In addition, as shown in Fig. 8a, pull-down assays with recombinant proteins revealed that there is a direct interaction between the CBD and the oestrogen receptor (ER). Moreover, mutation of this LxxLL motif abolished binding.

To explore the role of MVI in transcription of ER regulated genes, we switched to using ER positive MCF7 cells and monitored the expression of the ER target genes *PS2* and *GREB1*. Knockdown of MVI resulted in a specific 85% and 40% decrease in expression, respectively (Fig. 8b and Supplementary Fig. 8d), thereby suggesting a link between receptor binding and MVI's role in transcription. It is important to note that MVI knockdown does not lead to a general decrease in expression. To explore this relationship in a more general context, we also performed luciferase reporter assays driven by the ERE (ER response element) reporter. As shown in Fig. 8c, the stimulatory effect of estradiol is impeded upon a knockdown of MVI. We therefore suggest MVI may have the potential to regulate genes under ERE control.

Discussion

Here we have explored the function and regulation of nuclear MVI. The association of MVI with RNAPII is dependent upon its ability to bind DNA, which is regulated by putative transcription co-activator NDP52. NDP52 alters the MVI oligomeric and mechanical properties. We suggest MVI may function as an auxiliary motor in transcription, with a bipartite coupling to the RNAPII complex through NDP52-DNA, as well as RNAPII-bound actin. Finally, MVI interacts with nuclear receptors for specific gene targeting (Fig. 8d). These processes are structurally confined to the nuclear localising NI isoform, frequently found in cancer cells.

We have shown how a myosin can directly bind DNA. This occurs through two sites on the CBD that are inaccessible in FL-MVI. We observed MVI adopting a folded conformation consistent with previous analysis^{24, 26, 35}. Importantly, we have provided evidence this occurs *in vivo* using FLIM. Here we present a model whereby binding partners can unfold MVI to expose these sites. Unfortunately, the direct DNA binding by NDP52 prevented the direct measurement of a partner regulating this process. Nevertheless, we have revealed a mechanism whereby NDP52 can unfold MVI. The non-specific selectivity for substrate and the relatively weak binding affinity for nucleic acids suggests that DNA binding is likely to be driven through partners and their abilities to bind specific DNA targets.

Here we have defined that activation of MVI occurs through unfolding to enable both its motility and mechanical work. However, no change in ATPase activity has been observed. It is here that the role of Ca²⁺-calmodulin are likely to participate to fine-tune the motor activity in order to increase or reduce the ATPase activity, as required.

Our regulatory mechanism also enabled us to look into MVI oligomerisation. Here we report that MVI can be both a monomer and dimer dependent upon binding partner, with the latter controlled by the innate ability of the protein to dimerise. Our model is in agreement with the previous conclusions^{28, 36}, where it was proposed that MVI adopts a folded conformation and cargo bridges two motors, with the close proximity leading to internal dimerisation³⁷. We found that NDP52 triggered this process, and it occurred by exposing the dimerisation domain through unfolding. We suggest dimerisation occurs within the _NMVI_{TAIL} (amino acids 814–1060), which is in agreement to the model proposed by Mukherjee⁸ where the authors proposed dimerisation occurring distal to the 3HB between residues 917–942. Moreover, a later study confirmed this site was necessary for MVI to function *in vivo*³⁸ and the SAH domain (residues 842–978) was redundant.

The dissociation constant for dimerisation within the _NMVI_{TAIL} is essentially identical to the MVI_{TAIL} in the presence of NDP52, where the latter must be initially unfolded. This assessment is in agreement with molecular dynamics simulations, which showed self-association within this region of the MVI_{TAIL}³⁹. Moreover, our data agree with the experimental evidence from Spink²⁶, whereby the tail was monomeric at 1 μM. However, at higher concentrations we observed dimerisation (Fig. 5a and Supplementary Table 4).

We have also explored the nuclear role of NDP52 and linked the protein to both MVI and RNAPII. Many of our results suggest NDP52 participates in transcription: (i) its DNA-binding ability, (ii) its high homology to transcription co-activator CoCoA, (iii) its colocalisation with RNAPII, (iv) its binding to the RNAPII complex and (v) the observation that its depletion decreases mRNA yield *in vitro*. We suggest NDP52 can function similar to CoCoA. Likewise, we revealed that CoCoA is also a MVI partner. Further investigation is now required to define the nuclear role of NDP52.

MVI was previously linked to transcription initiation and elongation, whereby depletion reduced transcription³. We have expanded upon this study, firstly by dissecting its effect in a quantitative manner and secondly, by determining the domains of MVI responsible for its interaction with RNAPII. We have revealed that the CBD is associated with the RNAPII complex, requiring both the RRL motif and the DNA-binding sites. We suggest that NDP52, and/or CoCoA, bind to the RRL motif to unfold MVI.

Importantly, RNAPII interactions are not limited to the C terminus of MVI. The motor domain is likely to associate with RNAPII through actin. Due to the presence of actin on the RNAPII complex^{31, 32}, it is highly likely for MVI to bind this

actin population. Whilst the oligomeric state of this actin remains unknown, it has been suggested that it consists of short polymers⁴⁰, thereby providing several binding interfaces across the complex. The importance of the MVI-actin interaction is more relevant when we used the TIP inhibitor to target the motor activity. Inhibition resulted in a transcription decrease equivalent to depletion. Therefore, we conclude that MVI is an active motor in transcription.

Our finding that suggests a bipartite association between MVI and the RNAPII complex would enable mechanical work to be performed, whereby MVI could either hold the complex in situ, or act as an auxiliary motor driving RNAPII (Fig. 7e). MVI can perform both functions, switching between them depending on the force exerted on it⁴¹. We speculate that MVI could help propel the RNAPII complex, but should the complex encounter a stall, it could exert a load upon MVI, triggering a switch to a 'tether mode' until transcription begins again. Indeed, MVI has been associated with transcription pause-restart²¹.

MVI has previously been linked to the androgen receptor (AR), with evidence for a direct interaction between the two³⁴. We identified a nuclear receptor binding motif at the C terminus of MVI which enabled ER binding, suggesting a wider link to nuclear receptors beyond the AR. A link between MVI and nuclear receptors is of particular importance, given their role in cell proliferation, which is reduced after MVI knockdown^{18, 20}. We found that MVI knockdown led to a decreased expression of ER target genes. Moreover, luciferase reporter assays showed that MVI is involved in regulating expression from ERE promoters. Therefore, MVI may participate in the activation of ER-driven gene expression (Fig. 8d), which drives tumour development and maintains the tumorigenic potential of cells. A wider genomic study is required to reveal the extent of this effect.

In summary, we have revealed how the motor protein can bind DNA in a process regulated by NDP52. The binding partner releases an autoinhibited state, which also enables dimerisation. This couples MVI to the RNAPII complex, where it can function as a tethering factor and/or auxiliary motor driving transcription. Lastly, we have revealed how MVI interacts with nuclear receptors with the potential to modulate gene expression.

Methods

Constructs. A list of constructs and PCR primers are provided in Supplementary Tables 5 and 8, respectively. Human MVI_{TAIL} and α MVI_{TAIL} were generated using directional TOPO cloning in to pET151 using pEGFP-NI-MVI as a template. The CBD, α CBD₁₉₀₋₁₁₂₉ and α CBD₁₁₂₁₋₁₂₅₃ were isolated by PCR using pET151 MVI_{TAIL} as a template, restriction digested by NheI and NotI and cloned into pET28. MVI_{TAIL} (large insert) and CBD (large insert) were cloned by PCR and restriction digestion using NheI and NotI in to pET28 using pEGFP-C3-LI-MVI as a template. CBD M1062Q (large insert) was cloned in the same manner from pEGFP-C3-LI-MVI M1062Q. CBD Δ Site A was cloned as above from pEGFP-C3-NI-MVI WSKNKKR/WASANNRR. MVI, Motor₁₋₈₁₄ and Motor₁₋₁₀₆₉ were cloned by PCR and restriction digest (NotI and XhoI) into pFastbacHTB using pFastbacHTB-NI-GFP-MVI as template. pET28 calmodulin was cloned by PCR and restriction digestion from pFastbacCalmodulin.

Modified CBD and MVI_{TAIL} constructs were made by site-directed mutagenesis using standard Quick-Change site-directed mutagenesis protocol. All plasmids were verified by DNA sequencing.

The dual-labelled full-length myosin VI construct was generated by restriction digest of pEGFP-NI-MVI with XcmI (within MVI) and SacII (in vector) to remove the last 67 residues at the C terminus of myosin VI. A synthetic gene was produced (pMXMVI C terminus) containing the C terminus with both cut sites but mRFP was introduced prior to the SacII site. The construct was then assembled to yield PL pEGFP-NI-MVI-RFP.

Protein expression and purification in *Escherichia coli*. Recombinant constructs were expressed in *E. coli* BL21 DE3 cells (Invitrogen) in Luria Bertani media. Proteins were purified by affinity chromatography (HisTrap FF, GE Healthcare). The purest fractions were desalted through a PD10 column (GE Healthcare) to remove imidazole before treatment with TEV protease for 4 h at 25 °C. The samples were then passed through a second HisTrap column. The cleaved protein was further purified through a Superdex 200 16/600 column (GE Healthcare).

Note: TEV cleavage was not performed when the His-tag was needed for pull-down experiments.

Protein expression using baculovirus system. Full-length myosin VI, Motor₁₋₈₁₄, Motor₁₋₁₀₆₉ and *Xenopus* calmodulin were expressed in Sf9 and Sf21 (*Spartopoda frugiperda*) insect cells using the Baculovirus expression system. Sf9 cells were cultured in suspension in sf900 media (Gibco) at 27 °C to generate the P1-3 recombinant baculovirus stocks. Finally, expression of recombinant proteins was set up by infecting Sf21 cells with the P3 viral stock in ExCell 420 media (Sigma). The cells were harvested by centrifugation for protein purification after 4 days. Prior to sonication, an additional 5 mg Calmodulin was added with 2 mM DTT. After sonication, 5 mM ATP and 10 mM MgCl₂ were added and the solution was rotated at 4 °C for 30 min before centrifugation (20,000 × g, 4 °C, 30 min). Then, the cell lysate was subjected to the purification steps described above.

Protein labelling. Proteins were transferred into 50 mM Na-phosphate (pH 6.5) using a PD10 column. Samples were then incubated with a 5-fold excess of dye for 4 h, rotating at 4 °C. Excess dye was removed using a PD10 column pre-equilibrated with 50 mM Na-Phosphate, 150 mM NaCl and 1 mM DTT. Labelling efficiency was calculated based on the absorbance at 280 nm and the absorbance maximum of the dye. Typical efficiency was 90%, whereby the less than complete labelling was taken as an indicator for a single dye per protein. This was tested for isolated preparations in mass spectroscopy, which revealed both an unlabelled and single labelled population.

Cell culture and transfection. HeLa (ECACC 93021013) and MCF7 (ECACC 86012803) cells were cultured at 37 °C and 5% CO₂ in Gibco MEM Alpha medium with GlutaMAX (no nucleosides), supplemented with 10% Fetal Bovine Serum (Gibco), 100 units per ml penicillin and 100 µg ml⁻¹ streptomycin (Gibco). For the transient expression of MVI isoforms, HeLa cells grown on glass coverslips were transfected with EGFP-NI-MVI, EGFP-LI-MVI and EGFP-LI-MVI(M1062Q) constructs using Lipofectamine 2000 (Invitrogen), following the manufacturer's instructions. At 72 h post transfection, cells were subjected to nuclear staining, fixed and analysed or subjected to indirect immunofluorescence (see below). For MVI knock-down experiments, MCF7 monolayers, seeded to 30–50% confluency, were transfected with human myosin VI siRNA duplex (5'-GGUUUAGGU-GUUAAUGAAGTt-3') (Ambion) or AllStars Negative Control siRNA duplex (Qiagen) at a concentration of 50 nM, using Lipofectamine 2000 (Invitrogen), according to the manufacturer's guidelines. Cells were harvested after 48 h for immunoblot and RT-qPCR analysis.

Nuclei isolation. The nuclei isolation protocol was adapted from the Collas Lab protocol⁴². HeLa cells were washed once with ice-cold PBS, then washed in ice-cold Hypotonic Buffer N (10 mM Hepes pH 7.5, 2 mM MgCl₂, 25 mM KCl, supplemented with 1 mM PMSF, 1 mM DTT and 1x Halt Protease Inhibitor Cocktail (Thermo Fisher Scientific)). Cells were then re-suspended in ice-cold hypotonic buffer N and incubated for 1 h on ice. Cells were then homogenised on ice with a glass Dounce homogeniser (Wheaton). Cell lysate was supplemented with 2 M sucrose solution and mixed well by inversion before centrifugation. The supernatant which corresponded to the cytoplasmic fraction, was aliquoted and stored at -80 °C. The pellet, which corresponded to isolated nuclei, was further cleaned by washing in ice-cold buffer N (10 mM Hepes pH 7.5, 2 mM MgCl₂, 25 mM KCl, 250 mM sucrose, supplemented with 1 mM PMSF, 1 mM DTT and 1x Halt Protease Inhibitor Cocktail). The nuclei pellet was re-suspended either in ice-cold Buffer N and used immediately or in freezing medium (70% glycerol in buffer N), to yield a concentration of 4 × 10⁶ nuclei per ml. Nuclei were aliquoted on ice and stored at -80 °C.

Nuclear staining and immunofluorescence. Purified fresh or defrosted nuclei were immobilised on Poly-D-lysine (MW 70,000–150,000, Sigma)-coated glass coverslips (ThermoFisher) by 30 min incubation at 37 °C. Glass coverslips were coated with 0.1 mg ml⁻¹ Poly-D-lysine solution in H₂O, for 30 min, at room temperature, washed and dried. Immobilised nuclei were stained with 1 µg ml⁻¹ Hoechst 33342 (ThermoFisher) and/or 5 µl ml⁻¹ Vybrant® DiD Cell Labeling Solution (ThermoFisher) in Buffer N. Transfected and non-transfected HeLa cells grown on glass coverslips were incubated for 10 min at 37 °C with 1 µg ml⁻¹ Hoechst 33342 in growth medium. Stained cells or nuclei were fixed for 15 min at room temperature in 4% (w/v) paraformaldehyde (PFA) and residual PFA was quenched for 15 min with 50 mM ammonium chloride. All subsequent steps were performed at room temperature. Cells or nuclei were permeabilised and simultaneously blocked for 15 min with 0.1% (v/v) Triton X-100 and 2% (w/v) BSA in TBS. Cells or nuclei were then immune-stained against the endogenous proteins by 1 h incubation with the indicated primary and subsequently the appropriate fluorophore-conjugated secondary antibody (details below), both diluted in 2% (w/v) BSA in TBS. The following antibodies were used at the indicated dilutions: Rabbit anti-MVI (1:200, Atlas-Sigma HPA0354863-100UL), mouse-NDP52 (1:200, Abcam Ab124372), rabbit anti-RNAPII phospho S5 (1:500, Abcam Ab5131), donkey anti-mouse Alexa Fluor 647-conjugated (1:500, Abcam Ab150103) and donkey anti-rabbit Alexa Fluor 555-conjugated antibody (1:500, Abcam).

Ab150074). For actin staining, fixed and permeabilised cells or nuclei were stained prior to immunofluorescence with 165 nM Rhodamine-Phalloidin (ThermoFisher) for 20 min. Coverslips were mounted on microscope slides with Mowiol (10% (w/v) Mowiol 4-88, 25% (w/v) glycerol, 0.2 M Tris-HCl, pH 8.5), supplemented with 2.5% (w/v) of the anti-fading reagent DABCO (Sigma).

For colocalisation analysis, ROIs were drawn around the nuclei of individual cells, or around whole cells in the case of Fig. 4g and Supplementary Fig. 5c (5 cells and 5 stacks per cell). Pearson's coefficients were obtained with the JACoP plugin⁴³ for ImageJ.

Immunoblot analysis. The total protein concentration of the cytoplasmic and nuclei fraction was determined by Bradford Assay (Sigma) following the manufacturer's instructions. Nuclei, cytoplasmic fractions and cell lysates were heat-denatured and resolved by SDS-PAGE. The membrane was probed against the endogenous proteins by incubation with the indicated rabbit polyclonal primary and subsequently a goat anti-rabbit antibody coupled to horseradish peroxidase (1:15,000 Abcam Ab6721). The following primary antibodies were used at the indicated dilutions: Rabbit anti-MVI (1:500, Atlas-Sigma HPA0354863-100UL), Rabbit anti-NDP52 (1:2000, GeneTex GTX115378), Rabbit anti-alpha tubulin (1:1000, Santa Cruz sc5286), Rabbit anti-Lamin B (1:1000, Abcam ab16048) and rabbit anti-RNAP II phospho S5 (1:1000, Abcam Ab5131). The bands were visualised using the ECL Western Blotting Detection Reagents (Invitrogen) and the images were taken using Syngene GBox system. Images were processed in ImageJ. Uncropped blots are shown in Supplementary Figs. 9 and 10.

Co-immunoprecipitation. Immunoprecipitation was performed using rabbit anti-myosin VI (Sigma), or rabbit anti-NDP52 (Genetex). Antibodies were bound to Protein A and G dynabeads, respectively, according to the manufacturer's instructions. Immunoprecipitation was performed from total protein extract for 2 h in a buffer containing 50 mM Tris-HCl, 150 mM NaCl, 1 mM DTT, 1 mM PMSF and 1% Triton X-100. Samples were subjected to immunoblot for RNAPII, as described above. Where steps were compared between conditions, equal total protein concentrations were used.

Imaging. Cells and nuclei were visualised using Olympus IX71 microscope with PlanApo 100xOTIRPM-SP 1.49 NA lens mounted on a PIFOC z-axis focus drive (Physik Instrumente, Karlsruhe, Germany), and illuminated with an automated 300 W Xenon light source (Sutter, Novato, CA) with appropriate filters (Chroma, Bellows Falls, VT). Images were acquired using a QuantEM (Photometrics) EMCCD camera, controlled by the Metamorph software (Molecular Devices). The whole volume of cells and nuclei was imaged by acquiring images at z-steps of 200 nm. Using the Hoechst 33342 staining, the lower and upper sections at which the nucleus was in focus were defined. Unless stated otherwise, images presented here correspond to a middle section between these two limits, which ensures imaging within the nucleus. Images were deconvolved with the Autoquant X software applying blind deconvolution and analysed by ImageJ.

FLIM sample preparation and data acquisition. Transfections were performed as above with the exception that 1 mg ml⁻¹ sodium borohydride (Sigma) was used for quenching. All time correlated single photon counting mode (TCSPC) images were acquired using the custom-built multifocal multiphoton fluorescence lifetime imaging system (MM-FLIM) as described previously⁴⁴. In brief, light generated from a Chameleon Ultra II Ti:Sapphire laser source (Coherent Inc.) is coupled with a spatial light modulator (SLM) to generate a uniform 8 × 8 array of beamlets. This beamlet array is then relayed through a set of galvanometer scanners (providing x-y raster scanning capability) onto the back-pupil plane of a 40 × 1.3 N.A. Plan Fluor oil objective (Nikon) where it is projected onto the sample. The two-photon generated fluorescence is collected and descanned where it is directed with a dichroic mirror and focused onto the Megaframe SPAD array using a 10 × 0.3 N.A. Plan Fluor air objective (Nikon).

For each individual image acquisition, the system processed 64 × 64 data points for 8 × 8 detectors producing 512 × 512 pixel images. Lifetime data was acquired operating the Megaframe camera in TCSPC mode. In TCSPC mode, on-pixel TDCs generate raw time-correlated data, which are stored and then post-processed offline to generate an image. Full details on TCSPC data acquisition can be found in ref. ⁴⁴. Once processed, these data are saved and then subsequently analysed using TR12 lifetime analysis software⁴⁵.

RNA extraction and RT-qPCR. RNA from MCF7 cells transfected with MVI or siRNA and negative control duplexes was extracted using Gene Jet RNA purification kit (Thermo scientific) according to the manufacturer's protocol. The RNA concentration was measured using Geneflow Nanophotometer and RT-qPCR was performed with one-step QuantiFast SYBR Green qPCR kit (Qiagen) using 50 ng of RNA in each sample. A list of qPCR primers is given in Supplementary Table 6.

Dual-luciferase assay. MCF7 cells were seeded in a 24-well plate at a density of 1.0 × 10⁵ cells per well in no phenol red MEM media (Gibco) with 5% double

charcoal stripped FCS (First Link UK) and 1% Penicillin-Streptomycin. After 48 h of starvation, the cells were co-transfected with 3X-ERE-TATA-Luc expression plasmid (400 ng per well), RL-CMV plasmid (400 ng per well) and human myosin VI siRNA duplex (5'-GGUUUAGGUGUUAAUGAAGT-3') (Ambion) or AllStars Negative Control siRNA duplex (Qiagen) at a concentration of 50 nM, using Lipofectamine 2000 (Invitrogen), according to the manufacturer's guidelines. In the control wells, cells were co-transfected with 3X-ERE-TATA-Luc and RL-CMV expression plasmids only. After 24 h of transfection, cells were treated with 10 nM of Estradiol or vehicle control and the luciferase activity was measured the following day using Dual-Glo luciferase reporter assay kit (Promega). Levels of firefly luciferase were standardised to those of Renilla. All samples were measured in triplicates.

DNA substrates. Labelled and unlabelled oligonucleotides were purchased from Sigma-Aldrich. To form duplex DNA substrates, oligonucleotides were mixed at equimolar concentrations at either 50 μM in water or a buffer containing 50 mM Tris.HCl at pH 7.5, 150 mM NaCl, and 3 mM MgCl₂. A list of DNA substrates is given in Supplementary Table 7.

In vitro transcription. The DNA template was the pEGFP-C3 linearised plasmid containing the CMV promoter that would generate a 130-base run-off transcript. The HelaScribe (Promega) reactions were performed in triplicates, through two independent experiments, according to the manufacturer's instructions. The reactions were performed for 60 min at 25 °C.

Reactions were also performed following pre-clearance with the stated antibodies. Protein G or A Dynabeads (Invitrogen) were prepared according to the manufacturer's instructions before being loaded with 4 μg antibody. Samples were incubated for 30 min on ice and beads were extracted immediately before performing the transcription reaction.

For quantification, mRNA was purified using Gene Jet RNA purification kit (Thermo Scientific) according to the manufacturer's protocol and RT-qPCR was performed with One-step QuantiFast SYBR Green qPCR kit (Qiagen).

Preparation of liposomes. Mixed brain liposomes—Folch fraction 1 (Sigma) were re-suspended in 20 mM HEPES (pH 7.4), 150 mM NaCl and 1 mM DTT to a final concentration of 1 mg ml⁻¹. The mixture was then extruded using a 100 nm filter. Liposomes were stored at 4 °C and used within 4 days.

Actin-pelleting assay. The assay was modified from Morriswood et al. Full length MVI was incubated with the tail construct at the specified concentrations in reaction buffer (150 mM NaCl, 50 mM Tris HCl (pH 7.5), 1 mM MgCl₂ and 1 mM DTT), for 30 min at 4 °C. 5 μM F-actin (from M. Gees) was added to the mixture before centrifugation at 190,000 × g for 15 min at 4 °C. The pellet was re-suspended in 50 μl reaction buffer and samples were analysed by SDS-PAGE and densitometry using ImageJ.

Protein-protein and protein-DNA isolation. His-tagged protein-protein pull downs. 10 μM His-tagged bait protein was bound to His Mag Sepharose Ni beads (GE Healthcare) according to the manufacturer's instructions. Samples were incubated in 50 mM Tris-HCl (pH 7.5), 500 mM NaCl and 40 mM imidazole and 1 mM DTT for 30 min shaking (400 rpm) at 25 °C. Beads were isolated and samples volumes were normalised with NuPAGE Sample buffer before SDS-PAGE.

Pull-down from nuclear extract. His-tagged bait protein was prepared as above. Frozen nuclei aliquots were defrosted as described above and re-suspended in 50 mM Tris-HCl (pH 7.5), 500 mM NaCl and 40 mM imidazole, 1 mM DTT and 1% Triton X. Nuclei were incubated on ice for 15 min for lysis to occur. Samples were then incubated for 30 min as above before proceeding with immunoblot analysis.

GST-tagged protein-protein. 10 μM GST-tagged bait protein was bound to glutathione sepharose resin (GE Healthcare) according to the manufacturer's instructions. Samples were incubated in PBS supplemented with 1 mM DTT, shaking at 25 °C for 30 min. Beads were isolated by centrifugation (1000 × g for 5 min) and samples volumes were equalised with NuPAGE sample buffer before SDS-PAGE.

DNA protein. A single biotin labelled 500 bp DNA substrate was generated by PCR with 5' biotin-TEG primer using pSG1365 as a template. Free biotin primers were removed using a QiaQuick PCR purification kit (Qiagen). 1 mg Streptavidin Dynabeads (M-280) (Invitrogen) were washed three times in wash buffer (10 mM Tris-HCl pH 7.5, 1 mM EDTA and 2 M NaCl). 1 μg DNA was added in an equal volume to bring the final NaCl concentration to 1 M and incubated for 15 min at room temperature. Beads were washed three times in wash buffer before re-suspension in binding buffer (50 mM Tris-HCl pH 7.5, 3 mM MgCl₂, 1 mM DTT and 50 mM NaCl). Protein was added to the beads and incubated shaking (400 rpm) for 30 min, at 25 °C. Beads were extracted and samples volumes were normalised with NuPAGE sample buffer before SDS-PAGE.

Gliding filament assays. Motility assays were performed at 30 °C. Antibody immobilisation was achieved using rabbit anti-myosin VI (Atlas-Sigma HPA0354863-100UL) against the C terminus that was pre-absorbed to

nitrocellulose (0.1% v/v). NDP52 immobilisation was achieved by flowing 0.1, 0.5 or 1 μM NDP52 onto nitrocellulose. Subsequently, 100 $\mu\text{g ml}^{-1}$ MVI was added to the flow cells in 50 mM Tris-HCl (pH 7.5), 20 mM Imidazole, 1 mM EGTA, 5 mM MgCl_2 and 5 mM DTT. TRITC-phalloidin-labelled actin filaments were added in the same buffer plus oxygen scavenger (5 U ml^{-1} Glucose oxidase and 800 U ml^{-1} Catalase) and 2 mM ATP. Filaments were visualised every 5 s for a total period of 500 s. Individual trajectories were tracked and velocities extracted using GMImPro (www.mashanov.uk).

Steady-state ATPase activity of MVI. Ca^{2+} -actin monomers were converted to Mg^{2+} -actin with 0.2 mM EGTA and 50 μM MgCl_2 before polymerising by dialysis into 20 mM Tris-HCl (pH 7.5), 20 mM Imidazole (pH 7.4), 25 mM NaCl and 1 mM DTT. A 1:1 molar equivalent of phalloidin (Sigma) was used to stabilise actin filaments.

Steady-state ATPase activities were measured at 25 °C in KMg50 buffer (50 mM KCl, 1 mM MgCl_2 , 1 mM EGTA, 1 mM DTT, and 10 mM Imidazole, pH 7.0). Supplemented with the NADH-coupled assay components, 0.2 mM NADH, 2 mM phosphoenolpyruvate, 3.3 U ml^{-1} lactate dehydrogenase, 2.3 U ml^{-1} pyruvate kinase and various actin concentrations (0–30 μM). The final [Mg-ATP] was 5 mM and MVI concentration was 100–300 nM. The assay was started by the addition of MVI. The change in absorbance at OD₃₄₀ nm was followed for 5 min. The k_{cat} and K_{actin} values were determined by fitting the data.

$$\text{Rate} = V_o + \frac{k_{\text{cat}}[\text{Actin}]}{K_{\text{actin}} + [\text{Actin}]}$$

V_o is the basal ATPase activity of MVI, k_{cat} is the maximum actin-activated ATPase rate and K_{actin} is the concentration of actin needed to reach half maximal ATPase activity.

Stopped flow measurements. A HiTech SP61DX2 apparatus (TgK Scientific Ltd, Bradford-on-Avon, UK) with a mercury-xenon light source and HiTech Kinetic Studio 2 software was used^{46–50}. Anisotropy was measured with the instrument in the ‘T’ format, allowing simultaneous acquisition of horizontal (I_H) and perpendicular (I_V) components. This enabled anisotropy $(I_H - I_V)/(I_H + I_V)$, and intensity $(I_H + I_V)$ to be calculated from the same set of data. The G-factor was accounted for by normalising the detectors prior to performing measurements. Excitation was at 495 nm with emission through a 515 nm cut-off filter (Schott Glass). In all experiments, the quoted concentrations are those in the mixing chamber, except when stated. All experiments were performed at 25 °C in 50 mM Tris-HCl, 150 mM NaCl, 1 mM DTT and 3 mM MgCl_2 . The dead time of the stopped-flow instrument was ~2 ms; during this initial time no change in fluorescence can be observed.

Titration measurements. All reactions were performed at 25 °C in a buffer containing 50 mM Tris-HCl (pH 7.5), 150 mM sodium chloride and 1 mM DTT in a final volume of 100 μl . Measurements were performed using a ClarioStar Plate Reader (BMG Labtech) with the exception of the tryptophan measurements which were performed in a Cary Spectrophotometer (Varian).

Intensity measurements were performed at the following wavelengths: Tryptophan (ex. 295 nm), GFP (ex. 490 nm), RFP (ex. 585 nm), FITC (ex. 490 nm), Alexa Fluor 555 (ex. 555 nm). FITC to Alexa Fluor 555 FRET measurements were performed using the following wavelengths ex. 470 nm and em. 575 nm. Anisotropy was measured with the instrument in the T format, allowing simultaneous acquisition of parallel (I_H) and perpendicular (I_V) components using BMG filter-sets for fluorescein (Ex. 482/16–10, Dichroic LP504 and em. 530/-40).

Analysis of kinetic data. For fluorescence anisotropy titrations: anisotropy was calculated, as described below, based upon established procedures^{46, 47, 51, 52}.

Total fluorescence intensity (F_t) is given by:

$$F_t = \sum c_i F_i$$

Total anisotropy (A_t) is given by:

$$A_t = \frac{\sum c_i F_i A_i}{F_t}$$

Where c_i is the concentration of species i , F_i is the fluorescence intensity per unit of concentration and A_i is the anisotropy. This is calculated from the parallel and perpendicular fluorescence intensity (I) in relation to the plane of excitation by:

$$A_i = \frac{I_{\text{parallel}} - I_{\text{perpendicular}}}{I_{\text{parallel}} + 2I_{\text{perpendicular}}}$$

As anisotropy is additive for multiple fluorescence species in solution, it is used to give a measure of their relative concentrations. For MVI (and various constructs) there are two fluorescence species, DNA and MVI.DNA. The total anisotropy can

then be calculated in terms of the dissociation constant (K_d) for the MVI.DNA complex:

$$A_t = \frac{A_{\text{DNA}}([\text{DNA}]_t - [\text{MVI.DNA}]) + A_{\text{MVI.DNA}}Q[\text{MVI.DNA}]}{[\text{DNA}]_t - [\text{MVI.DNA}] + Q[\text{MVI.DNA}]}$$

where

$$[\text{MVI.DNA}] = \frac{([\text{MVI}]_t + [\text{DNA}]_t + K_d) - \sqrt{([\text{MVI}]_t + [\text{DNA}]_t + K_d)^2 - 4[\text{MVI}]_t[\text{DNA}]_t}}{2}$$

And where $[\text{MVI}]_t$ and $[\text{DNA}]_t$ are the total concentrations for each reactant. $[\text{MVI.DNA}]$ is the concentration of the protein-bound DNA complex. Q is the fluorescence intensity of MVI.DNA relative to DNA. The anisotropy data were fitted to obtain dissociation constants based on the above equations using GraFit fitting software⁵³.

For the FRET titrations: the 575 nm intensity data were corrected for the increase in intensity due to a small direct excitation. This background signal was subtracted from the dataset to leave the FRET values. The titration curves for the MVI-TALIN interactions were fitting to a binding quadratic equation:

$$[\text{Complex}] = \frac{([\text{FITC}]_t + [\text{AP555}]_t + K_d) - \sqrt{([\text{FITC}]_t + [\text{AP555}]_t + K_d)^2 - 4[\text{FITC}]_t[\text{AP555}]_t}}{2}$$

For lipid titrations: curves were fitted to a 1 site plus background equation:

$$[\text{Fluorescence}] = \frac{\text{Amplitude} \cdot [\text{Lipid}]}{K_d + [\text{Lipid}]} + \text{Background}$$

Data availability. The data supporting the findings of this study are available from the corresponding author on request.

Received: 10 January 2017 Accepted: 30 October 2017

Published online: 30 November 2017

References

- Wells, A. L. et al. Myosin VI is an actin-based motor that moves backwards. *Nature* **401**, 505–508 (1999).
- Roberts, R. et al. Myosin VI: cellular functions and motor properties. *Philos. Trans. R. Soc. Lond. B Biol. Sci.* **359**, 1931–1944 (2004).
- Vreugde, S. et al. Nuclear myosin VI enhances RNA polymerase II-dependent transcription. *Mol. Cell* **23**, 749–755 (2006).
- Avraham, K. B. et al. The mouse Snell's waltzer deafness gene encodes an unconventional myosin required for structural integrity of inner ear hair cells. *Nat. Genet.* **11**, 369–375 (1995).
- Dunn, T. A. et al. A novel role of myosin VI in human prostate cancer. *Am. J. Pathol.* **169**, 1843–1854 (2006).
- Mohiddin, S. A. et al. Novel association of hypertrophic cardiomyopathy, sensorineural deafness, and a mutation in unconventional myosin VI (MYO6). *J. Med. Genet.* **41**, 309–314 (2004).
- Yoshida, H. et al. Lessons from border cell migration in the Drosophila ovary: a role for myosin VI in dissemination of human ovarian cancer. *Proc. Natl. Acad. Sci. USA* **101**, 8144–8149 (2004).
- Mukherjee, M. et al. Myosin VI dimerization triggers an unfolding of a three-helix bundle in order to extend its reach. *Mol. Cell* **35**, 305–315 (2009).
- Knight, P. J. et al. The predicted coiled-coil domain of myosin 10 forms a novel elongated domain that lengthens the head. *J. Biol. Chem.* **280**, 34702–34708 (2005).
- Buss, F., Arden, S. D., Lindsay, M., Luzio, J. P. & Kendrick-Jones, J. Myosin VI isoform localized to clathrin-coated vesicles with a role in clathrin-mediated endocytosis. *EMBO J.* **20**, 3676–3684 (2001).
- Morriswood, B. et al. T6BP and NDP52 are myosin VI binding partners with potential roles in cytokine signalling and cell adhesion. *J. Cell Sci.* **120**, 2574–2585 (2007).
- Naccache, S. N., Hasson, T. & Horowitz, A. Binding of internalized receptors to the PDZ domain of GIPC/synectin recruits myosin VI to endocytic vesicles. *Proc. Natl. Acad. Sci. USA* **103**, 12735–12740 (2006).
- Spudich, G. et al. Myosin VI targeting to clathrin-coated structures and dimerization is mediated by binding to Disabled-2 and PtdIns(4,5)P₂. *Nat. Cell Biol.* **9**, 176–183 (2007).

14. Koriath, P., Gieffers, C., Maul, G. G. & Frey, J. Molecular characterization of NDP52, a novel protein of the nuclear domain 10, which is redistributed upon virus infection and interferon treatment. *J. Cell Biol.* **130**, 1–13 (1995).
15. Sternsdorf, T., Jensen, K., Zuchner, D. & Will, H. Cellular localization, expression, and structure of the nuclear dot protein 52. *J. Cell Biol.* **138**, 435–448 (1997).
16. Mostowy, S. et al. p62 and NDP52 proteins target intracytosolic Shigella and Listeria to different autophagy pathways. *J. Biol. Chem.* **286**, 26987–26995 (2011).
17. Yang, C. K., Kim, J. H. & Stallcup, M. R. Role of the N-terminal activation domain of the coiled-coil coactivator in mediating transcriptional activation by beta-catenin. *Mol. Endocrinol.* **20**, 3251–3262 (2006).
18. Wang, H., Wang, B., Zhu, W. & Yang, Z. Lentivirus-mediated knockdown of myosin VI inhibits cell proliferation of breast cancer cell. *Cancer Biother. Radiopharm.* **30**, 330–335 (2015).
19. Puri, C. et al. Overexpression of myosin VI in prostate cancer cells enhances PSA and VEGF secretion, but has no effect on endocytosis. *Oncogene* **29**, 188–200 (2010).
20. Wang, D. et al. MYO6 knockdown inhibits the growth and induces the apoptosis of prostate cancer cells by decreasing the phosphorylation of ERK1/2 and PRAS40. *Oncol. Rep.* **36**, 1285–1292 (2016).
21. Zorca, C. E. et al. Myosin VI regulates gene pairing and transcriptional pause release in T cells. *Proc. Natl Acad. Sci. USA* **112**, E1587–E1593 (2015).
22. Wollscheid, H. P. et al. Diverse functions of myosin VI elucidated by an isoform-specific alpha-helix domain. *Nat. Struct. Mol. Biol.* **23**, 300–308 (2016).
23. Wang, L. & Brown, S. J. BindN: a web-based tool for efficient prediction of DNA and RNA binding sites in amino acid sequences. *Nucleic Acids Res.* **34**, W243–W248 (2006).
24. Batters, C., Brack, D., Ellrich, H., Averbeck, B. & Veigel, C. Calcium can mobilize and activate myosin VI. *Proc. Natl Acad. Sci. USA* **113**, E1162–E1169 (2016).
25. Lister, I. et al. A monomeric myosin VI with a large working stroke. *EMBO J.* **23**, 1729–1738 (2004).
26. Spink, B. J., Sivaramakrishnan, S., Lipfert, J., Doniach, S. & Spedich, J. A. Long single alpha-helical tail domains bridge the gap between structure and function of myosin VI. *Nat. Struct. Mol. Biol.* **15**, 591–597 (2008).
27. Arden, S. D., Tumbarello, D. A., Butt, T., Kendrick-Jones, J. & Buss, P. Loss of cargo binding in the human myosin VI deafness mutant (R1166X) leads to increased actin filament binding. *Biochem. J.* **473**, 3307–3319 (2016).
28. Phichith, D. et al. Cargo binding induces dimerization of myosin VI. *Proc. Natl Acad. Sci. USA* **106**, 17320–17324 (2009).
29. Lupas, A., Van Dyke, M. & Stock, J. Predicting coiled coils from protein sequences. *Science* **252**, 1162–1164 (1991).
30. Sweeney, H. L. et al. How myosin VI coordinates its heads during processive movement. *EMBO J.* **26**, 2682–2692 (2007).
31. Fomproix, N. & Percipalle, P. An actin-myosin complex on actively transcribing genes. *Exp. Cell Res.* **294**, 140–148 (2004).
32. Kukuliev, A., Nord, Y., Palmberg, C., Bergman, T. & Percipalle, P. Actin and hnRNP U cooperate for productive transcription by RNA polymerase II. *Nat. Struct. Mol. Biol.* **12**, 238–244 (2005).
33. Heissler, S. M. et al. Kinetic properties and small-molecule inhibition of human myosin-6. *FEBS Lett.* **586**, 3208–3214 (2012).
34. Loikkanen, I. et al. Myosin VI is a modulator of androgen-dependent gene expression. *Oncol. Rep.* **22**, 991–995 (2009).
35. Song, C. F., Sader, K., White, H., Kendrick-Jones, J. & Trinick, J. Nucleotide-dependent shape changes in the reverse direction motor, myosin VI. *Biophys. J.* **99**, 3326–3344 (2010).
36. Park, H. et al. Full-length myosin VI dimerizes and moves processively along actin filaments upon monomer clustering. *Mol. Cell* **21**, 331–336 (2006).
37. Sweeney, H. L. & Houdusse, A. Myosin VI rewrites the rules for myosin motors. *Cell* **141**, 573–582 (2010).
38. Mukherjee, M. et al. Myosin VI must dimerize and deploy its unusual lever arm in order to perform its cellular roles. *Cell Rep.* **8**, 1522–1532 (2014).
39. Kim, H., Hsin, J., Liu, Y., Selvin, P. R. & Schulten, K. Formation of salt bridges mediates internal dimerization of myosin VI medial tail domain. *Structure* **18**, 1443–1449 (2010).
40. McDonald, D., Carrero, G., Andrin, C., de Vries, G. & Hendzel, M. J. Nucleoplasmic beta-actin exists in a dynamic equilibrium between low-mobility polymeric species and rapidly diffusing populations. *J. Cell Biol.* **172**, 541–552 (2006).
41. Altman, D., Sweeney, H. L. & Spudich, J. A. The mechanism of myosin VI translocation and its load-induced anchoring. *Cell* **116**, 737–749 (2004).
42. Hakelien, A. M., Gaustad, K. G. & Collas, P. Modulation of cell fate using nuclear and cytoplasmic extracts. *Methods Mol. Biol.* **325**, 99–114 (2006).
43. Boite, S. & Cordelières, F. P. A guided tour into subcellular colocalization analysis in light microscopy. *J. Microsc.* **224**, 213–232 (2006).
44. Poland, S. P. et al. A high speed multifocal multiphoton fluorescence lifetime imaging microscope for live-cell FRET imaging. *Biomed. Opt. Express* **6**, 277–296 (2015).
45. Barber, P. R. et al. Multiphoton time-domain fluorescence lifetime imaging microscopy: practical application to protein-protein interactions using global analysis. *J. R. Soc. Interface* **6**, S93–S105 (2009).
46. Toseland, C. P. Fluorescence to study the ATPase mechanism of motor proteins. *EXS* **105**, 67–86 (2014).
47. Toseland, C. P. & Geeves, M. A. Rapid reaction kinetic techniques. *EXS* **105**, 49–65 (2014).
48. Toseland, C. P., Martinez-Senac, M. M., Slatter, A. P. & Webb, M. R. The ATPase cycle of PcrA helicase and its coupling to translocation on DNA. *J. Mol. Biol.* **392**, 1020–1032 (2009).
49. Toseland, C. P., Powell, B. & Webb, M. R. ATPase cycle and DNA unwinding kinetics of RecG helicase. *PLoS ONE* **7**, e38270 (2012).
50. Toseland, C. P. & Webb, M. R. Fluorescence tools to measure helicase activity in real time. *Methods* **51**, 259–268 (2010).
51. Brownbridge, G. G., Lowe, P. N., Moore, K. J., Skinner, R. H. & Webb, M. R. Interaction of GTPase activating proteins (GAPs) with p21ras measured by a novel fluorescence anisotropy method. Essential role of Arg-903 of GAP in activation of GTP hydrolysis on p21ras. *J. Biol. Chem.* **268**, 10914–10919 (1993).
52. Soh, Y. M. et al. Molecular basis for SMC rod formation and its dissolution upon DNA binding. *Mol. Cell* **57**, 290–303 (2015).
53. Leatherbarrow, R. J. *Graftit Version 5* (Erithacus Software Ltd., Horley, UK, 2001).
54. Yu, C. Myosin VI undergoes cargo-mediated dimerization. *Cell* **138**, 537–548 (2009).

Acknowledgements

We thank the MRC (MR/M020606/1 to C.P.T.) and (MR/K015664/1 to M.P./S.M.A.B.), Royal Society (RG150801) and Leverhulme Trust (ECF-2014-688) for funding. N.F. was supported by Royal Society Newton International Fellowship (NF151167). We thank D. Mulvihill and D. Griffin for sharing equipment and G. Brooke for help with ER qPCR and luciferase assays. We also thank B. Goult and M. Geeves for sharing equipment and critical reading of this manuscript.

Author contributions

N.F., Y.H.-G. and C.P.T. conceived the experiments. N.F., Y.H.-G., A.d.S. and C.P.T. performed experiments and analysed the data. A.C. provided reagents. S.P., S.M.A.-B. and M.P. performed FLIM. N.F. and C.P.T. wrote the manuscript.


Additional information

Supplementary Information accompanies this paper at <https://doi.org/10.1038/s41467-017-02050-w>.

Competing interests: The authors declare no competing financial interests.

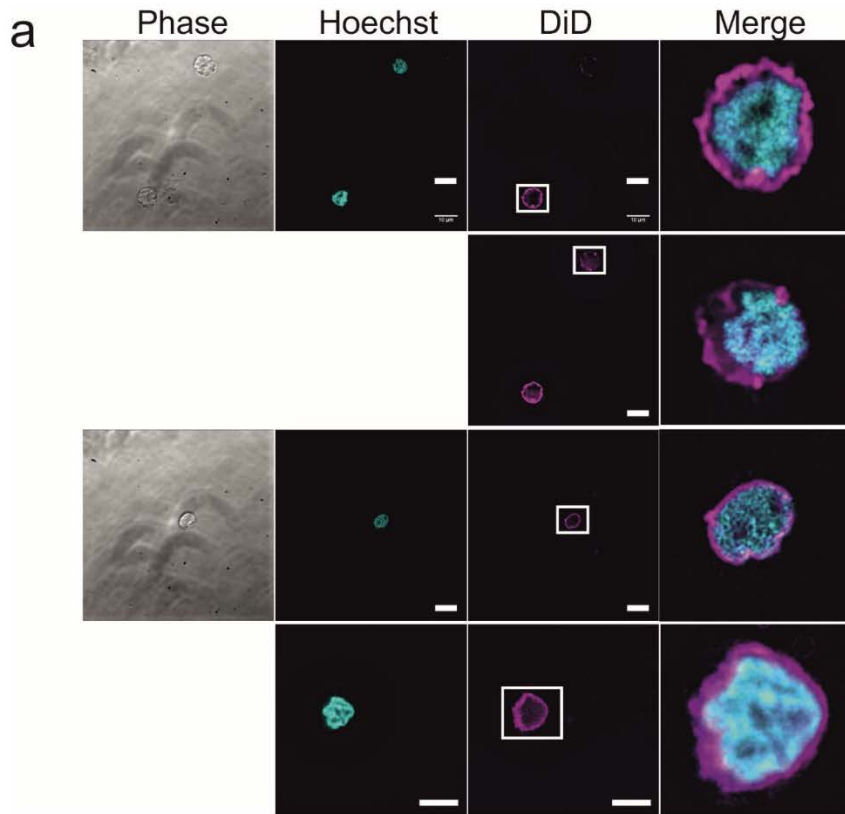
Reprints and permission information is available online at <http://npg.nature.com/reprintsandpermissions/>

Publisher's note: Springer Nature remains neutral with regard to jurisdictional claims in published maps and institutional affiliations.

 **Open Access** This article is licensed under a Creative Commons Attribution 4.0 International License, which permits use, sharing, adaptation, distribution and reproduction in any medium or format, as long as you give appropriate credit to the original author(s) and the source, provide a link to the Creative Commons license, and indicate if changes were made. The images or other third party material in this article are included in the article's Creative Commons license, unless indicated otherwise in a credit line to the material. If material is not included in the article's Creative Commons license and your intended use is not permitted by statutory regulation or exceeds the permitted use, you will need to obtain permission directly from the copyright holder. To view a copy of this license, visit <http://creativecommons.org/licenses/by/4.0/>.

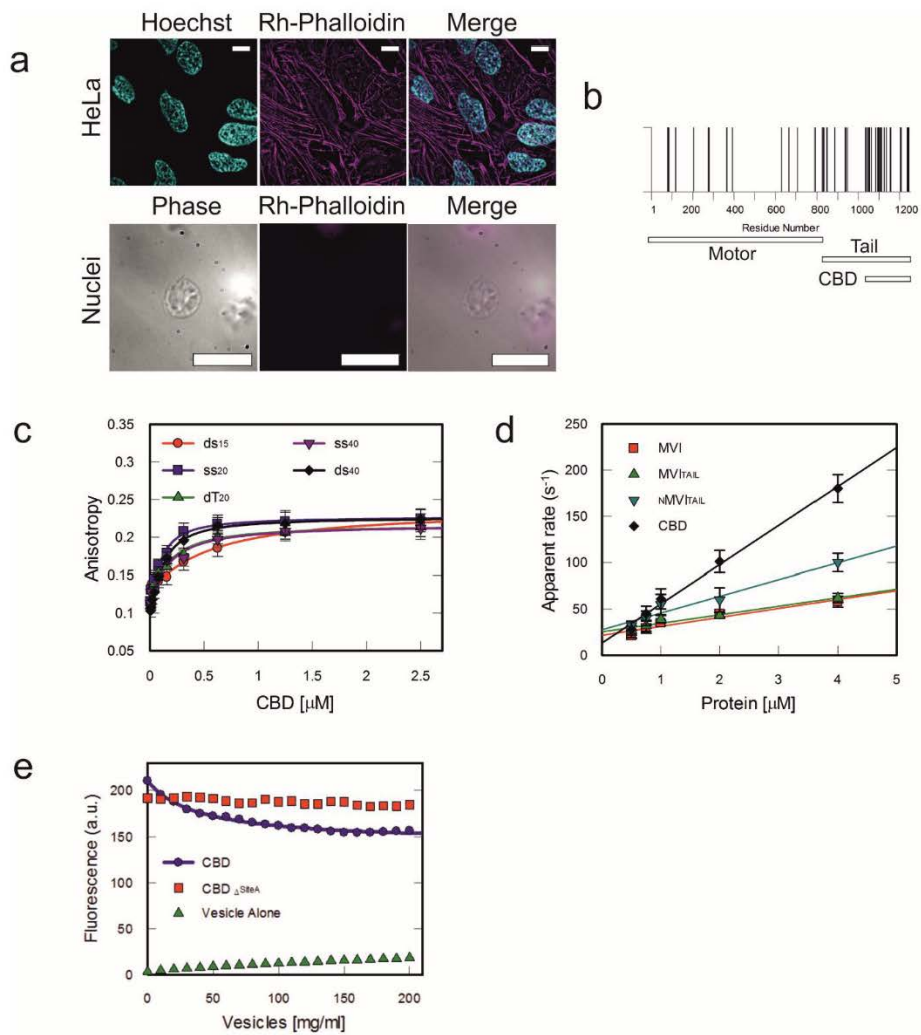
© The Author(s) 2017

4.2.1.1. Supplementary Material for Manuscript 3



Supplementary Figure 1.

(a) Examples of purified HeLa nuclei. Nuclei were stained with the DNA dye Hoechst 33342 and the lipophilic dye DiD. The staining showed that the purified nuclei appeared intact 3-D organelles, surrounded by membrane and maintaining not only their DNA content, but also preserving structures like the nucleoli (See Supplementary Movie 3 and 4). Images were acquired at the mid-point of the nucleus. Scale bar 10 μm .



Supplementary Figure 2.

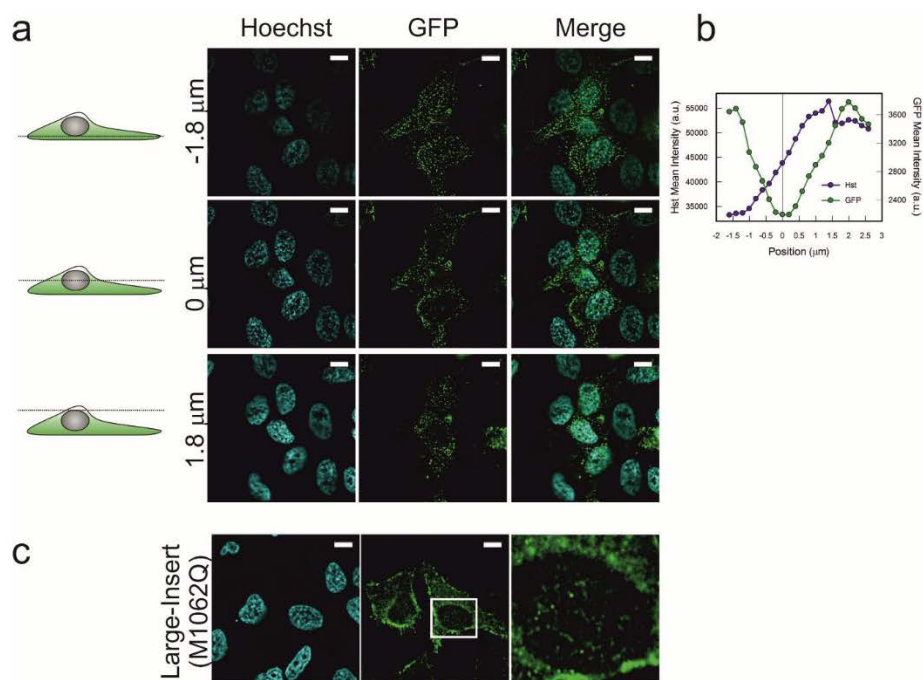
(a) Staining for filamentous actin. To assess whether the filamentous structures seen by the immunofluorescence staining of MVI were nuclear actin filaments, fixed HeLa cells and isolated nuclei were stained with Rhodamine-Phalloidin and Hoechst 3342. However, the lack of phalloidin staining in the nucleus suggested that these structures are not actin-based. Images were acquired at the mid-point of the nucleus. Scale bar 10 μ m.

(b) Prediction of DNA binding residues using BindN (<http://bioinformatics.k-state.edu/bindn/>). Bars indicate residues with a predicted confidence greater than 70%. A full list of residues are presented in Supplementary Table 1. A majority of sites are clustered in the CBD.

(c) Fluorescence anisotropy titrations of the CBD domain against various FAM-DNA substrates (50 nM). Data fitting was performed as described in Methods. K_d : ds₁₅ 500 +/- 45 nM, ss₂₀ 110 +/- 35 nM, dT₂₀ 120 +/- 25 nM, ss₄₀ 120 +/- 35 nM and ds₄₀ 100 +/- 20 nM. Data were averaged from three independent experiments.

(d) Fluorescence anisotropy was measured in stopped flow pre-steady-state measurements. MVI domains were rapidly mixed against 50 nM 40 bp FAM-DNA. Traces were fitted as described in the Methods to yield the rate constants plotted in d. Association and dissociation rate constants were calculated from linear fits to the data (Supplementary Table 3). Data were averaged from three independent experiments.

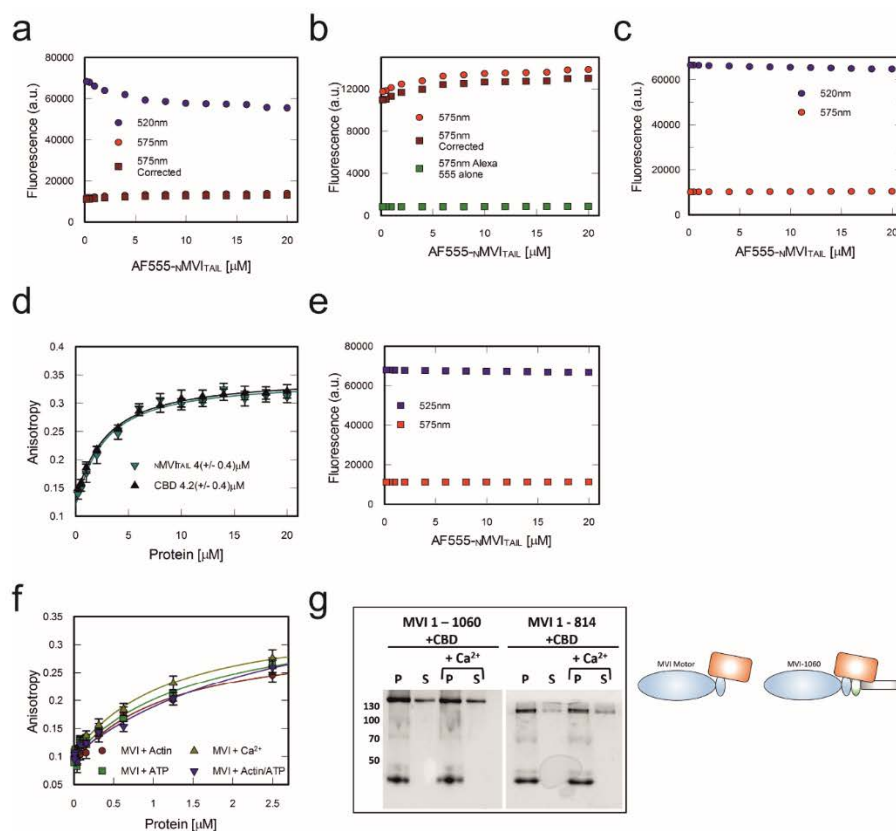
(e) Titration of Folch vesicles against 1 μ M CBD or CBD $_{\Delta$ SiteA. Data were fitted as described in Methods, following background subtraction of the folch auto-fluorescence. Fitting gives an indication of the affinity with K_d 39 +/- 4 mg/ml. Due to the unknown mixed composition, it was not possible to have molar concentrations. Poor binding by CBD $_{\Delta$ SiteA means data could not be fitted to the model.



Supplementary Figure 3.

(a-b) Intracellular distribution of EGFP-LI-MVI transiently expressed in HeLa cells. The EGFP-LI-MVI localisation was restricted to the cell periphery, being excluded from the nucleus. This is highlighted by the plot of mean intensity of Hoechst (Hst) and EGFP across each image stack. The position is measured relative to the mid-point of the nucleus. The intensity was measured within a region of interest through the centre of the nucleus. Scale bar 10 μm .

(c) Intracellular distribution of EGFP-LI-MVI(M1062Q). The mutant, in which the LI helix is destabilised, displayed a similar distribution to the NI isoform. Images were acquired at the mid-point of the nucleus. Scale bar 10 μm .



Supplementary Figure 4.

(a) Raw fluorescence intensity data for titration of nMVI_{TAIL} against CBD in Fig. 3a.

(b) Raw intensity data as shown in (a) but on a smaller scale.

(c) Raw fluorescence intensity data for titration of nMVI_{TAIL} against CBD in the presence of DNA (Blue is FITC intensity and Red is AF555 intensity).

(d) Fluorescence anisotropy titration of nMVI_{TAIL} against FITC-CBD and CBD against FITC-nMVI_{TAIL}. Data were fitted as described in Methods for the DNA substrates with K_d +/- SEM.

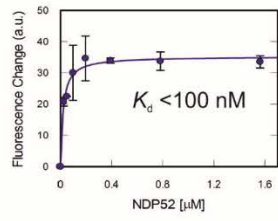
(e) Raw fluorescence intensity data for titration of nMVI_{TAIL} against CBD in the presence of NDP52. (Blue is FITC intensity and Red is AF555 intensity)

(f) Fluorescence anisotropy titrations of FL MVI against a 40 bp FAM-DNA (50 nM) in the presence of F-Actin (5 μ M), Ca²⁺ (1 mM), ATP (2 mM) and Actin-ATP. Data fitting

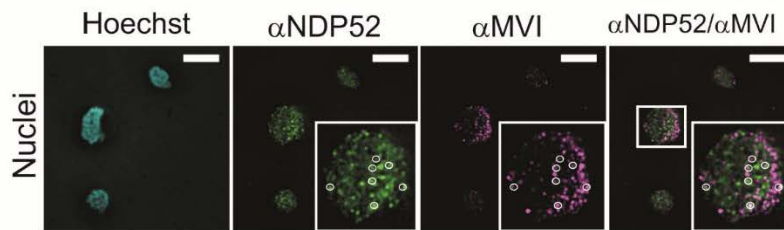
was performed as described in Methods. Data were averaged from three independent experiments.

(g) Pull-down of CBD (5 μ M) by His-tagged Motor₁₋₁₀₆₀ and Motor₁₋₈₁₄ both at 10 μ M +/- 1 mM Ca²⁺. P and S represent pellet and supernatant fractions, respectively. Interaction of the CBD with the motor constructs is shown in the cartoon scheme.

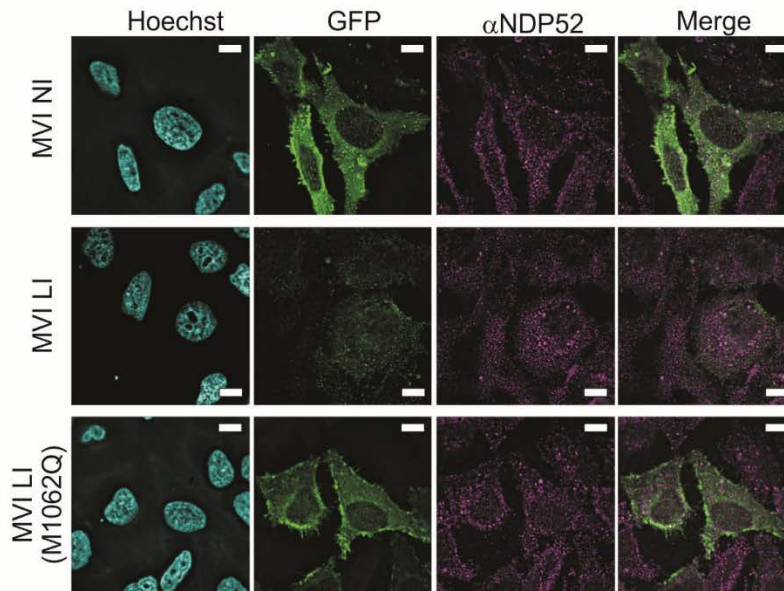
a



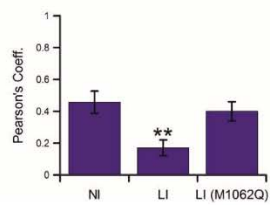
b



c



d



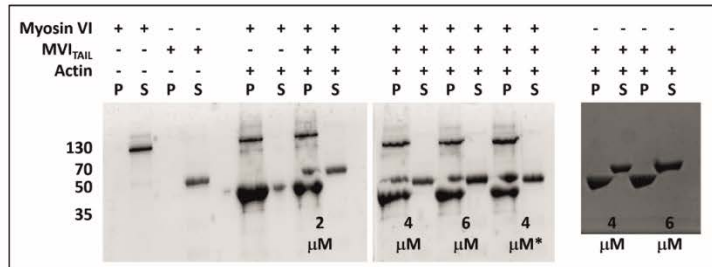
Supplementary Figure 5.

(a) Fluorescence intensity titration of NDP52 against a 40 bp FAM-DNA substrate (50 nM). Data fitting was performed as described in Methods. Data were averaged from three independent experiments. K_d : ds₄₀ 80 +/- 25 nM

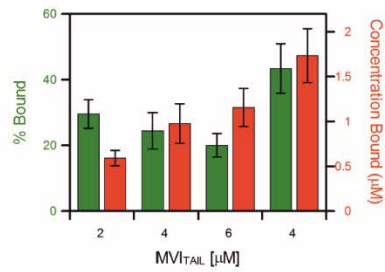
(b) Immunofluorescence staining against NDP52 (green), MVI (magenta) and DNA (cyan) on isolated HeLa nuclei, as performed in Fig. 1b. Insert depicts co-localising foci. Scale bar 10 μ m.

(c) Representative images of transiently expressed NI-, LI- and LI (M1062Q) -EGFP-MVI in HeLa cells stained against DNA (Cyan) and immune-stained against endogenous NDP52 (magenta). Scale bar 10 μ m. These images were used to assess the significance of the Pearson's coefficient regarding MVI and NDP52 co-localisation. We have established how the NI and LI (M1062Q) can form interactions with NDP52. Therefore, to assess this *in vivo* through imaging, we performed the Pearson's coefficient test (d) with the three MVI constructs. Here a region of interest was drawn around the cells and images were analysed from 5 different stacks. LI MVI shows a significantly lower co-localisation than the NI or mutant **p <0.001.

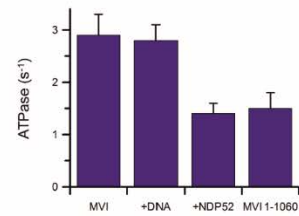
a



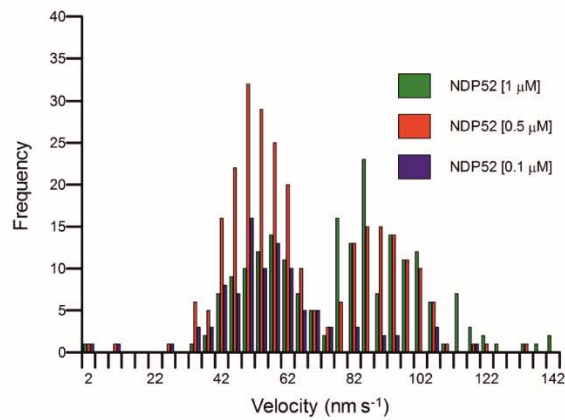
b



c



d



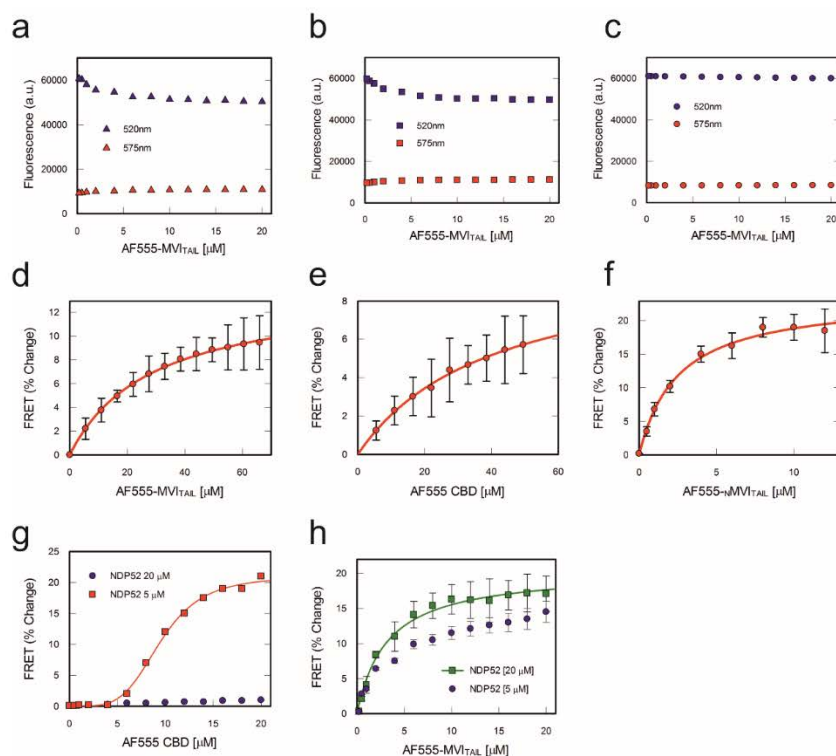
Supplementary Figure 6.

(a) Actin co-sedimentation assay. 1 μM MVI was incubated with the indicated concentrations of MVI_{TAIL} before sedimentation in the presence of 5 μM F-actin, as described in the Methods. Except for the 4 μM^* condition where 2 μM MVI was used. P and S represent pellet and supernatant fractions, respectively.

(b) Gel densitometry was used to determine the relative % of MVI_{TAIL} in the actin pellet (Green bars). The % bound was then converted into the concentration of bound species (Red bars) (Error bars represent SEM).

(c) Plots of MVI or Motor₁₋₁₀₆₀ ATPase rate constants in the presence of 5 μ M DNA or NDP52 under conditions described in the Methods. Error bars represent SEM.

(d) Velocity histogram from sliding filament assay with MVI immobilised through the stated concentrations of NDP52.



Supplementary Figure 7.

(a) Raw fluorescence intensity data for titration of AF555-MV_{TAIL} against FITC-MV_{TAIL} in the presence of 20 μ M NDP52. (a-c) Blue is FITC intensity and Red is AF555 intensity.

(b) Raw fluorescence intensity data for titration of AF555-MV_{TAIL} against FITC-MV_{TAIL} in the presence of 20 μ M DNA/NDP52.

(c) Raw fluorescence intensity data for titration of AF555-MV_{TAIL} against FITC-MV_{TAIL}.

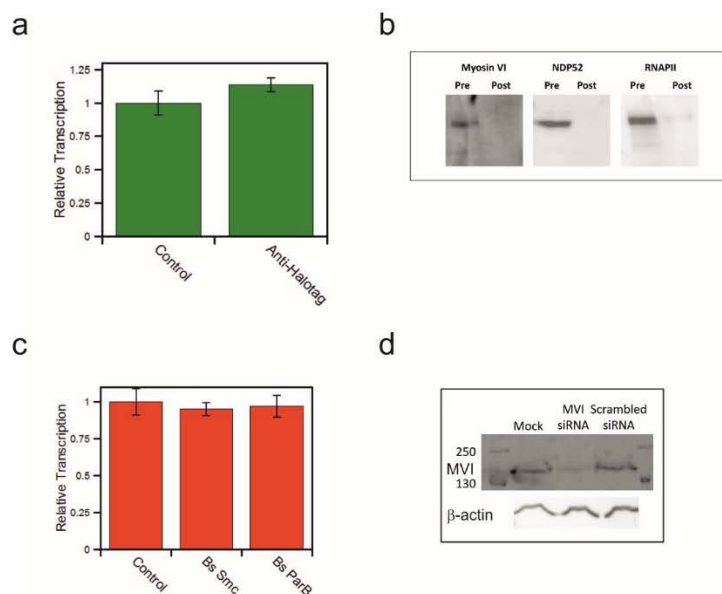
(d) FRET titration of AF555-MV_{TAIL} against FITC-MV_{TAIL} over a larger concentration range.

(e) FRET titration of AF555-CBD against FITC-CBD.

(f) FRET titration of AF555-NMV_{TAIL} against FITC-NMV_{TAIL}.

(g) FRET titration of AF555-CBD against FITC-CBD in the presence of 5 μ M or 20 μ M NDP52. For F-G, fitting was performed as described in the Methods.

(h) FRET titration of AF555-MV_{TAIL} against FITC-MV_{TAIL} in the presence of 5 μ M or 20 μ M NDP52.



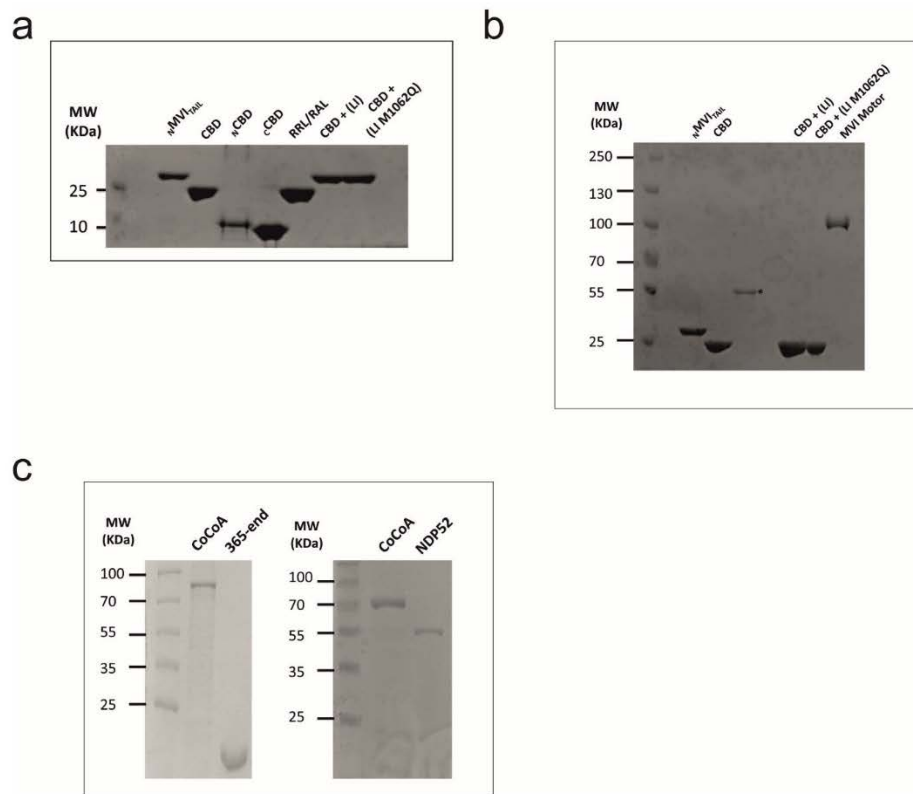
Supplementary Figure 8.

(a) *In vitro* transcription by HeLaScribe extracts. A control reaction was performed under standard manufacturer's instructions. Antibody depletion was performed as described in Methods. Here, Anti-HaloTag represents an antibody negative control to highlight the specific isolation of target proteins. Samples were normalized to a non-depleted control reaction (error bars represent SEM).

(b) Confirmation of antibody depletion. Western-blots are shown confirming the presence of MVI, NDP52 and RNAPII in the HeLaScribe extracts (Pre). Depletion of the proteins by the corresponding antibodies is shown in the Post samples.

(c) *In vitro* transcription by HeLaScribe extracts in the presence of competitor *Bacillus subtilis* Smc and ParB at 25 μ M. Both proteins were used as controls for DNA binding which may block transcription. As no decrease in transcription occurred, we conclude that the decrease in transcription observed with the CBD is related to its interaction with the RNAPII complex and not the interference by DNA binding. Samples were normalized to the control sample in Fig. 6e (error bars represent SEM).

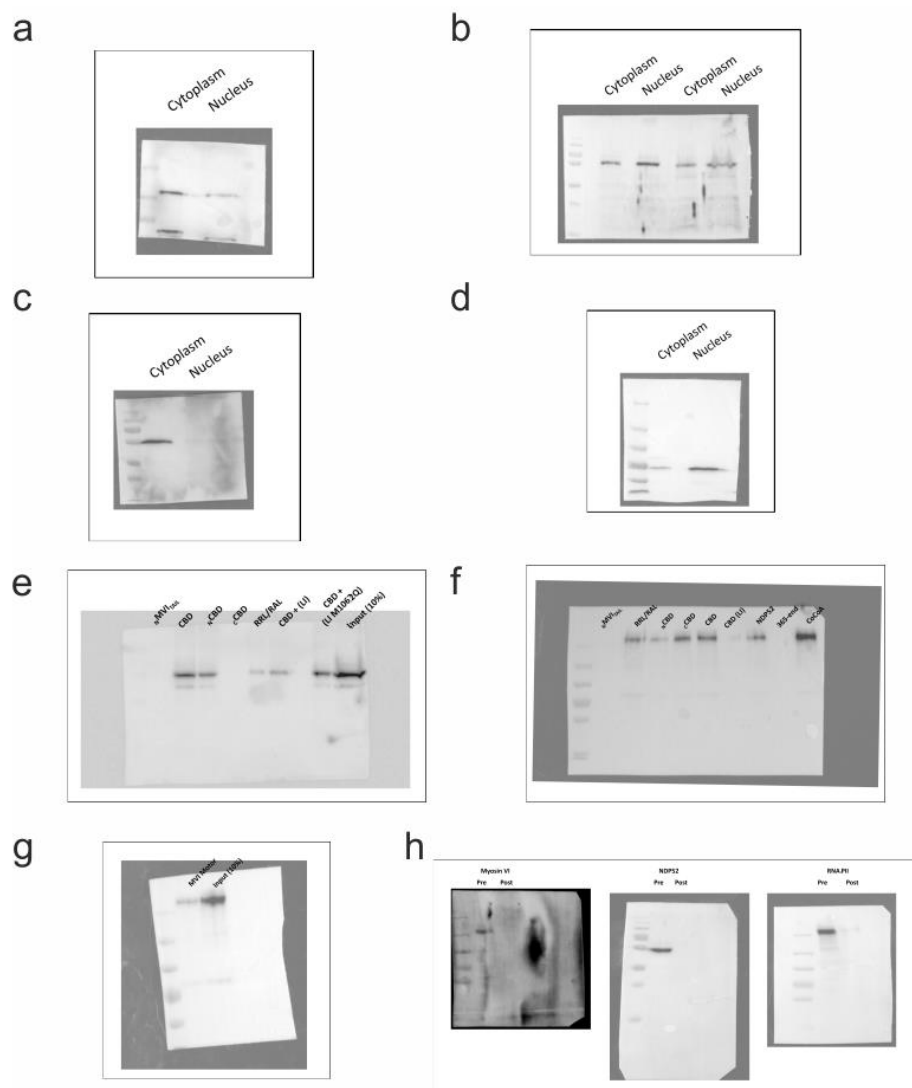
(d) siRNA Knock-down of myosin VI. Western-blot on myosin VI in MCF7 cells under mock conditions and following transfection with MVI siRNA and control scrambled siRNA.



Supplementary Figure 9.

(a-b) Loading controls of recombinant proteins for assays performed in Fig. 4f and 7c.

(c) Loading controls of recombinant proteins for assay performed in Fig. 6c.



Supplementary Figure 10.

Uncropped Western-blots. (a) MVI From Fig. 1c. (b) NDP52 From Fig. 4c. (c) Tubulin from cell fractionation Fig. 1c and 4c. (d) Lamin B from cell fractionation Fig. 1c and 4c. (e) From Fig. 4f. (f) From Fig. 6c and 7c. (g) From Fig. 7c. (h) From Supplementary Fig. 8b.

Supplementary Table 1. DNA Binding Prediction

Residue	Amino acid	Output	Prediction	Confidence (0-1)
80	R	1.6914	+	0.9539
83	K	1.4826	+	0.9152
85	R	2.0163	+	0.9862
118	K	1.5894	+	0.9373
205	R	1.6289	+	0.9447
276	R	1.7193	+	0.9594
280	R	1.9585	+	0.9825
365	K	1.6639	+	0.9493
368	S	1.4254	+	0.9005
393	R	1.854	+	0.9705
632	K	1.4439	+	0.9023
667	R	1.4925	+	0.9189
708	R	1.9088	+	0.9788
792	R	1.7813	+	0.965
825	R	1.5331	+	0.9309
831	R	1.4709	+	0.9124
832	R	1.3556	+	0.8839
834	K	1.1633	+	0.8166
847	K	1.1978	+	0.8341
849	R	1.2752	+	0.8553
886	K	1.1943	+	0.8313
937	R	1.2846	+	0.8627
940	R	1.1816	+	0.824
948	R	1.1761	+	0.823
1035	R	0.9922	+	0.8235
1036	R	1.038	+	0.8475
1044	K	0.9667	+	0.806
1049	T	0.9875	+	0.8217
1050	K	1.0849	+	0.8714
1055	S	0.9608	+	0.8041
1056	K	1.1173	+	0.8862
1063	R	1.1307	+	0.8917
1085	R	1.0471	+	0.8548
1094	S	1.4206	+	0.8995
1095	K	1.9281	+	0.9816
1096	N	1.3317	+	0.8774
1097	K	1.4436	+	0.9023
1098	K	1.7798	+	0.965
1099	R	1.6503	+	0.9484
1100	N	1.2231	+	0.8433
1106	R	1.0999	+	0.8797
1109	K	1.507	+	0.9235
1112	T	1.0336	+	0.8447
1126	R	1.0418	+	0.8502
1137	R	1.1627	+	0.8147
1155	S	1.1766	+	0.823
1156	K	1.539	+	0.9318
1157	K	1.1108	+	0.8797
1158	K	1.5536	+	0.9336
1205	T	0.9608	+	0.8041
1206	R	1.8287	+	0.9687
1207	K	1.1256	+	0.8908
1208	R	1.4658	+	0.9115
1237	R	1.4731	+	0.9134
1240	R	1.7045	+	0.9548
1242	T	1.1889	+	0.8286
1243	Y	1.2152	+	0.8424
1245	T	1.2904	+	0.8645

Supplementary Table 2. DNA Binding dissociation constants.

Construct	DNA Substrate	Conditions	Figure	<i>K_d</i> (μM)
MVI	ds40		2a	3.5 +/- 0.7
Motor1-814	ds40		2a	-
MVITAIL	ds40		2a	2.5 +/- 0.4
NMVITAIL	ds40		2b	1.2 +/- 0.35
CBD	ds40		2b	0.1 +/- 0.02
CBD $\Delta\Sigma\text{I}\tau\epsilon\text{A}$	ds40		2e	0.11 +/- 0.04
NCBD	ds40		2e	1.3 +/- 0.7
CCBD	ds40		2e	0.12 +/- 0.03
CCBD $\Delta\Sigma\text{I}\tau\epsilon\text{B}$	ds40		2f	0.7 +/- 0.18
CCBD $\Delta\Sigma\text{I}\tau\epsilon\text{X}$	ds40		2f	0.5 +/- 0.15
MVITAIL (W1221A)	ds40		3e	0.3 +/- 0.03
CBD	ds15		Sup Fig 2a	0.5 +/- 0.045
CBD	ss20		Sup Fig 2a	0.11 +/- 0.035
CBD	dT20		Sup Fig 2a	0.12 +/- 0.025
CBD	ss40		Sup Fig 2a	0.12 +/- 0.035
MVI	ds40	5 μM F-actin	Sup Fig 3f	2.4 +/- 1.3
MVI	ds40	1 mM Ca^{2+}	Sup Fig 3f	1.7 +/- 0.9
MVI	ds40	2 mM ATP	Sup Fig 3f	2.5 +/- 1.1
MVI	ds40	F-actin + ATP	Sup Fig 3f	2.7 +/- 1.3
NDP52	ds40		Sup Fig 4f	0.08 +/- 0.025

Supplementary Table 3. Myosin VI – DNA Pre-steady-state kinetics.

Construct	Association rate constant ($\mu\text{M}^{-1} \text{s}^{-1}$)	Dissociation rate constant (s^{-1})
MVI	9.1 +/- 1.5	21.3 +/- 3.3
MVITAIL	9.4 +/- 1	25.6 +/- 2.2
NMVITAIL	17.4 +/- 2.2	27.8 +/- 4.7
CBD	42.2 +/- 3.8	13.3 +/- 3.9

Supplementary Table 4. Protein-protein dissociation constants.

Construct A	Construct B	Technique	Conditions	Figure	<i>K_d</i> (μ M)
NMVITAIL	CBD	FRET		3a	4.5 +/- 0.6
NMVITAIL	CBD	Anisotropy		Sup Fig 3d	4 +/- 0.4
CBD	NMVITAIL	Anisotropy		Sup Fig 3d	4.2 +/- 0.4
NDP52	MVITAIL	FRET		4d	3.2 +/- 1.2
NDP52	MVITAIL (LI)	FRET		4d	9.8 +/- 4.3
NDP52	MVITAIL (RRL/ARL)	FRET		4d	4.6 +/- 1.2
NDP52	MVITAIL (RRL/RAL)	FRET		4d	55 +/- 23
NDP52	MVITAIL (RRL/RRA)	FRET		4d	21 +/- 11
NDP52	MVITAIL (RRL/AAA)	FRET		4d	63 +/- 15
AF555-MVITAIL	FITC-MVITAIL	FRET		5a	27 +/- 4.3
AF555-MVITAIL	FITC-MVITAIL	FRET	20 μ M NDP52	5a	2.3 +/- 0.8
AF555-MVITAIL	FITC-MVITAIL	FRET	20 μ M DNA	5a	29 +/- 5
AF555-MVITAIL	FITC-MVITAIL	FRET	20 μ M NDP52/DNA	5a	2.5 +/- 1.2
AF555-CBD	FITC-CBD	FRET		Sup Fig 5g	58 +/- 9.5
AF555-CBD	FITC-CBD	FRET	20 μ M NDP52	Sup Fig 5i	51 +/- 7
AF555-NMVITAIL	FITC-NMVITAIL	FRET		Sup Fig 5f	3.1 +/- 1.4

Supplementary Table 5. Recombinant DNA.

Construct (Residue numbers)	Source
Human pEGFP-C3 myosin VI (large insert) (1-1284)	F. Buss (CIMR)
Human pEGFP-C3 myosin VI M1062Q (large insert) (1-1284)	S. Polo (IFOM)
Human pEGFP-C3 myosin VI (non insert) (1-1253)	F. Buss (CIMR)
Human pEGFP-C3 myosin VI WKSKNKKR/WASANNNR (1-1253)	F. Buss (CIMR)
Human pFastBacHTB GFP NI myosin VI	F. Buss (CIMR)
Xenopus pFastBac1 Calmodulin (1-end)	J. Sellers (NIH)
Bacillus subtilis pET28 Smc hinge	S.Gruber (MPIB)
Bacillus subtilis pET28 ParB (1-end)	S.Gruber (MPIB)
pSG1365	S.Gruber (MPIB)
Human pET151 GST ERalpha (1-end)	Synthetic Gene – This Study
Human pET151 NDP52 (1-end)	Synthetic Gene – This Study
Human pET151 NDP52 (365-end)	Synthetic Gene – This Study
Human pET151 EGFP-MVI _{TAIL} -RFP (814-1253)	Synthetic Gene – This Study
Human pET151 MVI _{TAIL} (814-1253) W1221A	Synthetic Gene – This Study
Human pET151 CBD (1060-end) W1221A	Synthetic Gene – This Study
Human pET151 CoCoA (1-end)	Synthetic Gene – This Study
Human pMX MVI (1184-1253)	Synthetic Gene – This Study
Human pET151 MVI _{TAIL} 814-1253	This Study
Human pET151 _N MVI _{TAIL} 814-1060	This Study
Human pET28 CBD 1060-1253	This Study
Human pET28 _N CBD ₁₀₆₀₋₁₁₂₀	This Study
Human pET28 _C CBD ₁₁₂₁₋₁₂₅₃	This Study
Human pET28 MVI _{TAIL} (large insert) (814-1284)	This Study
Human pET28 CBD (large insert) (1037-1284)	This Study
Human pET28 CBD M1062Q (large insert) (1037-1284)	This Study
Human pFastbacHTB NI MVI (1-1253)	This Study
Human pFastbacHTB Motor ₁₋₈₁₄	This Study
Human pFastbacHTB Motor ₁₋₁₀₆₀	This Study
Human pET28 CBD ΔSite A WKSKNKKR/WASANNNR (1060-	This Study
Xenopus pET28 Calmodulin	This Study
Human pET28 _C CBD ΔSite B SKKK/AAAA	This Study
Human pET28 _C CBD ΔSite C TRKR/AAAA	This Study
Human pET28 CBD RRL/RAL	This Study
Human pET28 CBD LQSL/AQSAA	This Study
Human pET28 MVI _{TAIL} RRL/RAL	This Study
Human pET28 MVI _{TAIL} RRL/ARL	This Study
Human pET28 MVI _{TAIL} RRL/RRA	This Study
Human pET28 MVI _{TAIL} RRL/AAA	This Study

Supplementary Table 6. Primers for qPCR.

Sequence	Use
CATGGAGAACAAGGTGATCTG	TFF1/PS2 qPCR For
CACTGTACACGTCTCTGTCTG	TFF1/PS2 qPCR Rev
ATGGGAAATTCTTACGCTGGAC	GREB1 qPCR For
CACTCGGCTACCACCTTCT	GREB1 qPCR Rev
AGAGCTACGAGCTGCCTGAC	Human B-Actin qPCR For
AGCACTGTGTTGGCGTACAG	Human B-Actin qPCR Rev
AAGCTTCGATGATGGGCTTA	ESR1 qPCR For
AGGTGGACCTGATCATGGAG	ESR1 qPCR Rev
CCGAGCTCATCAGTGATGAGGC	Myosin VI qPCR For
CCAAGCATGATACACTTTTAGTCTCC	Myosin VI qPCR Rev
AAGGGCATCGACTTCAAGGA	CMV GFP RT-qPCR For In vitro Transcription
GGCGGATCTTGAAGTTCACC	CMV GFP RT-qPCR Rev In vitro Transcription

Supplementary Table 7. DNA Substrates.

Sequence	Use
TTAGTTGTTCTAGTGTCTCGTCTGGCTCTGGATTACCCGC*	ds40 A 3'FAM
GCGGGTAATCCAGAGCCAGACGAGCACTACGAACAATAA	ds40 B
TTAGTTGTTCTAGTGTCTCGTCTGGCTCTGGATTACCCGC*	ss40 A 3'FAM
TCTGGCTCTGGATTACCCGC*	ds20 A 3'FAM
GCGGGTAATCCAGAGCCAGA	ds20 B
TCTGGCTCTGGATTACCCGC*	ss20 A 3'FAM
TTAGTTGTTCTCTGG*	15 bp A 3'FAM
CCAGAGAACAATAA	15 bp B
TTTTTTTTTTTTTTTTTTTT	dT ₂₀

Supplementary Table 8. PCR Primers.

Sequence	Use
AGCTAGCTGCATGGCTGACCAACTG	pET28 Calmodulin For
TTTTGCGGCCGCTCACTTTGCTGTCATC	pET28 Calmodulin Rev
CTAGGCGGCCGCCCCGAGGATGGAAAGCCCGTTTG	pFastbacHTB NI Myosin VI
TTTTCTCGAGTTATTTCAACAGGTTCTGCAGCATG	pFastbacHTB NI Myosin VI
CACC GAAGCCTGCATTAATAATGC	MVI _{TAIL} 814-1253 For
CTATTTCAACAGGTTCTGCAGCAT	MVI _{TAIL} 814-1253 Rev
CTAGGCGGCCGCCCCGAGGATGGAAAGCCCGTTTG	pFastBacHTB NI MVI
TTTTCTCGAGCTAGCATTTTAAATGCAGGCTTC	pFastBacHTB NI MVI
CTAGGCGGCCGCCCCGAGGATGGAAAGCCCGTTTG	pFastBacHTB NI MVI
TTTTCTCGAGCTAGATGGTATCACGTAGTTCTGC	pFastBacHTB NI MVI
AGCTAGCGCAGAACTACGTGATACCATC	CBD For
TTTTGCGGCCGCTATTTCAACAGGTTCTGCAGCAT	CBD Rev
AGCTAGCGCAGAACTACGTGATACCATC	_N CBD For
TTTTGCGGCCGCTATGCTGGTTTTGCTGAGG	_N CBD Rev
AGCTAGCGCTCAGATTCCTGCCAGG	_C CBD For
TTTTGCGGCCGCTATTTCAACAGGTTCTGCAGCAT	_C CBD Rev
AGCTAGCGGGCAGAACTCAGCACTG	CBD Plus LI For
TTTTGCGGCCGCTATTTCAACAGGTTCTGCAGCAT	CBD Plus LI Rev
CACC GAAGCCTGCATTAATAATGC	_N MVI _{TAIL} For 814-1060
CTAGATGGTATCACGTAGTTCTGC	_N MVI _{TAIL} Rev 814-1060
AGCTAGCGCCGAAGTGCATGATACCA	CBD W1221A For
TTTTGCGGCCGCTATTTTTCAGCAGGCTCTGCAGC	CBD W1221A Rev
CTTGACAGAGAAGAATTTTCATGCGGCAGCAAAGTGTATCATGC	RRL/AAA For
GATTTCCAAGCATGATACACTTTTGCTGCCGCATGAAATTCTTC	RRL/AAA Rev
CTTGACAGAGAAGAATTTTCATAGGAGAGCAAAGTGTATCATGC	RRL/RRA For (L1118A)
GATTTCCAAGCATGATACACTTTTGCTCTCCTATGAAATTCTTC	RRL/RRA Rev (L1118A)
CTTGACAGAGAAGAATTTTCATGCGGACTAAAAGTGTATCATGC	RRL/ARL For (R1116A)
GATTTCCAAGCATGATACACTTTTAGTCTCGCATGAAATTCTTC	RRL/ARL Rev (R1116A)
GCAGAGAAGAATTTTCATAGGGCACTAAAAGTGTATCATGCTTG	RRL/RAL Rev (R1117A)
CCAAGCATGATACACTTTTAGTGCCTATGAAATTCTTCTCTGC	RRL/RAL Rev (R1117A)
GACCCTCAGAGTGCAGCAGGCTGGTGGTATGC	SKKK/SAAA For
GCATACCACCAGCCTGCTGCCGCACTCTGAGGGTC	SKKK/SAAA Rev
GACTGGCCTGACTCGGAAGCGTGGTGCTGAGATCTTG	TRKR/TAAA For
CAAGATCTCAGCACCACGCTTCCGAGTCAGGCCAGTC	TRKR/TAAA Rev
GCCATGGCGCAGAACGCGGCGAAATAAGCCGAAG	LQSLI/AQSAA For
CTTCGGCTTATTTTCGCCGCTTCTGCGCCATGGC	LQSLI/AQSAA Rev
GATCGATAGTACATAAGGATTTCTTACGCG	500bp 5'Bio-Teg
CCAATTTTCGTTTGTGAACATAATGGGTGC	500 bp Rev

4.2.2. Manuscript 4 - Competition between two high-and low-affinity protein-binding sites in myosin VI controls its cellular function.



Competition between two high- and low-affinity protein-binding sites in myosin VI controls its cellular function

Received for publication, July 10, 2019, and in revised form, November 15, 2019. Published, Papers in Press, November 19, 2019, DOI 10.1074/jbc.RA119.010142

Natalia Fili^{†1}, Yukti Hari-Gupta^{§1}, Bjork Aston[§], Ália dos Santos[‡], Rosemarie E. Gough[‡], Bana Alamad[§], Lin Wang[¶], Marisa L. Martin-Fernandez[‡], and Christopher P. Toseland^{†2}

From the [†]Sheffield Cancer Centre, Department of Oncology and Metabolism, University of Sheffield, Sheffield S10 2RX, United Kingdom, the [§]School of Biosciences, University of Kent, Canterbury CT2 7NZ, United Kingdom, and the [‡]Central Laser Facility, Research Complex at Harwell, Science and Technology Facilities Council, Rutherford Appleton Laboratory, Harwell, Didcot, Oxford OX11 0QX, United Kingdom

Edited by Enrique M. De La Cruz

Myosin VI is involved in many cellular processes ranging from endocytosis to transcription. This multifunctional potential is achieved through alternative isoform splicing and through interactions of myosin VI with a diverse network of binding partners. However, the interplay between these two modes of regulation remains unexplored. To this end, we compared two different binding partners and their interactions with myosin VI by exploring the kinetic properties of recombinant proteins and their distribution in mammalian cells using fluorescence imaging. We found that selectivity for these binding partners is achieved through a high-affinity motif and a low-affinity motif within myosin VI. These two motifs allow competition among partners for myosin VI. Exploring how this competition affects the activity of nuclear myosin VI, we demonstrate the impact of a concentration-driven interaction with the low-affinity binding partner DAB2, finding that this interaction blocks the ability of nuclear myosin VI to bind DNA and its transcriptional activity *in vitro*. We conclude that loss of DAB2, a tumor suppressor, may enhance myosin VI-mediated transcription. We propose that the frequent loss of specific myosin VI partner proteins during the onset of cancer leads to a higher level of nuclear myosin VI activity.

Myosin VI (MVI)³ is an actin-based molecular motor that performs numerous vital roles in key cellular processes such as cell migration, endocytosis, exocytosis, and transcription (1–3). Defects in MVI lead to various diseases including hypertrophic cardiomyopathy, deafness, and cancer (4–7).

MVI consists of the highly conserved actin-binding motor domain, a neck region, and a C-terminal globular cargo-binding domain (CBD) (see Fig. 1*a*). We have recently shown that

MVI can adopt a back-folded conformation, in which the CBD is brought in close proximity to the motor domain (see Fig. 1*b*) (3). Moreover, two regions within the tail (MVI_{TAIL}, aa 814–1253) can be alternatively spliced, resulting in a 31-residue insertion (large insert, LI) adjacent to the CBD and/or a 9-residue insertion in the middle of the CBD (small insert, SI) (8). This leads to several splice isoforms, namely the noninsert (NI), SI, LI, and LI + SI, each with distinct intracellular distributions and functions (8, 9). For example, the NI isoform is able to enter the nucleus, whereas the LI is confined to the cell periphery (3).

The intracellular localization and function of MVI is also regulated through its interaction with a broad range of binding partners, such as DAB2 (disabled-2), GIPC (GAIP-interacting protein C terminus), and NDP52 (nuclear dot protein 52). These partners specifically bind to one of two established motifs within the CBD of MVI, namely the RRL and WWY (10–12).

NDP52, also known as CALCOCO2, is an RRL-binding partner of MVI. It was initially identified in the nucleus (13), but it was later found to be mostly cytoplasmic (14), with roles in cell adhesion and autophagy (10, 15). NDP52 has been shown to release the back-folded conformation of MVI, allowing MVI to dimerize and to interact with DNA, both of which enable coupling of MVI to RNA polymerase II. Moreover, NDP52 has been shown to have a role in regulating transcription (3), possibly as a coactivator, similarly to its highly conserved family member CoCoA (16).

DAB2, also known as DOC-2 (differentially expressed in ovarian carcinoma), links MVI to clathrin-coated vesicles at the early stages of endocytosis (12), through interaction with the WWY motif. DAB2 is down-regulated in majority of breast and ovarian cancers. Moreover, depletion and re-expression of DAB2 can trigger tumorigenesis or suppress growth, respectively (17). Therefore, DAB2 is considered as a tumor suppressor.

The selectivity of MVI for its binding partners is, in part, regulated by isoform splicing. The LI encodes an α -helix that sits upon, and therefore blocks, the RRL motif (18). This prevents partners, such as NDP52, interacting with the protein, and therefore the binding partner interactions of this isoform are driven by the WWY motif. In contrast, in the NI isoform, both the RRL and WWY motifs are available for binding. In this case, binding partner selectivity would be an important regula-

This work was supported by Medical Research Council Grant MR/M020606/1 and Science and Technology Facilities Council Grant 19130001. The authors declare that they have no conflicts of interest with the contents of this article.

This article contains Tables S1–S3 and Fig. S1–S3.

¹ These authors contributed equally to this work.

² To whom correspondence should be addressed: Sheffield Cancer Centre, Dept. of Oncology and Metabolism, University of Sheffield, Sheffield, S10 2RX, UK. E-mail: c.toseland@sheffield.ac.uk

³ The abbreviations used are: MVI, myosin VI; CBD, cargo-binding domain; LI, large insert; SI, small insert; NI, non insert; ER, estrogen receptor; RFP, red fluorescent protein; qPCR, quantitative PCR.

This is an Open Access article under the [CC BY](https://creativecommons.org/licenses/by/4.0/) license.



© 2020 Fili et al. Published under exclusive license by The American Society for Biochemistry and Molecular Biology, Inc.

J. Biol. Chem. (2020) 295(2) 337–347 337

Binding partner regulation of myosin VI

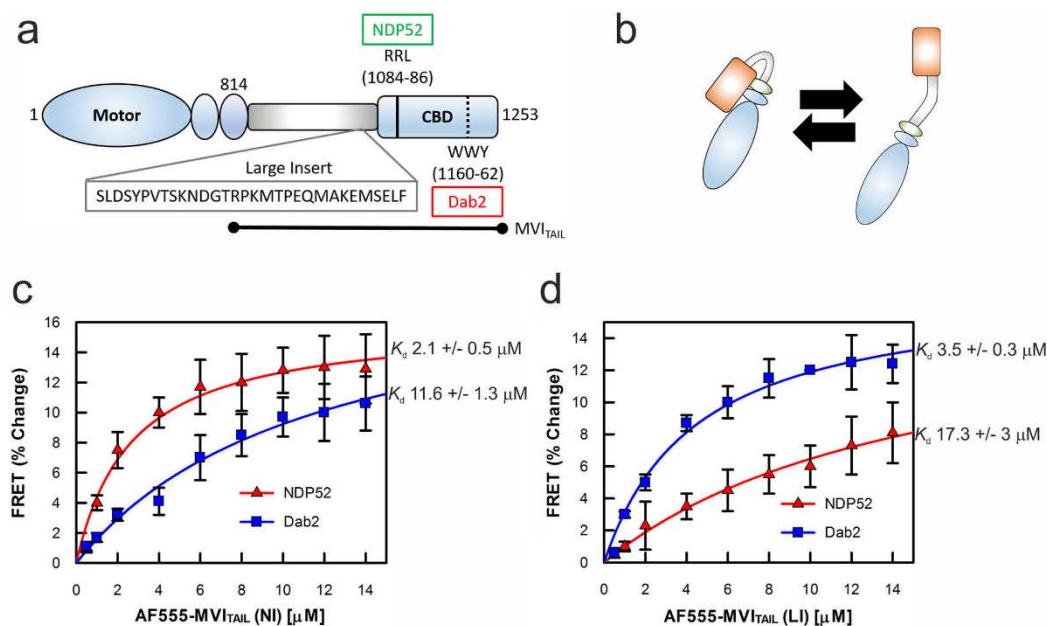


Figure 1. Interaction between myosin VI and binding partners NDP52 and DAB2. *a*, cartoon depiction of the key regions of the MVI_{TAIL}, as discussed in the text. This highlights the position of the large insert, along with the NDP52 and DAB2 binding sites. *b*, cartoon depiction of MVI backfolding with contacts between the CBD and motor, as described in Ref. 3. *c*, FRET titration of MVI_{TAIL(NI)} against 1 μ M NDP52 (red triangles) or tDAB2 (blue squares). *d*, FRET titration of MVI_{TAIL(LI)} against 1 μ M NDP52 (red triangles) or tDAB2 (blue squares). All titration data fitting was performed as described under "Materials and methods," giving a K_d as plotted. Error bars represent S.E. from three independent experiments.

tory mechanism. In the light of our recent work on the regulation of the NI isoform by NDP52 (3) and with the aim to unravel such a regulatory mechanism, we have established how competition between the two binding sites is achieved and how this can impact upon the role of nuclear MVI in gene expression.

Results

Interactions between binding partners and myosin VI

To establish how the selectivity of MVI for its binding partners is regulated, we compared its interactions with two binding partners, namely NDP52 and DAB2, as representatives of RRL- and WWY-binding proteins, respectively. Given our recent work on the interaction of the NI isoform with NDP52 (3); here we focus on the interaction with DAB2.

Before investigating the effect of DAB2 upon MVI, we first assessed their interaction. Recombinant full-length DAB2 was highly unstable and unable to yield sufficient amounts of protein for biochemical characterization. Therefore, we used the stable C-terminal region of the protein (residues 649–770), which contains the MVI binding site (12). This truncation of DAB2 will be referred to as tDAB2 throughout the manuscript, unless stated. To characterize the interaction between MVI and tDAB2, we performed an *in vitro* FRET assay by titrating Alexa 555–MVI_{TAIL(NI)} or Alexa 555–MVI_{TAIL(LI)} against FITC–DAB2. As demonstrated by the binding curves in Fig. 1 (*c* and

d), tDAB2 displayed relatively weak binding to the MVI_{TAIL(NI)} ($K_d = 11.6 \mu\text{M}$). Binding was noticeably enhanced for the MVI_{TAIL(LI)} ($K_d = 3.5 \mu\text{M}$), suggesting that the LI stabilizes the interaction with tDAB2. For comparison, measurements were also performed with NDP52. Consistent with the previous results (3), MVI_{TAIL(NI)} bound to NDP52 with a low micromolar affinity ($K_d = 2.1 \mu\text{M}$). In contrast, binding to the MVI_{TAIL(LI)} was over 8-fold weaker ($K_d = 17.3 \mu\text{M}$), indicating that NDP52 selectively interacts with MVI_{TAIL(NI)} rather than the MVI_{TAIL(LI)}. Based on these data, the differential affinity between the WWY and RRL sites suggests that the NI isoform would selectively bind RRL binding partners over its WWY competitors. In contrast, the LI isoform shows preferential binding to the WWY partners because the LI helix (i) masks the higher affinity RRL motif (18), thereby impeding NDP52 binding, and (ii) may provide additional interaction sites to increase the DAB2 affinity.

To further explore these interactions with full-length proteins, we assessed their association within cells. In HeLa cells, which only express the NI isoform (19), endogenous MVI shows little colocalization with endogenous DAB2, if any (Fig. 2*a*). In contrast, transiently expressed GFP-LI showed significant colocalization with endogenous DAB2, as highlighted by the 10-fold increase in Pearson's coefficient (Fig. 2, *b* and *d*). Consistent with the titration measurements, these observations

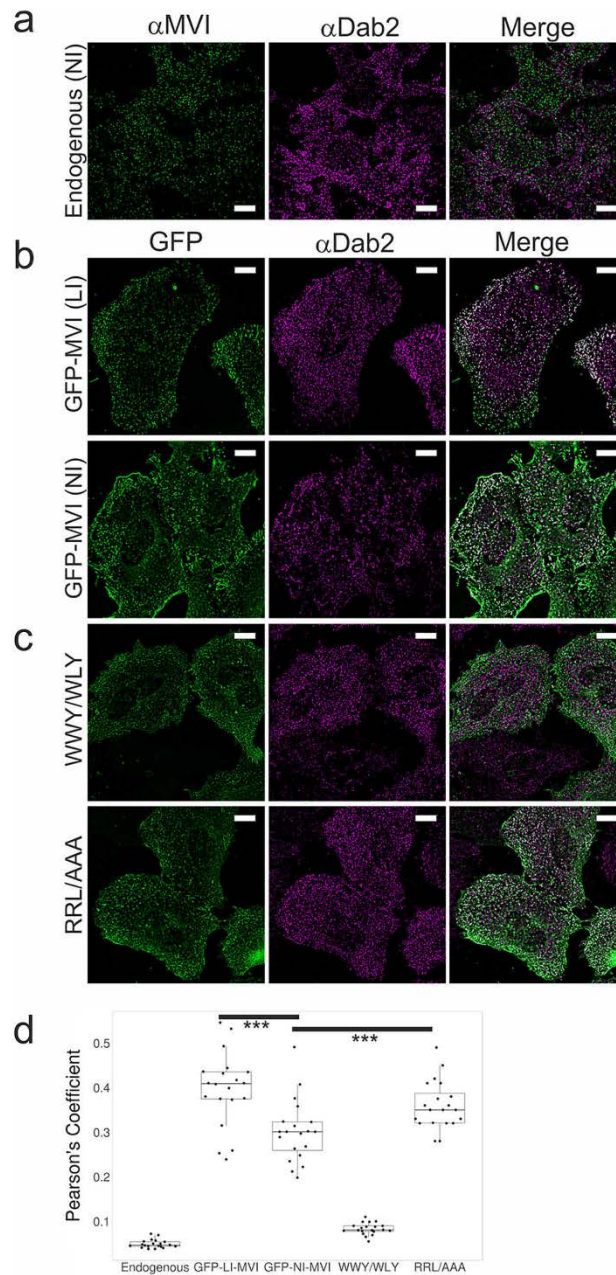


Figure 2. Myosin VI interaction with DAB2 in HeLa cells. *a*, immunofluorescence staining against MVI (green) and DAB2 (purple) in HeLa cells. White foci depict colocalization. *b*, representative images of transiently expressed NI- and LI-GFP-MVI in HeLa cells combined with immunofluorescence staining against DAB2. *c*, representative images of transiently expressed NI-MVI mutants WWY/WLY and RRL/AAA in HeLa cells combined with immunofluorescence staining against DAB2. Scale bars, 10 μ m in all images. *d*, Pearson's coefficient for MVI colocalization with DAB2 from images in *a*–*c*. The figure was generated using Ref. 26. Each data point represents a field of view consisting of 2–4 cells. *** represents a $p < 0.001$ by two-tailed *t* test.

Binding partner regulation of myosin VI

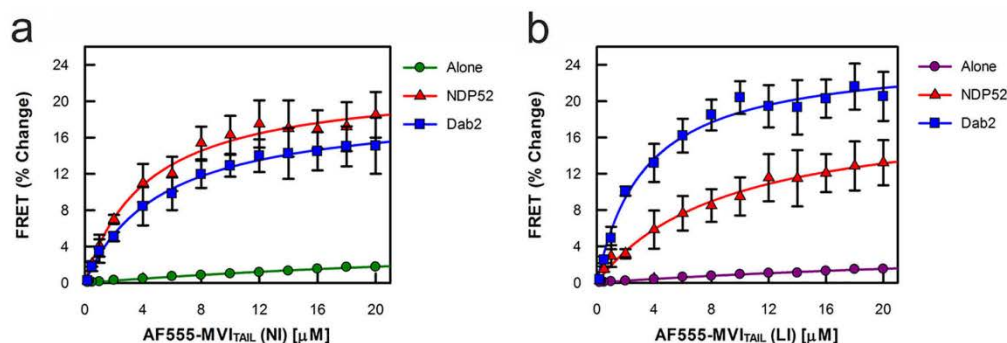


Figure 3. Binding partner-driven dimerization of myosin VI. *a*, FRET titration of AF555-MVITAIL(NI) against 1 μM FITC-MVITAIL(NI) \pm tDAB2 (20 μM) and NDP52 (20 μM). Data fitting generated NDP52 K_d^{DIMER} as 4.3 μM and tDAB2 K_d^{DIMER} as 5.3 μM . *b*, FRET titration of AF555-MVITAIL(LI) against 1 μM FITC-MVITAIL(LI) \pm tDAB2 (20 μM) and NDP52 (20 μM). Data fitting generated NDP52 K_d^{DIMER} as 9.3 μM and tDAB2 K_d^{DIMER} as 3.3 μM . All titration data fitting was performed as described under "Materials and methods." (Error bars represent S.E. from three independent experiments.)

support that the selectivity of MVI for its partners differs depending on the isoform.

Our biochemical data suggested that the association of MVI with its partners is a concentration-dependent process. To address this in the cellular environment, we artificially increased the intracellular levels of the NI isoform by transient overexpression of GFP-NI-MVI and assessed its colocalization with endogenous DAB2. Consistent with our titration data, increase in the NI intracellular levels shifted the extent of colocalization between the two proteins at levels comparable with the LI-MVI (Fig. 2, *b* and *d*). To confirm the specificity of this observation, we also assessed the effect of transiently overexpressing two mutants of the NI isoform, each carrying mutations that abolish one of the two binding motifs (Fig. 2, *c* and *d*). As expected, GFP-NI-MVI (WWY/WLY), in which the WWY binding site is abolished, did not show any colocalization with DAB2. In contrast, mutation of the RRL motif did not affect the colocalization with DAB2. In fact, there was a slight increase in colocalization, which may relate to an increase in free MVI available to interact with WWY-binding partners. Overall, these observations are consistent with the conclusions from the titration measurements suggesting that significant interactions between the NI MVI_{TAIL} and tDAB2 can occur at higher protein concentrations. Therefore, our data support that the WWY-binding site has a weaker affinity for protein-protein interactions.

DAB2 mediates myosin VI large insert isoform dimerization

We have previously revealed how NDP52 interacts with MVI-NI to bring about its unfolding (3). Unfolding subsequently exposes dimerization sites, leading to protein oligomerization. However, the ability of the LI isoform to dimerize has not been yet explored. The presence of the additional α -helix in this isoform may perturb its dimerization. To test whether DAB2 can oligomerize both isoforms, we performed a FRET assay, whereby two pools of MVI_{TAIL(NI)} or MVI_{TAIL(LI)} were labeled, one with FITC and the other one with Alexa 555. Titrations revealed a weak association between the two tail pools (Fig. 3, *a* and *b*), consistent with our previous results

(3). Upon addition of 20 μM excess tDAB2, a change in FRET signal was observed, indicating the formation of a dimer complex. This occurred with both the NI and LI tails, with the LI signal being higher possibly because of the higher association with tDAB2. 20 μM excess of NDP52 was able to trigger dimerization of MVI_{TAIL(NI)} but failed to significantly dimerize the MVI_{TAIL(LI)}, consistent with the poor binding of NDP52 to the LI isoform.

Taking all our data together, we propose the following model: NDP52 specifically associates with MVI-NI through the RRL motif to trigger unfolding of the protein and subsequent dimerization. Similarly, binding of DAB2 to the LI isoform through the WWY motif also leads to dimerization. Although DAB2 has also the ability to bind the NI isoform, its weaker affinity for the WWY motif makes this interaction less favorable compared with the high-affinity binding of NDP52 to the RRL motif. In this way, the unfolding and dimerization of the NI isoform is preferentially assigned to the RRL binding partners.

Effect of binding partner competition upon the biochemical properties of nuclear myosin VI

We have shown that association of a binding partner with either the RRL or the WWY motif can bring about dimerization. We have also shown that the selectivity of MVI for its binding partners is regulated by the differential affinity between the two motifs. However, what is the biological impact of this binding partner selectivity and what would be the effect if it gets disrupted? More specifically, what is the effect of DAB2 upon the function of nuclear MVI, which we previously identified as the NI isoform? We have established that DAB2 can interact with this isoform at high protein concentrations. Interestingly, DAB2 can also be detected in the nucleus (Fig. 4*a*), and therefore it could interact with nuclear MVI.

We have previously shown that MVI contains a DNA-binding site on two conserved loops in the CBD (Fig. S1*a*) (3). These sites are only exposed upon unfolding of the tail domain, and therefore, DNA binding depends upon the interaction with a binding partner (3). First, we wanted to assess the effect of binding partners upon the ability of MVI to bind DNA, which is

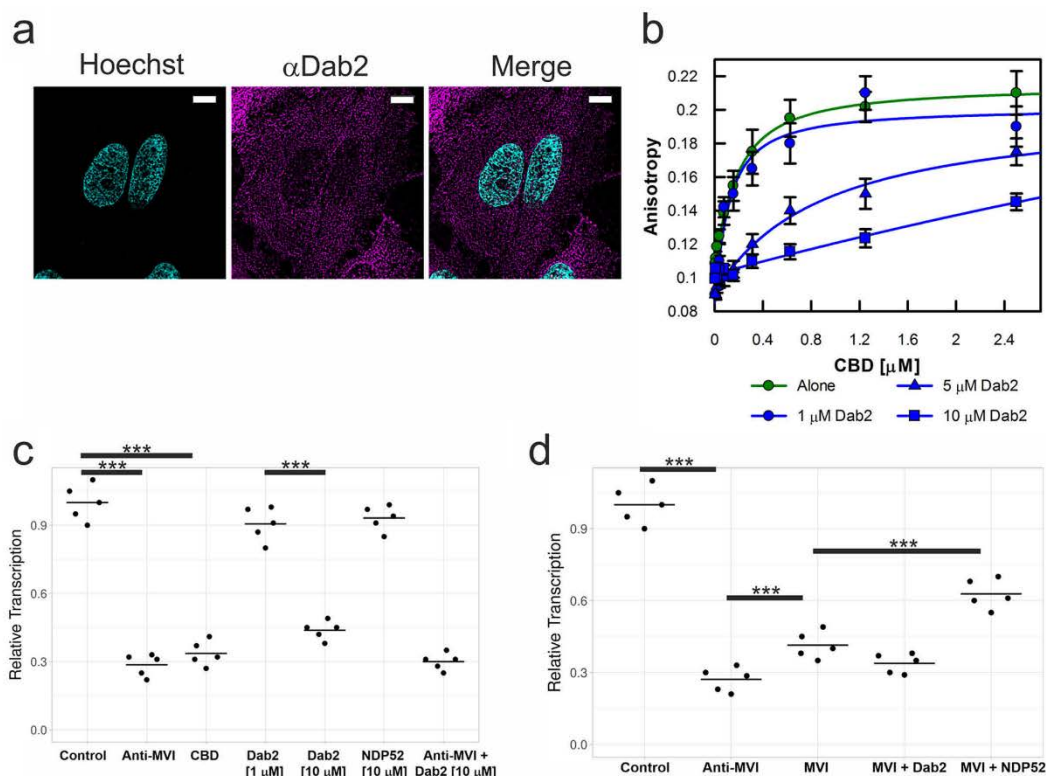


Figure 4. DAB2 represents the *in vitro* activity of nuclear myosin VI. *a*, immunofluorescence staining against DAB2 (purple) combined with DNA staining (cyan) in HeLa cells. Scale bar, 10 μm in all images. *b*, fluorescence anisotropy titrations of the CBD against a 40-bp fluorescein amidite-DNA (50 nM) with the highlighted concentrations of tDAB2. Data fitting was performed as described under "Materials and methods" ($K_d \pm \text{S.E.}$, $n = 3$ independent experiments). *c*, *in vitro* transcription by HeLaScribe extracts following antibody depletion as described under "Materials and methods" or in the presence of CBD at 25 μM , tDAB2 at 1 or 10 μM , and NDP52 at 10 μM . The samples were normalized to a nondepleted control reaction. *** represents a $p < 0.001$ by two-tailed *t* test. *d*, *in vitro* transcription following antibody depletion and rescue using recombinant MVI (NI) (1 μM), NDP52 (10 μM), or tDAB2 (10 μM), as described under "Materials and methods." *** represents a $p < 0.001$ by two-tailed *t* test.

critical for its role in transcription (3). To determine DNA binding, we measured the fluorescence anisotropy of labeled DNA. As reported previously (3), NDP52 independently binds to DNA itself, and therefore, it is unsuitable for this purpose. In contrast, tDAB2 does not bind DNA (Fig. 1*b*), and therefore it can be used to determine its impact upon MVI binding DNA. To this end, we monitored the binding of MVI CBD to fluorescently labeled DNA (Fig. 4*b*). Whereas the CBD alone could bind to DNA with strong affinity ($K_d = 140 \text{ nM}$), the presence of DAB2 inhibited DNA binding in a concentration-dependent manner. Interestingly, the DNA-binding sites of MVI are in close proximity to the WWY motif where DAB2 binds (Fig. S1*a*). Therefore, the interaction of DAB2 with MVI might induce a steric hindrance or a structural change within the CBD, which prevents the complex from binding DNA.

The ability of MVI to bind DNA is important for efficient *in vitro* transcription (3). Therefore, to assess the effect of DAB2 on the transcription activity of MVI, we performed *in vitro* transcription assays using the HeLaScribe nuclear extracts (Fig.

4*c*). Antibody depletion of MVI leads to a 70% decrease in transcription yield. A similar impact is achieved through the addition of recombinant CBD to displace MVI. Interestingly, addition of 10 μM recombinant tDAB2 leads to a 60% decrease in transcription. We therefore propose that this effect is due to tDAB2 interfering with the DNA-binding ability of MVI in the HeLaScribe lysate. This effect was observed in a concentration-dependent manner, consistent with our anisotropy data. The addition of 10 μM NDP52 did not decrease the transcription yield, suggesting that the tDAB2 effect is not due to sequestering MVI through binding to the protein. Moreover, no further decrease in transcription yield was found when tDAB2 was added following antibody depletion of MVI.

The compromised transcription activity that we observed following antibody depletion of MVI can be partially rescued through the addition of recombinant MVI (Fig. 4*d*). The addition of recombinant MVI and NDP52 together can restore transcription to $\sim 60\%$ (Fig. 4*d*), possibly because of the unfolding and dimerization of the protein. However, addition of recom-

Binding partner regulation of myosin VI

binant MVI and tDAB2 together failed to rescue the transcription yield, reinforcing that the observed effect is specific to DAB2, possibly through its interference with DNA binding. Taken together, our data suggest that DAB2 is a negative regulator of the transcription activity of MVI.

Effect of binding partner competition upon the nuclear functions of myosin VI

We have shown how two different binding partners can have contrasting effects on the biochemical properties and activity of MVI *in vitro*. On this basis, we then wanted to explore the impact of different binding partners on the cellular function of MVI and in particular its nuclear role in breast cancer cell line MCF-7. MVI is also distributed throughout the cell body, including the nucleus (Fig. 5a). In these cells, MVI has been already shown to be required for the expression of genes responsive to estrogen receptor (ER) signaling. When MCF-7 cells underwent siRNA knockdown of MVI or treatment with TIP, the small molecule inhibitor of MVI, there was a decrease in the expression of estrogen-activated *PS2* and *GREB1* (Fig. 5b). The impact of both treatments was similar, with a decrease of 70–80% for *PS2* and 30–40% for *GREB1*. Inhibition of MVI with TIP has already been shown to decrease the transcription yield *in vitro* (20). Based on our data, we can now suggest that the motor activity of MVI is required for ER signaling.

The genes that are under the control of the estrogen receptor relate, among others, to cell growth. Given the role of MVI in the expression of these genes, we then assessed the effect of MVI knockdown on MCF-7 growth (Fig. 5c). Indeed, the loss of MVI attenuates cell growth, which suggests there is a correlation between the role in gene expression and overall cell growth.

MCF-7 cells, along with many other estrogen receptor positive breast and ovarian cancer cell lines, have lost or attenuated DAB2 expression (Fig. S2a). Moreover, the reintroduction of DAB2 to these cell lines has been suggested to suppress tumorigenicity (17). Based upon the impact of MVI on the ER-driven gene expression and our *in vitro* data demonstrating the impact of DAB2 upon MVI associated transcription, we wished to explore whether reintroduction of DAB2 in MCF-7 could lead to a perturbation of the expression of ER target genes. To this end, we transiently expressed full-length DAB2–mRFP in MCF-7 cells (Fig. S2, a and b) and then monitored the expression of *PS2* and *GREB1*. Interestingly, the presence of DAB2 in MCF-7 resulted in a 20–30% decrease in the expression of these ER-target genes.

To confirm that this decrease is due to the targeting of MVI, we transiently expressed in MCF-7 two truncations of DAB2 (Fig. S2c): the DAB2_{649–770} region, which contains the MVI binding site and is the one used in our biochemical assays, and the DAB2_{1–648}, which cannot associate with MVI (12). As expected, the DAB2_{649–770} resulted in a 40–50% decrease in the expression of the two ER target genes, whereas the DAB2_{1–648} did not have any effect, confirming that the observed decrease in gene expression is indeed due to the interaction of DAB2 with MVI. Overall, our observations suggest that DAB2 can function in the cell as a negative regulator of MVI in the expression of ER-target genes.

Discussion

The structural regulation of MVI controls its biochemical properties and therefore directly impacts on the cellular function of this motor protein. Here, we have explored what is the impact of binding partners on the conformation of MVI, how these interactions are regulated, and how this regulation varies between isoforms. We have then investigated how the selectivity of MVI for its binding partner can affect its biochemical properties and intracellular functions.

The structural regulation of MVI seems to follow a single general mechanism, which is summarized by the following model: MVI exists as a folded monomer that interacts with binding partners through the CBD. These interactions lead to MVI unfolding and subsequent dimerization of the protein through its tail domain. As shown previously, this generates a processive motor protein (3).

Moreover, here we have shown that this widely applied mechanism of structural regulation is under the control of a finely tuned interplay between binding partners and the MVI isoforms. In the case of the LI isoform, structural studies have revealed how the RRL motif is blocked by the LI helix (18), allowing only the WWY partners, such as DAB2, to bind to MVI. We have confirmed this here biochemically, by measuring the binding partner interactions at each site, using DAB2 as a representative example. In contrast, the NI isoform, in which both the RRL and WWY motif are readily accessible, should be able to associate with any partner. We have therefore explored the mechanism underlying the partner selectivity in this case. We have revealed that the NI isoform can enact selectivity through the differential affinity between the two sites, with the RRL motif having stronger binding affinity over the WWY. In this way, the selectivity for binding partners is based upon the relative concentration of WWY *versus* RRL partners, although the overall cellular concentrations of DAB2 is unlikely to be in the micromolar range. However, it is possible for there to be local high-protein concentrations, which can generate micromolar concentrations within a defined volume. In these instances interactions between MVI and binding partners would be observed. Moreover, cellular interactions may be supported by additional protein/cargo factors, thereby increasing the affinity. There could also be a global change in protein expression levels. For instance, the loss of a WWY partner would perturb the dynamics leading to an enhanced role of RRL binding partners.

This mechanism of selectivity is particularly relevant for the regulation of nuclear MVI, which is the NI isoform (3). Here, we have demonstrated the impact of a concentration-driven interaction with the low-affinity binding partner DAB2. Indeed, interaction with DAB2 blocked the ability of MVI to bind DNA and subsequently its transcription activity *in vitro*.

The impact of DAB2 on the biochemical properties of MVI raised questions about its impact on the cellular functions of MVI. DAB2 has been proposed to function as a tumor suppressor; however, the underlying mechanism remains elusive. Here, we have proposed that at least part of this activity could relate to the down-regulation of nuclear MVI in transcription. Because nuclear MVI is linked to estrogen receptor gene expression, this would in turn attenuate the activity of the estrogen receptor,

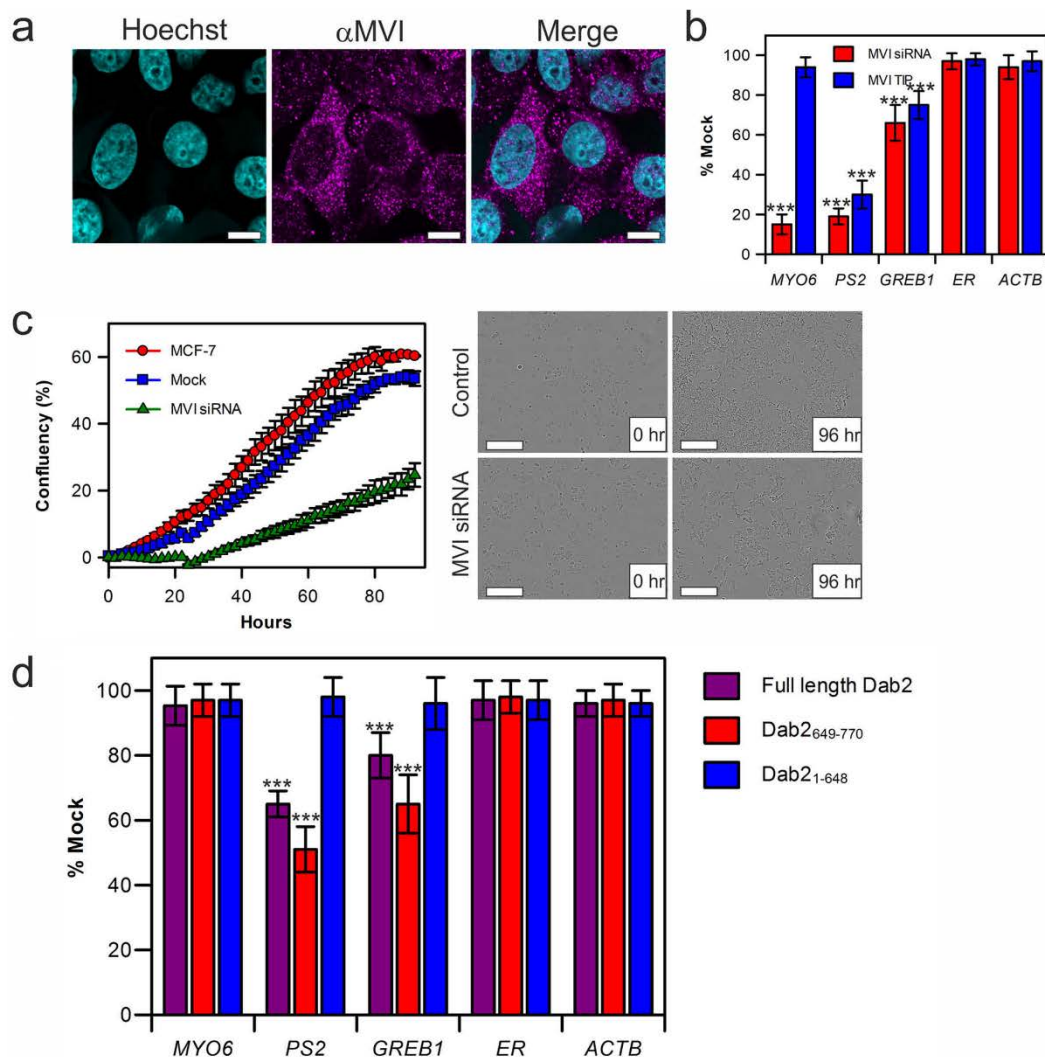


Figure 5. Inhibition of myosin VI in estrogen-linked gene expression. *a*, immunofluorescence staining against MVI (purple) combined with DNA staining (cyan) in MCF7 cells. Scale bar, 10 μ m in all images. *b*, expression of estrogen receptor gene targets following siRNA knockdown of MVI (red) or TIP treatment (blue) in MCF-7 cells. Expression is plotted as a percentage of expression in mock cells. *MYO6* reports on the success of the siRNA knockdown, whereas *ESR1* and *ACTB* were used to reflect global changes in transcription. *** represents a $p < 0.001$ by two-tailed *t* test. *c*, real-time growth of MCF-7 cells (red) and corresponding measurements following MVI siRNA knockdown (green) and mock transfection control (blue). The data represent three independent measurements, and error bars show S.E. Example images at start and end time points are shown. Scale bar, 300 μ m in all images. Western blot against DAB2 following transient transfection into MCF-7 cells is shown in Fig. S2*a*. *d*, Expression of estrogen receptor target genes following transient transfections of DAB2 (purple), DAB2₁₋₆₄₈ (blue), and DAB2₆₄₉₋₇₇₀ (red) in to MCF-7 cells. Expression is plotted as a percentage of expression in nontransfected cells. *MYO6*, *ESR1*, and *ACTB* were used to reflect global changes in transcription. (Error bars represent S.E. from three independent experiments. *** represents a $p < 0.001$ by two-tailed *t* test.).

subsequently leading to a decrease in tumorigenicity. Conversely, loss of a DAB2 would perturb the dynamics leading to an enhanced role of RRI binding partners, like NDP52 leading to enhanced MVI transcription activity. Cancer cell lines, such as the MCF-7, overexpress the NI isoform of MVI, which is the

one able to translocate to the nucleus, and they are therefore primed for transcriptional activity. This is further enhanced in MCF-7 cells by the loss of DAB2 expression, which relieves the DAB2-mediated negative regulation. Overall, this would lead to a high level of ER activity, which is MVI-dependent. Interest-

Binding partner regulation of myosin VI

ingly, reintroduction of DAB2 in these cells has an effect on their tumorigenic potential (17). In this study, we have confirmed that reintroduction of DAB2 perturbs the transcription landscape downstream the ER and revealed that this is due to MVI targeting. We therefore suggest that the down-regulation of the transcriptional activity of MVI is indeed part of the role of DAB2 as a tumor suppressor.

In summary, this study has allowed us to gain new insights into the regulation of MVI. The mechanism of selectivity of binding partners is isoform dependent. Although the LI-MVI employs a structural selection for its binding partners, the selectivity of the NI isoform is regulated by the relative expression levels of the partners. Finally, we provide an example of how the intracellular levels of MVI binding partners can modulate the cellular function of the protein. We propose that the tumor suppressor activity of DAB2 is, in part, related to the down-regulation of estrogen receptor target gene activation by nuclear MVI. These insights open new avenues for exploring how the activity of this multifunctional motor protein is regulated within the nucleus and the cytoplasm, as well.

Materials and methods

Constructs

Lists of constructs and PCR primers are provided in Tables S1 and S2, respectively. Constructs generated in this work are described below. The following human full-length myosin VI mutants (EGFP-C3-NI-MVI-RRL-AAA and EGFP-C3-NI-MVI-WWY-WLY) were a kind gift from F. Buss (Cambridge Institute for Medical Research). The full-length human DAB2-mRFP was isolated by PCR from pET28a-DAB2-RFP plasmid, restriction-digested with NheI and NotI, and cloned into the pZsGreen1-N1 backbone following removal of ZsGreen1. The human DAB2 truncations were generated by PCR isolation of the DAB2 fragment containing the myosin VI-binding site (aa 649–770) and the rest of DAB2 (aa 1–648), which does not contain the myosin VI-binding site from the above DAB2-mRFP plasmid. The PCRs were restriction-digested by XhoI and SacII and cloned into pEGFP-C3.

Protein expression and purification in *Escherichia coli*

Recombinant constructs were expressed in *E. coli* BL21 DE3 cells (Invitrogen) in Luria Bertani media. Proteins were purified by affinity chromatography (HisTrap FF; GE Healthcare). The purest fractions were further purified through a Superdex 200 16/600 column (GE Healthcare). Example gels are shown in Fig. S3.

Protein expression using Baculovirus system

Full-length myosin VI-NI and -LI and *Xenopus* calmodulin were expressed in *Sf9* and *Sf21* (*Spodoptera frugiperda*) insect cells using the Baculovirus expression system. *Sf9* cells were cultured in suspension in sf900 medium (Gibco) at 27 °C to generate the P1–3 recombinant baculovirus stocks. Finally, expression of recombinant proteins was set up by infecting *Sf21* cells with the P3 viral stock in ExCell 420 medium (Sigma). The cells were harvested by centrifugation (as above) for protein purification after 4 days. Prior to sonication, an additional 5 mg

of calmodulin was added with 2 mM DTT. After sonication, 5 mM ATP and 10 mM MgCl₂ were added, and the solution was rotated at 4 °C for 30 min before centrifugation (20,000 - *g* at 4 °C for 30 min). Then the cell lysate was subjected to the purification steps described above.

Protein labeling

Proteins were transferred into 50 mM sodium phosphate (pH 6.5) using a PD10 desalting column. The samples were then incubated with a 5-fold excess of dye for 4 h, rotating at 4 °C. Excess dye was removed using a PD10 desalting column pre-equilibrated with 50 mM sodium phosphate, 150 mM NaCl, and 1 mM DTT. Labeling efficiency was calculated based on the absorbance at 280 nm and the absorbance maximum of the dye. Typical efficiency was 90%, whereby the less than complete labeling was taken as an indicator for a single dye per protein. This was tested for isolated preparations in MS, which revealed both an unlabeled and single labeled population.

Cell culture and transfection

HeLa (ECACC 93021013) and MCF7 (ECACC 86012803) cells were cultured at 37 °C and 5% CO₂, in Gibco α -minimum Eagle's medium with GlutaMAX (no nucleosides), supplemented with 10% fetal bovine serum (Gibco), 100 units/ml penicillin, and 100 μ g/ml streptomycin (Gibco). For the transient expression of MVI isoforms and mutants, full-length DAB2, and truncations, HeLa cells and/or MCF7 cells grown on glass coverslips were transfected with EGFP-NI-MVI, EGFP-LI-MVI, EGFP-NI-MVI-RRL-AAA, EGFP-NI-MVI-WWY-WLY, DAB2-mRFP, EGFP-DAB2-1-648, and EGFP-DAB2-649-770 constructs using Lipofectamine 2000 (Invitrogen), following the manufacturer's instructions. Depending on the construct, 24–72 h after transfection, the cells were subjected to nuclear staining using Hoechst 33342 (Thermo Scientific), fixed, and analyzed or subjected to indirect immunofluorescence (see below).

Full-length DAB2-RFP cDNA was electroporated into MCF7 cells using Bio-Rad Gene Pulser Xcell™ electroporation system. After trypsinization, harvested cells were washed with 1 \times PBS and counted; 1.5 \times 10⁶ cells were resuspended in 800 μ l of cold Opti-MEM medium; and the cell suspension was kept on ice. 10 μ g of DNA was added to the cell suspension, and the mixture was transferred to the Bio-Rad 4-mm cuvette. The cells were then pulsed using exponential-decay protocol with a voltage of 300 V and a capacitance of 350 microfarads. The cells were allowed to recover for 5 min, after which warm complete medium (minimum Eagle's medium) was added to them, and they were plated in a 6-well plate at a density of 0.5 \times 10⁶ cells/well. The cells were collected for protein or RNA extraction after 48 h.

Immunofluorescence

Transfected and nontransfected HeLa or MCF-7 cells were fixed for 15 min at room temperature in 4% (w/v) paraformaldehyde, and residual paraformaldehyde was quenched for 15 min with 50 mM ammonium chloride. All subsequent steps were performed at room temperature. The cells were permeabilized and simultaneously blocked for 15 min with 0.1% (v/v)

Triton X-100 and 2% (w/v) BSA in PBS. The cells were then immunostained against the endogenous proteins by 1 h of incubation with the indicated primary and subsequently the appropriate fluorophore-conjugated secondary antibody (details below), both diluted in 2% (w/v) BSA in PBS. The following antibodies were used at the indicated dilutions: rabbit anti-MVI (1:200, Atlas–Sigma HPA0354863–100UL), mouse anti-DAB2 (1:100, Abcam ab88590), donkey anti-mouse Alexa Fluor 488–conjugated (1:500, Abcam Ab181289), donkey anti-mouse Alexa Fluor 555–conjugated (1:500, Abcam Ab150110), donkey anti-rabbit Alexa Fluor 488–conjugated antibody (1:500, Abcam Ab181346), and donkey anti-rabbit Alexa Fluor 555–conjugated antibody (1:500, Abcam Ab150074). Coverslips were mounted on microscope slides with Mowiol (10% (w/v) Mowiol 4–88, 25% (w/v) glycerol, 0.2 M Tris-HCl, pH 8.5), supplemented with 2.5% (w/v) of the anti-fading reagent DABCO (Sigma).

For colocalization analysis, 20 fields of view were recorded with 2–4 cells/field. We ensured that all cells were transfected within the field. Pearson's coefficients were obtained with the JACoP plugin (21) for ImageJ.

Immunoblot analysis

The total protein concentration was determined by Bradford assay (Sigma) following the manufacturer's instructions. Cell lysates were heat-denatured and resolved by SDS-PAGE. The membrane was probed against the endogenous proteins by incubation with mouse anti-DAB2 polyclonal antibody (1:1000, Abcam ab88590) and subsequently a goat anti-mouse antibody coupled to horseradish peroxidase (1:15,000, Abcam ab97023). The bands were visualized using the ECL Western blotting detection reagents (Invitrogen), and the images were taken using Syngene GBox system. Images were processed in ImageJ.

Fluorescence imaging

The cells were visualized using either the Zeiss LSM 880 confocal microscope or the wide-field Olympus IX71 microscope. The former was equipped with a Plan-Apochromat 63× 1.4 NA oil immersion lens (Carl Zeiss, 420782-9900-000). Three laser lines, *i.e.* 405, 488, and 561 nm, were used to excite the fluorophores, *i.e.* Hoechst, GFP, and RFP, respectively. The built-in dichroic mirrors (Carl Zeiss, MBS-405, MBS-488, and MBS-561) were used to reflect the excitation laser beams on to cell samples. The emission spectral bands for fluorescence collection were 410–524 nm (Hoechst), 493–578 nm (GFP) and 564–697 nm (RFP). The detectors consisted of two multianode photomultiplier tubes and one gallium arsenide phosphide detector. The green channel (GFP) was imaged using the gallium arsenide phosphide detector, whereas the blue (Hoechst) and red (RFP) channels were imaged using multianode photomultiplier tubes. ZEN software (Carl Zeiss, ZEN 2.3) was used to acquire and render the confocal images. The later was equipped with an PlanApo 100× OTIRFM-SP 1.49 NA lens mounted on a PIFOC *z* axis focus drive (Physik Instrumente, Karlsruhe, Germany), and illuminated with an automated 300W Xenon light source (Sutter, Novato, CA) with appropriate filters (Chroma, Bellows Falls, VT). The images were acquired using a QuantEM (Photometrics) EMCCD camera,

controlled by the Metamorph software (Molecular Devices). The whole volume of cells was imaged by acquiring images at *z*-steps of 200 nm. Wide-field images were deconvolved with the Huygens Essential version 17.10 software. Confocal images were deconvolved using the Zeiss Zen2.3 Blue software, using the regularized inverse filter method. All images were then analyzed by ImageJ.

IncuCyte

The cells were seeded onto 96-well tissue culture dishes at equal densities in six replicates. After attachment overnight, the cells were transfected with MVI siRNA. Photomicrographs were taken every hour using an IncuCyte live cell imager (Essen Biosciences, Ann Harbor, MI), and confluency of cultures was measured using IncuCyte software. Confluency values between wells were normalized to initial confluency for comparison.

RNA extraction and RT-qPCR

RNA from DAB2-RFP transfected or nontransfected MCF7 cells was extracted using Gene Jet RNA purification kit (Thermo scientific) according to the manufacturer's protocol. The RNA concentration was measured using a Geneflow nanophotometer and RT-qPCR was performed with one-step QuantiFast SYBR Green qPCR kit (Qiagen) using 50 ng of RNA in each sample. A list of qPCR primers is given in Table S3.

DNA substrates

DNA substrate ds40 consisted of labeled (TTAGTTGTTCTGTAGTGTCTCGTCTGGCTCTGGATTACCCGC*FAM) and unlabeled (GCGGGTAATCCAGAGCCAGACGAGCACTACGAACAATAA) oligonucleotides purchased from IDT. To form duplex DNA substrates, the oligonucleotides were mixed at equimolar concentrations at either 50 μ M in water or a buffer containing 50 mM Tris-HCl (pH 7.5), 150 mM NaCl, and 3 mM MgCl₂.

In vitro transcription

The DNA template was the pEGFP-C3 linearized plasmid containing the cytomegalovirus promoter, which would generate a 130-base run-off transcript. The HeLaScribe (Promega) reactions were performed in triplicate, through two independent experiments, according to the manufacturer's instructions. The reactions were performed for 60 min at 25 °C.

The reactions were also performed following preclearance with the MVI antibody. Protein G Dynabeads (Invitrogen) were prepared according to the manufacturer's instructions before being loaded with 4 μ g of antibody. The samples were incubated for 30 min on ice, and beads were extracted immediately before performing the transcription reaction. For quantification, mRNA was purified using a Gene Jet RNA purification kit (Thermo scientific) according to the manufacturer's protocol, and RT-qPCR was performed with a one-step QuantiFast SYBR Green qPCR kit (Qiagen).

Titration measurements

All reactions were performed at 25 °C in a buffer containing 50 mM Tris-HCl (pH 7.5), 150 mM sodium chloride, and 1

Binding partner regulation of myosin VI

mM DTT in a final volume of 100 μ l. Measurements were performed using a ClarioStar plate reader (BMG Labtech).

Intensity measurements were performed at the following wavelengths: FITC (excitation, 490 nm) and Alexa Fluor 555 (excitation, 555 nm). FITC to Alexa Fluor 555 FRET measurements were performed using the wavelength excitation of 470 nm and the emission of 575 nm. Anisotropy was measured with the instrument in the T format, allowing simultaneous acquisition of parallel (I_{\parallel}) and perpendicular (I) components using BMG filter sets for fluorescein (excitation, 482/16-10, Dichroic LP504; and emission, 530/-40).

Analysis of kinetic data

For fluorescence anisotropy titrations: Anisotropy was calculated, as described below, based upon established procedures (22–25).

Total fluorescence intensity (F_t) is given by the following.

$$F_t = \sum c_i F_i \quad (\text{Eq. 1})$$

Total anisotropy (A_t) is given by the following.

$$A_t = \frac{\sum c_i F_i A_i}{F_t} \quad (\text{Eq. 2})$$

where c_i is the concentration of species i , F_i is the fluorescence intensity per unit of concentration, and A_i is the anisotropy. This is calculated from the parallel and perpendicular fluorescence intensity (I) in relation to the plane of excitation by the following.

$$A_i = \frac{I_{\parallel} - I_{\perp}}{I_{\parallel} + 2I_{\perp}} \quad (\text{Eq. 3})$$

Because anisotropy is additive for multiple fluorescence species in solution, it is used to give a measure of their relative concentrations. For MVI (and various constructs) there are two fluorescence species: DNA and MVI-DNA. The total anisotropy can then be calculated in terms of the dissociation constant (K_d) for the MVI-DNA complex,

$$A_t = \frac{A_{\text{DNA}}([\text{DNA}]_t - [\text{MVI-DNA}]_t) + A_{\text{MVI-DNA}}Q[\text{MVI-DNA}]_t}{[\text{DNA}]_t - [\text{MVI-DNA}]_t + Q[\text{MVI-DNA}]_t} \quad (\text{Eq. 4})$$

where

$$[\text{MVI-DNA}]_t = \frac{([\text{MVI}]_t + [\text{DNA}]_t + K_d) - \sqrt{([\text{MVI}]_t + [\text{DNA}]_t + K_d)^2 - 4[\text{MVI}]_t[\text{DNA}]_t}}{2} \quad (\text{Eq. 5})$$

and where $[\text{MVI}]_t$ and $[\text{DNA}]_t$ are the total concentrations for each reactant. $[\text{MVI-DNA}]_t$ is the concentration of the protein-bound DNA complex. Q is the fluorescence intensity of MVI-DNA relative to DNA. The anisotropy data were fitted to obtain dissociation constants based on the above equations using GraFit fitting software (27).

For the FRET titrations, the 575-nm intensity data were corrected for the increase in intensity caused by a small direct excitation. This background signal was subtracted from the dataset to leave the FRET values. The titration curves for the MVI_{TAIL} interactions were fitting to a binding quadratic equation.

[Complex]

$$= \frac{([\text{FITC}]_t + [\text{AF555}]_t + K_d) - \sqrt{([\text{FITC}]_t + [\text{AF555}]_t + K_d)^2 - 4[\text{FITC}]_t[\text{AF555}]_t}}{2} \quad (\text{Eq. 6})$$

Data availability

The data supporting the findings of this study are available from the corresponding author on request.

Author contributions—N. F., Y. H.-G., B. Aston, and C. P. T. conceptualization; N. F., Y. H.-G., B. Aston, Á. d. S., R. E. G., and C. P. T. formal analysis; N. F., Y. H.-G., and C. P. T. supervision; N. F., Y. H.-G., and C. P. T. funding acquisition; N. F., Y. H.-G., B. Aston, Á. d. S., R. E. G., B. Alamad, L. W., and C. P. T. investigation; N. F., Y. H.-G., and C. P. T. writing-original draft; N. F., Y. H.-G., B. Aston, and C. P. T. writing-review and editing; L. W., M. L. M.-F., and C. P. T. resources.

Acknowledgments—We thank Darren Griffin and Anastasios Tsaousis for sharing of equipment.

References

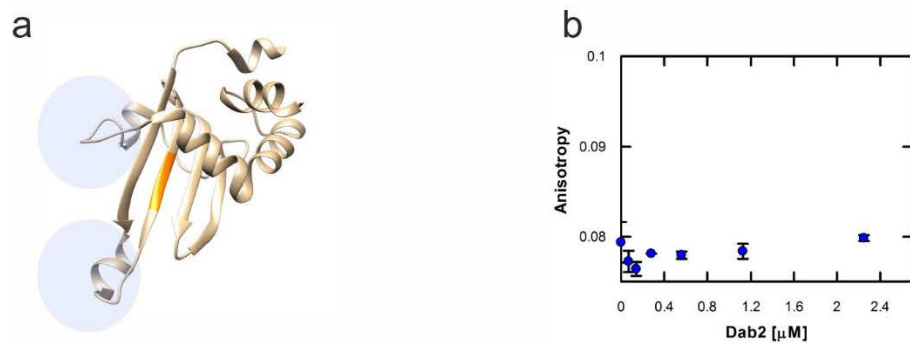
- Roberts, R., Lister, I., Schmitz, S., Walker, M., Veigel, C., Trinick, J., Buss, F., and Kendrick-Jones, J. (2004) Myosin VI: cellular functions and motor properties. *Philos. Trans. R. Soc. Lond. B Biol. Sci.* **359**, 1931–1944 CrossRef Medline
- Vreugde, S., Ferrai, C., Miluzio, A., Hauben, E., Marchisio, P. C., Crippa, M. P., Bussi, M., and Biffo, S. (2006) Nuclear myosin VI enhances RNA polymerase II-dependent transcription. *Mol. Cell* **23**, 749–755 CrossRef Medline
- Fili, N., Hari-Gupta, Y., Dos Santos, Á., Cook, A., Poland, S., Ameer-Beg, S. M., Parsons, M., and Toseland, C. P. (2017) NDP52 activates nuclear myosin VI to enhance RNA polymerase II transcription. *Nat. Commun.* **8**, 1871 CrossRef Medline
- Avraham, K. B., Hasson, T., Steel, K. P., Kingsley, D. M., Russell, L. B., Mooseker, M. S., Copeland, N. G., and Jenkins, N. A. (1995) The mouse Snell's waltzer deafness gene encodes an unconventional myosin required for structural integrity of inner ear hair cells. *Nat. Genet.* **11**, 369–375 CrossRef Medline
- Dunn, T. A., Chen, S., Faith, D. A., Hicks, J. L., Platz, E. A., Chen, Y., Ewing, C. M., Sauvageot, J., Isaacs, W. B., De Marzo, A. M., and Luo, J. (2006) A novel role of myosin VI in human prostate cancer. *Am. J. Pathol.* **169**, 1843–1854 CrossRef Medline
- Mohiddin, S. A., Ahmed, Z. M., Griffith, A. J., Tripodi, D., Friedman, T. B., Fananapazir, L., and Morell, R. J. (2004) Novel association of hypertrophic cardiomyopathy, sensorineural deafness, and a mutation in unconventional myosin VI (MYO6). *J. Med. Genet.* **41**, 309–314 CrossRef Medline
- Yoshida, H., Cheng, W., Hung, J., Montell, D., Geisbrecht, E., Rosen, D., Liu, J., and Naora, H. (2004) Lessons from border cell migration in the *Drosophila* ovary: a role for myosin VI in dissemination of human ovarian cancer. *Proc. Natl. Acad. Sci. U.S.A.* **101**, 8144–8149 CrossRef Medline
- Buss, F., Arden, S. D., Lindsay, M., Luzio, J. P., and Kendrick-Jones, J. (2001) Myosin VI isoform localized to clathrin-coated vesicles with a role in clathrin-mediated endocytosis. *EMBO J.* **20**, 3676–3684 CrossRef Medline
- Au, J. S., Puri, C., Ihrke, G., Kendrick-Jones, J., and Buss, F. (2007) Myosin VI is required for sorting of AP-1B-dependent cargo to the basolateral

- domain in polarized MDCK cells. *J. Cell Biol.* **177**, 103–114 [CrossRef](#) [Medline](#)
10. Morriswood, B., Ryzhakov, G., Puri, C., Arden, S. D., Roberts, R., Dendrou, C., Kendrick-Jones, J., and Buss, F. (2007) T6BP and NDP52 are myosin VI binding partners with potential roles in cytokine signalling and cell adhesion. *J. Cell Sci.* **120**, 2574–2585 [CrossRef](#) [Medline](#)
 11. Naccache, S. N., Hasson, T., and Horowitz, A. (2006) Binding of internalized receptors to the PDZ domain of GIPC/synectin recruits myosin VI to endocytic vesicles. *Proc. Natl. Acad. Sci. U.S.A.* **103**, 12735–12740 [CrossRef](#) [Medline](#)
 12. Spudich, G., Chibalina, M. V., Au, J. S., Arden, S. D., Buss, F., and Kendrick-Jones, J. (2007) Myosin VI targeting to clathrin-coated structures and dimerization is mediated by binding to Disabled-2 and PtdIns(4,5)P₂. *Nat. Cell Biol.* **9**, 176–183 [CrossRef](#) [Medline](#)
 13. Koriath, F., Gieffers, C., Maul, G. G., and Frey, J. (1995) Molecular characterization of NDP52, a novel protein of the nuclear domain 10, which is redistributed upon virus infection and interferon treatment. *J. Cell Biol.* **130**, 1–13 [CrossRef](#) [Medline](#)
 14. Sternsdorf, T., Jensen, K., Züchner, D., and Will, H. (1997) Cellular localization, expression, and structure of the nuclear dot protein 52. *J. Cell Biol.* **138**, 435–448 [CrossRef](#) [Medline](#)
 15. Mostowy, S., Sancho-Shimizu, V., Hamon, M. A., Simeone, R., Brosch, R., Johansen, T., and Cossart, P. (2011) p62 and NDP52 proteins target intracytosolic Shigella and Listeria to different autophagy pathways. *J. Biol. Chem.* **286**, 26987–26995 [CrossRef](#) [Medline](#)
 16. Yang, C. K., Kim, J. H., and Stallcup, M. R. (2006) Role of the N-terminal activation domain of the coiled-coil coactivator in mediating transcriptional activation by β -catenin. *Mol. Endocrinol.* **20**, 3251–3262 [CrossRef](#) [Medline](#)
 17. He, J., Smith, E. R., and Xu, X. X. (2001) Disabled-2 exerts its tumor suppressor activity by uncoupling c-Fos expression and MAP kinase activation. *J. Biol. Chem.* **276**, 26814–26818 [CrossRef](#) [Medline](#)
 18. Wollscheid, H. P., Biancospino, M., He, F., Magistrati, E., Molteni, E., Lupia, M., Soffientini, P., Rottner, K., Cavallaro, U., Pozzoli, U., Mapelli, M., Walters, K. J., and Polo, S. (2016) Diverse functions of myosin VI elucidated by an isoform-specific α -helix domain. *Nat. Struct. Mol. Biol.* **23**, 300–308 [CrossRef](#) [Medline](#)
 19. Puri, C., Chibalina, M. V., Arden, S. D., Kruppa, A. J., Kendrick-Jones, J., and Buss, F. (2010) Overexpression of myosin VI in prostate cancer cells enhances PSA and VEGF secretion, but has no effect on endocytosis. *Oncogene* **29**, 188–200 [CrossRef](#) [Medline](#)
 20. Cook, A., Hari-Gupta, Y., and Toseland, C. P. (2018) Application of the SSB biosensor to study in vitro transcription. *Biochem. Biophys. Res. Commun.* **496**, 820–825 [CrossRef](#) [Medline](#)
 21. Bolte, S., and Cordelières, F. P. (2006) A guided tour into subcellular colocalization analysis in light microscopy. *J. Microsc.* **224**, 213–232 [CrossRef](#) [Medline](#)
 22. Brownbridge, G. G., Lowe, P. N., Moore, K. J., Skinner, R. H., and Webb, M. R. (1993) Interaction of GTPase activating proteins (GAPs) with p21ras measured by a novel fluorescence anisotropy method. Essential role of Arg-903 of GAP in activation of GTP hydrolysis on p21ras. *J. Biol. Chem.* **268**, 10914–10919 [Medline](#)
 23. Soh, Y. M., Bürmann, F., Shin, H. C., Oda, T., Jin, K. S., Toseland, C. P., Kim, C., Lee, H., Kim, S. J., Kong, M. S., Durand-Diebold, M. L., Kim, Y. G., Kim, H. M., Lee, N. K., Sato, M., *et al.* (2015) Molecular basis for SMC rod formation and its dissolution upon DNA binding. *Mol. Cell* **57**, 290–303 [CrossRef](#) [Medline](#)
 24. Toseland, C. P. (2014) Fluorescence to study the ATPase mechanism of motor proteins. *Exs* **105**, 67–86 [Medline](#)
 25. Toseland, C. P., and Geeves, M. A. (2014) Rapid reaction kinetic techniques. *Exs* **105**, 49–65 [Medline](#)
 26. Postma, M., and Goedhart, J. (2019) PlotsOfData: a web app for visualizing data together with their summaries. *PLoS Biol.* **17**, e3000202 [CrossRef](#) [Medline](#)
 27. Leatherbarrow, R. J. (2001) *GrafFit*, version 5, EriThacus Software Ltd, Hordley, UK

4.2.2.1. Supplementary Material for Manuscript 4

SUPPLEMENTARY INFORMATION

SUPPLEMENTARY FIGURES

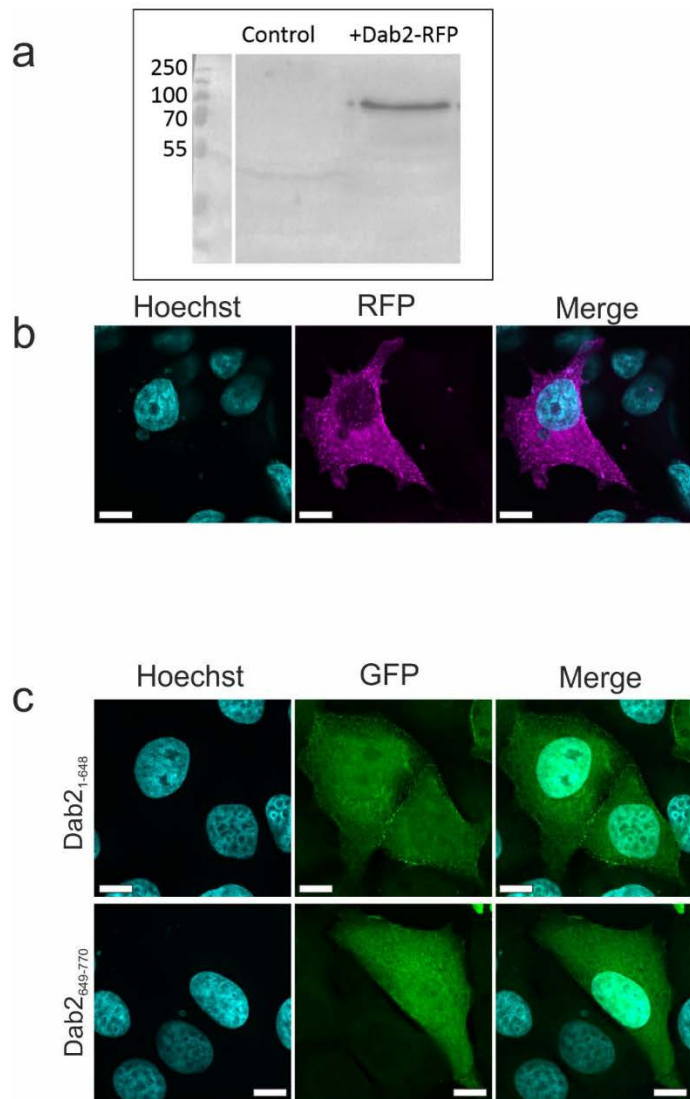


Supplementary Figure 1 Characterisation of Dab2 DNA binding.

(a) Structure of the C-terminal CBD with DNA binding sites highlighted (blue circles).

The WWY motif which binds Dab2 is shown in orange. (PDB:2KIA(27)).

(b) Fluorescence anisotropy titrations of Dab2 against a 40 bp fluorescein amidite (FAM)-DNA (50 nM). Data fitting was performed as described in Methods (K_d +/- SEM $n = 3$ independent experiments).

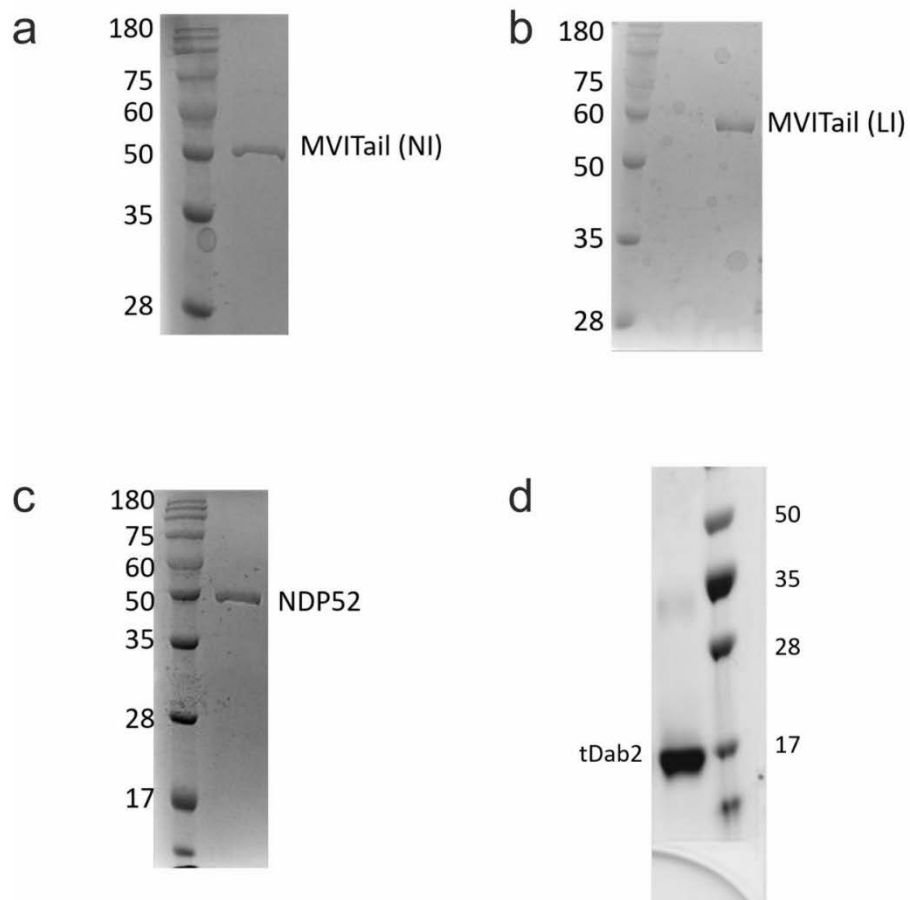


Supplementary Figure 2 Transfection of Dab2 in MCF-7 cells.

(a) Western Blot against Dab2 in MCF-7 cells (Control) and MCF-7 cells transiently transfected with Dab2-RFP.

(b) Representative images of transiently expressed Dab2-RFP in MCF-7 cells combined with DNA staining (Cyan).

(c) Representative images of transiently expressed GFP-Dab2₁₋₆₄₈ and GFP-Dab2₆₄₉₋₇₇₀ in MCF-7 cells combined with DNA staining (Cyan). Scale bar 10 μm in all images.



Supplementary Figure 3 Example gels for recombinant proteins.

These gels represent examples of the recombinant proteins used in the binding studies in Fig1, 3, 4 and Supplementary Fig. 1.(a) MVITail(NI). (b) MVITail(LI). (c) NDP52. (d) tDab2

Supplementary Table 1. Recombinant DNA.

Construct (Residue numbers)	Source
Human pEGFP-C3 myosin VI (large insert) (1-1284)	F. Buss (CIMR)
Human pEGFP-C3 myosin VI (non insert) (1-1253)	F. Buss (CIMR)
Human pFastBacHTB GFP NI myosin VI	F. Buss (CIMR)
Human pFastBacHTB GFP LI myosin VI	F. Buss (CIMR)
Xenopus pFastBac1 Calmodulin (1-end)	J. Sellers (NIH)
Human pET151 NDP52 (1-end)	Ref Fili et al 2017
Human pET151 MVI _{TAIL} 814-1253	Ref Fili et al 2017
Human pET28 CBD 1060-1253	Ref Fili et al 2017
Human pET28 MVI _{TAIL} (large insert) (814-1284)	Ref Fili et al 2017
Human pFastbachHTB NI MVI (1-1253)	Ref Fili et al 2017
Xenopus pET28 Calmodulin	Ref Fili et al 2017
Human pET151 Dab2 (649-770)	Synthetic Gene – This Study
Human pZsGreen1 backbone Dab2 RFP	This Study
Human pEGFP-C3 myosin VI (non insert) WWY-WLY	This Study
Human pEGFP-C3 myosin VI (non insert) RRL-AAA	This Study
Human pEGFP-C3 Dab2 (1-648)	This Study
Human pEGFP-C3 Dab2 (649-770)	This Study
Human pET28 Dab2 RFP	F. Buss (CIMR)

Supplementary Table 2. PCR Primers.

Sequence	Use
CTTGCAGAGAAGAATTCATGCGGCAGCAAAAGTGTAT	RRL/AAA For
GATTTCCAAGCATGATACACTTTTGCTGCCGCATGAAAT	RRL/AAA Rev
CCCTCAGAGTAAGAAAAAAGGCTGGTTGTATGCCCAT	WWY/WLY For
GGTCCATCAAAATGGGCATACAACCAGCCTTTTTCTTA	WWY/WLY Rev
AGCTAGCATGTCTAACGAAGTAGAAACAAGTGC	Dab2 RFP For
TTTTGCGGCCGCTTAGGCAAAAGGATTTCCAAATGG	Dab2 RFP Rev
AAAACCTCGAGATGTCTAACGAAGTAGAAACAAGTGC	pEGFP-C3 Dab2 (1-648) For
AAAACCGCGGTTAGATCTCTTTATCCCCAAGTGGG	pEGFP-C3 Dab2 (1-648) Rev
AAAACCTCGAGAAGGATGTGAAAGAAATGTTTAAGG	pEGFP-C3 Dab2 (649-770) For
AAAACCGCGGTTAGGCAAAAGGATTTCCAAATGG	pEGFP-C3 Dab2 (649-770) Rev

Supplementary Table 3. Primers for qPCR.

Sequence	Use
CATGGAGAACAAGGTGATCTG	TFF1/PS2 qPCR For
CACTGTACACGTCTCTGTCTG	TFF1/PS2 qPCR Rev
ATGGGAAATTCTTACGCTGGAC	GREB1 qPCR For
CACTCGGCTACCACCTTCT	GREB1 qPCR Rev
AGAGCTACGAGCTGCCTGAC	Human B-Actin qPCR For
AGCACTGTGTTGGCGTACAG	Human B-Actin qPCR Rev
AAGCTTCGATGATGGGCTTA	ESR1 qPCR For
AGGTGGACCTGATCATGGAG	ESR1 qPCR Rev
CCGAGCTCATCAGTGATGAGGC	Myosin VI qPCR For
CCAAGCATGATACACTTTTAGTCTCC	Myosin VI qPCR Rev
AAGGGCATCGACTTCAAGGA	CMV GFP RT-qPCR For In vitro Transcription
GGCGGATCTTGAAGTTCACC	CMV GFP RT-qPCR Rev In vitro Transcription

4.2.3. Manuscript 5 – Binding Partners Regulate Unfolding of Myosin VI to Activate the Molecular Motor

Binding partners regulate unfolding of myosin VI to activate the molecular motor

Ália dos Santos^{1#}, Natalia Fili^{1#%}, Yukti Hari-Gupta^{2§}, Rosemarie E. Gough¹, Lin Wang³, Marisa Martin-Fernandez³, Jesse Aaron⁴, Eric Wait⁴, Teng-Leong Chew⁴ and Christopher P. Toseland^{1*}

¹Department of Oncology and Metabolism, University of Sheffield, Sheffield, S10 2RX, UK.

²School of Biosciences, University of Kent, Canterbury, CT2 7NJ, UK.

³Central Laser Facility, Research Complex at Harwell, Science and Technology Facilities Council, Rutherford Appleton Laboratory, Harwell, Didcot, Oxford OX11 0QX, UK.

⁴Advanced Imaging Center, HHMI Janelia Research Campus, Ashburn, USA.

[§]Current address: MRC LMCB, University College London, Gower Street, London, WC1E 6BT, UK.

[%]Current address: School of Life Sciences, University of Lincoln, Lincoln, LN6 7DL, UK.

[#] Equal contribution.

***Corresponding Author:** Department of Oncology and Metabolism, University of Sheffield, Sheffield, S10 2RX, UK c.toseland@sheffield.ac.uk

Key Words: Myosin VI, Dab2, NDP52, molecular motor

ABSTRACT

Myosin VI is the only minus-end actin motor and is coupled to various cellular processes ranging from endocytosis to transcription. This multi-potent nature is achieved through alternative isoform splicing and interactions with a network of binding partners. There is a complex interplay between isoforms and binding partners to regulate myosin VI. Here, we have compared the regulation of two myosin VI splice isoforms by two different binding partners. By combining biochemical and single-molecule approaches, we propose that myosin VI regulation follows a generic mechanism, independently of the spliced isoform and the binding partner involved. We describe how myosin VI adopts an autoinhibited backfolded state which is released by binding partners. This unfolding activates the motor, enhances actin binding and can subsequently trigger dimerization. We have further expanded our study by using single molecule imaging to investigate the impact of binding partners upon myosin VI molecular organisation and dynamics.

INTRODUCTION

Myosins are actin-based molecular motors which perform vital roles in numerous of cellular processes [1]. Myosin VI (MVI) is associated with several cellular functions, ranging from endocytosis to transcription [2-9]. MVI is unique, in that it is the only member of the myosin family with the ability to move towards the minus end of actin filaments [10] and its functional diversity relies on its association with various binding partners [11, 12].

MVI is comprised of a motor domain, followed by a neck region consisting of a unique insert, which confers the reverse directionality, and an IQ domain (Figure 1A). Both of these domains bind calmodulin. The N-terminal tail domain contains three structural domains: a three-helix-bundle (amino acids 835-916)[13], a single-alpha-helix (amino acids 942-978), followed by a short coiled-coil [14]. The C-terminal tail domain consists of the globular cargo binding domain (CBD 1060-end). In addition, two regions within the tail can be alternatively spliced resulting in a 31-residue insertion (large-insert, LI) proximal to the CBD, and/or an 9-residue insertion within the CBD (small-insert, SI). This leads to four splice isoforms, the non-insert (NI), SI, LI and LI+SI [15], each with distinct intracellular distributions and functions [15, 16]. For example, the MVI-NI isoform is able to enter the nucleus, whereas the MVI-LI is confined to the cell periphery [4].

The CBD domain enables interactions with several binding partners which control the intracellular localisation and function of MVI [1]. This diverse list of partners includes disabled-2 (Dab2) and nuclear dot protein 52 (NDP52). These partners predominantly bind to one of the two established motifs within the CBD of MVI, the WWY and RRL, respectively [8, 17, 18]. However, interactions occur over wider regions. Binding partner selectivity is driven by isoform splicing, whereby the MVI-LI encodes an alpha helix which occludes the RRL motif [19]. This prevents partners, such as NDP52, from interacting with the protein, and therefore interactions for this isoform can be driven by the WWY motif. In contrast, in the MVI-NI isoform, both motifs are available for binding. However, the RRL site can display higher affinity for partners over the WWY motif, in order to select for those interactions [6]. We have previously revealed that MVI-NI can adopt a back-folded conformation, in which the CBD is brought into close proximity to the motor domain [4, 20, 21]. NDP52 then interacts through the RRL binding motif, which leads to unfolding and subsequent dimerization of MVI through an internal dimerization site.

Several questions remain unanswered: It is unknown if the structurally distinct MVI-LI isoform is regulated in the same manner, or whether the WWY site can trigger the same structural rearrangements in MVI. Do binding partners enable unfolding of MVI or stabilise an open conformation? How do micromolar protein affinities regulate MVI in the cell? Lastly, how does the release of backfolding regulate motor activity?

To this end, we have now expanded our studies to assess whether this mechanism applies generally to MVI, independent of partner and isoform preference. We have also further explored the molecular basis for this mechanism, and investigated the cellular organisation and dynamics with respect to binding partners. Overall, we present a detailed generic model governing the activation of MVI from an inactive back-folded state to an active motor capable of actin binding and dimerization.

RESULTS

Myosin VI back-folding is independent of isoform

We have previously shown that the MVI-NI isoform is back-folded *in vitro* and in cells [4]. To address whether back-folding is a generic feature of MVI, independent of the isoform, we investigated the conformation of MVI-LI. We utilised a previously employed FRET-based assay [4, 6, 22] by titrating Alexa555-CBD against FITC-

MVI₈₁₄₋₁₀₉₁ (containing the LI) to assess whether there is an interaction between the N- and C-terminal tail domains, as would occur in a back-folded state. A significant concentration-dependent change in FRET was measured, indicating that the two domains are in close proximity (Figure 1B). The same was observed for the MVI-NI isoform MVI₈₁₄₋₁₀₆₀ (Figure 1C), consistent with previous results [4]. The calculated equilibrium dissociation constants (K_d) corresponding to these data were 5.98 (+/- 0.58) μ M and 4.8 (+/- 0.61) μ M for MVI-LI- and MVI-NI, respectively. These are relatively low micromolar affinities, suggesting the interactions are likely to be dynamic.

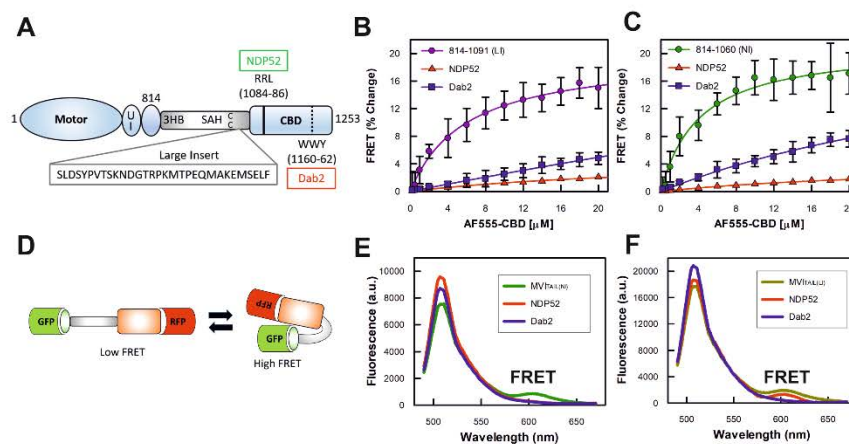


Figure 1: Backfolding of the myosin VI tail

(A) Cartoon depiction of the key regions of MVI, as discussed in the text. UI Unique Insert; 3HB Three Helix Bundle; SAH Stable Alpha Helix; CC Coiled-coil; CBD Cargo Binding Domain. This highlights position of the large insert (LI), along with NDP52 and Dab2 binding sites. (B) FRET titration of Alexa555-CBD against 1 μ M of FITC-MVI_{TAIL(LI)}, large insert (LI) containing MVI_{TAIL} (residues 814-1091), in the presence of NDP52 or tDab2, at 10 μ M. (C) FRET titration of Alexa555-CBD against 1 μ M of FITC-MVI_{TAIL(NI)} non-insert (NI) MVI_{TAIL} (residues 814-1060), in the presence of NDP52 or tDab2, at 10 μ M. All titration data fitting was performed as described in Methods (error bars represent SEM from three independent experiments). (D) Schematic representation of FRET assay to measure backfolding of the MVI_{TAIL}. (E) Representative fluorescence spectra of 1 μ M GFP-MVI_{TAIL(NI)}-RFP +/- 5 μ M NDP52, or 20 μ M tDab2. (F) Representative fluorescence spectra of 1 μ M GFP-MVI_{TAIL(LI)}-RFP (right) +/- 5 μ M NDP52, or tDab2.

Binding partners regulate back-folded myosin VI.

We have previously shown [4] that unfolding of the MVI-NI tail is directly driven by NDP52 following its interaction with the RRL motif and not through Calcium-

Calmodulin interactions, as proposed by a different study [20], and we have previously addressed this discrepancy [4]. To address whether regulation of backfolding by binding partners is a generic mechanism, we followed a similar approach for both MVI-LI and MVI-NI isoforms, but now focusing upon the WWY partner of MVI, Dab2. Due to the instability of recombinant full-length Dab2, we used a recombinant C-terminal truncation of the protein (residues 649-770), which contains the MVI binding site [8], as performed previously [6]. This truncation of Dab2 will be referred to as tDab2 throughout the manuscript. To assess whether Dab2 can regulate back-folding, the FRET assay between the CBD and the MVI₈₁₄₋₁₀₉₁ (LI) or the MVI₈₁₄₋₁₀₆₀ (NI) tail was repeated following pre-incubation of the CBD with an excess of tDab2. As with NDP52, tDab2 sequestered the CBD, preventing the interaction between the two domains (Figures 1B and 1C), suggesting that Dab2 is also able to disrupt the intramolecular back-folding in both isoforms. However, tDab2 was not as efficient as NDP52, which is consistent with its weaker affinity for MVI [6].

To further confirm the direct effect of binding partners upon MVI unfolding, we used the FRET-based MVI tail conformation reporter, which we have previously developed [4]. Our reporter was based on a GFP-RFP FRET pair with the MVI_{TAIL(NI)} or MVI_{TAIL(LI)}, placed in the middle (Figure 1D). As shown by the fluorescent spectra, a high FRET population was observed with both of these reporters, supporting the conclusion that the tails of both isoforms have the ability to back-fold (Figure 1E and 1F). The addition of 5 μ M NDP52 to the MVI_{TAIL(NI)} FRET reporter, resulted in loss of the high FRET population. Similarly, 5 μ M tDab2 was able to deplete the FRET population of the MVI_{TAIL(LI)}. However, 20 μ M of tDab2 were required to induce an equivalent effect on MVI_{TAIL(NI)}, given its low affinity for this tail [6]. Also as expected, NDP52 induced little, if any, loss of the high FRET population of the MVI_{TAIL(LI)} reporter, given that the RRL site is masked by the LI [19].

Altogether, these data demonstrate that the intramolecular backfolding of MVI is not isoform specific, but rather an intrinsic feature of the protein. Moreover, binding partners interacting at either motif can regulate this backfolding by triggering the unfolding step.

Binding partners associate to back-folded myosin VI and trigger unfolding.

Stopped-flow transient kinetics were then employed to further explore the role of binding partner interactions during the unfolding process. In particular, we endeavoured to determine whether binding partners first interact with the backfolded MVI triggering its unfolding, or whether they bind to spontaneously unfolded MVI stabilising the conformation. Given that both MVI isoforms showed the same response for either binding partner tested, further experiments only focused upon the NI isoform and NDP52.

First, FITC-MVI_{TAIL(NI)} and AF555-NDP52 were used as a FRET pair to report upon the interaction. 1 μM FITC-MVI_{TAIL(NI)} was mixed with excess AF555-NDP52 under pseudo-first order conditions (Figure 2A). The fluorescence traces were characterised by two phases: an increase in FRET signal, followed by a partial decrease (Figure 2B). The first phase was fitted to a signal exponential function (Figure 2C) and the observed rate constant was found to be dependent on the concentration of NDP52 (Figure 2D). We extracted an association rate constant of $1.72 \mu\text{M}^{-1} \text{s}^{-1}$ and dissociation rate constant of 3.3s^{-1} , giving a K_d of $1.9 \mu\text{M}$. This is consistent with the Equilibrium Dissociation constant previously derived from titrations [6]. The second phase in all three traces was also fitted to a single exponential function (Figure 2C), however the derived rate constants (average 2.1s^{-1}) were independent of NDP52 concentration (Figure 2D). This indicates that the second phase corresponds to a first order process, such as a conformation change. We therefore propose that these biphasic traces directly report upon a two-step process: first, binding of the partner onto backfolded MVI, corresponding to the initial increase in FRET, and second, the subsequent unfolding of the myosin, corresponding to the consequent decrease in FRET due to a greater distance between the donor-acceptor dyes (Figure 2E). This suggests that direct binding of the unfolded MVI is unlikely to occur.

To further understand this partner-induced conformation change, we used fluorescently labelled calmodulin bound to the MVI_{TAIL(NI)} as an environmental reporter. This approach would enable the probe to report upon either the partner binding step or the MVI unfolding step, or both processes (Figure 2F and G). Cy3B-calmodulin was pre-mixed with MVI_{TAIL(NI)} in a 2:1 molar excess. 1 μM Cy3B-calmodulin MVI_{TAIL(NI)} was then mixed against an excess of non-fluorescent NDP52, under pseudo-first order

conditions. A single exponential decrease in fluorescence was observed for all concentrations tested (Figure 2F), suggesting a single step process, which does not arise solely due to Cy3B-calmodulin reacting to NDP52 (Supplementary Figure 1). Interestingly, the derived rate constants (2 s^{-1}) were independent of NDP52 concentration (Figure 2H) and were identical to the rate of constants of the second exponential phase observed in the AF555-NDP52 experiments (Figure 2D). We therefore propose that the Cy3B-calmodulin probe reports upon unfolding. This is not unanticipated because unfolding would lead to the largest local environmental change for the dye, as the partner itself binds to the CBD not the neck region. These observations are consistent with the partners not binding to a spontaneously unfolded MVI but rather to its backfolded conformation, which then triggers the unfolding of the protein (Figure 2E).

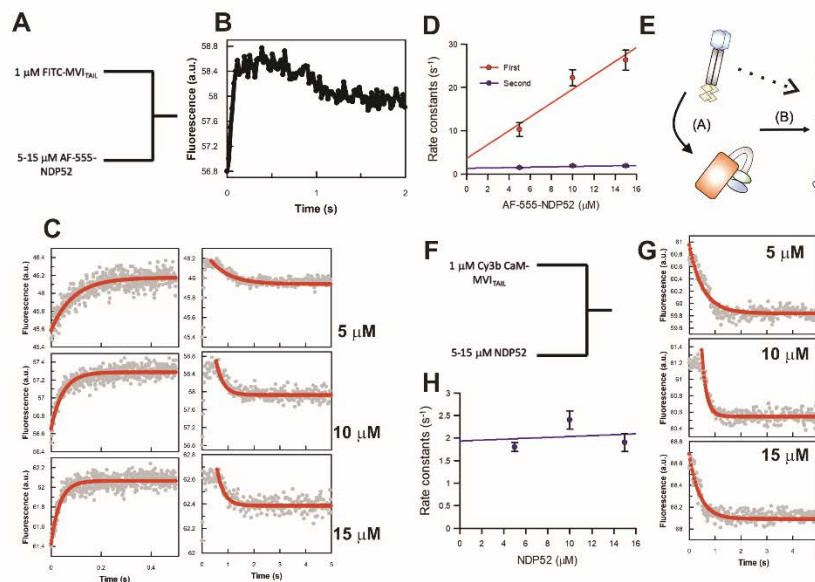


Figure 2: NDP52 association kinetics with the myosin VI tail.

(A) Schematic of the experiments for rapid mixing of the FITC labelled MVI_{TAIL} and Alexa-Fluor555 labelled NDP52. Experiments were performed as described in the methods. (B) Representative stopped-flow fluorescence trace depicting both changes in FRET signal, as described in the text. (C) Representative stopped-flow fluorescence traces and exponential fitting to both transitions when the FITC- MVI_{TAIL} is mixed with the stated concentrations of NDP52. (D) The individual traces were fitted to single exponentials and the dependence of the rate constants on concentration was then fitted to a straight line, as shown. The points shown are averages of at least 3

7

measurements, where error bars represent SEM. The fit for the first phase gives a slope of $1.72 \mu\text{M}^{-1} \text{s}^{-1}$ and an intercept of 3.3s^{-1} . The second phase is independent of NDP52 concentration and gives an average rate constant of 2.1s^{-1} . (E) Cartoon depicting the two processes reported by the stopped-flow experiments. Step A represents NDP52 binding to the MVI_{TAIL} , which is dependent upon NDP52 concentration. Step B represents the subsequent unfolding of MVI with a rate constant of 2.1s^{-1} , which is independent of NDP52 concentration. The dotted line represents an alternative model where NDP52 would bind to spontaneously unfolding MVI_{TAIL} . (F) Schematic of the experiments for rapid mixing of $1 \mu\text{M}$ Cy3B-calmodulin-bound $\text{MVI}_{\text{TAIL(NI)}}$ (pre-mix molar ratio 2:1) and unlabelled NDP52. Experiments were performed as described in the methods. (G) Representative stopped-flow fluorescence traces and exponential fitting to the fluorescence decrease when Cy3B-calmodulin $\text{MVI}_{\text{TAIL(NI)}}$ is mixed with the stated concentrations of NDP52. (H) The individual traces were fitted to single exponentials and the dependence of the rate constants on NDP52 concentration was then fitted to a straight line, as shown. The points shown are averages of at least 3 measurements, where error bars represent SEM. The rate constants are independent of NDP52 concentration, with an average value of 2s^{-1} .

Myosin VI dimerization is an intrinsic property.

Unfolding of the NI isoform subsequently exposes dimerization sites, leading to protein oligomerization [4], similar to the LI isoform with binding partners [6]. There is a debate as to whether MVI dimerizes intrinsically or through a binding partner mediator [4, 13, 23-25]. We have previously reported that a tail region ahead of the CBD (Figure 3A) of MVI can dimerize independently of binding partners, but we also suggested that this region is blocked until interactions with binding partners occur [4].

NDP52 is a dimeric protein (Figure 3B) and therefore capable of dimerizing MVI with one CBD bound to each monomer. However, tDab2, which also has been previously shown to be able to dimerize MVI [6], is monomeric (Figure 3B). This finding reinforces our previous conclusion that dimerization is an intrinsic property of MVI. This allowed us to estimate that the complex would consist of one binding partner (monomer or dimer) per MVI molecule. For example, we would expect 4 NDP52 molecules (or 2 NDP52 dimers) in complex with 2 MVI proteins.

To explore this hypothesis, we performed ATPase measurements on two MVI constructs, namely MVI_{1-814} and MVI_{1-1060} , with the latter lacking the CBD and therefore having the proposed dimerization region exposed (Figure 3C). The ATPase rates for MVI_{1-814} ($k_{\text{cat}} 4.4 \text{s}^{-1}$) were similar to full-length MVI ($k_{\text{cat}} 4.1 \text{s}^{-1}$), while MVI_{1-1060} displayed a lower ATPase rate ($k_{\text{cat}} 2.79 \text{s}^{-1}$), as expected for a dimeric protein. This occurs due to molecular gating, whereby the ATPase activity of the individual motors

is coordinated so that only a single motor turns over ATP at any given moment [26]. This rate was also similar to those measured for full-length MVI in the presence of dimeric NDP52 (k_{cat} 2.11 s^{-1}) and monomeric tDab2 (k_{cat} 2.55 s^{-1}). Overall, these ATPase measurements show that dimerization is a feature of MVI and not due to binding partner crosslinking. In addition, size-exclusion chromatography strongly supported the formation of MVI₁₋₁₀₆₀ dimers. Full-length MVI eluted as a single peak around 13 ml, whereas MVI₁₋₈₁₄ eluted at 15.6 ml (Figure 3D), consistent with this construct being smaller in size. However, MVI₁₋₁₀₆₀ eluted earlier than both full length MVI and MVI₁₋₈₁₄ constructs, suggesting it has adopted a distinct structure which supports its dimeric nature observed in the ATPase measurements. Experiments were also performed with MVI and NDP52, however the proteins separated during the chromatography, so a complex could not be resolved. Finally, size-exclusion chromatography also showed that MVI₈₁₄₋₁₀₆₀ elutes in two equal peaks, indicating monomer and dimer species. In contrast, MVI_{TAIL(NI)} and CBD elute as largely single species (Figure 3E), further supporting our finding that dimerization occurs within amino acids 814-1060. Taken together, the ATPase and size-exclusion chromatography data further support the presence of a dimerization site between amino acids 814-1060, consistent with our previous FRET experiments [4, 6].

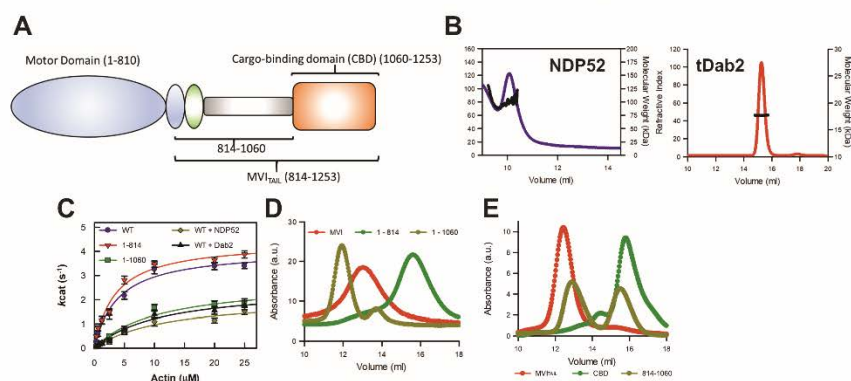


Figure 3: Dimerization of myosin VI.

(A) Cartoon depiction of the key domains of MVI which are used in the ATPase and size-exclusion chromatography measurements. (B) Representative SEC-MALS traces for NDP52 and tDab2 giving molecular weights of 102 kDa and 17 kDa, respectively. This corresponds to dimeric NDP52 and monomeric tDab2. (C) Michaelis-Menten plot displaying steady-state actin-activated ATPase activity for the MVI constructs. Error bars represent SEM from three-independent experiments. (D) Representative SEC traces for 1 mg/ml of the MVI constructs. (E) Representative SEC traces for 1 mg/ml of the MVI_{TAIL} constructs.

9

Lastly, in order to follow the binding partner induced dimerization in real-time, we performed a FRET-based stopped flow assay. 1 μM FITC-MV_{TAIL(NI)} and 1 μM AF555-MV_{TAIL(NI)} were pre-mixed, before being mixed in the stopped-flow with an excess of NDP52, under pseudo-first order conditions (Figure 4A). The fluorescence trace revealed a single exponential increase in FRET signal, with an observed rate constant of 2.2 s⁻¹ (Figure 4B, C). This was independent of NDP52 concentration (Figure 4C), but importantly, it was similar to the unfolding kinetics of the MV_{TAIL(NI)} (Figure 2C and 2G). Altogether, we propose that dimerization is an intrinsic property of MVI and is a rapid process that occurs once unfolding has been triggered by the interaction with the binding partners, exposing the otherwise masked dimerization site (Figure 4D).

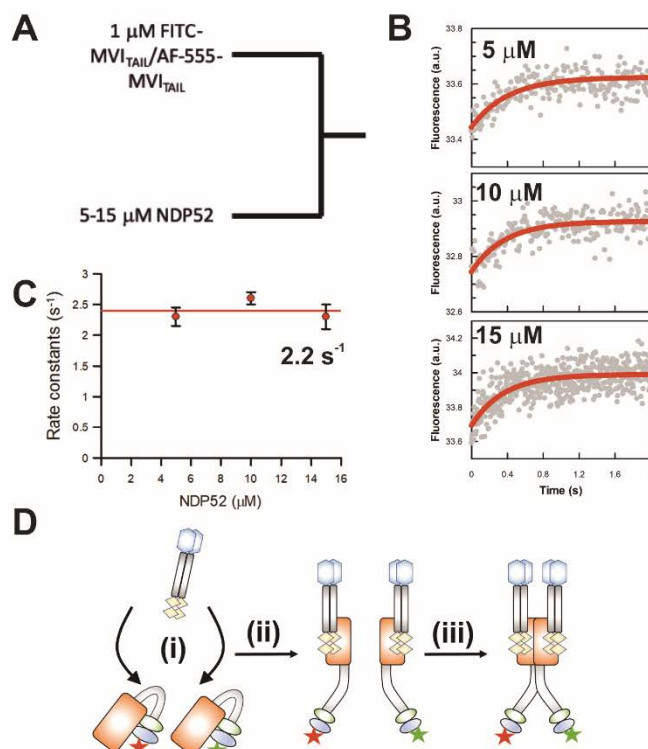


Figure 4: Binding partner driven dimerization of Myosin VI.

(A) Schematic of the experiments for rapid mixing of premixed FITC-MV_{TAIL} and Alexa-Fluor555--MV_{TAIL} with unlabelled NDP52. Experiments were performed as described in the methods. (B) Representative stopped-flow fluorescence traces and exponential fitting to the fluorescence increase, when the two labelled pools of MV_{TAIL} are mixed with the stated concentrations of NDP52. (C) The individual traces were

fitted to single exponentials and the dependence of the rate constants on concentration was then fitted to a straight line, as shown. The points shown are averages of at least 3 measurements and error bars represent SEM. The rate constants are independent of NDP52 concentration, with an average value of 2.2 s^{-1} . (D) Cartoon depicting binding partner driven dimerization based upon the experiments in Figure 2, 3 and 4. Both pools of labelled MVI_{TAIL} are folded. NDP52 binds to either Tail (i) and then triggers their unfolding (ii). This then enables dimerization of the MVI_{TAIL} domains (iii).

Clustering of myosin VI generates high local densities within the cell

We have explored the molecular mechanism underpinning MVI unfolding and dimerization. However, the affinities determined here and previously [6] are in the low micromolar range. Whilst it is possible that these interactions are part of large multi-valent complexes which enhances the overall complex affinities, the biochemical constants defined here suggest that binding partner interactions and subsequent dimerization would be rare events. We therefore focused upon investigating the *in cellulo* spatial organisation of MVI and NDP52 using super resolution imaging – Stochastic Optical Reconstruction Microscopy (STORM) to investigate cellular interactions.

Widefield imaging against endogenous NDP52 and MVI showed that both proteins are distributed throughout HeLa cells (Figure 5A). STORM imaging of both proteins resolved NDP52 and MVI clusters (Figure 5B). To determine whether this distribution is indeed clustered or random (Figure 5C), we performed cluster analysis using the linearized form of Ripley's K function [27] $L(r)-r$, where r is the radius. A plot of $L(r)-r$ versus r gives a value of zero for a random distribution (blue spots), but deviates from zero, due to molecular clustering (Figure 5C). This analysis showed that both NDP52 and MVI assemble into clusters, rather than being randomly distributed. To further understand this clustering behaviour, we used the Clus-DoC software [27], which allows to quantify the spatial distribution of a protein by generating cluster maps (Figure 5D). In this way, we calculated that, in the cytoplasm, 65 % and 70 % of MVI and NDP52 molecules, respectively, are in clusters (Figure 5E). Overexpression of Halo-MVI reveals an increase in the mean number percentage of MVI molecules in clusters (Figure 5E), which suggests clustering is concentration dependent. Interestingly, mutation of the RRL binding sites leads to a 50% reduction in the percentage of molecules in clusters (Figure 5E), which links binding partner interactions to molecular clustering. Lastly, treatment with small molecule inhibitor,

TIP, results in a significant decrease in the percentage of molecules in a cluster (Figure 5E). Moreover, TIP leads to a significant decrease in the total number of clusters and number of molecules per cluster (Supplementary Figure 2), suggesting that molecular clustering requires MVI activity.

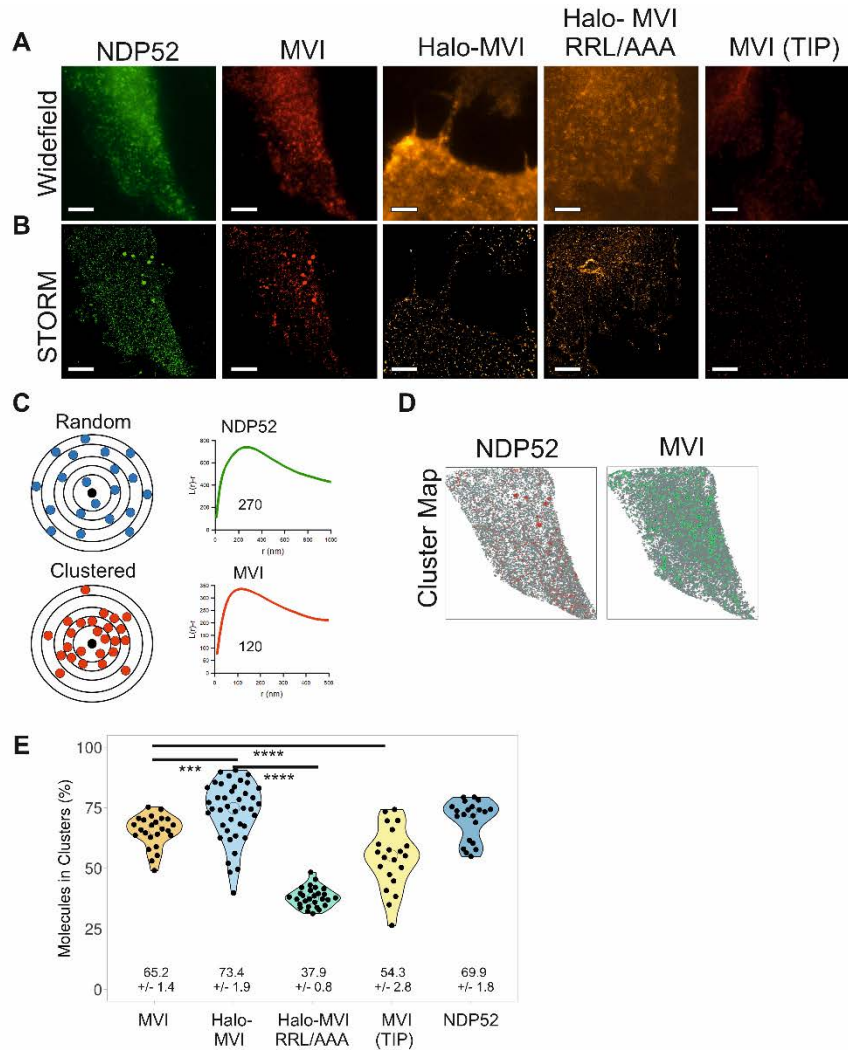


Figure 5: Cellular clustering of myosin VI and NDP52.

(A) Widefield Immunofluorescence imaging against endogenous NDP52 (green) and MVI (red) in the presence and absence of TIP, and JF549 staining against transfected Halo-MVI and Halo-MVI(RRL/AAA) in the cytoplasm of HeLa cells (Scale bar 10 μ m). (B) STORM render images of the cells shown in (A) (Scale bar 10 μ m). Images were

acquired as described in the methods. (C) Depiction of a theoretical example of molecular clustering and random distribution. Molecular clustering is assessed by the linearized plot of Ripley's K function $L(r)-r$, versus r , where r is the radius. Distribution can be plotted as an L-function, where a randomly distributed set of molecules is a flat line with a value of zero. The green curve corresponds to the organisation of NDP52 (peak at $r=270$ nm) and the red curve corresponds to the organisation of MVI (peak at $r=120$ nm). (D) Cluster maps based upon the STORM render in (B). Clusters are shown in Red (NDP52) and Green (MVI). (E) Cluster analysis representing the percentage of molecules in a cluster for the conditions in (B). Individual data points correspond to the average number of molecules per cluster in the selected ROI, in an individual cell. The values represent the mean from all the ROIs for each protein ($n > 20$). (**p < 0.001 ****p < 0.0001 by two-tailed t-test).

To explore the interaction between MVI and NDP52 within the cell, we performed colocalization analysis of the clusters (Figure 6). Colocalization can be represented by transforming the STORM images (Figure 6A) into colocalization heat maps (Figure 6B), which assigns a different colour to the clusters of each protein depending on the level of colocalization between them. TIP has a clear impact on the fraction of MVI which is colocalised with NDP52, resulting in an almost two-third reduction (Figure 6C). Exploring the cluster data further revealed that, for each protein, the colocalized clusters represent approximately 20 % of all clusters (colocalised and non-colocalised) (Figure 6D). This is not a surprise given that both proteins interact with various other partners and are also involved in distinct pathways. However, the MVI colocalized clusters are 3-fold larger than the non-colocalized ones, and contain 15-fold more molecules. Treatment with TIP reduces the colocalised cluster area by a third and reduces the number of molecules per cluster by 50%. For NDP52, the colocalized clusters are 2-fold larger than the non-colocalized ones, and contain almost 7-fold more molecules.

Taken together, the cluster analysis suggests that molecular clustering of MVI does occur within the cell and is promoted by binding partners, while require motor activity. As clustered MVI does not represent freely diffusing molecules, the high local density generated by clustering would enhance the impact of its biochemical properties. Within the confined and denser environment of the clusters, the low affinity interactions of MVI with its partners are more likely to occur. In this way, clustering would ensure that the subsequent unfolding and dimerization of MVI is readily facilitated and implemented, when needed.

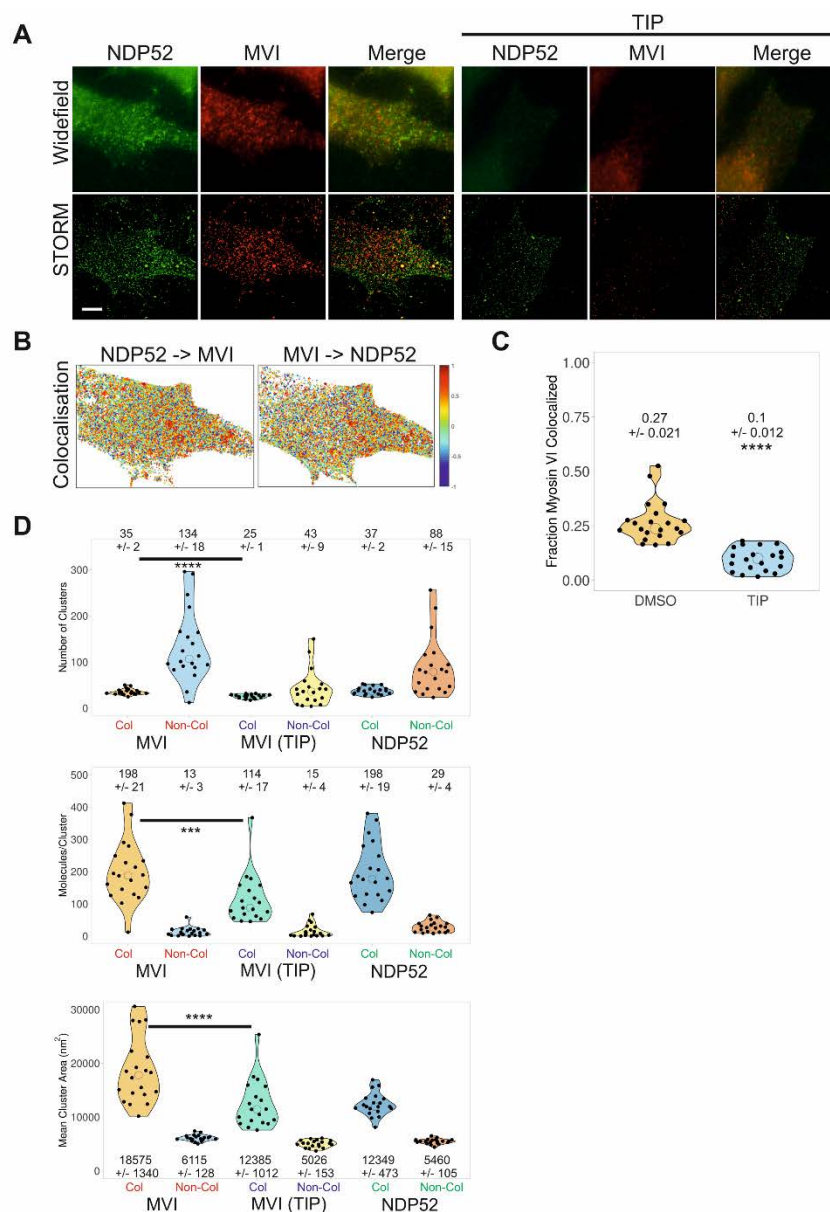


Figure 6: Cluster analysis and colocalization of myosin VI and NDP52.

(A) Examples of widefield immunofluorescence imaging against endogenous NDP52 (green) and MVI (red) in the presence and absence of TIP in HeLa cells (Scale bar 10 μ m), with their corresponding STORM render. Images were acquired as described in the methods. (B) Cluster colocalization heatmaps corresponding to the STORM renders shown in (A), depicting the colocalisation scores for each molecular cluster

for MVI and NDP52. Here, values of 1 (dark red) correspond to perfectly colocalised clusters and -1 (dark blue) to clusters separated from each other. (C) Fraction of MVI colocalised with NDP52 in the presence and absence of TIP. (D) Results of cluster analysis of MVI +/- TIP and NDP52, displaying the distribution and mean values of the number of clusters per cell ROI, number of molecules per cluster and cluster area. The data are broken down into MVI and NDP52 colocalized and non-colocalized clusters. Individual data points correspond to the corresponding average value per cell ROI. The values represent the mean (+/- s.d.) from the ROIs ($n = 20$) for each condition (**** $p < 0.0001$ by two-tailed t-test compared to non-colocalized clusters).

Interactions with binding partners regulate the cellular dynamics of myosin VI.

Following the single molecule localisation experiments, we performed live-cell 3D single molecule tracking to observe the impact of binding partners on the dynamics of MVI, using an aberration-corrected multi-focal microscope (acMFM) system [28]. This technique allows the simultaneous acquisition of 9 focal planes covering $4 \mu\text{m}$ in the z axis, with a $20 \times 20 \mu\text{m}$ field of view. We visualised NI isoform of MVI in HeLa using an N-terminal HaloTag fusion [7] labelled with JF549 [29] and then performed single particle tracking.

The trajectories of MVI revealed different populations of molecules, some undergoing confined motion, some random diffusion and others directed movement (Figure 7A). The diffusion constants (D) extracted from these trajectories had a mean value of $0.3 \mu\text{m}^2 \text{s}^{-1}$, under normal conditions, with the large majority of molecules exhibiting slow diffusion (Figure 7B). To better understand the diffusion properties of MVI, we further split these diffusion constants into three groups: a) static/slow moving molecules with D below $0.1 \mu\text{m}^2 \text{s}^{-1}$, b) molecules with D between 0.1 and $2 \mu\text{m}^2 \text{s}^{-1}$ and c) fast moving molecules with D above $2 \mu\text{m}^2 \text{s}^{-1}$ (Figure 7C). We found that MVI molecules are almost equally split between the first two categories, indicating that MVI mainly exists in a static/slow and medium diffusive state. In addition, we assessed the type of particle motion exhibited by MVI by calculating the anomalous diffusion alpha value (Figure 7D). Values below 1 are indicative of confined motion, values above 1 are suggestive of directed motion, whereas values of 1 occur for random diffusion. The alpha value for MVI under normal conditions had a mean value of 0.69, therefore suggesting it mainly undergoes confined movement. This confined motion was further represented using a roseplot (Figure 7E) to depict the angular change in direction within the trajectories. Angles around 180 degrees were enriched and represented

trajectories where molecules reversed direction, as would more likely occur for a confined molecule.

To assess the role of binding partners in the cellular dynamics of MVI, we tracked the movement of two MVI mutants in which Dab2 and NDP52 binding was disrupted, namely MVI_{WWW/WLY} and MVI_{RRL/AAA}, respectively. MVI_{WWW/WLY} did not show any significant change in its diffusion properties compared to wild type MVI (Figure 7B and C). This is not surprising since, as shown previously, the NI isoform displays selectivity for RRL binding partners, rather than the lower affinity WWY-mediated interactions [6]. Conversely, MVI_{RRL/AAA} led to a significant shift in the distribution of diffusion constants, with a 30 % increase in the mean diffusion constant to a value of $0.39 \mu\text{m}^2 \text{s}^{-1}$ (Figure 7B). This can also be seen by the decrease in the static/slow moving population ($<0.1 \mu\text{m}^2 \text{s}^{-1}$) and the increase in the medium and highly diffusive pools ($0.1 - 2 \mu\text{m}^2 \text{s}^{-1}$ and $>2 \mu\text{m}^2 \text{s}^{-1}$) (Figure 7C). This was also matched by the significant change in the type of anomalous diffusion exhibited by the MVI mutant molecules, with an increase in the mean anomalous diffusion alpha value to 0.79 (Figure 7D). As evidenced by the dramatic change in the shape of the distribution, disruption of MVI interaction with its RRL binding partners caused a significant shift from confined motion towards random diffusion.

As expected from the biochemical parameters, these data suggest that there is an impact of the binding partners upon the activity of MVI, which influences its cellular dynamics. This was further supported by the effect of transiently over-expressed GFP-tagged CBD into cells stably expressing wild type Halo-MVI. Over-expression of this construct is known to have a dominant negative effect by displacing wild type MVI from binding partner and lipid-based interactions [30]. Indeed, the presence of the CBD led to a considerable increase in the diffusion constant of MVI to a mean value of $0.43 \mu\text{m}^2 \text{s}^{-1}$ (Figure 7B), an increase in the population of highly diffusive species (Figure 7C), and a shift of the alpha value to mean of 0.85 (Figure 7D). Once again, this is consistent with the STORM measurements which revealed less clustering of MVI RRL mutant. To assess the contribution of actin to the pool of static/slow diffusing molecules, the dynamics of MVI were observed following treatment with an actin polymerization inhibitor, Latrunculin B. Not surprisingly, there was a significant increase in MVI diffusion (Figure 7B and 7C), due to the loss of actin-based interactions.

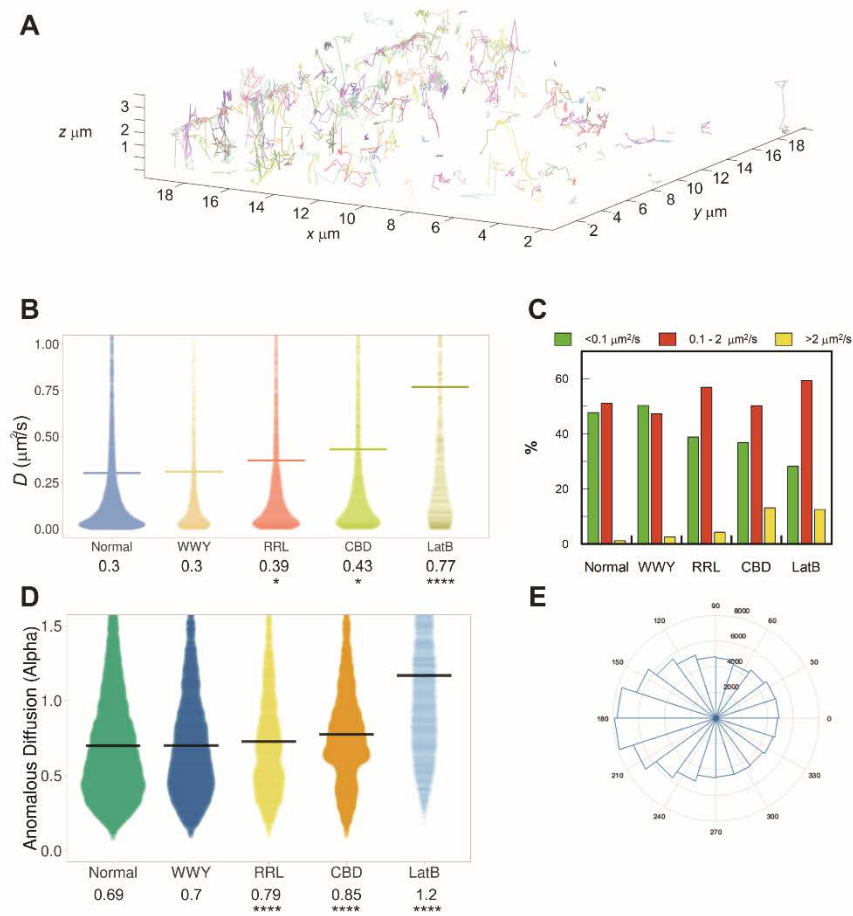


Figure 7: Live cell single-molecule dynamics of myosin VI.

(A) Example render of 3D single-molecule trajectories for JF549-labelled Halo-tagged MVI, stably expressed in HeLa cells, under normal conditions. (B) Plot of diffusion constants for wild type (WT) MVI (normal), MVI WWY/WLY (WWY), MVI RRL/AAA (RRL), WT MVI following transient over-expression of GFP-CBD (CBD) and WT MVI following treatment with latrunculin B (LatB). Diffusion constants were derived from fitting trajectories to an anomalous diffusion model, as described in methods. The data represent all trajectories from 100 cells (* $p < 0.05$, **** $p < 0.0001$ by two-tailed t-test compared to normal conditions). (C) Diffusion constants (D) were split into three categories corresponding to static/slow moving ($D < 0.1 \mu\text{m}^2 \text{s}^{-1}$), mobile ($0.1 < D < 2 \mu\text{m}^2 \text{s}^{-1}$) and hyper-mobile fractions ($D > 2 \mu\text{m}^2 \text{s}^{-1}$). The percentage of molecules from the experiments in (B) falling into each group were then plotted. (D) Plot of anomalous diffusion alpha values derived from the same experimental set shown in (B), for the indicated conditions. (**** $p < 0.0001$ by two-tailed t-test compared to normal conditions). (E) Roseplot representing the angular change in WT MVI diffusion from

the trajectories analysed in (B). Angles close to 180° are enriched which suggests molecules are moving backwards and forwards within a space.

Overall, our data demonstrate that the interaction of MVI with its binding partners plays an important role in regulating the cellular dynamics of the protein. The increase in random diffusion observed following disruption of these interactions could reflect a loss of interaction with cargo and anchoring sites. It could also reflect loss of direct interactions with actin, given that MVI would then be in a back-folded inactive state.

Binding partner interactions enhance actin binding

To directly test how binding partners impact actin binding, we performed actin isolation assays with recombinant proteins (Figure 8A/B). As expected, MVI is isolated by F-actin. The amount of MVI bound to actin is 50%. The addition of an excess of NDP52 led to above 80% of MVI being bound to actin. As expected, the RRL-AAA mutant did not show the enhanced binding in the presence of NDP52. Whilst these experiments are in alignment with our assays above, this finding contradicts the claims in (Arden 2016) where actin pelleting assays were performed in cell lysates. Based on the findings from Arden et al, we would expect to find these mutant proteins decorating actin filaments. To this end, we transfected HeLa cells with eGFP-WT, RRL-AAA and WWY-WLY MVI (Figure 8C). Some colocalization with actin filaments are observed but there are no obvious differences between mutants and wild type MVI. We therefore conclude we are not enhancing actin binding above wild type levels.

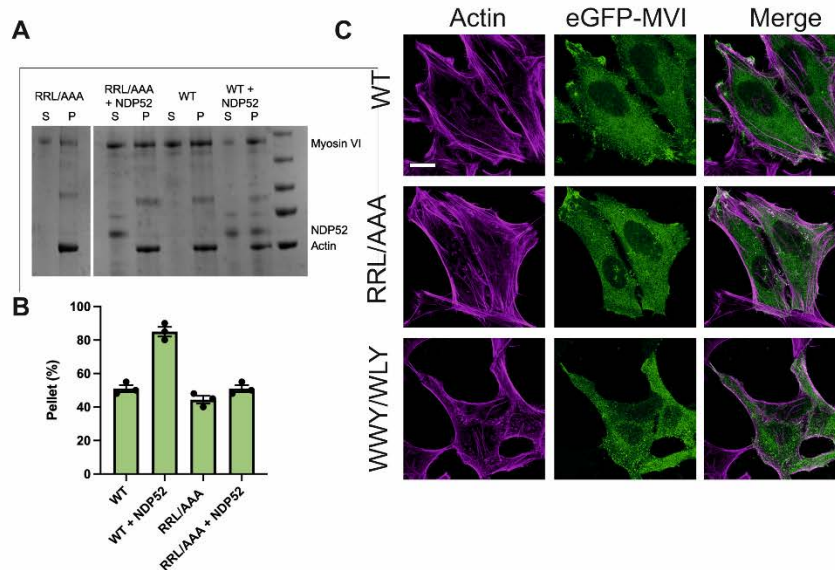


Figure 8: Binding partners enhance actin binding.

(A) Actin pull-down of 5 μ M myosin VI wild type (WT) or mutant RRL/AAA in the presence and absence of 15 μ M NDP52. P and S represent pellet and supernatant, respectively. (B) Quantification of pull-downs in A. (C) Representative images of transiently transfected eGFP-MVI wild type (WT), RRL/AAA and WWY/WLY MVI in HeLa cells combined with phalloidin staining against actin (magenta). Scale bar 10 μ m.

DISCUSSION

This study has provided novel insights into the mechanisms underlying the regulation of MVI and its function within a cell. We have revealed that binding partners directly regulate the structural transitions of MVI from an auto-inhibited backfolded monomer to an active motor, which is linked to actin and cargo (Figure 8A). Our data suggest that this mechanism is generic, irrespective of MVI isoform or choice of binding partners. Importantly, this model does not assume that binding partners must be dimeric. Moreover, pre-steady-state kinetics has allowed us to define that binding partners first bind to the backfolded MVI and subsequently trigger unfolding, rather than binding to a spontaneously unfolded MVI and stabilising that state. This is an important regulatory step which enables binding partners to turn myosin VI on and off.

We have shown that once MVI is unfolded, it has the intrinsic ability to dimerize, as it has been reported before [4, 6, 13, 24, 25, 31]. Here, we have further clarified these models by showing that MVI dimerizes internally and that binding partner

dimerization is not the driving factor. We therefore propose that the complex stoichiometry exists as one active binding partner (monomer or dimer) per MVI molecule (Figure 9A). This stoichiometry has been reported from structural studies [25, 32]. Greater differences in oligomerization status may occur between binding partners where monomers or dimers can be favoured. Moreover, larger oligomers, while maintaining 1:1 stoichiometry, could also be produced [32].

Rapid mixing kinetics allowed us to probe the individual mechanistic steps and therefore propose that dimerization can occur rapidly following unfolding of MVI, with unfolding being the rate-limiting step once binding partner interaction occurs.

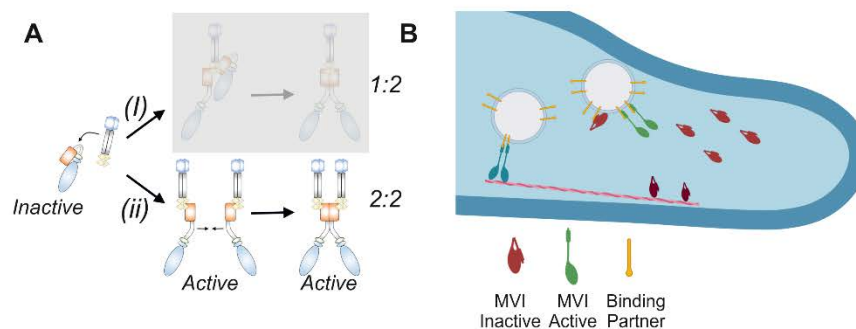


Figure 9: Model describing the activation of myosin VI by binding partners.

(A) Two routes of binding partner-dependent dimerization of MVI. (i) Dimeric binding partner (e.g. NDP52) binds to backfolded MVI and triggers its unfolding. A second MVI molecule is then recruited through the binding partner, due to its dimeric nature. This results in a stoichiometry of 1 dimeric partner to 2 MVI motors. This mechanism does not require MVI internal dimerization. (ii) Each MVI molecule is unfolded by an individual binding partner. Unfolding then exposes internal dimerization sequences within MVI, which can result in a dimer complex with a stoichiometry of 2 partners and 2 motors. The data presented here allow option (i) to be excluded. Our data also allows us to propose that the folded state is inactive (non-actin bound) and that the unfolded state (monomer and dimer) becomes active with the ability to bind actin. (B) Recruitment and activation of myosin VI to cellular cargo by binding partners. Monomeric backfolded (inactive) myosin VI (red) can be found freely diffusing in the cytoplasm or bound to actin (dark red). The inactive myosin VI associates with cargo-bound binding partners. This triggers unfolding and activation of the motor in monomeric (green) or dimeric (blue) populations. The active myosin VI can interact with actin filaments and undergo processive movement to facilitate cargo transportation.

MVI exists as four alternative spliced isoforms and interacts with a wide range of binding partners. In our study, we assessed the generic nature of MVI unfolding and

dimerization, using examples of two MVI isoforms, which represent the two largest structural variants, and two binding partners, which bind at alternative motifs. Although we cannot exclude potential differences in behaviour in other isoforms and with other MVI partners.

Our biochemical analysis has furthered our understanding of how MVI interacts with its binding partners and highlighted the impact of these interactions upon MVI activity. We have previously shown that this relies on the interplay between isoform splicing and the differential affinities between the RRL and WWY binding sites motifs [6]. Here, we have provided insights into the order of events occurring during partner binding, unfolding and dimerization. However, by nature, all these biochemical studies occur under an environment allowing free molecular diffusion, which is strikingly different from the crowded cellular environment. Our high-resolution imaging data shed light on how the biochemical features of MVI measured *in vitro* could translate into the complex cellular context. They revealed that over 60% of MVI molecules are clustered within the mammalian cell. The high local densities within these clusters enhance the probability of interactions with its binding partners, which have been biochemically shown to be in the micromolar range. Moreover, our data have shown that association with binding partners further increases these clusters in size and molecular density. Although this was tested here only for the partner NDP52, it is very likely to apply for all binding partners. The reason is that, within such clusters, multivalent interactions of MVI to cargo through various binding partners would lead to stable complexes capable of long-range processive movement. Enzymatic clustering has been reported for many cellular processes [33, 34], where it is hypothesised to increase local concentrations to enhance efficiency. Therefore, given the multifunctional and complex nature of MVI intracellular activity, it would not be surprising that this myosin follows a mechanism, which allows stability, efficiency and high level of regulation.

In addition to what was demonstrated biochemically, the impact of binding partners upon MVI is also evident from the live cell single-molecule tracking data. Here, we have shown how mutations, or truncations that lead to the disruption of interactions between MVI and binding partners have a profound effect on the dynamics of the protein inside the cell, leading to loss of the static and slow-moving molecules, which display restrictive diffusion, for more rapidly diffusing molecules exhibiting random motion. To account for such a behavioural switch, we propose that the direct

association with the actin cytoskeleton and cellular cargo is decreased when interactions with binding partners are disrupted. In this manner, a backfolded MVI would freely diffuse around the cell and then interact with the cytoplasm when activated by a binding partner on a cargo.

It was previously reported that disruption of MVI – binding partner/cargo interactions leads to an increase in actin binding using a cell-based pull-down assays [35]. However, while imaging was performed with other mutations within their study to show enhanced actin binding, those targeting the RRL and WWY sites were not observed. We performed imaging of these mutations and could not find them decorating actin filaments, as would have been expected based on the study. Instead, the results are consistent with the data presented here, and with our recombinant actin binding assays, where we find that binding partners enhance actin associations.

These observations allowed us to further expand our activation model of MVI. We propose that the back-folded MVI, being inactive, can randomly diffuse in the cell. In this state, MVI can be sequestered by binding partners to cellular cargo or organelles, and get subsequently activated (Figure 9B). Diffusion of MVI in its inactive state is important because it allows sampling of various regions of the cell before recruitment by its partners to function in specific biological processes. Interestingly, we would expect to observe a decrease in ATPase activity if the protein is not bound to actin. However, these changes have not been observed through biochemical analysis, possibly due to the marked differences between the chemical environment of biochemical assays and the cellular environment. Also, within the complex cellular environment, other processes, such as further regulation of the motor by calcium-calmodulin or changes in the phosphorylation status of MVI upon perturbation of binding partner interactions, could lead to inhibition of the ATPase activity, and these would not be observed *in vitro*. These factors remain to be determined.

In summary, our multidisciplinary study provides new insights into the regulation of MVI by binding partners in the cell. The regulation is complex and our knowledge is not complete. It remains unknown as to how monomeric or dimeric states of the protein are selected within the cell, which may be the role of the binding partners to fulfil. Interestingly, due to the internal dimerization of MVI, we suggest that monomeric activities would arise from binding partners activity halting dimerization. Given the established impact of MVI in several diseases, including cancer [19, 36-39] and deafness [35, 40], defining the mechanistic details of its regulation and function is

critical for understanding the impact of mutations, truncations, or altered expression of MVI or partners during disease. Overall, these insights provide new avenues for exploring how the activity of this multi-functional motor protein is regulated within the cell and how these processes may be perturbed during disease.

ACKNOWLEDGEMENTS

We thank the UKRI-MRC (MR/M020606/1) and UKRI-STFC (19130001) for funding. Aberration-corrected multi-focal microscopy was performed in collaboration with the Advanced Imaging Center at Janelia Research Campus, a facility jointly supported by the Howard Hughes Medical Institute and the Gordon and Betty Moore Foundation. We also thank Darren Griffin (University of Kent) and Mike Geeves (University of Kent) for sharing of equipment and reagents, and Satya Khuon (Janelia Research Campus) for assisting with cell culture. The JF549 dye was kindly provided by Luke Lavis (Janelia Research Campus).

AUTHOR CONTRIBUTIONS

C.P.T. conceived the study. A.dS., N.F., Y.H-G. and C.P.T. designed experiments. N.F. and C.P.T. designed and cloned constructs. A.dS., N.F., Y.H-G., R.E.G. and C.P.T. performed single molecule imaging experiments. Imaging was supported by L.W., M.M-F. and J.A. N.F., R.E.G. and C.P.T. expressed, purified and performed experiments with recombinant proteins. L.W., J.A., T-L.C., A.dS. and C.P.T. contributed to single molecule data analysis. C.P.T. supervised the study. C.P.T. wrote the manuscript with comments from all authors.

Competing financial interests: The authors declare no competing financial interests.

METHODS

Constructs

A list of constructs and PCR primers are provided in Supplementary Table 1 and 2, respectively. Constructs generated in this work are described below: RRL/AAA and WWY/WLY mutations were made by site-directed mutagenesis using standard Quick-Change site-directed mutagenesis protocol with pLV-Tet0-Halo MVI as the template. All plasmids were verified by DNA sequencing.

Protein expression and purification in Escherichia coli

Recombinant constructs were expressed in *E. coli* BL21 DE3 cells (Invitrogen) in Luria Bertani media. Proteins were purified by affinity chromatography (HisTrap FF, GE Healthcare). The purest fractions were desalted through a PD10 column (GE Healthcare) to remove imidazole before treatment with TEV protease for 4 hr at 25°C. The samples were then passed through a second HisTrap column. The cleaved protein was further purified through a Superdex 200 16/600 column (GE Healthcare).

Protein Expression using Baculovirus system

Full-length MVI NI, MVI₁₋₈₁₄, MVI₁₋₁₀₆₀, MVI_{RRL/AAA} and *Xenopus* calmodulin were expressed in Sf9 and Sf21 (*Spodoptera frugiperda*) insect cells using the Bac-to-Bac® Baculovirus Expression System (Invitrogen). Sf9 cells were cultured in Sf900 media (Gibco). Recombinant bacmids were generated following the manufacturer's instructions and were transfected into adherent Sf9 cells to generate the P1 viral stock. Sf9 cells were infected in suspension at 27°C and 100 rpm with 1 in 50 dilution of P1 and P2 viral stocks to yield P2 and P3 stocks, respectively. Finally, expression of recombinant proteins was set up by infecting sf21 cells with the P3 viral stock in Spodopan media (PAN Biotech). To ensure correct folding of the MVI constructs, cells were simultaneously infected with P3 viral stock of the MVI constructs together with calmodulin at a 0.75 ratio. The cells were harvested after 3 days by centrifugation for 15 min at 700xg and at 4 °C and resuspended in ice cold myosin extraction buffer (90 mM KH₂PO₄, 60 mM K₂HPO₄, 300 mM KCl, pH 6.8), supplemented with Proteolock protease inhibitor cocktail (Expedeon) and 100 µM PMSF, before proceeding to protein purification. Prior to sonication, an additional 5 mg recombinant calmodulin was added together with 2 mM DTT. After sonication, 5 mM ATP and 10 mM MgCl₂ were added and the solution was rotated at 4 °C for 30 min before centrifugation (20,000g, 4°C, 30 min). Then, the cell lysate was subjected to the purification. Proteins were purified by affinity chromatography (HisTrap FF, GE Healthcare). The purest fractions were further purified through a Superdex 200 16/600 column (GE Healthcare).

Protein labelling

Proteins were transferred into 50 mM Na-phosphate (pH 6.5) using a PD10 desalting column. Samples were then incubated with a 5-fold excess of dye for 4 hours, rotating at 4°C. Excess dye was removed using a PD10 desalting column pre-equilibrated with 50 mM Na-Phosphate, 150 mM NaCl and 1 mM DTT. Labelling efficiency was calculated based on the absorbance at 280 nm and the absorbance maximum of the dye. Typical efficiency was 90%, whereby the less than complete labelling was taken as an indicator for a single dye per protein. This was tested for isolated preparations in mass spectroscopy, which revealed both an unlabelled and single labelled population.

Cell culture and Transfection

HeLa (ECACC 93021013) cells were cultured at 37°C and 5% CO₂, in Gibco MEM Alpha medium with GlutaMAX (no nucleosides), supplemented with 10% Fetal Bovine Serum (Gibco), 100 units/ml penicillin and 100 µg/ml streptomycin (Gibco). For the transient expression of MVI mutants, HeLa cells grown on glass coverslips were transfected using Lipofectamine 2000 (Invitrogen), following the manufacturer's instructions. Depending on the construct, 24 h - 72 h after transfection, cells were subjected to further analysis. To inhibit actin polymerization, cells were treated with 1 µM Latrunculin B (Sigma) for 1h at 37 °C.

Immunofluorescence

HeLa cells were fixed for 15 min at room temperature in 4% (w/v) paraformaldehyde (PFA) in PBS and residual PFA was quenched for 15 min with 50 mM ammonium chloride in PBS. All subsequent steps were performed at room temperature. Cells were permeabilised and simultaneously blocked for 15 min with 0.1 % (v/v) Triton X-100 and 2 % (w/v) BSA in PBS. Cells were then immuno-stained against the endogenous proteins by 1 h incubation with the indicated primary and subsequently the appropriate fluorophore-conjugated secondary antibody (details below), both diluted in 2 % (w/v) BSA in PBS. The following antibodies were used at the indicated dilutions: Rabbit anti-myosin VI (1:200, Atlas-Sigma HPA0354863), Mouse anti-NDP52 (1:250 Abcam ab124372), Donkey anti-mouse Alexa Fluor 488-conjugated (1:250, Abcam Ab181289), Donkey anti-rabbit Alexa Fluor 647-conjugated (1:250, Abcam Ab181347). Coverslips were mounted on microscope slides with Mowiol (10%

(w/v) Mowiol 4-88, 25% (w/v) glycerol, 0.2 M Tris-HCl, pH 8.5), supplemented with 2.5% (w/v) of the anti-fading reagent DABCO (Sigma).

STORM Imaging

Cells were seeded on pre-cleaned No 1.5, 25-mm round glass coverslips, placed in 6-well cell culture dishes. Glass coverslips were cleaned by incubating them for 3 hours, in etch solution, made of 5:1:1 ratio of H₂O : H₂O₂ (50 wt. % in H₂O, stabilized, Fisher Scientific) : NH₄OH (ACS reagent, 28-30% NH₃ basis, Sigma), placed in a 70°C water bath. Cleaned coverslips were repeatedly washed in filtered water and then ethanol, dried and used for cell seeding. Cells were fixed in pre-warmed 4% (w/v) PFA in PBS and residual PFA was quenched for 15 min with 50 mM ammonium chloride in PBS. Immunofluorescence (IF) was performed in filtered sterilised PBS. Cells were permeabilized and simultaneously blocked for 30 min with 3% (w/v) BSA in PBS supplemented with 0.1 % (v/v) Triton X-100. Permeabilized cells were incubated for 1h with the primary antibody and subsequently the appropriate fluorophore-conjugated secondary antibody, at the desired dilution in 3% (w/v) BSA, 0.1% (v/v) Triton X-100 in PBS. The antibody dilutions used were the same as for the normal IF protocol (see above). Following incubation with both primary and secondary antibodies, cells were washed 3 times, for 10 min per wash, with 0.2% (w/v) BSA, 0.05% (v/v) Triton X-100 in PBS or TBS. Cells were further washed in PBS and fixed for a second time with pre-warmed 4% (w/v) PFA in PBS for 10 min. Cells were washed in PBS and stored at 4 °C, in the dark, in 0.02% NaN₃ in PBS, before proceeding to STORM imaging.

Before imaging, coverslips were assembled into the Attofluor® cell chambers (Invitrogen). Imaging was performed in freshly made STORM buffer consisting of 10 % (w/v) glucose, 10 mM NaCl, 50 mM Tris - pH 8.0, supplemented with 0.1 % (v/v) 2-mercaptoethanol and 0.1 % (v/v) pre-made GLOX solution which was stored at 4 °C for up to a week (5.6 % (w/v) glucose oxidase and 3.4 mg/ml catalase in 50 mM NaCl, 10 mM Tris - pH 8.0). All chemicals were purchased from Sigma.

Imaging was undertaken using the Zeiss Elyra PS.1 system. Illumination was from a HR Diode 642 nm (150 mW) and HR Diode 488 nm (100 mW) lasers where power density on the sample was 7-14 kW/cm² and 7-12 kW/cm², respectively

Imaging was performed under highly inclined and laminated optical (HILO) illumination to reduce the background fluorescence with a 100x NA 1.46 oil immersion objective lens (Zeiss alpha Plan-Apochromat) with a BP 420-480/BP495-550/LP 650 filter. The

final image was projected on an Andor iXon EMCCD camera with 25 msec exposure for 20000 frames.

Image processing was performed using the Zeiss Zen software. Where required, two channel images were aligned following a calibration using a calibration using pre-mounted MultiSpec bead sample (Carl Zeiss, 2076-515). The channel alignment was then performed in the Zeiss Zen software using the Affine method to account for lateral, tilting and stretching between the channels. The calibration was performed during each day of measurements.

The images were then processed through our STORM analysis pipeline using the Zen software. Single molecule detection and localisation was performed using a 9 pixel mask with a signal to noise ratio of 6 in the "Peak finder" settings while applying the "Account for overlap" function. This function allows multi-object fitting to localise molecules within a dense environment. Molecules were then localised by fitting to a 2D Gaussian.

The render was then subjected to model-based cross-correlation drift correction. Typical localisation precision was 20 nm for Alexa-Fluor 647 and 30 nm for Alexa-Fluor 488. The final render was then generated at 10 nm/pixel and displayed in Gauss mode where each localisation is presented as a 2D gaussian with a standard deviation based on its precision. The localisation table was exported as a txt for import in to Clus-DoC.

Clus-DoC

The single molecule positions were exported from Zeiss black version and imported into the Clus-DoC analysis software [27] (<https://github.com/PRNicovich/ClusDoC>). Cytoplasmic areas were selected as ROIs for cluster analysis. First the Ripley K function was completed on each channel identifying the r max. The r max was then assigned for DBSCAN if one channel was being analysed or Clus-Doc if two channel colocalisation was being analysed. The clustering size was set to a minimum of 5 molecules, with smoothing set at 7 nm and epsilon set at the mean localization precision for the dye. All other analyses parameters remained at default settings. Data concerning each cluster was exported and graphed using Plots of Data.

Size-exclusion Chromatography and Multi-Angle Light Scattering

100 µl samples of 2mg/ml purified protein, was applied to a Superdex 200 (30 x 1 cm) analytical column (GE Healthcare) equilibrated in 150 mM NaCl, 50 mM Tris.HCl (pH 7.5) and 1 mM DTT and controlled using Waters 626 HPLC at room temperature. Eluted proteins were analysed with Viscotek SEC-MALS 9 and Viscotek RI detector VE3580 (Malvern Panalytical). Molecular mass was determined using OmniSEC software.

Actin-pelleting Assay

Constructs were incubated at the specified concentrations in reaction buffer (150 mM NaCl, 50 mM Tris.HCl (pH 7.5), 1 mM MgCl₂ and 1 mM DTT), for 10 min at RT. 5 µM F-actin (mixture 20% Biotinylated actin (Cytoskeleton Inc.)) was added to the mixture and incubated at RT for 10 min. Streptavidin Dynabeads (M-280) (Invitrogen) were washed 3 times according to the manufacturer's instructions and then finally in reaction buffer. 0.2 mg/ml beads were added to the samples. The samples were incubated for 5 min at RT before magnetic isolation. The isolated sample was re-suspended in an equal volume to the supernatant. The samples were analyzed by SDS-PAGE.

Multi-focal Imaging and Particle Tracking Analysis

Cells stably or transiently expressing Halo-tag constructs were labelled for 15 min with 10 nM HaloTag-JF549 ligand, in cell culture medium at 37°C, 5% CO₂. Cells were washed for 3 times with warm cell culture medium and then incubated for further 30 min at 37°C, 5% CO₂. Cells were then washed three times in pre-warmed FluoroBrite DMEM imaging medium (ThermoFisher Scientific), before proceeding to imaging. Single molecule imaging was performed using an aberration-corrected multifocal microscope (acMFM), as described by Abrahamsson et al. [28]. Briefly, samples were imaged using 561nm laser excitation, with typical irradiance of 4-6 kW/cm² at the back aperture of a Nikon 100x 1.4 NA objective. Images were relayed through a custom optical system appended to the detection path of a Nikon Ti microscope with focus stabilization. The acMFM detection path includes a diffractive multifocal grating in a conjugate pupil plane, a chromatic correction grating to reverse the effects of spectral dispersion, and a nine-faceted prism, followed by a final imaging lens.

The acMFM produces nine simultaneous, separated images, each representing successive focal planes in the sample, with ca. 20 μm field of view and nominal axial separation of ca. 400nm between them. The nine-image array is digitized via an electron multiplying charge coupled device (EMCCD) camera (iXon Du897, Andor) at up to 32ms temporal resolution, with typical durations of 30 seconds.

3D+t images of single molecules were reconstructed via a calibration procedure, implemented in Matlab (MathWorks), that calculates and accounts for (1) the inter-plane spacing, (2) affine transformation to correctly align each focal plane in the xy plane with respect to each other, and (3) slight variations in detection efficiency in each plane, typically less than $\pm 5\text{-}15\%$ from the mean.

Reconstructed data were then subject to pre-processing, including background subtraction, mild deconvolution (3-5 Richardson-Lucy iterations), and/or Gaussian denoising prior to 3D particle tracking using the MOSAIC software suite [41]. Parameters were set where maximum particle displacement was 400 nm and a minimum of 10 frames was required. Tracks were reconstructed, and diffusion constants were extracted via MSD analysis [42] using custom Matlab software assuming an anomalous diffusion model.

Steady-state ATPase Activity of MVI

Ca^{2+} -actin monomers were converted to Mg^{2+} -actin with 0.2 mM EGTA and 50 μM MgCl_2 before polymerizing by dialysis into 20 mM Tris.HCl (pH7.5), 20 mM imidazole (pH 7.4), 25 mM NaCl and 1 mM DTT. A 1.1 molar equivalent of phalloidin (Sigma) was used to stabilize actin filaments, as previously described [43].

Steady-state ATPase activities were measured at 25 $^\circ\text{C}$ in KMg50 buffer (50 mM KCl, 1 mM MgCl_2 , 1 mM EGTA, 1 mM DTT, and 10 mM imidazole, pH 7.0). Supplemented with the NADH-coupled assay components, 0.2 mM NADH, 2 mM phosphoenolpyruvate, 3.3 U ml^{-1} lactate dehydrogenase, 2.3 U ml^{-1} pyruvate kinase and various actin concentrations (0 – 30 μM). The final $[\text{Mg.ATP}]$ was 5 mM and MVI concentration was 100–300 nM. The assay was started by the addition of MVI. The change in absorption at OD₃₄₀ nm was followed for 5 min. The k_{cat} and K_{actin} values were determined by fitting the data to equation 1.

$$[1] \quad \text{Rate} = V_0 + \left(\frac{k_{\text{cat}}[\text{Actin}]}{K_{\text{actin}} + [\text{Actin}]} \right)$$

V_0 is the basal ATPase activity of MVI, k_{cat} is the maximum actin-activated ATPase rate and K_{actin} is the concentration of actin needed to reach half maximal ATPase activity.

Titration measurements

All reactions were performed at 25 °C in a buffer containing 50 mM Tris-HCl (pH 7.5), 150 mM sodium chloride and 1 mM DTT in a final volume of 100 μ L. Measurements were performed using a ClarioStar Plate Reader (BMG Labtech). Intensity measurements were performed at the following wavelengths: FITC (ex. 490nm), Alexa Fluor 555 (ex. 555nm). FITC to Alexa Fluor 555 FRET measurements were performed using the following wavelengths ex. 470nm and em. 575nm.

Stopped flow measurements

A HiTech SF61DX2 apparatus (TgK Scientific Ltd, Bradford-on-Avon, UK) with a mercury-xenon light source and HiTech Kinetic Studio 2 software was used [44, 45]. For FRET experiments, excitation was at 495 nm with emission through a 570 nm cut-off filter (Schott Glass). For Cy3B, excitation was at 550 nm with emission through a 570 nm cut-filter (Schott Glass). In all experiments, the quoted concentrations are those in the mixing chamber, except when stated. All experiments were performed at 25°C in 50 mM Tris-HCl, 150 mM NaCl, 1 mM DTT and 3 mM MgCl₂. The dead time of the stopped-flow instrument was ~2 ms: during this initial time no change in fluorescence can be observed.

Analysis of kinetic data

For the FRET titrations: The 575 nm intensity data was corrected for the increase in intensity due to a small direct excitation. This background signal was subtracted from the dataset to leave the FRET values. The titration curves for the MVI_{TAIL} interactions were fitting to a binding quadratic equation, Equation 2:

[2]

[Complex]

$$= \frac{([FITC]_t + [AF555]_t + K_d) - \sqrt{([FITC]_t + [AF555]_t + K_d)^2 - 4[FITC]_t[AF555]_t}}{2}$$

Graphics

Unless stated, data fitting and plotting was performed using Plots of data [46] and Grafit Version 5 (Erithacus Software Ltd). Cartoons were generated using the BioRender software.

Data Availability

The data supporting the findings of this study are available from the corresponding author on request.

REFERENCES

1. Fili, N. and C.P. Toseland, *Unconventional Myosins: How Regulation Meets Function*. Int J Mol Sci, 2019. **21**(1).
2. Roberts, R., et al., *Myosin VI: cellular functions and motor properties*. Philos Trans R Soc Lond B Biol Sci, 2004. **359**(1452): p. 1931-44.
3. Vreugde, S., et al., *Nuclear myosin VI enhances RNA polymerase II-dependent transcription*. Mol Cell, 2006. **23**(5): p. 749-55.
4. Fili, N., et al., *NDP52 activates nuclear myosin VI to enhance RNA polymerase II transcription*. Nat Commun, 2017. **8**(1): p. 1871.
5. Cook, A., Y. Hari-Gupta, and C.P. Toseland, *Application of the SSB biosensor to study in vitro transcription*. Biochem Biophys Res Commun, 2018. **496**(3): p. 820-825.
6. Fili, N., et al., *Competition between two high- and low-affinity protein-binding sites in myosin VI controls its cellular function*. J Biol Chem, 2020. **295**(2): p. 337-347.
7. Große-Berkenbusch, A., et al., *Myosin VI moves on nuclear actin filaments and supports long-range chromatin rearrangements*. bioRxiv, 2020: p. 2020.04.03.023614.
8. Spudich, G., et al., *Myosin VI targeting to clathrin-coated structures and dimerization is mediated by binding to Disabled-2 and PtdIns(4,5)P2*. Nat Cell Biol, 2007. **9**(2): p. 176-83.
9. Hari-Gupta, Y., et al., *Nuclear myosin VI regulates the spatial organization of mammalian transcription initiation*. bioRxiv, 2020: p. 2020.04.21.053124.
10. Wells, A.L., et al., *Myosin VI is an actin-based motor that moves backwards*. Nature, 1999. **401**(6752): p. 505-8.
11. Buss, F., G. Spudich, and J. Kendrick-Jones, *Myosin VI: cellular functions and motor properties*. Annu Rev Cell Dev Biol, 2004. **20**: p. 649-76.
12. Finan, D., M.A. Hartman, and J.A. Spudich, *Proteomics approach to study the functions of Drosophila myosin VI through identification of multiple cargo-binding proteins*. Proc Natl Acad Sci U S A, 2011. **108**(14): p. 5566-71.
13. Mukherjee, M., et al., *Myosin VI dimerization triggers an unfolding of a three-helix bundle in order to extend its reach*. Mol Cell, 2009. **35**(3): p. 305-15.
14. Knight, P.J., et al., *The predicted coiled-coil domain of myosin 10 forms a novel elongated domain that lengthens the head*. J Biol Chem, 2005. **280**(41): p. 34702-8.
15. Buss, F., et al., *Myosin VI isoform localized to clathrin-coated vesicles with a role in clathrin-mediated endocytosis*. EMBO J, 2001. **20**(14): p. 3676-84.
16. Au, J.S., et al., *Myosin VI is required for sorting of AP-1B-dependent cargo to the basolateral domain in polarized MDCK cells*. J Cell Biol, 2007. **177**(1): p. 103-14.
17. Morriswood, B., et al., *T6BP and NDP52 are myosin VI binding partners with potential roles in cytokine signalling and cell adhesion*. J Cell Sci, 2007. **120**(Pt 15): p. 2574-85.

18. Naccache, S.N., T. Hasson, and A. Horowitz, *Binding of internalized receptors to the PDZ domain of GIPC/synectin recruits myosin VI to endocytic vesicles*. Proc Natl Acad Sci U S A, 2006. **103**(34): p. 12735-40.
19. Wollscheid, H.P., et al., *Diverse functions of myosin VI elucidated by an isoform-specific alpha-helix domain*. Nat Struct Mol Biol, 2016. **23**(4): p. 300-8.
20. Batters, C., et al., *Calcium can mobilize and activate myosin-VI*. Proc Natl Acad Sci U S A, 2016. **113**(9): p. E1162-9.
21. Spink, B.J., et al., *Long single alpha-helical tail domains bridge the gap between structure and function of myosin VI*. Nat Struct Mol Biol, 2008. **15**(6): p. 591-7.
22. Toseland, C.P., *Fluorescent labeling and modification of proteins*. J Chem Biol, 2013. **6**(3): p. 85-95.
23. Mukherjee, M., et al., *Myosin VI must dimerize and deploy its unusual lever arm in order to perform its cellular roles*. Cell Rep, 2014. **8**(5): p. 1522-32.
24. Phichith, D., et al., *Cargo binding induces dimerization of myosin VI*. Proc Natl Acad Sci U S A, 2009. **106**(41): p. 17320-4.
25. Yu, C., et al., *Myosin VI undergoes cargo-mediated dimerization*. Cell, 2009. **138**(3): p. 537-48.
26. Altman, D., H.L. Sweeney, and J.A. Spudich, *The mechanism of myosin VI translocation and its load-induced anchoring*. Cell, 2004. **116**(5): p. 737-49.
27. Pagoon, S.V., et al., *Clus-DoC: a combined cluster detection and colocalization analysis for single-molecule localization microscopy data*. Mol Biol Cell, 2016. **27**(22): p. 3627-3636.
28. Abrahamsson, S., et al., *Fast multicolor 3D imaging using aberration-corrected multifocus microscopy*. Nat Methods, 2013. **10**(1): p. 60-3.
29. Grimm, J.B., et al., *Bright photoactivatable fluorophores for single-molecule imaging*. Nat Methods, 2016. **13**(12): p. 985-988.
30. Bond, L.M., et al., *Myosin VI and its binding partner optineurin are involved in secretory vesicle fusion at the plasma membrane*. Mol Biol Cell, 2011. **22**(1): p. 54-65.
31. Park, H., et al., *Full-length myosin VI dimerizes and moves processively along actin filaments upon monomer clustering*. Mol Cell, 2006. **21**(3): p. 331-6.
32. Shang, G., et al., *Structure analyses reveal a regulated oligomerization mechanism of the PlexinD1/GIPC/myosin VI complex*. Elife, 2017. **6**.
33. Carmo-Fonseca, M., *The contribution of nuclear compartmentalization to gene regulation*. Cell, 2002. **108**(4): p. 513-21.
34. Cook, P.R., *A model for all genomes: the role of transcription factories*. J Mol Biol, 2010. **395**(1): p. 1-10.
35. Arden, S.D., et al., *Loss of cargo binding in the human myosin VI deafness mutant (R1166X) leads to increased actin filament binding*. Biochem J, 2016. **473**(19): p. 3307-19.
36. Dunn, T.A., et al., *A novel role of myosin VI in human prostate cancer*. Am J Pathol, 2006. **169**(5): p. 1843-54.
37. Loikkanen, I., et al., *Myosin VI is a modulator of androgen-dependent gene expression*. Oncol Rep, 2009. **22**(5): p. 991-5.
38. Maddugoda, M.P., et al., *Myosin VI and vinculin cooperate during the morphogenesis of cadherin cell cell contacts in mammalian epithelial cells*. J Cell Biol, 2007. **178**(3): p. 529-40.
39. Wang, H., et al., *Lentivirus-Mediated Knockdown of Myosin VI Inhibits Cell Proliferation of Breast Cancer Cell*. Cancer Biother Radiopharm, 2015. **30**(8): p. 330-5.
40. Avraham, K.B., et al., *The mouse Snell's waltzer deafness gene encodes an unconventional myosin required for structural integrity of inner ear hair cells*. Nat Genet, 1995. **11**(4): p. 369-75.
41. Sbalzarini, I.F. and P. Koumoutsakos, *Feature point tracking and trajectory analysis for video imaging in cell biology*. J Struct Biol, 2005. **151**(2): p. 182-95.
42. Aaron, J., et al., *Practical Considerations in Particle and Object Tracking and Analysis*. Curr Protoc Cell Biol, 2019. **83**(1): p. e88.

43. Batters, C., et al., *Cloning, expression, and characterization of a novel molecular motor, Leishmania myosin-XXI*. *J Biol Chem*, 2012. **287**(33): p. 27556-66.
44. Toseland, C.P., *Fluorescence to study the ATPase mechanism of motor proteins*. *EXS*, 2014. **105**: p. 67-86.
45. Toseland, C.P. and M.A. Geeves, *Rapid reaction kinetic techniques*. *EXS*, 2014. **105**: p. 49-65.
46. Postma, M. and J. Goedhart, *PlotsOfData-A web app for visualizing data together with their summaries*. *PLoS Biol*, 2019. **17**(3): p. e3000202.

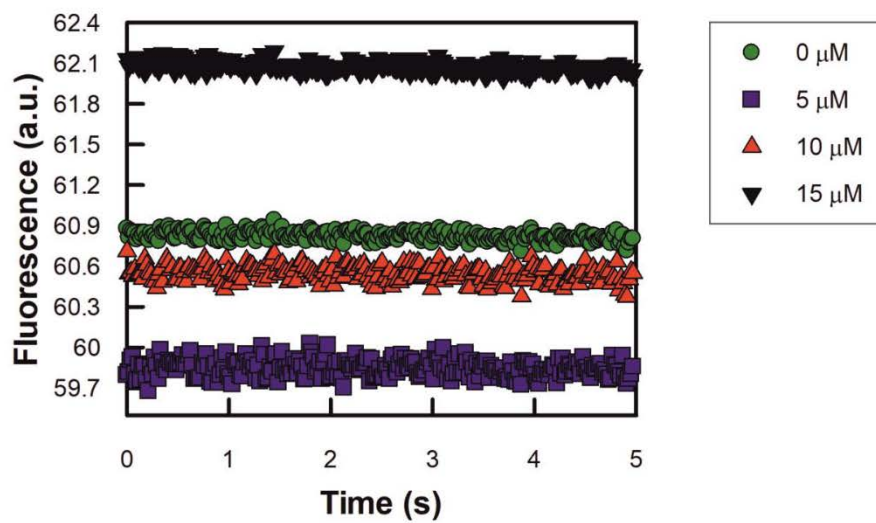
4.2.3.1. Supplementary Material for Manuscript 5

Supplementary Table 1. Recombinant DNA.

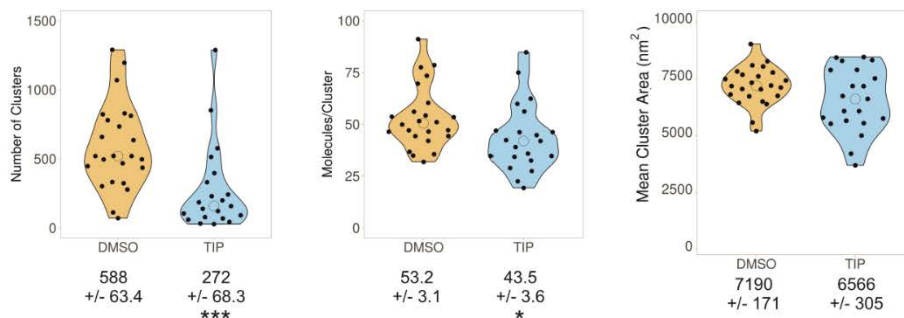
Construct (Residue numbers)	Source
Xenopus pFastBac1 Calmodulin (1-end)	J. Sellers (NIH)
Human pET151 NDP52 (1-end)	Ref Fili et al 2017
Human pET151 EGFP-MV _{TAIL(NI)} -RFP (814-1253)	Ref Fili et al 2017
Human pET151 EGFP-MV _{TAIL(LI)} -RFP (814-1284)	Synthetic Gene – This study
Human pET151 MV _{TAIL} 814-1253	Ref Fili et al 2017
Human pET151 MV _{TAIL} 814-1060(NI)	Ref Fili et al 2017
Human pET151 MV _{TAIL} 814-1091(LI)	Synthetic Gene – This study
Human pET28 CBD 1060-1253	Ref Fili et al 2017
Human pFastbacHTB NI MVI (1-1253)	Ref Fili et al 2017
Human pFastbacHTB MVI (1-814)	Ref Fili et al 2017
Human pFastbacHTB MVI (1-1060)	Ref Fili et al 2017
Xenopus pET28 Cys Calmodulin	Ref Fili et al 2017
Human pET151 Dab2 (649-770)	Ref Fili et al 2020
Human pEGFP-C3 CBD 1060-1253	F. Buss (CIMR)
Human pLV-Tet0-Halo-MVI RRL/AAA	This study
Human pLV-Tet0-Halo-MVI WWY/WLY	This study
Human pEGFP-C3 NI MVI	Ref Fili et al 2017
Human pEGFP-C3 NI MVI RRL/AAA	Ref Fili et al 2020
Human pEGFP-C3 NI MVI WWY/WLY	Ref Fili et al 2020
Human pcDNA3.1 Halo-MVI	Synthetic Gene – This study

Supplementary Table 2. PCR Primers.

Sequence	Use
CTTG CAGAGAAGAATTCATGCGGCAGCAAAGTGTATCATGC	RRL/AAA For
GATTTCCAAGCATGATACACTTTTGCTGCCGCATGAAATTCCTC	RRL/AAA Rev
CCCTCAGAGTAAGAAAAAAGGCTGGTTGTATGCCCATTTTGA	WWY/WLY For
GGTCCATCAAAATGGGCATACAACCAGCCTTTTTCTTACTCT	WWY/WLY Rev



Supplementary Figure 1. Representative stopped-flow fluorescence traces following rapid mixing of 1 μM Cy3B-calmodulin and unlabelled NDP52 at the stated concentrations. Experiments were performed as described in the methods.



Supplementary Figure 2. Cluster analysis of MVI in the presence and absence of TIP, as described in Figure 5. Individual data points correspond to the average number of molecules per cluster in the selected ROI, in an individual cell. The values represent the mean from all the ROIs for each protein ($n = \geq 20$). (* $p < 0.05$ *** $p < 0.001$ by two-tailed t-test).

5. Myosin VI regulates the spatial organization of mammalian transcription

5.1. Context of Research and Contributions

This chapter is a continuation of the work described in Chapter 4. In particular, in Fili *et al.* (2017) we proposed an early model of how MVI might regulate transcriptional activity. Our model was as follows: MVI is recruited to sites of transcription (*e.g.*, ERE sites) and activated through interactions at the C-terminal with binding partners, such as NDP52. This then enables binding to RNAPII through actin, which is present in the transcription complex, via the N-terminal. As we also show that MVI motor activity is essential for its role in transcription, we postulated that MVI could act as either as an auxiliary motor – helping RNAPII propel - or, alternatively, as an anchor for stabilising the RNAPII complex. Importantly, this points towards a role in the overall dynamics and/or organisation of RNAPII during transcription. Hence, the work presented in this chapter tries to answer the following questions: *How important is MVI motor function for the spatial organisation and molecular dynamics of RNAPII? Is MVI-actin binding ability necessary for its transcriptional activity? Does MVI force sensing and molecular anchor function play a role in its regulatory role?*

This chapter comprises one manuscript, for which I am a co-main contributor, as listed below. My specific contributions are also listed below.

Hari-Gupta Y*, Fili N*, **dos Santos Á***, Cook AW, Gough RE, Reed HCW, Wang L, Aaron J, Venit T, Wait E, Grosse-Berkenbusch A, Gebhardt JCM, Percipalle P, Chew TL, Martin-Fernandez M, Toseland CP; Nuclear myosin VI regulates the spatial organization of mammalian transcription initiation. (**equal contribution*) **Nat Commun** 13, 1346 (2022). <https://doi.org/10.1038/s41467-022-28962-w>

We show that MVI has an important role in the nanoscale organisation of transcription initiation. Upon MVI depletion or motor inhibition, RNAPII-Ser5P becomes more dynamic and transcription factory formation is severely disrupted. Furthermore, we found that this is linked to changes in chromatin organisation and gene expression levels. MVI has the ability to switch from a motile state to an anchoring state, depending on how much force

is applied to the molecule. In our updated model for the regulation of transcription by MVI, we propose that this is an essential characteristic in its regulatory role and that MVI has the ability to anchor RNAPII at sites of transcription initiation. This molecular anchoring of RNAPII would allow increased binding times of transcription machinery at transcription sites, subsequent cluster formation and more efficient gene expression. In this model we keep our previous view that MVI could be simultaneously interacting with DNA and/or transcription coactivators via its C-terminal and RNAPII through actin via its N-terminal domain.

Contributions

This project was a joint effort between Dr Yukti Hari-Gupta, Dr Natalia Fili and me. The work performed herein is heavily based on single-molecule data to understand the nanoscale organisation and molecular dynamics of RNAPII, and this is where my main contribution lies. I designed experiments, prepared samples and performed single-molecule data acquisition (STORM and acMFM). I also developed the cluster analysis protocol used for STORM data analysis, using open access tools developed by Pajeon *et al* (Pajeon *et al.*, 2016). With support from the Advanced Imaging facility at HHMI Janelia Research Campus, Dr Christopher Toseland and I performed acMFM data analysis. Together with Dr Hari-Gupta, I designed and performed cell proliferation assays - I then performed the analysis of proliferation data. I also designed and performed confocal imaging experiments.

5.2. Manuscript

(see below)

5.2.1. Manuscript 6 - Myosin VI regulates the spatial organization of mammalian transcription

Nuclear myosin VI regulates the spatial organization of mammalian transcription initiation.

Yukti Hari-Gupta^{#1}, Natalia Fili^{#2}, Ália dos Santos^{#2}, Alexander W. Cook², Rosemarie E. Gough², Hannah C. W. Reed¹, Lin Wang³, Jesse Aaron⁴, Tomas Venit⁵, Eric Wait⁴, Andreas Grosse-Berkenbusch⁶, J. Christof M. Gebhardt⁶, Piergiorgio Percipalle^{5,7}, Teng-Leong Chew⁴, Marisa Martin-Fernandez³ and Christopher P. Toseland^{2*}

¹School of Biosciences, University of Kent, Canterbury, CT2 7NJ, UK. ²Sheffield Cancer Centre, Department of Oncology and Metabolism, University of Sheffield, Sheffield, S10 2RX, UK. ³Central Laser Facility, Research Complex at Harwell, Science and Technology Facilities Council, Rutherford Appleton Laboratory, Harwell, Didcot, Oxford OX11 0QX, UK. ⁴Advanced Imaging Center, HHMI Janelia Research Campus, Ashburn, USA. ⁵Science Division, Biology Program, New York University Abu Dhabi (NYUAD), Abu Dhabi, United Arab Emirates. ⁶Institute of Biophysics, Ulm University, Ulm, Germany. ⁷Current address: MRC LMCB, University College London, London, WC1E 6BT, UK. ⁸Department of Molecular Bioscience, The Wenner Gren Institute, Stockholm University, SE 10691, Sweden. [#]Equal contribution

*Corresponding Author: Christopher P. Toseland c.toseland@sheffield.ac.uk

Key Words: Myosin VI, RNA Polymerase II, Transcription, Nuclear organisation, Gene expression.

SUMMARY

During transcription, RNA Polymerase II (RNAPII) is spatially organised within the nucleus into clusters that correlate with transcription activity. While this is a hallmark of genome regulation in mammalian cells, the mechanisms concerning the assembly, organisation and stability which underpin the function these transcription factories remain unknown. Here, we have used combination of single molecule imaging and genomic approaches to explore the role of nuclear myosin VI in the nanoscale organisation of RNAPII. We reveal that myosin VI acts as the molecular anchor that holds RNAPII into transcription factories. Perturbation of myosin VI leads to the disruption of RNAPII localisation, changes in chromatin organisation and subsequently a decrease in gene expression. Overall, we uncover the fundamental role of myosin VI in the spatial regulation of gene expression during the rapid response to changes in the cellular environment.

INTRODUCTION

The tight regulation of gene expression is critical for the maintenance of cellular homeostasis. This is fundamental during organism development and for the prevention of disease. In eukaryotic cells, RNA polymerase II (RNAPII) directs the flow of genetic information from DNA to messenger RNA (mRNA). Detailed genetic and biochemical assays have revealed a multi-level regulation of transcription, including *cis* control elements within the DNA and *trans* factors, such as general transcription factors, activators, repressors and a large number of coactivators. More recently, the actin-based molecular motors, myosins, have been also shown to act as transcription regulators (de Lanerolle, 2012, de Lanerolle and

Serebryanny, 2011, Fomproix and Percipalle, 2004, Hofmann et al., 2006, Kukalev et al., 2005). Myosins modulate their interaction with actin through their ATPase activity, which occurs within their highly conserved motor domain (Figure 1A). They are involved in multiple cellular processes including cell migration, endocytosis and exocytosis (Fili and Toseland, 2019). More recently, they have also been identified within the cell nucleus, where they have roles in transcription, DNA damage and chromosome organisation (de Lanerolle, 2012).

The minus-end directed myosin, Myosin VI (Figure 1A), has been shown to bind DNA through its cargo binding domain (CBD) and couple itself to RNAPII in an actin-dependent manner through the motor domain (Fili et al., 2017). It has been revealed that the ability of myosin VI to bind DNA and its ATPase activity are both critical for transcription *in vitro* (Cook et al., 2018, Fili et al., 2017, Fili et al., 2020), and myosin VI can function in gene pairing (Zorca et al., 2015). Recently, myosin VI has been shown to actively undergo directed motion in the nucleus in response to transcription stimulation (Große-Berkenbusch et al., 2020). However, the precise role that this motor protein has in transcription has remained elusive.

The spatial organization of transcription has been debated and studied by both imaging and immunoprecipitation methods for over two decades (Cho et al., 2016a, Jackson et al., 1993, Papantonis and Cook, 2013). The formation of transcription centres has been suggested to increase the local concentration of enzymes and render these nuclear processes more efficient (Mao et al., 2011). Enzymatic clustering occurs in many cellular processes, particularly in the nucleus, with examples in replication (Kennedy et al., 2000) and DNA repair (Misteli and Soutoglou, 2009). Therefore, it is not surprising that clusters

of RNAPII have been observed. The lifetime and composition of these clusters has been a matter of debate, with discrepancies between antibody staining in fixed cells, versus live cell observations (Jackson et al., 1993, Kimura et al., 2002, Papanonis and Cook, 2013, Sugaya et al., 2000, Sutherland and Bickmore, 2009, Zhao et al., 2014). More recently, RNAPII has been found to transiently cluster during transcription (Cho et al., 2016a, Cho et al., 2016b) and active RNAPII has been found to constrain chromatin dynamics (Nagashima et al., 2019). Yet, detailed molecular mechanisms of how these clusters form and how they are maintained remain unknown.

Interestingly, the biochemical properties of myosin VI can be tuned by the load applied to the motor (Altman et al., 2004), which allows it to switch from an active transporter to an actin anchor when tension is applied. We therefore hypothesised that myosin VI could act as either an anchor to stabilise RNAPII or as an auxiliary motor to drive RNAPII through the gene body. In either case, this would impact the organisation of RNAPII within the nucleus.

To this end, this study set out to explore whether myosin VI activity is responsible for the spatial organization of RNAPII. Through a combination of single molecule imaging and genomic studies, we have endeavoured to provide general mechanistic insight into how this form of nuclear organisation is achieved and what is the role of a myosin in this process.

RESULTS

The nuclear organisation of myosin VI

Myosin VI is present throughout the mammalian cell, including the nucleus (Figure 1B). To gain better understanding of the spatial organization of myosin VI, we used super resolution imaging, specifically Stochastic Optical Reconstruction Microscopy (STORM) (Figure 1C). Using this approach, individual myosin VI molecules within the nucleus could be resolved, quantified and their functional clustering behaviour assessed. To determine whether myosin VI assembles into clusters or is randomly distributed, we performed cluster analysis using the linearized form of Ripley's K function (Pageon et al., 2016) (Figure 1D). This analysis demonstrated that nuclear myosin VI is clustered, rather than randomly distributed. To further understand this clustering behaviour, we used the Clus-DoC software (Pageon et al., 2016), which allows to quantify the spatial distribution of a protein by generating cluster maps (Figure 1E). We were able to determine that 81% (± 12) of nuclear myosin VI is clustered, with an average of 504 (± 178) clusters per nuclei. Each cluster, with an average cluster size of 1.2 μm^2 (± 0.578), consists of 64 (± 24)

myosin VI molecules, (Figure 1F). Of note, all the parameters quantified showed a large cell-to-cell variation, which may be attributed to the cells not being synchronized.

Given the well-established role of myosin VI in transcription (Cook et al., 2018, Fili et al., 2020, Fili et al., 2017, Große-Berkenbusch et al., 2020, Vreugde et al., 2006), we assessed whether stimulation of transcription can alter its clustering and thus functional properties. Indeed, stimulation with serum induced a significant increase in the nuclear distribution of myosin VI, as evidenced by both the STORM images and cluster maps (Figure 1C and E). Consistent with the noticeable increase in its nuclear recruitment, the number of clusters and their area increased significantly to 678 (± 122) clusters per nuclei and 1.7 μm^2 (± 0.327), respectively (Figure 1F). However, the number of molecules per cluster and the overall percentage of molecules in a cluster remained unchanged, suggesting that new clusters are formed upon serum stimulation but that there may be an upper limit on the number of molecules within a cluster. Interestingly, the cell-to-cell variation decreased, potentially due to a more synchronised cellular response to serum.

Since myosin VI is an ATPase, we then explored whether its nuclear distribution and clustering behaviour was dependent upon its myosin motor activity. To this end, we used the small molecule inhibitor 2,4,6-triiodophenol (TIP) which is known to perturb the motor activity of myosin VI (Heissler et al., 2012) and impact upon transcription (Cook et al., 2018, Fili et al., 2020, Fili et al., 2017). TIP treatment disrupted the nuclear organisation of myosin VI (Figure 1C). STORM imaging and cluster analysis showed a significant decrease in all parameters, except for the number of clusters (Figure 1C, E-F). This suggests that inhibition of myosin VI motor activity interferes with its ability to assemble into clusters. This motor-dependent clustering behaviour indicates that actin could participate in the formation of these structures.

Having observed that transcription stimulation drives myosin VI cluster formation, we turned our attention to RNAPII to explore if there is a relationship between the clustering of both proteins. Firstly, we imaged RNAPII in the transcription initiation state (pSer5) using STORM and performed cluster analysis (Figure 2A). As it has previously been shown (Cho et al., 2016a, Jackson et al., 1993), we also observed clusters of RNAPII under normal growth conditions, whereby 42 (± 17) % of RNAPII was clustered, into 246 (± 140) clusters per cell, each containing 60 (± 27) molecules in an area of 2.7 (± 0.8) μm^2 , on average (Figure 2B). Interestingly, these clusters partially colocalized with the myosin VI clusters. In order to quantify this

colocalization, we employed the Degree of Colocalisation (DoC) analysis which is available in the ClusDoC software (Pageon et al., 2016). The colour-coded co-localization cluster map highlights these regions, where, $15 (\pm 3) \%$ of myosin VI and $22 (\pm 3) \%$ of RNAPII colocalise (Figure 2C). The single-molecule nature of these measurements allowed us to further interrogate the data by comparing the features of colocalised and non-colocalised clusters. Whilst the number of colocalised clusters for both proteins is lower than the non-colocalised ones, these clusters are

up to 2-fold larger in size for RNAPII and up to 10-fold larger for myosin VI, compared to the non-colocalised subpopulation (Supplementary Figure 1A and B). This also correlates with an approximate 50% and 100% increase in RNAPII and myosin VI molecules, respectively, within the colocalised clusters. We also determined that, in the colocalised clusters, there is a ratio of two myosin proteins for each RNAPII. Overall, this suggests there is synergy between the two proteins.

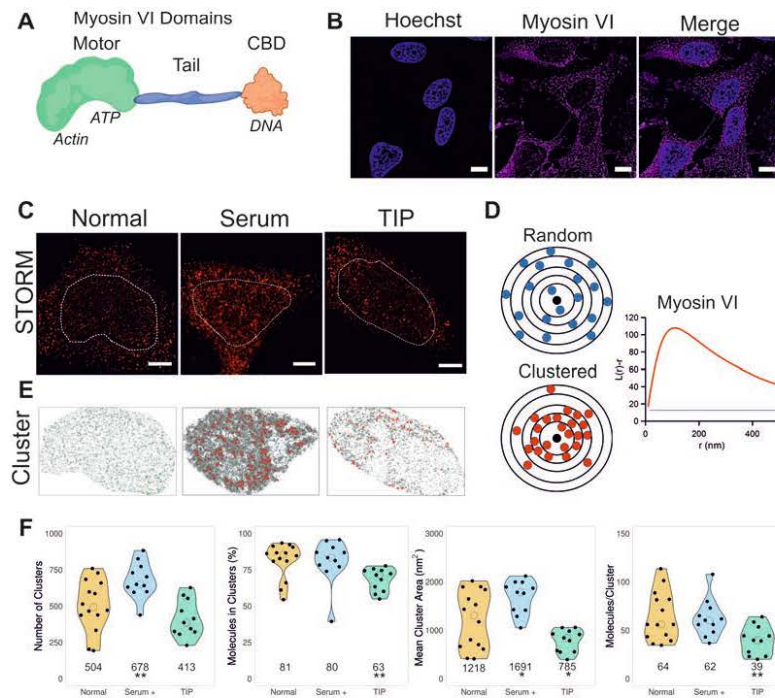


Figure 1 Nuclear organisation of myosin VI. (A) Cartoon depiction of the myosin VI domains and key features discussed in the text. The motor domain has ATPase activity regulates actin binding within the domain. The motor is connected to a cargo binding domain (CBD) in the myosin tail which has the ability to bind DNA. (B) Widefield Immunofluorescence staining against myosin VI (magenta) and DNA (cyan) in HeLa cells. Images were acquired at the mid-point of the nucleus (Scale bar 10 μm). (C) Example STORM render images of myosin VI under normal, serum- and TIP-treated conditions, as described in the Experimental Procedures (scale bar 2 μm). Dotted lines represent a region of interest (ROI) containing the nucleus which are taken forward for cluster analysis. The nucleus was identified using either Hoechst or RNAPII staining. (D) Depiction of molecular clustering and random distribution. We performed cluster analysis using the linearized form of Ripley's K function (Pageon et al., 2016) $L(r)-r$, where r is the radius. A plot of $L(r)-r$ versus r gives a value of zero for a random distribution (blue line), but deviates from zero, towards positive values, due to molecular clustering (red). The organisation of myosin VI is seen with a peak at 125 nm. (E) Cluster maps based upon the selected ROI in (c). Clusters are shown in green (Normal) or red (Serum and TIP treatment). (F) Cluster analysis of myosin VI nuclear organisation under normal, serum- and TIP-treated conditions. Individual data points correspond to the average value for a cell ROI ($n = 14$ for normal, 11 for serum- and TIP-treated). The values represent the mean from the ROIs for each condition (Only statistically significant changes are highlighted * $p < 0.05$, ** $p < 0.01$ by two-tailed t-test compared to normal conditions).

To further understand the functional relevance of the myosin VI-RNAPII co-localization, we stimulated transcription using serum (Figure 2D). Similar to myosin VI, there was a noticeable change in the RNAPII distribution. Serum stimulation led to an increase in cluster size and number of clusters of RNAPII, while the total number of molecules per cluster remained the same (Figure 2B). Moreover, we observed a significant increase in positive colocalization

between the clusters, where $31 (\pm 7) \%$ and $35 (\pm 6) \%$ of myosin VI and RNAPII colocalized, respectively (Figure 2C). Furthermore, comparison of colocalised and non-colocalised subpopulations showed that the synergy between the two proteins is maintained following serum stimulation (Supplementary Figure 1A and B).

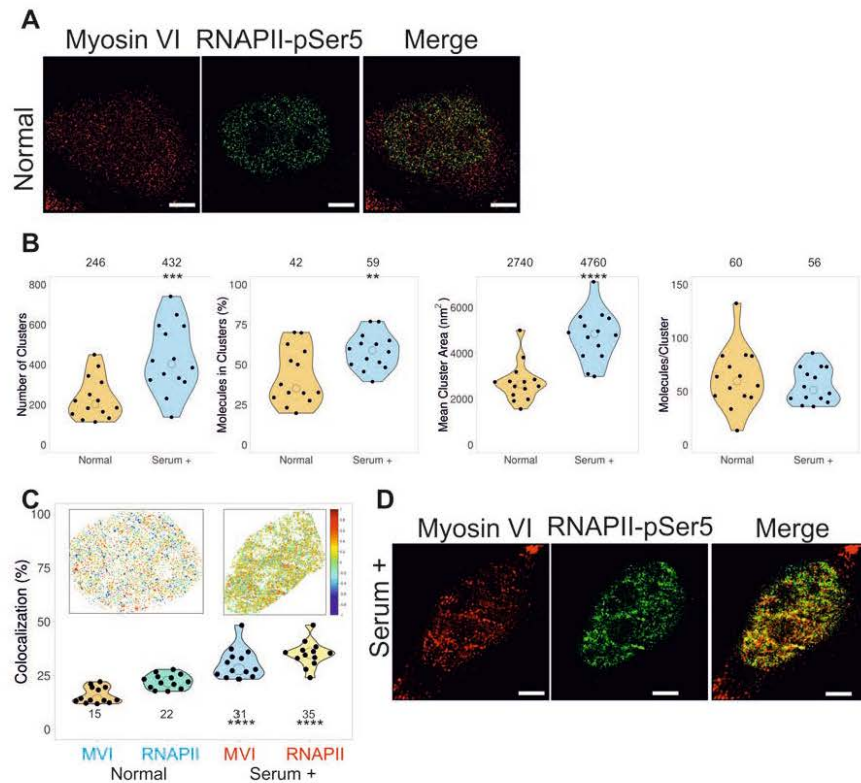


Figure 2 Nuclear organisation of RNAPII and colocalization with myosin VI. (A) Example STORM render image of myosin VI and RNAPII-pSer5 under normal conditions (scale bar 2 μ m). (B) Cluster analysis of RNAPII nuclear organisation under normal and serum-treated conditions. Individual data points correspond to the average value for a cell ROI (n=14). The values represent the mean from the ROIs for each condition. (Only statistically significant changes are highlighted $^{**}p < 0.01$, $^{***}p < 0.001$, $^{****}p < 0.0001$ by two-tailed t-test compared to normal conditions). (C) Colocalisation analysis of myosin VI (MVI) and RNAPII-pSer5 clusters under normal and serum-treated conditions. Inset is a representative cluster colocalization heatmap whereby values of 1 are perfectly colocalised and -1 are separated from each other. Individual data points represent the percentage of each protein which is colocalized and correspond to the average value for a cell ROI (n=13). The values represent the mean from the ROIs for each protein (Only statistically significant changes are highlighted $^{****}p < 0.0001$ by two-tailed t-test compared to normal conditions for each protein). (D) Example STORM render image of myosin VI and RNAPII-pSer5 under serum-treated conditions (scale bar 2 μ m).

Myosin VI regulates the spatial organisation of RNA Polymerase II.

After observing the correlation between RNAPII and myosin VI clustering, and building upon the established role of myosin VI in transcription, we wanted to explore how myosin VI activity may impact the spatial organisation of RNAPII which underpins mammalian gene expression.

Treatment with the myosin VI inhibitor TIP induced a significant disruption of the spatial distribution and organisation of RNAPII, whereby the protein was aggregated at the nuclear periphery, while it was significantly decreased in the centre of the nucleus (Figure 3A and Supplementary Figure 2A). Not surprisingly, based on the visual redistribution of RNAPII, parameters such as the number, size, area and number of molecules per cluster were significantly decreased, compared to normal conditions (Figure 3B). We also confirmed that, while TIP impacts the clustering activity of myosin VI (Figure 1C), it does not lead to protein degradation (Figure 3C). We therefore conclude that the motor activity of myosin VI is required for RNAPII clustering. To further support this finding, we performed siRNA transient knockdown of myosin VI (Figure 3C, Supplementary Figure 2B and 3). Similar to the effect of the inhibitor, absence of myosin VI had a significant impact on the RNAPII distribution (Figure 3A). Based on the number of localisations in the STORM imaging and western-blot analysis, we confirmed that the total amount of RNAPII-pSer5 did not change following either treatment (Figure 3D and E). Therefore, perturbation of myosin VI causes destabilisation of RNAPII clusters. Consistently, TIP treatment also led to a decrease in myosin VI-RNAPII colocalization (Supplementary Figure 1C). Overall, our data indicated a role for myosin VI in the nuclear organisation of RNAPII.

We next sought to establish whether the redistribution of RNAPII also correlated with its loss from chromatin. To this end, Chromatin Immunoprecipitation (ChIP) against RNAPII-pSer5 was performed under normal conditions and following TIP treatment. Indeed, myosin VI inhibition induced a decrease of several orders of magnitude in RNAPII occupancy from all tested loci (Figure 3F and G).

Both myosin VI knockdown and inhibition by TIP have an impact on the cytoplasmic and nuclear populations of myosin VI. To determine the specific role of the nuclear population of myosin VI in the spatial organisation of RNAPII, we transfected cells with NLS-tagged truncations of myosin VI, namely NLS-CBD (Cargo-binding domain) and NLS-Motor. Based on *in vitro*

transcription assays (Fili et al., 2017), over-expression of these constructs and their targeting to the nucleus was expected to have a dominant negative impact upon the endogenous nuclear myosin VI by displacing the protein. Indeed, similar to TIP treatment and myosin knockdown, over-expression of either construct disrupted the nuclear distribution of RNAPII, as observed by widefield microscopy (Supplementary Figure 4A and B). We therefore concluded that it is the nuclear pool of myosin VI that is directly involved into the nuclear organisation of RNAPII.

We next explored whether the impact of myosin VI on RNAPII is also dependent upon nuclear actin. It has been well-established that actin is bound to RNAPII (de Lanerolle, 2012, Fomproix and Percipalle, 2004, Kukalev et al., 2005) and nuclear actin was recently found to support clustering of RNAPII (Wei et al., 2020). The association of myosin VI to RNAPII is also actin-dependent, *in vitro* (Fili et al., 2017). Moreover, as previously mentioned, the effect of TIP also suggests that actin filaments are involved. We therefore performed two types of actin perturbation experiments: (a) Treatment with latrunculin B to prevent actin polymerisation, which would reveal whether actin polymers are important for transcription. (b) Transient expression of a nuclear targeted monomeric actin mutant, namely NLS-YFP-R62D-actin (Serebryanny et al., 2016). This mutant would bind to endogenous nuclear G-actin, thereby preventing its polymerisation. Both of these perturbations caused disruption of RNAPII organisation, revealing that polymerization of nuclear actin is critical to transcription (Figure 4A, 4B and Supplementary Figure 2C), as shown recently (Wei et al., 2020). Cluster analysis (Figure 4C) shows that all cluster parameters are significantly decreased in both conditions, as is the colocalization between myosin VI and RNAPII with latrunculin B (Supplementary Figure 1C). These results were also supported by the impact of latrunculin B treatment on the nuclear organisation of myosin VI. Similar to RNAPII, all clustering parameters for myosin VI were significantly decreased (Figure 4D), leading to a greater impact than TIP treatment (Figure 1). This suggests, that the nuclear roles of myosin VI involve its interaction with filaments or short polymers of actin. Overall, these results indicate that the myosin VI - actin interaction is required for the correct spatial organisation of RNAPII.

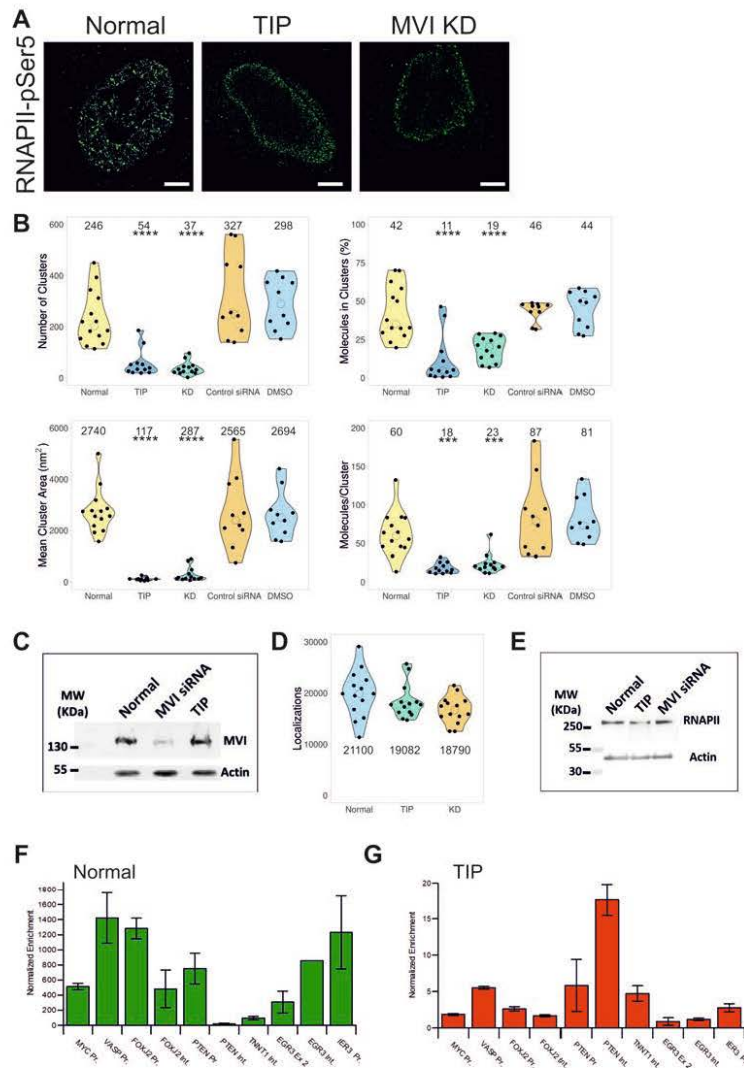


Figure 3 Spatial organisation of RNAPII depends upon MVI. (A) Example STORM render image of RNAPII-pSer5 under normal, TIP-treated and myosin VI (MVI) knockdown conditions (scale bar 2 µm). Further widefield example images are shown in Supplementary Figure 2A and B. (B) Cluster analysis of RNAPII nuclear organisation under the conditions described in (A). Individual data points correspond to the average value for a cell ROI (n=14 for normal, 12 for TIP, 13 for KD, 10 for Control siRNA and DMSO). The values represent the mean from the ROIs for each condition (Only statistically significant changes are highlighted ***p < 0.001, ****p < 0.0001 by two-tailed t-test compared to normal conditions). (C) Western-blot against MVI under normal, MVI-knockdown and TIP-treated conditions. Example widefield images of myosin VI under knockdown conditions are shown in Supplementary Figure 3. (D) Number of localisations of RNAPII-pSer5 under the different conditions. Individual data points correspond to the value for a cell ROI (n=14). The values represent the mean from the ROIs for each condition. (E) Western-blot against RNAPII-pSer5 under normal, TIP-treated and MVI knockdown conditions. (F) RNAPII-pSer5 ChIP against labelled loci. Values are the average of two independent experiments. Error bars represent SEM from two independent experiments. (G) RNAPII-pSer5 ChIP against labelled loci following TIP-treatment. Values are the average of two independent experiments. Error bars represent SEM from two independent experiments.

Myosin VI controls the nuclear dynamics of RNA Polymerase II.

Having revealed the role of myosin VI in the nuclear organisation of RNAPII, we then assessed its role in the dynamics of RNAPII in living cells to understand the assembly of the transcription factories.

To achieve this, we performed single molecule tracking of Halo-tagged or SNAP-tagged Rbp1, the largest RNAPII subunit, using an aberration-corrected multi-focal microscope (acMFM) system (Abrahamsson et al., 2013) (Figure 5A). This technique allows the simultaneous acquisition of 9 focal planes covering 4 μm in the z axis, with a 20 x 20 μm field of view, which is essentially the size of the HeLa cell nucleus. In this way, we were able to observe and track the 3D dynamics of RNAPII across the whole nucleus, in live cells (Figure 5B). Clustering of RNAPII was not observed in these live cell

experiments due to the low labelling density required in order to achieve single-molecule detection in the crowded nuclear environment. Moreover, all populations of RNAPII were visible, compared to solely the pSer5 population in the STORM measurements. We observed pools of spatially confined RNAPII molecules and pools of molecules diffusing freely within the nucleus (Figure 5C). We determined the diffusion constant for each track by measuring the Mean Squared Displacement (MSD) and then plotted the average diffusion constant per cell (Figure 5D). Under normal conditions, we found that, on average, RNAPII diffuses relatively slowly ($0.41 \mu\text{m}^2 \text{s}^{-1}$) and this decreases further during transcription stimulation ($0.35 \mu\text{m}^2 \text{s}^{-1}$).

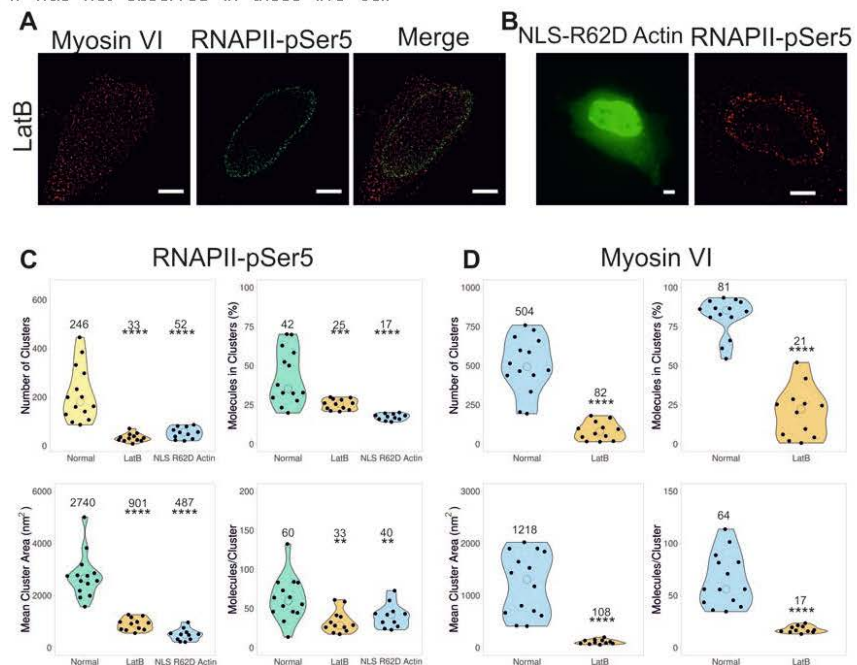


Figure 4 Impact of nuclear actin upon the organisation of RNAPII. (A) Example STORM render image of myosin VI and RNAPII-pSer5 following treatment with Latrunculin B (LatB), as described in the methods (scale bar 2 μm). Further widefield example images are shown in Supplementary Figure 2C. (B) (left) Example widefield image of YFP-NLS-R62D actin following transfection. (right) Example STORM render image of RNAPII-pSer5 following transfection of YFP-NLS-R62D actin (scale bar 2 μm). (C) Cluster analysis of RNAPII-pSer5 nuclear organisation following treatment with LatB (n=12) or transfection with YFP-NLS-R62D Actin (n=11). (D) Cluster analysis of myosin VI nuclear organisation following treatment with LatB (n=12). Individual data points correspond to the average value for a cell ROI. The values represent the mean from the ROIs for each condition (Only statistically significant changes are highlighted **p < 0.01, ***p < 0.001, ****p < 0.0001 by two-tailed t-test compared to normal conditions).

When we interrogate the individual tracks for each cell, we observed several populations of RNAPII which we termed as (i) static $D < 0.1 \mu\text{m}^2 \text{s}^{-1}$, (ii) diffusive $0.1 > D < 5 \mu\text{m}^2 \text{s}^{-1}$ and (iii) hyper mobile (not quantified) (Figure 5E). These findings are consistent with the previous reports using this technique (Abrahamsson et al., 2013). To further investigate RNAPII dynamics, the total numbers of static ($< 0.1 \mu\text{m}^2 \text{s}^{-1}$) and mobile ($> 0.1 \mu\text{m}^2 \text{s}^{-1}$) RNAPII molecules were plotted as a ratio (Figure 5F). Under normal conditions, just over half of the RNAPII population (52%) was static, probably corresponding to molecules confined at sites of transcription activation. Interestingly, this value was similar to the percentage of RNAPII molecules in clusters detected by STORM.

Similar to the STORM experiments, we then observed the dynamics of RNAPII following TIP treatment, siRNA knockdown of myosin VI and actin perturbations. These treatments led to a 2-fold increase in the RNAPII average diffusion constant (Figure 5D) and 3 to 4-fold increase in the motile fraction (Figure 5F). Visually, the impact was also clear and could be observed through the loss of spatially confined molecules and the gain of diffusive tracks (Figure 5B). This was further quantified by plotting the anomalous diffusion alpha values whereby TIP treatment leads to an increase in freely diffusing species (Supplementary Figure 5A). In order to assess whether TIP has a global impact on molecular diffusion in the nucleus, we transiently expressed an isolated SNAP-tag domain to act as a diffusion reporter for the nuclear environment (Supplementary Figure 5B). We would not expect any impact on the diffusion of this isolated protein domain when cells are treated with TIP. Indeed, no changes were observed, confirming that the detected changes in RNAPII behaviour relate solely to the activity of myosin VI. We also observed the RNAPII dynamics in cells transiently expressing the dominant negative NLS-motor and NLS-CBD constructs. Consistent with the effect of TIP and myosin VI knockdown, there was an almost 2-fold increase in RNAPII diffusion in both cases, as well as an increase in the motile fraction of RNAPII (Figure 5D and F). This increased mobility of RNAPII following perturbation of myosin VI would be expected to lead to a decrease in the number of clusters, which is what we observed with the STORM measurements. Moreover, the greater mobility of RNAPII would also account for its relocation to the nuclear periphery, where it may non-specifically associate with the nuclear membrane or lamina. Overall, our observations suggest a model whereby myosin VI stabilises the RNAPII at sites of transcription initiation.

Finally, we also explored the nuclear dynamics of myosin VI and its interplay with RNAPII (Figure

5G). Overall, myosin VI is relatively static, with a mean diffusion constant of $0.4 \mu\text{m}^2 \text{s}^{-1}$. However, treatment with TIP, or perturbation of actin, resulted in an increased mean diffusion to approximately $1 \mu\text{m}^2 \text{s}^{-1}$, which is consistent with the STORM measurements, that show a reduction in clustering behaviour. Interestingly, a 2-fold increase in mean myosin VI diffusion was observed when cells were treated with the RNAPII inhibitor α -amanitin, that inhibits transcription through RNAPII degradation. The impact of RNAPII on myosin VI dynamics indicates a two-way communication between the two proteins, as it would be expected for two interacting molecules.

RNA Polymerase II spatial distribution is coupled to transcription activity.

We then explored the impact of the perturbed nuclear organisation of RNAPII on the underlying chromatin which could fundamentally alter the cellular properties. We performed a high-content screening assay, using antibodies against histones H3K9ac and H3K27ac, positive epigenetic marks of active gene expression, and H3K9me3, a mark of repressed transcription (Wang et al., 2008). Fluorescent intensity was used as a readout for the level of each marker in cells grown under normal conditions and upon treatment with TIP (Figure 6A). Treatment with TIP led to a decrease in active transcription markers by 35% and 10% for H3K9ac and H3K27ac, respectively, and an increase in the repressive marker H3K9me3 by 100% (Figure 6B). To assess the overall impact on cell function, we performed live-cell growth assays under normal and myosin VI knockdown conditions. A 3-fold decrease in growth was observed following knockdown (Figure 6C). The increase in growth rate after 3 days is consistent with the end of the transient knockdown. Overall, this change is indicative of a larger cellular response to the perturbation of RNAPII and the resulting decrease in gene expression.

To explore the global changes in gene expression, RNA-seq measurements were performed under normal and myosin VI knockdown conditions. In total, we observed a significant change in the expression of 1947 genes ($\text{Log}_2 \text{FC} > 0.5$ or < -0.5 with adjusted p value < 0.05). From this set, 489 genes were up-regulated and 1458 were down-regulated (Figure 7A), which highlights the extensive negative impact on transcription due to the disruption of myosin VI. This is consistent with the STORM data that demonstrated disruption of the spatial organisation of RNAPII under these conditions (Figure 3A and 3B). The down-regulated genes were taken forward to Gene Ontology analysis.

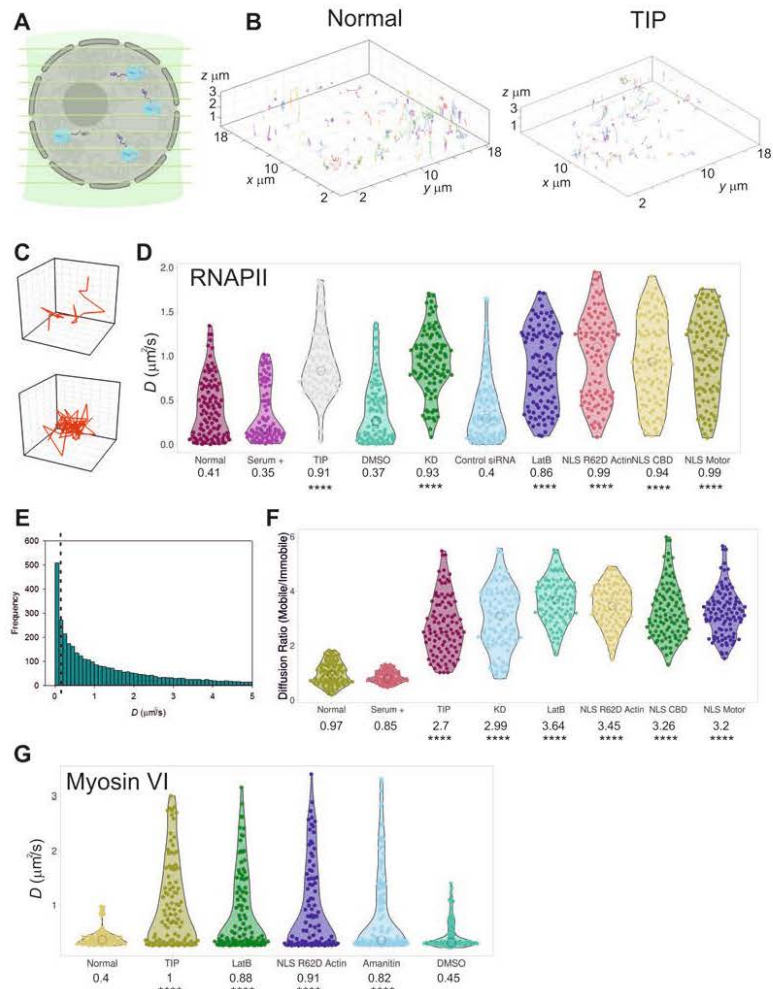


Figure 5 Live cell single molecule dynamics of RNAPII. (A) Cartoon depicting simultaneous acquisition of 9 focal planes covering 4 μm to perform live cell 3D single molecule tracking of RNAPII. (B) Example render of 3D single molecule trajectories under normal and TIP-treated conditions. (C) Example of trajectory of a diffusive and spatially confined molecule which can be identified in (B). (D) Plot of Halo-RNAPII or SNAP-RNAPII diffusion constants under the stated conditions derived from fitting trajectories to an anomalous diffusion model, as described in methods. NLS-R62D Actin, NLS CBD and NLS Motor refer to tracking of RNAPII following transfection of these constructs. NLS CBD and NLS motor were transfected in to SNAP-RNAPII cells. Individual data points correspond to the average value for a cell ROI (n = 100). The values represent the mean from the ROIs for each condition (Only statistically significant changes are highlighted ****p <0.0001 by two-tailed t-test compared to normal conditions). (E) Example histogram of diffusion constants arising from a single cell. The dotted line represents the threshold applied to segregate static and dynamic molecules. (F) Using the threshold defined in (e), trajectories were plotted as a ratio of mobile and immobile species. Individual data points correspond to the average value for a cell ROI. The values represent the mean from the ROIs for each condition (Only statistically significant changes are highlighted ****p <0.0001 by two-tailed t-test compared to normal conditions). (G) Plot of Halo-myosin VI diffusion constants under the stated conditions derived from fitting trajectories to an anomalous diffusion model, as described in methods. Individual data points correspond to the average value for a cell ROI (n = 100). The values represent the mean from the ROIs for each condition (Only statistically significant changes are highlighted ****p <0.0001 by two-tailed t-test compared to normal conditions).

The breakdown for GO Biological Process reveals that affected genes are significantly enriched to processes such as "Regulation of signalling", "Regulation of cell communication", "Response to stimulus" and "Regulation of cell proliferation" (Figure 7B and Supplementary Table 1). Overall, the majority of the processes affected are coupled to cell response pathways, rather than to housekeeping ones. Hence, disruption of myosin VI perturbs expression of specific genes, but it does not completely halt transcription.

We observed that transcription stimulation with serum had a significant impact on the nuclear organisation of both myosin VI and RNAPII (Figure 1 and 2). Interestingly, the RNA-seq data also revealed that, out of 22 serum-responsive genes, two thirds were down-regulated when myosin VI was perturbed (Figure 7C). To investigate the role of myosin VI under conditions of transcription stimulation, we performed serum stimulation on cells where myosin VI had been knocked down. We then used RT-qPCR to monitor the expression of serum responsive

genes. Control measurements showed that serum stimulation increases the expression of CDC42BPA, TNNT1, EGR3, INHA and VASP genes (Figure 7D). In all cases, knockdown of myosin VI completely abrogated this response. Taken together, the data shows that perturbation of myosin VI, which impacts the spatial organisation of RNAPII, impedes gene expression under stimulatory conditions. Therefore, myosin VI is critical for the cell's response to stimulus.

Myosin VI acts as a molecular anchor

We have revealed that myosin VI is a key regulator of RNAPII spatial organisation. However, how mechanism governing how myosin VI achieves this fundamental role is unknown. Based on previously conducted biochemical analysis, we hypothesised that myosin VI is bound to chromatin and/or transcription regulators through its CBD, and to RNAPII through actin (Fili et al., 2017).

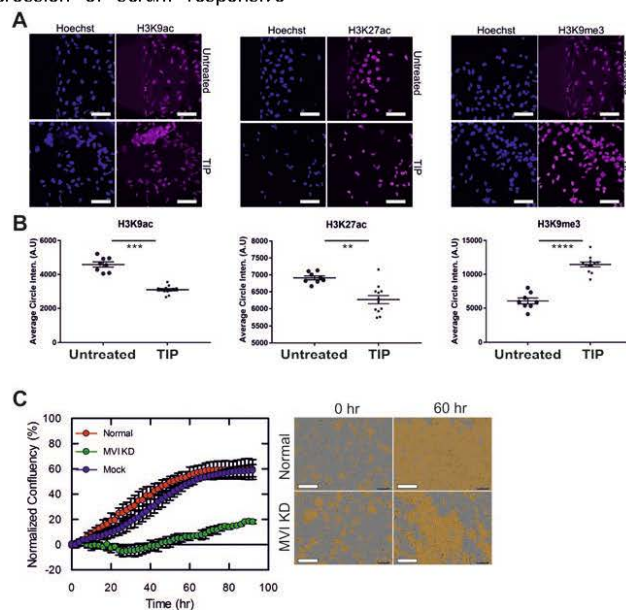


Figure 6 Perturbation of myosin VI impacts chromatin organisation and cell growth. (A) Example widefield Immunofluorescence staining against stated histones (magenta) and DNA (blue) in HeLa cells under normal and TIP-treated conditions (scale bar 100 μ m). (B) The fluorescence intensity within the nucleus was measured for each histone marker under untreated and TIP-treated conditions, and each data point represents the average from a minimum of 1000 nuclei (Only statistically significant changes are highlighted **p <0.01, ***p <0.001, ****p <0.0001 by two-tailed t-test compared to untreated conditions). (C) Real-time growth of HeLa cells (red) and corresponding measurements following myosin VI (MVI) siRNA knockdown (green) and mock transfection control (blue). Data represent three independent measurements and error bars show SEM. Example images at start and 60 hr time points are shown (scale bar 300 μ m in all images).

Myosin VI is a rare motor protein with the ability to switch from a motile state to a molecular anchor, when forces greater than 2pN are applied to the molecule (Altman et al., 2004). This property prevents the unwanted dissociation from actin by increasing the affinity of the interaction. RNAPII is a large macromolecular machine which could diffuse or potentially move along DNA, away from transcription initiation sites. Such a movement would apply load upon myosin VI and then trigger the motor protein to anchor RNAPII *in situ*. To test this hypothesis, we set out to disrupt the ability of myosin VI to respond to force. To achieve this, we inserted a molecular spring consisting of a repeated penta-peptide sequence from spider-silk flagelliform into the myosin VI tail (Figure 8A). The repeat sequence has been widely used as a calibrated tension sensor (Grashoff et al., 2010). The spring unfolds as tension up to 10 pN is exerted across the

molecule (Grashoff et al., 2010), thereby preventing load-induced changes on myosin VI. Therefore, this myosin VI construct should not be responsive to force up to 10 pN.

We first explored the impact of the insertion upon the biochemical properties of myosin VI. Firstly, CD spectroscopy confirmed that the recombinant protein is folded and stable (Supplementary Figure 6A), similar to wild type (WT) myosin VI (Supplementary Figure 6B). Moreover, the actin-activated ATPase activity was not affected by the presence of the insert, with k_{cat} 5.9 s^{-1} and 5.5 s^{-1} for myosin VI spring and WT, respectively (Supplementary Figure 6C). To assess whether the spring insert disrupts the load-induced anchoring ability in myosin VI, we then compared the ATPase rate of two stable dimeric constructs of the protein, one containing and one lacking the insert.

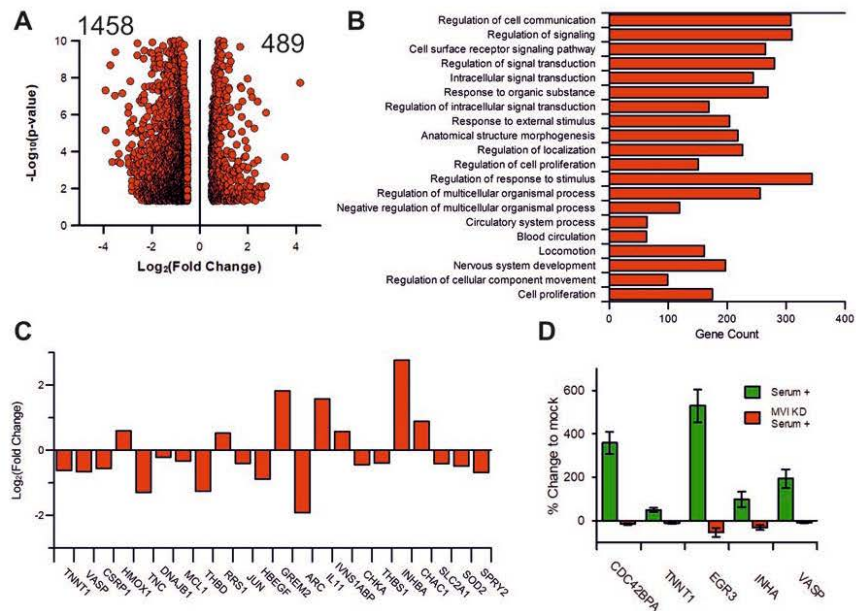


Figure 7 Impact of myosin VI perturbation on gene expression. (A) Volcano plot of differentially expressed genes following myosin VI knockdown. (B) GO terms, with gene count, for Biological Process corresponding to the genes negatively expressed following myosin VI knockdown. GO Terms are plotted based on significant enrichment, as shown in Supplementary Table 1. (C) Plot of gene expression changes for serum-responsive genes within the list of differentially expressed genes following myosin VI knockdown. (D) RT-qPCR Gene expression analysis of 5 serum-responsive genes with treatment of serum alone, or serum following a myosin VI (MVI KD) knockdown. Data are plotted relative to non-stimulated expression from three independent experiments. Error bars represent SEM from three independent experiments.

The stable dimeric myosin VI, in which a leucine zipper replaces the myosin VI C-terminal domain at residue 920 to dimerize the protein, has been widely used in myosin VI studies (Große-Berkenbusch et al., 2020, Mukherjea et al., 2014, Mukherjea et al., 2009, Park et al., 2006, Phichith et al., 2009). We first confirmed that the spring dimeric construct is indeed dimeric, as shown by a similar size-exclusion chromatography elution profile to wild type dimeric myosin VI (Supplementary Figure 6D).

As previously observed (Sweeney et al., 2007), the dimeric form of myosin VI displayed gating ATPase activity, whereby only one motor domain within the dimer hydrolyses ATP at a given point. Therefore, the observed ATPase rate was half of that of the monomeric myosin VI (k_{cat} 2.84 s⁻¹), as seen in Supplementary Figure 6C. This gating behaviour results from load-induced conformation changes: the conformation of the leading motor is in a state which prevents ADP dissociation and therefore remains bound to actin (Altman et al., 2004). However, the insertion of the spring within the dimer construct showed an ATPase rate 4.9 s⁻¹, which is similar to that of the monomeric myosin VI (Supplementary Figure 6C). This suggests the two motor domains are functioning independently. We propose that the spring-induced flexibility and the resulting inability to respond to load prevents the communication between the leading and the rear motor domains within the dimer.

Having assessed the biochemical properties of the spring construct, we transiently overexpressed it into mammalian cells where endogenous myosin VI had been knocked down (Figure 8B and Supplementary Figure 6E). The spring construct was localised throughout the cytoplasm and the nucleus. We then assessed the ability of the spring construct to rescue the disrupted RNAPII nuclear organisation, in comparison to the transiently overexpressed wild type myosin VI. Unlike wild type myosin VI (Figure 8B), the spring construct was unable to fully rescue the RNAPII nuclear distribution. As demonstrated by the STORM imaging and cluster analysis (Figure 8C and D), this partial rescue was evidenced in terms of number of clusters, cluster area and molecules per cluster. These results suggest that the ability of myosin VI to respond to force is required for rescuing the disrupted RNAPII distribution. In further support of this, the over-expression of wild type myosin VI was not only able to rescue RNAPII distribution, but to also increase RNAPII clusters number, size and percentage of molecules in clusters (Figure 8C and D). A possible explanation for the partial rescue by the spring construct could be that, at selected locations within the nucleus, the forces

exerted upon myosin VI exceed the 10 pN limit, above which the spring insert would be fully unfolded and therefore responsive to forces and able to anchor. Therefore, we propose that the force-induced anchoring ability of myosin VI is critical for the nuclear organisation of RNAPII and that myosin VI physically holds RNAPII at sites of transcription initiation.

DISCUSSION

Following a multidisciplinary approach, we have been able to shed light on to the regulation of transcription by addressing how the spatial organisation of transcription factories is achieved and the role of nuclear myosins in this process. We have observed that the molecular motor myosin VI is clustered within the nucleus and we showed that this activity is linked to the spatial organisation of RNAPII into transcription factories. We have also been able to show that the spatial and dynamic changes in RNAPII behaviour are dependent upon myosin VI and relate to wider chromatin and transcriptome changes.

For over a decade, myosin VI has been linked to transcription (Cook et al., 2018, Fili et al., 2020, Fili et al., 2017, Große-Berkenbusch et al., 2020, Vreugde et al., 2006) and here we have gained further understanding of its nuclear function, including its interaction with nuclear receptors and DNA (Fili et al., 2017). Furthermore, until now, it has not been possible to determine the precise role that myosin VI plays in this vital process and why the properties of a myosin would be required for transcription. As with many nuclear proteins (Carmo-Fonseca, 2002, Cook, 2010, Cremer et al., 2006, Verschure et al., 1999), we have shown that myosin VI forms molecular clusters, possibly to enhance its activity and the efficiency of biochemical processes. The formation of these clusters is ATP and actin-dependent and, therefore, relies on the motor properties of myosin VI. Here, we have dissected the molecular mechanistic need for myosin VI to be capable of switching from a transporter to an anchor in a force induced manner. Therefore, we have been able to directly address why a nuclear myosin, with its biophysical properties to sense and respond to force, is required in transcription in order to hold RNAPII *in situ*.

Overall, we present a model, whereby myosin VI anchors RNAPII at, or near, sites of transcription initiation (Figure 9) within the nucleus. This approach could enable enhanced RNAPII binding to initiate transcription and facilitate rapid recycling of RNAPII to drive higher expression levels.

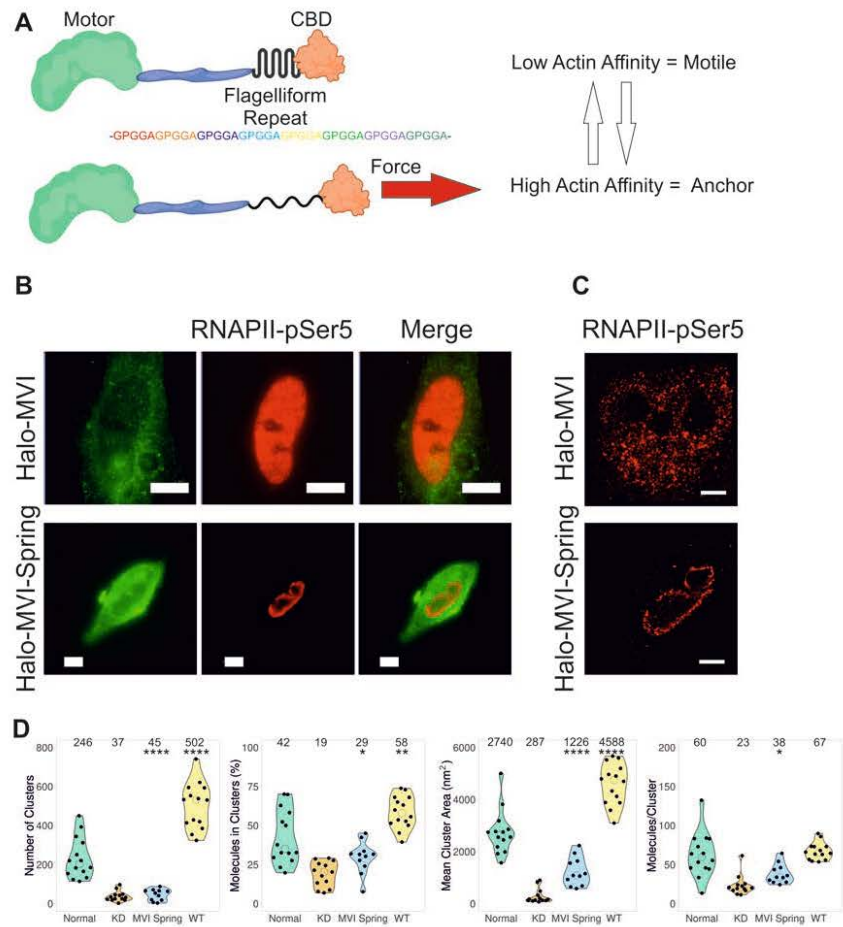


Figure 8 Myosin VI anchors RNAPII at transcription sites. (A) Cartoon depiction of myosin VI (MVI) containing the molecular spring (Flagelliform repeat) inserted proximal to the CBD. At low force, the spring is folded and myosin VI is in a low actin affinity mode. The application of force leads to extension of the spring which triggers the high affinity actin binding mode. (B) Example widefield imaging of Halo-MVI and Halo-MVI-spring stained with JF549 (green) and corresponding immunofluorescence staining against RNAPII-pSer5 (red) in HeLa cells (Scale bar 10 μ m). Further example images are in Supplementary Figure 6E. (C) Example STORM render image of RNAPII-pSer5 following transfection of Halo-MVI and Halo-MVI-spring, as described in the methods (scale bar 2 μ m). (D) Cluster analysis of RNAPII-pSer5 nuclear organisation following treatment in (c). WT refers to Halo-MVI transfection. Individual data points correspond to the average value for a cell ROI. (n = 14 for Normal, 13 for KD, 11 for MVI Spring and 14 for WT) The values represent the mean from the ROIs for each condition (Only statistically significant changes are highlighted *p < 0.05, **p < 0.01, ****p < 0.0001 by two-tailed t-test compared to normal conditions).

Such a mechanism would also fit with the observation that myosin VI functions in gene pairing (Zorca et al., 2015). We have previously shown that myosin VI interacts with RNAPII through actin (Fili et al., 2017), present within the RNAPII complex. Given that the interaction of myosin VI with nuclear receptors and DNA is

mediated by its CBD, we propose that myosin VI could be bound to DNA and/or transcription regulators via the CBD, whilst simultaneously interacting with RNAPII through actin. We propose that the myosin VI orientation is critical to enable force-induced anchoring of RNAPII. These results are consistent with recent reports of

nuclear actin clustering during transcription stimulation (Wei et al., 2020). Interestingly, myosin VI is the only actin minus-end motor protein, therefore actin polymerizing from these

sites of transcription would also provide a framework to recruit myosin VI to these sites and subsequently to RNAPII.

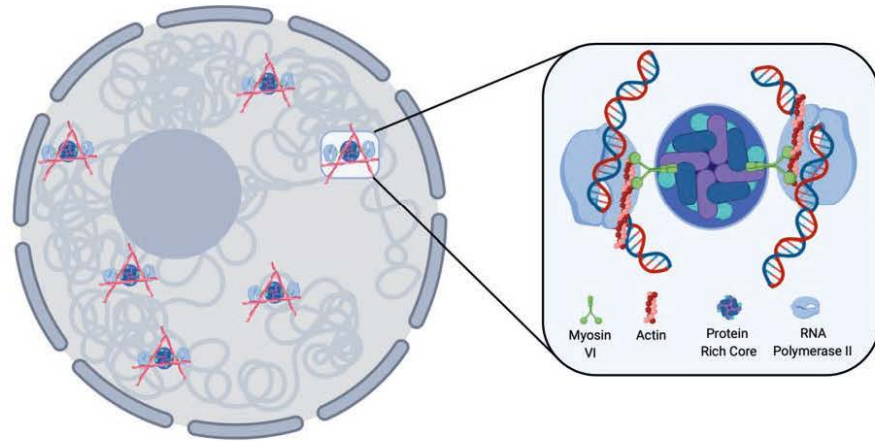


Figure 9 Schematic of myosin VI anchoring RNAPII at transcription factories. Based on the data presented here we can propose this model for RNAPII clustering. Transcription sites within the nucleus are marked by clustering of RNAPII and actin filaments. Focusing on the clusters: The protein rich core consists of transcription regulators which the DNA would also contact. Myosin VI interacts with these proteins and DNA via its C-terminal domain. Myosin VI then interacts with RNAPII through nuclear actin filaments thereby providing a framework for mechanical linkage to RNAPII.

It would be interesting to address whether RNAPII moves along the DNA, or whether DNA is trafficked through the factories. Published ChIP data (Vreugde et al., 2006) showed that myosin VI is present throughout the gene body. Based on the clustering behaviour of myosin VI and our model, we would expect DNA to be trafficked through these static factories. Maintaining the interaction would support rapid recycling of RNAPII, as mentioned above.

Nuclear Myosin I, has a well-established role in transcription and this family of myosins is also capable of acting as force-induced anchors (Greenberg and Ostap, 2013). It remains to be explored if both proteins interact with RNAPII simultaneously to stabilise the complex or if, conversely, the different myosin proteins interact with distinct populations of RNAPII. Overall, it would not be surprising if nuclear myosins are deployed in a similar way in other nuclear processes such as DNA repair, where myosin proteins are also known to function (Caridi et al., 2018, Kulashreshtha et al., 2016, Venit et al., 2020).

Upon perturbation of myosin VI, RNAPII was observed around the nuclear periphery, which highlights the key role of myosin VI in maintaining the nuclear organisation of RNAPII. The basis for

this localisation is not yet clear, but we can postulate two mechanisms. The protein may be en-route for nuclear export as part of a degradation process which initiates once transcription is disrupted (Muratani and Tansey, 2003). Alternatively, RNAPII may be excluded from the chromatin body as DNA condensation takes place, through the increase of repressive transcription histone markers. This would assume that the loss of transcription triggers a default to a repressive marker. In this manner, the now highly dynamic RNAPII would move into less dense chromatin regions, which may speculatively be present at the periphery. Moreover, an increase in chromatin condensation would further increase RNAPII dynamics, by reducing RNAPII interacts with DNA and lead to an increase in non-specific interactions. In our model, myosin VI anchoring would also lead to a reduction in these non-specific interactions by holding the complex at the active regions.

The ability of RNAPII to cluster has been shown to be important for transcription (Cho et al., 2016a, Cho et al., 2016b). Our findings further support this, given the disruptive effect of myosin VI perturbation on the organisation of RNAPII and, subsequently, on transcription. The simultaneous expression of genes from a single

transcription factory ensures that numerous proteins required for a specific pathway are efficiently produced in a co-ordinated fashion. Clustering of RNAPII has been shown to be dynamic with structures lasting around 10 seconds (Cho et al., 2016a, Cho et al., 2016b) and myosin VI has also been shown to display dynamic binding (up to 20 seconds) (Große-Berkenbusch et al., 2020). We therefore conclude that there is likely to be turnover of proteins within these clusters, however we suggest that myosin VI enhances the RNAPII binding time to enable transcription initiation. Phase separation drives the formation of membraneless compartments through cooperative interactions between molecules (Hnisz et al., 2017). This process has been shown to contribute to the regulation of transcription, with impacts upon enhancers, mediators and the RNAPII C-Terminal-Domain (Boehning et al., 2018, Cho et al., 2018, Sabari et al., 2018). In contrast, our results suggest there are underlying mechanical processes contributing to the establishment of transcription factories with regard to RNAPII. Importantly, phase separation observations are still consistent with our conclusions because these processes can occur locally within the factories and may contribute to larger genomic rearrangements by bringing chromatin to the factories.

The formation of transcription factories has been proposed to be linked to transcription stimulation events. According to our model, we expect the need for myosins to be deployed in conditions of high transcriptional load to increase activate and/or recycling of RNAPII. Indeed, our RNA-seq analysis suggests that myosin VI plays a key role during stimulation and the downstream cell response processes. We therefore propose that the function of myosin VI is particularly critical when cells are under high transcription load and undergo rapid changes in the gene expression landscape. This is consistent with previous observations of myosin VI being over-expressed in several cancers, along with interacting with nuclear receptors and participating in the expression of target genes (Dunn et al., 2006, Loikkanen et al., 2009, Puri et al., 2010, Wang et al., 2016, Wang et al., 2015, Wollscheid et al., 2016).

With regard to the factories, various key questions remain unanswered, for instance how the clustering sites are selected and how they are brought together? What is the internal structure of the clusters with regard to positioning of myosin VI, RNAPII, DNA and transcription factors? Although processes such as chromatin condensation and genome organisation such as Topologically Associating Domains, could play a role in dictating where the clustering sites form,

the underlying mechanism remains elusive. Myosin VI has been shown to interact with nuclear receptors therefore it could be that myosin VI is recruited to these binding sites and clusters subsequently build around these locations. Loop exclusion may then have the ability to cluster local sites together (Schoenfelder and Fraser, 2019). Moreover, as it has been proposed (Große-Berkenbusch et al., 2020), we could speculate that the cargo transportation ability of nuclear myosins, including myosin VI, could be harnessed in combination with actin filaments, in order to bring genes together across large distances. Understanding the internal organisation of the clusters would require high-resolution structure characterisation in the cell and with reconstituted complexes.

In summary, we have investigated the function of nuclear myosin VI and uncovered a fundamental role in the spatial organisation of gene expression. This appears to be critical for transcription stimulation events where multiple genes are simultaneously expressed and cells rapidly adapt to environmental changes.

ACKNOWLEDGEMENTS

We thank the UKRI-MRC (MR/M020606/1), UKRI-STFC (19130001) and the Royal Society (IES/R3/183138) for funding to C.P.T. ERC StG 637987 and SPP 2202 GE 2631/1-1 for funding to J.C.M.G. Aberration-corrected multi-focal microscopy was performed in collaboration with the Advanced Imaging Center at Janelia Research Campus, a facility jointly supported by the Howard Hughes Medical Institute and the Gordon and Betty Moore Foundation. We also thank Darren Griffin (University of Kent) and Alessia Buscaino (University of Kent) for sharing of equipment, and Satya Khuon (Janelia Research Campus) for assisting with cell culture. JF549 dyes were kindly provided by Luke Lavis (Janelia Research Campus). We also thank grant from NYU Abu Dhabi, The Swedish Research Council and Cancerfonden to P.P. and we acknowledge technical help from the NYU Abu Dhabi Center for Genomics and Systems Biology, in particular Marc Arnoux and Mehar Sultana. We appreciate the computational platform provided by NYUAD HPC team and are especially thankful to Nizar Drou for technical help.

AUTHOR CONTRIBUTIONS

C.P.T. conceived the study. Y.H-G., N.F., A.dS., R.E.G., A.W.C. and C.P.T. designed experiments. N.F., Y.H-G. and C.P.T. designed and cloned constructs. Y.H-G., A.G-B. and J.C.M.G. created cell lines. Y.H-G., N.F., A.dS. and C.P.T. performed single molecule imaging experiments. Imaging was supported by L.W., M.M-F. and J.A. Y.H-G., A.W.C., T.V., and P.P. performed and analyzed the genomics experiments. N.F., R.E.G., H.C.W.R. and C.P.T. expressed, purified and performed experiments with recombinant proteins. L.W., J.A., E.W., T-L.C., A.dS. and C.P.T. contributed to single molecule data

analysis. C.P.T. supervised the study. C.P.T. wrote the manuscript with comments from all authors.

Competing financial interests: The authors declare no competing financial interests.

EXPERIMENTAL PROCEDURES

Constructs

A list of constructs are provided in Supplementary Table 2. Constructs generated in this work are described below. Halo or SNAP tags were used through to provide a specific protein labeling strategy for live cells (Toseland, 2013). The SNAP-Rpb1 construct was generated by sub-cloning the SNAP tag from the pSNAP-C1 plasmid (Addgene 58186) into the NheI and SacII of the pHalo-Rpb1 plasmid (A gift from Darzacq lab), following removal of the Halo tag. pcDNA3.1 Halo-MVI, pcDNA3.1 Halo-MVI-Spring, pFastbac Halo-MVI-Spring, and pFastbac Halo-MVI-Spring bZip were ordered as synthetic constructs.

Protein Expression using Baculovirus system

Full-length MVI NI, MVI Spring, MVI Spring bZip (1-914) and *Xenopus* calmodulin were expressed in *Sf9* and *Sf21* (*Spodoptera frugiperda*) insect cells using the Bac-to-Bac® Baculovirus Expression System (Invitrogen). *Sf9* cells were cultured in Sf900 media (Gibco). Recombinant bacmids were generated following the manufacturer's instructions and were transfected into adherent *Sf9* cells to generate the P1 viral stock. *Sf9* cells were infected in suspension at 27°C and 100 rpm with 1 in 50 dilution of P1 and P2 viral stocks to yield P2 and P3 stocks, respectively. Finally, expression of recombinant proteins was set up by infecting *Sf21* cells with the P3 viral stock in Spodopan media (PAN Biotech). To ensure correct folding of the myosin VI constructs, cells were simultaneously infected with P3 viral stock of the myosin VI constructs together with calmodulin at a 0.75 ratio. The cells were harvested after 3 days by centrifugation for 15 min at 700xg and at 4 °C and resuspended in ice cold myosin extraction buffer (90 mM KH₂PO₄, 60 mM K₂HPO₄, 300 mM KCl, pH 6.8), supplemented with Proteolock protease inhibitor cocktail (Expedeon) and 100 μM PMSF, before proceeding to protein purification. Prior to sonication, an additional 5 mg recombinant calmodulin was added together with 2 mM DTT. After sonication, 5 mM ATP and 10 mM MgCl₂ were added and the solution was rotated at 4 °C for 30 min before centrifugation (20,000g, 4°C, 30 min). Then, the cell lysate was subjected to the purification. Proteins were purified by affinity chromatography (HisTrap FF, GE Healthcare). The purest fractions were further purified through a Superdex 200 16/600 column (GE Healthcare).

Cell culture and Transfection

HeLa (ECACC 93021013) cells were cultured at 37°C and 5% CO₂ in Gibco MEM Alpha medium with GlutaMAX (no nucleosides), supplemented with 10% Fetal Bovine Serum (Gibco), 100 units/ml penicillin and 100 μg/ml streptomycin (Gibco). For the transient expression of myosin VI and mutants, HeLa cells grown on glass coverslips were transfected using Lipofectamine 2000 (Invitrogen), following the manufacturer's instructions. Depending on the

construct, 24 h - 72 h after transfection, cells were subjected to nuclear staining using Hoechst 33342 (Thermo Scientific), fixed and analysed or subjected to indirect immunofluorescence (see below).

Cell Treatments

For MVI knock-down experiments, HeLa cell monolayers, seeded to 30 – 50 % confluency, were transfected with human myosin VI siRNA duplex (5'GGUUUAGGUGUUAUGAAGtt-3') (Ambion) or AllStars Negative Control siRNA duplex (Qiagen) at a concentration of 50 nM, using Lipofectamine 2000 (Invitrogen), according to the manufacturer's guidelines. Cells were fixed or harvested after 48 h for further analysis. To inhibit myosin VI, cells were treated with 25 μM TIP (Sigma) for 1 h at 37 °C. To inhibit actin polymerization, cells were treated with 1 μM Latrunculin B (Sigma) for 1h at 37 °C. To inhibit RNAPII transcription, cells were treated with 5 μg/ml α-amanitin (Sigma) for 4h at 37 °C. For serum stimulation, 4.8x10⁵ HeLa cells were seeded in DMEM complete media in 6 well plates to achieve 70-80% confluency on the following day. For serum starvation, cells were grown in DMEM with 0.5% FBS at 37 °C for 24 h. To stimulate the starved cells, media was replaced with complete media containing 10% FBS for another 24 h after which cells were fixed for immunofluorescence.

Stable cell line generation

The stable cell lines used in this study are named as HeLa-Halo MVI (pHalo-MVI vector stably expressed in HeLa) and HeLa-Halo Rpb1 (pHalo-Rpb1 vector stably expressed in HeLa). The HeLa-Halo MVI were generated as described in (Große-Berkenbusch et al., 2020). To generate HeLa cells stably expressing pHalo-Rpb1, the plasmid was transfected in 6-well plates using lipofectamine 2000 protocol (Thermo Fisher Scientific). The transfected cells were selected using optimal concentrations of G418 antibiotic (G418 Sulfate, Gibco) in the complete media (0.5mg/ml) for 9-10 days until most of the untransfected cells were dead and those survived would have integrated the desired plasmid. The cells were harvested when they reached about 60-70% confluency and were expanded into multiple T75 flasks with 1:10 ratio. Some cells at this stage were seeded onto coverslips and stable transfection of desired plasmids was confirmed by using specific fluorescent ligands to Halo-tag (TMR, Promega). The cells seeded in T75 flasks were allowed to grow for further 3-4 weeks in complete media with G418 replaced twice a week. When the cells reached high confluency, they were frozen down as polyclonal stable cell line.

Immunofluorescence

Transfected and non-transfected HeLa cells were fixed for 15 min at room temperature in 4% (w/v) paraformaldehyde (PFA) in PBS and residual PFA was quenched for 15 min with 50 mM ammonium chloride in PBS. All subsequent steps were performed at room temperature. Cells were permeabilised and simultaneously blocked for 15 min with 0.1 % (v/v) Triton X-100 and 2 % (w/v) BSA in PBS. Cells were then immuno-stained against the endogenous proteins by 1 h incubation with the indicated primary and subsequently the appropriate fluorophore-conjugated secondary antibody (details below), both diluted in 2 %

(w/v) BSA in PBS. When using anti-phospho antibodies, immunofluorescence protocol was performed in TBS. The following antibodies were used at the indicated dilutions: Rabbit anti-myosin VI (1:200, Atlas-Sigma HPA0354863), Rabbit anti-Histone H3 (tri methyl K9) (1:500, Abcam ab8898), Rabbit anti-Histone H3 (acetyl K27) (1:500, Abcam ab4729), Rabbit anti-Histone H3 (acetyl K9) (1:200, Abcam ab4441), Rabbit anti-RNAPII phospho Ser5 (1:500, Abcam Ab5131), Mouse anti-RNAPII phospho Ser5 (1:500, Abcam Ab5408), Donkey anti-mouse Alexa Fluor 488-conjugated (1:500, Abcam Ab181289), Donkey anti-rabbit Alexa Fluor 647-conjugated (1:500, Abcam Ab181347) and Donkey anti-rabbit Alexa Fluor 488-conjugated antibody (1:500, Abcam Ab181346). Coverslips were mounted on microscope slides with Mowiol (10% (w/v) Mowiol 4-88, 25% (w/v) glycerol, 0.2 M Tris-HCl, pH 8.5), supplemented with 2.5% (w/v) of the anti-fading reagent DABCO (Sigma).

Immunoblot Analysis

The total protein concentration was determined by Bradford Assay (Sigma) following the manufacturer's instructions. Cell lysates were heat-denatured and resolved by SDS-PAGE. The membrane was probed against the endogenous proteins by incubation with primary Rabbit anti-myosin VI (1:500, Atlas-Sigma HPA0354863-100UL) or Mouse anti-RNAPII phospho Ser5 (1:500, Abcam Ab5408) and subsequently secondary Goat anti-rabbit antibody (1:15000 Abcam ab6721) or Goat anti-mouse antibody (1:15000, Abcam ab97023) coupled to horseradish peroxidase. The bands were visualised using the ECL Western Blotting Detection Reagents (Invitrogen) and the images were taken using Syngene GBox system. Images were processed in ImageJ.

Fluorescence Imaging

Cells were visualised using either the ZEISS LSM 880 confocal microscope or the widefield Olympus IX71 microscope. The former was equipped with a Plan-Apochromat 63x 1.4 NA oil immersion lens (Carl Zeiss, 420782-9900-000). Three laser lines, i.e. 405 nm, 488 nm and 561 nm, were used to excite the fluorophores, i.e. Hoechst, GFP and RFP, respectively. The built-in dichroic mirrors (Carl Zeiss, MBS-405, MBS-488 and MBS-561) were used to reflect the excitation laser beams on to cell samples. The emission spectral bands for fluorescence collection were 410 nm-524 nm (Hoechst), 493 nm-578 nm (GFP) and 564 nm-697 nm (RFP). The detectors consisted of two multi anode photomultiplier tubes (MA-PMT) and 1 gallium arsenide phosphide (GaAsP) detector. The green channel (GFP) was imaged using GaAsP detector, while the blue (Hoechst) and red (RFP) channels were imaged using MA-PMTs. ZEN software (Carl Zeiss, ZEN 2.3) was used to acquire and render the confocal images. The later was equipped with an PlanApo 100xOTIRFM-SP 1.49 NA lens mounted on a PIFOC z-axis focus drive (Physik Instrumente, Karlsruhe, Germany), and illuminated with an automated 300W Xenon light source (Sutter, Novato, CA) with appropriate filters (Chroma, Bellows Falls, VT). Images were acquired using a QuantEM (Photometrics) EMCCD camera, controlled by the Metamorph software (Molecular Devices). The whole volume of cells was imaged by acquiring images at z-steps of 200

nm. Widefield images were deconvolved with the Huygens Essential version 17.10 software. Confocal Images were deconvolved using the Zeiss Zen2.3 Blue software, using the regularised inverse filter method. All images were then analysed by ImageJ.

STORM Imaging

Cells were seeded on pre-cleaned No 1.5, 25-mm round glass coverslips, placed in 6-well cell culture dishes. Glass coverslips were cleaned by incubating them for 3 hours, in etch solution, made of 5:1:1 ratio of H₂O : H₂O₂ (50 wt. % in H₂O, stabilized, Fisher Scientific) : NH₄OH (ACS reagent, 28-30% NH₃ basis, Sigma), placed in a 70°C water bath. Cleaned coverslips were repeatedly washed in filtered water and then ethanol, dried and used for cell seeding. Transfected or non-transfected cells were fixed in pre-warmed 4% (w/v) PFA in PBS and residual PFA was quenched for 15 min with 50 mM ammonium chloride in PBS. Immunofluorescence (IF) was performed in filtered sterilised PBS, unless when anti-phospho antibodies were used. Then, IF was performed in filtered sterilised TBS. Cells were permeabilized and simultaneously blocked for 30 min with 3% (w/v) BSA in PBS or TBS, supplemented with 0.1 % (v/v) Triton X-100. Permeabilized cells were incubated for 1h with the primary antibody and subsequently the appropriate fluorophore-conjugated secondary antibody, at the desired dilution in 3% (w/v) BSA, 0.1% (v/v) Triton X-100 in PBS or TBS. The antibody dilutions used were the same as for the normal IF protocol (see above), except from the secondary antibodies which were used at 1:250 dilution. Following incubation with both primary and secondary antibodies, cells were washed 3 times, for 10 min per wash, with 0.2% (w/v) BSA, 0.05% (v/v) Triton X-100 in PBS or TBS. Cells were further washed in PBS and fixed for a second time with pre-warmed 4% (w/v) PFA in PBS for 10 min. Cells were washed in PBS and stored at 4 °C, in the dark, in 0.02% Na₃N in PBS, before proceeding to STORM imaging.

Before imaging, coverslips were assembled into the Attofluor® cell chambers (Invitrogen). Imaging was performed in freshly made STORM buffer consisting of 10 % (w/v) glucose, 10 mM NaCl, 50 mM Tris - pH 8.0, supplemented with 0.1 % (v/v) 2-mercaptoethanol and 0.1 % (v/v) pre-made GLOX solution which was stored at 4 °C for up to a week (5.6 % (w/v) glucose oxidase and 3.4 mg/ml catalase in 50 mM NaCl, 10 mM Tris - pH 8.0). All chemicals were purchased from Sigma. Imaging was undertaken using the Zeiss Elyra PS.1 system. Illumination was from a HR Diode 642 nm (150 mW) and HR Diode 488 nm (100 mW) lasers where power density on the sample was 7-14 kW/cm² and 7-12 kW/cm², respectively

Imaging was performed under highly inclined and laminated optical (HILO) illumination to reduce the background fluorescence with a 100x NA 1.46 oil immersion objective lens (Zeiss alpha Plan-Apochromat) with a BP 420-480/BP495-550/LP 650 filter. The final image was projected on an Andor iXon EMCCD camera with 25 msec exposure for 20000 frames.

Image processing was performed using the Zeiss Zen software. Where required, two channel images were aligned following a calibration using a calibration using pre-mounted MultiSpec bead sample (Carl Zeiss,

2076-515). For calibration, a 2 μm Z-stack was acquired at 100 nm steps. The channel alignment was then performed in the Zeiss Zen software using the Affine method to account for lateral, tilting and stretching between the channels. The calibration was performed during each day of measurements.

The images were then processed through our STORM analysis pipeline using the Zen software. Single molecule detection and localisation was performed using a 9 pixel mask with a signal to noise ratio of 6 in the "Peak finder" settings while applying the "Account for overlap" function. This function allows multi-object fitting to localise molecules within a dense environment. Molecules were then localised by fitting to a 2D Gaussian.

The render was then subjected to model-based cross-correlation drift correction and detection grouping to remove detections within multiple frames. Typical localisation precision was 20 nm for Alexa-Fluor 647 and 30 nm for Alexa-Fluor 488. The final render was then generated at 10 nm/pixel and displayed in Gauss mode where each localisation is presented as a 2D gaussian with a standard deviation based on its precision. The localisation table was exported as a csv for import in to Clus-DoC.

Clus-DoC

The single molecule positions were exported from Zeiss Zen Black version and imported into the Clus-DoC analysis software (Pageon et al., 2016) (<https://github.com/PRNicovich/ClusDoC>). The region of interest was determined by the nuclear staining. First the Ripley K function was completed on each channel identifying the r_{max} . The r_{max} was then assigned for DBSCAN if one channel was being analysed or Clus-DoC if two channel colocalisation was being analysed. The clustering size was set to a minimum of 5 molecules within a cluster with a smoothing of a cluster being set at 7 nm. All other analyses parameters remained at default settings. Data concerning each clusters was exported and graphed using Plots of Data.

High content imaging

Cells were seeded onto Corning® 384 well microplates at a density of 5,000 cells per well. The cells were grown for 24 hours, followed by the necessary treatments. The cells were fixed and immunofluorescence was undertaken as described above, due to the cells being grown directly on the plates no mounting of coverslips was required. Stained cells in plate were scanned via Cellomics ArrayScan™ XTI High Content Analysis (HCS) platform (Thermo Fisher Scientific), with a 20x Objective. Compartment Analysis Bio Application software (Cellomics) was applied to quantitatively analyse the immunostaining spots in the nucleus based on a mask created using the nuclear Hoechst staining. For each experiment, at least 1000 valid single cells per culture well were quantified and at least 10 independent culture wells (10 biological replicates) were analysed, fluorescence intensities were then plotted using Prism 8, Graphpad.

Size-exclusion Chromatography

100 μl samples of 2mg/ml purified protein, was applied to a Superdex 200 (30 x 1 cm) analytical column (GE Healthcare) equilibrated in 150 mM NaCl, 50 mM Tris.HCl (pH 7.5) and 1 mM DTT and controlled using

Waters 626 HPLC and OMNISEC (Malvern Panalytical) at room temperature.

Multi-focal Imaging and Particle Tracking Analysis

Cells stably or transiently expressing Halo-tag or SNAP-tag constructs were labelled for 15 min with HaloTag-JF549 or SNAP-tag-JF549 ligand, respectively, in cell culture medium at 37°C, 5% CO₂. 10 nM ligand was used to label Halo-tagged myosin VI constructs, whereas 50 nM ligand was used to label Halo- or SNAP-tagged RNAPII. Cells were washed for 3 times with warm cell culture medium and then incubated for further 30 min at 37°C, 5% CO₂. Cells were then washed three times in pre-warmed FluoroBrite DMEM imaging medium (ThermoFisher Scientific), before proceeding to imaging.

Single molecule imaging was performed using an aberration-corrected multifocal microscope (acMFM), as described by Abrahamsson et al. (Abrahamsson et al., 2013). Briefly, samples were imaged using 561nm laser excitation, with typical irradiance of 4-6 kW/cm² at the back aperture of a Nikon 100x 1.4 NA objective. Images were relayed through a custom optical system appended to the detection path of a Nikon Ti microscope with focus stabilization. The acMFM detection path includes a diffractive multifocal grating in a conjugate pupil plane, a chromatic correction grating to reverse the effects of spectral dispersion, and a nine-faceted prism, followed by a final imaging lens.

The acMFM produces nine simultaneous, separated images, each representing successive focal planes in the sample, with ca. 20 μm field of view and nominal axial separation of ca. 400nm between them. The nine-image array is digitized via an electron multiplying charge coupled device (EMCCD) camera (iXon Du897, Andor) at up to 32ms temporal resolution, with typical durations of 30 seconds.

3D+t images of single molecules were reconstructed via a calibration procedure, implemented in Matlab (MathWorks), that calculates and accounts for (1) the inter-plane spacing, (2) affine transformation to correctly align each focal plane in the xy plane with respect to each other, and (3) slight variations in detection efficiency in each plane, typically less than $\pm 5-15\%$ from the mean.

Reconstructed data were then subject to pre-processing, including background subtraction, mild deconvolution (3-5 Richardson-Lucy iterations), and/or Gaussian de-noising prior to 3D particle tracking using the MOSAIC software suite (Sbalzarini and Koumoutsakos, 2005). Parameters were set where maximum particle displacement was 400 nm and a minimum of 10 frames was required. Tracks were reconstructed, and diffusion constants were extracted via MSD analysis (Aaron et al., 2019) using custom Matlab software assuming an anomalous diffusion model.

Circular dichroism Spectroscopy

1 mgmL⁻¹ of protein was analysed using far UV spectra (190nm-270nm) measured by a Jasco J715 Circular Dichroism Spectrometer (Jasco Inc.). Spectra were taken at 20°C. 4 readings were taken for each measurement and averaged by the software provided. For spectra analysis the following equation was used.

$$[\theta]_{MRW} = \frac{\frac{MW}{(n-1)} \times \theta}{l \times c \times 10}$$

Where θ_{MRW} is the mean residue ellipticity, MW is the molecular weight of the protein, n is the number of amino acids, θ is the degrees in ellipticity, l is the path length and c is the concentration.

Incucyte live cell imaging

Cells were seeded onto 96-well tissue culture dishes at equal densities in 6 replicates. After attachment overnight, cells were transfected with MVI siRNA, or scrambled siRNA (Qiagen). Photomicrographs were taken every hour using an IncuCyte live cell imager (Essen Biosciences, Ann Harbor, MI) and confluency of cultures was measured using IncuCyte software. Confluency values between wells were normalised to initial confluency for comparison.

RNA extraction and RT-qPCR

RNA from HeLa cells was extracted using Gene Jet RNA purification kit (Thermo scientific) according to manufacturer's protocol. The RNA concentration was measured using Geneflow Nanophotometer and RT-qPCR was performed with one-step QuantiFast SYBR Green qPCR kit (Qiagen) using 50ng of RNA in each sample. A list of qPCR primers is given in Supplementary Table 3.

RNA-seq and analysis

Total RNA was extracted from three replicates of WT, MVI KD and Scrambled siRNA. Ice cold TRIzol reagent was added to each culture and homogenised. The mixture was then incubated for 5 mins at room temperature then chloroform was added to the lysis and incubated for 3 mins. The samples were then centrifuged at 12,000 x g at 4°C. The colourless aqueous phase was collected. The RNA was then precipitated with incubation for 10 mins with isopropanol before centrifugation for a further 10 mins at 12,000 x g at 4°C. The pellet was washed in 75% (v/v) ethanol, vortexed and centrifuged for 5 mins at 7500 x g at 4°C. The RNA pellet is air dried for 10 mins. The pellet is then resuspended in 50µL of RNase-free water containing 0.1mM EDTA and incubated at 55°C for 15 mins to allow the RNA to dissolve. The RNA was then quantified using then 260nm absorbance, ensuring the A260/A280 ratio was approximately 2, therefore implying the sample is pure. The sample was then further purified using the RNeasy kit (Qiagen) where the manufacturers protocol was followed exactly. Once the purity and stability had been measured the RNA was then stored at -80°C.

The RNA-seq libraries were prepared with TruSeq RNA Library Prep kit v2 as per protocol instructions. Resulting libraries concentration, size distribution and quality were assessed on a Qubit fluorometer with a dsDNA high sensitivity kit and on an Agilent 2100 bioanalyzer using a DNA 7500 kit. Then libraries were normalized, pooled and quantified with a KAPA Library quantification kit for Illumina platforms on a ABI StepOnePlus qPCR machine, then loaded on a high output flow cell and paired-end sequenced (2x75 bp) on an Illumina NextSeq 550 next generation sequencer (performed at the NYUAD Sequencing Center). The raw FASTQ reads were quality trimmed using Trimmomatic (version 0.36) (Bolger et al., 2014) to trim

low quality bases, systematic base calling errors, as well sequencing adapter contamination. FastQC (www.bioinformatics.babraham.ac.uk/projects/fastqc) was used to assess the quality of the sequenced reads pre/post quality trimming. Only the reads that passed quality trimming in pairs were retained for downstream analysis. The quality trimmed RNAseq reads were aligned to the Homo sapiens GRCh38.p4 genome using HISAT2 (version 2.0.4) (Kim et al., 2015). The resulting SAM alignment files were then converted to BAM format and sorted by coordinate using SAMtools (version 0.1.19) (Li et al., 2009). The BAM alignment files were processed using HTseq-count (Anders et al., 2015) using the reference annotation file to produce raw counts for each sample. The raw counts were then analyzed using the online analysis portal NASQAR (<http://nasqar.abudhabi.nyu.edu/>) in order to merge, normalize and identify differentially expressed genes by using the START app (Nelson et al., 2017). Differentially expressed genes by at least 2-fold $\log_2(FC) \geq 1$ and adjusted p-value of < 0.05 for upregulated genes and $\log_2(FC) \leq -1$ and adjusted p-value of < 0.05 for downregulated genes) between the samples which were then subjected to Gene Ontology (GO) enrichment using ShinyGo v0.60 (<http://bioinformatics.sdstate.edu/go/>) (Ge et al., 2019).

Chromatin Immunoprecipitation (ChIP)

To identify specific RNAPII-DNA interactions, ChIP was performed using mouse anti-RNAPII-pSer5 antibody (Abcam Ab5408). A confluent T175 flask ($10 \times 10^6 - 30 \times 10^6$) of HeLa cells was crosslinked by adding formaldehyde dropwise directly to the media to a final concentration of 0.75% and was left for gentle rotation at room temperature (RT) for 10min. To stop the reaction, glycine was added to a final concentration of 125 mM and was incubated with shaking for 5 min at RT. The cells were washed twice with 10 ml of cold PBS and were scraped in 5-8 ml of cold PBS. All cells were collected and centrifuged at 1000xg, 4°C for 5 min. The pellet was re-suspended in ChIP lysis buffer (750 µL per 1×10^7 cells) (lysis buffer: 50 mM HEPES-KOH pH 7.5, 140 mM NaCl, 1 mM EDTA pH8, 1 % TritonX-100, 0.1 % Sodium Deoxycholate, 0.1 % SDS and Protease Inhibitors) and was incubated on ice for 10 min. The cells were sonicated using the diagenode bioruptor sonicator in order to shear DNA to an average fragment size of 200-800 bp. The fragment size was analysed on a 1.5 % agarose gel. After sonication, cell debris was removed by centrifugation for 10 min, 4°C, 8000xg and the supernatant (chromatin) was used for the immunoprecipitation. The sonicated chromatin was snap frozen on dry ice and was stored at -80°C until further use (max storage 3 months).

The chromatin prepared above was diluted 1:10 with RIPA buffer (50 mM Tris-HCl pH8, 150 mM NaCl, 2 mM EDTA pH8, 1% NP-40, 0.5% Sodium Deoxycholate, 0.1% SDS and Protease Inhibitors) and was distributed into 6 tubes (approximately 1×10^6 cells per IP) - 3 samples for specific antibody (MVI) and 3 samples for the no antibody control (beads only). 10% of diluted chromatin was removed to serve as input sample and was stored at -20°C until further use. All chromatin samples were pre-cleared using the protein A magnetic beads (Thermo Fisher Scientific) for 30 min after which 20 µl of mouse anti-RNAPII-pSer5 antibody

was added to each of the triplicate Ab samples (1 in 50 dilution) and the tubes were rotated at 4°C, overnight. Next day, 40 µl of protein A magnetic beads (washed three times in RIPA buffer) were added to each of the samples including the no antibody control tubes and were put on rotation at 4°C for 1 h. After 1h, the beads were collected using a magnetic rack and were washed twice in low salt buffer (0.1 % SDS, 1 % Triton X-100, 2 mM EDTA, 20 mM Tris-HCl pH 8, 150 mM NaCl), once in high salt buffer (0.1 % SDS, 1 % Triton X-100, 2 mM EDTA, 20 mM Tris-HCl pH 8, 500 mM NaCl), once in LiCl wash buffer (0.25 M LiCl, 1 % NP-40, 1 % Sodium Deoxycholate, 1 mM EDTA, 10 mM Tris-HCl pH 8) and finally in TE (10mM Tris pH8, 1mM EDTA). DNA was eluted by adding 120 µl of elution buffer (1 % SDS, 100 mM NaHCO₃) to the beads and vortexing them slowly for 15 min at 30°C. To reverse crosslink the protein-DNA complexes, 4.8 µl of 5M NaCl and 2 µl RNase A (10mg/ml) was added to the elutes including the input sample that was stored at -20°C and they were incubated while shaking at 65°C overnight followed by proteinase K treatment at 60°C for 1 h. The DNA was then purified using phenol:chloroform extraction and the samples were analysed by qPCR using primers in Supplementary Table 3.

Steady-state ATPase Activity

Ca²⁺-actin monomers were converted to Mg²⁺-actin with 0.2 mM EGTA and 50 µM MgCl₂ before polymerizing by dialysis into 20 mM Tris.HCl (pH7.5), 20 mM imidazole (pH 7.4), 25 mM NaCl and 1 mM DTT. A 1.1 molar equivalent of phalloidin (Sigma) was used to stabilize actin filaments (Batters et al., 2012, Toseland, 2014).

Steady-state ATPase activities were measured at 25 °C in KMg50 buffer (50 mM KCl, 1 mM MgCl₂, 1 mM EGTA, 1 mM DTT, and 10 mM imidazole, pH 7.0). Supplemented with the NADH-coupled assay components, 0.2 mM NADH, 2 mM phosphoenolpyruvate, 3.3 U ml⁻¹ lactate dehydrogenase, 2.3 U ml⁻¹ pyruvate kinase and various actin concentrations (0 – 30 µM). The final [Mg.ATP] was 5 mM and MVI concentration was 100–300 nM. The assay was started by the addition of MVI. The change in absorption at OD₃₄₀ nm was followed for 5 min. The *k*_{cat} and *K*_{actin} values were determined by fitting the data to equation:

$$Rate = V_0 + \left(\frac{k_{cat}[Actin]}{K_{actin} + [Actin]} \right)$$

*V*₀ is the basal ATPase activity of MVI, *k*_{cat} is the maximum actin-activated ATPase rate and *K*_{actin} is the concentration of actin needed to reach half maximal ATPase activity.

Graphics

Unless stated, data fitting and plotting was performed using Plots of data (Postma and Goedhart, 2019) and Graft Version 5 (Erihtacus Software Ltd). Cartoons were generated using the BioRender software (www.biorender.com).

Data Availability

The data supporting the findings of this study are available from the corresponding author on request.

REFERENCES

- AARON, J., WAIT, E., DESANTIS, M. & CHEW, T. L. 2019. Practical Considerations in Particle and Object Tracking and Analysis. *Curr Protoc Cell Biol*, 83, e88.
- ABRAHAMSSON, S., CHEN, J., HAJI, B., STALLINGA, S., KATSOV, A. Y., WISNIEWSKI, J., MIZUGUCHI, G., SOULE, P., MUELLER, F., DUGAST DARZACQ, C., DARZACQ, X., WU, C., BARGMANN, C. I., AGARD, D. A., DAHAN, M. & GUSTAFSSON, M. G. 2013. Fast multicolor 3D imaging using aberration-corrected multifocus microscopy. *Nat Methods*, 10, 60-3.
- ALTMAN, D., SWEENEY, H. L. & SPUDICH, J. A. 2004. The mechanism of myosin VI translocation and its load-induced anchoring. *Cell*, 116, 737-49.
- ANDERS, S., PYL, P. T. & HUBER, W. 2015. HTSeq—a Python framework to work with high-throughput sequencing data. *Bioinformatics*, 31, 166-9.
- BATTERS, C., WOODALL, K. A., TOSELAND, C. P., HUNDSCHHELL, C. & VEIGEL, C. 2012. Cloning, expression, and characterization of a novel molecular motor, Leishmania myosin-XXI. *J Biol Chem*, 287, 27556-66.
- BOEHNING, M., DUGAST-DARZACQ, C., RANKOVIC, M., HANSEN, A. S., YU, T., MARIE-NELLY, H., MCSWIGGEN, D. T., KOKIC, G., DAILEY, G. M., CRAMER, P., DARZACQ, X. & ZWECKSTETTER, M. 2018. RNA polymerase II clustering through carboxy-terminal domain phase separation. *Nat Struct Mol Biol*, 25, 833-840.
- BOLGER, A. M., LOHSE, M. & USADEL, B. 2014. Trimmomatic: a flexible trimmer for Illumina sequence data. *Bioinformatics*, 30, 2114-20.
- CARIDI, C. P., D'AGOSTINO, C., RYU, T., ZAPOTOCZNY, G., DELABAERE, L., LI, X., KHODAVERDIAN, V. Y., AMARAL, N., LIN, E., RAU, A. R. & CHIOLIO, I. 2018. Nuclear F-actin and myosins drive relocalization of heterochromatic breaks. *Nature*, 559, 54-60.
- CARMO-FONSECA, M. 2002. The contribution of nuclear compartmentalization to gene regulation. *Cell*, 108, 513-21.
- CHO, W. K., JAYANTH, N., ENGLISH, B. P., INOUE, T., ANDREWS, J. O., CONWAY, W., GRIMM, J. B., SPILLE, J. H., LAVIS, L. D., LIONNET, T. & CISSE, II 2016a. RNA Polymerase II cluster dynamics predict mRNA output in living cells. *Elife*, 5.
- CHO, W. K., JAYANTH, N., MULLEN, S., TAN, T. H., JUNG, Y. J. & CISSE, II 2016b. Super-resolution imaging of fluorescently labeled, endogenous RNA Polymerase II in living cells with CRISPR/Cas9-mediated gene editing. *Sci Rep*, 6, 35949.
- CHO, W. K., SPILLE, J. H., HECHT, M., LEE, C., LI, C., GRUBE, V. & CISSE, II 2018. Mediator and RNA polymerase II clusters associate in transcription-dependent condensates. *Science*, 361, 412-415.
- COOK, A., HARI-GUPTA, Y. & TOSELAND, C. P. 2018. Application of the SSB biosensor to study in vitro transcription. *Biochem Biophys Res Commun*, 496, 820-825.
- COOK, P. R. 2010. A model for all genomes: the role of transcription factories. *J Mol Biol*, 395, 1-10.

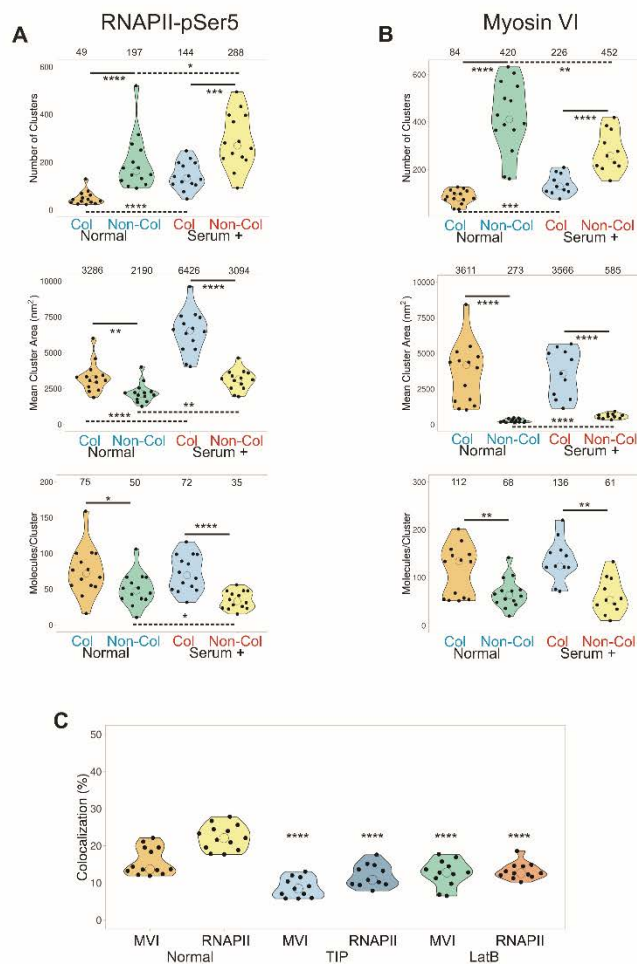
- CREMER, T., CREMER, M., DIETZEL, S., MULLER, S., SOLOVEI, I. & FAKAN, S. 2006. Chromosome territories--a functional nuclear landscape. *Curr Opin Cell Biol*, 18, 307-16.
- DE LANEROLLE, P. 2012. Nuclear actin and myosin at a glance. *J Cell Sci*, 125, 4945-9.
- DE LANEROLLE, P. & SEREBRYANNYY, L. 2011. Nuclear actin and myosins: life without filaments. *Nat Cell Biol*, 13, 1282-8.
- DUNN, T. A., CHEN, S., FAITH, D. A., HICKS, J. L., PLATZ, E. A., CHEN, Y., EWING, C. M., SAUVAGEOT, J., ISAACS, W. B., DE MARZO, A. M. & LUO, J. 2006. A novel role of myosin VI in human prostate cancer. *Am J Pathol*, 169, 1843-54.
- FILI, N., HARI-GUPTA, Y., ASTON, B., DOS SANTOS, A., GOUGH, R. E., ALAMAD, B., WANG, L., MARTIN-FERNANDEZ, M. L. & TOSELAND, C. P. 2020. Competition between two high- and low-affinity protein-binding sites in myosin VI controls its cellular function. *J Biol Chem*, 295, 337-347.
- FILI, N., HARI-GUPTA, Y., DOS SANTOS, A., COOK, A., POLAND, S., AMEER-BEG, S. M., PARSONS, M. & TOSELAND, C. P. 2017. NDP52 activates nuclear myosin VI to enhance RNA polymerase II transcription. *Nat Commun*, 8, 1871.
- FILI, N. & TOSELAND, C. P. 2019. Unconventional Myosins: How Regulation Meets Function. *Int J Mol Sci*, 21.
- FOMPROIX, N. & PERCIPALLE, P. 2004. An actin-myosin complex on actively transcribing genes. *Exp Cell Res*, 294, 140-8.
- GE, S. X., JUNG, D. & YAO, R. 2019. ShinyGO: a graphical enrichment tool for animals and plants. *Bioinformatics*.
- GRASHOFF, C., HOFFMAN, B. D., BRENNER, M. D., ZHOU, R., PARSONS, M., YANG, M. T., MCLEAN, M. A., SLIGAR, S. G., CHEN, C. S., HA, T. & SCHWARTZ, M. A. 2010. Measuring mechanical tension across vinculin reveals regulation of focal adhesion dynamics. *Nature*, 466, 263-6.
- GREENBERG, M. J. & OSTAP, E. M. 2013. Regulation and control of myosin-I by the motor and light chain-binding domains. *Trends Cell Biol*, 23, 81-9.
- GROSS-BERKENBUSCH, A., HETTICH, J., KUHN, T., FILI, N., COOK, A. W., HARI-GUPTA, Y., PALMER, A., STREIT, L., ELLIS, P. J. I., TOSELAND, C. P. & GEBHARDT, J. C. M. 2020. Myosin VI moves on nuclear actin filaments and supports long-range chromatin rearrangements. *bioRxiv*, 2020.04.03.023614.
- HEISSLER, S. M., SELVADURAI, J., BOND, L. M., FEDOROV, R., KENDRICK-JONES, J., BUSS, F. & MANSTEIN, D. J. 2012. Kinetic properties and small-molecule inhibition of human myosin-6. *FEBS Lett*, 586, 3208-14.
- HNISZ, D., SHRINIVAS, K., YOUNG, R. A., CHAKRABORTY, A. K. & SHARP, P. A. 2017. A Phase Separation Model for Transcriptional Control. *Cell*, 169, 13-23.
- HOFMANN, W. A., VARGAS, G. M., RAMCHANDRAN, R., STOJILJKOVIC, L., GOODRICH, J. A. & DE LANEROLLE, P. 2006. Nuclear myosin I is necessary for the formation of the first phosphodiester bond during transcription initiation by RNA polymerase II. *J Cell Biochem*, 99, 1001-9.
- JACKSON, D. A., HASSAN, A. B., ERRINGTON, R. J. & COOK, P. R. 1993. Visualization of focal sites of transcription within human nuclei. *EMBO J*, 12, 1059-65.
- KENNEDY, B. K., BARBIE, D. A., CLASSON, M., DYSON, N. & HARLOW, E. 2000. Nuclear organization of DNA replication in primary mammalian cells. *Genes Dev*, 14, 2855-68.
- KIM, D., LANGMEAD, B. & SALZBERG, S. L. 2015. HISAT: a fast spliced aligner with low memory requirements. *Nat Methods*, 12, 357-60.
- KIMURA, H., SUGAYA, K. & COOK, P. R. 2002. The transcription cycle of RNA polymerase II in living cells. *J Cell Biol*, 159, 777-82.
- KUKALEV, A., NORD, Y., PALMBERG, C., BERGMAN, T. & PERCIPALLE, P. 2005. Actin and hnRNP U cooperate for productive transcription by RNA polymerase II. *Nat Struct Mol Biol*, 12, 238-44.
- KULASHRESHTHA, M., MEHTA, I. S., KUMAR, P. & RAO, B. J. 2016. Chromosome territory relocation during DNA repair requires nuclear myosin 1 recruitment to chromatin mediated by Upsilon-H2AX signaling. *Nucleic Acids Res*, 44, 8272-91.
- LI, H., HANDSAKER, B., WYSOKER, A., FENNEL, T., RUAN, J., HOMER, N., MARTH, G., ABECASIS, G., DURBIN, R. & GENOME PROJECT DATA PROCESSING, S. 2009. The Sequence Alignment/Map format and SAMtools. *Bioinformatics*, 25, 2078-9.
- LOIKKANEN, I., TOLJAMO, K., HIRVIKOSKI, P., VAISANEN, T., PAAVONEN, T. K. & VAARALA, M. H. 2009. Myosin VI is a modulator of androgen-dependent gene expression. *Oncol Rep*, 22, 991-5.
- MAO, Y. S., ZHANG, B. & SPECTOR, D. L. 2011. Biogenesis and function of nuclear bodies. *Trends Genet*, 27, 295-306.
- MISTELI, T. & SOUTOGLU, E. 2009. The emerging role of nuclear architecture in DNA repair and genome maintenance. *Nat Rev Mol Cell Biol*, 10, 243-54.
- MUKHERJEA, M., ALI, M. Y., KIKUTI, C., SAFER, D., YANG, Z., SIRKIA, H., ROPARS, V., HOUDUSSE, A., WARSHAW, D. M. & SWEENEY, H. L. 2014. Myosin VI must dimerize and deploy its unusual lever arm in order to perform its cellular roles. *Cell Rep*, 8, 1522-32.
- MUKHERJEA, M., LLINAS, P., KIM, H., TRAVAGLIA, M., SAFER, D., MENETREY, J., FRANZINI-ARMSTRONG, C., SELVIN, P. R., HOUDUSSE, A. & SWEENEY, H. L. 2009. Myosin VI dimerization triggers an unfolding of a three-helix bundle in order to extend its reach. *Mol Cell*, 35, 305-15.
- MURATANI, M. & TANSEY, W. P. 2003. How the ubiquitin-proteasome system controls transcription. *Nat Rev Mol Cell Biol*, 4, 192-201.
- NAGASHIMA, R., HIBINO, K., ASHWIN, S. S., BABOKHOV, M., FUJISHIRO, S., IMAI, R., NOZAKI, T., TAMURA, S., TANI, T., KIMURA, H., SHRIBAK, M., KANEMAKI, M. T., SASAI, M. & MAESHIMA, K. 2019. Single nucleosome imaging reveals loose genome chromatin networks via active RNA polymerase II. *J Cell Biol*, 218, 1511-1530.

- NELSON, J. W., SKLENAR, J., BARNES, A. P. & MINNIER, J. 2017. The START App: a web-based RNAseq analysis and visualization resource. *Bioinformatics*, 33, 447-449.
- PAGEON, S. V., NICOVICH, P. R., MOLLAZADE, M., TABARIN, T. & GAUS, K. 2016. Clus-DoC: a combined cluster detection and colocalization analysis for single-molecule localization microscopy data. *Mol Biol Cell*, 27, 3627-3636.
- PAPANTONIS, A. & COOK, P. R. 2013. Transcription factories: genome organization and gene regulation. *Chem Rev*, 113, 8683-705.
- PARK, H., RAMAMURTHY, B., TRAVAGLIA, M., SAFER, D., CHEN, L. Q., FRANZINI-ARMSTRONG, C., SELVIN, P. R. & SWEENEY, H. L. 2006. Full-length myosin VI dimerizes and moves processively along actin filaments upon monomer clustering. *Mol Cell*, 21, 331-6.
- PHICHITH, D., TRAVAGLIA, M., YANG, Z., LIU, X., ZONG, A. B., SAFER, D. & SWEENEY, H. L. 2009. Cargo binding induces dimerization of myosin VI. *Proc Natl Acad Sci U S A*, 106, 17320-4.
- POSTMA, M. & GOEDHART, J. 2019. PlotsOfData-A web app for visualizing data together with their summaries. *PLoS Biol*, 17, e3000202.
- PURI, C., CHIBALINA, M. V., ARDEN, S. D., KRUPPA, A. J., KENDRICK-JONES, J. & BUSS, F. 2010. Overexpression of myosin VI in prostate cancer cells enhances PSA and VEGF secretion, but has no effect on endocytosis. *Oncogene*, 29, 188-200.
- SABARI, B. R., DALL'AGNESE, A., BOJIA, A., KLEIN, I. A., COFFEY, E. L., SHRINIVAS, K., ABRAHAM, B. J., HANNETT, N. M., ZAMUDIO, A. V., MANTEIGA, J. C., LI, C. H., GUO, Y. E., DAY, D. S., SCHUIJERS, J., VASILE, E., MALIK, S., HNISZ, D., LEE, T. I., CISSE, II, ROEDER, R. G., SHARP, P. A., CHAKRABORTY, A. K. & YOUNG, R. A. 2018. Coactivator condensation at super-enhancers links phase separation and gene control. *Science*, 361.
- SBALZARINI, I. F. & KOUMOUTSAKOS, P. 2005. Feature point tracking and trajectory analysis for video imaging in cell biology. *J Struct Biol*, 151, 182-95.
- SCHOENFELDER, S. & FRASER, P. 2019. Long-range enhancer-promoter contacts in gene expression control. *Nat Rev Genet*, 20, 437-455.
- SEREBRYANNYY, L. A., PARILLA, M., ANNIBALE, P., CRUZ, C. M., LASTER, K., GRATTON, E., KUDRYASHOV, D., KOSAK, S. T., GOTTARDI, C. J. & DE LANEROLLE, P. 2016. Persistent nuclear actin filaments inhibit transcription by RNA polymerase II. *J Cell Sci*, 129, 3412-25.
- SUGAYA, K., VIGNERON, M. & COOK, P. R. 2000. Mammalian cell lines expressing functional RNA polymerase II tagged with the green fluorescent protein. *J Cell Sci*, 113 (Pt 15), 2679-83.
- SUTHERLAND, H. & BICKMORE, W. A. 2009. Transcription factories: gene expression in unions? *Nat Rev Genet*, 10, 457-66.
- SWEENEY, H. L., PARK, H., ZONG, A. B., YANG, Z., SELVIN, P. R. & ROSENFELD, S. S. 2007. How myosin VI coordinates its heads during processive movement. *EMBO J*, 26, 2682-92.
- TOSELAND, C. P. 2013. Fluorescent labeling and modification of proteins. *J Chem Biol*, 6, 85-95.
- TOSELAND, C. P. 2014. Fluorescence to study the ATPase mechanism of motor proteins. *EXS*, 105, 67-86.
- VENIT, T., SEMESTA, K., FARRUKH, S., ENDARA-COLL, M., HAVALDA, R., HOZAK, P. & PERCIPALLE, P. 2020. Nuclear myosin 1 activates p21 gene transcription in response to DNA damage through a chromatin-based mechanism. *Commun Biol*, 3, 115.
- VERSCHURE, P. J., VAN DER KRAAN, I., MANDERS, E. M. & VAN DRIEL, R. 1999. Spatial relationship between transcription sites and chromosome territories. *J Cell Biol*, 147, 13-24.
- VREUGDE, S., FERRAI, C., MILUZIO, A., HAUBEN, E., MARCHISIO, P. C., CRIPPA, M. P., BUSSI, M. & BIFFO, S. 2006. Nuclear myosin VI enhances RNA polymerase II-dependent transcription. *Mol Cell*, 23, 749-55.
- WANG, D., ZHU, L., LIAO, M., ZENG, T., ZHUO, W., YANG, S. & WU, W. 2016. MYO6 knockdown inhibits the growth and induces the apoptosis of prostate cancer cells by decreasing the phosphorylation of ERK1/2 and PRAS40. *Oncol Rep*, 36, 1285-92.
- WANG, H., WANG, B., ZHU, W. & YANG, Z. 2015. Lentivirus-Mediated Knockdown of Myosin VI Inhibits Cell Proliferation of Breast Cancer Cell. *Cancer Biother Radiopharm*, 30, 330-5.
- WANG, Z., ZANG, C., ROSENFELD, J. A., SCHONES, D. E., BARSKI, A., CUDDAPAH, S., CUI, K., ROH, T. Y., PENG, W., ZHANG, M. Q. & ZHAO, K. 2008. Combinatorial patterns of histone acetylations and methylations in the human genome. *Nat Genet*, 40, 897-903.
- WEI, M., FAN, X., DING, M., LI, R., SHAO, S., HOU, Y., MENG, S., TANG, F., LI, C. & SUN, Y. 2020. Nuclear actin regulates inducible transcription by enhancing RNA polymerase II clustering. *Science Advances*, 6, eaay6515.
- WOLLSCHIED, H. P., BIANCOSPINO, M., HE, F., MAGISTRATI, E., MOLTENI, E., LUPIA, M., SOFFIENTINI, P., ROTTNER, K., CAVALLARO, U., POZZOLI, U., MAPELLI, M., WALTERS, K. J. & POLO, S. 2016. Diverse functions of myosin VI elucidated by an isoform-specific alpha-helix domain. *Nat Struct Mol Biol*, 23, 300-8.
- ZHAO, Z. W., ROY, R., GEBHARDT, J. C., SUTER, D. M., CHAPMAN, A. R. & XIE, X. S. 2014. Spatial organization of RNA polymerase II inside a mammalian cell nucleus revealed by reflected light-sheet superresolution microscopy. *Proc Natl Acad Sci U S A*, 111, 681-6.
- ZORCA, C. E., KIM, L. K., KIM, Y. J., KRAUSE, M. R., ZENKLUSEN, D., SPILIANAKIS, C. G. & FLAVELL, R. A. 2015. Myosin VI regulates gene pairing and transcriptional pause release in T cells. *Proc Natl Acad Sci U S A*, 112, E1587-93.

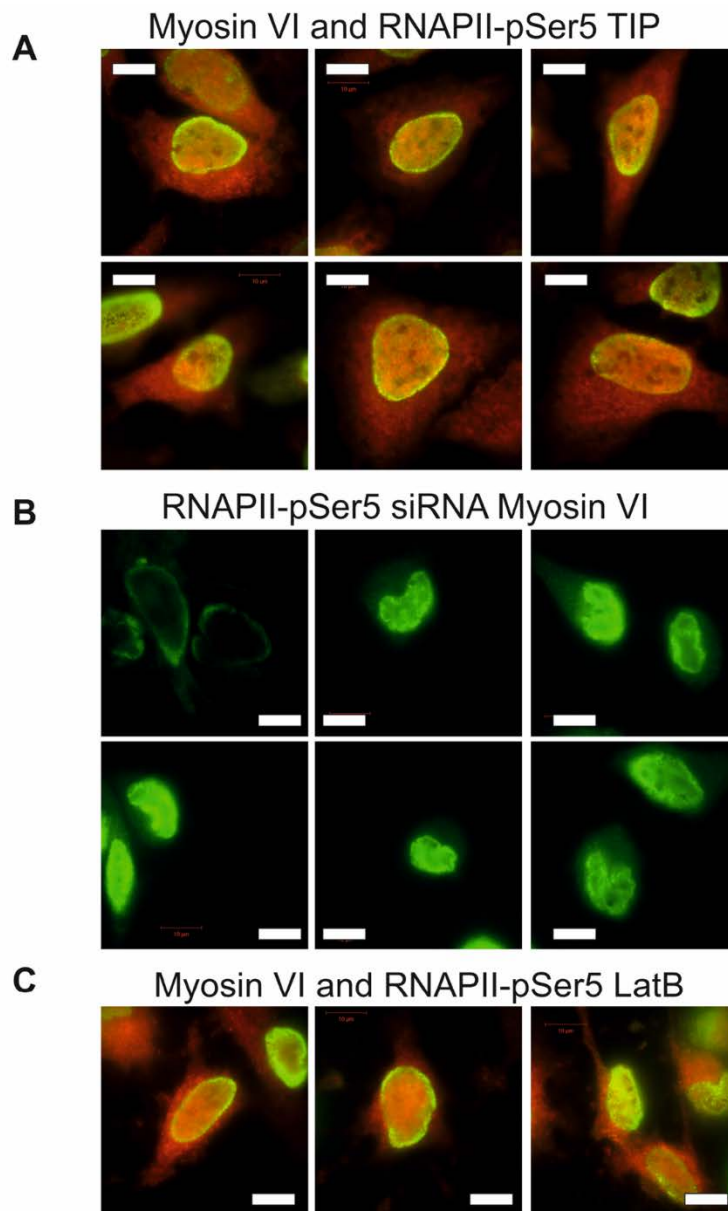
5.2.1.1. Supplementary Material for Manuscript 6

Nuclear myosin VI regulates the spatial organization of mammalian transcription initiation.

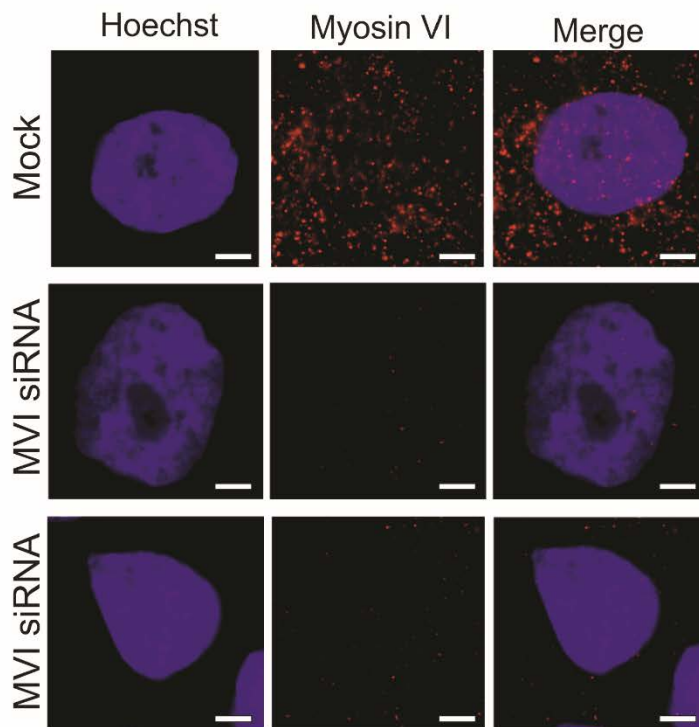
SUPPLEMENTARY INFORMATION



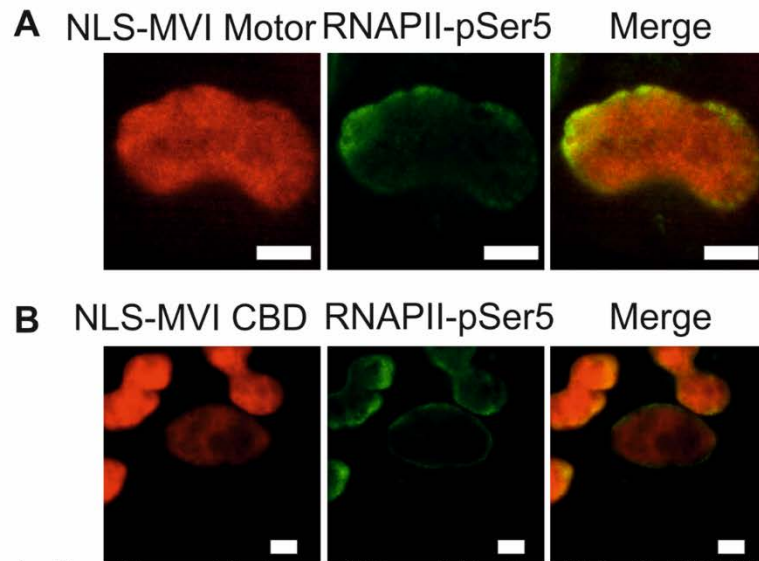
Supplementary Figure 1 Colocalization analysis of RNAPII with MVI. (A) Cluster analysis of RNAPII-pSer5 nuclear organisation under normal and serum-treated conditions. The data are broken down into myosin VI colocalized and non-colocalized clusters. Individual data points correspond to the average value for a cell ROI (n=14). The values represent the mean from the ROIs for each condition (Only statistically significant changes are highlighted *p < 0.05, **p < 0.01, ***p < 0.001, ****p < 0.0001 by two-tailed t-test compared to normal conditions). (B) Cluster analysis of myosin VI nuclear organisation under normal and serum-treated conditions. The data are broken down into RNAPII-pSer5 colocalized and non-colocalized clusters. Individual data points correspond to the average value for a cell ROI (n=14). The values represent the mean from the ROIs for each condition (Only statistically significant changes are highlighted **p < 0.01, ***p < 0.001, ****p < 0.0001 by two-tailed t-test compared to normal conditions). (C) Colocalization analysis of myosin VI (MVI) and RNAPII-pSer5 clusters under normal (n=13), TIP- (n=11) and LatB-treated (n=11) conditions. Individual data points represent the percentage of each protein which is colocalized and correspond to the average value for a cell ROI. The values represent the mean from the ROIs for each condition (Only statistically significant changes are highlighted ****p < 0.0001 by two-tailed t-test compared to normal conditions for each protein).



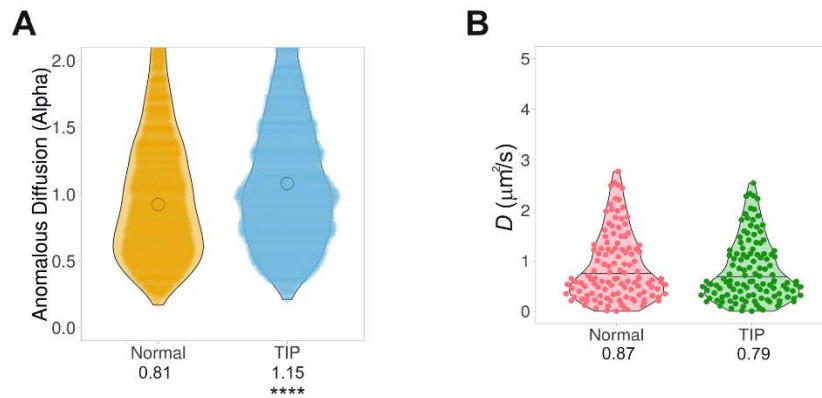
Supplementary Figure 2 Representative images of myosin VI and RNAPII under treatments. (A) Widefield Immunofluorescence staining against myosin VI (red) and RNAPII-pSer5 (green) in HeLa cells when treated with TIP. Images were acquired at the mid-point of the nucleus (scale bar 10 μm). (B) Widefield Immunofluorescence staining against RNAPII-pSer5 (green) in HeLa cells following siRNA knockdown of myosin VI. Please see Supplementary Figure 3 for myosin VI controls. Images were acquired at the mid-point of the nucleus (scale bar 10 μm). (C) Widefield Immunofluorescence staining against myosin VI (red) and RNAPII-pSer5 (green) in HeLa cells when treated with LatB. Images were acquired at the mid-point of the nucleus (scale bar 10 μm).



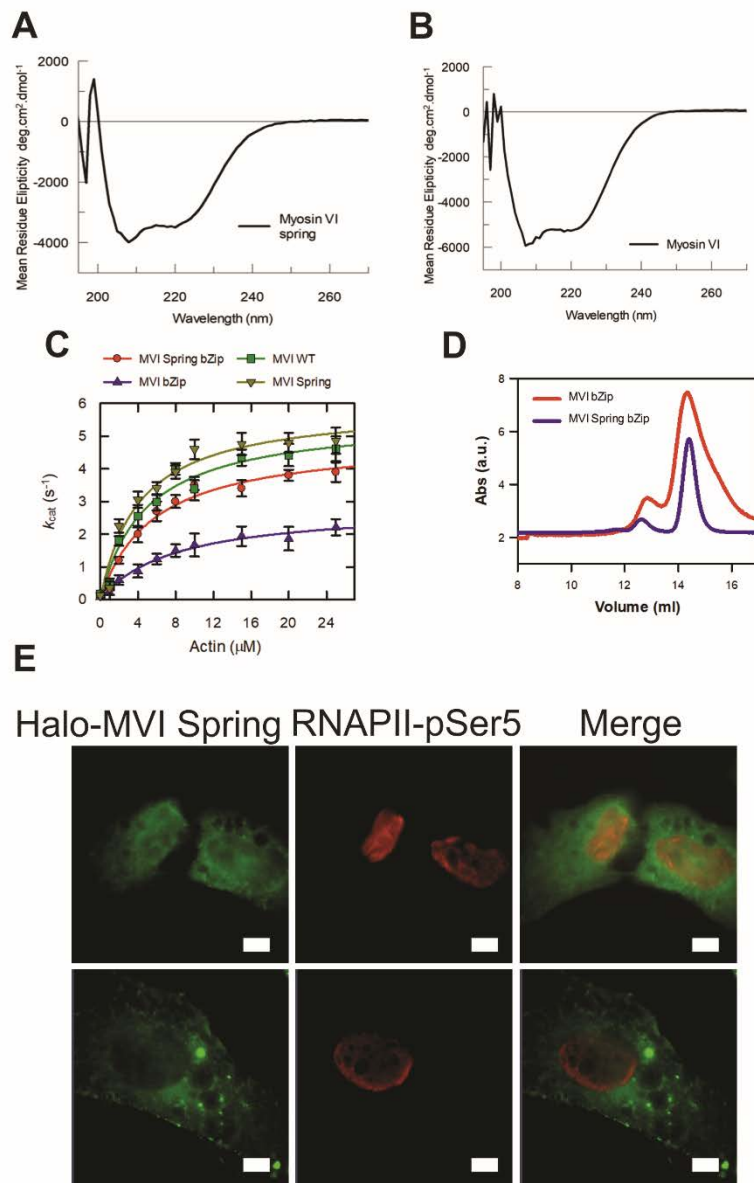
Supplementary Figure 3 Representative images of myosin VI following siRNA knockdown. Widefield Immunofluorescence staining against myosin VI (MVI) (magenta) and DNA (cyan) in HeLa cells under mock (control siRNA treatment) and siRNA conditions following 48 hr transfection. Images were acquired at the mid-point of the nucleus (scale bar 5 μm).



Supplementary Figure 4 Representative images of NLS myosin VI motor and CBD with RNAPII. (A) Widefield Halo-TMR and Immunofluorescence staining against NLS myosin VI motor (red) and RNAPII-pSer5 (green) in HeLa cells. Images were acquired at the mid-point of the nucleus (scale bar 5 μm). (B) Widefield Halo-TMR and Immunofluorescence staining against NLS myosin VI CBD (red) and RNAPII-pSer5 (green) in HeLa cells. Images were acquired at the mid-point of the nucleus (scale bar 5 μm).



Supplementary Figure 5 Controls for Live cell single molecule tracking. (A) Plot of Halo-RNAPII anomalous diffusion alpha value under normal and TIP treated conditions. Values were derived from fitting trajectories to an anomalous diffusion model, as described in methods. Data points correspond to the individual tracks across all cells ($n = 100$). The values represent the mean from the ROIs for each condition. (**** $p < 0.0001$ by two-tailed t-test compared to normal conditions) (B) Plot of SNAP-tag diffusion constants under the stated conditions derived from fitting trajectories to an anomalous diffusion model, as described in methods. Data points correspond to the average value for a cell ROI ($n=100$). The values represent the mean from the ROIs for each condition. There is not a statistically significant change between the datasets.



Supplementary Figure 6 Characterisation of myosin VI spring construct. (A) Representative CD spectra for recombinant full-length myosin VI spring. (B) Representative CD spectra for recombinant full-length wild type myosin VI. (C) Michaelis-Menten plot of displaying steady-state actin-activated ATPase activity for the myosin VI (MVI) constructs. Error bars represent SEM from three-independent experiments. (D) Representative size exclusion chromatography trace for 1 mg/ml myosin VI bZip and myosin VI spring bZip constructs. (E) Representative widefield Halo-TMR and Immunofluorescence staining against Myosin VI Spring (green) and RNAPII-pSer5 (red) in HeLa cells. Images were acquired at the mid-point of the nucleus (scale bar 5 μ m).

Supplementary Table 1. GO Gene Expression analysis

p value (FDR corrected)	Genes in List	Total Genes	Functional Category	GO Term
2.88E-09	308	3903	Regulation of cell communication	GO:0010646
2.88E-09	310	3952	Regulation of signaling	GO:0023051
7.76E-09	265	3287	Cell surface receptor signaling pathway	GO:0007166
7.76E-09	280	3529	Regulation of signal transduction	GO:0009966
7.20E-07	244	3113	Intracellular signal transduction	GO:0035556
1.71E-06	269	3547	Response to organic substance	GO:0010033
2.78E-06	169	2027	Regulation of intracellular signal transduction	GO:1902531
2.78E-06	204	2561	Response to external stimulus	GO:0009605
2.78E-06	218	2785	Anatomical structure morphogenesis	GO:0009653
2.78E-06	226	2905	Regulation of localization	GO:0032879
2.78E-06	151	1756	Regulation of cell proliferation	GO:0042127
2.78E-06	344	4820	Regulation of response to stimulus	GO:0048583
2.78E-06	256	3382	Regulation of multicellular organismal process	GO:0051239
2.78E-06	119	1286	Negative regulation of multicellular organismal process	GO:0051241
2.78E-06	64	551	Circulatory system process	GO:0003013
3.08E-06	63	542	Blood circulation	GO:0008015
3.85E-06	161	1921	Locomotion	GO:0040011
3.90E-06	197	2474	Nervous system development	GO:0007399
4.67E-06	99	1028	Regulation of cellular component movement	GO:0051270
9.19E-06	175	2165	Cell proliferation	GO:0008283

Supplementary Table 2. Recombinant DNA.

Construct	Source
Xenopus pFastBac1 Calmodulin (1-end)	Sellers Lab
Human pFastbacHTB MVI (1-1253)	Fili et al 2017
Human pFastbacHTB MVI bzip	Sellers Lab
Human pFastbacHTB MVI Spring	Synthetic Gene - This Study
Human pFastbacHTB MVI Spring bzip	Synthetic Gene - This Study
pHalo-Rpb1	Darzacq lab
pSNAP-C1	Addgene 58186
pSNAP-Rpb1	This Study
YFP-NLS-R62D Actin	De Lanerolle Lab
pLV-Tet0-Halo-NLS-Motor (1-814)	Große-Berkenbusch et al 2020
pLV-Tet0-Halo-NLS-CBD (1060-1253)	Große-Berkenbusch et al 2020
pcDNA3.1 MVI	Synthetic Gene - This Study
pcDNA3.1 MVI Spring	Synthetic Gene - This Study

Supplementary Table 3. Primers for qPCR.

Sequence	Use
CTGCTGCAGGAACCTCTCAT	VASP For
CTTCCTGGGGAGAATGTGG	VASP Rev
GACAACCTCCTGGTTGGGAGA	FOXJ2 Pro. For
GGAGGTCTACTTGGGGAAG	FOXJ2 Pro. Rev
AGGGGAATCTCTAGGCAAA	PTEN Pro. For
TGCATTCGCTCTTTCCTTTT	PTEN Pro. Rev
GAATGGTTTGTGGCTCAGGT	PTEN Int. For
CCCCTGGGTTGAAATATGG	PTEN Int. Rev
GGTGCCTGAGAAGAGGTGAG	EGR3 ex2 For
CCATGTGGATGAATGAGGTG	EGR3 ex2 Rev
TCACGTACCACACACACACG	EGR3 Int. For
TCCGGGTCTGAACTACCTG	EGR3 Int. Rev
CCCCTGCTTCTTCTCAGTTG	IER3 Pro. For
AAAAGATGCACGGATTGGAG	IER3 Pro. Rev
CTCACCTTCCTCCTCCTCCT	TNNT1 Int. For
GTCCAGCAGAGACTGGAACC	TNNT1 Int. Rev
GGCTCACCCCTTGCTGATGCT	Myc For
GCTCTGGGCACACACATTGG	Myc Rev
GCTTTCCTGCCTCACCATTA	FOXJ2 Int. For
AAGGCCAAGTCAGATGAAGC	FOXJ2 Int. Rev
GGAGAAGAACAGCACAACCT	VASP RT-qPCR For
CCCTCTGTAGGTCCGAGTAAT	VASP RT-qPCR Rev
TGGTCAAGGCAGAACAGAAG	TNNT1 RT-qPCR For
CCCATGTAGTCAATGTCCAGAG	TNNT1 RT-qPCR Rev
CTCGGATGGAGTTACTCTTTC	INHA RT-qPCR For
CACCAGCCATGGGATTAAGA	INHA RT-qPCR Rev
TCAGCCCAGTGTGTCATTAG	CDC42BPA RT-qPCR For
TCTTCCGACTTGCATGGATAA	CDC42BPA RT-qPCR Rev
GGCTCCTTTGAAGTGGAGTAATA	EGR3 RT-qPCR For
CACAGGAGAAGTAACGCTAACA	EGR3 RT-qPCR Rev

6. Autophagy receptor NDP52 modulates RNA Polymerase II transcription

6.1. Context of Research and Contributions

After exploring the role of MVI in the regulation of transcription in Chapters 4 and 5, the work presented here focuses on MVI binding partner NDP52 and its nuclear roles. As mentioned earlier, in the cytoplasm, NDP52 is an autophagy receptor and binding partner of MVI. During our initial investigation of the role of nuclear MVI (Chapter 4), we used NDP52 to study the activation of this molecular motor in the nucleus (Fili *et al.*, 2017). In addition to our findings regarding MVI activation and nuclear function, in Fili *et al.* (2017) we show that NDP52 can bind to double-stranded DNA; is present in the nucleus and can be co-immunoprecipitated with RNAPII-Ser5P. Moreover, antibody depletion of NDP52 significantly reduced *in vitro* transcription levels – by approximately 50%. These data strongly pointed to a role for NDP52 in transcription. Furthermore, as it is described in Chapter 1 and in Fili *et al.* (2017), NDP52 is a gene paralog and shares high sequence homology with CoCoA, a transcription coactivator for nuclear receptors. This led us to propose that in addition to being an important binding partner and activator of MVI motor activity, NDP52 could have important roles in transcription regulation. In the final chapter we followed-up on these findings and attempt to answer the following questions: *How does the nuclear organisation and molecular dynamics of NDP52 relate to transcriptional activity? Does disruption of NDP52 impact gene expression? What is the nuclear interactome of NDP52? Could the ability of NDP52 to bind DNA be important for its nuclear role? How do the biochemical properties of the protein contribute to its nuclear role?*

This chapter is composed of one manuscript, listed below, for which I am the sole main contributor.

dos Santos Á, Rollins DE, Hari-Gupta Y, Reed HCW, Du M, Ru SYZ, Pidlisna K, Stranger A, Lorgat F, Brown I, Howland K, Aaron J, Wang L, Ellis PJI, Chew TL, , Martin-Fernandez ML, Pyne ALB, Toseland CP.

Autophagy receptor NDP52 modulates RNA Polymerase II transcription. **BioRxiv (2022)**
<https://doi.org/10.1101/2022.02.01.478690>

In this Chapter we provide evidence that NDP52 is a regulator of transcription, by showing that its molecular clustering and relatively slow/static molecular dynamics are tightly coupled to transcriptional activity. Furthermore, we show NDP52 clustering at transcription initiation sites with RNAPII-Ser5P and that overexpression of NDP52 leads to an increase in transcriptional clusters. Furthermore, depletion of NDP52 has a global effect on gene expression. Interestingly, NDP52 binding to DNA appears to cause changes in DNA structure and create bridging events between DNA molecules. This, together with a nuclear interactome that is enriched for chromatin regulators led us to propose that one of the possible ways NDP52 is regulating transcription is through changes in chromatin structure/organisation.

Contributions

This project was conceived by myself and Dr Christopher Toseland, as we discussed emerging NDP52 data used in Fili *et al.* (2017). I led this project, initiated contacts with collaborators and coordinated the work between multiple research groups. I designed and performed experiments with additional contributions as follows: I supervised students Hannah Reed and Sabrina Yong Zi Ru, who contributed to recombinant protein data, as well as Kseniia Pidllisna, who contributed to LC-MS/MS sample preparation. AFM imaging of both DNA and proteins was performed by myself and Daniel E Rollins. AFM data analysis was performed by myself, Mingxue Du and Dr Alice Pyne. Kevin Howland ran LC-MS/MS samples prepared by myself. I performed data analysis of all recombinant proteomics data. Anne Stranger helped with analysis of endogenous co-immunoprecipitation proteomics data, under my guidance. Ian Brown performed electron microscopy sample preparation, from cells prepared by myself. Both Ian Brown and myself acquired electron microscopy images. Dr Yukti Hari-Gupta prepared RNA-Seq samples for MCF-7 cell line, I prepared RNA-Seq samples for HeLa. Faeza Lorgat contributed to recombinant protein biochemical data. I prepared samples for both STORM and acMFM. Dr Christopher Toseland and myself performed STORM and acMFM imaging experiments with support of HHMI Janelia and Research Complex at Harwell facility staff. I analysed all STORM data. Both myself and Dr Toseland used single-molecule tracking analysis tools developed by Dr Aaron to analyse acMFM data. Dr Christopher Toseland performed mass photometry data and data analysis. All other experiments were performed by myself. I wrote the manuscript with Dr Christopher Toseland and included input from all other authors.

6.2. Manuscript

(see below)

6.2.1. Manuscript 7 - Autophagy receptor NDP52 modulates RNA Polymerase II transcription

Autophagy receptor NDP52 modulates RNA Polymerase II transcription

Ália dos Santos¹, Daniel E. Rollins², Yukti Hari-Gupta^{3,3}, Hannah C. W. Reed³, Sabrina Yong Zi Ru³, Kseniia Pidlisna³, Ane Stranger³, Faeza Lorgat¹, Ian Brown³, Kevin Howland³, Jesse Aaron⁴, Lin Wang⁵, Peter J. I. Ellis³, Teng-Leong Chew⁴, Alice L. B. Pyne², Marisa Martin-Fernandez⁵, Christopher P. Toseland^{1*}

¹Department of Oncology and Metabolism, University of Sheffield, Sheffield, S10 2RX, UK

²Department of Material Science and Engineering, University of Sheffield, Sheffield, S1 3JD, UK

³School of Biosciences, University of Kent, Canterbury, CT2 7NJ, UK

⁴Advanced Imaging Center, HHMI Janelia Research Campus, Ashburn, VA 20147, USA

⁵Central Laser Facility, Research Complex at Harwell, Science and Technology Facilities Council, Rutherford Appleton Laboratory, Harwell, Didcot, Oxford OX11 0QX, UK

[§]Current address: MRC LMCB, University College London, Gower Street, London, WC1E 6BT, UK.

***Corresponding Author:** Christopher P. Toseland, Department of Oncology and Metabolism, University of Sheffield, Sheffield, S10 2RX, UK
c.toseland@sheffield.ac.uk

Key Words: NDP52, RNA Polymerase II, Transcription, Nuclear organisation, Gene expression, Chromatin.

Abstract

NDP52 is an autophagy receptor involved in the recognition and degradation of invading pathogens and damaged organelles. Although NDP52 was first identified in the nucleus and is expressed throughout the cell, to date, there is no clear nuclear function for NDP52.

Here, we use a multidisciplinary approach to characterise the biochemical properties and nuclear roles of NDP52. We found that NDP52 clusters with RNA Polymerase II (RNAPII) at transcription initiation sites and that its overexpression promotes the formation of additional transcriptional clusters. We also show that depletion of NDP52 impacts overall gene-expression levels in two model mammalian cells, and that transcription inhibition affects the

spatial organisation and molecular dynamics of NDP52 in the nucleus. This directly links NDP52 to a role in RNAPII-dependent transcription.

Furthermore, we also show that NDP52 binds specifically and with high affinity to double-stranded DNA (dsDNA) and that this interaction leads to changes in DNA structure *in vitro*. This, together with our proteomics data indicating enrichment for interactions with nucleosome remodelling proteins and DNA structure regulators, suggests a possible function for NDP52 in chromatin regulation. We propose this could be a mechanism through which NDP52 can regulate RNAPII transcription.

Overall, here we uncover novel nuclear roles for NDP52 in gene expression and DNA structure regulation.

Introduction

NDP52/CALCOCO2, a 446 amino-acid autophagy receptor, was first identified in the nucleus, as a component of nuclear dots – multiprotein sub-compartments that respond to environmental stresses, such as viral infections (Korioth et al., 1995). However, later reports showed that the protein is distributed throughout the cell, with higher levels in the cytoplasm (Sternsdorf et al., 1997). NDP52 has since been linked to cytoplasmic roles in autophagy and cell adhesion, where it is known to be required for pathogen-containing autophagosome maturation and membrane ruffle formation (Morriswood et al., 2007; Mostowy et al., 2011; Tumbarello et al., 2012); however, no nuclear function has been attributed to this protein.

NDP52 comprises a skeletal muscle and kidney enriched inositol phosphatase (SKIP) carboxyl homology (SKICH) domain, which facilitates membrane localisation (Morriswood et al., 2007); a long coiled-coil (CC) region that includes a predicted leucine-zipper (LZ) domain, and two zinc finger domains at the C-terminal - ZF1 and ZF2 (Fig.1A) (Korioth et al., 1995). The CC region of NDP52 has been identified as a potential homo-dimerisation domain for the protein (Kim et al., 2013). At the C-terminal, ZF1 has been characterised as an unconventional dynamic zinc finger, whilst ZF2 is a canonical C₂H₂-type zinc finger (Xie et al., 2015). The C-terminal domains of NDP52 are responsible for interactions with ubiquitin, which allows binding to ubiquitylated pathogens, as well as interactions with actin-based motor Myosin VI (MVI) (Fili and Toseland, 2019; Morriswood et al., 2007; Xie et al., 2015). In the cytoplasm, interactions between NDP52 and MVI allow autophagosome maturation (Tumbarello et al., 2012). However, there is little information available regarding the biochemical and structural properties of the full-length protein, which limits our understanding of its functions.

NDP52 is a member of the Calcium-binding and coiled-coil domain containing (CALCOCO) family. Other members are TAX1BP1 and CoCoA. NDP52 shares high sequence homology with both TAX1BP1 and CoCoA, and all three proteins have similar domain structure. Interestingly, whilst TAX1BP1 is also a known autophagy receptor (Morriswood et al., 2007; Tumbarello et al., 2015), CoCoA is a well-characterised transcription coactivator (Kim et al., 2003). Recently, CoCoA has also been linked to roles in autophagy, further highlighting potential functional similarities between these proteins (Nthiga et al., 2020; Stefely et al., 2020). Moreover, NDP52 binding partner MVI, has important nuclear roles in transcription, DNA repair and chromatin regulation (Cook et al., 2020). Furthermore, a recent study by Fili

et al. has revealed that the interaction between NDP52 and MVI enhances RNA Polymerase II (RNAPII) transcriptional activity *in vitro* (Fili et al., 2017).

Here, we explore the spatial organisation of NDP52 in the nucleus, as well as its dynamic behaviour; and assess how perturbation of this protein affects gene expression in cells. We found that NDP52 forms clusters in the nucleus at RNAPII transcription initiation sites and that knockdown of NDP52 significantly affects gene expression in both HeLa and MCF-7 cells. Furthermore, our biochemical analysis shows that NDP52 binds to double-stranded DNA with high affinity and this results in changes to DNA shape and structure *in vitro*. We have also explored the nuclear interactome of NDP52, which shows enrichment for proteins involved in DNA structure and nucleosome regulation. We suggest that NDP52 has a regulatory role in RNAPII-dependent transcription, and that this arises both from direct interactions with chromatin as well as from protein-protein interactions with chromatin regulators and transcription factors. Overall, this highlights a wider role of NDP52 across the cell and it remains to be determined if there are links between its cytoplasmic and nuclear functions.

Methods

Constructs

A list of constructs is provided in Supplementary table 1.

Cell culture and Transfection

HeLa (ECACC 93021013) and MCF-7 (ECACC 86012803) cells were cultured in MEM Alpha medium (Gibco), with GlutaMax (no nucleosides), supplemented with 10% Fetal Bovine Serum (Gibco), 100 µg/mL streptomycin (Gibco) and 100 units/mL penicillin, at 37°C and 5% CO₂. To inhibit transcription, cells were treated with 5µg/mL α -amanitin for 4 hours at 37°C and 5% CO₂.

For transient transfection of Halo-NDP52, HeLa cells cultured in Nunc LabTek dishes (Merk) were transfected using Lipofectamine 2000 (Invitrogen) for 24h. Following this, cells were used for live-cell imaging using Fluorescence Recovery After Photobleaching (FRAP) or aberration-corrected Multi-Focal Microscopy (acMFM).

Immunofluorescence

Following nuclear staining using Hoechst 33342 (Thermo Scientific), HeLa and MCF-7 cells cultured on glass coverslips were fixed for 15 minutes at room temperature, in 4%(w/v) paraformaldehyde (PFA) in Phosphate-buffered saline (PBS). Residual PFA was then quenched for 15 minutes using 50mM Ammonium Chloride in PBS.

Cells were permeabilised and blocked in 2% (w/v) BSA, 0.1% (v/v) Triton X-100 in PBS for 30 minutes. Cells were then labelled against endogenous proteins for 1 hour in 2% (w/v) BSA, with appropriate primary antibody and, subsequently, with appropriate fluorophore-conjugated secondary antibodies. When using anti-phospho antibodies, the immunofluorescence protocol was performed in Tris-buffered saline (TBS).

For endogenous NDP52, rabbit anti-NDP52 (1:200, Genetex GTX115378) antibodies were used. For RNA Polymerase II, mouse anti-RNAPII phospho Ser 5 (1:500, Abcam, ab5408) was used. Secondary conjugated antibodies Donkey anti-rabbit Alexa 647 (1:500, Abcam, 181347) and Donkey anti-mouse Alexa 488 (1:500, Abcam, ab181289) were used.

Coverslips were then mounted on microscope slides in Mowiol solution (10%(w/v) mowiol 4-88, 25%(v/v) glycerol, 0.2M Tris-HCl, pH 8.5) with 2.5%(w/v) DABCO (Sigma).

Confocal Microscopy

Fixed cells were imaged using a Zeiss LSM980, with a Plan-Achromat 63 x 1.4 NA oil immersion objective (Carl Zeiss, 420782-9900-000). Three laser lines: 405, 488 and 561 were used for excitation of Hoechst, Alexa-fluor 488 and Alexa-fluor 647 fluorophores. Built-in multi-band dichroic mirror MBS405/488/561 (Carl Zeiss, 1784-995) were used to reflect excitation laser beams onto samples. For fluorescence signal collection, the used emission spectral bands were: 410–524 nm (Hoechst), 493–578 nm (Alexa-fluor 488) and 564–697 nm (Alexa-fluor 647). The green channel (Alexa-fluor 488) was imaged using a 1 gallium arsenide phosphide (GaAsP) detector, while the blue (Hoechst) and red (Alexa-fluor 647) channels were imaged using two multi-anode photomultiplier tubes (MA-PMTs). For imaging acquisition and rendering, Zeiss ZEN software was used. Confocal Images were deconvolved using the Zeiss Zen2.3 Blue software, using the regularized inverse filter method.

Stochastic Optical Reconstruction Microscopy

No. 1.5, 25mm round glass coverslips were cleaned by incubation with etch solution (5:1:1 ratio of H₂O : H₂O₂ (50% wt in H₂O stabilised, Fisher Scientific) : NH₄OH (ACS reagent, 29-30% NH₃ basis, Sigma) for 2 hours in a 70°C water bath. Cleaned coverslips were washed in filtered water and ethanol and allowed to dry before cell seeding.

Cells were fixed for 15 minutes in 4%(w/v) PFA in PBS and residual PFA was quenched with 50mM Ammonium Chloride in PBS for 15 minutes. Immunofluorescence was performed using filtered TBS. Cells were first permeabilised and blocked for 30 minutes in 3% (w/v) BSA, 0.1% (v/v) Triton X-100. Cells were then incubated in primary antibody for 1 hour, at the same dilution as for the normal immunofluorescence protocol. Cells were washed three times (10 minutes each wash) with 0.2% (w/v) BSA, 0.05% (v/v) Triton X-100 in TBS. Cells were subsequently incubated in an appropriate fluorophore-conjugated secondary antibody for 1 hour, at a 1:250 dilution, in 3% (w/v) BSA, 0.1% (v/v) Triton X-100. Cells were washed in TBS and PBS and fixed in 4% (w/v) PFA in PBS a second time. Cells were stored in PBS supplemented with 0.02% (w/v) NaN₃ in the dark until STORM imaging.

Before imaging, coverslips were washed in filtered H₂O and assembled into Attofluor cell chambers (Invitrogen). Imaging was performed in STORM buffer - 10% (w/v) glucose, 10mM NaCl, 50mM Tris-HCl pH8.0 - supplemented with GLOX solution (5.6% (w/v) glucose oxidase and 3.4 mg/mL catalase in 50mM NaCl, 10mM Tris-HCl pH 8.0) and 0.1% (v/v) 2-mercaptoethanol.

STORM imaging was performed using a Zeiss Elyra PS.1 system. For sample illumination HR Diode 488 nm (100mW) and HR Diode 642 nm (150mW) lasers were used, where power density on the sample was 7-12kW/cm² and 7-14kW/cm², respectively. Built-in multi-band

dichroic mirror MBS 405/488/642 (Carl Zeiss 1784-996) were used to reflect excitation laser beams onto samples. To reduce background fluorescence levels, imaging was performed using Highly Inclined and Laminated (HILO) illumination with a 100x NA 1.46 oil immersion objective (Carl Zeiss alpha Plan-Apochromat, 420792-9800-000). For fluorescence signal collection, a BP 420-480/BP 495-550/LP 650 multi-bandpass emission filter (Carl Zeiss 1769-207) was used and a final image was acquired using an Andor iXon DU 897 EMCCD camera with 25msec exposure, for 25000 frames.

Image processing was performed in Zeiss Zen software. For two-colour STORM images, channel alignment was performed following a calibration procedure using pre-mounted MultiSpec beads (Carl Zeiss, 2076-515). For the calibration procedure, the affine method was performed, to account for lateral stretching and tilting between the two channels. This was performed for each day of acquisitions.

Blinking event detection was then performed in Zeiss Zen software using a 9-pixel mask with a signal-to-noise ratio of 6, accounting for overlap, to allow localisation of molecules in dense environments. Final molecule positions were then determined through fitting of a 2D Gaussian function. Molecule positions were subjected to model-based cross-correlation drift correction. For Alexa-fluor-647 and Alexa-fluor-488 labelled molecules, the typical mean value of localisation precision was 20 nm and 30 nm, respectively. Molecule localisation tables were exported as .txt files for further analysis using ClusDoC software.

ClusDoC

Following export of molecule positions from Zeiss ZEN software, STORM data were further analysed using ClusDoC software (<https://github.com/PRNicovich/ClusDoC>) (Pageon et al., 2016). The nucleus was selected as an ROI for cluster analysis. The Ripley K function was first calculated for the ROI selected, to identify the r_{max} . This value was then used in DBSCAN analysis for single-channel images or ClusDoC analysis for two-channel images. Minimum cluster size was set to 5 molecules with a smoothing value set at 7 and an epsilon value set at the mean localisation precision value for the dye. Other parameters remained at default values.

Aberration Corrected Multi-Focal Microscopy

Cells transiently expressing Halo-NDP52 were labelled for 15 minutes with 10 nM Halo tag-JF549 ligand in cell culture medium at 37°C, 5% CO₂. Cells were then washed three times in complete media and incubated for at least 30 minutes at 37°C, 5% CO₂ before imaging. For imaging, cell media was replaced with FluoroBrite DMEM medium (Thermo Fisher Scientific).

Single-molecule tracking experiments were performed using an aberration-corrected multi-focal microscope (acMFM), described in Abrahamsson *et al.*, (Abrahamsson et al., 2013). Briefly, a custom optical system appended to the detection path of an optical Nikon Ti microscope was used. The detection path of the microscope included a diffractive multifocal grating in a conjugate pupil plane, a chromatic correction grating, to reverse spectral dispersion, and a nine-faceted prism followed by the final imaging lens. A 561 nm laser was used for excitation, with a 4-6 kW/cm² power density at the back aperture of a 100x 1.4NA objective (Nikon).

AcMFM imaging produces nine separate, simultaneous images, each representing a separate focal plane, with an axial separation of ca. 400 nm between them. Field of view is ca. 20 μm . The nine-image array was digitised via an EMCCD camera (iXon Du897, Andor), at up to 32msec temporal resolution, with a typical duration of 30 seconds.

3D+t single-molecule images were reconstructed via a calibration procedure in Matlab (MathWorks) that accounts and calculates (1) inter-plane spacing, (2) affine transformation for the correct alignment of each focal plane in xy and (3) slight variations in the detection efficiency in each plane - typically less than 5-15% from the mean.

Reconstructed data were pre-processed, including background subtraction and deconvolution (3-5 Richardson-Lucy iterations) and/or Gaussian de-noising prior to 3D particle tracking using the MOSAIC software suite. Maximum particle displacement was set at 400 nm and a minimum 10 frames was required. Detected tracks were reconstructed and diffusion constants calculated through MSD analysis using custom Matlab software assuming an anomalous diffusion model.

Fluorescence Recovery After Photobleaching

Cells transiently expressing Halo-NDP52 were labelled for 15 minutes with 10 nM Halo tag-JF549 ligand in cell culture medium at 37°C, 5% CO₂. Cells were then washed three times in CO₂-independent medium (ThermoFisher) before imaging.

FRAP measurement was performed using a Zeiss LSM 880 system equipped with a 100x NA 1.46 oil immersion objective (Carl Zeiss alpha Plan-Apochromat, 420792-9800-000). For sample illumination a 20 mW 561 nm diode laser was used. Built-in multi-band dichroic mirror MBS 458/561 was used to reflect excitation laser beams onto samples. For fluorescence signal collection, the wavelengths from 566 nm to 685 nm were captured using a multi-anode photomultiplier tube (MA-PMT) with 0.96 μs pixel dwell time. The detector master gain was 900, and digital gain was 1.

Ten frames of confocal microscopy image under 8 mW 561 nm laser illumination were acquired before photobleaching. Selected regions of interest (ROIs) were exposed to full laser power, followed by 100 seconds of confocal microscopy image acquisition. The time course of fluorescence intensity from the selected ROIs was recorded by Zeiss ZEN 2.3 Blue software. Fluorescence intensity time traces from ROIs, whole cell areas and background areas were exported as .txt files, and then were analysed using easyFRAP Software (<https://easyfrap.vimnet.upatras.gr/?AspxAutoDetectCookieSupport=1>) (Koulouras et al., 2018).

RNA-Sequencing and Analysis

Total RNA was extracted from three replicates of NDP52 KD (using CALCOCO2 siRNA, Ambion, 4392420) and scrambled siRNA (using control siRNA, Qiagen, 1027280) in MCF-7 and HeLa cells. Ice cold TRIzol reagent was added to each cell culture dish and homogenised. The mixture was incubated at room temperature for 10 minutes. Chloroform was then added to the mixture and incubated at room temperature for 5 minutes. The samples were centrifuged at 8,000 $\times g$. The top, aqueous layer was collected and isopropanol was added. The mixture was then centrifuged at 12,000 $\times g$ for 30 minutes and the supernatant discarded. The pellet

was washed in 75% (v/v) ethanol and centrifuged at 7,500 $\times g$ for 5 minutes. The pellet was air dried and resuspended in RNase-free H₂O. RNA concentration and quality was then assessed by measuring absorbance at 260 nm and A260/A280 ratio. RNA samples were stored at -80°C.

The following procedures were performed by GENEWIZ and Glasgow Polyomics. The RNA-seq libraries were prepared using Poly-A selection. Resulting libraries concentration, size distribution and quality were assessed on a Qubit fluorometer and on an Agilent 2100 bioanalyzer. Paired-end sequencing (2x150 bp) was then performed on an Illumina NovaSeq next generation sequencer for HeLa cells (GENEWIZ) and (2x75 bp) on a HiSeq sequencer for MCF7 cells (Glasgow Polyomics).

Sequence reads were trimmed to remove possible adapter sequences and nucleotides with poor quality using Trimmomatic v.0.36. The trimmed reads were mapped to the Homo sapiens GRCh38 reference genome available on ENSEMBL using the STAR aligner v.2.5.2b. BAM files were generated as a result of this step. Unique gene hit counts were calculated by using featureCounts from the Subread package v.1.5.2. After extraction of gene hit counts, the gene hit counts table was used for downstream differential expression analysis. Using DESeq2, a comparison of gene expression between the customer-defined groups of samples was performed. The Wald test was used to generate p-values and log₂ fold changes. Genes with an adjusted p-value < 0.05 and absolute log₂ fold change > 1 were called as differentially expressed genes for each comparison.

Differentially expressed genes by at least 1.5-fold ($-0.5 \geq \log_2 FC \geq 0.5$) and adjust p-value < 0.05 were subjected to Gene Ontology analysis, using iDEP93 (<http://bioinformatics.sdstate.edu/idep93/>) (Ge et al., 2018).

RNA-Seq data were deposited in the Gene Expression Omnibus (GEO) database under the accession number.

Chromatin Immunoprecipitation and qPCR

To identify NDP52-DNA interactions, ChIP was performed using anti-rabbit NDP52 antibody (Genetex GTX115378). HeLa cells were crosslinked by adding formaldehyde directly to the cell medium, to a final concentration of 0.75% (v/v). Cells were left to incubate with gentle rotation at room temperature for 10 minutes. The reaction was stopped by adding glycine to a final concentration of 125 mM and incubating the mixture for 5 minutes at room temperature with rotation. Cells were washed twice with cold PBS and scraped in cold PBS. All cells were collected by centrifugation at 1,000 $\times g$ at 4°C for 5 minutes. The pellet was resuspended in ChIP lysis buffer - 50 mM HEPES-KOH pH 7.5, 140 mM NaCl, 1 mM EDTA pH 8.0, 1% (v/v) Triton X-100, 0.1% (m/v) Sodium Deoxycholate, 0.1% (m/v) SDS - supplemented with protease inhibitors, using 750 μ L per 1×10^7 cells. Cells were sonicated using a diagenode bioruptor sonicator to shear DNA until an average DNA fragment size of 200-800bp was achieved. Fragment size was determined using a 1.5% agarose gel.

Cell debris were removed through centrifugation of samples at 8,000 $\times g$ for 10 minutes at 4°C. The supernatant, enriched for chromatin, was stored at -80°C until used for immunoprecipitation experiments.

Chromatin fractions were diluted 1:10 in RIPA buffer - 50 mM Tris-HCl pH 8.0, 150 mM NaCl, 2 mM EDTA pH 8.0, 1% (v/v) NP40, 0.5% (m/v) Sodium Deoxycholate, 0.1% (m/v) SDS - supplemented with protease inhibitors. Three samples were used for immunoprecipitation with NDP52 and three samples for no-antibody control (beads only). 10 % of total chromatin was removed as input sample and stored at -20°C. All samples were pre-cleared using protein A magnetic beads (Thermo Fisher Scientific) for 30 minutes at 4°C with end-to-end rotation. Immunoprecipitation replicates were incubated overnight with NDP52 antibody (1:50 dilution) at 4°C with end-to-end rotation. The following day, 40 µL of protein A magnetic beads, pre-equilibrated in RIPA buffer, were added to each sample, including the no-antibody controls. Samples were incubated with end-to-end rotation at 4°C for 1 hour. Following this, beads were collected using a magnetic rack and washed twice in low-salt buffer (20 mM Tris-HCl pH 8.0, 150 mM NaCl, 0.1% (m/v) SDS, 1% (v/v) Triton X-100, 2 mM EDTA) followed by a wash in high-salt (20 mM Tris-HCl pH 8.0, 500 mM NaCl, 0.1% (m/v) SDS, 1% (v/v) Triton X-100, 2 mM EDTA), a wash in LiCl buffer (10 mM Tris-HCl pH 8.0, 250 mM LiCl, 1% (m/v) Sodium deoxycholate, 1% (v/v) NP40, 1 mM EDTA pH 8.0) and, finally, in TE buffer (10 mM Tris-HCl pH 8.0; 1 mM EDTA pH 8.0).

DNA was eluted by incubating the beads with 120 µL elution buffer (1%(w/v) SDS; 100mM NaHCO₃) at 30°C, with shaking. To reverse crosslinking, eluted protein-DNA complexes and input samples were incubated overnight with 4.8 µL NaCl (5M) and 2 µL RNase A (10mg/mL) at 65°C with shaking. The following day, samples were incubated with Proteinase K for 1 hour at 60°C.

The DNA was purified using phenol:chloroform extraction and samples analysed using QuantiNova SYBR Green qPCR kit (Qiagen). A list of qPCR primers for ChIP is supplied in supplementary table 2.

Protein expression and purification in *Escherichia coli*

Recombinant protein expression was performed in *E. coli* BL21 DE3 cell (Invitrogen) in Luria Bertani media. Proteins were purified by affinity chromatography, using HisTrap FF columns (GE Healthcare). Protein fractions were further purified using Size Exclusion Chromatography, using a Superdex 200 16/600 column (GE Healthcare).

Size Exclusion Chromatography and Multi-Angle Light Scattering

100 µL samples of recombinant proteins, at concentrations of 1mg/mL (NDP52-FL and CoCoA) and 5mg/mL (_NNDP52, _CNDP52 and ZF2) were loaded onto a Superdex 200 (30 x 1cm) analytical gel filtration column (GE Healthcare), equilibrated in 50mM Tris pH7.5, 150 mM NaCl, 1mM DTT and controlled by Waters 626 HPLC at room temperature. A Viscotek SEC-MALS 9 and Viscotek RI detector VE3580 (Malvern Panalytical) were used for detection. Analysis was performed using Omnisec software (Malvern Panalytical).

Dynamic Light Scattering

Dynamic light scattering measurements were performed at 20°C, using a Zetasizer Nano ZS DLS system (Malvern Panalytical). Before measuring light scattering intensity at 90° angle, samples were centrifuged at 20 000xg for 10 minutes. Analysis was undertaken using the Zetasizer software.

Microscale Thermophoresis

Recombinantly purified protein constructs were labelled with RED-tris NTA dye (NanoTemper Technologies GmbH) in PBS to a concentration of 100 nM. A 20 μ M stock of non-labelled protein was also prepared. This stock was used in a 16-step serial dilution in PBS buffer. For oligomerisation studies, 10 μ M of protein was used as the highest ligand concentration, with Red-tris-NTA labelled protein kept at a final concentration of 50 nM for all reactions.

Reactions were incubated for 15 minutes at room temperature in the dark and loaded into Monolith NT.115 Capillaries (NanoTemper Technologies GmbH). Microscale thermophoresis measurements were performed using a Monolith NT.115 (NanoTemper Technologies GmbH) with 20%(RED) LED and high MST power. Binding assays were run as three independent experiments and the data were fitted using a K_D model with ligand-induced initial fluorescence change, as described by Jerabek-Willemsen *et al.* (Jerabek-Willemsen *et al.*, 2014).

Circular Dichroism

Recombinantly purified constructs were prepared in 50mM Tris-HCl pH7.5, 150 mM NaCl. Circular dichroism spectra were obtained from 200 μ L samples in a 1-mm cuvette, in a J175 spectropolarimeter from Jasco, with data collected at 0.5 nm intervals with averaging of 16 scans. For thermostability data, spectra were collected between 20 and 90 $^{\circ}$ C, and mean residue ellipticity values at 222 nm or 215 nm wavelength were fitted to a simple sigmoidal curve.

Electrophoretic Mobility Shift Assay

Reactions were performed in a final volume of 30 μ L, with 250 nM ds40 and increasing concentrations of NDP52-FL (between 0.5 and 3 μ M) in 50 mM Tris-HCl pH 7.5, 50 mM NaCl and 3 mM MgCl₂. After 5 minutes incubation, reactions were supplemented with 3 μ L of 30% (v/v) glycerol, loaded on a 3% agarose gel and run in Tris-Borate buffer at 60V. Gels were incubated for 30 minutes in ethidium bromide, washed for 20 minutes with H₂O and visualised under UV light.

Nano-Differential Scanning Fluorimetry

Thermostability of recombinantly produced proteins NDP52-FL, c NDP52 and ZF2 was assessed using nano-DSF, at protein concentrations 50 μ M, 75 μ M and 100 μ M, respectively. Samples were prepared in 50 mM Tris-HCl pH 7.5, 150 mM NaCl and loaded in nanoDSF Grade Standard Capillaries (NanoTemper Technologies GmbH), for NDP52-FL, or nanoDSF Grade High Sensitivity Capillaries (NanoTemper Technologies GmbH), for c NDP52 and ZF2. Data were acquired using a Prometheus NT.48 (NanoTemper Technologies GmbH).

Thermal denaturation of proteins was detected with heating in a linear thermal ramp (2 $^{\circ}$ C \cdot min⁻¹) between 20 and 90 $^{\circ}$ C, with an excitation power of 60-90%. Temperature unfolding was detected by following fluorescence emission at 350 and 330 nm wavelength. Melting temperatures were determined as the maxima of the first derivative of the ratio 350nm/330nm, using NanoTemper software (NanoTemper Technologies GmbH).

Mass Photometry

Before measurements, samples were centrifuged at 20 000 xg for 10 min. The samples were then diluted to 10 nM immediately prior to measurements in 50mM Tris-HCl pH7.5, 150 mM NaCl. Measurements were performed on clean glass coverslips and recorded on the OneMP mass photometer (Refeyn Ltd) for 60 s. Each measurement was repeated at least 3 times. The recorded videos were analyzed using DiscoverMP (Refeyn Ltd) to quantify protein binding events. The molecular weight was obtained by contrast comparison with known mass standards (BSA, Urease and IgG) measured on the same day.

Atomic Force Microscopy

Preparation of samples for imaging was carried out as described fully in a published protocol (Pyne et al., 2021) <https://doi.org/10.17504/protocols.io.bncemate>. Linear 339 bp DNA molecules, NDP52-FL and cNDP52 were adsorbed onto freshly cleaved mica disks (diameter 5 mm, Agar Scientific, UK), separately and in combination, at room temperature using poly-L-lysine (PLL) 0.01% solution (Sigma-Aldrich) (Pyne and Hoogenboom, 2016). 20 μ L of 20 mM HEPES pH 7.4 or 50 mM TRIS, 150 mM NaCl buffer solution was deposited on the surface. The sample solution was then added to the deposited buffer solution with approximate sample masses of 7ng of DNA for DNA alone, 10 ng of NDP52 with 6 ng of DNA and 10 ng of cNDP52 with 14 ng of DNA. For NDP52-FL and cNDP52 imaged in the absence of DNA 20 μ L of 50 mM TRIS, 150 mM NaCl was placed on the PLL surface and between 3 and 8 ng of either protein was added to the buffer. Samples were adsorbed for approximately 10 minutes followed by four washes in buffer.

All AFM measurements were performed in liquid <https://doi.org/10.17504/protocols.io.bncemate>. Experiments were carried out in PeakForce Tapping mode on a Dimension XR with a FastScan AFM head (Bruker) with FastScan D AFM probes (Bruker). Continuous force–distance curves were recorded with the tip-sample feedback set by the peak force as referenced to the force baseline. Force–distance curves were recorded over 40 nm (PeakForce Tapping amplitude of 20 nm), at a frequency of 8 kHz with PeakForce setpoints in the range of 5–12 mV. Images were recorded at 512 \times 512 pixels to ensure a resolution \geq 1 nm/pixel at line rates of 1–4 Hz.

The Python software package TopoStats (Beton et al., 2021) was used to automate processing and tracing of DNA, with the code available at <https://github.com/AFM-SPM/TopoStats>. AFM images were processed using a user-designed Python script (pygwytracing.py), which utilises the Gwyddion 'pygwy' module (Nečas and Klapeček, 2012) for automated image correction, DNA and protein molecule identification and morphological analysis.

Size measurements were performed in ImageJ.

DNA binding Assays

FITC-labelled and unlabelled oligonucleotides were purchased from Sigma-Aldrich. For dsDNA preparation, equimolar concentrations of complementary ssDNA oligonucleotides were mixed. A list of oligonucleotides is provided in Supplementary table 3.

Recombinant NDP52 (NDP52-FL, _cNDP52, _NNDP52 and ZF2) and CoCoA constructs were titrated into 100nM of FITC labelled ssDNA 40 bp or dsDNA, 15 or 40 bp, in 50mM Tris-HCl pH7.5, 150mM NaCl, 1mM DTT. Measurements were performed using a ClarioStar microplate reader (BMG Labtech). Fluorescence excitation was performed at 495 nm wavelength and emission spectra were measured between 515 and 570 nm wavelength, with fluorescence intensity values taken at 520 nm. Change in fluorescence was plotted in function of protein concentration, using three independent replicates for each experiment. Titration curves for NDP52-FL, CoCoA and _NNDP52 were fitted to a binding quadratic equation:

$$\frac{[Protein.DNA]}{[Protein]_t + [DNA]_t + K_d} = \frac{([Protein]_t + [DNA]_t + K_d) - \sqrt{([Protein]_t + [DNA]_t + K_d)^2 - 4[Protein]_t[DNA]_t}}{2}$$

For _cNDP52 and ZF2, a modified quadratic equation, accounting for a linear portion of the curve was used:

$$\frac{[Protein.DNA]}{[Protein]_t + [DNA]_t + K_d} = \frac{([Protein]_t + [DNA]_t + K_d) - \sqrt{([Protein]_t + [DNA]_t + K_d)^2 - 4[Protein]_t[DNA]_t}}{2} + (a + (b[DNA]_t))$$

Small-Angle X-Ray Scattering and Ab initio envelope calculation

Recombinantly expressed and purified NDP52-FL in SAXS buffer (50mM Tris-HCl pH7.5, 150mM NaCl, 1 mM DTT) was used for SEC-SAXS experiments at a concentration of 5mg/mL. NDP52-FL was analysed using a Superdex 200 increase 3.2/300 column, at a flow rate of 0.075mL/min (Cytiva Life Sciences), using an Agilent 1200 HPLC system (Agilent LC). SEC-SAXS experiments were performed at the B21 Beamline, Diamond Light Source UK, by core facility staff. For SEC-SAXS analysis and envelope generation, ScÅtter software (Version J) was used in combination with the ATSAS package (Manalastas-Cantos et al., 2021).

Nuclear isolation and extract preparation

Nuclear isolation was performed as previously described and characterised (Fili et al., 2017; Lherbette et al., 2017). Briefly, HeLa cells were collected and washed once with ice-cold PBS, then washed with ice cold Hypotonic buffer N (10 mM Hepes pH 7.5, 2 mM MgCl₂, 25 mM KCl supplemented with 1 mM PMSF, 1 mM DTT and Protease Inhibitors (Thermo Fisher Scientific)). Cells were resuspended in cold Hypotonic buffer N and incubated on ice for 1h. Following this, cells were homogenised on ice using a glass Dounce homogeniser (Wheaton) and cell lysate was supplemented with sucrose solution to a final concentration

of 220 mM, before centrifugation. The pellet, corresponding to isolated nuclei, was washed with cold Buffer N (10 mM Hepes pH 7.5, 2 mM MgCl₂, 25 mM KCl, 250mM sucrose, 1 mM PMSF, 1 mM DTT, supplemented with Protease Inhibitor Cocktail).

For nuclear extract preparation, nuclei were incubated in nuclear 'Hypotonic lysis buffer' (10 mM Hepes pH 7.5, 2 mM MgCl₂, 25 mM KCl, 0.1%(V/V) Triton X-100, 0.1%(V/V) NP-40, supplemented with 1 mM PMSF, 1 mM DTT and Protease Inhibitors) for 1 hour on ice. Lysed nuclei were then used for recombinant protein pull-downs.

Immunoblotting

Cell pellets from HeLa and MCF-7 cells, following NDP52 KD or control siRNA, were heat-denatured and resolved by SDS-PAGE. Membranes were probed against actin (Abcam, ab6276) and NDP52 by incubation with rabbit polyclonal primary antibody (1:2000 dilution, GeneTex, GTX115378) and, subsequently, a goat anti-rabbit antibody, coupled to horseradish peroxidase (1:15 000 dilution, Abcam, ab6721). Bands were visualised with ECL Western Blotting detection reagents (Invitrogen) using a ChemiDoc gel imager (Bio-Rad). For Ponceau S staining, membranes were incubated for 5 minutes in Ponceau S reagent (Sigma), washed three times with water and then imaged.

Co-immunoprecipitation

HeLa cells (non-treated or following α -amanitin treatment for 4 hours) were collected and centrifuged at 500xg for 5 minutes at 4 °C. 1x10⁶ cells were used per co-immunoprecipitation assay. Each pellet was resuspended in 200 μ L of Lysis buffer (10mM Hepes pH7.5, 2 mM MgCl₂, 25mM KCl, 0.1mM DTT, 0.01mM PMSF, 0.1%(V/V) Triton X-100, 0.1%(V/V) NP40 and supplemented with protease inhibitors). Cells were left in Lysis buffer, on ice, for 1 hour. All samples were pre-cleared using protein A magnetic beads (Thermo Fisher Scientific) for 30 minutes at 4°C with end-to-end rotation. Immunoprecipitation replicates were incubated overnight with NDP52 antibody (1:100 dilution) at 4°C with end-to-end rotation. The following day, 50 μ L of protein A magnetic beads, pre-equilibrated in Lysis buffer, were added to each sample, including the no-antibody controls, and incubated at 4°C with end-to-end rotation for 2 hours. Following this, beads were collected using a magnetic rack and washed three times with PBS. After removing all PBS, 50 μ L of loading buffer (NuPAGE LDS sample buffer supplemented with 50 mM DTT) were added and samples were incubated at 95°C for 10 minutes. Samples were then loaded on SDS-PAGE gels for in-gel protein digestion for LC-MS/MS.

Recombinant protein pull-downs

Following recombinant protein purification, 2.5mg of protein, per replicate, were incubated with nuclear extract (2x10⁶ nuclei per pull-down) at 4°C with end-to-end rotation, for 4 hours. Following this, 100 μ L of Ni²⁺ magnetic beads (HisPur Ni-NTA ThermoFisher), pre-equilibrated in equilibration buffer (50mM Tris-HCl pH 7.5, 150 mM NaCl, 20 mM imidazole, 1mM DTT), were added to each sample, including the no-protein controls, and incubated at 4°C with end-

to-end rotation for 2 hours. Following this, beads were collected using a magnetic rack and washed three times with 'low imidazole buffer' (50mM Tris-HCl pH 7.5, 150 mM NaCl, 40 mM imidazole, 1mM DTT). Following this step, three elutions were performed using 'high imidazole buffer' (50mM Tris-HCl pH 7.5, 150 mM NaCl, 400 mM imidazole, 1mM DTT). Eluted samples were loaded on SDS-PAGE gels for in-gel protein digestion for LC-MS/MS.

In-gel digestion and LC-MS/MS

Following co-immunoprecipitation or recombinant protein pull-downs, samples were run only within the stacking portion of SDS-PAGE gels. Following this, gels were then stained, leaving a single band in the stacking portion of the gel, with all the protein content of each sample. Gel bands for each replicate were extracted, cut into 1x1mm squares and transferred into clean 1.5mL tubes. Gel particles were incubated with 50mM ammonium bicarbonate and acetonitrile in a 1:1 ratio at room temperature for 15 minutes and then centrifuged at 8,000 xg for 60 seconds and the supernatant discarded. Samples were then incubated in acetonitrile for 15 minutes and centrifuged to remove supernatant. Gel particles were then incubated in 10mM DTT, 50mM ammonium bicarbonate and incubated at 56°C for 30 mins. Following this, the samples were centrifuged, the supernatant removed, and samples briefly incubated in acetonitrile until gel pieces shrunk. Samples were centrifuged and 55mM iodoacetamide in 50mM ammonium bicarbonate solution was added so that all gel particles were submerged. Samples were incubated in the dark, at room temperature, for 20 minutes. Following centrifugation, the supernatant was removed and washed in 50mM ammonium bicarbonate solution:acetonitrile (1:1) for 15 minutes, followed by 50mM ammonium bicarbonate for 15 minutes and acetonitrile for 15 minutes (between each step samples were centrifuged and supernatant discarded). Samples were then centrifuged and all liquid removed.

For tryptic digestion, gel particles were incubated in digestion buffer (25 mM ammonium bicarbonate, 10%(V/V) acetonitrile and 10ng/ μ L Trypsin (Sigma Aldrich, EMS0006)) for 30 minutes on ice. Digestion buffer was replenished as needed during this process to ensure gel particles were covered in solution. After 30 minutes, excess digestion buffer was removed from each sample and replaced with 25mM ammonium bicarbonate, 10%(V/V) acetonitrile solution. Samples were incubated overnight at room temperature.

The next day, acetonitrile was added to each tube and samples were sonicated in an ultrasound bath for 15 minutes. Samples were then centrifuged and the supernatant, containing digested protein for mass spectrometry, was transferred into clean 1.5mL tubes. 50%(v/v) acetonitrile and 5%(v/v) formic acid solution was added to gel particles and these were sonicated again. The supernatant from this step was combined with the previously collected sample into the same tube. Extracted protein samples were vacuum dried and resuspended in 10%(v/v) acetonitrile, 0.1%(v/v) trifluoroacetic acid for nanoLC-MS.

Peptides were separated on a HSS T3 Acquity column (Waters) 75 μ m i.d. x 15 cm (1.8 μ m, 100A) using an Acquity M-Class UPLC (Waters), elution was performed with a linear gradient from 3 to 40% B over 40 mins (solvent A = 0.1% formic acid, solvent B = 0.1% formic acid, acetonitrile) and the eluate directed via a nanospray source to a Synapt G2-Si (Waters) with data collected in UDMSe mode. Mass spectrometry data were imported into the software package Progenesis QI (Non-Linear Dynamics) and searched against a protein database using an MSe Search algorithm with an FDR set to 4%. Progenesis QI software (Waters)

provided quality control information and quantification of peptides. The peptides were assigned using the 'human proteome including enolase v5 2017' from UNIPROT as a reference library, accounting for trypsin cleavage, carbamidomethyl modifications to cysteine residues and methionine oxidation. Maximum protein mass was set to 500kDa with a maximum of one missed cleavage allowed.

For peptide and protein assignments, a minimum of 3 fragments per peptide was required and a minimum of 5 fragments per protein. All assigned proteins contained at least one unique peptide. Following PCA analysis, replicates that didn't cluster were excluded. Hits with a $\log_2FC > 1$ and ANOVA $p < 0.05$, compared to controls (protein A or Ni^{2+} magnetic beads-pull downs) were considered for further analysis. Protein hits were submitted to Gene Ontology analysis using Gene Ontology Resource (<https://geneontology.org>).

Electron Microscopy

Cells grown on Aclar membrane (Agar Scientific) were fixed in 2% (w/v) formaldehyde and 0.5% glutaraldehyde in CAB (100mM Sodium cacodylate buffer pH7.2) for 2h at RT. The sample was washed 2 x 10 minutes in CAB. Cells were dehydrated by incubation in an ethanol gradient, 50% EtOH for 10 min, 70% EtOH overnight, and 90% EtOH for 10 min followed by three 10-min washes in 100% dry EtOH. Cells were then suspended in LR White resin medium grade (London Resin Company) for 4h and then in fresh LR White resin overnight. Following 2 x 4h changes in fresh LR White resin samples were placed in sealed gelatine capsules and were polymerised upright at 60°C for 20 hours. Ultrathin sections were cut using a Leica EM UC7 ultramicrotome equipped with a diamond knife (DiATOME 45°). Sections (80 nm) were collected on uncoated 400-mesh gold grids.

Samples were blocked in a 20 μ l drop of 2% BSA in TBST (20mM Tris, 500mM NaCl, 0.1% BSA and 0.05% Tween 20) at room temperature for 30 min. Grids were then transferred directly into a 20 μ l drop of Rabbit anti-NDP52 (1:200 dilution, Genetex GTX115378) TBST and incubated for 1 hr. Grids were washed in 6 x TBST. Grids were then moved into a drop of goat anti-rabbit IgG 5nm gold (British Biocell International) diluted 1:50 and then moved to a fresh drop of the same antibody and incubated for 30 min. Excess antibody was removed by washing in 6 x 20 μ l drops of TBST and 6 x 20 μ l drops of milliQ water and dried.

Grids were stained for 15 min in 4.5% uranyl acetate in 1% acetic acid solution and then washed in 6 x 20 μ l drops of milliQ water. Grids were then stained with Reynolds lead citrate for 3 min and washed in 6 x 20 μ l drops of milliQ water. Electron microscopy was performed using a JEOL-1230 transmission electron microscope operated at an accelerating voltage of 80 kV equipped with a Gatan One View digital camera.

Results

Nuclear organisation and dynamics of NDP52

To attribute a nuclear function to NDP52, we first assessed its nuclear localisation in two example mammalian cell lines. As expected, immunofluorescence staining of NDP52 in both HeLa and MCF-7 cells shows that NDP52 is distributed throughout the cytoplasm and nucleus (Fig.1B). Confocal imaging of different focal planes also shows distribution of the protein throughout the organelle (Fig.1C). To further confirm this, we also used electron microscopy with gold-immunolabelling of endogenous NDP52. Imaging of negative stained HeLa sections (c.a. 70 nm thickness) (Fig.1D) clearly shows NDP52 particles in nuclear regions, which can be observed in zoomed-in sections in Fig.1E. The presence of NDP52 in the nucleus is consistent with previous reports (Fili et al., 2017; Koriath et al., 1995; Sternsdorf et al., 1997).

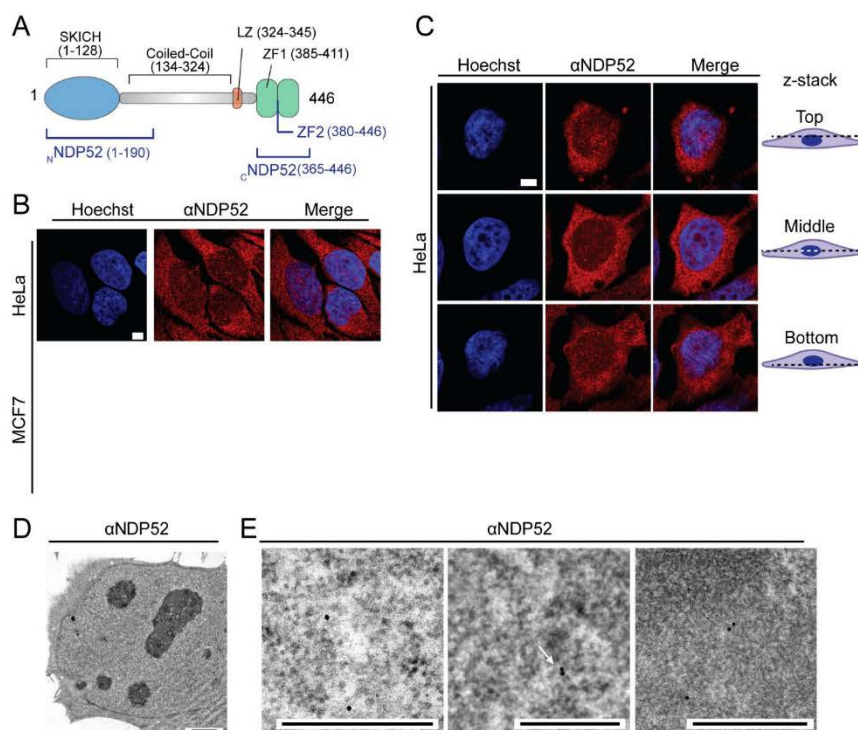


Figure 1 – NDP52 is distributed throughout the nucleus. (A) Diagram of NDP52 displaying protein domains and key features, as well as recombinant constructs used in this study (in blue). (B) Confocal imaging of HeLa and MCF-7 cells labelled by immunofluorescence against NDP52 (red), with DNA staining shown in blue. Scale bar = 5µm. (C) Confocal imaging of the intracellular distribution of NDP52 at different z points in HeLa. Scale bar = 5µm. (D) Electron microscopy of HeLa cells following gold immuno-labelling of NDP52. Scale bar = 2µm. Approximate thickness = 70-100 nm (E) Electron microscopy detail images of immuno-labelled NDP52 (black dots) in the nucleus. Scale bar = 500 nm.

Within the nuclear region, NDP52 appears to cluster into small punctate regions of high fluorescence intensity (Fig.2A). To explore the nuclear organisation of NDP52, we used Stochastic Optical Reconstruction Microscopy (STORM) in both HeLa and MCF-7 cells (Fig.2B). STORM allows us to visualise with high spatial precision and quantify individual molecules of NDP52 within a specified region of interest (ROI) (Fig. 2C), in this case the nuclear region. Furthermore, in-depth analysis of STORM data can also provide information regarding the clustering behaviour of the protein (Fig.2D). Protein clustering is often related to the molecular function of a protein and is particularly important in the enhancement of enzymatic processes such as transcription, DNA repair and DNA replication (Carmo-Fonseca, 2002; Cook, 2010; Meister et al., 2003; Schrank et al., 2018; Sporbert et al., 2002). Hence, as we investigate a nuclear function for NDP52, it is important to study its spatial organisation and how this might be linked to its nuclear role. To determine if NDP52 is randomly distributed or forms clusters (Fig.2D), we used a linearised Ripley's K function (Pageon et al., 2016). In both cell lines we observe a high probability for nuclear clustering of NDP52, as the Ripley's K function deviates from zero towards positive values (Fig.2E and F). To further understand the organisation of NDP52 clusters in the nucleus, we used ClusDoC software (Pageon et al., 2016). We defined NDP52 clusters, as regions where a minimum of 5 neighbouring molecules are spaced at a distance smaller than the mean value of localisation precision from STORM acquisition (described Methods). This allowed us to generate cluster maps for selected nuclear regions (Fig.2G) and determine that approximately 45% (± 6) and 79% (± 3) of NDP52 molecules are clustered in HeLa and MCF-7 cells, respectively. This corresponds to an average of 1604 (± 307) and 2285 (± 478) clusters per cell in HeLa and MCF-7 cells, respectively, with an average size of 3513 nm² (± 249) and 6190 nm² (± 890), and 44 (± 6) and 109 (± 64) molecules of NDP52 per cluster (Fig.2H-K). In both HeLa and MCF-7 cells, we observe large cell-to-cell variation for clustering data. Although STORM provides detailed information regarding the spatial organisation of molecules, it is also a low-throughput technique. Cell variability could be a result of cells not being synchronised; however, due to this limited throughput, it is also not possible to identify multiple subpopulations within the data. To assess how the spatial distribution of NDP52 relates to its molecular dynamics in the nucleus, we transiently expressed Halo-NDP52 in HeLa cells. This allowed us to use Fluorescence Recovery After Photobleaching (FRAP) to assess how dynamic NDP52 molecules are in the nucleus of live-cells (Fig.3A). Our data show that NDP52 has a recovery half-time of 7.5 s (± 0.8) (Fig.3B and SFig.1A) and a mobile fraction of 0.65 (± 0.02) (Fig.3C). This is in agreement with molecular clustering data showing that approximately 45% of NDP52 molecules are clustered, and would therefore be expected to be less dynamic. To obtain more detailed information on the dynamic behaviour of nuclear NDP52, we used aberration-corrected Multi-Focal Microscopy (acMFM). This technique allows us to simultaneously track single-molecules across nine focal planes in live-cells, covering 4 μ m in the z axis and 20 x 20 μ m in xy (Fig.3D). We obtained 3D trajectories of Halo-NDP52 molecules in the nucleus of HeLa cells (Fig.3E). Analysis of the different trajectories can then provide information on how confined or diffuse molecules are (Fig. 3F). By measuring the Mean Squared Displacement (MSD) of each molecule (SFig.1B), we were also able to calculate diffusion coefficients (Fig.3G) and anomalous diffusion constants (α) (SFig.1C) for each track. These were then plotted as the average diffusion coefficient or average α per cell (Fig.3H and I). Under normal conditions, NDP52 nuclear diffusion is relatively slow ($D = 0.24 (\pm 0.008) \mu\text{m}^2/\text{s}$) and molecules are mostly confined, displaying an α value lower than 1 ($\alpha = 0.7 (\pm 0.006)$) (Fig.3H and I).

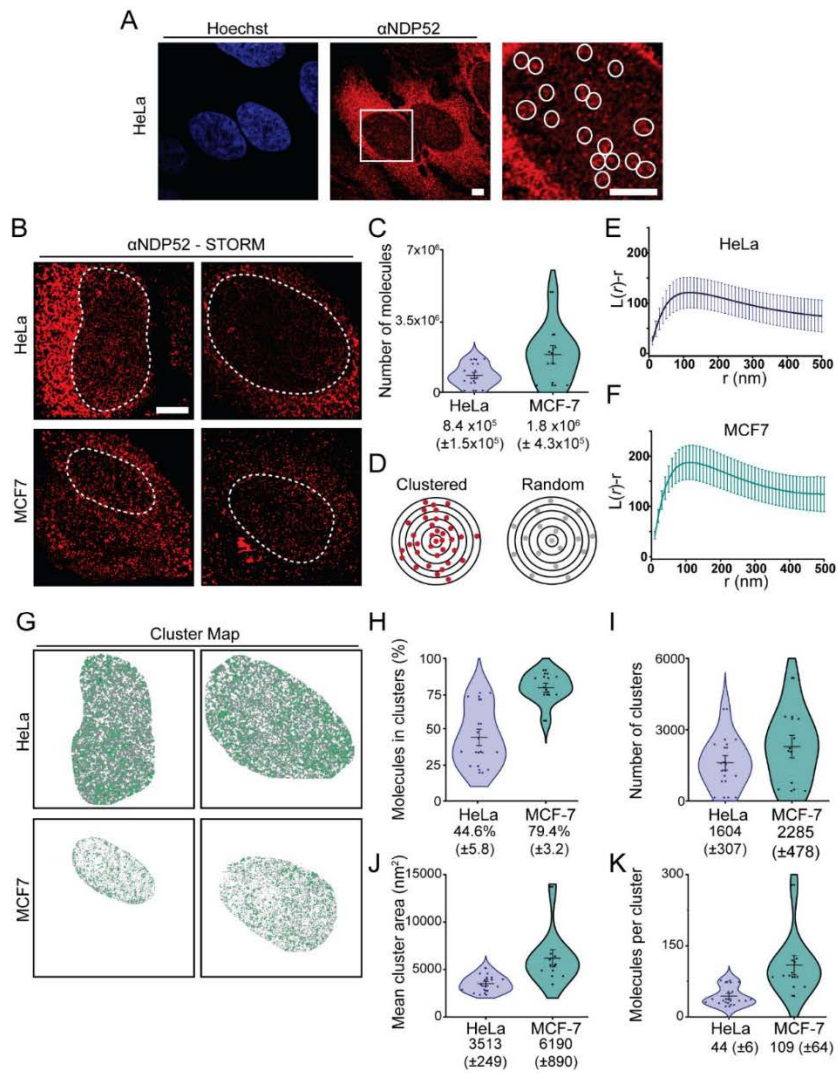


Figure 2 – Spatial organisation of NDP52 in the nucleus. (A) Confocal image of NDP52 in HeLa cells showing detail of dense nuclear staining in white circles (zoomed-in right panel). Scale bar = 5µm (B) Example STORM images of NDP52 in HeLa and MCF-7 cells. Dotted lines represent selected regions of interest (ROIs) for the nucleus. These regions were used for cluster analysis. Scale bar = 5µm (C) Linearized Ripley's K Function, $L(r)-r$ (where r is the radius), calculated for selected ROIs from STORM images in HeLa and MCF-7. A value of zero in this plot signifies molecules are randomly distributed, whilst positive values indicate molecular clustering. Mean values are plotted \pm SEM. $n = 12$ (HeLa), $n = 10$ (MCF-7) (D) Diagram depicting molecular clustering and random distribution. (E) Cluster maps generated for ROIs displayed in (C), using parameters specified in Methods. Clustered molecules are shown in green. (F-J) Cluster analysis of NDP52 in the nucleus of HeLa and MCF-7 showing: (F) total number of molecules; (G) percentage of molecules in clusters; (H) number of clusters in ROIs; (I) mean cluster area in nm^2 and (J) number of molecules per clusters. Mean \pm SEM values are shown. $n = 12$ (HeLa), $n = 10$ (MCF-7).

are static ($D < 0.1 \mu\text{m}^2/\text{s}$), which closely relates to the estimated percentage of clustered molecules calculated from STORM data.

Overall, the clustering behaviour and confined dynamics of NDP52 molecules in the nucleus support our hypothesis of a nuclear function for this protein.

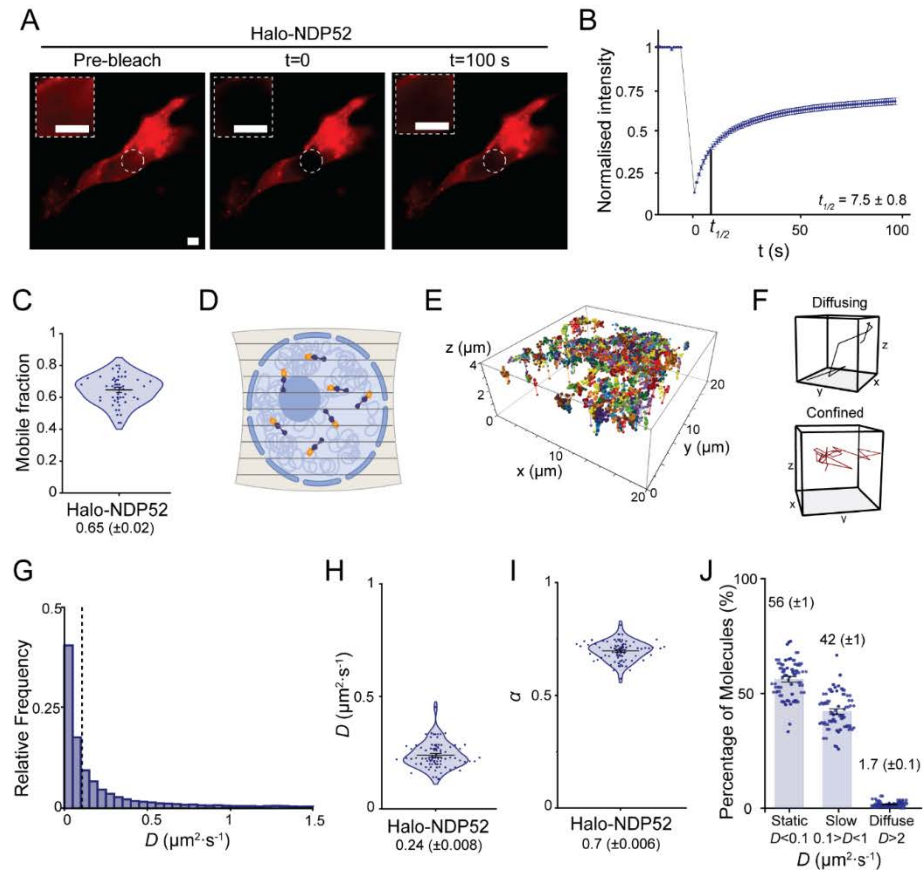


Figure 3 – Molecular dynamics of NDP52 in the nucleus. (A) Example of Fluorescence Recovery After Photobleaching (FRAP) image acquired in HeLa cells transiently expressing Halo-NDP52. Insets display zoomed-in detail of nuclear area selected for photobleaching. Scale bar= $5 \mu\text{m}$. (B) Normalised fluorescence intensity profile, in function of time for FRAP experiments. Estimated value of fluorescence recovery $t_{1/2}$ is shown on the graph. Mean values \pm SEM are shown. $n = 27$ cells. (C) Calculated mobile fraction from FRAP data. Mean values \pm SEM are shown. $n = 27$ cells. (D) Diagram depicting simultaneous acquisition of nine focal planes (covering $4 \mu\text{m}$ in z and $20 \mu\text{m} \times 20 \mu\text{m}$ in xy) for 3D single-molecule tracking of Halo-NDP52 in the nucleus. (E) Example of 3D reconstructed trajectories for a single nucleus over time. (F) Example of diffusive and confined trajectories over time. (G) Histogram of diffusion constants from the nucleus of HeLa cells transiently expressing Halo-NDP52. Dotted lines represent the applied threshold to differentiate between static and dynamic molecules (14 322 molecules from 51 cells). (H) Diffusion coefficient values for Halo-NDP52. Each data point represents the mean diffusion coefficient for a cell. (I) Anomalous diffusion constant, α , values. Each data point represents the mean α value per cell. (J) Percentage of molecules considered static ($D < 0.1 \mu\text{m}^2/\text{s}$), slow moving ($0.1 < D < 1 \mu\text{m}^2/\text{s}$) or diffuse ($D > 1 \mu\text{m}^2/\text{s}$) per cell. $n = 51$ cells.

NDP52 oligomerisation

Having investigated the spatial organisation and molecular dynamics of nuclear NDP52, which suggests a nuclear function, we wanted to investigate the biochemical properties of the protein to understand its potential roles. For this, we used different recombinant NDP52 constructs, including the full-length protein (NDP52-FL), an N-terminal truncated region ($_N$ NDP52), which includes the SKICH domain and part of the coiled-coil region (amino acid residues 1-190), a C-terminal region ($_C$ NDP52), which includes both zinc finger domains (amino acid residues 365-446) and the last zinc finger domain (ZF2 – amino acid residues 380-446) (Fig.4A). All the recombinant proteins presented stable secondary structure, as shown by circular dichroism and/or nano-differential scanning fluorimetry (nano-DSF) (SFig.2A-K). The first zinc finger domain of NDP52 (ZF1) was not selected for biochemical studies, as it lacked a stable secondary structure. This is in agreement with previous structural reports for this domain (Xie et al., 2015).

Previous work showed that full-length NDP52 is mainly a dimer in solution (dos Santos et al., 2020; Kim et al., 2013). To confirm this, we used Size-Exclusion Chromatography with Multi-Angle Light Scattering (SEC-MALS). SEC-MALS allows us to obtain accurate molecular weight information from gel filtration elution profiles and to identify different oligomeric species in solution. Our SEC-MALS data show that the majority of NDP52 is present in the dimeric form (second peak average molecular weight = 117kDa), but it also shows the presence of higher oligomeric forms, such as trimers and tetramers (first elution peak with an average molecular weight of 333 kDa) (Fig.4B). Through titrations of RED-tris-NTA labelled NDP52-FL with unlabelled NDP52-FL, microscale thermophoresis (MST) confirms oligomerisation of the full-length protein, with an estimated K_D value of $0.21\mu\text{M}$ (± 0.006) (Fig.4C). Mass photometry data further support this, by showing that at low concentrations (100nM) NDP52 is mostly dimeric, with a small population of trimers also present (Fig. 4D).

From the SEC profile, NDP52 appears to be an elongated protein, eluting at a much earlier elution volume than expected for a globular protein. The estimated radii of gyration from SEC-MALS data are 11.7nm, for the second peak (corresponding to NDP52 dimers) and 14.8nm for the higher-oligomeric forms (first elution peak) of NDP52 (Fig.4E). This translates into an approximate end-to-end measurement of 23 nm for dimeric NDP52. Dynamic Light-Scattering (DLS) data also show that NDP52-FL particles can be measured at a range of diameters between 10-43nm, with a maximum at 15.5 nm (Fig.4F). To obtain more information regarding the overall shape and measurements of NDP52-FL, we used Small-Angle X-Ray Scattering (SAXS). SEC-SAXS is a robust technique for the study of macromolecule conformation in solution. Our SAXS data estimate a radius of gyration for NDP52 between 9-15 nm (end-to-end value 18-30 nm) (Fig.4G), predicting a rod-shape structure for the protein. Variability in radii measurements for NDP52 could be a direct consequence of its elongated shape, as measurements for different profiles of the protein will be more varied than in a globular protein. Using SAXS we were also able to generate an envelope model for NDP52-FL, showing the predicted elongated shape (Fig. 4H and I).

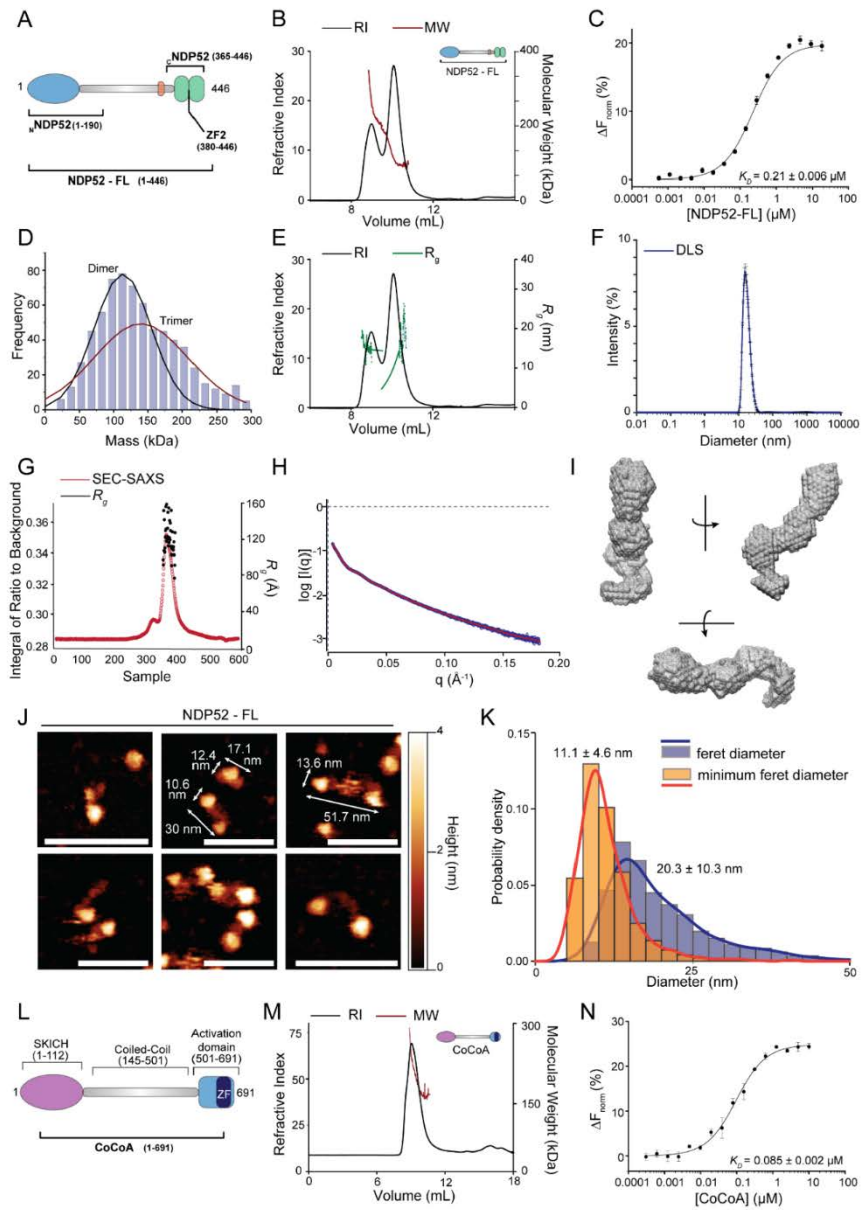


Figure 4 – Oligomerisation of NDP52. (A) Diagram of NDP52 showing recombinant constructs used for biochemical assays with NDP52. (B) Size-exclusion chromatography with multi-angle light scattering (SEC-MALS) profile for recombinant full-length NDP52 (NDP52-FL). Refractive index (RI) trace is shown in black, as well as the calculated molecular weight values, across the peaks (in red). (C) Microscale thermophoresis, showing oligomerisation of NDP52. Calculated K_D (as specified in Methods) is displayed in the graph. Values plotted represent average \pm SEM of three individual experiments. (D) Histogram showing calculated mass of NDP52-FL from mass photometry assays. Two Gaussian curves could be fitted to the data set. Mean values of Gaussian

To directly visualise and measure protein shape and size, we used Atomic Force Microscopy (AFM) imaging. As expected, under AFM imaging, NDP52-FL displays an elongated shape with a variable range of sizes (Fig.4J). Furthermore, it is also possible to visualise different domains for the NDP52-FL and oligomeric forms of the protein (Fig.4J). Analysis of NDP52-FL particles reveals a large range of maximum diameters for the protein (feret diameter), with the most likely value for the protein at 20.3nm (Fig.4K). In agreement with other biochemical data (Fig.4B-H), AFM analysis shows a large distribution of maximum lengths for NDP52-FL, indicative of different possible conformations for the protein, as well as a variety of oligomeric associations (Fig.4K). Furthermore, a relatively flexible coiled-coil region that allows bending of the protein, could also account for some of the variability observed in AFM measurements. Conversely, the most likely minimum feret value (caliper diameter) for NDP52-FL was calculated at 11.1 nm (Fig.4K), in agreement with the observed elongated shape for the protein. Minimum feret values of NDP52-FL also display a narrower distribution compared to maximum lengths for the protein. It is likely that these values correspond to the lengths of globular domains at NDP52-FL ends (Fig.4J).

α -helical coiled-coil domains are often drivers of protein oligomerisation (Ciani et al., 2010; Lupas and Gruber, 2005). To test which regions of NDP52 are capable of oligomerising, we used different truncated regions of the protein (Fig.4A). SEC-MALS of c NDP52 shows that this region is mostly present in dimeric and monomeric forms, although trimers could also be detected (SFig.3A). MST data confirms oligomerisation of this domain, generating a K_D of 0.05 μ M (\pm 0.006) (SFig.3B). Oligomerisation of c NDP52, which lacks the presence of the coiled-coil region, suggests that these domains might also be important for interactions between monomers during dimerization of the full-length protein. To visualise c NDP52 region, we used AFM imaging. In agreement with SEC-MALS and MST data, we could identify monomeric, dimeric and trimeric forms of c NDP52 (SFig.3C). AFM measurements of maximum lengths and minimum feret diameters for c NDP52 are largely overlapping, with most likely values of 11.7nm and 7.8nm, respectively, indicating relatively globular conformations (SFig.3D). Interestingly, maximum length values for c NDP52 (11.7nm) closely resemble the minimum feret diameter of NDP52-FL (11.1 nm) (SFig. 3E and Fig.4K).

(Figure 4 Legend – continuation)

curves closely correspond to dimeric and trimeric molecular weights of NDP52 (Gaussian max values = 105kDa and 140kDa, respectively). **(E)** Radius of gyration (R_g) calculated from SEC-MALS data shown in (B). Estimated R_g for peak one was 14.84nm and 11.7nm for the second peak. RI trace shown again for NDP52-FL in black, and R_g across peaks shown in green. **(F)** Dynamic light scattering trace for NDP52-FL showing calculated diameter for the protein, with values between 10 and 43 nm and maximum at 15.5 nm. **(G)** SEC-Small-angle X-ray light scattering (SEC-SAXS) for NDP52-FL showing R_g values across peaks. Radii values between 9-15nm. **(H)** Experimental SAXS curve for NDP52-FL. **(I)** Beads model of NDP52-FL obtained from SEC-SAXS data. **(J)** Atomic force microscopy imaging (AFM) of NDP52-FL showing the protein in monomeric, dimeric and higher oligomeric forms. Example measurements for individual protein molecules are also shown. Scale bar = 50 nm. Height scale also shown. **(K)** Probability distributions for feret diameter and minimum feret diameter of NDP52-FL molecules, calculated from AFM imaging. Data were fitted to Gaussian distributions to calculate particle size, displayed as Mean \pm SD. n=1 511 molecules. **(L)** Diagram depicting CALCOCO2/CoCoA, which belongs to the same family as NDP52 and has high sequence and domain similarity. Domains and key features are specified. A recombinant full-length CoCoA construct was used in biochemical assays. **(M)** SEC-MALS trace for CoCoA. RI trace is shown in black and calculated molecular weight values are shown in red (MW values between 140 and 300kDa). **(N)** Microscale thermophoresis, showing oligomerisation of CoCoA, with the calculated K_D displayed in the graph. Curve fitting was performed as described in Methods. Values represent average \pm SEM of three individual experiments.

We also investigated the ability of the ZF2 domain to oligomerise, using SEC-MALS and MST. Our data show that this domain can also homo-oligomerise, presenting itself as a monomer, dimer and trimer in solution, with an oligomerisation K_D of 0.18 μM (± 0.017) (SFig.3E and F). When testing oligomerisation of the N-terminal region of NDP52, ${}_N\text{NDP52}$, containing the SKICH domain and part of the coiled-coil region, we observe a clearer preference for the dimeric form (SFig. 3G and H). Interestingly, we could also observe an interaction between ${}_C\text{NDP52}$ and ${}_N\text{NDP52}$ (SFig. 3I). It is possible that these two opposing regions interact in the full-length protein, due to the presence of a relatively flexible central coiled-coil region, or between homo-oligomers of NDP52.

As previously mentioned, NDP52 shares high sequence identity with its family member CoCoA - a protein with known nuclear functions in transcription co-activation (Kim et al., 2003). However, very little is known regarding the oligomeric states of CoCoA, or how this may align with NDP52. To test if recombinant CoCoA (Fig.4L) can also form dimers, we used SEC-MALS. Our data show that the main peak for CoCoA is a complex mixture of molecular weights, ranging from 148kDa (equivalent to the dimeric form of CoCoA) to 300kDa (Fig.4M). Using MST, we further confirmed the ability of CoCoA to oligomerise, with a calculated K_D of 0.085 μM (± 0.002) (Fig.4N). Essentially, CoCoA and NDP52 display similar biochemical properties.

NDP52 binds and oligomerises with double-stranded DNA

Having determined the oligomeric state of NDP52-FL and clarified its nuclear localisation, we decided to test NDP52 binding to DNA. Previously, Fili *et al.* showed that NDP52 can bind to double-stranded DNA (dsDNA) with high-affinity (Fili et al., 2017). As we have established that NDP52 is present in confined clusters within the nucleus, DNA binding could be an essential part of its nuclear role. Hence, we used an electrophoretic mobility shift assay (EMSA) to investigate the formation of NDP52-dsDNA complexes. Using 250nM of dsDNA 40bp long (ds40) and concentrations of NDP52-FL ranging from 50 nM to 3 μM , we show that NDP52 can form complexes with dsDNA, *in vitro*, evident by the formation of a higher band in the EMSA (Fig.5A). To explore this interaction in a quantitative manner, we used fluorescence spectroscopy. For this, NDP52-FL was titrated against two different lengths of FITC labelled DNA - 40 and 15bp (ds40 and ds15, respectively). Our data confirmed a high-affinity interaction between NDP52 and DNA, with K_D values < 100nM for both DNA lengths (Fig.5B). To directly visualise this interaction, once again we employed AFM imaging. We used linearised dsDNA 339 bp long (ds339) - approximately 115 nm long. As shown in Fig.5C, we can observe direct interactions between NDP52-FL and ds339. Furthermore, we can also observe that more than one molecule of NDP52-FL can interact with DNA (Fig.5C and Fig.6A-C). This agrees with mass photometry measurements that show that when incubated with ds40, the measured mass for NDP52-FL increases from its dimer/trimer values (112 and 157 kDa, calculated for NDP52-FL alone, to 1334 kDa) (Fig.5D). Similar to NDP52, when testing CoCoA for dsDNA binding, we also observe high-affinity interactions in fluorescence spectroscopy assays (Fig.5E).

Zinc finger domains are well-known for their ability to bind DNA (Cassandri et al., 2017). To test if these domains are responsible for DNA binding abilities of full-length NDP52, we used the ${}_C\text{NDP52}$ and ZF2 recombinant constructs in fluorescence spectroscopy assays. As

expected, both constructs interact tightly with dsDNA, with K_D values in the low nM range (Fig.5F and H). However, DNA binding curves for these constructs do not reach saturation at higher concentrations of protein, as they do for NDP52-FL. This could be explained by the clustering behaviour of c NDP52 around DNA, that we observe when performing AFM imaging of this domain with ds339 (Fig.5G). c NDP52 oligomerises with, and around dsDNA, to a much larger extent than the full-length protein, creating very large complexes of DNA-protein.

Although some degree of interaction could be detected for n NDP52-dsDNA, this presents much lower affinity than NDP52-FL or C-terminal domains. This is represented by lower K_D values estimated from fluorescence spectroscopy assays, and relatively poor fitting of these curves (Fig.5I).

Interestingly, we also observe specificity of NDP52-FL towards dsDNA. Although fluorescence spectroscopy assays using FITC labelled single-stranded DNA 40 bases (ss40) show changes in fluorescence, the data are highly variable and could not be fitted to a binding equation (Fig. 5J). This suggests that although some interaction may occur, NDP52-FL preferentially binds dsDNA.

Since we have established that NDP52 can bind to DNA *in vitro*, we hypothesised that this could also occur in cells, whereby NDP52 could directly interact with genomic regions. To test this, we performed chromatin immunoprecipitation (ChIP) with NDP52. Using this approach, we could detect the presence of NDP52 bound to chromatin-enriched cellular fractions (SFig. 4A). We also tested different genomic *loci* for the presence of NDP52, through ChIP-qPCR, including genes regulated by nuclear receptors (previously linked to coactivator functions of CoCoA) (Kim et al., 2003), and inflammation-related targets, where NDP52 has been shown to have a role (Ellinghaus et al., 2013; Till et al., 2013). Our ChIP-qPCR data suggest that NDP52 is present throughout the gene body of different genes (SFig. 4B). This supports our hypothesis that NDP52 can bind DNA *in vitro* and *in cellulo* and this could be a mechanism through which the protein could impact gene expression.

NDP52 can alter DNA shape

Having established that NDP52-FL can interact with DNA through its zinc finger domains, we then investigated if these interactions could cause local changes to DNA shape or structure. Using AFM imaging, we observed several instances where NDP52 appears to be able to bridge and crosslink individual linearised strands of dsDNA (Fig.6A). We could also observe looping of DNA (Fig.6B) following incubation with NDP52-FL, and bending of DNA structures (Fig.6C). Indeed, we found that at binding sites with NDP52-FL, DNA was more likely to be found with local angles of $129.2^\circ \pm 3.3^\circ$, followed by $91.7^\circ \pm 11.9^\circ$, showing a clear preference for bent conformation at interacting regions (Fig.6D and E).

To test if NDP52-FL is actively changing DNA structure upon binding, we measured end-to-end ds339 distances in the absence of NDP52-FL (bare DNA) and following incubation with the protein. Kernel distributions show a clear shift towards lower end-to-end distances of ds339 in the presence of NDP52-FL, indicating a higher degree of bending of DNA molecules (Fig.6F). This supports the hypothesis that NDP52 binding can change DNA structure. The observed bimodal distribution for ds339-NDP52-FL measurements indicates a mixed-population of DNA molecules. This could be the result of binding dynamics of NDP52 to DNA.

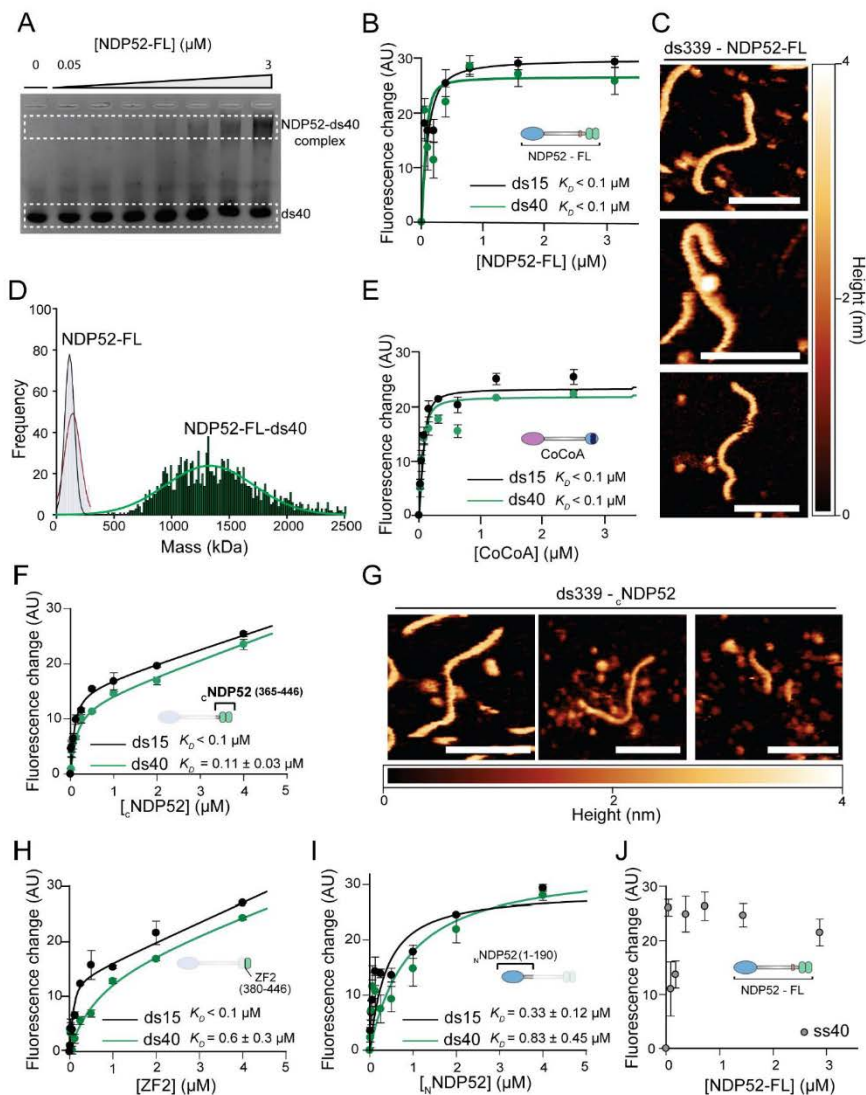


Figure 5 – NDP52 binds to and oligomerises with double-stranded DNA through its C-terminal domain. (A) Electrophoretic-mobility shift assay (EMSA) for NDP52-FL with ds40. dsDNA was used at 250 nM, with increasing concentrations of NDP52-FL run in each well (0.05; 0.1; 0.2; 0.5; 1; 2 and 3 μM). Lower band represents free ds40 and top band represents DNA in complex with NDP52-FL. **(B)** Fluorescence spectroscopy titrations of NDP52-FL against 40bp or 15bp fluorescein amidite double-stranded DNA (ds40 and ds15, respectively). **(C)** Example images of direct visualisation of NDP52-FL binding to dsDNA, using AFM. Linearised 339bp DNA (ds339) was used for imaging. Scale bar = 50 nm. Height scale is also shown. **(D)** Mass photometry histogram for NDP52 showing a large shift in detected mass when NDP52-FL is incubated with ds40. Histograms and Gaussian fittings for NDP52 alone are the same as the ones shown in Figure 4D (in black and red). Histogram for NDP52-FL-ds40 (green) was also fitted to a Gaussian function. Mean value calculated as 1 334kDa). **(E)** Fluorescence spectroscopy titrations of CoCoA against ds40 and ds15DNA. **(F)** Fluorescence spectroscopy titrations of cNDP52 against ds40 and ds15. Calculated K_D values are shown. **(G)** Example images of cNDP52 binding and clustering around ds339, using AFM. Scale bar = 50 nm. Height scale is also shown. **(H)** Fluorescence spectroscopy titrations of ZF2 against ds40 and

For example, DNA that is still interacting with NDP52 could present a higher degree of bending, whilst DNA that has lost interactions with NDP52 could have become more relaxed, accounting for the second peak of the distribution. Alternatively, a variability in the number of NDP52-FL molecules per ds339 strand could also explain differences in DNA bending populations; as it is expected that with more molecules of NDP52-FL, more DNA bending will occur. Location of NDP52 binding on the DNA molecule could also impact global ds339 conformations. To test if NDP52-FL has a preferential binding location on DNA (DNA ends vs middle) we divided ds339 molecules into two regions: edge – accounting for 50% of the DNA molecule (25% at each end) and middle – accounting for the central 50% of ds339 (Fig.6G diagram). We observed that NDP52-FL preferentially binds at the ends of linearised dsDNA, approximately 20-25 nm into the ds339 molecule (corresponding to $19.39 \pm 0.86\%$ of ds339 length) (Fig. 6G and H).

Interestingly, we could also observe changes in DNA structure when incubating ds339 with cNDP52, with instances of DNA bending and looping observed (SFig.4C and D). This, together with the fact that the N-terminal of NDP52 only displays low affinity for dsDNA in biochemical studies, strongly suggests that changes to DNA shape caused by the full-length protein are most likely induced by the zinc finger domains at the C-terminal of NDP52.

NDP52 is involved in RNAPII-dependent transcription

As previously mentioned, one of the most well-known binding partners of NDP52 is MVI. Previous work has linked the interaction between NDP52 and MVI to the enhancement of RNA Polymerase II (RNAPII) activity (Fili et al., 2017). Furthermore, colocalising foci of NDP52 and RNAPII have been previously observed in the nucleus (Fili et al., 2017), also shown in Fig.7A. To further explore the role of NDP52 in RNAPII-related transcription, we used STORM. STORM not only allows us to improve colocalisation estimates between NDP52 and RNAPII molecules, relative to conventional optical microscopy, but also allows us to measure colocalisation of clusters for both proteins. Here, we used phospho-Ser5-RNAPII immunofluorescence staining, which selects for the pool of RNAPII molecules involved in transcription initiation. STORM data show that, under normal conditions, approximately 28.7% (± 1.7) of NDP52 is colocalised with RNAPII, and 20.2% (± 2.8) of RNAPII is found colocalising with NDP52 (Fig. 7B and C). Colocalisation of clusters between NDP52 and RNAPII can also be observed in ClusDoC-generated heat maps and histograms (Fig. 7D and SFig.5A), with nuclear regions of high colocalisation density for each channel represented in red. Interestingly, our data show that NDP52 clusters that colocalise with RNAPII clusters are approximately 6.5 times larger than non-colocalised clusters, and RNAPII clusters colocalised with NDP52 approximately 12-fold larger (Fig. 7E). Although there are more non-colocalised clusters than colocalised between NDP52 and RNAPII, colocalised clusters also have higher density of molecules (2.5 times higher density for NDP52 and 2 times higher for RNAPII) (SFig. 5B-E) This further suggests a relationship between the nuclear organisation of NDP52 and transcription.

(Figure 5 Legend – continuation)

ds16 DNA. (I) Fluorescence spectroscopy titrations of nNDP52 against ds40 and ds15 DNA. (J) Fluorescence spectroscopy titrations of NDP52-FL with single-stranded 40bases DNA (ss40). For all protein-DNA fluorescent assays, DNA concentration was kept at 100 nM and K_D values represent mean \pm SEM of n=3 independent experiments. Data fitting was performed as described in Methods.

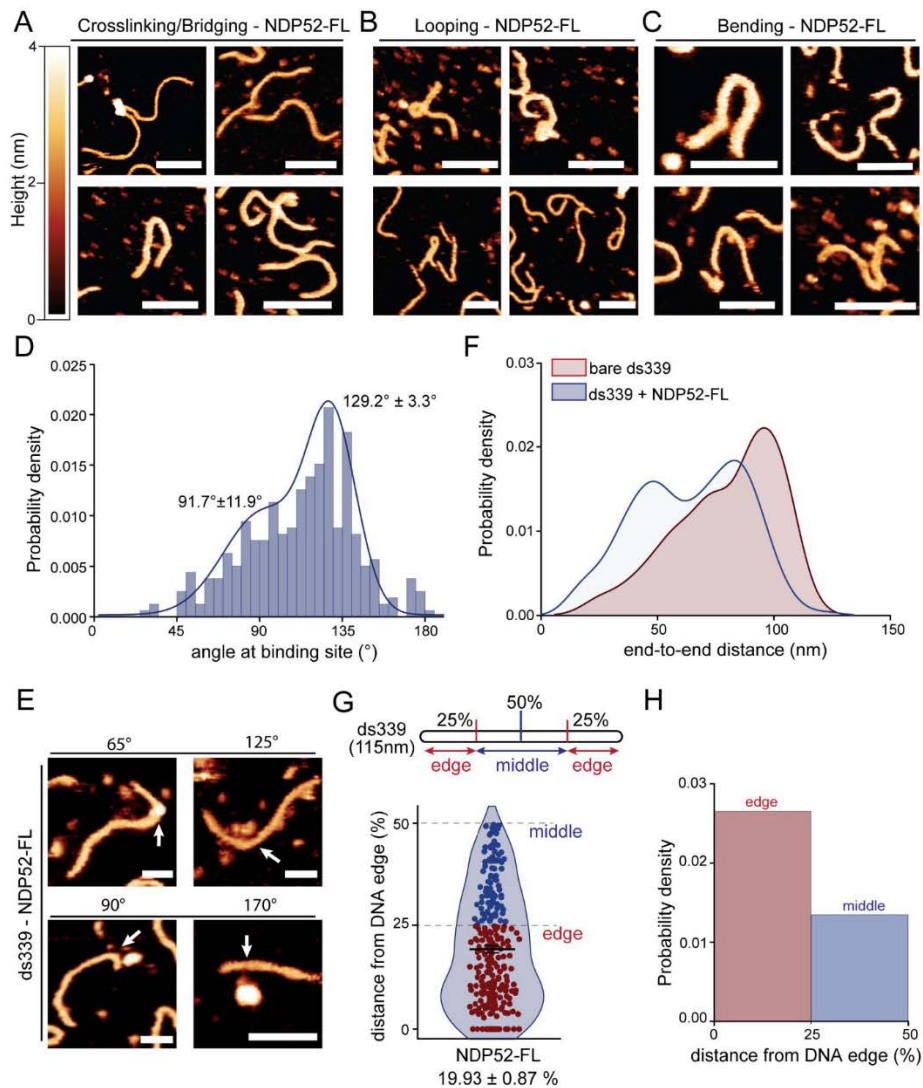


Figure 6 – NDP52 changes DNA conformation *in vitro*. (A) AFM example images of NDP52-FL bridging strands of linear (339 bp) dsDNA. (B) Examples of ds339 DNA looped following incubation with NDP52-FL. (C) AFM examples of NDP52-FL bending dsDNA. (D) Probability density distribution of local DNA angles at sites of NDP52-FL binding. Mean values of bimodal distribution are shown \pm SE. $n=319$ binding events. (E) Examples AFM images showing local DNA angles at binding sites. (F) Kernel distributions of end-to-end measurements of bare ds339 versus ds339 incubated with NDP52-FL, quantified from AFM images. Shorter distances indicate higher degree of bending. $n=394$ DNA molecules (bare ds339) $n=393$ DNA molecules (ds339+NDP52-FL) (G) Preference for NDP52-FL binding on ds339 molecule. Diagram shows ds339 edge and middle references on linear DNA. Violin plot shows %distance from DNA edge values for NDP52-FL binding. Mean \pm SEM is shown for $n=270$ binding events. (H) Probability density for data shown in (G). Scale bars = 50nm. Height scale for AFM images shown in (A).

To test if NDP52 can affect the spatial organisation of RNAPII, we overexpressed the nuclear pool of NDP52. For this, we used a Halo-NLS-NDP52 construct (SFig. 5F). We then used STORM and cluster analysis to quantify changes in the distribution of RNAPII in the nucleus (Fig.7F). Overexpression of nuclear NDP52 did not have an effect on the number of molecules of RNAPII, or the propensity for RNAPII to form clusters (Fig.7G, SFig.5H-J). However, we did observe a significant increase in the number of RNAPII clusters in cells transiently expressing Halo-NLS-NDP52 (Fig.7H). This suggests that overexpression of NDP52 might allow the formation of new transcription hubs in the cell, but the overall size of each cluster is not dependent on NDP52.

Having determined that NDP52 can be found clustering at transcription initiation sites, we set out to explore how depletion of NDP52 would affect global gene expression. For this, we performed RNA-Seq in both HeLa and MCF-7 cells, following siRNA knockdown of NDP52 (SFig.6 and SFig.7). Overall, we observed significant changes in gene expression levels for both cell lines, with 1420 genes and 1140 genes differentially expressed in HeLa and MCF-7, respectively ($-0.5 > \log_2FC < 0.5$, and $p_{adj} < 0.05$) (SFig.6A, SFig.7A). In both HeLa and MCF-7 datasets, more genes are downregulated than upregulated, also showing an overall negative impact on transcription caused by depletion of NDP52. Gene Ontology analysis for both up and downregulated genes was then performed for both cell lines (SFig.6B, SFig.7B). For HeLa, genes involved in the 'regulation of transcription', as well as 'cell migration' and 'tissue development' were significantly affected (SFig.6B). In MCF-7, NDP52 knockdown was shown to also affect the expression of genes involved in 'cell migration', 'tissue development', as in HeLa, but also 'cell cycle', 'DNA replication' and 'chromosome segregation' (SFig.7B). This suggests that whilst some genes and processes are equally affected by NDP52 knockdown in both cell lines, others might be more susceptible depending on the unique characteristics of the cell line.

NDP52 nuclear interactome

Following our observation that NDP52 colocalises and clusters at RNAPII transcription initiation sites, and can drive the formation of additional RNAPII clusters when overexpressed, we decided to explore the nuclear interactome of NDP52. To identify partners of NDP52, we used label-free quantitative LC-MS/MS to analyse pull-downs of recombinant NDP52-FL, Δ NDP52, CoCoA and ZF2 from HeLa nuclear extracts (SFig.8A, Fig. 8A-D, SFig.8B and C). Proteins were identified using Progenesis software (Waters), as described in Methods. Following protein identification, we selected proteins enriched in NDP52-FL pull-downs, compared to control beads without recombinant protein. We used $\log_2FC > 1$ and $p_{adj} < 0.05$ as a threshold to investigate the interactome of NDP52. Following this, we performed GO analysis to determine novel biological processes that could shed light on a new nuclear role for NDP52. Interestingly, the top enriched biological processes for NDP52 interactions were 'DNA geometric change' and 'DNA duplex unwinding', with 'chromosome organisation' also scoring high (SFig.9A). Top enriched molecular functions also relate to 'nucleosome-dependent ATPase activity', 'DNA helicase activity' or DNA binding (SFig.9B). These data reinforce the concept that NDP52 has significant roles in DNA binding and structure, as indicated in our biochemical studies and AFM imaging, which could, in turn, impact gene expression. Although several known transcription factors were identified in proteomics (Fig.8B), gene expression-related GO functions were not particularly enriched. This suggests that although NDP52 might

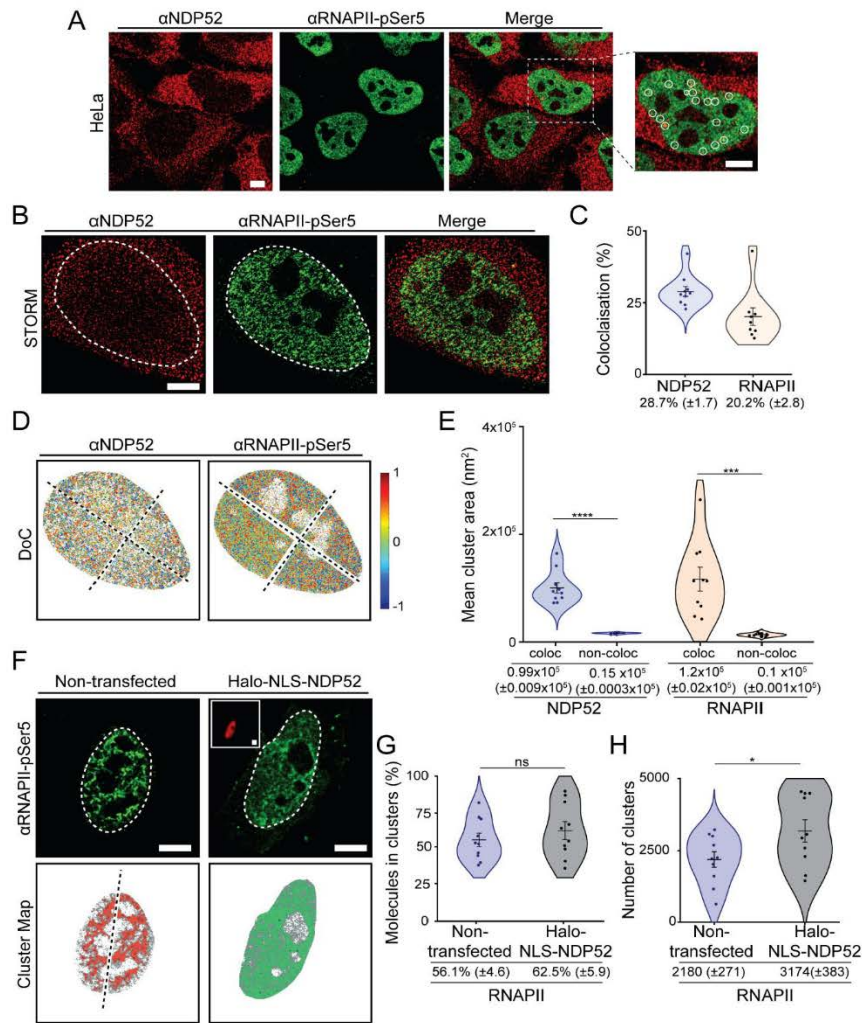


Figure 7 – Colocalisation of NDP52 with RNAPII-pSer5. (A) Immunofluorescence confocal image of NDP52 (red) and RNAPII-pSer5 (green) in HeLa cells, showing detail of colocalising foci in white circles (zoomed-in right panel). Scale bar = 5µm (B) Example STORM images of NDP52 and RNAPII-pSer5 in HeLa. The nuclear region (determined by RNAPII-pSer5 fluorescence) was used for ClusDoC analysis (shown as dotted white line). Scale bar = 5µm (C) Colocalisation analysis of NDP52 and RNAPII-pSer5 clusters. (D) Cluster colocalisation heat maps for NDP52 and RNAPII-pSer5 generated from the STORM data shown in (B). DoC score of 1 represents perfect colocalisation between molecules, and DoC score -1 represents segregation. A DoC score of 0.4 was used as threshold for colocalisation. Due to high molecular density the nucleus was split into four ROIs for ClusDoC analysis. Axis of separation for the images are shown as dotted lines. (E) Mean cluster area is shown for colocalised and non-colocalised clusters of NDP52 and RNAPII-pSer5. n = 10 cells. (F) STORM rendering for RNAPII-pSer5 and generated cluster maps for HeLa cells non-transfected or transiently expressing a Halo-NLS-NDP52 construct. Inset in Halo-NLS-NDP52 panel shows wide-field channel Halo ligand-JF549 labelled cells. Scale bar = 5µm. (G) Percentage of RNAPII-pSer5 molecules in clusters in non-transfected or transiently expressing Halo-NLS-NDP52 HeLa cells. (H) Number of RNAPII-pSer5 clusters in non-transfected or transiently expressing Halo-NLS-NDP52 HeLa cells. Mean ± SEM values are shown. Each point represents the average value per cell. n = 10 cells (Non-transfected) n = 10 cells (Halo-NLS-NDP52). *p<0.05; ***p<0.001; ****p<0.0001 by two-tailed t-test.

directly interact with transcription-related proteins and also affect gene expression through these interactions, its largest contribution might, instead, arise through regulation of DNA structure.

We were able to map 16% of NDP52-FL interactions to the C-terminal of NDP52 (cNDP52), also through LC-MS/MS with recombinant cNDP52 (Fig.8A). Figure 8B shows examples of top hits for NDP52-FL and the identification of some of these hits in cNDP52 proteomics. Fold change values, are relative to control beads for pull-downs, with infinity fold-change (∞) indicating hits only present in pull-downs and not in control samples.

We also compared how the interactome of NDP52 relates to its close family member CoCoA (Fig.8C). Similar to NDP52, the nuclear interactome of CoCoA also showed enrichment for 'DNA duplex unwinding' and 'DNA geometric change'. However, 'gene expression' was clearly enriched for CoCoA (SFig.10A and B). Furthermore, when comparing CoCoA and NDP52 interactions, a quarter of CoCoA hits were common to NDP52 (Fig.8C), showing a degree of overlap between both interactomes, as expected for proteins with high homology. Importantly, our data show that whilst both proteins could have similar functions and overlapping interactomes, they do not appear to be redundant. Figure 8D shows some of the top hits for CoCoA and identification in NDP52-FL pull-downs.

As ZF2 is highly conserved in both NDP52 and CoCoA, we also tested if some of the interactions in common between CoCoA and NDP52 could be mapped to this domain (SFig.8B). Interestingly, only 5% of common interactions between NDP52 and CoCoA occur independently of ZF2-binding, suggesting that this domain could account for similarities in the interactomes between both proteins. Furthermore, 86% of proteomics common hits between NDP52-FL and cNDP52, could be mapped to ZF2. This, together with the fact that ZF1 is largely unstructured, could indicate that protein-protein interactions at the C-terminal of NDP52 are mostly sustained by ZF2. Examples of top hits for CoCoA and NDP52 are shown for ZF2 proteomics in SFig.8C.

Changes to the nuclear organisation and dynamics of NDP52 following transcription inhibition

As we have established that NDP52 has a role in transcription, and can impact the organisation of RNAPII, we tested whether transcription inhibition would affect its nuclear organisation and dynamics. To address this, we used α -amanitin, an irreversible RNAPII inhibitor that promotes degradation of RNAPII (Bushnell et al., 2002). As expected, α -amanitin treatment leads to depletion not only of RNAPII molecules, but also of its clusters (Fig. 9A-D and SFig.11A-C).

We then used STORM to compare the spatial organisation of NDP52 in the nucleus of non-treated HeLa cells versus cells treated with α -amanitin (Fig. 9E-F). The linearised Ripley's K function clearly shows that, compared to non-treated cells, there is a reduced probability for NDP52 clustering in the nucleus, following α -amanitin treatment (Fig. 9G). This is further confirmed through cluster analysis, which shows a reduction from 44.6% (± 5.8) to 20.8% (± 4.2) in the percentage of NDP52 molecules forming clusters following α -amanitin treatment (Fig. 9H).

We also explored how reduced clustering of NDP52 in the nucleus, following transcription inhibition, would affect its molecular dynamics. As the number of NDP52 in clusters is

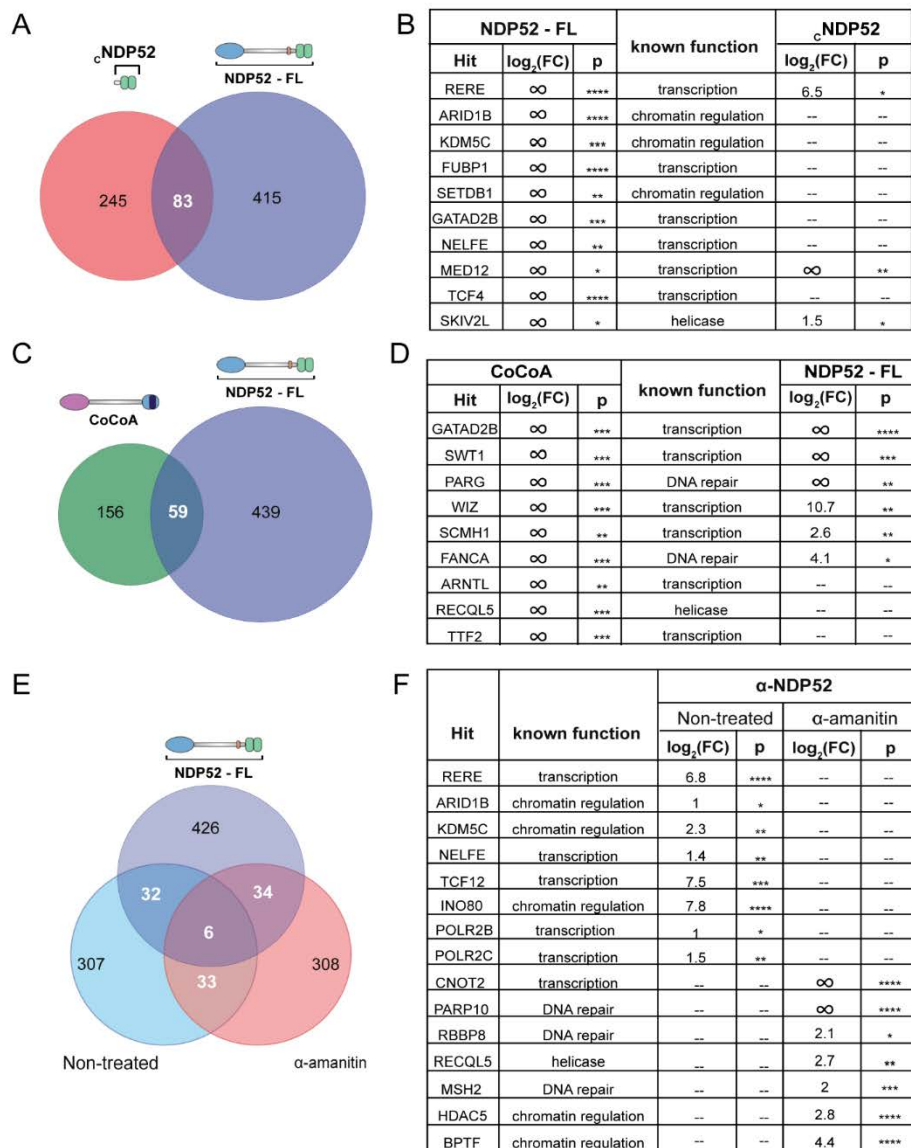


Figure 8 – NDP52-FL, CoCoA and cNDP52 interactomes from HeLa nuclear extract. (A) Venn diagram of hits found in NDP52-FL and cNDP52 **(B)** Examples of top hits for NDP52, and their identification in cNDP52 proteomics data. log₂FC is relative to beads control. **(C)** Venn diagram of hits found in NDP52-FL and CoCoA **(D)** Examples of top hits for CoCoA, and their identification in NDP52-FL proteomics data. log₂FC is relative to beads control. **(E)** Venn diagram showing overlap of identified hits between recombinant NDP52-FL proteomics and co-immunoprecipitation of endogenous NDP52 for non-treated and α-amanitin treated cells. **(F)** Examples of hits identified in non-treated and α-amanitin treated cells. log₂FC is relative to beads control. *FDR<0.05, **FDR<0.01, ***FDR<0.001, ****FDR<0.0001.

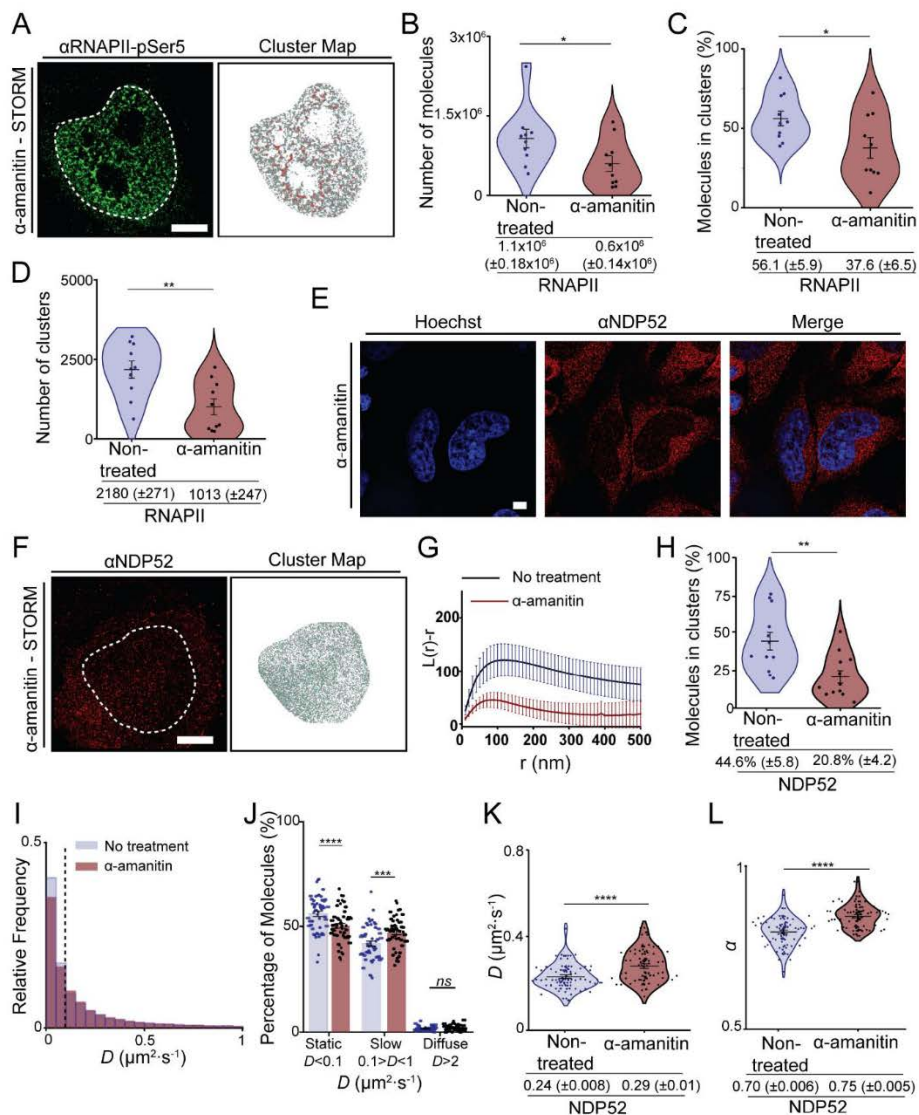


Figure 9 – Organisation and dynamics of nuclear NDP52 following transcription inhibition. (A) Example of STORM rendering and cluster map, generated following DBSCAN analysis, of RNAPII-pSer5 following α -amanitin treatment. Scale bar = 5 μ m. (B) Calculated number of RNAPII-pSer5 molecules in the nucleus of non-treated vs α -amanitin treated cells. (C) Percentage of RNAPII-pSer5 molecules in clusters for non-treated vs α -amanitin treated cells. (D) Number of clusters in selected ROIs for RNAPII-pSer5 in non-treated vs α -amanitin treated cells. $n = 10$ cells (non-treated) $n = 10$ cells (α -amanitin). (E) Confocal image of NDP52 in HeLa cells following treatment with transcription inhibitor α -amanitin. Scale bar = 5 μ m. Hoechst DNA stain is shown in blue. (F) Example STORM image of NDP52 in HeLa cells treated with α -amanitin and corresponding cluster map. Scale bar = 5 μ m. Clustered molecules are shown in green. (G) Linearized Ripley's K Function, $L(r)-r$, calculated for selected ROIs from STORM images. Ripley's K values are shown in red for α -amanitin treated cells and in blue for non-treated cells. For non-treated cells, values are the same as shown in Figure 2C. Mean values are plotted \pm SEM. $n = 11$ (α -amanitin) $n = 12$ (non-treated). (H) Percentage of molecules in clusters in non-treated HeLa cells compared to α -amanitin treatment.

Values for non-treated cells are the same as shown in Figure 2G. Mean \pm SEM values are shown. $n = 11$ (α -amanitin) $n = 12$ (non-treated) ** $p < 0.01$ by a two-tailed t-test. (I) Histogram of diffusion constants from the nucleus of non-treated and α -amanitin-treated HeLa cells transiently expressing Halo-NDP52 in blue and red, respectively. Dotted lines represent the applied threshold to differentiate between static and dynamic molecules (14 322 molecules from 51 cells for non-treated condition and 14 492 molecules from 50 cells). Non-treated cell values are the same as shown in Figure 3G (J) Percentage of molecules considered static ($D < 0.1 \mu\text{m}^2/\text{s}$), slow moving ($0.1 < D < 1 \mu\text{m}^2/\text{s}$) or diffuse ($D > 1 \mu\text{m}^2/\text{s}$) per cell. $n = 51$ cells. (non-treated – same as Figure 3J) and $n = 50$ (α -amanitin). (K) Diffusion coefficient values for Halo-NDP52 under normal conditions and after α -amanitin treatment. Each data point represents the mean diffusion coefficient for a cell. $n = 51$ (non-treated – same as Figure 3H) and $n = 50$ (α -amanitin). (L) Anomalous diffusion constant, α , values under normal conditions and after α -amanitin treatment.

(Figure 9 Legend – continuation)

markedly reduced, we expected an increase in the dynamic behaviour of the protein. To test this hypothesis, we used acMFM to determine diffusion coefficient and anomalous diffusion changes in cells transiently expressing Halo-NDP52, in non-treated and α -amanitin-treated cells. As expected, loss of NDP52 clusters, observed in STORM data, correlated with a significant increase in the diffusion coefficient and anomalous diffusion constant, α , for Halo-NDP52 in the nucleus of α -amanitin-treated cells (Fig. 9I-L, SFig.11D). A proportion of static NDP52 molecules was lost following α -amanitin treatment (reduction from 56.3% (± 1.2) in non-treated to 50.5% (± 1.1) in α -amanitin-treated) (Fig.9J). This was accompanied by a significant increase in molecules in slow diffusion (increase from 42.1% (± 1.2) in non-treated to 47.4 (± 1.0) in α -amanitin-treated) and a small, non-significant, increase in diffuse molecules (from 1.7% (± 0.1) in non-treated to 2.1 (± 0.2) in α -amanitin-treated). Overall, our data show that transcription inhibition by α -amanitin disrupts global nuclear NDP52 clustering, which correlates with higher molecular diffusion of the protein.

Having shown that the spatial organisation of nuclear NDP52 is altered following transcription inhibition, we also tested if this would also cause changes to the interactome of the protein. For this we used label-free quantitative LC-MS/MS of co-immunoprecipitation assays, for endogenous NDP52 from whole-cell HeLa extracts, with and without α -amanitin treatment (Fig.9E). Co-immunoprecipitation assays were performed as six replicates and compared to protein A controls. The same $\log_2\text{FC} > 1$ and $p_{adj} < 0.05$ threshold was used to identify enriched GO processes. Interestingly, whilst in non-treated cells we can observe 'gene expression' as an enriched process, α -amanitin treatment disrupts this and appears to change NDP52 interactome to 'regulation of DNA replication', 'signal transduction in response to DNA damage', and 'chromosome organisation' (SFig.11E and F). Figure 9F shows examples of top hits for endogenous NDP52 pull-downs in non-treated versus α -amanitin treated cells. The shift observed in interacting partners suggests that NDP52 preferentially interacts with different proteins, depending on cell state, and could change its interactome in response to environmental stresses. Interestingly, in non-treated cells we observe different GO enrichments to those observed in recombinant protein pull-down assays (SFig.9A and SFig.11E). The high concentration of recombinant NDP52-FL used could have allowed the identification of different interactions, that under normal conditions and cellular levels of NDP52 are less enriched.

Overall, our data show NDP52 as a novel transcription regulator, with functions in DNA structure.

Discussion

In this study, we used a multidisciplinary approach to shed light on the nuclear role of autophagy receptor NDP52. Although NDP52 was first observed in the nucleus (Korioth et al., 1995), until now, no clear nuclear function had been attributed to this protein. By investigating its nuclear organisation, dynamics, interactome and biochemical characteristics, we have been able to link its function to transcription and DNA regulation.

To enhance their activity and functional efficiency, many nuclear proteins involved in transcription and other nuclear processes form molecular clusters (Carmo-Fonseca, 2002; Cook, 2010; Cremer et al., 2006; Leake, 2018; Wollman et al., 2017). Here, we have determined that nuclear NDP52 clusters at regions of transcription initiation with RNAPII, and that its overexpression can increase the number of transcriptional clusters available in the nucleus. RNAPII clustering is directly related to transcription activity (Cho et al., 2016a; Cho et al., 2016b; Cho et al., 2018) and changes to its spatial organisation and clustering behaviour impact whole gene-expression levels (Hari-Gupta et al., 2020). This provides a direct association between NDP52 and transcriptional regulation. Furthermore, we have also shown that knockdown of NDP52 impacts gene expression in both HeLa and MCF-7 cells. Altogether, these data support a role for NDP52 in RNAPII-related transcription.

Although future studies will be necessary to determine a mechanism for the regulatory role of NDP52 in transcription, here we propose two different strategies: i) through interactions with transcriptional machinery and regulatory factors at transcriptional sites and/or ii) through direct DNA structure regulation and interaction with chromatin remodellers (Fig. 10). In support of our first hypothesis, we show that NDP52 colocalises with RNAPII at transcription initiation sites and that clustering of NDP52 is abrogated following transcription inhibition. Although we observed more non-colocalised clusters of NDP52-Ser5 RNAPII than colocalised, it is important to note that not all Ser5-RNAPII represents actively transcribing complexes, and that part of this population is stalled/paused. Hence, it is possible that NDP52 preferentially localises with a subset of RNAPII clusters, for example, with molecules that are going through initiation into active elongation. Following transcription inhibition with α -amanitin treatment, the observed increase in NDP52 molecular dynamics suggests a reduction in binding sites available for the protein in the nucleus. These data indicate that loss of RNAPII molecules, due to its degradation, directly affects the nuclear organisation of NDP52. Furthermore, our proteomics data, both with recombinant and endogenous NDP52, also shows interactions with different transcriptional regulators. These interactions are markedly reduced in endogenous NDP52 pull-downs when cells are pre-treated with α -amanitin, which further supports the hypothesis that interactions between NDP52 and transcriptional regulators are an important part of the regulatory function of this protein.

Equally, we also show that NDP52 binds specifically and with high affinity to dsDNA and we believe this interaction to be crucial for its observed role in transcription. Importantly, we have shown that NDP52 can be isolated in complex with different genomic *loci*, through ChIP-qPCR, and this could be a regulatory strategy for the protein. In fact, CoCoA, a gene paralog of NDP52 and known transcription co-activator, has been found present at different genes

regulated by nuclear receptors, such as the *TFF1/PS2* gene (Kim et al., 2008). Although our biochemical studies also show for the first time that CoCoA can directly bind DNA, previous studies have determined that interactions of this protein with histone methyltransferases and acetyltransferases at the gene body allows the recruitment of basal transcriptional machinery, thus promoting transcriptional activity (Kim et al., 2003; Kim et al., 2008; Kim et al., 2006). It will be interesting, in future studies, to produce a more comprehensive analysis of NDP52-genomic DNA interactions, through ChIP-Seq. There are also no available ChIP-Seq data for CoCoA. It would be informative to determine how similar the genomic targets of these two proteins are, given their biochemical likeness.

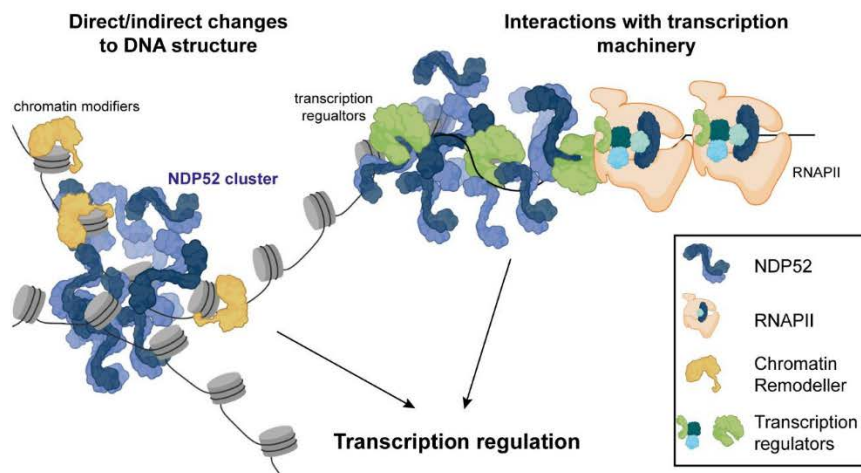


Figure 10 – Model of possible mechanism for NDP52's activity in transcription. NDP52 could directly interact with DNA in the nucleus, or with chromatin modifiers (e.g. histone modifiers), to cause local changes to chromatin structure. Conversely, interactions with transcription factors/coactivators and transcription machinery could also modulate transcription activity of genes.

Interestingly, when exploring NDP52 binding to DNA, we observed that NDP52 promotes changes in DNA structure *in vitro* - through bending, bridging and DNA looping. This, together with our proteomics data showing regulators of chromatin and DNA structure as possible binding partners of NDP52, suggests a role in chromatin regulation for NDP52. Chromatin conformation and structure are important determinants of accessibility to transcriptional machinery (Imbalzano et al., 1994); as a result, chromatin regulation is directly linked to transcriptional activity. Our data suggest that, in addition to direct regulation at transcriptional sites - either through direct interactions with RNAPII or other transcription factors -, NDP52 activity in DNA structure and links to chromatin organisation could also drive transcriptional regulation. This could also explain how overexpression of NDP52 leads to an increase in RNAPII clusters, as changes to chromatin accessibility might occur. In future studies, it will be important to address specifically the role of NDP52 in chromatin structure and regulation and explore some of the possible new interactions with DNA binding proteins and regulators identified in our proteomics data.

Our work has also provided a detailed biochemical analysis of NDP52. We show that NDP52, in solution, is predominantly dimeric, as previously suggested (Kim et al., 2013); although it can also associate into higher oligomeric forms, such as trimers and tetramers. We also found that, in addition to its coiled-coil region, the C-terminal and N-terminal domains can also independently interact and form oligomeric structures. Furthermore, we provide evidence that NDP52 interacts with DNA through its zinc finger domains and that both the full-length and C-terminal domains of NDP52 can oligomerise with and around DNA *in vitro*. In cells, this could provide a mechanism for a possible function of NDP52 in chromatin structure regulation, by increasing local concentrations of the protein around DNA. Moreover, given that the C-terminal domain is the main region for interactions with DNA, it is possible that, in the cell, NDP52 binds to DNA through this region whilst simultaneously sustaining interactions with other proteins through its N-terminal and coiled-coil regions. AFM data suggests a variety of spatial orientations might be available during oligomerisation of the protein, but further studies will be necessary.

Whilst the C-terminal of NDP52 is crucial for its DNA binding activity, our proteomics data also indicate that many important regulatory protein-protein interactions also occur through this region. In fact, previous studies have identified the C-terminal domain of NDP52 as the main interacting region with Myosin VI and ubiquitin (Vargas et al., 2019). Interestingly, the majority of common hits found in recombinant proteomics between full-length NDP52 and CoCoA arise from the C-terminal domain region of the protein. This is not surprising as this region displays high levels of amino acid homology in both proteins.

Interestingly, our proteomics data with endogenous NDP52 following treatment with α -amanitin, showed an enrichment for proteins involved in cell stress and DNA damage response. Although this was not explored in this study, it will be interesting to understand, in the future, how nuclear NDP52 responds to different cellular stresses. In the cytoplasm, NDP52 is known to be activated by certain cell stresses, namely in response to bacterial or viral infections or the presence of damaged organelles (Thurston et al., 2009; Vargas et al., 2019; Verlhac et al., 2015). It is not yet known how cell stress might affect nuclear levels, organisation or the nuclear activity of NDP52. It is possible that NDP52 has a dual cytoplasmic-nuclear role in cells and that its nuclear activity is linked to its cytoplasmic function in autophagy. Following cellular infection innate immunity and apoptotic pathways are activated in the cytoplasm that lead to the translocation of different proteins into the nucleus for their activity in transcription, chromatin and DNA repair regulation (Liang and Clarke, 2001; Mercurio and Manning, 1999; Shim et al., 2020). Understanding the molecular role of NDP52 and its nuclear activity in context of its already known cytoplasmic function in autophagy will be important in future studies.

Overall, here, we provide evidence for NDP52 as a novel transcriptional regulator, with possible functions in chromatin structure and organisation.

ACKNOWLEDGEMENTS

We thank the UKRI-MRC (MR/M020606/1) and UKRI-STFC (19130001) for funding to C.P.T. Aberration-corrected multi-focal microscopy was performed in collaboration with the Advanced Imaging Center at Janelia Research Campus, a facility jointly supported by the Howard Hughes Medical Institute and the Gordon and Betty Moore Foundation. We also thank Darren Griffin (University of Kent) and Alessia Buscaino (University of Kent) for sharing of equipment, and Satya Khuon (Janelia Research Campus) for assisting with cell culture. The JF549 dyes were kindly provided by Luke Lavis (Janelia Research Campus).

AUTHOR CONTRIBUTIONS

A.dS and C.P.T. conceived the study. A.dS, E.R, A.L.B.P., Y.H-G. and C.P.T. designed experiments. A.dS and C.P.T. performed single molecule imaging experiments. Imaging was supported by L.W., M.M-F., T-L.C., and J.A. A.dS and Y.H-G. performed and analyzed the genomics experiments. A.dS, H.C.W.R., K.P., S.Y.Z.R and F.L. expressed, purified and performed experiments with recombinant proteins. L.W., J.A., A.dS. and C.P.T. contributed to single molecule data analysis. A.dS, A.S., P.I.J.E., and K.H. performed and analyzed the mass spectroscopy experiments. I.B. prepared samples and performed electron microscopy. C.P.T. supervised the study. A.dS and C.P.T. wrote the manuscript with comments from all authors.

Competing financial interests: The authors declare no competing financial interests.

References

- Abrahamsson, S., Chen, J., Hajj, B., Stallinga, S., Katsov, A.Y., Wisniewski, J., Mizuguchi, G., Soule, P., Mueller, F., Darzacq, C.D., *et al.* (2013). Fast multicolor 3D imaging using aberration-corrected multifocus microscopy. *Nature methods* *10*, 60-63.
- Beton, J.G., Moorehead, R., Helfmann, L., Gray, R., Hoogenboom, B.W., Joseph, A.P., Topf, M., and Pyne, A.L.B. (2021). TopoStats – A program for automated tracing of biomolecules from AFM images. *Methods* *193*, 68-79.
- Bushnell, D.A., Cramer, P., and Kornberg, R.D. (2002). Structural basis of transcription: alpha-amanitin-RNA polymerase II cocrystal at 2.8 Å resolution. *Proc Natl Acad Sci U S A* *99*, 1218-1222.
- Carmo-Fonseca, M. (2002). The Contribution of Nuclear Compartmentalization to Gene Regulation. *Cell* *108*, 513-521.
- Cassandri, M., Smirnov, A., Novelli, F., Pitolli, C., Agostini, M., Malewicz, M., Melino, G., and Raschellà, G. (2017). Zinc-finger proteins in health and disease. *Cell Death Discovery* *3*, 17071.
- Cho, W.-K., Jayanth, N., English, B.P., Inoue, T., Andrews, J.O., Conway, W., Grimm, J.B., Spille, J.-H., Lavis, L.D., Lionnet, T., *et al.* (2016a). RNA Polymerase II cluster dynamics predict mRNA output in living cells. *eLife* *5*, e13617.
- Cho, W.-K., Jayanth, N., Mullen, S., Tan, T.H., Jung, Y.J., and Cissé, I.I. (2016b). Super-resolution imaging of fluorescently labeled, endogenous RNA Polymerase II in living cells with CRISPR/Cas9-mediated gene editing. *Scientific Reports* *6*, 35949.
- Cho, W.K., Spille, J.H., Hecht, M., Lee, C., Li, C., Grube, V., and Cisse, I.I. (2018). Mediator and RNA polymerase II clusters associate in transcription-dependent condensates. *Science* *361*, 412-415.
- Ciani, B., Bjelić, S., Honnappa, S., Jawhari, H., Jaussi, R., Payapilly, A., Jowitt, T., Steinmetz, M.O., and Kammerer, R.A. (2010). Molecular basis of coiled-coil oligomerization-state specificity. *Proceedings of the National Academy of Sciences* *107*, 19850.
- Cook, A.W., Gough, R.E., and Toseland, C.P. (2020). Nuclear myosins – roles for molecular transporters and anchors. *Journal of Cell Science* *133*.
- Cook, P.R. (2010). A model for all genomes: the role of transcription factories. *Journal of molecular biology* *395*, 1-10.
- Cremer, T., Cremer, M., Dietzel, S., Müller, S., Solovei, I., and Fakan, S. (2006). Chromosome territories – a functional nuclear landscape. *Current Opinion in Cell Biology* *18*, 307-316.
- dos Santos, Á., Fili, N., Hari-Gupta, Y., Gough, R.E., Wang, L., Martin-Fernandez, M., Aaron, J., Waite, E., Chew, T.-L., and Toseland, C.P. (2020). Binding partners regulate unfolding of myosin VI to activate the molecular motor. *bioRxiv*, 2020.2005.2010.079236.
- Ellinghaus, D., Zhang, H., Zeissig, S., Lipinski, S., Till, A., Jiang, T., Stade, B., Bromberg, Y., Ellinghaus, E., Keller, A., *et al.* (2013). Association between variants of PRDM1 and NDP52 and Crohn's disease, based on exome sequencing and functional studies. *Gastroenterology* *145*, 339-347.
- Fili, N., Hari-Gupta, Y., Dos Santos, Á., Cook, A., Poland, S., Ameer-Beg, S.M., Parsons, M., and Toseland, C.P. (2017). NDP52 activates nuclear myosin VI to enhance RNA polymerase II transcription. *Nat Commun* *8*, 1871.
- Fili, N., and Toseland, C.P. (2019). Unconventional Myosins: How Regulation Meets Function. *International journal of molecular sciences* *21*.
- Ge, S.X., Son, E.W., and Yao, R. (2018). iDEP: an integrated web application for differential expression and pathway analysis of RNA-Seq data. *BMC Bioinformatics* *19*, 534.
- Hari-Gupta, Y., Fili, N., dos Santos, Á., Cook, A.W., Gough, R.E., Reed, H.C.W., Wang, L., Aaron, J., Venit, T., Wait, E., *et al.* (2020). Nuclear myosin VI regulates the spatial organization of mammalian transcription initiation. *bioRxiv*, 2020.2004.2021.053124.
- Imbalzano, A.N., Kwon, H., Green, M.R., and Kingston, R.E. (1994). Facilitated binding of TATA-binding protein to nucleosomal DNA. *Nature* *370*, 481-485.

Jerabek-Willemsen, M., André, T., Wanner, R., Roth, H.M., Duhr, S., Baaske, P., and Breitsprecher, D. (2014). MicroScale Thermophoresis: Interaction analysis and beyond. *Journal of Molecular Structure* 1077, 101-113.

Kim, B.W., Hong, S.B., Kim, J.H., Kwon, D.H., and Song, H.K. (2013). Structural basis for recognition of autophagic receptor NDP52 by the sugar receptor galectin-8. *Nat Commun* 4, 1613.

Kim, J.H., Li, H., and Stallcup, M.R. (2003). CoCoA, a Nuclear Receptor Coactivator which Acts through an N-Terminal Activation Domain of p160 Coactivators. *Molecular cell* 12, 1537-1549.

Kim, J.H., Yang, C.K., Heo, K., Roeder, R.G., An, W., and Stallcup, M.R. (2008). CCAR1, a Key Regulator of Mediator Complex Recruitment to Nuclear Receptor Transcription Complexes. *Molecular cell* 31, 510-519.

Kim, J.H., Yang, C.K., and Stallcup, M.R. (2006). Downstream signaling mechanism of the C-terminal activation domain of transcriptional coactivator CoCoA. *Nucleic Acids Res* 34, 2736-2750.

Korioth, F., Gieffers, C., Maul, G.G., and Frey, J. (1995). Molecular characterization of NDP52, a novel protein of the nuclear domain 10, which is redistributed upon virus infection and interferon treatment. *J Cell Biol* 130, 1-13.

Koulouras, G., Panagopoulos, A., Rapsomaniki, M.A., Giakoumakis, N.N., Taraviras, S., and Lygerou, Z. (2018). EasyFRAP-web: a web-based tool for the analysis of fluorescence recovery after photobleaching data. *Nucleic Acids Research* 46, W467-W472.

Leake, M.C. (2018). Transcription factors in eukaryotic cells can functionally regulate gene expression by acting in oligomeric assemblies formed from an intrinsically disordered protein phase transition enabled by molecular crowding. *Transcription* 9, 298-306.

Lherbette, M., dos Santos, Á., Hari-Gupta, Y., Fili, N., Toseland, C.P., and Schaap, I.A.T. (2017). Atomic Force Microscopy micro-rheology reveals large structural inhomogeneities in single cell-nuclei. *Scientific Reports* 7, 8116.

Liang, S.H., and Clarke, M.F. (2001). Regulation of p53 localization. *European journal of biochemistry* 268, 2779-2783.

Lupas, A.N., and Gruber, M. (2005). The structure of alpha-helical coiled coils. *Advances in protein chemistry* 70, 37-78.

Manalastas-Cantos, K., Konarev, P.V., Hajizadeh, N.R., Kikhney, A.G., Petoukhov, M.V., Molodenskiy, D.S., Panjkovich, A., Mertens, H.D.T., Gruzinov, A., Borges, C., *et al.* (2021). ATSAS 3.0: expanded functionality and new tools for small-angle scattering data analysis. *Journal of Applied Crystallography* 54, 343-355.

Meister, P., Poidevin, M., Francesconi, S., Tratner, I., Zarzov, P., and Baldacci, G. (2003). Nuclear factories for signalling and repairing DNA double strand breaks in living fission yeast. *Nucleic acids research* 31, 5064-5073.

Mercurio, F., and Manning, A.M. (1999). NF- κ B as a primary regulator of the stress response. *Oncogene* 18, 6163-6171.

Morriswood, B., Ryzhakov, G., Puri, C., Arden, S.D., Roberts, R., Dendrou, C., Kendrick-Jones, J., and Buss, F. (2007). T6BP and NDP52 are myosin VI binding partners with potential roles in cytokine signalling and cell adhesion. *J Cell Sci* 120, 2574-2585.

Mostowy, S., Sancho-Shimizu, V., Hamon, M.A., Simeone, R., Brosch, R., Johansen, T., and Cossart, P. (2011). p62 and NDP52 proteins target intracytosolic *Shigella* and *Listeria* to different autophagy pathways. *The Journal of biological chemistry* 286, 26987-26995.

Nečas, D., and Klapetek, P. (2012). Gwyddion: an open-source software for SPM data analysis. *Central European Journal of Physics* 10, 181-188.

Nthiga, T.M., Kumar Shrestha, B., Sjøttem, E., Bruun, J.A., Bowitz Larsen, K., Bhujabal, Z., Lamark, T., and Johansen, T. (2020). CALCOCO1 acts with VAMP-associated proteins to mediate ER-phagy. *Embo j* 39, e103649.

Pageon, S.V., Nicovich, P.R., Mollazade, M., Tabarin, T., and Gaus, K. (2016). Clus-DoC: a combined cluster detection and colocalization analysis for single-molecule localization microscopy data. *Molecular biology of the cell* 27, 3627-3636.

Pyne, A.L., and Hoogenboom, B.W. (2016). Imaging DNA Structure by Atomic Force Microscopy. *Methods in molecular biology* (Clifton, NJ) *1431*, 47-60.

Pyne, A.L.B., Noy, A., Main, K.H.S., Velasco-Berrelleza, V., Piperakis, M.M., Mitchenall, L.A., Cugliandolo, F.M., Beton, J.G., Stevenson, C.E.M., Hoogenboom, B.W., *et al.* (2021). Base-pair resolution analysis of the effect of supercoiling on DNA flexibility and major groove recognition by triplex-forming oligonucleotides. *Nature Communications* *12*, 1053.

Schrank, B.R., Aparicio, T., Li, Y., Chang, W., Chait, B.T., Gundersen, G.G., Gottesman, M.E., and Gautier, J. (2018). Nuclear ARP2/3 drives DNA break clustering for homology-directed repair. *Nature* *559*, 61-66.

Shim, M.S., Nettesheim, A., Hirt, J., and Liton, P.B. (2020). The autophagic protein LC3 translocates to the nucleus and localizes in the nucleolus associated to NUFIP1 in response to cyclic mechanical stress. *Autophagy* *16*, 1248-1261.

Sporbert, A., Gahl, A., Ankerhold, R., Leonhardt, H., and Cardoso, M.C. (2002). DNA Polymerase Clamp Shows Little Turnover at Established Replication Sites but Sequential De Novo Assembly at Adjacent Origin Clusters. *Molecular cell* *10*, 1355-1365.

Stefely, J.A., Zhang, Y., Freiburger, E.C., Kwiecien, N.W., Thomas, H.E., Davis, A.M., Lowry, N.D., Vincent, C.E., Shishkova, E., Clark, N.A., *et al.* (2020). Mass spectrometry proteomics reveals a function for mammalian CALCOCO1 in MTOR-regulated selective autophagy. *Autophagy* *16*, 2219-2237.

Sternsdorf, T., Jensen, K., Züchner, D., and Will, H. (1997). Cellular localization, expression, and structure of the nuclear dot protein 52. *J Cell Biol* *138*, 435-448.

Thurston, T.L., Ryzhakov, G., Bloor, S., von Muhlinen, N., and Randow, F. (2009). The TBK1 adaptor and autophagy receptor NDP52 restricts the proliferation of ubiquitin-coated bacteria. *Nature immunology* *10*, 1215-1221.

Till, A., Lipinski, S., Ellinghaus, D., Mayr, G., Subramani, S., Rosenstiel, P., and Franke, A. (2013). Autophagy receptor CALCOCO2/NDP52 takes center stage in Crohn disease. *Autophagy* *9*, 1256-1257.

Tumbarello, D.A., Manna, P.T., Allen, M., Bycroft, M., Arden, S.D., Kendrick-Jones, J., and Buss, F. (2015). The Autophagy Receptor TAX1BP1 and the Molecular Motor Myosin VI Are Required for Clearance of Salmonella Typhimurium by Autophagy. *PLOS Pathogens* *11*, e1005174.

Tumbarello, D.A., Waxse, B.J., Arden, S.D., Bright, N.A., Kendrick-Jones, J., and Buss, F. (2012). Autophagy receptors link myosin VI to autophagosomes to mediate Tom1-dependent autophagosome maturation and fusion with the lysosome. *Nat Cell Biol* *14*, 1024-1035.

Vargas, J.N.S., Wang, C., Bunker, E., Hao, L., Maric, D., Schiavo, G., Randow, F., and Youle, R.J. (2019). Spatiotemporal Control of ULK1 Activation by NDP52 and TBK1 during Selective Autophagy. *Molecular cell* *74*, 347-362.e346.

Verlhac, P., Grégoire, I.P., Azocar, O., Petkova, D.S., Baguet, J., Viret, C., and Faure, M. (2015). Autophagy receptor NDP52 regulates pathogen-containing autophagosome maturation. *Cell host & microbe* *17*, 515-525.

Wollman, A.J., Shashkova, S., Hedlund, E.G., Friemann, R., Hohmann, S., and Leake, M.C. (2017). Transcription factor clusters regulate genes in eukaryotic cells. *eLife* *6*, e27451.

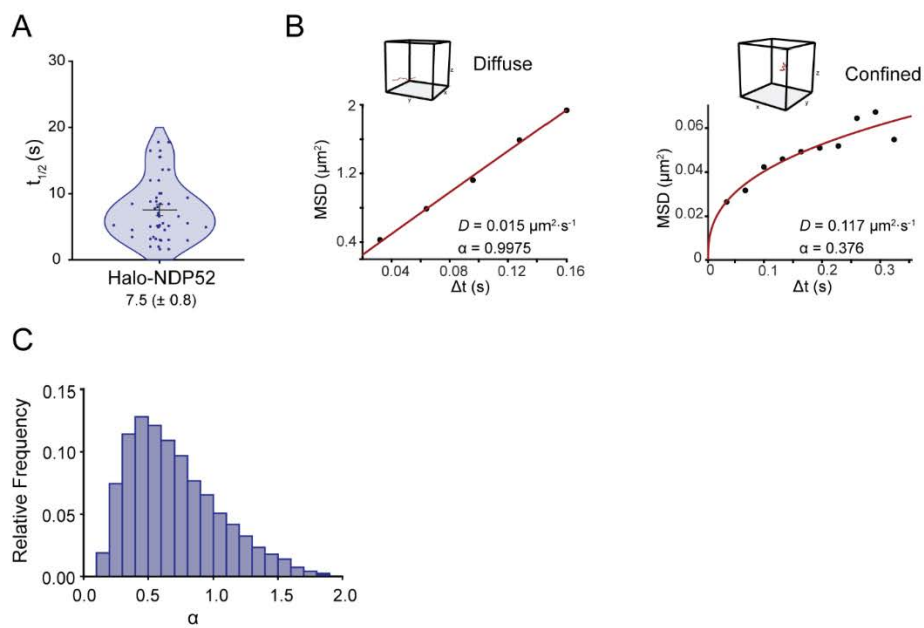
Xie, X., Li, F., Wang, Y., Wang, Y., Lin, Z., Cheng, X., Liu, J., Chen, C., and Pan, L. (2015). Molecular basis of ubiquitin recognition by the autophagy receptor CALCOCO2. *Autophagy* *11*, 1775-1789.

6.2.1.1. Supplementary Material for Manuscript 7

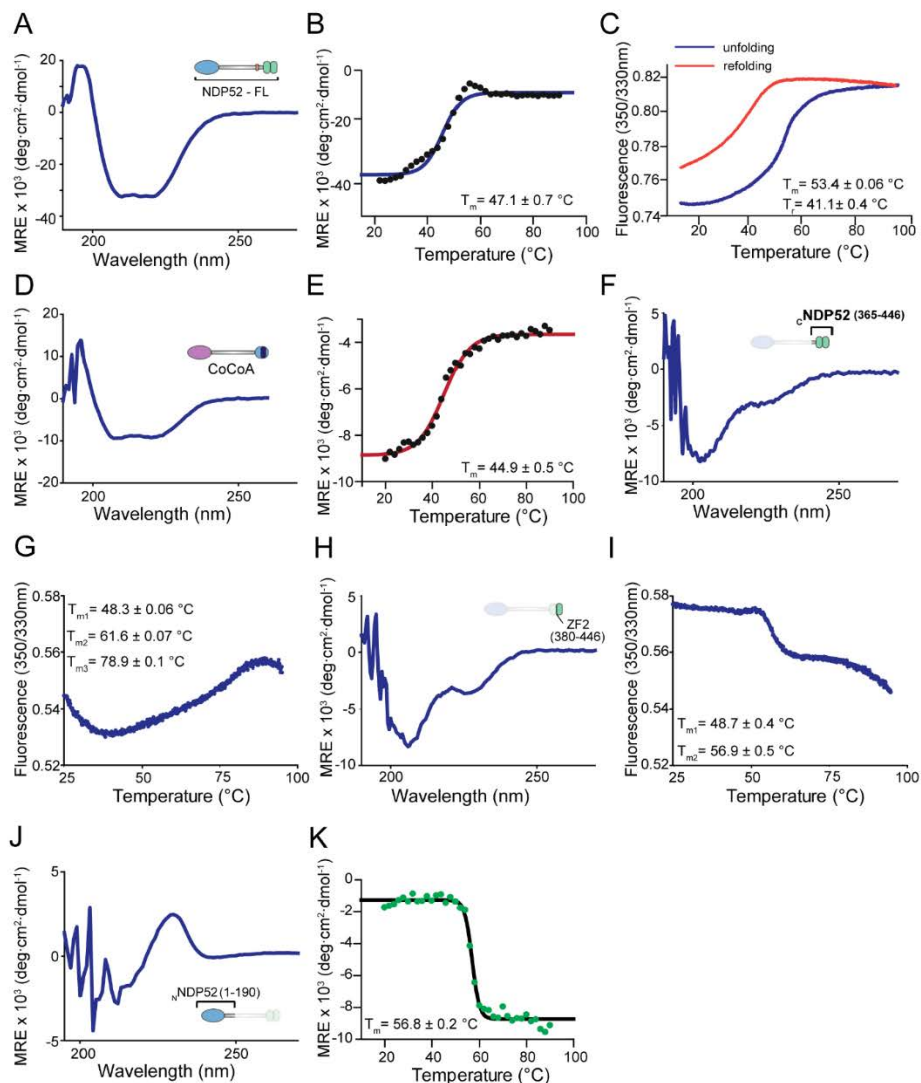
Supplementary Material

Autophagy receptor NDP52 modulates RNA Polymerase II transcription

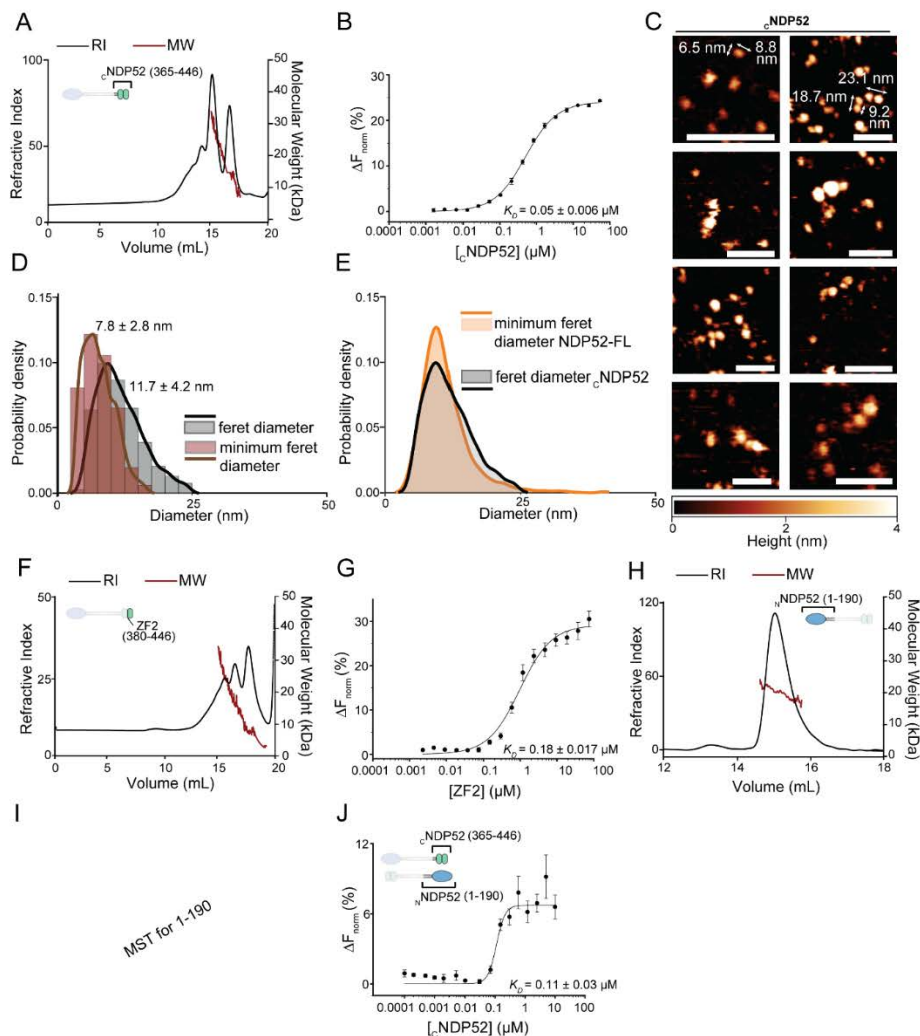
Ália dos Santos¹, Daniel E. Rollins², Yukti Hari-Gupta^{3,3}, Hannah C. W. Reed³, Sabrina Yong Zi Ru³, Kseniia Pidlisna³, Ane Stranger³, Faeza Lorgat¹, Ian Brown³, Kevin Howland³, Jesse Aaron⁴, Lin Wang⁵, Peter J. I. Ellis³, Teng-Leong Chew⁴, Alice L. B. Pyne², Marisa Martin-Fernandez⁵, Christopher P. Toseland^{1*}



Supplementary Figure 1 – Nuclear dynamics of NDP52. (A) Violin plot of recovery time ($t_{1/2}$) calculated from FRAP data for Halo NDP52. Each individual point represents one cell. Mean \pm SEM value is shown. $n = 27$ cells. (B) Example MSD curves extracted and fitted from acMFM single-molecule tracks. 3D trajectory of each example is shown above the graph and calculated values for diffusion coefficient (D) and anomalous diffusion (α) are shown. (C) Histogram of calculated α values for all molecules using acMFM. Graph represents values for 14 322 molecules from 51 cells.

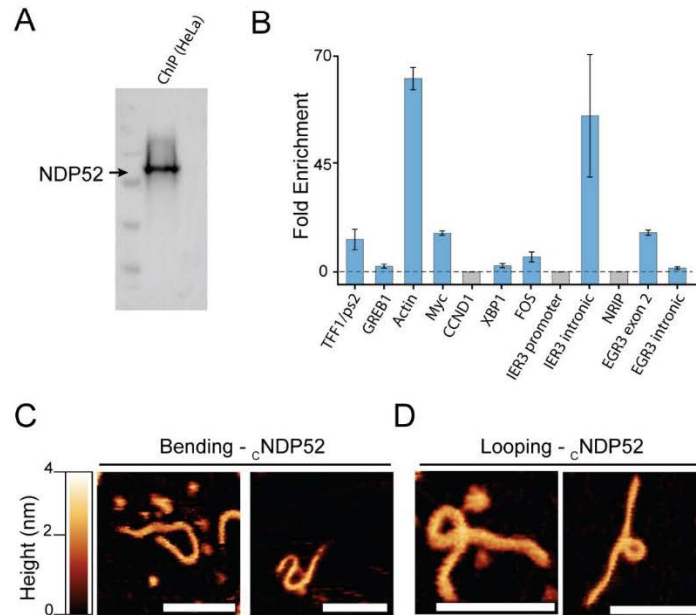


Supplementary Figure 2 – Folding and stability of NDP52 and CoCoA recombinant constructs. (A) CD spectra of NDP52-FL. (B) Thermal denaturation of NDP52-FL following MRE values at 222 nm wavelength. (C) Nano-DSF curves for NDP52 thermal denaturation and refolding. (D) CoCoA CD spectra. (E) Thermal denaturation of CoCoA, following MRE values at 222nm wavelength. (F) cNDP52 CD spectra. (G) Nano-Differential Scanning Fluorimetry (nano-DSF) for cNDP52 during thermal denaturation. (H) ZF2 CD spectra. (I) Nano-DSF for ZF2 during thermal denaturation. (J) nNDP52 CD spectra. (K) Thermal denaturation of nNDP52, following MRE values at 215nm wavelength.

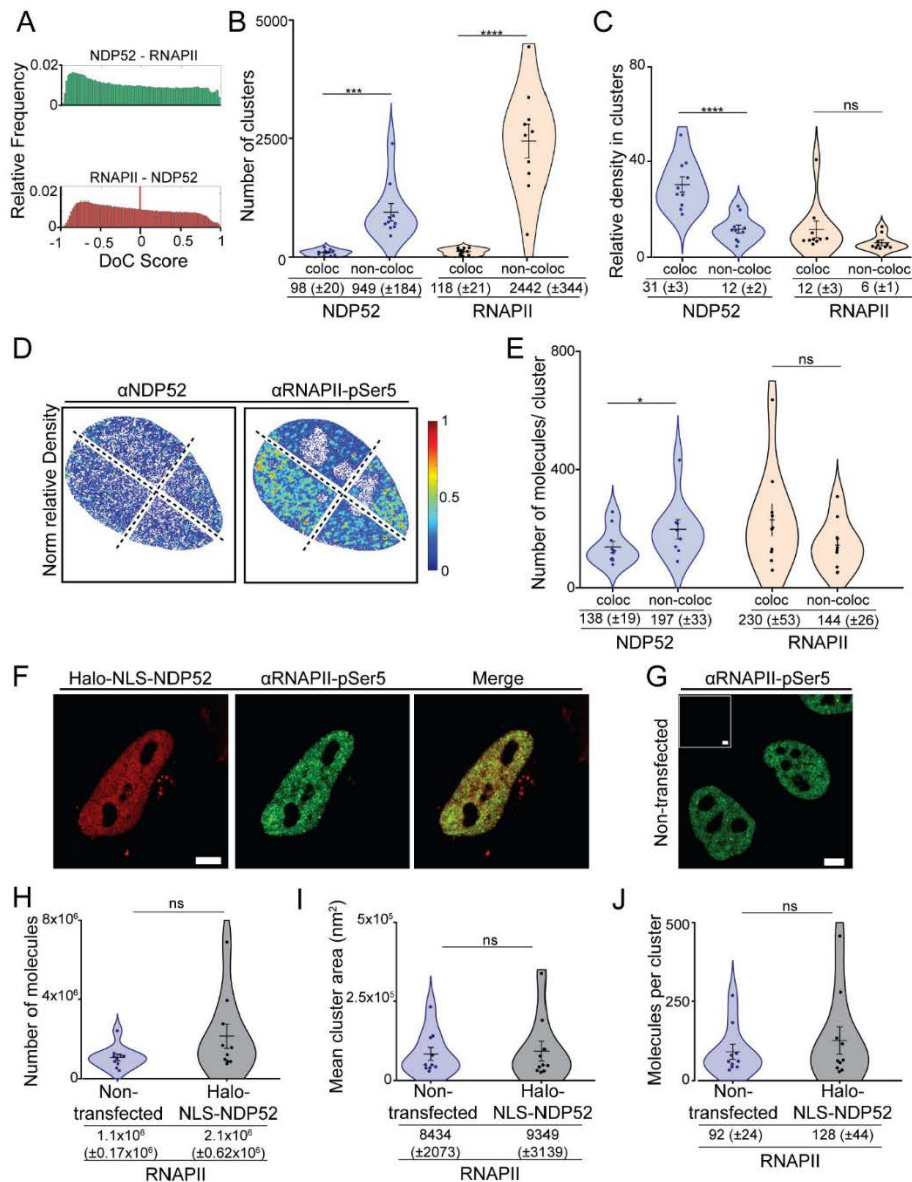


Supplementary Figure 3 – Oligomerisation of individual NDP52 domains. (A) SEC-MALS profile for the C-terminal of NDP52 (cNDP52), which encompasses both zinc finger domains. Refractive index (RI) trace is shown in black, as well as the calculated molecular weight values, across the peaks (in red). (B) Microscale thermophoresis, showing oligomerisation of cNDP52, with the calculated K_D displayed in the graph. Values plotted represent average \pm SEM of three individual experiments. (C) Atomic force microscopy imaging (AFM) of cNDP52 showing monomeric, dimeric and higher oligomeric forms of the protein. Example measurements for individual protein molecules are shown. Scale bar = 50 nm. Height scale also shown. (D) Kernel distributions of feret diameter and minimum feret diameter for cNDP52, calculated from AFM imaging. $n = 1\,149$ molecules. Values shown represent Mean \pm SD. (E) Kernel distribution showing feret diameter of cNDP52 (shown in (D)) compared to minimum feret diameter calculated for NDP52-FL shown in Figure 4K. (F) SEC-MALS trace for ZF2. RI trace is shown in black and calculated molecular weight values are shown in red. (G) Microscale thermophoresis, showing oligomerisation of ZF2, with the calculated K_D displayed in the graph. Values represent average \pm SEM of three individual experiments. (H) SEC-MALS trace for the N-terminal of NDP52 (nNDP52), comprising the SKICH domain and a small portion of the coiled-coil region. RI trace is shown in black and calculated molecular weight values are shown in red. (I) Microscale thermophoresis, showing oligomerisation of nNDP52, with the calculated K_D displayed

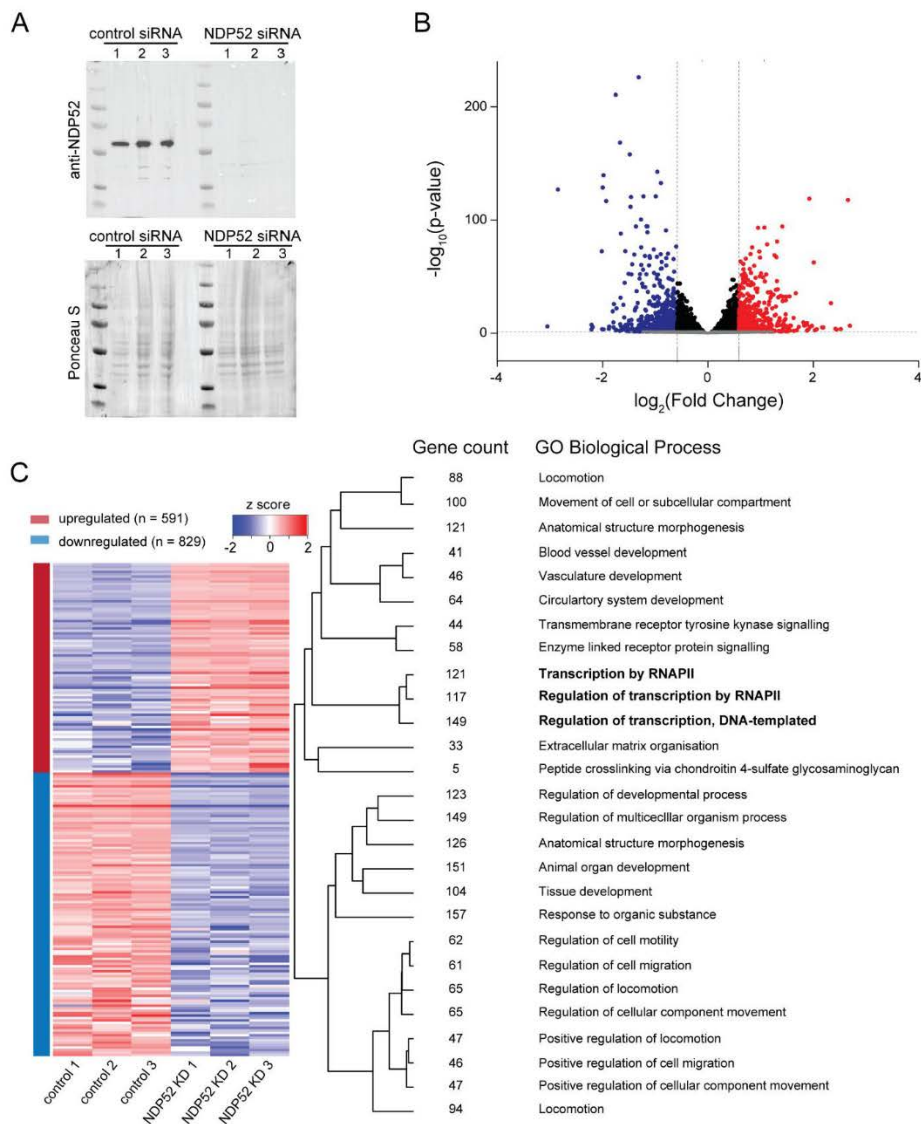
in the graph. **(J)** MST curve showing interaction between labelled nNDP52 titrated with cNDP52, with the calculated K_D displayed in the graph. Values represent average \pm SEM of three individual experiments.



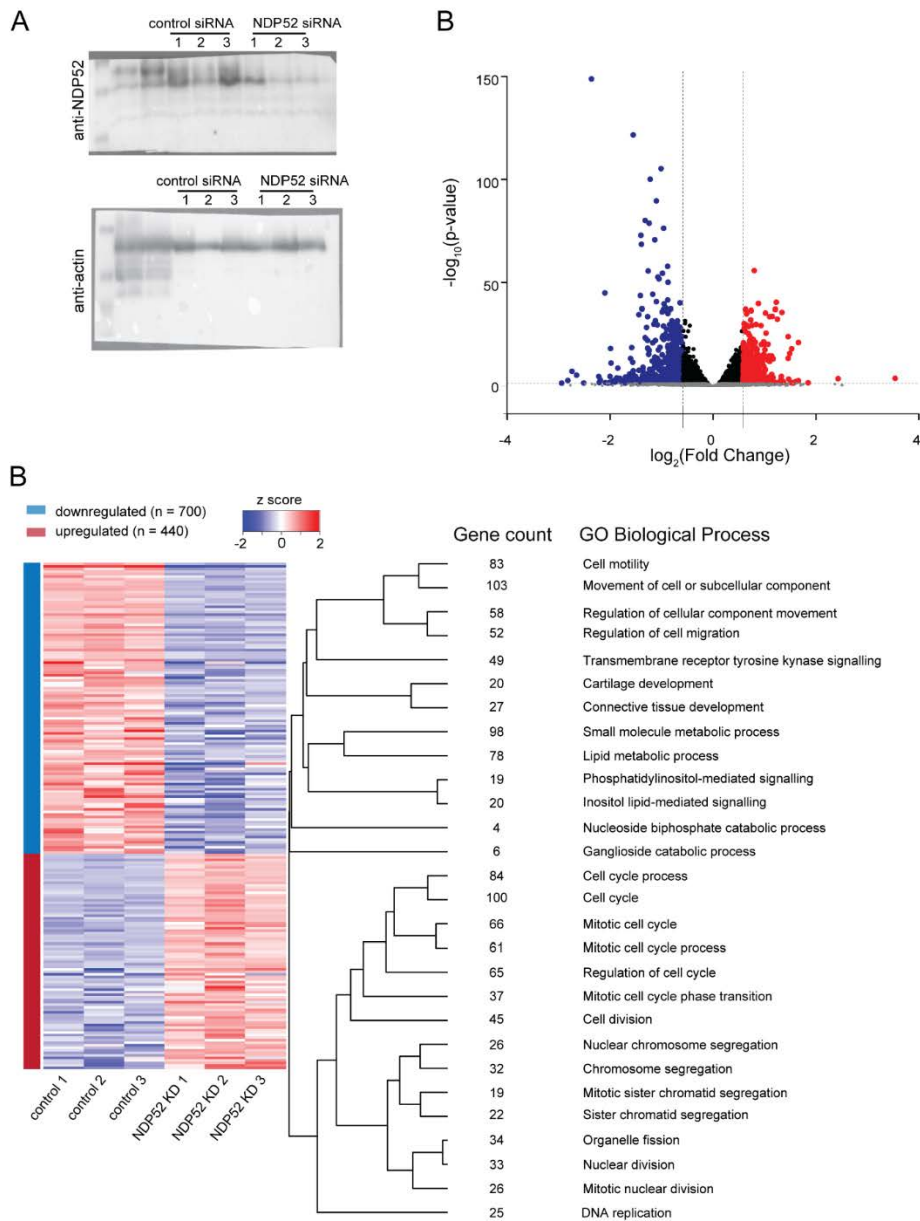
Supplementary Figure 4 – NDP52 binding to DNA *in vitro* and in cells. (A) Western blot showing presence of NDP52 in chromatin-enriched ChIP sample. **(B)** NDP52 ChIP-qPCR against *loci* specified in the label. Enriched *loci* are shown in blue. Values represent mean \pm SEM of three individual experiments. **(C)** AFM images of examples of cNDP52 bending DNA. Scale bars = 50 nm and height scale shown. **(D)** Example images of DNA looping by cNDP52. Scale bars = 50 nm. Height scale shown in (A).



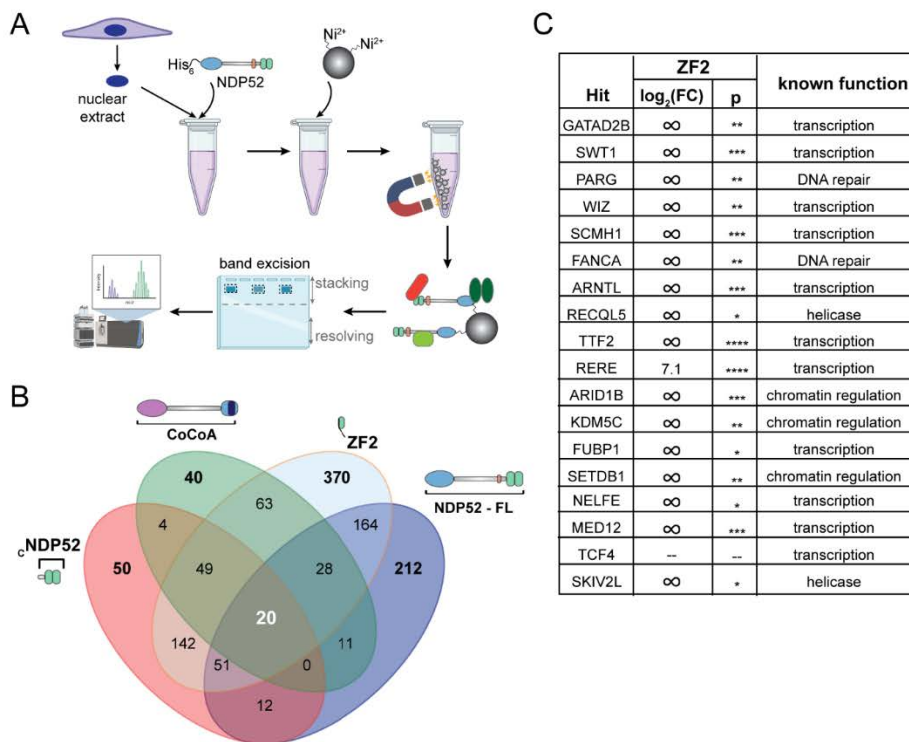
Supplementary Figure 5 – Colocalisation of NDP52 with RNAPII-pSer5. (A) DoC score histogram for example STORM rendering in Figure 8B and colocalisation map shown in Figure 8D. DoC score of 1 represents perfect colocalisation between molecules, and DoC score -1 represents segregation. DoC score of 0.4 was used as colocalisation threshold. (B) Number of clusters considered colocalised or non-colocalised for both NDP52 and RNAPII-pSer5. (C) Relative density of molecules in colocalised and non-colocalised NDP52 or RNAPII-pSer5 clusters. (D) Example of normalised relative density heat maps for NDP52 and RNAPII-pSer5. Heat maps correspond to the same cell shown in Figure 8B and D. Red represents regions of high molecular density and blue of low molecular density. (E) Mean number of molecules per colocalised or non-colocalised clusters for NDP52 or RNAPII-pSer5. $n = 10$ cells (F) Confocal images of HeLa cell transiently expressing Halo-NLS-NDP52 and immunofluorescently stained with RNAPII-pSer5. Scale bar = 5 μ m. (G) Confocal image of non-transfected HeLa cell with immunofluorescent staining of RNAPII-pSer5. Scale bar = 5 μ m. (H) Number of RNAPII-pSer5 molecules in non-transfected or transiently expressing Halo-NLS-NDP52 HeLa cells. (I) Mean cluster area in nm² for RNAPII-pSer5 molecules in non-transfected or transiently expressing Halo-NLS-NDP52 HeLa cells. (J) Number of molecules per RNAPII-pSer5 cluster in non-transfected or transiently expressing Halo-NLS-NDP52 HeLa cells. Mean \pm SEM values are shown. Each point represents the average value per cell. $n = 10$ cells (Non-transfected) $n = 10$ cells (Halo-NLS-NDP52). * $p < 0.05$; *** $p < 0.001$; **** $p < 0.0001$ by two-tailed t-test.



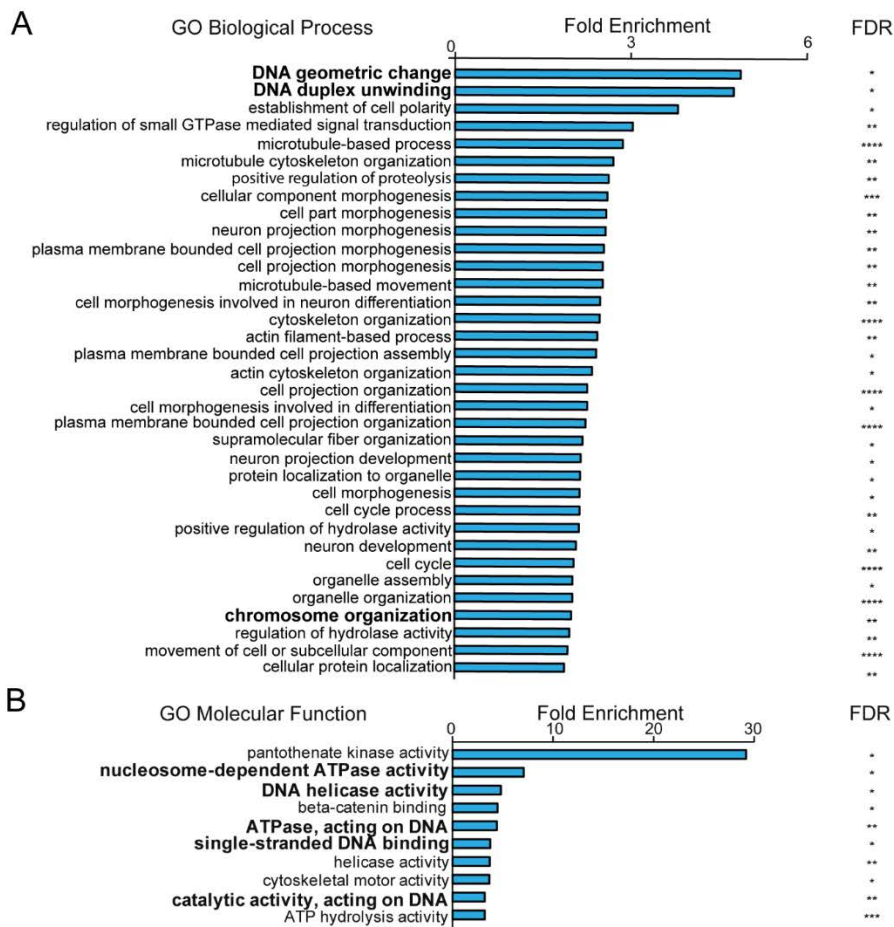
Supplementary Figure 6 – Impact of NDP52 knockdown in gene expression in HeLa cells. (A) Western blot showing NDP52 KD replicates for RNA-Seq. On top, immunoblot against NDP52 is shown and, on the bottom panel, the same blot stained with Ponceau S is shown as loading control. **(B)** Volcano plot of differentially expressed genes following NDP52 KD. **(C)** Heat map showing top down and upregulated genes in HeLa cells showing z-score values for control siRNA and NDP52 KD, obtained from three independent experiments. Dendrogram and enriched GO terms are shown. Number of genes differentially expressed for each GO term is also displayed. All GO terms shown have FDR<0.01. For details see Supplementary Table 4.



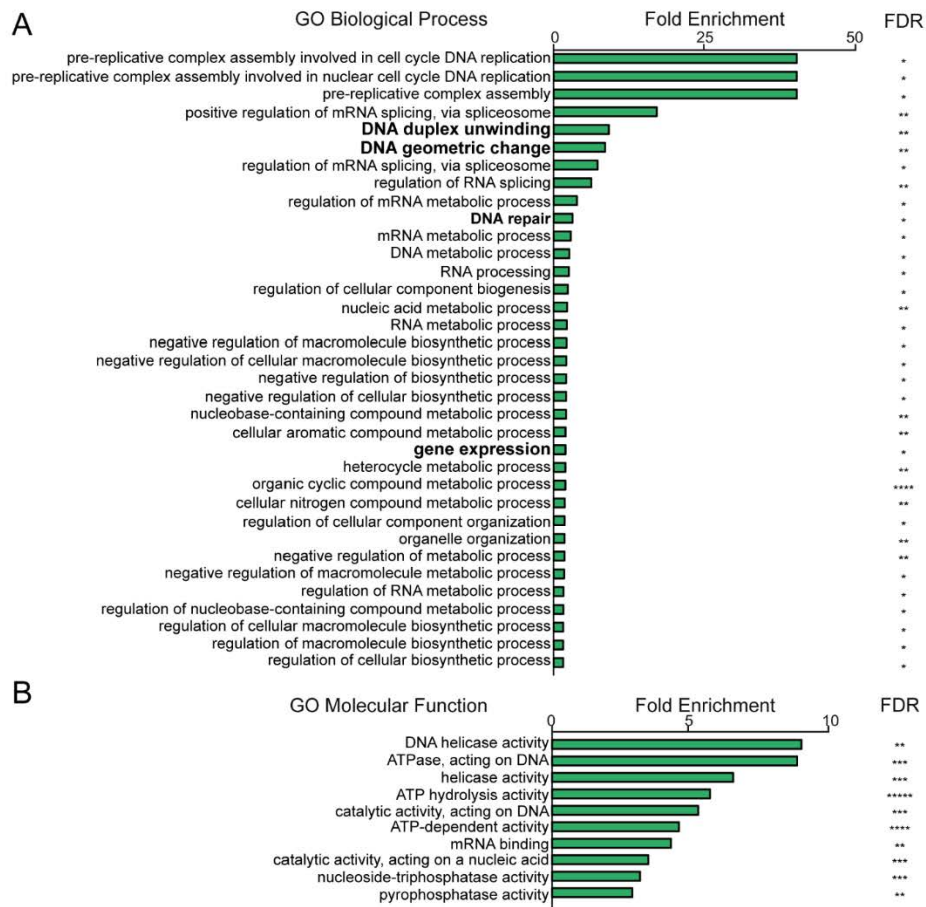
Supplementary Figure 7 – Impact of NDP52 knockdown in gene expression in MCF-7 cells. (A) Western blot showing NDP52 KD replicates for RNA-Seq. On top, immunoblot against NDP52 is shown and, on the bottom panel, anti-actin immunoblot is shown. **(B)** Volcano plot of differentially expressed genes following NDP52 KD in MCF-7 cells. **(C)** Heat map showing top down and upregulated genes and z-score values for control siRNA and NDP52 KD from three independent experiments. Dendrogram and enriched GO terms are shown. Number of genes differentially expressed for each GO term is also displayed. All GO terms shown have FDR<0.01. For details see Supplementary Table 5.



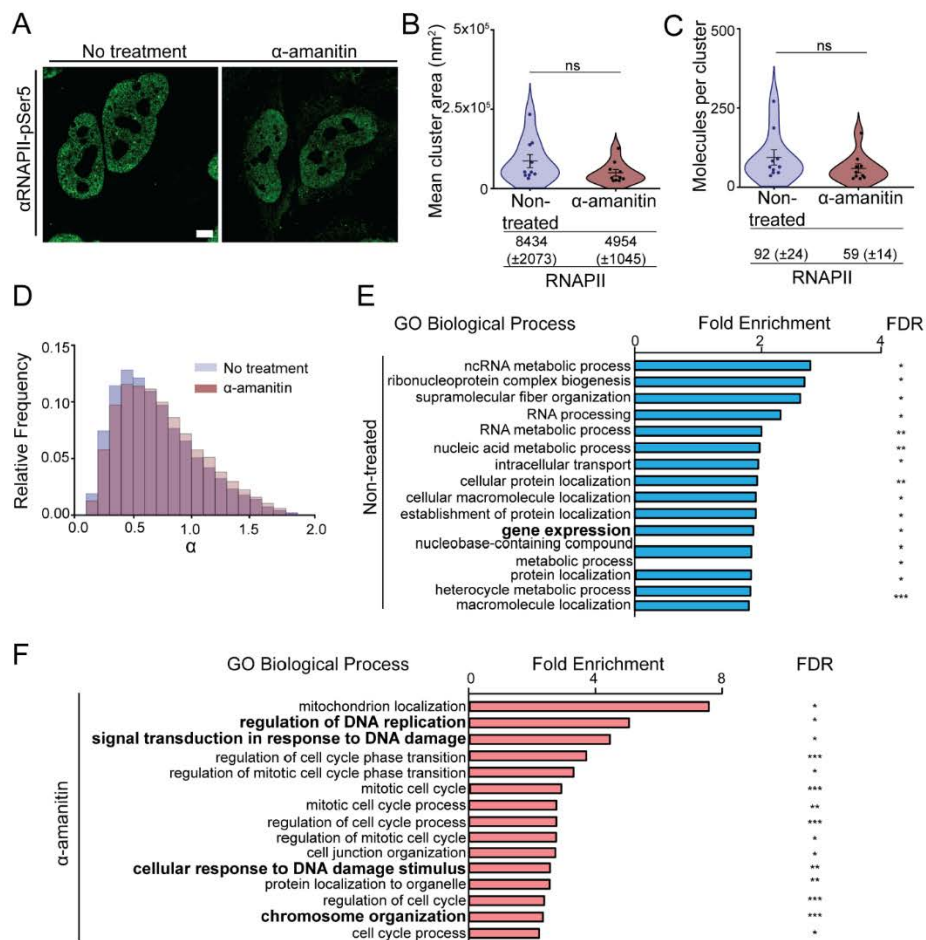
Supplementary Figure 8 – Recombinant and endogenous NDP52 interactomes in non-treated and α -amanitin treated HeLa (A) Diagram depicting recombinant protein proteomics protocol. Briefly, following nuclear isolation from HeLa cells, recombinant constructs were incubated with nuclear extract. His-tagged constructs bound to interacting partners were pulled-down using magnetic Ni-NTA beads. Samples were run in SDS-PAGE gels and all proteins from each replicate were excised as a single band from the stacking portion of the polyacrylamide gel, for LC-MS/MS experiments. (B) Venn diagram of hits found in label-free quantitative LC-MS/MS data for pull-downs of recombinant protein from HeLa nuclear extract. (C) Examples of top hits for CoCoA and NDP52 shown in Figures 12D and 13D, and their identification in ZF2 proteomics data. log₂FC is relative to beads control.



Supplementary Figure 9 – GO Biological Process and Molecular Function analysis for NDP52-FL-interacting proteins in HeLa nuclear extract. (A) Top 35 Gene Ontology Biological Process annotation terms for NDP52-FL interactions. **(B)** Top 10 Gene Ontology molecular function terms for identified interactors of NDP52-FL. Fold enrichment and FDR values are shown. * FDR<0.05, ** FDR<0.01, *** FDR<0.001, **** FDR<0.0001. For full lists refer to Supplementary tables 6 and 7.



Supplementary Figure 10 – GO Biological Process and Molecular Function analysis for CoCoA-interacting proteins in HeLa nuclear extract. (A) Top 35 Gene Ontology Biological Process annotation terms for CoCoA interactions. **(B)** Top 10 Gene Ontology molecular function terms for identified interactors of CoCoA. Fold enrichment and FDR values are shown. * FDR<0.05, ** FDR<0.01, *** FDR<0.001, **** FDR<0.0001. For full lists refer to Supplementary tables 8 and 9.



Supplementary Figure 11 - Effect on transcription inhibition on the nuclear spatial organisation and dynamics of NDP52. **(A)** Confocal images of RNAPII-pSer5 in non-treated and α -amanitin treated HeLa cells. **(B)** Mean cluster area in nm² for RNAPII-pSer5 in non-treated and α -amanitin treated cells. **(C)** Number of RNAPII-pSer5 per cluster in non-treated and α -amanitin treated cells. Mean \pm SEM values are shown. Each point represents the average value per cell. $n = 10$ cells (non-treated) $n = 10$ cells (α -amanitin). **(D)** Anomalous diffusion (α) histograms for cells transiently expressing Halo-NLS-NDP52, non-treated or following α -amanitin treatment. Histogram represents values for 14 322 molecules from 51 cells non-treated condition (in blue – same as shown in Supplementary Figure 2C) and 14 492 molecules from 50 cells for α -amanitin treatment (in red). **(E-F)** Changes in the interactome of endogenous NDP52 in non-treated and α -amanitin treated HeLa cells. **(E)** Top 15 Gene Ontology Biological Process annotation terms for NDP52 interactions in non-treated HeLa cells. **(F)** Top 15 Gene Ontology molecular function terms for identified for interactions of NDP52 following α -amanitin treatment. Fold enrichment and FDR values are shown. * FDR<0.05, ** FDR<0.01, *** FDR<0.001, **** FDR<0.0001. For full lists refer to Supplementary tables 10 and 11.

Supplementary Tables

Supplementary Table 1 – List of constructs.

Construct	Source
Human pET151 Halo-NDP52	Synthetic Gene
Human pET151 Halo-NLS-NDP52	Synthetic Gene
Human pET151 NDP52-FL (1-end)	Synthetic Gene
Human pET151 CoCoA (1-end)	Synthetic Gene
Human pET151 _c NDP52 (365-end)	Synthetic Gene
Human pET151 ZF2 (380-end)	Synthetic Gene
Human pET151 _N NDP52 (1-190)	Synthetic Gene

Supplementary Table 2 – ChIP-qPCR primers

Description	Oligonucleotide sequence
TFF1/PS2 Forward	CCATGTTGGCCAGGCTAGTC
TFF1/PS2 Reverse	ACAACAGTGGCTCACGGGGT
GREB1 Forward	GCAGTGAAAAAAGTGTGGCAACTGGG
GREB1 Reverse	GACCCACAGAAATGAAAAGGCAGCAAAC
Actin Forward	GACCTTCAACACCCCAGCC
Actin Reverse	GTCACGCACGATTTCCCGCT
Myc Forward	GGCTCACCCCTTGCTGATGCT
Myc Reverse	GCTCTGGGCACACACATTGG
CCND1 Forward	GCCAGACAACATTAGCCACA
CCND1 Reverse	CCCATTTCTTAGCTGGGTCA
XBP1 Forward	ATACTTGGCAGCCTGTGACC
XBP1 Reverse	GGTCCACAAAGCAGGAAAAA
FOS Forward	GGGCACTTACACACACATGC
FOS Reverse	ATGATACTCGCGAGCAGAGG
IER3 Promoter Forward	CCCCTGCTTCTTCTCAGTTG
IER3 Promoter Reverse	AAAAGATGCACGGATTGGAG
IER3 Intronic Forward	CGCCGAAGTCTCACACAGTA
IER3 Intronic Reverse	AGGAGAAGAAATGGGGAGGA
NRIP Forward	GACCTGGCCCAGATAGATCA

NRIP Reverse	TATAATGTAGGGGCGCAACC
EGR3 exon 2 Forward	GGTGCCTGAGAAGAGGTGAG
EGR3 exon 2 Reverse	CCATGTGGATGAATGAGGTG
EGR3 Intronic Forward	TCACGTACCACACACACACG
EGR3 Intronic Reverse	TCCGGGTCTGAAACTACCTG

Supplementary Table 3 – List of DNA constructs.

Description	Oligonucleotide sequence
ds15A 3'FAM	TTAGTTGTTCTCTGG*
ds15B	CCAGAGAACAATAA
ds40A 3'FAM	TTAGTTGTTTCGTAGTGCTCGTCTGGCTCTGGATTACCCGC*
ds40B	GCGGGTAATCCAGAGCCAGACGAGCACTACGAACAATAA
ss40 3'FAM	TTAGTTGTTTCGTAGTGCTCGTCTGGCTCTGGATTACCCGC*

Supplementary Table 4 – HeLa RNA-Seq enriched GO Biological processes

P _{adj}	Gene count	Pathways
6.12E-13	157	Response to organic substance
1.23E-11	149	Regulation of multicellular organismal process
6.06E-11	126	Anatomical structure morphogenesis
6.06E-11	46	Positive regulation of cell migration
9.75E-11	61	Regulation of cell migration
9.75E-11	65	Regulation of locomotion
9.75E-11	47	Positive regulation of locomotion
9.75E-11	47	Positive regulation of cellular component movement
1.34E-10	104	Tissue development
2.83E-10	62	Regulation of cell motility
3.50E-10	123	Regulation of developmental process
3.74E-10	65	Regulation of cellular component movement
6.00E-10	151	Animal organ development
8.97E-10	94	Locomotion
0.000123	64	Circulatory system development
0.000173	5	Peptide cross-linking via chondroitin 4-sulfate glycosaminoglycan
0.000219	33	Extracellular matrix organization
0.000362	46	Vasculature development
0.000963	121	Anatomical structure morphogenesis
0.001308	117	Regulation of transcription by RNA polymerase II
0.00131	100	Movement of cell or subcellular component
0.001842	121	Transcription by RNA polymerase II

0.001842	58	Enzyme linked receptor protein signaling pathway
0.001842	44	Transmembrane receptor protein tyrosine kinase signaling pathway
0.002537	88	Locomotion
0.003258	41	Blood vessel development
0.003744	149	Regulation of transcription, DNA-templated

Supplementary Table 5 – MCF-7 RNA-Seq enriched GO Biological processes

p_{adj}	Gene count	Pathways
7.33E-05	27	Connective tissue development
0.000519	49	Transmembrane receptor protein tyrosine kinase signaling pathway
0.00239	6	Ganglioside catabolic process
0.00239	20	Cartilage development
0.002642	78	Lipid metabolic process
0.002642	103	Movement of cell or subcellular component
0.002642	20	Inositol lipid-mediated signaling
0.002904	52	Regulation of cell migration
0.002904	4	Nucleoside bisphosphate catabolic process
0.002904	98	Small molecule metabolic process
0.002904	58	Regulation of cellular component movement
0.002955	19	Phosphatidylinositol-mediated signaling
0.002955	83	Cell motility
2.69E-16	100	Cell cycle
4.74E-16	84	Cell cycle process
7.62E-14	61	Mitotic cell cycle process
7.97E-14	66	Mitotic cell cycle
2.62E-11	45	Cell division
7.52E-11	32	Chromosome segregation
4.30E-10	65	Regulation of cell cycle
7.62E-09	22	Sister chromatid segregation
9.57E-09	26	Nuclear chromosome segregation
2.36E-08	33	Nuclear division
5.40E-08	26	Mitotic nuclear division
7.25E-08	25	DNA replication
7.25E-08	34	Organelle fission
8.16E-08	19	Mitotic sister chromatid segregation
2.36E-07	37	Mitotic cell cycle phase transition

Supplementary Table 6 – Enriched GO Biological processes from recombinant NDP52-FL nuclear interactome

Fold Enrichment	Genes in list	FDR	Functional Category – Biological Process
4.75	11	0.0142	DNA geometric change (GO:0032392)
3.8	10	0.0315	DNA duplex unwinding (GO:0032508)
3.03	12	0.0407	establishment of cell polarity (GO:0030010)
2.86	24	0.00249	regulation of small GTPase mediated signal transduction (GO:0051056)
2.7	56	3.17E-08	microtubule-based process (GO:0007017)
2.62	36	2.63E-04	microtubule cytoskeleton organization (GO:0000226)
2.6	25	0.01	positive regulation of proteolysis (GO:0045862)
2.58	38	2.40E-04	cellular component morphogenesis (GO:0032989)
2.57	32	0.00194	cell part morphogenesis (GO:0032990)
2.54	30	0.00305	neuron projection morphogenesis (GO:0048812)
2.52	30	0.00511	plasma membrane bounded cell projection morphogenesis (GO:0120039)
2.52	30	0.00535	cell projection morphogenesis (GO:0048858)
2.48	23	0.0303	microtubule-based movement (GO:0007018)
2.47	26	0.0197	cell morphogenesis involved in neuron differentiation (GO:0048667)
2.43	74	1.22E-08	cytoskeleton organization (GO:0007010)
2.41	37	0.00142	actin filament-based process (GO:0030029)
2.34	24	0.0411	plasma membrane bounded cell projection assembly (GO:0120031)
2.26	32	0.0102	actin cytoskeleton organization (GO:0030036)
2.26	65	3.72E-06	cell projection organization (GO:0030030)
2.23	30	0.023	cell morphogenesis involved in differentiation (GO:0000904)
2.18	61	2.57E-05	plasma membrane bounded cell projection organization (GO:0120036)
2.15	29	0.0413	supramolecular fiber organization (GO:0097435)
2.14	36	0.0119	neuron projection development (GO:0031175)
2.13	35	0.0166	protein localization to organelle (GO:0033365)
2.13	37	0.0143	cell morphogenesis (GO:0000902)
2.12	44	0.00294	cell cycle process (GO:0022402)
2.07	32	0.0353	positive regulation of hydrolase activity (GO:0051345)
2.03	43	0.0068	neuron development (GO:0048666)
2.01	63	2.44E-04	cell cycle (GO:0007049)
2.01	38	0.028	organelle assembly (GO:0070925)
1.99	173	4.25E-16	organelle organization (GO:0006996)
1.96	52	0.00292	chromosome organization (GO:0051276)
1.93	52	0.00423	regulation of hydrolase activity (GO:0051336)
1.87	70	2.45E-04	movement of cell or subcellular component (GO:0006928)
1.87	66	0.00143	cellular protein localization (GO:0034613)

1.86	46	0.0318	biological adhesion (GO:0022610)
1.84	66	0.00211	cellular macromolecule localization (GO:0070727)
1.84	45	0.0404	cell adhesion (GO:0007155)
1.83	45	0.0397	regulation of cellular component biogenesis (GO:0044087)
1.83	56	0.00954	regulation of organelle organization (GO:0033043)
1.81	56	0.0094	protein-containing complex assembly (GO:0065003)
1.79	105	6.16E-06	cellular component assembly (GO:0022607)
1.79	243	1.15E-18	cellular component organization (GO:0016043)
1.77	114	2.75E-06	cellular component biogenesis (GO:0044085)
1.75	61	0.0108	protein-containing complex subunit organization (GO:0043933)
1.7	247	2.10E-18	cellular component organization or biogenesis (GO:0071840)
1.66	83	0.00228	protein localization (GO:0008104)
1.65	69	0.0208	cell development (GO:0048468)
1.6	96	0.00143	cellular localization (GO:0051641)
1.6	97	0.00299	regulation of cellular component organization (GO:0051128)
1.59	90	0.00614	nervous system development (GO:0007399)
1.51	98	0.00314	regulation of catalytic activity (GO:0050790)
1.5	119	0.00295	regulation of molecular function (GO:0065009)

Supplementary Table 7 – Enriched GO Molecular Functions from recombinant NDP52-FL nuclear interactome

Fold Enrichment	Genes in list	FDR	Functional Category – Molecular Function
29.2	3	0.0468	pantothenate kinase activity (GO:0004594)
7.08	6	0.0372	nucleosome-dependent ATPase activity (GO:0070615)
4.8	9	0.0213	DNA helicase activity (GO:0003678)
4.47	10	0.0173	beta-catenin binding (GO:0008013)
4.41	12	0.00517	ATPase, acting on DNA (GO:0008094)
3.74	12	0.0182	single-stranded DNA binding (GO:0003697)
3.7	15	0.00408	helicase activity (GO:0004386)
3.66	11	0.0373	cytoskeletal motor activity (GO:0003774)
3.2	19	2.85E-03	catalytic activity, acting on DNA (GO:0140097)
3.2	23	4.85E-04	ATP hydrolysis activity (GO:0016887)
3.13	16	0.0125	phosphatase binding (GO:0019902)
2.8	22	4.03E-03	mRNA binding (GO:0003729)
2.76	33	1.01E-04	GTPase activator activity (GO:0005096)
2.74	36	4.11E-05	ATP-dependent activity (GO:0140657)
2.68	34	1.14E-04	GTPase regulator activity (GO:0030695)

2.68	34	1.09E-04	nucleoside-triphosphatase regulator activity (GO:0060589)
2.59	18	0.0366	microtubule binding (GO:0008017)
2.53	21	0.0184	cadherin binding (GO:0045296)
2.39	33	0.00139	cell adhesion molecule binding (GO:0050839)
2.18	41	0.00144	enzyme activator activity (GO:0008047)
2.16	33	0.00824	catalytic activity, acting on a nucleic acid (GO:0140640)
2.15	25	0.0483	actin binding (GO:0003779)
2.14	39	2.85E-03	structural molecule activity (GO:0005198)
2.14	55	6.53E-05	cytoskeletal protein binding (GO:0008092)
2.07	83	9.42E-07	adenyl ribonucleotide binding (GO:0032559)
2.06	79	1.52E-06	ATP binding (GO:0005524)
2.05	83	9.16E-07	adenyl nucleotide binding (GO:0030554)
2	32	3.13E-02	nucleoside-triphosphatase activity (GO:0017111)
1.99	86	1.63E-06	RNA binding (GO:0003723)
1.85	91	9.13E-06	purine ribonucleotide binding (GO:0032555)
1.84	87	1.97E-05	purine ribonucleoside triphosphate binding (GO:0035639)
1.84	91	1.37E-05	purine nucleotide binding (GO:0017076)
1.84	91	1.30E-05	ribonucleotide binding (GO:0032553)
1.84	62	0.00117	protein-containing complex binding (GO:0044877)
1.81	58	2.94E-03	enzyme regulator activity (GO:0030234)
1.78	104	6.38E-06	carbohydrate derivative binding (GO:0097367)
1.76	98	2.05E-05	nucleotide binding (GO:0000166)
1.75	98	1.96E-05	nucleoside phosphate binding (GO:1901265)
1.64	87	1.29E-03	enzyme binding (GO:0019899)
1.62	100	4.22E-04	anion binding (GO:0043168)
1.61	104	2.46E-04	small molecule binding (GO:0036094)
1.49	153	5.15E-05	nucleic acid binding (GO:0003676)
1.46	223	3.07E-07	heterocyclic compound binding (GO:1901363)
1.45	225	2.42E-07	organic cyclic compound binding (GO:0097159)
1.27	198	1.24E-02	ion binding (GO:0043167)
1.17	432	7.60E-07	protein binding (GO:0005515)
0.43	18	0.0057	molecular transducer activity (GO:0060089)
0.43	18	5.56E-03	signaling receptor activity (GO:0038023)
0.36	13	2.75E-03	transmembrane signaling receptor activity (GO:0004888)
0.09	2	1.92E-05	G protein-coupled receptor activity (GO:0004930)

Supplementary Table 8 – Enriched GO Biological Processes from recombinant CoCoA nuclear interactome

Fold Enrichment	Genes in list	FDR	Functional Category – Biological Process
40.3	3	0.0489	pre-replicative complex assembly involved in cell cycle DNA replication (GO:1902299)
40.3	3	0.0478	pre-replicative complex assembly involved in nuclear cell cycle DNA replication (GO:0006267)
40.3	3	0.0467	pre-replicative complex assembly (GO:0036388)
17.1	4	0.0498	positive regulation of mRNA splicing, via spliceosome (GO:0048026)
9.17	8	0.00699	DNA duplex unwinding (GO:0032508)
8.55	8	0.0089	DNA geometric change (GO:0032392)
7.3	8	0.0191	regulation of mRNA splicing, via spliceosome (GO:0048024)
6.27	10	0.00944	regulation of RNA splicing (GO:0043484)
3.88	12	0.0398	regulation of mRNA metabolic process (GO:1903311)
3.15	16	0.034	DNA repair (GO:0006281)
2.84	17	0.0491	mRNA metabolic process (GO:0016071)
2.63	20	0.0415	DNA metabolic process (GO:0006259)
2.55	23	0.0295	RNA processing (GO:0006396)
2.37	24	0.049	regulation of cellular component biogenesis (GO:0044087)
2.25	48	0.00101	nucleic acid metabolic process (GO:0090304)
2.21	33	0.0182	RNA metabolic process (GO:0016070)
2.17	36	0.0159	negative regulation of macromolecule biosynthetic process (GO:0010558)
2.13	35	0.0205	negative regulation of cellular macromolecule biosynthetic process (GO:2000113)
2.11	37	0.0164	negative regulation of biosynthetic process (GO:0009890)
2.09	36	0.0201	negative regulation of cellular biosynthetic process (GO:0031327)
2.09	55	0.00169	nucleobase-containing compound metabolic process (GO:0006139)
1.99	57	0.0012	cellular aromatic compound metabolic process (GO:0006725)
1.98	42	0.0165	gene expression (GO:0010467)
1.97	55	0.00232	heterocycle metabolic process (GO:0046483)
1.96	61	8.69E-04	organic cyclic compound metabolic process (GO:1901360)
1.86	63	0.00204	cellular nitrogen compound metabolic process (GO:0034641)
1.83	46	0.0341	regulation of cellular component organization (GO:0051128)
1.82	65	0.00189	organelle organization (GO:0006996)
1.82	57	0.00862	negative regulation of metabolic process (GO:0009892)
1.75	51	0.0312	negative regulation of macromolecule metabolic process (GO:0010605)
1.65	65	0.0199	regulation of RNA metabolic process (GO:0051252)
1.63	68	0.02	regulation of nucleobase-containing compound metabolic process (GO:0019219)

1.61	67	0.0273	regulation of cellular macromolecule biosynthetic process (GO:2000112)
1.6	67	0.0331	regulation of macromolecule biosynthetic process (GO:0010556)
1.59	69	0.0327	regulation of cellular biosynthetic process (GO:0031326)
1.58	92	0.00213	cellular component organization or biogenesis (GO:0071840)
1.56	88	0.00597	cellular component organization (GO:0016043)
1.5	76	0.0424	regulation of gene expression (GO:0010468)

Supplementary Table 9 – Enriched GO Molecular Functions from recombinant CoCoA nuclear interactome

Fold Enrichment	Genes in list	FDR	Functional Category – Biological Process
9.02	7	0.0035	DNA helicase activity (GO:0003678)
8.87	10	1.14E-04	ATPase, acting on DNA (GO:0008094)
6.55	11	4.08E-04	helicase activity (GO:0004386)
5.71	17	1.49E-05	ATP hydrolysis activity (GO:0016887)
5.29	13	4.30E-04	catalytic activity, acting on DNA (GO:0140097)
4.59	25	5.28E-07	ATP-dependent activity (GO:0140657)
4.3	14	0.00157	mRNA binding (GO:0003729)
3.48	22	1.61E-04	catalytic activity, acting on a nucleic acid (GO:0140640)
3.18	21	9.63E-04	nucleoside-triphosphatase activity (GO:0017111)
2.9	21	0.00322	pyrophosphatase activity (GO:0016462)
2.88	21	0.00338	hydrolase activity, acting on acid anhydrides, in phosphorus-containing anhydrides (GO:0016818)
2.88	21	0.00326	hydrolase activity, acting on acid anhydrides (GO:0016817)
2.79	50	6.17E-08	RNA binding (GO:0003723)
2.58	41	1.93E-05	ATP binding (GO:0005524)
2.47	41	4.09E-05	adenyl ribonucleotide binding (GO:0032559)
2.45	41	4.43E-05	adenyl nucleotide binding (GO:0030554)
2.35	46	3.13E-05	purine ribonucleoside triphosphate binding (GO:0035639)
2.29	47	3.42E-05	ribonucleotide binding (GO:0032553)
2.26	46	7.87E-05	purine ribonucleotide binding (GO:0032555)
2.25	52	1.73E-05	nucleotide binding (GO:0000166)
2.25	52	1.55E-05	nucleoside phosphate binding (GO:1901265)
2.24	46	8.08E-05	purine nucleotide binding (GO:0017076)
2.15	55	2.07E-05	anion binding (GO:0043168)
2.06	55	7.10E-05	small molecule binding (GO:0036094)
2	85	5.46E-08	nucleic acid binding (GO:0003676)
1.94	47	0.00209	carbohydrate derivative binding (GO:0097367)
1.79	113	1.12E-08	heterocyclic compound binding (GO:1901363)
1.76	113	1.86E-08	organic cyclic compound binding (GO:0097159)
1.21	185	1.48E-04	protein binding (GO:0005515)

Supplementary Table 10 – Enriched GO Biological processes from endogenous NDP52 interactome in non-treated HeLa cells

Fold Enrichment	Genes in list	FDR	Functional Category – Biological Process
2.77	24	0.00874	ncRNA metabolic process (GO:0034660)
2.68	21	0.0354	ribonucleoprotein complex biogenesis (GO:0022613)
2.61	25	0.0127	supramolecular fiber organization (GO:0097435)
2.3	36	0.00466	RNA processing (GO:0006396)
2	52	0.00234	RNA metabolic process (GO:0016070)
1.97	73	7.16E-5	nucleic acid metabolic process (GO:0090304)
1.95	45	0.0179	intracellular transport (GO:0046907)
1.93	49	0.0117	cellular protein localization (GO:0034613)
1.91	49	0.0122	cellular macromolecule localization (GO:0070727)
1.91	45	0.0223	establishment of protein localization (GO:0045184)
1.87	69	5.52E-4	gene expression (GO:0010467)
1.84	84	8.18E-5	nucleobase-containing compound metabolic process (GO:0006139)
1.82	64	0.00324	protein localization (GO:0008104)
1.81	88	9.04E-5	heterocycle metabolic process (GO:0046483)
1.8	77	5.44E-4	macromolecule localization (GO:0033036)
1.79	75	9.15E-4	cellular localization (GO:0051641)
1.77	88	1.38E-4	cellular aromatic compound metabolic process (GO:0006725)
1.71	101	8.49E-5	cellular nitrogen compound metabolic process (GO:0034641)
1.7	92	3.51E-4	organic cyclic compound metabolic process (GO:1901360)
1.62	71	0.0248	regulation of cellular component organization (GO:0051128)
1.59	73	0.0459	cellular component biogenesis (GO:0044085)
1.56	158	1.03E-5	cellular component organization or biogenesis (GO:0071840)
1.54	151	3.12E-5	cellular component organization (GO:0016043)
1.51	160	2.61E-5	macromolecule metabolic process (GO:0043170)

Supplementary Table 11 – Enriched GO Biological processes from endogenous NDP52 interactome in HeLa cells following α -amanitin treatment

Fold Enrichment	Genes in list	FDR	Functional Category – Biological Process
7.49	7	0.0339	mitochondrion localization (GO:0051646)
5	10	0.0279	regulation of DNA replication (GO:0006275)
4.39	11	0.0339	signal transduction in response to DNA damage (GO:0042770)
3.65	25	1.66E-4	regulation of cell cycle phase transition (GO:1901987)
3.28	17	0.0205	regulation of mitotic cell cycle phase transition (GO:1901990)
2.86	32	4.76E-4	mitotic cell cycle (GO:0000278)
2.73	26	0.00629	mitotic cell cycle process (GO:1903047)
2.73	32	8.54E-4	regulation of cell cycle process (GO:0010564)
2.72	22	0.0214	regulation of mitotic cell cycle (GO:0007346)
2.7	24	0.0142	cell junction organization (GO:0034330)
2.53	34	0.00241	cellular response to DNA damage stimulus (GO:0006974)
2.52	30	0.00806	protein localization to organelle (GO:0033365)
2.35	44	5.72E-4	regulation of cell cycle (GO:0051726)
2.31	44	7.19E-4	chromosome organization (GO:0051276)
2.19	33	0.0276	cell cycle process (GO:0022402)
2.17	49	8.66E-4	cell cycle (GO:0007049)

1.99	50	0.00578	protein-containing complex subunit organization (GO:0043933)
1.93	43	0.029	protein-containing complex assembly (GO:0065003)
1.89	49	0.0162	cellular macromolecule localization (GO:0070727)
1.88	42	0.0468	negative regulation of signal transduction (GO:0009968)
1.87	48	0.0282	cellular protein localization (GO:0034613)
1.82	114	5.61E-7	organelle organization (GO:0006996)
1.79	49	0.0389	intracellular signal transduction (GO:0035556)
1.79	67	0.00423	nucleic acid metabolic process (GO:0090304)
1.76	50	0.0479	cellular response to stress (GO:0033554)
1.74	179	2.7E-12	cellular component organization or biogenesis (GO:0071840)
1.73	73	0.00542	cellular localization (GO:0051641)
1.72	80	0.00233	cellular component biogenesis (GO:0044085)
1.72	170	7.99E-11	cellular component organization (GO:0016043)
1.68	71	0.0129	cellular component assembly (GO:0022607)
1.6	74	0.028	nucleobase-containing compound metabolic process (GO:0006139)

7. Discussion and Future Perspectives

The work presented here aimed to investigate the biochemical and physical properties of the nucleus – from nuclear mechanics to the nanoscale organisation of nuclear processes. This work focused on four different aspects, addressed in Chapters 3-6:

- 1) first, we explored how the nucleus responds to force and what structural components contribute to its viscoelastic behaviour. We also investigated the relationship between the mechanical properties of the nucleus, DNA damage and activation of DDR signalling (Chapter 3);
- 2) we then investigated the role of molecular motor MVI in transcription, with a special focus on its biochemical regulation and activation by binding partners (Chapter 4);
- 3) we then assessed MVI role in the spatial organisation and molecular dynamics of RNAPII during transcription initiation (Chapter 5);
- 4) and, finally, we propose NDP52, an autophagy receptor and binding partner of MVI, as a novel transcriptional regulator with roles in chromatin structure and organisation (Chapter 6).

7.1. Contribution of chromatin to nuclear mechanics and impact of DNA damage and repair on nuclear stiffness

The first aim of this work focused on the mechanical properties of the nucleus. In order to investigate the viscoelastic properties of the nucleus, we used a micro-rheology AFM method. This allowed us to probe how the nucleus responds to strains at different length- and time-scales. With this, we were able to show that both the nuclear lamina and chromatin packaging/crosslinking contribute to the mechanical properties of the nucleus (Lherbette *et al.*, 2017). An important outcome of this study was the observation that the nuclear interior is not uniform and that chromatin organisation is an important factor in nuclear response to mechanical strains. The nucleus could be separated into two different contributing regions, in addition to the nuclear lamina. Surprisingly, we observed a softer, more viscous nuclear periphery (several microns thick), and a more

elastic inner core. This was true for nuclei of different cell lines - whilst quantitatively nuclei varied, with some nuclei being stiffer than others, the qualitative response, showing this mechanical separation within chromatin, was consistently observed.

The observation of an outer, softer region was unexpected, as compact heterochromatin is thought to be substantially stiffer than decondensed chromatin, and heterochromatin usually occupies peripheric positions within the nucleus (Bannister and Kouzarides, 2011; Melters Daniël et al., 2019; Ranade *et al.*, 2019; Strom *et al.*, 2020). The work shown here, led by both Michael Lherbette and myself proposes that these two different mechanical environments are likely the result of the highly regulated spatial organisation of chromatin in the nucleus, whereby different chromatin packaging is observed at different nuclear positions (Bannister and Kouzarides, 2011; Crosetto and Bienko, 2020; dos Santos and Toseland, 2021). Different degrees of chromatin crosslinking, caused by the activity of protein-DNA interactions and the formation of molecular clusters for different nuclear processes could contribute to the two-regime chromatin system observed (Ashwin *et al.*, 2020; Maya-Miles et al., 2019; Nagashima *et al.*, 2019; Strom *et al.*, 2020). It is important to note that chromatin crosslinking can occur in active chromatin regions, and local stiffening has been observed at genomic regions of high transcriptional activity (Ashwin *et al.*, 2020; Nagashima *et al.*, 2019). This makes the relationship between nuclear processes, surrounding chromatin stiffness and overall nuclear stiffness a complex question.

It would be interesting, in the future, to explore the reasons behind the observed variation in chromatin stiffness across the nucleus. Investigating how chromatin is organised in isolated nuclei, which is the model I use in this study, could help elucidate some unanswered questions that remain. For example, do we still observe a higher level of heterochromatin at the nuclear periphery (*e.g.*, H3K9me3 heterochromatin distribution) in isolated nuclei, as we do in whole cells? How does the process of nuclear extraction affect chromatin arrangements? Furthermore, I believe it would be also important to explore how changing nuclear processes, such as transcriptional activity might affect the variation in the mechanical behaviour of the nucleus, at different depths. As one of our postulations is that chromatin crosslinking, due to molecular clustering and LLPS formation during nuclear activity might change local stiffness, we should be able to test this, by disrupting these processes.

A main limitation of this study was the use of isolated nuclei. Whilst this is a useful way to obtain information on the mechanical properties of the nucleus without interference from other cellular components, the physiological environment of the nucleus is lost.

Moreover, the process of extracting nuclei could also cause a certain degree of DNA damage, through mechanical stress, and we do not yet fully understand the consequences of this in terms of chromatin organisation. In Fili *et al.* (Fili *et al.*, 2017) Supplementary Figure 1 (Chapter 3) we use Hoechst and DID (a lipophilic dye) to show that isolated nuclei are relatively intact following the extraction process. Furthermore, subnuclear structures such as the nucleoli appear to be well preserved in isolated nuclei (Fili *et al.*, 2017). Nevertheless, it is unclear if some nuclei still present reminiscent endoplasmic reticulum associated to the organelle and we cannot completely exclude the possibility of small ruptures on the nuclear lamina that we cannot easily observe, or loss of some integral components of the NE. Damage to the nuclear lamina during the extraction process could result in changes to nuclear mechanics, either by directly affecting NE components or indirectly by disrupting chromatin organisation (*e.g.*, LAD organisation at the nuclear periphery). This is why it will be important in the future to explore, in live-cells, how these two different mechanical regimes of chromatin in the nucleus are associated to the regulation nuclear processes such as transcription and to levels of heterochromatin/euchromatin.

The nuclei I isolated from different cell lines for the work shown here displayed different heights and diameters (Lherbette *et al.*, 2017), which was in accordance to their original size within the cell. It is not clear what the reason behind nuclear size variation and here we did not investigate this. In terms of DNA content, we do not expect that the cells we tested to have enough DNA content variability to warrant this variation. Additionally, it is thought that DNA content is not a major determinant of nuclear size, but that cytoplasmic size, instead, could be a more important parameter (Edens *et al.*, 2013; Walters *et al.*, 2012). In Lherbette *et al.* we do, however, observe a correlation between size of the nucleus and stiffness with the smaller nuclei tested being stiffer than larger nuclei (Lherbette *et al.*, 2017). In this work, we propose that since chromatin and lamina content are relatively uniform across cell lines, the higher confinement of chromatin and a thicker lamina in smaller nuclei might account for this increased stiffness.

Having showed that chromatin crosslinking levels can alter whole nuclear mechanics, we decided to investigate how activation of nuclear processes would affect the physical properties of the organelle. To investigate this, I focused on DNA damage, in specific the induction of double-strand breaks by chemotherapy agent cisplatin, and DNA repair. Both DNA damage/DDR and gene expression changes are known to induce chromatin changes. My focus on DNA damage, as an alternative to transcriptional stimulation or disruption, allowed us to have higher control over our experimental design, as the time-scales for DNA damage drug treatments are well defined and relatively short.

Furthermore, it also allowed us to induce responses of different severities from the organelle, by using different time points (4 hours and 24 hours) for cisplatin treatment.

To study the impact of cisplatin and DDR on nuclear mechanics it was important to perform these measurements with the nucleus in its physiological environment – the cell. However, measuring nuclear mechanics in adhered-cells poses a major limitation to the field. This stems from the presence of a fully-formed cytoskeleton that surrounds the nucleus and exerts forces on the organelle, thus masking the real physical properties of the nucleus. To circumvent this and avoid the use of cytoskeletal drugs that could have unknown effects in our study, we performed initially-adhered measurements. This allowed us to measure nuclear stiffness relatively free from cytoskeletal contributions and detect changes to mechanics caused by cytotoxic drug treatment.

In dos Santos *et al.*, I did not explore the dependence of nuclear mechanics on AFM probing frequencies. Although in this work I was able to avoid contributions from cytoskeletal actin fibres by using initially-adhered cells, micro-rheology measurements of the nucleus within initially adhered cells will also include contributions from all cytoplasmic components that surround the organelle. Conclusions from these data might be less straightforward to interpret and require complex mathematical models to explain the observed measurements.

In dos Santos *et al.*, I show that cisplatin treatment causes nuclear softening and that this is linked to large-scale chromatin decondensation. Furthermore, I found that this effect was dependent on ATM-kinase activity and not a direct consequence of the damage itself. This further confirms the importance of chromatin architecture for nuclear mechanics and highlights the impact of the activation of nuclear pathways for organelle stiffness and mechano-sensing ability.

We do not yet know the mechanism through which the observed global rearrangement of chromatin occurs, following DNA damage. In agreement with our study, a more recent report by Fortuny *et al.* showed that damage at pericentric heterochromatin causes large-scale histone displacement and massive chromatin unfolding. This was caused by the recruitment of UV damage sensor DDB2 to the lesion (Fortuny *et al.*, 2021). However, many different repair factors and chromatin remodelling complexes, such as INO80 and SWI/SNF, have been shown to be recruited to DSBs (dos Santos and Toseland, 2021; Kruhlak *et al.*, 2006; Lou *et al.*, 2019; Strickfaden *et al.*, 2016; Ziv *et al.*, 2006), and it is possible that they also contribute to the mechanical changes detected in this study. Additionally, molecular motors such as NM1 have been linked to chromatin reorganisation following DNA damage in an ATM and γ H2AX signalling-dependent

manner (Kulashreshtha *et al.*, 2016). Importantly, we observed that chromatin changes caused by ATM signalling lead to higher levels of molecular diffusion in the nucleus, as measured using a reporter tag (SNAP tag), which does not sustain specific interactions with other proteins (Bosch *et al.*, 2014). This may be important to increase the efficiency of DNA repair, as it will allow higher accessibility of the lesions to repair factors.

It will be interesting in future studies to investigate how different proteins and complexes involved in ATM-dependent chromatin remodelling might specifically contribute to the observed mechanical changes in the nucleus.

In this study, I did not explore other types of DNA damage or cytotoxic drugs (*e.g.*, single-strand breaks, oxidative or UV damage, bleomycin etc.). Hence, it is not clear if the chromatin relaxation that I observed is common across different types of DNA damage. It would be important to determine if this is a common mechanism or if it is restricted to DSBs or even more exclusively to cisplatin. Furthermore, I did not investigate the reversibility of chromatin decondensation. Other studies report that chromatin returns to its initial state of compaction, after an initial relaxation upon DDR activation (Burgess *et al.*, 2014; Fortuny *et al.*, 2021; Kruhlak *et al.*, 2006; Lu *et al.*, 2019; Murga *et al.*, 2007). I believe this to be an important question for future studies.

An important finding of this study was that nuclear relaxation, prior to treatment with cytotoxic drugs, appears to be protective for DNA damage. Cells grown on softer surfaces, or with inhibited cytoskeletal formation, presented lower levels of DNA damage mark γ H2AX following cisplatin treatment. It is not clear why this is the case, or if this is true of other types of damage, such as oxidative damage. One hypothesis is that replication is slower in cells growing on softer surfaces (Klein *et al.*, 2009; Kocgozlu *et al.*, 2010; Mih *et al.*, 2012). As cisplatin's main mechanism for DSB induction is through replication force collapse, this could be an explanation for the lower damage incidence. Other types of damage, that are independent of replication rates in cells, could help elucidate the role of extracellular stiffness and nuclear tension on DNA damage. Furthermore, whilst γ H2AX signal is a widely used mark of DSB (Bennett and Peterson, 2015; Burma *et al.*, 2001; Chen *et al.*, 2018; Kulashreshtha *et al.*, 2016), direct visualisation of cisplatin, for example using fluorescently labelled cisplatin, to measure direct intercalation into DNA, could provide additional information on kinetics of DNA damage in cells growing on different surfaces.

Whilst we do have some understanding of mechanotransduction processes between the extracellular environment and the cell, our knowledge of how the mechanical state of the nucleus may affect cellular function and disease development is still limited. As

shown here, changes in nuclear activity such as DDR, lead to global mechanical changes to the organelle. This is especially important in cancer development and cancer therapy, where changes to nuclear processes, such as transcription and DNA repair are often misregulated and where nuclear stiffness could be important in determining cell migration and proliferation or affect chemotherapy treatment and drug resistance.

7.2. Activation of Myosin VI by binding partners in transcription

The work presented in Chapter 4 aimed to investigate the regulation of MVI activity in the nucleus. Our work not only contributed to the current knowledge of the role of MVI in RNAPII transcription, but also shed light on some unanswered questions on the general regulation and activation of MVI, which is essential to understand the nuclear roles of this molecular motor.

We were able to determine that, of the four possible splice-isoforms of MVI (NI, SI, LI, SI+LI), the NI-MVI isoform is the one present in the nucleus and responsible for the transcriptional activity of the protein. In the NI-MVI isoform both binding motifs – RRL and WWY – are readily accessible for interactions with binding partners. However, our studies show that this isoform has preferential interactions with RRL-binding proteins, such as NDP52, due to higher molecular affinity presented by this site. Conversely, interactions occurring through the WWY motif (*e.g.*, interaction with Dab2) are more likely in the LI isoform due to the masking of the RRL site by the additional α -helix encoded in this isoform. We also show that interactions with Dab2 attenuate the nuclear role of MVI, by blocking MVI-DNA binding, a property that we found to be crucial in its role in transcription.

Understanding how different isoforms and binding affinities contribute to MVI activity in transcription is important because in many cancers the NI-MVI isoform is specifically overexpressed (Wollscheid *et al.*, 2016). For many years it has been assumed that misregulation of the many cytoplasmic roles of MVI is the main cause of disease development. However, the fact that MVI is linked to cancer development (for example, breast, ovarian and prostate cancer) (Dunn *et al.*, 2006; Puri *et al.*, 2010; Wang *et al.*, 2015; Yoshida *et al.*, 2004), and some cancer cells only express the nuclear isoform of the protein (NI-MVI) (Wollscheid *et al.*, 2016), provides new insights into disease mechanisms. This is further supported by the fact that we also found NI-MVI to be involved in oestrogen-receptor transcription, a nuclear receptor that is hyperactive in

some cancers. The work led by Fili *et al.* shows that MVI interacts with the ER through an LxxLL nuclear receptor-binding motif. Furthermore, depletion of MVI leads to significantly reduced proliferation in breast cancer cell line MCF-7. It will be important in future studies to further explore the role of MVI in ER-related gene expression, to understand how MVI levels and activity might be linked to ER positive cancer development.

Another important contribution of the work shown here, was the finding that MVI motor activity is essential for its role in transcription. Although previous work had linked MVI to RNAPII transcription, until Fili *et al.*, (Fili *et al.*, 2017) it was unclear whether MVI motor activity was necessary for its regulatory role in transcription. Both depletion and inhibition of ATPase activity by small-drug inhibitor, TIP, led to reduced transcription levels. This indicates that the main mechanism for MVI nuclear role is linked to its motor activity. With this we postulated that MVI could act as a motor propelling RNAPII during transcription, or as a molecular anchor for transcription machinery. As this is the case, it is also important that we understand how activation of motor processivity occurs in MVI.

As previously described in Chapter 1, MVI has been observed both in monomeric and dimeric forms *in vitro*. In the monomeric form, MVI is in an auto-inhibited backfolded state, whilst as a dimer, processive motor activity can occur (Mukherjea *et al.*, 2014; Mukherjea *et al.*, 2009; Park *et al.*, 2006; Spink *et al.*, 2008; Yu *et al.*, 2009). Importantly, in the work presented in Chapter 4, we confirm that both these conformations of MVI occur in the cell and that they are regulated by the ability of MVI to bind its binding partners. Our data are in agreement with previous models, proposing that dimerization of MVI occurs through the N-terminal region of the tail domain (Mukherjea *et al.*, 2009). However, unlike a recent study proposing that MVI backfolding is regulated by Ca^{2+} (Batters *et al.*, 2016), our data do not support this. Instead, we show that binding partners interacting at either WWY or RRL motifs are responsible for the unfolding of MVI, which allows the subsequent dimerization of the protein. Furthermore, we show that dimerisation is an intrinsic ability of MVI that occurs through exposure of an oligomerisation region in the tail domain and is not dependent on the oligomeric state of binding partners. Disruption of WWY and RRL motifs led to loss of static and slow diffusing MVI molecules, possibly indicating a loss of interactions with cargoes or inability of the protein to anchor.

Finally, we also highlight the importance of molecular clustering, not only of MVI but also of its interacting partners, in determining the cellular functions of MVI. The increased

local concentration of molecules due to their physical clustering can drive interactions that otherwise would not be possible to occur. Whilst in our studies we show this for NDP52, the same is likely to be true for, for example, Dab2 interactions with NI-MVI. Although NI-MVI-Dab2 interaction is less favoured than NI-MVI-NDP52, local high concentrations of Dab2, through molecular clustering, could shift this preference. Once again, this is important because it highlights another way in which MVI function can be regulated. Dab2 is present in the nucleus and is thought to act as a tumour suppressant (He *et al.*, 2001). Additionally, in breast cancer cells MCF-7, Dab2 is either lost or its expression attenuated (Fili *et al.*, 2020; He *et al.*, 2001). Our study revealed that the tumour suppressant activity of Dab2, previously observed by He *et al.* (He *et al.*, 2001), is tightly linked to its ability to bind to MVI. Therefore, it could be possible that under normal expression levels, Dab2 has a mild negative effect on the regulation of MVI for the expression of ER-target genes.

Interestingly, during work performed in this chapter, we made our first observations regarding the potential of NDP52 as a transcriptional regulator. We observed that depletion of NDP52 significantly reduced *in vitro* transcription; NDP52 can tightly interact with dsDNA; NDP52 is distributed throughout the cell, including the nucleus; a pool of nuclear NDP52 colocalises with RNAPII, and the two proteins can be co-immunoprecipitated. These findings led to the work presented in Chapter 6 and discussed below.

Comments on data fitting and model assumptions

In dos Santos *et al.*, (dos Santos *et al.*, 2020) we assume a biphasic model for the interaction between NDP52 and MVI tail (Figure 2C). This assumption results from the observed curve profile in Figure 2B, where an initial increase in FRET signal (first phase), followed by a decrease (second phase). The two phases of the curve were fitted separately in order to calculate rate constants, as specified in the Methods section (dos Santos *et al.*, 2020). As described, the calculated rate constants were plotted and fitted to a straight line, to determine their dependency on the concentration of NDP52. In order to improve fitting of these lines, a larger range of concentrations could have been used.

Overall, in this chapter we provide a new perspective for MVI regulation in transcription and a new avenue for future studies in cancer development, where the nuclear role of MVI might take a central place.

7.3. Myosin VI regulates the spatial organisation of RNA Polymerase II clusters during transcription initiation

Following this initial assessment of how nuclear MVI is activated, we explored how MVI regulates the spatial organisation and dynamics of transcription by RNAPII. Our previous observation that motor activity of MVI is essential in transcription (Fili *et al.*, 2017) led us to postulate that this molecular motor might have anchoring activity or aid the motility of RNAPII transcription machinery. From this, it follows that MVI will have an impact in the molecular dynamics and organisation of RNAPII.

As mentioned in Chapter 1, cluster formation is an essential phenomenon in transcription. RNAPII associates into high-density clusters, which also contain a number of transcription factors and coactivators (Boehning *et al.*, 2018; Cho *et al.*, 2018; Cisse *et al.*, 2013; Pancholi *et al.*, 2021). This enables better regulation of gene expression and higher transcriptional efficiency. Additionally, binding times of RNAPII machinery at promoters directly correlate to levels of newly transcribed mRNA indicating that, in the first steps of transcription, RNAPII molecules and associated factors must be in a relatively confined state at initiation sites (Cho *et al.*, 2016a; Jackson *et al.*, 1993; Popp *et al.*, 2020; Zhao *et al.*, 2014).

MVI had previously been observed at transcription factories by Vreugde *et al.* (Vreugde *et al.*, 2006). Our data show that not only MVI is present at these sites, but has an important regulatory role that impacts their formation and dynamics. We saw that KD of MVI or inhibition of its motor activity, leads to abrogation of RNAPII-Ser5P clusters. RNAPII levels are not affected by either depletion or inhibition of MVI but its spatial distribution is severely impacted, with RNAPII being relocated to the nuclear periphery in a diffuse manner. This correlates with a large decrease in RNAPII binding to chromatin and overall changes in gene expression profiles. Interestingly, we show that this role of MVI in the spatial organisation of transcription is also linked to actin polymerisation. We show that nuclear MVI colocalises with nuclear actin clusters and that perturbation of actin polymerisation, both in the whole-cell (through LatB treatment) or exclusively of the nuclear pool (expression of NLS-R36D-actin mutant) causes similar disruption of RNAPII clusters. We therefore propose that MVI-actin interactions have a central role in RNAPII transcription. Interestingly, at the time we concluded this study, a report by Wei *et al.*, also showed how nuclear actin filament formation is crucial to enhance RNAPII clustering upon serum stimulation of cells, or interferon- γ treatment. The authors describe how the formation and localisation of new RNAPII clusters at newly-induced

gene *loci* is dependent upon nuclear actin polymerisation, and suggest that nuclear F-actin might act as a scaffold for transcriptional machinery (Wei *et al.*, 2020). Whilst this is largely in agreement with our work, the authors do not explore how actin binding proteins, known to be present in the nucleus, might help regulate RNAPII clustering following actin filament formation. MVI, and other nuclear myosins (*e.g.*, NM1, Myosin V, Myosin X) (Cook *et al.*, 2020) are likely to bind actin filaments in the nucleus, as they do in the cytoplasm. It is possible that actin filament formation in the nucleus provides the necessary structure for these proteins to deploy their motor activity in the regulation of nuclear processes. In my opinion, future work exploring how different nuclear myosins might utilise dynamic actin filaments to perform their nuclear function will be important for the field.

In line with this, when we measured the 3D molecular dynamics of Rbp1 – the largest subunit of RNAPII – we observed that depletion of MVI; inhibition of its motor domain; or disruption of nuclear actin filament formation, lead to higher molecular diffusion. This points to shorter binding times of Rbp1 at promoter regions, which, based on previous studies (Cho *et al.*, 2016a) and our data, translates into lower transcriptional efficiency.

Finally, we were able to show that the molecular mechanism through which MVI has this organisational role lies on its ability to act as a molecular anchor under load. When a load over 2pN is applied to a MVI molecule, MVI shifts its function from a motile motor to a molecular anchor (Altman *et al.*, 2004). Disruption of this ability, through engineering of a tension-sensor spring, led to the same spatial disruption of RNAPII as depletion or inhibition of MVI. Hence, we propose a model whereby MVI can anchor RNAPII at transcription initiation sites, to reduce its molecular diffusion and enable the formation of concentrated clustered regions of transcription machinery. As a result, although intrinsically disordered regions of proteins are known as main drivers for protein clustering and LLPS (Boehning *et al.*, 2018; Lin *et al.*, 2017; Pancholi *et al.*, 2021), our work here also shows that additional mechanisms might contribute to their formation and regulation. Proteins, such as MVI, with the ability to generate force and act as anchors, could act as stabilisers of these assemblies.

Similar to what was observed for nuclear F-actin formation (Wei *et al.*, 2020), MVI nuclear activity could be especially important for cells undergoing simultaneous activation of several genes or gene expression pathways. Our work supports this by showing that when transcriptional activity is stimulated, through serum stimulation, there is an increase in MVI nuclear clustering, which correlates with higher RNAPII clustering and higher transcriptional activity. Once again, this may be of particular importance in

cancer studies. As increased levels of MVI appear to drive the formation of RNAPII clusters, overexpression of MVI in several cancer is of particular concern (Dunn *et al.*, 2006; Wang *et al.*, 2015; Wollscheid *et al.*, 2016; Yoshida *et al.*, 2004). Observations in both Chapters 3 and 4 showing that MVI KD reduces cell growth support the concept that high levels of MVI might drive cancer proliferation. Furthermore, its link to nuclear receptor-related transcription (Fili *et al.*, 2017) could make MVI an interesting drug target in future studies. Inhibition or depletion of nuclear receptors are common treatments in hormone-responsive cancers (e.g., tamoxifen or fulvestrant treatments for ER positive cancers). Since we show that MVI can enhance transcription through nuclear-receptor activity, exploring combination treatments between these drugs and MVI inhibition could help us better understand the therapeutic potential of MVI as a treatment target.

Finally, we also observed that epigenetic marks and chromatin accessibility are altered in cells following inhibition of MVI. This could also help explain the relocation of RNAPII to the nuclear periphery, following transcription MVI inhibition and transcription shut down. In general, MVI is thought to have an important role in chromatin organisation (Große-Berkenbusch *et al.*, 2020; Zorca *et al.*, 2015). Previous work by Zorca *et al.* described how MVI is involved in the relocation of gene *loci* in the nucleus for coordinated transcription events (Zorca *et al.*, 2015). This attributes MVI a role in long-distance chromosome organisation. Chromatin organisation by MVI could directly contribute to the assembly of RNAPII clusters. This could give MVI a dual role in transcription. By bringing together distal regions of the genome, MVI could allow the formation of super-enhancers and promote condensate formation following the recruitment of the large number of auxiliary factors that assemble in these regions. Then, through its molecular anchoring abilities, MVI could help stabilise transcriptional machinery at these sites to allow efficient transcription initiation. The recent work by Große-Berkenbusch *et al.* confirms chromatin movement by MVI and, importantly, also links this activity to nuclear actin filaments (Große-Berkenbusch *et al.*, 2020). This further supports our findings that both MVI and actin disruption have a negative impact in transcription.

In spite of MVI role in chromatin organisation and its ability to coordinate transcriptional clustering throughout the nucleus, we are yet to know what impact this protein has in overall nuclear architecture and mechanics. Future work, focusing on the impact of MVI activity on overall mechanics will help our understanding of its nuclear function. Long-distance chromatin relocation and altered levels of euchromatin/heterochromatin upon depletion or inhibition of MVI could be sufficient to affect nuclear stiffness and this would be an interesting question to pursue. Some of my preliminary, unpublished data (Figure

15) from AFM measurements performed in initially-adhered cells, show a reduction in nuclear stiffness when cells are treated with TIP. Transcriptional condensates, although they occur in open regions of chromatin, are highly crosslinked assemblies, known to increase local chromatin constraints, promote the formation of chromatin bridges and to increase local stiffness (Ashwin *et al.*, 2020; Nagashima *et al.*, 2019). Although further investigation is necessary, the disruption of RNAPII spatial organisation, caused by inhibition or depletion of MVI could lead to the observed nuclear softening (Figure 13) through loss of local chromatin crosslinks. Interestingly, this may suggest that transcriptionally inactive cells are softer. This agrees with earlier work, presented in Chapter 3, where we observed that the nuclear core, which, is transcriptionally more active than the periphery, had a more elastic, stiffer response (Lherbette *et al.*, 2017). Based on this, transcriptional levels in the cell could be manipulated to change nuclear mechanics, or adapt to enable cell migration in confined spaces.

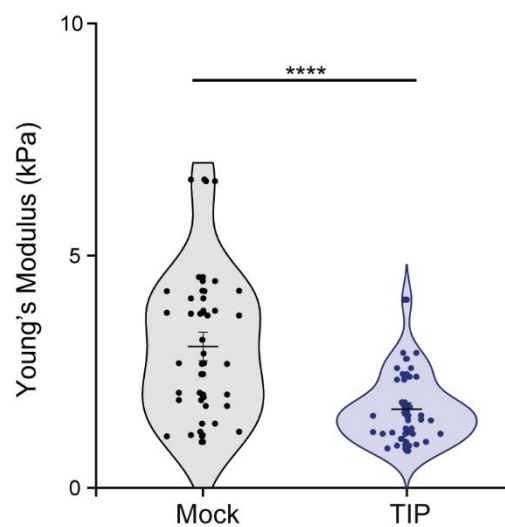


Figure 15 – Nuclear softening following MVI inhibition. Young's modulus calculated from AFM measurements on initially-adhered HeLa cells treated with 1 μ M TIP for 1 hour. n=26 (mock) n=30 (TIP). ****p<0.0001 (two-tailed t-test).

7.4. Autophagy receptor NDP52 modulates RNA Polymerase II transcription

For Chapter 6 of this thesis, we proposed that NDP52, a cytoplasmic autophagy receptor and binding partner of MVI, has nuclear roles, possibly in transcription. The rationale for this was two-fold: i) NDP52 belongs to the same family and shares high homology with a known coactivator of transcription CoCoA (Kim *et al.*, 2003); and ii) NDP52 is an important binding partner of MVI, a molecular motor that, as described above, has important nuclear roles in transcription and chromatin regulation (Fili *et al.*, 2017).

One of the approaches used in this study was to investigate the nanoscale organisation and molecular dynamics of NDP52 in the nucleus. Our data show that NDP52 forms relatively static nuclear clusters. Importantly, a proportion of these clusters is present at transcription initiation sites (colocalised with RANP11-Ser5P) and these supramolecular assemblies are much larger than non-colocalised clusters. This insight into the spatial organisation of NDP52 is important because, as clustering of molecules is usually linked to their functional activity, this clearly supports a role in RNAP11 transcription. As further evidence, when we inhibited transcription, through the use of Rbp1 inhibitor α -amanitin, we observed disruption of NDP52 cluster formation and increased nuclear diffusion of this protein. Differential gene expression experiments in two different example mammalian cell lines support this further by showing that NDP52 KD has an overall impact in transcription. Interestingly, we also found that overexpression of the nuclear pool of NDP52 led to an increase in the number of RNAP11-Ser5P clusters. Although we did not explore the mechanism through which this occurs here, it will be interesting, in future studies to assess how NDP52 can promote novel transcriptional hub formation.

The findings described above not only support our previous work, showing that NDP52 can promote transcription enhancement through activation of MVI, but also instate NDP52 as a regulator of transcription in its own right.

To investigate the molecular mechanisms through which NDP52 performs its nuclear function, we performed a biochemical characterisation of the protein. In agreement with previous work, we found that NDP52 is a dimer (dos Santos *et al.*, 2020; Kim *et al.*, 2013a) of elongated shape, although we also observed that higher oligomeric forms can co-exist in solution. We also determined that NDP52 can bind tightly to dsDNA through its ZF domains at the C-terminal of the protein. This could be of particular relevance for its nuclear role of as we were able to show that binding of NDP52 induces structural changes to DNA – bridging and looping. Additionally, as we were able to detect NDP52

bound to genomic regions in cells, through ChIP-qPCR, this could be a possible mechanism for NDP52 to regulate transcription.

In addition to interactions with DNA, the ZF domains also act as interfaces for protein-protein interactions. Previous observations show that NDP52 can interact with MVI and ubiquitin through its C-terminal region (Morriswood *et al.*, 2007; Xie *et al.*, 2015). Hence, further insight into NDP52 nuclear functions might also arise from proteomics data collected during this study. Using both recombinant NDP52 for pull-downs from nuclear extract and co-immunoprecipitation from whole cells, we investigated the interactome of this protein. Putative new binding partners included coactivators of transcription, histone methyl and acetyltransferases, as well as subunits of ATP-dependent chromatin remodellers. Future experiments, will be necessary not only validate some of the interactions found, but to understand how they relate to the nuclear role of NDP52.

Based on this work, we propose two possible mechanisms for NDP52 in the regulation of transcription. One through direct or indirect interactions and changes to chromatin structure and another through modulation of transcriptional coactivators. A combination of these two mechanisms is also possible. CoCoA, a gene paralog of NDP52, acts by recruiting additional transcription coactivators to active sites of transcription. Interacting partners of CoCoA include both transcriptional machinery and proteins with DNA-binding activity that can change DNA landscape to facilitate transcription (Kim *et al.*, 2003; Kim *et al.*, 2006; Yang *et al.*, 2006b).

Some of my recently collected preliminary data (unpublished) support that the ability of NDP52 to change chromatin structure might be the main mechanism through which transcription regulation is achieved. Overexpression of nuclear NDP52 appears to lead to large-scale chromatin decondensation. Cells expressing Halo-NLS-NDP52 present lower levels of heterochromatin mark H3K9me3, increased nuclear size, nuclear aberrations and, in extreme cases, nuclear rupture (Figure 16A-E). The higher levels of decondensed chromatin from preliminary data could also explain our observation showing the formation of additional RNAPII clusters in cells expressing NLS-NDP52. Chromatin decondensation induced by NDP52 could allow formation of additional RNAPII clusters at sites which were previously inaccessible to transcription machinery, due to restrictive chromatin structures. An interesting question is, if NDP52 can induce changes to chromatin structure, whether NDP52 can change local mechanics of chromatin. Although we have not yet tested this, the degree of chromatin decondensation that we observe when overexpressing nuclear NDP52 is likely to affect nuclear mechanics. Similar to what we observe with NDP52 (Figure 16 A-E), a study on

the nucleosomal binding protein HMGN5 showed that overexpression of this protein in the nucleus caused massive-scale chromatin decondensation, nuclear aberrations, frequent NE rupture and overall softening of the organelle (Furusawa *et al.*, 2015). It will be interesting in the future to understand how NDP52 regulates chromatin organisation and the impact of this to nuclear architecture and mechanics.

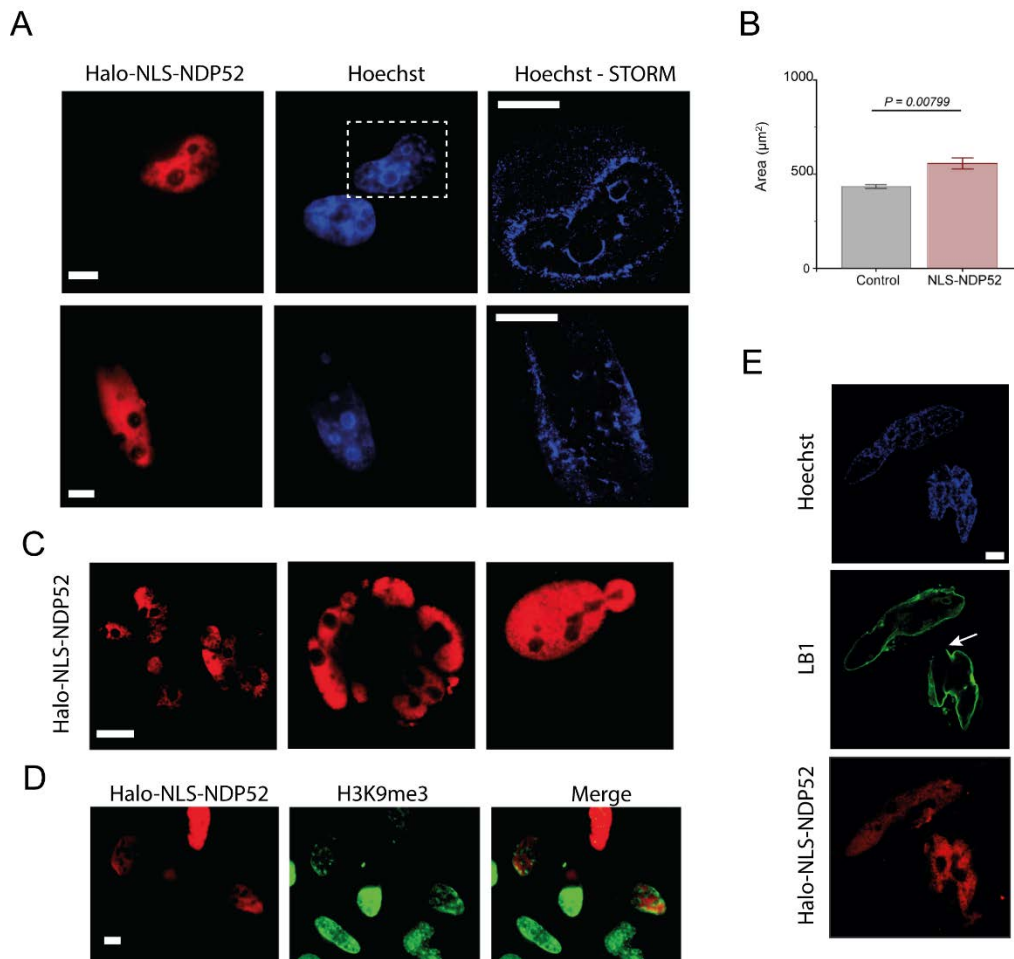


Figure 16 – Chromatin decondensation by nuclear overexpression of NDP52. (A) Hoechst staining of HeLa nuclei expressing Halo-NLS-NDP52 following 24 hours of transfection. **(B)** Cross-sectional area of non-transfected vs Halo-NLS-NDP52 expressing nuclei. control: n=4 biological replicates, 230 cells Halo-NLS-NDP52 n=4 biological replicates, 267 cells. *p*-value shown (two-tailed t-test) **(C)** Aberrant shapes of nuclei expressing Halo-NLS-NDP52. **(D)** H3K9me3 in nuclei expressing Halo-NLS-NDP52. **(E)** Lamin B1 (LB1) labelling of nuclei expressing Halo-NLS-NDP52. Arrow shows nuclear rupture. Scale bar = 5 μm .

An interesting future focus for NDP52 will also be to investigate its nuclear role in response to cell stress. In the cytoplasm NDP52 responds to both external and internal stresses to initiate autophagy. Furthermore, proteomics data presented in this study show that, following α -amanitin treatment, there is an enrichment for interactions of NDP52 with DNA repair proteins. Future experiments, with DNA damage drugs, such as cisplatin, could shed light on how nuclear NDP52 functions are modulated by these

stimuli. In dos Santos *et al.* (dos Santos *et al.*, 2021) – Chapter 3 – we showed that cisplatin treatment causes large-scale chromatin decondensation events. Although the mechanism through which this occurs is still not clear, it is possible that the coordinated action of many different factors is involved. As we collect more evidence of NDP52 role in chromatin organisation, it will be interesting to explore this in the context of cellular stress.

Overall, this thesis explored different aspects of nuclear architecture – from the physical properties of the nucleus to the nanoscale organisation of enzymatic nuclear processes. The works presented here shed light on how structural components, in particular chromatin, and the activation of nuclear processes contribute to overall nuclear mechanics. Additionally, this thesis also contributed to the knowledge of how RNAPII transcription is organised at a nanoscale, linking this to overall nuclear structure and function. This work lays the foundation for bridging the spatial organisation of nuclear proteins and the physical properties of the nucleus, therefore, highlighting the existence of bidirectional mechanotransduction, outside-in and inside-out across the cell. In the future, it will be important to shed light on these mechanisms and consider their impact on cellular function as well as their consequence for disease and therapeutic strategies.

8. Non-Manuscript References

- A, P., and Weber, S.C. (2019). Evidence for and against Liquid-Liquid Phase Separation in the Nucleus. *Non-coding RNA* 5. 10.3390/ncrna5040050.
- Aaron, J., Wait, E., DeSantis, M., and Chew, T.-L. (2019). Practical Considerations in Particle and Object Tracking and Analysis. *Current Protocols in Cell Biology* 83, e88. <https://doi.org/10.1002/cpcb.88>.
- Abbe, E. (1873). Beiträge zur Theorie des Mikroskops und der mikroskopischen Wahrnehmung. *Archiv für Mikroskopische Anatomie* 9, 413-468. 10.1007/BF02956173.
- Abercrombie, M., Heaysman, J.E.M., and Pegrum, S.M. (1971). The locomotion of fibroblasts in culture: IV. Electron microscopy of the leading lamella. *Experimental Cell Research* 67, 359-367. [https://doi.org/10.1016/0014-4827\(71\)90420-4](https://doi.org/10.1016/0014-4827(71)90420-4).
- Abrahamsson, S., Chen, J., Hajj, B., Stallinga, S., Katsov, A.Y., Wisniewski, J., Mizuguchi, G., Soule, P., Mueller, F., Darzacq, C.D., et al. (2013). Fast multicolor 3D imaging using aberration-corrected multifocus microscopy. *Nature methods* 10, 60-63. 10.1038/nmeth.2277.
- Adam, S., Dabin, J., and Polo, S.E. (2015). Chromatin plasticity in response to DNA damage: The shape of things to come. *DNA Repair* 32, 120-126. <https://doi.org/10.1016/j.dnarep.2015.04.022>.
- Adam, S.A., Butin-Israeli, V., Cleland, M.M., Shimi, T., and Goldman, R.D. (2013). Disruption of lamin B1 and lamin B2 processing and localization by farnesyltransferase inhibitors. *Nucleus (Austin, Tex.)* 4, 142-150. 10.4161/nucl.24089.
- Adcock, I.M., and Caramori, G. (2009). Chapter 31 - Transcription Factors. In *Asthma and COPD (Second Edition)*, P.J. Barnes, J.M. Drazen, S.I. Rennard, and N.C. Thomson, eds. (Academic Press), pp. 373-380. <https://doi.org/10.1016/B978-0-12-374001-4.00031-6>.
- Aebi, U., Cohn, J., Buhle, L., and Gerace, L. (1986). The nuclear lamina is a meshwork of intermediate-type filaments. *Nature* 323, 560-564. 10.1038/323560a0.
- Agrawal, A., and Lele, T.P. (2019). Mechanics of nuclear membranes. *Journal of Cell Science* 132, jcs229245. 10.1242/jcs.229245.
- Alagoz, M., Katsuki, Y., Ogiwara, H., Ogi, T., Shibata, A., Kakarougkas, A., and Jeggo, P. (2015). SETDB1, HP1 and SUV39 promote repositioning of 53BP1 to extend resection during homologous recombination in G2 cells. *Nucleic Acids Research* 43, 7931-7944. 10.1093/nar/gkv722.
- Alam, S.G., Zhang, Q., Prasad, N., Li, Y., Chamala, S., Kuchibhotla, R., Kc, B., Aggarwal, V., Shrestha, S., Jones, A.L., et al. (2016). The mammalian LINC complex regulates genome transcriptional responses to substrate rigidity. *Scientific Reports* 6, 38063. 10.1038/srep38063.
- Alberti, S., Gladfelter, A., and Mittag, T. (2019). Considerations and Challenges in Studying Liquid-Liquid Phase Separation and Biomolecular Condensates. *Cell* 176, 419-434. 10.1016/j.cell.2018.12.035.
- Almuzzaini, B., Sarshad, A.A., Farrants, A.K., and Percipalle, P. (2015). Nuclear myosin 1 contributes to a chromatin landscape compatible with RNA polymerase II transcription activation. *BMC Biol* 13, 35. 10.1186/s12915-015-0147-z.
- Alshareedah, I., Moosa, M.M., Pham, M., Potoyan, D.A., and Banerjee, P.R. (2021). Programmable viscoelasticity in protein-RNA condensates with disordered sticker-spacer polypeptides. *Nature Communications* 12, 6620. 10.1038/s41467-021-26733-7.
- Altman, D., Goswami, D., Hasson, T., Spudich, J.A., and Mayor, S. (2007). Precise Positioning of Myosin VI on Endocytic Vesicles In Vivo. *PLOS Biology* 5, e210. 10.1371/journal.pbio.0050210.
- Altman, D., Sweeney, H.L., and Spudich, J.A. (2004). The mechanism of myosin VI translocation and its load-induced anchoring. *Cell* 116, 737-749. 10.1016/s0092-8674(04)00211-9.
- Altman, D.G., and Bland, J.M. (2005). Standard deviations and standard errors. *BMJ* 331, 903-903. 10.1136/bmj.331.7521.903.
- Andrin, C., McDonald, D., Attwood, K.M., Rodrigue, A., Ghosh, S., Mirzayans, R., Masson, J.-Y., Dellaire, G., and Hendzel, M.J. (2012). A requirement for polymerized actin in DNA double-strand break repair. *Nucleus* 3, 384-395. 10.4161/nucl.21055.

Arden, S.D., Tumbarello, D.A., Butt, T., Kendrick-Jones, J., and Buss, F. (2016). Loss of cargo binding in the human myosin VI deafness mutant (R1166X) leads to increased actin filament binding. *The Biochemical journal* *473*, 3307-3319. 10.1042/bcj20160571.

Ashwin, S.S., Maeshima, K., and Sasai, M. (2020). Heterogeneous fluid-like movements of chromatin and their implications to transcription. *Biophysical Reviews* *12*, 461-468. 10.1007/s12551-020-00675-8.

Au, J.S., Puri, C., Ihrke, G., Kendrick-Jones, J., and Buss, F. (2007). Myosin VI is required for sorting of AP-1B-dependent cargo to the basolateral domain in polarized MDCK cells. *J Cell Biol* *177*, 103-114. 10.1083/jcb.200608126.

Axelrod, D., Koppel, D.E., Schlessinger, J., Elson, E., and Webb, W.W. (1976). Mobility measurement by analysis of fluorescence photobleaching recovery kinetics. *Biophys J* *16*, 1055-1069. 10.1016/s0006-3495(76)85755-4.

Aymard, F., Bugler, B., Schmidt, C.K., Guillou, E., Caron, P., Briois, S., Iacovoni, J.S., Daburon, V., Miller, K.M., Jackson, S.P., and Legube, G. (2014). Transcriptionally active chromatin recruits homologous recombination at DNA double-strand breaks. *Nature Structural & Molecular Biology* *21*, 366-374. 10.1038/nsmb.2796.

Baarlink, C., Plessner, M., Sherrard, A., Morita, K., Misu, S., Virant, D., Kleinschnitz, E.-M., Harniman, R., Alibhai, D., Baumeister, S., et al. (2017). A transient pool of nuclear F-actin at mitotic exit controls chromatin organization. *Nature Cell Biology* *19*, 1389-1399. 10.1038/ncb3641.

Baldeyron, C., Soria, G., Roche, D., Cook, A.J., and Almouzni, G. (2011). HP1alpha recruitment to DNA damage by p150CAF-1 promotes homologous recombination repair. *J Cell Biol* *193*, 81-95. 10.1083/jcb.201101030.

Banani, S.F., Lee, H.O., Hyman, A.A., and Rosen, M.K. (2017). Biomolecular condensates: organizers of cellular biochemistry. *Nature Reviews Molecular Cell Biology* *18*, 285-298. 10.1038/nrm.2017.7.

Banerjee, I., Zhang, J., Moore-Morris, T., Pfeiffer, E., Buchholz, K.S., Liu, A., Ouyang, K., Stroud, M.J., Gerace, L., Evans, S.M., et al. (2014). Targeted Ablation of Nesprin 1 and Nesprin 2 from Murine Myocardium Results in Cardiomyopathy, Altered Nuclear Morphology and Inhibition of the Biomechanical Gene Response. *PLOS Genetics* *10*, e1004114. 10.1371/journal.pgen.1004114.

Banjade, S., and Rosen, M.K. (2014). Phase transitions of multivalent proteins can promote clustering of membrane receptors. *eLife* *3*, e04123. 10.7554/eLife.04123.

Bannister, A.J., and Kouzarides, T. (2011). Regulation of chromatin by histone modifications. *Cell Research* *21*, 381-395. 10.1038/cr.2011.22.

Bartolomei, M.S., Halden, N.F., Cullen, C.R., and Corden, J.L. (1988). Genetic analysis of the repetitive carboxyl-terminal domain of the largest subunit of mouse RNA polymerase II. *Molecular and cellular biology* *8*, 330-339. 10.1128/mcb.8.1.330-339.1988.

Bates, M., Huang, B., and Zhuang, X. (2008). Super-resolution microscopy by nanoscale localization of photo-switchable fluorescent probes. *Current Opinion in Chemical Biology* *12*, 505-514. <https://doi.org/10.1016/j.cbpa.2008.08.008>.

Bates, M., Jones, S.A., and Zhuang, X. (2013a). Preparation of photoswitchable labeled antibodies for STORM imaging. *Cold Spring Harb Protoc* *2013*, 540-541. 10.1101/pdb.prot075168.

Bates, M., Jones, S.A., and Zhuang, X. (2013b). Stochastic Optical Reconstruction Microscopy (STORM): A Method for Superresolution Fluorescence Imaging. *Cold Spring Harbor Protocols* *2013*, pdb.top075143.

Batters, C., Brack, D., Ellrich, H., Averbek, B., and Veigel, C. (2016). Calcium can mobilize and activate myosin-VI. *Proc Natl Acad Sci U S A* *113*, E1162-1169. 10.1073/pnas.1519435113.

Bautista, M., Fernandez, A., and Pinaud, F. (2019). A Micropatterning Strategy to Study Nuclear Mechanotransduction in Cells. *Micromachines* *10*. 10.3390/mi10120810.

Belaghzal, H., Borrman, T., Stephens, A.D., Lafontaine, D.L., Venev, S.V., Weng, Z., Marko, J.F., and Dekker, J. (2021). Liquid chromatin Hi-C characterizes compartment-dependent chromatin interaction dynamics. *Nature Genetics*. 10.1038/s41588-021-00784-4.

Belin, B.J., Cimini, B.A., Blackburn, E.H., and Mullins, R.D. (2013). Visualization of actin filaments and monomers in somatic cell nuclei. *Mol Biol Cell* 24, 982-994. 10.1091/mbc.E12-09-0685.

Belin, B.J., Lee, T., and Mullins, R.D. (2015). DNA damage induces nuclear actin filament assembly by Formin-2 and Spire-1/2 that promotes efficient DNA repair. *eLife* 4, e07735. 10.7554/eLife.07735.

Bell, E.S., and Lammerding, J. (2016). Causes and consequences of nuclear envelope alterations in tumour progression. *European Journal of Cell Biology* 95, 449-464. <https://doi.org/10.1016/j.ejcb.2016.06.007>.

Bellush, J.M., and Whitehouse, I. (2017). DNA replication through a chromatin environment. *Philosophical Transactions of the Royal Society B: Biological Sciences* 372, 20160287. 10.1098/rstb.2016.0287.

Benjamini, Y., and Hochberg, Y. (1995). Controlling the False Discovery Rate: A Practical and Powerful Approach to Multiple Testing. *Journal of the Royal Statistical Society: Series B (Methodological)* 57, 289-300. <https://doi.org/10.1111/j.2517-6161.1995.tb02031.x>.

Bennett, G., and Peterson, C.L. (2015). SWI/SNF recruitment to a DNA double-strand break by the NuA4 and Gcn5 histone acetyltransferases. *DNA Repair* 30, 38-45. <https://doi.org/10.1016/j.dnarep.2015.03.006>.

Betzig, E., Patterson George, H., Sougrat, R., Lindwasser, O.W., Olenych, S., Bonifacino Juan, S., Davidson Michael, W., Lippincott-Schwartz, J., and Hess Harald, F. (2006). Imaging Intracellular Fluorescent Proteins at Nanometer Resolution. *Science* 313, 1642-1645. 10.1126/science.1127344.

Binnig, G., Quate, C.F., and Gerber, C. (1986). Atomic Force Microscope. *Physical Review Letters* 56, 930-933. 10.1103/PhysRevLett.56.930.

Black, J.C., Van Rechem, C., and Whetstine, J.R. (2012). Histone lysine methylation dynamics: establishment, regulation, and biological impact. *Molecular cell* 48, 491-507. 10.1016/j.molcel.2012.11.006.

Boehning, M., Dugast-Darzacq, C., Rankovic, M., Hansen, A.S., Yu, T., Marie-Nelly, H., McSwiggen, D.T., Kovic, G., Dailey, G.M., Cramer, P., et al. (2018). RNA polymerase II clustering through carboxy-terminal domain phase separation. *Nature Structural & Molecular Biology* 25, 833-840. 10.1038/s41594-018-0112-y.

Boija, A., Klein, I.A., Sabari, B.R., Dall'Agnese, A., Coffey, E.L., Zamudio, A.V., Li, C.H., Shrinivas, K., Manteiga, J.C., Hannett, N.M., et al. (2018). Transcription Factors Activate Genes through the Phase-Separation Capacity of Their Activation Domains. *Cell* 175, 1842-1855.e1816. 10.1016/j.cell.2018.10.042.

Bonner, J.J., Ballou, C., and Fackenthal, D.L. (1994). Interactions between DNA-bound trimers of the yeast heat shock factor. *Molecular and cellular biology* 14, 501-508. 10.1128/mcb.14.1.501-508.1994.

Born, M., and Wolf, E. (2013). Principles of optics: electromagnetic theory of propagation, interference and diffraction of light (Elsevier).

Bosch, P.J., Corrêa, I.R., Jr., Sonntag, M.H., Ibach, J., Brunsveld, L., Kanger, J.S., and Subramaniam, V. (2014). Evaluation of fluorophores to label SNAP-tag fused proteins for multicolor single-molecule tracking microscopy in live cells. *Biophys J* 107, 803-814. 10.1016/j.bpj.2014.06.040.

Botcherby, E.J., Juskaitis, R., Booth, M.J., and Wilson, T. (2007). Aberration-free optical refocusing in high numerical aperture microscopy. *Opt. Lett.* 32, 2007-2009. 10.1364/OL.32.002007.

Bowers, E.M., Yan, G., Mukherjee, C., Orry, A., Wang, L., Holbert, M.A., Crump, N.T., Hazzalin, C.A., Liszczak, G., Yuan, H., et al. (2010). Virtual ligand screening of the p300/CBP histone acetyltransferase: identification of a selective small molecule inhibitor. *Chemistry & biology* 17, 471-482. 10.1016/j.chembiol.2010.03.006.

Bracha, D., Walls, M.T., Wei, M.-T., Zhu, L., Kurian, M., Avalos, J.L., Toettcher, J.E., and Brangwynne, C.P. (2018). Mapping Local and Global Liquid Phase Behavior in Living Cells Using Photo-Oligomerizable Seeds. *Cell* 175, 1467-1480.e1413. <https://doi.org/10.1016/j.cell.2018.10.048>.

Brandt, A., Papagiannouli, F., Wagner, N., Wilsch-Bräuninger, M., Braun, M., Furlong, E.E., Loserth, S., Wenzl, C., Pilot, F., Vogt, N., et al. (2006). Developmental control of nuclear size and shape by Kugelkern and Kurzkern. *Current biology : CB* 16, 543-552. 10.1016/j.cub.2006.01.051.

Brookes, E., and Pombo, A. (2009). Modifications of RNA polymerase II are pivotal in regulating gene expression states. *EMBO Rep* 10, 1213-1219. 10.1038/embor.2009.221.

Brown, S.A., and Kingston, R.E. (1997). Disruption of downstream chromatin directed by a transcriptional activator. *Genes & Development* 11, 3116-3121.

Buratowski, S. (2003). The CTD code. *Nature Structural & Molecular Biology* 10, 679-680. 10.1038/nsb0903-679.

Buratowski, S. (2009). Progression through the RNA polymerase II CTD cycle. *Molecular cell* 36, 541-546. 10.1016/j.molcel.2009.10.019.

Burgess, Rebecca C., Burman, B., Kruhlak, Michael J., and Misteli, T. (2014). Activation of DNA Damage Response Signaling by Condensed Chromatin. *Cell Reports* 9, 1703-1717. <https://doi.org/10.1016/j.celrep.2014.10.060>.

Burma, S., Chen, B.P., Murphy, M., Kurimasa, A., and Chen, D.J. (2001). ATM phosphorylates histone H2AX in response to DNA double-strand breaks. *The Journal of biological chemistry* 276, 42462-42467. 10.1074/jbc.C100466200.

Burnham, N.A., and Colton, R.J. (1989). Measuring the nanomechanical properties and surface forces of materials using an atomic force microscope. *Journal of Vacuum Science & Technology A* 7, 2906-2913. 10.1116/1.576168.

Buss, F., Arden, S.D., Lindsay, M., Luzio, J.P., and Kendrick-Jones, J. (2001). Myosin VI isoform localized to clathrin-coated vesicles with a role in clathrin-mediated endocytosis. *The EMBO journal* 20, 3676-3684. 10.1093/emboj/20.14.3676.

Buss, F., Kendrick-Jones, J., Lionne, C., Knight, A.E., Côté, G.P., and Paul Luzio, J. (1998). The localization of myosin VI at the golgi complex and leading edge of fibroblasts and its phosphorylation and recruitment into membrane ruffles of A431 cells after growth factor stimulation. *J Cell Biol* 143, 1535-1545. 10.1083/jcb.143.6.1535.

Buss, F., Spudich, G., and Kendrick-Jones, J. (2004). MYOSIN VI: Cellular Functions and Motor Properties. *Annual Review of Cell and Developmental Biology* 20, 649-676. 10.1146/annurev.cellbio.20.012103.094243.

Buxboim, A., Swift, J., Irianto, J., Spinler, Kyle R., Dingal, P.C.Dave P., Athirasala, A., Kao, Y.-Ruei C., Cho, S., Harada, T., Shin, J.-W., and Discher, Dennis E. (2014). Matrix Elasticity Regulates Lamin-A,C Phosphorylation and Turnover with Feedback to Actomyosin. *Current Biology* 24, 1909-1917. 10.1016/j.cub.2014.07.001.

Cadet, J., and Wagner, J.R. (2013). DNA base damage by reactive oxygen species, oxidizing agents, and UV radiation. *Cold Spring Harbor perspectives in biology* 5, a012559. 10.1101/cshperspect.a012559.

Cai, D., McEwen, D.P., Martens, J.R., Meyhofer, E., and Verhey, K.J. (2009). Single molecule imaging reveals differences in microtubule track selection between Kinesin motors. *PLoS Biol* 7, e1000216. 10.1371/journal.pbio.1000216.

Cairns, B.R. (2004). Around the world of DNA damage INO80 days. *Cell* 119, 733-735. 10.1016/j.cell.2004.12.005.

Calo, E., and Wysocka, J. (2013). Modification of Enhancer Chromatin: What, How, and Why? *Molecular cell* 49, 825-837. <https://doi.org/10.1016/j.molcel.2013.01.038>.

Calvo, F., Ege, N., Grande-Garcia, A., Hooper, S., Jenkins, R.P., Chaudhry, S.I., Harrington, K., Williamson, P., Moeendarbary, E., Charras, G., and Sahai, E. (2013). Mechanotransduction and YAP-dependent matrix remodelling is required for the generation and maintenance of cancer-associated fibroblasts. *Nat Cell Biol* 15, 637-646. 10.1038/ncb2756.

Canzio, D., Chang, E.Y., Shankar, S., Kuchenbecker, K.M., Simon, M.D., Madhani, H.D., Narlikar, G.J., and Al-Sady, B. (2011). Chromodomain-mediated oligomerization of HP1 suggests a nucleosome-bridging mechanism for heterochromatin assembly. *Molecular cell* 41, 67-81. 10.1016/j.molcel.2010.12.016.

Caridi, C.P., Plessner, M., Grosse, R., and Chiolo, I. (2019). Nuclear actin filaments in DNA repair dynamics. *Nature Cell Biology* 21, 1068-1077. 10.1038/s41556-019-0379-1.

Castaneda, N., Park, J., and Kang, E.H. (2021). Regulation of Actin Bundle Mechanics and Structure by Intracellular Environmental Factors. *Frontiers in Physics* 9. 10.3389/fphy.2021.675885.

Cenni, V., Capanni, C., Mattioli, E., Schena, E., Squarzone, S., Bacalini, M.G., Garagnani, P., Salvioli, S., Franceschi, C., and Lattanzi, G. (2020). Lamin A involvement in ageing processes. *Ageing Res Rev* 62, 101073. 10.1016/j.arr.2020.101073.

Chakalova, L., and Fraser, P. (2010). Organization of transcription. *Cold Spring Harbor perspectives in biology* 2, a000729-a000729. 10.1101/cshperspect.a000729.

Chalut, Kevin J., Höpfner, M., Lautenschläger, F., Boyde, L., Chan, Chii J., Ekpenyong, A., Martinez-Arias, A., and Guck, J. (2012). Chromatin Decondensation and Nuclear Softening Accompany Nanog Downregulation in Embryonic Stem Cells. *Biophysical Journal* 103, 2060-2070. 10.1016/j.bpj.2012.10.015.

Chandrasekaran, A., Upadhyaya, A., and Papoian, G.A. (2019). Remarkable structural transformations of actin bundles are driven by their initial polarity, motor activity, crosslinking, and filament treadmill. *PLOS Computational Biology* 15, e1007156. 10.1371/journal.pcbi.1007156.

Chandrasekhar, S. (1943). Stochastic Problems in Physics and Astronomy. *Reviews of Modern Physics* 15, 1-89. 10.1103/RevModPhys.15.1.

Chang, L., Li, M., Shao, S., Li, C., Ai, S., Xue, B., Hou, Y., Zhang, Y., Li, R., Fan, X., et al. (2020). Nuclear peripheral chromatin-lamin B1 interaction is required for global integrity of chromatin architecture and dynamics in human cells. *Protein & Cell*. 10.1007/s13238-020-00794-8.

Charrier, E.E., Pogoda, K., Wells, R.G., and Janmey, P.A. (2018). Control of cell morphology and differentiation by substrates with independently tunable elasticity and viscous dissipation. *Nature Communications* 9, 449. 10.1038/s41467-018-02906-9.

Chaudhuri, O., Gu, L., Klumpers, D., Darnell, M., Bencherif, S.A., Weaver, J.C., Huebsch, N., Lee, H.P., Lippens, E., Duda, G.N., and Mooney, D.J. (2016). Hydrogels with tunable stress relaxation regulate stem cell fate and activity. *Nature materials* 15, 326-334. 10.1038/nmat4489.

Chen, B.C., Legant, W.R., Wang, K., Shao, L., Millie, D.E., Davidson, M.W., Janetopoulos, C., Wu, X.S., Hammer, J.A., 3rd, Liu, Z., et al. (2014). Lattice light-sheet microscopy: imaging molecules to embryos at high spatiotemporal resolution. *Science* 346, 1257998. 10.1126/science.1257998.

Chen, C.S., Mrksich, M., Huang, S., Whitesides, G.M., and Ingber, D.E. (1997). Geometric control of cell life and death. *Science* 276, 1425-1428. 10.1126/science.276.5317.1425.

Chen, N.Y., Kim, P., Weston, T.A., Edillo, L., Tu, Y., Fong, L.G., and Young, S.G. (2018). Fibroblasts lacking nuclear lamins do not have nuclear blebs or protrusions but nevertheless have frequent nuclear membrane ruptures. *Proceedings of the National Academy of Sciences U.S.A* 115, 10100. 10.1073/pnas.1812622115.

Chen, N.Y., Yang, Y., Weston, T.A., Belling, J.N., Heizer, P., Tu, Y., Kim, P., Edillo, L., Jonas, S.J., Weiss, P.S., et al. (2019). An absence of lamin B1 in migrating neurons causes nuclear membrane ruptures and cell death. *Proceedings of the National Academy of Sciences U.S.A* 116, 25870. 10.1073/pnas.1917225116.

Chiolo, I., Minoda, A., Colmenares, Serafin U., Polyzos, A., Costes, Sylvain V., and Karpen, Gary H. (2011). Double-Strand Breaks in Heterochromatin Move Outside of a Dynamic HP1a Domain to Complete Recombinational Repair. *Cell* 144, 732-744. 10.1016/j.cell.2011.02.012.

Cho, W.-K., Jayanth, N., English, B.P., Inoue, T., Andrews, J.O., Conway, W., Grimm, J.B., Spille, J.-H., Lavis, L.D., Lionnet, T., and Cisse, I.I. (2016a). RNA Polymerase II cluster dynamics predict mRNA output in living cells. *eLife* 5, e13617. 10.7554/eLife.13617.

Cho, W.-K., Jayanth, N., Mullen, S., Tan, T.H., Jung, Y.J., and Cissé, I.I. (2016b). Super-resolution imaging of fluorescently labeled, endogenous RNA Polymerase II in living cells with CRISPR/Cas9-mediated gene editing. *Scientific Reports* 6, 35949. 10.1038/srep35949.

Cho, W.K., Spille, J.H., Hecht, M., Lee, C., Li, C., Grube, V., and Cisse, I.I. (2018). Mediator and RNA polymerase II clusters associate in transcription-dependent condensates. *Science* 361, 412-415. 10.1126/science.aar4199.

Choi, J.M., Holehouse, A.S., and Pappu, R.V. (2020). Physical Principles Underlying the Complex Biology of Intracellular Phase Transitions. *Annu Rev Biophys* 49, 107-133. 10.1146/annurev-biophys-121219-081629.

Chopra, V.S., Hong, J.W., and Levine, M. (2009). Regulation of Hox gene activity by transcriptional elongation in *Drosophila*. *Current biology : CB* 19, 688-693. 10.1016/j.cub.2009.02.055.

Choquet, D., Felsenfeld, D.P., and Sheetz, M.P. (1997). Extracellular Matrix Rigidity Causes Strengthening of Integrin Cytoskeleton Linkages. *Cell* 88, 39-48. 10.1016/S0092-8674(00)81856-5.

Chuang, C.H., Carpenter, A.E., Fuchsova, B., Johnson, T., de Lanerolle, P., and Belmont, A.S. (2006). Long-range directional movement of an interphase chromosome site. *Current biology : CB* 16, 825-831. 10.1016/j.cub.2006.03.059.

Ciani, B., Bjelić, S., Honnappa, S., Jawhari, H., Jaussi, R., Payapilly, A., Jowitt, T., Steinmetz, M.O., and Kammerer, R.A. (2010). Molecular basis of coiled-coil oligomerization-state specificity. *Proceedings of the National Academy of Sciences* 107, 19850. 10.1073/pnas.1008502107.

Cisse, I.I., Izeddin, I., Causse, S.Z., Boudarene, L., Senecal, A., Muresan, L., Dugast-Darzacq, C., Hajj, B., Dahan, M., and Darzacq, X. (2013). Real-Time Dynamics of RNA Polymerase II Clustering in Live Human Cells. *Science* 341, 664. 10.1126/science.1239053.

Clapier, C.R., and Cairns, B.R. (2009). The Biology of Chromatin Remodeling Complexes. *Annual Review of Biochemistry* 78, 273-304. 10.1146/annurev.biochem.77.062706.153223.

Cleaver, J.E. (1977). Nucleosome structure controls rates of excision repair in DNA of human cells. *Nature* 270, 451-453. 10.1038/270451a0.

Clouaire, T., Rocher, V., Lashgari, A., Arnould, C., Aguirrebengoa, M., Biernacka, A., Skrzypczak, M., Aymard, F., Fongang, B., Dojer, N., et al. (2018). Comprehensive Mapping of Histone Modifications at DNA Double-Strand Breaks Deciphers Repair Pathway Chromatin Signatures. *Molecular cell* 72, 250-262.e256. 10.1016/j.molcel.2018.08.020.

Coffinier, C., Jung, H.-J., Nobumori, C., Chang, S., Tu, Y., Barnes, R.H., Yoshinaga, Y., de Jong, P.J., Vergnes, L., Reue, K., et al. (2011). Deficiencies in lamin B1 and lamin B2 cause neurodevelopmental defects and distinct nuclear shape abnormalities in neurons. *Molecular Biology of the Cell* 22, 4683-4693. 10.1091/mbc.e11-06-0504.

Connelly, S., and Manley, J.L. (1988). A functional mRNA polyadenylation signal is required for transcription termination by RNA polymerase II. *Genes Dev* 2, 440-452. 10.1101/gad.2.4.440.

Cook, A.W., Gough, R.E., and Toseland, C.P. (2020). Nuclear myosins – roles for molecular transporters and anchors. *Journal of Cell Science* 133. 10.1242/jcs.242420.

Cook, A.W., and Toseland, C.P. (2021). The roles of nuclear myosin in the DNA damage response. *Journal of biochemistry* 169, 265-271. 10.1093/jb/mvaa113.

Cook, P.R. (1999). The organization of replication and transcription. *Science* 284, 1790-1795. 10.1126/science.284.5421.1790.

Corden, J.L., Cadena, D.L., Ahearn, J.M., Jr., and Dahmus, M.E. (1985). A unique structure at the carboxyl terminus of the largest subunit of eukaryotic RNA polymerase II. *Proc Natl Acad Sci U S A* 82, 7934-7938. 10.1073/pnas.82.23.7934.

Cramer, L.P. (2000). Myosin VI: Roles for a minus End-Directed Actin Motor in Cells. *Journal of Cell Biology* 150, F121-F126. 10.1083/jcb.150.6.F121.

Creyghton, M.P., Cheng, A.W., Welstead, G.G., Kooistra, T., Carey, B.W., Steine, E.J., Hanna, J., Lodato, M.A., Frampton, G.M., Sharp, P.A., et al. (2010). Histone H3K27ac separates active from poised enhancers and predicts developmental state. *Proceedings of the National Academy of Sciences* 107, 21931. 10.1073/pnas.1016071107.

Crisp, M., Liu, Q., Roux, K., Rattner, J.B., Shanahan, C., Burke, B., Stahl, P.D., and Hodzic, D. (2005). Coupling of the nucleus and cytoplasm: Role of the LINC complex. *Journal of Cell Biology* 172, 41-53. 10.1083/jcb.200509124.

Crosetto, N., and Bienko, M. (2020). Radial Organization in the Mammalian Nucleus. *Frontiers in genetics* 11. 10.3389/fgene.2020.00033.

Curtis, A.S. (1964). THE MECHANISM OF ADHESION OF CELLS TO GLASS. A STUDY BY INTERFERENCE REFLECTION MICROSCOPY. *J Cell Biol* 20, 199-215. 10.1083/jcb.20.2.199.

d'Adda di Fagagna, F. (2008). Living on a break: cellular senescence as a DNA-damage response. *Nat Rev Cancer* 8, 512-522. 10.1038/nrc2440.

Dahl, K.N., Engler, A.J., Pajerowski, J.D., and Discher, D.E. (2005). Power-Law Rheology of Isolated Nuclei with Deformation Mapping of Nuclear Substructures. *Biophysical Journal* 89, 2855-2864. 10.1529/biophysj.105.062554.

Dahl, K.N., Ribeiro, A.J.S., and Lammerding, J. (2008). Nuclear Shape, Mechanics, and Mechanotransduction. *Circulation Research* 102, 1307-1318. 10.1161/CIRCRESAHA.108.173989.

Dahl, K.N., Scaffidi, P., Islam, M.F., Yodh, A.G., Wilson, K.L., and Misteli, T. (2006). Distinct structural and mechanical properties of the nuclear lamina in Hutchinson–Gilford progeria syndrome. *Proceedings of the National Academy of Sciences U.S.A* 103, 10271. 10.1073/pnas.0601058103.

Darzacq, X., Shav-Tal, Y., de Turris, V., Brody, Y., Shenoy, S.M., Phair, R.D., and Singer, R.H. (2007). In vivo dynamics of RNA polymerase II transcription. *Nature Structural & Molecular Biology* 14, 796-806. 10.1038/nsmb1280.

Das, A., Fischer, R.S., Pan, D., and Waterman, C.M. (2016). YAP Nuclear Localization in the Absence of Cell-Cell Contact Is Mediated by a Filamentous Actin-dependent, Myosin II- and Phospho-YAP-independent Pathway during Extracellular Matrix Mechanosensing. *The Journal of biological chemistry* 291, 6096-6110. 10.1074/jbc.M115.708313.

Dechassa, M.L., Sabri, A., Pondugula, S., Kassabov, S.R., Chatterjee, N., Kladde, M.P., and Bartholomew, B. (2010). SWI/SNF has intrinsic nucleosome disassembly activity that is dependent on adjacent nucleosomes. *Molecular cell* 38, 590-602. 10.1016/j.molcel.2010.02.040.

Decker, C.J., and Parker, R. (2012). P-bodies and stress granules: possible roles in the control of translation and mRNA degradation. *Cold Spring Harbor perspectives in biology* 4, a012286. 10.1101/cshperspect.a012286.

Dellino, G.I., Schwartz, Y.B., Farkas, G., McCabe, D., Elgin, S.C., and Pirrotta, V. (2004). Polycomb silencing blocks transcription initiation. *Molecular cell* 13, 887-893. 10.1016/s1097-2765(04)00128-5.

Denais, C.M., Gilbert, R.M., Isermann, P., McGregor, A.L., te Lindert, M., Weigel, B., Davidson, P.M., Friedl, P., Wolf, K., and Lammerding, J. (2016). Nuclear envelope rupture and repair during cancer cell migration. *Science* 352, 353-358. 10.1126/science.aad7297.

Deweese, J.E., and Osheroff, N. (2009). The DNA cleavage reaction of topoisomerase II: wolf in sheep's clothing. *Nucleic Acids Research* 37, 738-748. 10.1093/nar/gkn937.

Dietrich, C., Yang, B., Fujiwara, T., Kusumi, A., and Jacobson, K. (2002). Relationship of Lipid Rafts to Transient Confinement Zones Detected by Single Particle Tracking. *Biophysical Journal* 82, 274-284. [https://doi.org/10.1016/S0006-3495\(02\)75393-9](https://doi.org/10.1016/S0006-3495(02)75393-9).

Dittmer, T.A., and Misteli, T. (2011). The lamin protein family. *Genome Biology* 12, 222. 10.1186/gb-2011-12-5-222.

Dixon, J.R., Selvaraj, S., Yue, F., Kim, A., Li, Y., Shen, Y., Hu, M., Liu, J.S., and Ren, B. (2012). Topological domains in mammalian genomes identified by analysis of chromatin interactions. *Nature* 485, 376-380. 10.1038/nature11082.

Dong, X., and Weng, Z. (2013). The correlation between histone modifications and gene expression. *Epigenomics* 5, 113-116. 10.2217/epi.13.13.

Dopie, J., Skarp, K.-P., Kaisa Rajakylä, E., Tanhuanpää, K., and Vartiainen, M.K. (2012). Active maintenance of nuclear actin by importin 9 supports transcription. *Proceedings of the National Academy of Sciences* 109, E544. 10.1073/pnas.1118880109.

dos Santos, Á., Cook, A.W., Gough, R.E., Schilling, M., Olszok, Nora A., Brown, I., Wang, L., Aaron, J., Martin-Fernandez, M.L., Rehfeldt, F., and Toseland, C.P. (2021). DNA damage alters nuclear mechanics through chromatin reorganization. *Nucleic Acids Research* 49, 340-353. 10.1093/nar/gkaa1202.

dos Santos, Á., Fili, N., Hari-Gupta, Y., Gough, R.E., Wang, L., Martin-Fernandez, M., Aaron, J., Waite, E., Chew, T.-L., and Toseland, C.P. (2020). Binding partners regulate unfolding of myosin VI to activate the molecular motor. *bioRxiv*, 2020.2005.2010.079236. 10.1101/2020.05.10.079236.

dos Santos, Á., Rehfeldt, F., and Toseland, C.P. (In press). Measuring nuclear mechanics with Atomic Force Microscopy. *Methods in molecular biology* (Clifton, N.J.).

dos Santos, Á., Rollins, D.E., Hari-Gupta, Y., Reed, H.C.W., Du, M., Ru, S.Y.Z., Pidlisna, K., Stranger, A., Lorgat, F., Brown, I., et al. (2022). Autophagy receptor NDP52 alters DNA conformation to modulate RNA Polymerase II transcription. *bioRxiv*, 2022.2002.2001.478690. 10.1101/2022.02.01.478690.

dos Santos, Á., and Toseland, C.P. (2021). Regulation of Nuclear Mechanics and the Impact on DNA Damage. *International journal of molecular sciences* 22. 10.3390/ijms22063178.

Doss Bryant, L., Pan, M., Gupta, M., Greci, G., Mège, R.-M., Lim Chwee, T., Sheetz Michael, P., Voituriez, R., and Ladoux, B. (2020). Cell response to substrate rigidity is regulated by active and passive cytoskeletal stress. *Proceedings of the National Academy of Sciences* 117, 12817-12825. 10.1073/pnas.1917555117.

Driscoll, T.P., Cosgrove, B.D., Heo, S.J., Shurden, Z.E., and Mauck, R.L. (2015). Cytoskeletal to Nuclear Strain Transfer Regulates YAP Signaling in Mesenchymal Stem Cells. *Biophys J* 108, 2783-2793. 10.1016/j.bpj.2015.05.010.

Dunn, T.A., Chen, S., Faith, D.A., Hicks, J.L., Platz, E.A., Chen, Y., Ewing, C.M., Sauvageot, J., Isaacs, W.B., De Marzo, A.M., and Luo, J. (2006). A novel role of myosin VI in human prostate cancer. *Am J Pathol* 169, 1843-1854. 10.2353/ajpath.2006.060316.

Dunne, B., and Going, J.J. (2001). Scoring nuclear pleomorphism in breast cancer. *Histopathology* 39, 259-265. <https://doi.org/10.1046/j.1365-2559.2001.01220.x>.

Eberharter, A., and Becker, P.B. (2004). ATP-dependent nucleosome remodelling: factors and functions. *Journal of Cell Science* 117, 3707-3711. 10.1242/jcs.01175.

Edens, L.J., White, K.H., Jevtic, P., Li, X., and Levy, D.L. (2013). Nuclear size regulation: from single cells to development and disease. *Trends Cell Biol* 23, 151-159. 10.1016/j.tcb.2012.11.004.

Egloff, S., and Murphy, S. (2008). Cracking the RNA polymerase II CTD code. *Trends in Genetics* 24, 280-288. <https://doi.org/10.1016/j.tig.2008.03.008>.

Eichstaedt, K.E., Kovatch, K., and Maroof, D.A. (2013). A less conservative method to adjust for familywise error rate in neuropsychological research: the Holm's sequential Bonferroni procedure. *NeuroRehabilitation* 32, 693-696. 10.3233/nre-130893.

Ellinghaus, D., Zhang, H., Zeissig, S., Lipinski, S., Till, A., Jiang, T., Stade, B., Bromberg, Y., Ellinghaus, E., Keller, A., et al. (2013). Association between variants of PRDM1 and NDP52 and Crohn's disease, based on exome sequencing and functional studies. *Gastroenterology* 145, 339-347. 10.1053/j.gastro.2013.04.040.

Elosegui-Artola, A., Andreu, I., Beedle, A.E.M., Lezamiz, A., Uroz, M., Kosmalska, A.J., Oria, R., Kechagia, J.Z., Rico-Lastres, P., Le Roux, A.-L., et al. (2017). Force Triggers YAP Nuclear Entry by Regulating Transport across Nuclear Pores. *Cell* 171, 1397-1410.e1314. 10.1016/j.cell.2017.10.008.

Endesfelder, U., and Heilemann, M. (2015). Direct stochastic optical reconstruction microscopy (dSTORM). *Methods in molecular biology* (Clifton, N.J.) 1251, 263-276. 10.1007/978-1-4939-2080-8_14.

Engler, A.J., Rehfeldt, F., Sen, S., and Discher, D.E. (2007). Microtissue elasticity: measurements by atomic force microscopy and its influence on cell differentiation. *Methods Cell Biol* 83, 521-545. 10.1016/s0091-679x(07)83022-6.

Ester, M., Kriegel, H.-P., Sander, J., and Xu, X. (1996). A density-based algorithm for discovering clusters in large spatial databases with noise. *Proceedings of the Second International Conference on Knowledge Discovery and Data Mining*. AAAI Press.

Fernandez, A., Bautista, M., Wu, L., and Pinaud, F. (2022). Emerin self-assembly and nucleoskeletal coupling regulate nuclear envelope mechanics against stress. *bioRxiv*, 2021.2002.2012.429834. 10.1101/2021.02.12.429834.

Fernandez-Capetillo, O., Chen, H.T., Celeste, A., Ward, I., Romanienko, P.J., Morales, J.C., Naka, K., Xia, Z., Camerini-Otero, R.D., Motoyama, N., et al. (2002). DNA damage-induced G2-M checkpoint activation by histone H2AX and 53BP1. *Nat Cell Biol* 4, 993-997. 10.1038/ncb884.

Ferrera, D., Canale, C., Marotta, R., Mazzaro, N., Gritti, M., Mazzanti, M., Capellari, S., Cortelli, P., and Gasparini, L. (2014). Lamin B1 overexpression increases nuclear rigidity in autosomal dominant leukodystrophy fibroblasts. *The FASEB Journal* 28, 3906-3918. <https://doi.org/10.1096/fj.13-247635>.

Fili, N., Hari-Gupta, Y., Aston, B., Dos Santos, Á., Gough, R.E., Alamad, B., Wang, L., Martin-Fernandez, M.L., and Toseland, C.P. (2020). Competition between two high- and low-affinity protein-binding sites in myosin VI controls its cellular function. *The Journal of biological chemistry* 295, 337-347. 10.1074/jbc.RA119.010142.

Fili, N., Hari-Gupta, Y., Dos Santos, Á., Cook, A., Poland, S., Ameer-Beg, S.M., Parsons, M., and Toseland, C.P. (2017). NDP52 activates nuclear myosin VI to enhance RNA polymerase II transcription. *Nat Commun* 8, 1871. 10.1038/s41467-017-02050-w.

Fili, N., and Toseland, C.P. (2019). Unconventional Myosins: How Regulation Meets Function. *International journal of molecular sciences* 21. 10.3390/ijms21010067.

Flaim, C.J., Chien, S., and Bhatia, S.N. (2005). An extracellular matrix microarray for probing cellular differentiation. *Nature methods* 2, 119-125. 10.1038/nmeth736.

Fomproix, N., and Percipalle, P. (2004). An actin-myosin complex on actively transcribing genes. *Exp Cell Res* 294, 140-148. 10.1016/j.yexcr.2003.10.028.

Fornasiero, E.F., and Opazo, F. (2015). Super-resolution imaging for cell biologists. *BioEssays* 37, 436-451. <https://doi.org/10.1002/bies.201400170>.

Fortuny, A., Chansard, A., Caron, P., Chevallier, O., Leroy, O., Renaud, O., and Polo, S.E. (2021). Imaging the response to DNA damage in heterochromatin domains reveals core principles of heterochromatin maintenance. *Nature Communications* 12, 2428. 10.1038/s41467-021-22575-5.

Frank, D.J., Noguchi, T., and Miller, K.G. (2004). Myosin VI: a structural role in actin organization important for protein and organelle localization and trafficking. *Current Opinion in Cell Biology* 16, 189-194. <https://doi.org/10.1016/j.ceb.2004.02.001>.

Frank, F., Liu, X., and Ortlund, E.A. (2021). Glucocorticoid receptor condensates link DNA-dependent receptor dimerization and transcriptional transactivation. *Proceedings of the National Academy of Sciences* 118, e2024685118. 10.1073/pnas.2024685118.

Fritzsche, M., Li, D., Colin-York, H., Chang, V.T., Moeendarbary, E., Felce, J.H., Sezgin, E., Charras, G., Betzig, E., and Eggeling, C. (2017). Self-organizing actin patterns shape membrane architecture but not cell mechanics. *Nature Communications* 8, 14347. 10.1038/ncomms14347.

Fu, T., Liu, J., Wang, Y., Xie, X., Hu, S., and Pan, L. (2018). Mechanistic insights into the interactions of NAP1 with the SKICH domains of NDP52 and TAX1BP1. *Proceedings of the National Academy of Sciences* 115, E11651. 10.1073/pnas.1811421115.

Funsten, J.R., Murillo Brizuela, K.O., Swatzel, H.E., Ward, A.S., Scott, T.A., Eikenbusch, S.M., Shields, M.C., Meredith, J.L., Mitchell, T.Y., Hanna, M.L., et al. (2020). PKC signaling contributes to chromatin decondensation and is required for competence to respond to IL-2 during T cell activation. *Cell Immunol* 347, 104027. 10.1016/j.cellimm.2019.104027.

Furusawa, T., Rochman, M., Taher, L., Dimitriadis, E.K., Nagashima, K., Anderson, S., and Bustin, M. (2015). Chromatin decompaction by the nucleosomal binding protein HMG5 impairs nuclear sturdiness. *Nature Communications* 6, 6138. 10.1038/ncomms7138.

Gebhardt, J.C., Suter, D.M., Roy, R., Zhao, Z.W., Chapman, A.R., Basu, S., Maniatis, T., and Xie, X.S. (2013). Single-molecule imaging of transcription factor binding to DNA in live mammalian cells. *Nature methods* 10, 421-426. 10.1038/nmeth.2411.

Granger, E., McNee, G., Allan, V., and Woodman, P. (2014). The role of the cytoskeleton and molecular motors in endosomal dynamics. *Semin Cell Dev Biol* 31, 20-29. 10.1016/j.semdb.2014.04.011.

Grimm, J.B., English, B.P., Chen, J., Slaughter, J.P., Zhang, Z., Revyakin, A., Patel, R., Macklin, J.J., Normanno, D., Singer, R.H., et al. (2015). A general method to improve fluorophores for live-cell and single-molecule microscopy. *Nature methods* 12, 244-250, 243 p following 250. 10.1038/nmeth.3256.

Große-Berkenbusch, A., Hettich, J., Kuhn, T., Fili, N., Cook, A.W., Hari-Gupta, Y., Palmer, A., Streit, L., Ellis, P.J.I., Toseland, C.P., and Gebhardt, J.C.M. (2020). Myosin VI moves on nuclear actin filaments

and supports long-range chromatin rearrangements. *bioRxiv*, 2020.2004.2003.023614. 10.1101/2020.04.03.023614.

Guilluy, C., Osborne, L.D., Van Landeghem, L., Sharek, L., Superfine, R., Garcia-Mata, R., and Burrige, K. (2014). Isolated nuclei adapt to force and reveal a mechanotransduction pathway in the nucleus. *Nature Cell Biology* 16, 376-381. 10.1038/ncb2927.

Guo, Y.E., Manteiga, J.C., Henninger, J.E., Sabari, B.R., Dall’Agnese, A., Hannett, N.M., Spille, J.-H., Afeyan, L.K., Zamudio, A.V., Shrinivas, K., et al. (2019). Pol II phosphorylation regulates a switch between transcriptional and splicing condensates. *Nature* 572, 543-548. 10.1038/s41586-019-1464-0.

Gurung, R., Tan, A., Ooms, L.M., McGrath, M.J., Huysmans, R.D., Munday, A.D., Prescott, M., Whisstock, J.C., and Mitchell, C.A. (2003). Identification of a novel domain in two mammalian inositol-polyphosphate 5-phosphatases that mediates membrane ruffle localization. The inositol 5-phosphatase skip localizes to the endoplasmic reticulum and translocates to membrane ruffles following epidermal growth factor stimulation. *The Journal of biological chemistry* 278, 11376-11385. 10.1074/jbc.M209991200.

Ha, T., and Tinnefeld, P. (2012). Photophysics of fluorescent probes for single-molecule biophysics and super-resolution imaging. *Annu Rev Phys Chem* 63, 595-617. 10.1146/annurev-physchem-032210-103340.

Han, Y., Reyes, A.A., Malik, S., and He, Y. (2020). Cryo-EM structure of SWI/SNF complex bound to a nucleosome. *Nature* 579, 452-455. 10.1038/s41586-020-2087-1.

Harada, Y., Funatsu, T., Murakami, K., Nonoyama, Y., Ishihama, A., and Yanagida, T. (1999). Single-Molecule Imaging of RNA Polymerase-DNA Interactions in Real Time. *Biophysical Journal* 76, 709-715. [https://doi.org/10.1016/S0006-3495\(99\)77237-1](https://doi.org/10.1016/S0006-3495(99)77237-1).

Hari-Gupta, Y., Fili, N., dos Santos, Á., Cook, A.W., Gough, R.E., Reed, H.C.W., Wang, L., Aaron, J., Venit, T., Wait, E., et al. (2020). Nuclear myosin VI regulates the spatial organization of mammalian transcription initiation. *bioRxiv*, 2020.2004.2021.053124. 10.1101/2020.04.21.053124.

Hashiguchi, K., Matsumoto, Y., and Yasui, A. (2007). Recruitment of DNA repair synthesis machinery to sites of DNA damage/repair in living human cells. *Nucleic acids research* 35, 2913-2923. 10.1093/nar/gkm115.

Hatch, E.M., and Hetzer, M.W. (2016). Nuclear envelope rupture is induced by actin-based nucleus confinement. *Journal of Cell Biology* 215, 27-36. 10.1083/jcb.201603053.

Hauer, M.H., and Gasser, S.M. (2017). Chromatin and nucleosome dynamics in DNA damage and repair. *Genes & Development* 31, 2204-2221.

Hauer, M.H., Seeber, A., Singh, V., Thierry, R., Sack, R., Amitai, A., Kryzhanovska, M., Eglinger, J., Holcman, D., Owen-Hughes, T., and Gasser, S.M. (2017). Histone degradation in response to DNA damage enhances chromatin dynamics and recombination rates. *Nature Structural & Molecular Biology* 24, 99-107. 10.1038/nsmb.3347.

Hayashi, M.T., and Masukata, H. (2011). Regulation of DNA replication by chromatin structures: accessibility and recruitment. *Chromosoma* 120, 39-46. 10.1007/s00412-010-0287-4.

He, J., Smith, E.R., and Xu, X.-X. (2001). Disabled-2 Exerts Its Tumor Suppressor Activity by Uncoupling c-Fos Expression and MAP Kinase Activation*. *Journal of Biological Chemistry* 276, 26814-26818. <https://doi.org/10.1074/jbc.M101820200>.

Heintzman, N.D., Stuart, R.K., Hon, G., Fu, Y., Ching, C.W., Hawkins, R.D., Barrera, L.O., Van Calcar, S., Qu, C., Ching, K.A., et al. (2007). Distinct and predictive chromatin signatures of transcriptional promoters and enhancers in the human genome. *Nature Genetics* 39, 311-318. 10.1038/ng1966.

Heintzmann, R., and Gustafsson, M.G.L. (2009). Subdiffraction resolution in continuous samples. *Nature Photonics* 3, 362-364. 10.1038/nphoton.2009.102.

Hell Stefan, W. (2007). Far-Field Optical Nanoscopy. *Science* 316, 1153-1158. 10.1126/science.1137395.

Hell, S.W., Schmidt, R., and Egner, A. (2009). Diffraction-unlimited three-dimensional optical nanoscopy with opposing lenses. *Nature Photonics* 3, 381-387. 10.1038/nphoton.2009.112.

Henriques, R., Griffiths, C., Hesper Rego, E., and Mhlanga, M.M. (2011). PALM and STORM: unlocking live-cell super-resolution. *Biopolymers* 95, 322-331. 10.1002/bip.21586.

Heo, S.-J., Cosgrove, B.D., Dai, E.N., and Mauck, R.L. (2018). Mechano-adaptation of the stem cell nucleus. *Nucleus* 9, 9-19. 10.1080/19491034.2017.1371398.

Herráez-Aguilar, D., Madrazo, E., López-Menéndez, H., Ramírez, M., Monroy, F., and Redondo-Muñoz, J. (2020). Multiple particle tracking analysis in isolated nuclei reveals the mechanical phenotype of leukemia cells. *Scientific Reports* 10, 6707. 10.1038/s41598-020-63682-5.

Hertz, H. (1882). Ueber die Berührung fester elastischer Körper. 1882, 156-171. doi:10.1515/crll.1882.92.156.

Hess, S.T., Girirajan, T.P.K., and Mason, M.D. (2006). Ultra-High Resolution Imaging by Fluorescence Photoactivation Localization Microscopy. *Biophysical Journal* 91, 4258-4272. <https://doi.org/10.1529/biophysj.106.091116>.

Hinde, E., Pandžić, E., Yang, Z., Ng, I.H.W., Jans, D.A., Bogoyevitch, M.A., Gratton, E., and Gaus, K. (2016). Quantifying the dynamics of the oligomeric transcription factor STAT3 by pair correlation of molecular brightness. *Nature Communications* 7, 11047. 10.1038/ncomms11047.

Hnisz, D., Shrinivas, K., Young, R.A., Chakraborty, A.K., and Sharp, P.A. (2017). A Phase Separation Model for Transcriptional Control. *Cell* 169, 13-23. <https://doi.org/10.1016/j.cell.2017.02.007>.

Hobson, C.M., Kern, M., O'Brien, E.T., Stephens, A.D., Falvo, M.R., and Superfine, R. (2020). Correlating nuclear morphology and external force with combined atomic force microscopy and light sheet imaging separates roles of chromatin and lamin A/C in nuclear mechanics. *Molecular Biology of the Cell* 31, 1788-1801. 10.1091/mbc.E20-01-0073.

Hofmann, W.A., Stojiljkovic, L., Fuchsova, B., Vargas, G.M., Mavrommatis, E., Philimonenko, V., Kysela, K., Goodrich, J.A., Lessard, J.L., Hope, T.J., et al. (2004). Actin is part of pre-initiation complexes and is necessary for transcription by RNA polymerase II. *Nat Cell Biol* 6, 1094-1101. 10.1038/ncb1182.

Holmes, K.C., Popp, D., Gebhard, W., and Kabsch, W. (1990). Atomic model of the actin filament. *Nature* 347, 44-49. 10.1038/347044a0.

Hoogenboom, J.P., van Dijk, E., Hernando, J., van Hulst, N.F., and Garcia-Parajo, M.F. (2005). Power-law-distributed dark states are the main pathway for photobleaching of single organic molecules. *Physical review letters* 95 9, 097401.

Horigome, C., Oma, Y., Konishi, T., Schmid, R., Marcomini, I., Hauer, Michael H., Dion, V., Harata, M., and Gasser, Susan M. (2014). SWR1 and INO80 Chromatin Remodelers Contribute to DNA Double-Strand Break Perinuclear Anchorage Site Choice. *Molecular cell* 55, 626-639. <https://doi.org/10.1016/j.molcel.2014.06.027>.

House, N.C., Koch, M.R., and Freudenreich, C.H. (2014). Chromatin modifications and DNA repair: beyond double-strand breaks. *Frontiers in genetics* 5, 296. 10.3389/fgene.2014.00296.

Hsin, J.-P., and Manley, J.L. (2012). The RNA polymerase II CTD coordinates transcription and RNA processing. *Genes & development* 26, 2119-2137. 10.1101/gad.200303.112.

Hu, P., Wu, S., and Hernandez, N. (2004). A role for beta-actin in RNA polymerase III transcription. *Genes & development* 18, 3010-3015. 10.1101/gad.1250804.

Hu, X., Liu, Z.Z., Chen, X., Schulz, V.P., Kumar, A., Hartman, A.A., Weinstein, J., Johnston, J.F., Rodriguez, E.C., Eastman, A.E., et al. (2019). MKL1-actin pathway restricts chromatin accessibility and prevents mature pluripotency activation. *Nature Communications* 10, 1695. 10.1038/s41467-019-09636-6.

Huang, B., Bates, M., and Zhuang, X. (2009). Super-Resolution Fluorescence Microscopy. *Annual Review of Biochemistry* 78, 993-1016. 10.1146/annurev.biochem.77.061906.092014.

Hutter, J.L., and Bechhoefer, J. (1993). Calibration of atomic-force microscope tips. *Review of Scientific Instruments* 64, 1868-1873. 10.1063/1.1143970.

Hynes, R.O., and Lander, A.D. (1992). Contact and adhesive specificities in the associations, migrations, and targeting of cells and axons. *Cell* 68, 303-322. 10.1016/0092-8674(92)90472-o.

Imbalzano, A.N., Kwon, H., Green, M.R., and Kingston, R.E. (1994). Facilitated binding of TATA-binding protein to nucleosomal DNA. *Nature* 370, 481-485. 10.1038/370481a0.

Irianto, J., Pfeifer, C.R., Bennett, R.R., Xia, Y., Ivanovska, I.L., Liu, A.J., Greenberg, R.A., and Discher, D.E. (2016). Nuclear constriction segregates mobile nuclear proteins away from chromatin. *Mol Biol Cell* 27, 4011-4020. 10.1091/mbc.E16-06-0428.

Iwafuchi-Doi, M., and Zaret, K.S. (2016). Cell fate control by pioneer transcription factors. *Development* 143, 1833-1837. 10.1242/dev.133900.

Izzard, C.S., and Lochner, L.R. (1976). Cell-to-substrate contacts in living fibroblasts: an interference reflexion study with an evaluation of the technique. *J Cell Sci* 21, 129-159. 10.1242/jcs.21.1.129.

Jackson, D.A., Hassan, A.B., Errington, R.J., and Cook, P.R. (1993). Visualization of focal sites of transcription within human nuclei. *The EMBO Journal* 12, 1059-1065. <https://doi.org/10.1002/j.1460-2075.1993.tb05747.x>.

Jackson, S.P., and Bartek, J. (2009). The DNA-damage response in human biology and disease. *Nature* 461, 1071-1078. 10.1038/nature08467.

Jain, N., Iyer, K.V., Kumar, A., and Shivashankar, G.V. (2013). Cell geometric constraints induce modular gene-expression patterns via redistribution of HDAC3 regulated by actomyosin contractility. *Proceedings of the National Academy of Sciences U.S.A.*, 201300801. 10.1073/pnas.1300801110.

Jawerth, L.M., Ijavi, M., Ruer, M., Saha, S., Jahnel, M., Hyman, A.A., Jülicher, F., and Fischer-Friedrich, E. (2018). Salt-Dependent Rheology and Surface Tension of Protein Condensates Using Optical Traps. *Physical Review Letters* 121, 258101. 10.1103/PhysRevLett.121.258101.

Jha, D.K., and Strahl, B.D. (2014). An RNA polymerase II-coupled function for histone H3K36 methylation in checkpoint activation and DSB repair. *Nature Communications* 5, 3965. 10.1038/ncomms4965.

Johnson, H.E., King, S.J., Asokan, S.B., Rotty, J.D., Bear, J.E., and Haugh, J.M. (2015). F-actin bundles direct the initiation and orientation of lamellipodia through adhesion-based signaling. *Journal of Cell Biology* 208, 443-455. 10.1083/jcb.201406102.

Jovtchev, G., Schubert, V., Meister, A., Barow, M., and Schubert, I. (2006). Nuclear DNA content and nuclear and cell volume are positively correlated in angiosperms. *Cytogenet Genome Res* 114, 77-82. 10.1159/000091932.

Kalousi, A., and Soutoglou, E. (2016). Nuclear compartmentalization of DNA repair. *Current Opinion in Genetics & Development* 37, 148-157. <https://doi.org/10.1016/j.gde.2016.05.013>.

Kapoor, P., and Shen, X. (2014). Mechanisms of nuclear actin in chromatin-remodeling complexes. *Trends Cell Biol* 24, 238-246. 10.1016/j.tcb.2013.10.007.

Katzenellenbogen, J.A., and Katzenellenbogen, B.S. (1996). Nuclear hormone receptors: ligand-activated regulators of transcription and diverse cell responses. *Chemistry & biology* 3, 529-536. 10.1016/s1074-5521(96)90143-x.

Kelly, W.G., Dahmus, M.E., and Hart, G.W. (1993). RNA polymerase II is a glycoprotein. Modification of the COOH-terminal domain by O-GlcNAc. *The Journal of biological chemistry* 268, 10416-10424.

Keppler, A., Gendreizig, S., Gronemeyer, T., Pick, H., Vogel, H., and Johnsson, K. (2003). A general method for the covalent labeling of fusion proteins with small molecules in vivo. *Nat Biotechnol* 21, 86-89. 10.1038/nbt765.

Khadaroo, B., Teixeira, M.T., Luciano, P., Eckert-Boulet, N., Germann, S.M., Simon, M.N., Gallina, I., Abdallah, P., Gilson, E., Géli, V., and Lisby, M. (2009). The DNA damage response at eroded telomeres and tethering to the nuclear pore complex. *Nature Cell Biology* 11, 980-987. 10.1038/ncb1910.

Kidiyoor, G.R., Li, Q., Bastianello, G., Bruhn, C., Giovannetti, I., Mohamood, A., Beznoussenko, G.V., Mironov, A., Raab, M., Piel, M., et al. (2020). ATR is essential for preservation of cell mechanics and nuclear integrity during interstitial migration. *Nature Communications* 11, 4828. 10.1038/s41467-020-18580-9.

Kim, B.-W., Beom Hong, S., Hoe Kim, J., Hoon Kwon, D., and Kyu Song, H. (2013a). Structural basis for recognition of autophagic receptor NDP52 by the sugar receptor galectin-8. *Nature Communications* 4, 1613. 10.1038/ncomms2606.

Kim, B.-W., Jung, Y.O., Kim, M.K., Kwon, D.H., Park, S.H., Kim, J.H., Kuk, Y.-B., Oh, S.-J., Kim, L., Kim, B.H., et al. (2017). ACCORD: an assessment tool to determine the orientation of homodimeric coiled-coils. *Scientific Reports* 7, 43318. 10.1038/srep43318.

Kim, B.W., Hong, S.B., Kim, J.H., Kwon, D.H., and Song, H.K. (2013b). Structural basis for recognition of autophagic receptor NDP52 by the sugar receptor galectin-8. *Nat Commun* 4, 1613. 10.1038/ncomms2606.

Kim, D.-H., Khatau, S.B., Feng, Y., Walcott, S., Sun, S.X., Longmore, G.D., and Wirtz, D. (2012). Actin cap associated focal adhesions and their distinct role in cellular mechanosensing. *Scientific Reports* 2, 555. 10.1038/srep00555.

Kim, J., Han, K.Y., Khanna, N., Ha, T., and Belmont, A.S. (2019). Nuclear speckle fusion via long-range directional motion regulates speckle morphology after transcriptional inhibition. *J Cell Sci* 132. 10.1242/jcs.226563.

Kim, J.H., Li, H., and Stallcup, M.R. (2003). CoCoA, a Nuclear Receptor Coactivator which Acts through an N-Terminal Activation Domain of p160 Coactivators. *Molecular cell* 12, 1537-1549. [https://doi.org/10.1016/S1097-2765\(03\)00450-7](https://doi.org/10.1016/S1097-2765(03)00450-7).

Kim, J.H., Yang, C.K., and Stallcup, M.R. (2006). Downstream signaling mechanism of the C-terminal activation domain of transcriptional coactivator CoCoA. *Nucleic Acids Res* 34, 2736-2750. 10.1093/nar/gkl361.

Kim, T., and Buratowski, S. (2009). Dimethylation of H3K4 by Set1 recruits the Set3 histone deacetylase complex to 5' transcribed regions. *Cell* 137, 259-272. 10.1016/j.cell.2009.02.045.

Kimura, H., Sugaya, K., and Cook, P.R. (2002). The transcription cycle of RNA polymerase II in living cells. *Journal of Cell Biology* 159, 777-782. 10.1083/jcb.200206019.

Kirby, T.J., and Lammerding, J. (2018). Emerging views of the nucleus as a cellular mechanosensor. *Nature cell biology* 20, 373-381. 10.1038/s41556-018-0038-y.

Kitamura, A., and Kinjo, M. (2018). Determination of diffusion coefficients in live cells using fluorescence recovery after photobleaching with wide-field fluorescence microscopy. *Biophys Physicobiol* 15, 1-7. 10.2142/biophysico.15.0_1.

Klein, E.A., Yin, L., Kothapalli, D., Castagnino, P., Byfield, F.J., Xu, T., Levental, I., Hawthorne, E., Janmey, P.A., and Assoian, R.K. (2009). Cell-cycle control by physiological matrix elasticity and in vivo tissue stiffening. *Current biology : CB* 19, 1511-1518. 10.1016/j.cub.2009.07.069.

Klemm, S.L., Shipony, Z., and Greenleaf, W.J. (2019). Chromatin accessibility and the regulatory epigenome. *Nature Reviews Genetics* 20, 207-220. 10.1038/s41576-018-0089-8.

Klose, R.J., and Bird, A.P. (2006). Genomic DNA methylation: the mark and its mediators. *Trends in biochemical sciences* 31, 89-97. 10.1016/j.tibs.2005.12.008.

Knoll, K.R., Eustermann, S., Niebauer, V., Oberbeckmann, E., Stoehr, G., Schall, K., Tosi, A., Schwarz, M., Buchfellner, A., Korber, P., and Hopfner, K.-P. (2018). The nuclear actin-containing Arp8 module is a linker DNA sensor driving INO80 chromatin remodeling. *Nature Structural & Molecular Biology* 25, 823-832. 10.1038/s41594-018-0115-8.

Kocgozlu, L., Lavalley, P., Koenig, G., Senger, B., Haikel, Y., Schaaf, P., Voegel, J.C., Tenenbaum, H., and Vautier, D. (2010). Selective and uncoupled role of substrate elasticity in the regulation of replication and transcription in epithelial cells. *J Cell Sci* 123, 29-39. 10.1242/jcs.053520.

Komarnitsky, P., Cho, E.J., and Buratowski, S. (2000). Different phosphorylated forms of RNA polymerase II and associated mRNA processing factors during transcription. *Genes Dev* 14, 2452-2460. 10.1101/gad.824700.

Kontomaris, S.V., and Malamou, A. (2020). Hertz model or Oliver & Pharr analysis? Tutorial regarding AFM nanoindentation experiments on biological samples. *Materials Research Express* 7, 033001. 10.1088/2053-1591/ab79ce.

Korioth, F., Gieffers, C., Maul, G.G., and Frey, J. (1995). Molecular characterization of NDP52, a novel protein of the nuclear domain 10, which is redistributed upon virus infection and interferon treatment. *J Cell Biol* 130, 1-13. 10.1083/jcb.130.1.1.

Kornberg, R.D. (1977). Structure of Chromatin. *Annual Review of Biochemistry* 46, 931-954. 10.1146/annurev.bi.46.070177.004435.

Kornberg, R.D. (2005). Mediator and the mechanism of transcriptional activation. *Trends in biochemical sciences* 30, 235-239. 10.1016/j.tibs.2005.03.011.

Koushki, N., Ghagre, A., Srivastava, L.K., Sitaras, C., Yoshie, H., Molter, C., and Ehrlicher, A.J. (2020). Lamin A redistribution mediated by nuclear deformation determines dynamic localization of YAP. *bioRxiv*, 2020.2003.2019.998708. 10.1101/2020.03.19.998708.

Krasnov, A.N., Mazina, M.Y., Nikolenko, J.V., and Vorobyeva, N.E. (2016). On the way of revealing coactivator complexes cross-talk during transcriptional activation. *Cell & Bioscience* 6, 15. 10.1186/s13578-016-0081-y.

Kruhlak, M.J., Celeste, A., Dellaire, G., Fernandez-Capetillo, O., Müller, W.G., McNally, J.G., Bazett-Jones, D.P., and Nussenzweig, A. (2006). Changes in chromatin structure and mobility in living cells at sites of DNA double-strand breaks. *Journal of Cell Biology* 172, 823-834. 10.1083/jcb.200510015.

Krumm, A., Hickey, L.B., and Groudine, M. (1995). Promoter-proximal pausing of RNA polymerase II defines a general rate-limiting step after transcription initiation. *Genes Dev* 9, 559-572. 10.1101/gad.9.5.559.

Krzywinski, M., and Altman, N. (2014). Comparing samples—part II. *Nature methods* 11, 355-356. 10.1038/nmeth.2900.

Kukalev, A., Nord, Y., Palmberg, C., Bergman, T., and Percipalle, P. (2005). Actin and hnRNP U cooperate for productive transcription by RNA polymerase II. *Nat Struct Mol Biol* 12, 238-244. 10.1038/nsmb904.

Kulashreshtha, M., Mehta, I.S., Kumar, P., and Rao, B.J. (2016). Chromosome territory relocation during DNA repair requires nuclear myosin 1 recruitment to chromatin mediated by Y-H2AX signaling. *Nucleic Acids Research* 44, 8272-8291. 10.1093/nar/gkw573.

Kusumi, A., Sako, Y., and Yamamoto, M. (1993). Confined lateral diffusion of membrane receptors as studied by single particle tracking (nanovid microscopy). Effects of calcium-induced differentiation in cultured epithelial cells. *Biophys J* 65, 2021-2040. 10.1016/s0006-3495(93)81253-0.

Laflamme, G., and Mekhail, K. (2020). Biomolecular condensates as arbiters of biochemical reactions inside the nucleus. *Communications Biology* 3, 773. 10.1038/s42003-020-01517-9.

Lafontaine, D.L.J., Riback, J.A., Bascetin, R., and Brangwynne, C.P. (2021). The nucleolus as a multiphase liquid condensate. *Nature Reviews Molecular Cell Biology* 22, 165-182. 10.1038/s41580-020-0272-6.

Lallemant-Breitenbach, V., and de Thé, H. (2010). PML nuclear bodies. *Cold Spring Harbor perspectives in biology* 2, a000661. 10.1101/cshperspect.a000661.

Lam, A.P., and Dean, D.A. (2008). Cyclic stretch-induced nuclear localization of transcription factors results in increased nuclear targeting of plasmids in alveolar epithelial cells. *J Gene Med* 10, 668-678. 10.1002/jgm.1187.

Lamm, N., Read, M.N., Nobis, M., Van Ly, D., Page, S.G., Masamsetti, V.P., Timpson, P., Biro, M., and Cesare, A.J. (2020). Nuclear F-actin counteracts nuclear deformation and promotes fork repair during replication stress. *Nature Cell Biology* 22, 1460-1470. 10.1038/s41556-020-00605-6.

Lammerding, J., Schulze, P.C., Takahashi, T., Kozlov, S., Sullivan, T., Kamm, R.D., Stewart, C.L., and Lee, R.T. (2004). Lamin A/C deficiency causes defective nuclear mechanics and mechanotransduction. *The Journal of clinical investigation* 113, 370-378. 10.1172/jci19670.

Lans, H., Marteiijn, J.A., and Vermeulen, W. (2012). ATP-dependent chromatin remodeling in the DNA-damage response. *Epigenetics & Chromatin* 5, 4. 10.1186/1756-8935-5-4.

Larrieu, D., Britton, S., Demir, M., Rodriguez, R., and Jackson, S.P. (2014). Chemical inhibition of NAT10 corrects defects of laminopathic cells. *Science* 344, 527-532. 10.1126/science.1252651.

Larson, A.G., Elnatan, D., Keenen, M.M., Trnka, M.J., Johnston, J.B., Burlingame, A.L., Agard, D.A., Redding, S., and Narlikar, G.J. (2017). Liquid droplet formation by HP1 α suggests a role for phase separation in heterochromatin. *Nature* 547, 236-240. 10.1038/nature22822.

Larson, D.R., Fritzsche, C., Sun, L., Meng, X., Lawrence, D.S., and Singer, R.H. (2013). Direct observation of frequency modulated transcription in single cells using light activation. *eLife* 2, e00750. 10.7554/eLife.00750.

Lauberth, S.M., Nakayama, T., Wu, X., Ferris, A.L., Tang, Z., Hughes, S.H., and Roeder, R.G. (2013). H3K4me3 interactions with TAF3 regulate preinitiation complex assembly and selective gene activation. *Cell* 152, 1021-1036. 10.1016/j.cell.2013.01.052.

Lauffenburger, D.A., and Horwitz, A.F. (1996). Cell migration: a physically integrated molecular process. *Cell* 84, 359-369. 10.1016/s0092-8674(00)81280-5.

Lawrence, T. (2009). The nuclear factor NF-kappaB pathway in inflammation. *Cold Spring Harbor perspectives in biology* 1, a001651-a001651. 10.1101/cshperspect.a001651.

Leake, M.C. (2018). Transcription factors in eukaryotic cells can functionally regulate gene expression by acting in oligomeric assemblies formed from an intrinsically disordered protein phase transition enabled by molecular crowding. *Transcription* 9, 298-306. 10.1080/21541264.2018.1475806.

Lee, S.K., Fletcher, A.G.L., Zhang, L., Chen, X., Fischbeck, J.A., and Stargell, L.A. (2010). Activation of a Poised RNAPII-Dependent Promoter Requires Both SAGA and Mediator. *Genetics* 184, 659-672. 10.1534/genetics.109.113464.

Lee, Y.H., Kuo, C.Y., Stark, J.M., Shih, H.M., and Ann, D.K. (2013). HP1 promotes tumor suppressor BRCA1 functions during the DNA damage response. *Nucleic Acids Res* 41, 5784-5798. 10.1093/nar/gkt231.

Lees-Miller, S.P., Sakaguchi, K., Ullrich, S.J., Appella, E., and Anderson, C.W. (1992). Human DNA-activated protein kinase phosphorylates serines 15 and 37 in the amino-terminal transactivation domain of human p53. *Molecular and cellular biology* 12, 5041-5049. 10.1128/mcb.12.11.5041-5049.1992.

Lemaître, C., Grabarz, A., Tsouroula, K., Andronov, L., Furst, A., Pankotai, T., Heyer, V., Rogier, M., Attwood, K.M., Kessler, P., et al. (2014). Nuclear position dictates DNA repair pathway choice. *Genes & Development* 28, 2450-2463.

Leno, G.H. (1992). Regulation of DNA replication by the nuclear envelope. *Seminars in Cell Biology* 3, 237-243. [https://doi.org/10.1016/1043-4682\(92\)90025-Q](https://doi.org/10.1016/1043-4682(92)90025-Q).

Levone, B.R., Lenzken, S.C., Antonaci, M., Maiser, A., Rapp, A., Conte, F., Reber, S., Mechttersheimer, J., Ronchi, A.E., Mühlemann, O., et al. (2021). FUS-dependent liquid-liquid phase separation is important for DNA repair initiation. *J Cell Biol* 220. 10.1083/jcb.202008030.

Lherbette, M., dos Santos, Á., Hari-Gupta, Y., Fili, N., Toseland, C.P., and Schaap, I.A.T. (2017). Atomic Force Microscopy micro-rheology reveals large structural inhomogeneities in single cell-nuclei. *Scientific Reports* 7, 8116. 10.1038/s41598-017-08517-6.

Li, H., Zhang, Z., Wang, B., Zhang, J., Zhao, Y., and Jin, Y. (2007). Wwp2-mediated ubiquitination of the RNA polymerase II large subunit in mouse embryonic pluripotent stem cells. *Molecular and cellular biology* 27, 5296-5305. 10.1128/mcb.01667-06.

Liddane, A.G., and Holaska, J.M. (2021). The Role of Emerin in Cancer Progression and Metastasis. *International journal of molecular sciences* 22. 10.3390/ijms222011289.

Lieberman-Aiden, E., van Berkum Nynke, L., Williams, L., Imakaev, M., Ragoczy, T., Telling, A., Amit, I., Lajoie Bryan, R., Sabo Peter, J., Dorschner Michael, O., et al. (2009). Comprehensive Mapping of Long-Range Interactions Reveals Folding Principles of the Human Genome. *Science* 326, 289-293. 10.1126/science.1181369.

Lim, S., Quinton, R.J., and Ganem, N.J. (2016). Nuclear envelope rupture drives genome instability in cancer. *Molecular biology of the cell* 27, 3210-3213. 10.1091/mbc.E16-02-0098.

Lin, Y., Currie, S.L., and Rosen, M.K. (2017). Intrinsically disordered sequences enable modulation of protein phase separation through distributed tyrosine motifs. *The Journal of biological chemistry* 292, 19110-19120. 10.1074/jbc.M117.800466.

Lionnet, T., and Wu, C. (2021). Single-molecule tracking of transcription protein dynamics in living cells: seeing is believing, but what are we seeing? *Current Opinion in Genetics & Development* 67, 94-102. <https://doi.org/10.1016/j.gde.2020.12.001>.

Liu, P., Kenney, J.M., Stiller, J.W., and Greenleaf, A.L. (2010a). Genetic organization, length conservation, and evolution of RNA polymerase II carboxyl-terminal domain. *Molecular biology and evolution* 27, 2628-2641. 10.1093/molbev/msq151.

Liu, S., Wang, T., Shi, Y., Bai, L., Wang, S., Guo, D., Zhang, Y., Qi, Y., Chen, C., Zhang, J., et al. (2021). USP42 drives nuclear speckle mRNA splicing via directing dynamic phase separation to promote tumorigenesis. *Cell Death & Differentiation* 28, 2482-2498. 10.1038/s41418-021-00763-6.

Liu, Z., Lavis, L.D., and Betzig, E. (2015). Imaging live-cell dynamics and structure at the single-molecule level. *Molecular cell* 58, 644-659. 10.1016/j.molcel.2015.02.033.

Liu, Z., Legant, W.R., Chen, B.-C., Li, L., Grimm, J.B., Lavis, L.D., Betzig, E., and Tjian, R. (2014). 3D imaging of Sox2 enhancer clusters in embryonic stem cells. *eLife* 3, e04236. 10.7554/eLife.04236.

Liu, Z., van Grunsven, L.A., Van Rossen, E., Schroyen, B., Timmermans, J.-P., Geerts, A., and Reynaert, H. (2010b). Blebbistatin inhibits contraction and accelerates migration in mouse hepatic stellate cells. *Br J Pharmacol* 159, 304-315. 10.1111/j.1476-5381.2009.00477.x.

Loeb, L.A., and Monnat, R.J. (2008). DNA polymerases and human disease. *Nature Reviews Genetics* 9, 594-604. 10.1038/nrg2345.

Lombardi, M.L., Jaalouk, D.E., Shanahan, C.M., Burke, B., Roux, K.J., and Lammerding, J. (2011). The interaction between nesprins and sun proteins at the nuclear envelope is critical for force transmission between the nucleus and cytoskeleton. *The Journal of biological chemistry* 286, 26743-26753. 10.1074/jbc.M111.233700.

Los, G.V., Encell, L.P., McDougall, M.G., Hartzell, D.D., Karassina, N., Zimprich, C., Wood, M.G., Learish, R., Ohana, R.F., Urh, M., et al. (2008). HaloTag: a novel protein labeling technology for cell imaging and protein analysis. *ACS Chem Biol* 3, 373-382. 10.1021/cb800025k.

Lou, J., Scipioni, L., Wright, B.K., Bartolec, T.K., Zhang, J., Masamsetti, V.P., Gaus, K., Gratton, E., Cesare, A.J., and Hinde, E. (2019). Phasor histone FLIM-FRET microscopy quantifies spatiotemporal rearrangement of chromatin architecture during the DNA damage response. *Proceedings of the National Academy of Sciences U.S.A* 116, 7323. 10.1073/pnas.1814965116.

Lu, H., Saha, J., Beckmann, P.J., Hendrickson, E.A., and Davis, A.J. (2019). DNA-PKcs promotes chromatin decondensation to facilitate initiation of the DNA damage response. *Nucleic Acids Research* 47, 9467-9479. 10.1093/nar/gkz694.

Lu, H., Yu, D., Hansen, A.S., Ganguly, S., Liu, R., Heckert, A., Darzacq, X., and Zhou, Q. (2018). Phase-separation mechanism for C-terminal hyperphosphorylation of RNA polymerase II. *Nature* 558, 318-323. 10.1038/s41586-018-0174-3.

Luijsterburg, M.S., Dinant, C., Lans, H., Stap, J., Wiernasz, E., Lagerwerf, S., Warmerdam, D.O., Lindh, M., Brink, M.C., Dobrucki, J.W., et al. (2009). Heterochromatin protein 1 is recruited to various types of DNA damage. *Journal of Cell Biology* 185, 577-586. 10.1083/jcb.200810035.

Luk, E., Ranjan, A., Fitzgerald, P.C., Mizuguchi, G., Huang, Y., Wei, D., and Wu, C. (2010). Stepwise histone replacement by SWR1 requires dual activation with histone H2A.Z and canonical nucleosome. *Cell* 143, 725-736. 10.1016/j.cell.2010.10.019.

Ma, L., Gao, Z., Wu, J., Zhong, B., Xie, Y., Huang, W., and Lin, Y. (2021). Co-condensation between transcription factor and coactivator p300 modulates transcriptional bursting kinetics. *Molecular cell* 81, 1682-1697.e1687. <https://doi.org/10.1016/j.molcel.2021.01.031>.

Mahaffy, R.E., Park, S., Gerde, E., Käs, J., and Shih, C.K. (2004). Quantitative analysis of the viscoelastic properties of thin regions of fibroblasts using atomic force microscopy. *Biophysical journal* 86, 1777-1793. 10.1016/S0006-3495(04)74245-9.

Mahaffy, R.E., Shih, C.K., MacKintosh, F.C., and Käs, J. (2000). Scanning Probe-Based Frequency-Dependent Microrheology of Polymer Gels and Biological Cells. *Physical Review Letters* 85, 880-883. 10.1103/PhysRevLett.85.880.

Majewski, L., Nowak, J., Sobczak, M., Karatsai, O., Havrylov, S., Lenartowski, R., Suszek, M., Lenartowska, M., and Redowicz, M.J. (2018). Myosin VI in the nucleus of neurosecretory PC12 cells: Stimulation-dependent nuclear translocation and interaction with nuclear proteins. *Nucleus* 9, 125-141. 10.1080/19491034.2017.1421881.

Makhija, E., Jekhun, D.S., and Shivashankar, G.V. (2016). Nuclear deformability and telomere dynamics are regulated by cell geometric constraints. *Proceedings of the National Academy of Sciences U.S.A* *113*, E32. 10.1073/pnas.1513189113.

Mammoto, A., Mammoto, T., and Ingber, D.E. (2012). Mechanosensitive mechanisms in transcriptional regulation. *Journal of cell science* *125*, 3061-3073. 10.1242/jcs.093005.

Maniotis, A.J., Chen, C.S., and Ingber, D.E. (1997). Demonstration of mechanical connections between integrins, cytoskeletal filaments, and nucleoplasm that stabilize nuclear structure. *Proceedings of the National Academy of Sciences U.S.A* *94*, 849. 10.1073/pnas.94.3.849.

Manley, S., Gillette, J.M., Patterson, G.H., Shroff, H., Hess, H.F., Betzig, E., and Lippincott-Schwartz, J. (2008). High-density mapping of single-molecule trajectories with photoactivated localization microscopy. *Nature methods* *5*, 155-157. 10.1038/nmeth.1176.

Maréchal, A., and Zou, L. (2013). DNA damage sensing by the ATM and ATR kinases. *Cold Spring Harbor perspectives in biology* *5*. 10.1101/cshperspect.a012716.

Martin, R.M., Rino, J., Carvalho, C., Kirchhausen, T., and Carmo-Fonseca, M. (2013). Live-cell visualization of pre-mRNA splicing with single-molecule sensitivity. *Cell reports* *4*, 1144-1155. 10.1016/j.celrep.2013.08.013.

Martins, F., Sousa, J., Pereira, C.D., da Cruz e Silva, O.A.B., and Rebelo, S. (2020). Nuclear envelope dysfunction and its contribution to the aging process. *Aging Cell* *19*, e13143. <https://doi.org/10.1111/accel.13143>.

Masters, T.A., and Buss, F. (2017). Filopodia formation and endosome clustering induced by mutant plus-end-directed myosin VI. *Proceedings of the National Academy of Sciences* *114*, 1595. 10.1073/pnas.1616941114.

Maya-Miles, D., Andújar, E., Pérez-Alegre, M., Murillo-Pineda, M., Barrientos-Moreno, M., Cabello-Lobato, M.J., Gómez-Marín, E., Morillo-Huesca, M., and Prado, F. (2019). Crosstalk between chromatin structure, cohesin activity and transcription. *Epigenetics & Chromatin* *12*, 47. 10.1186/s13072-019-0293-6.

Mazumder, A., Roopa, T., Basu, A., Mahadevan, L., and Shivashankar, G.V. (2008). Dynamics of Chromatin Decondensation Reveals the Structural Integrity of a Mechanically Prestressed Nucleus. *Biophysical Journal* *95*, 3028-3035. 10.1529/biophysj.108.132274.

Mehta, I.S., Kulashreshtha, M., Chakraborty, S., Kolthur-Seetharam, U., and Rao, B.J. (2013). Chromosome territories reposition during DNA damage-repair response. *Genome Biol* *14*, R135. 10.1186/gb-2013-14-12-r135.

Meininghaus, M., Chapman, R.D., Horndasch, M., and Eick, D. (2000). Conditional expression of RNA polymerase II in mammalian cells. Deletion of the carboxyl-terminal domain of the large subunit affects early steps in transcription. *The Journal of biological chemistry* *275*, 24375-24382. 10.1074/jbc.M001883200.

Meister, P., Poidevin, M., Francesconi, S., Tratner, I., Zarzov, P., and Baldacci, G. (2003). Nuclear factories for signalling and repairing DNA double strand breaks in living fission yeast. *Nucleic acids research* *31*, 5064-5073. 10.1093/nar/gkg719.

Melak, M., Plessner, M., and Grosse, R. (2017). Actin visualization at a glance. *Journal of Cell Science* *130*, 525-530. 10.1242/jcs.189068.

Melters Daniël, P., Pitman, M., Rakshit, T., Dimitriadis Emiliós, K., Bui, M., Papoian Garegin, A., and Dalal, Y. (2019). Intrinsic elasticity of nucleosomes is encoded by histone variants and calibrated by their binding partners. *Proceedings of the National Academy of Sciences* *116*, 24066-24074. 10.1073/pnas.1911880116.

Metzler, R., Jeon, J.-H., Cherstvy, A.G., and Barkai, E. (2014). Anomalous diffusion models and their properties: non-stationarity, non-ergodicity, and ageing at the centenary of single particle tracking. *Physical chemistry chemical physics : PCCP* *16* *44*, 24128-24164.

Metzler, R., and Klafter, J. (2000). The random walk's guide to anomalous diffusion: a fractional dynamics approach. *Physics Reports* *339*, 1-77. [https://doi.org/10.1016/S0370-1573\(00\)00070-3](https://doi.org/10.1016/S0370-1573(00)00070-3).

Mieczkowski, J., Cook, A., Bowman, S.K., Mueller, B., Alver, B.H., Kundu, S., Deaton, A.M., Urban, J.A., Larschan, E., Park, P.J., et al. (2016). MNase titration reveals differences between nucleosome occupancy and chromatin accessibility. *Nature Communications* 7, 11485. 10.1038/ncomms11485.

Mih, J.D., Marinkovic, A., Liu, F., Sharif, A.S., and Tschumperlin, D.J. (2012). Matrix stiffness reverses the effect of actomyosin tension on cell proliferation. *Journal of cell science* 125, 5974-5983. 10.1242/jcs.108886.

Milenkovic, L., Weiss, L.E., Yoon, J., Roth, T.L., Su, Y.S., Sahl, S.J., Scott, M.P., and Moerner, W.E. (2015). Single-molecule imaging of Hedgehog pathway protein Smoothed in primary cilia reveals binding events regulated by Patched1. *Proc Natl Acad Sci U S A* 112, 8320-8325. 10.1073/pnas.1510094112.

Miné-Hattab, J., Heltberg, M., Villemeur, M., Guedj, C., Mora, T., Walczak, A.M., Dahan, M., and Taddei, A. (2021). Single molecule microscopy reveals key physical features of repair foci in living cells. *eLife* 10, e60577. 10.7554/eLife.60577.

Mischo, H.E., and Proudfoot, N.J. (2013). Disengaging polymerase: terminating RNA polymerase II transcription in budding yeast. *Biochim Biophys Acta* 1829, 174-185. 10.1016/j.bbagr.2012.10.003.

Mitchell, J.A., and Fraser, P. (2008). Transcription factories are nuclear subcompartments that remain in the absence of transcription. *Genes & Development* 22, 20-25.

Mitchison, T.J., and Cramer, L.P. (1996). Actin-based cell motility and cell locomotion. *Cell* 84, 371-379. 10.1016/s0092-8674(00)81281-7.

Miyamoto, K., Nguyen, K.T., Allen, G.E., Jullien, J., Kumar, D., Otani, T., Bradshaw, C.R., Livesey, F.J., Kellis, M., and Gurdon, J.B. (2018). Chromatin Accessibility Impacts Transcriptional Reprogramming in Oocytes. *Cell Reports* 24, 304-311. <https://doi.org/10.1016/j.celrep.2018.06.030>.

Moore, L.D., Le, T., and Fan, G. (2013). DNA Methylation and Its Basic Function. *Neuropsychopharmacology* 38, 23-38. 10.1038/npp.2012.112.

Morriswood, B., Ryzhakov, G., Puri, C., Arden, S.D., Roberts, R., Dendrou, C., Kendrick-Jones, J., and Buss, F. (2007). T6BP and NDP52 are myosin VI binding partners with potential roles in cytokine signalling and cell adhesion. *J Cell Sci* 120, 2574-2585. 10.1242/jcs.007005.

Mostowy, S., Sancho-Shimizu, V., Hamon, M.A., Simeone, R., Brosch, R., Johansen, T., and Cossart, P. (2011). p62 and NDP52 proteins target intracytosolic Shigella and Listeria to different autophagy pathways. *The Journal of biological chemistry* 286, 26987-26995. 10.1074/jbc.M111.223610.

Mu, X., Tseng, C., Hambright, W.S., Matre, P., Lin, C.-Y., Chanda, P., Chen, W., Gu, J., Ravuri, S., Cui, Y., et al. (2020). Cytoskeleton stiffness regulates cellular senescence and innate immune response in Hutchinson–Gilford Progeria Syndrome. *Aging Cell* 19, e13152. <https://doi.org/10.1111/acer.13152>.

Mukherjea, M., Ali, M.Y., Kikuti, C., Safer, D., Yang, Z., Sirkia, H., Ropars, V., Houdusse, A., Warshaw, D.M., and Sweeney, H.L. (2014). Myosin VI must dimerize and deploy its unusual lever arm in order to perform its cellular roles. *Cell reports* 8, 1522-1532. 10.1016/j.celrep.2014.07.041.

Mukherjea, M., Llinas, P., Kim, H., Travaglia, M., Safer, D., Ménétrey, J., Franzini-Armstrong, C., Selvin, P.R., Houdusse, A., and Sweeney, H.L. (2009). Myosin VI dimerization triggers an unfolding of a three-helix bundle in order to extend its reach. *Molecular cell* 35, 305-315. 10.1016/j.molcel.2009.07.010.

Murga, M., Jaco, I., Fan, Y., Soria, R., Martinez-Pastor, B., Cuadrado, M., Yang, S.-M., Blasco, M.A., Skoultchi, A.I., and Fernandez-Capetillo, O. (2007). Global chromatin compaction limits the strength of the DNA damage response. *J Cell Biol* 178, 1101-1108. 10.1083/jcb.200704140.

Nader, G.P.F., Williard, A., and Piel, M. (2021). Nuclear deformations, from signaling to perturbation and damage. *Curr Opin Cell Biol* 72, 137-145. 10.1016/j.ceb.2021.07.008.

Naetar, N., Ferraioli, S., and Foisner, R. (2017). Lamins in the nuclear interior – life outside the lamina. *Journal of Cell Science* 130, 2087-2096. 10.1242/jcs.203430.

Nagashima, R., Hibino, K., Ashwin, S.S., Babokhov, M., Fujishiro, S., Imai, R., Nozaki, T., Tamura, S., Tani, T., Kimura, H., et al. (2019). Single nucleosome imaging reveals loose genome chromatin networks via active RNA polymerase II. *Journal of Cell Biology* 218, 1511-1530. 10.1083/jcb.201811090.

Nakajima, H. (2011). Role of transcription factors in differentiation and reprogramming of hematopoietic cells. *Keio J Med* 60, 47-55. 10.2302/kjm.60.47.

Nambiar, R., McConnell, R.E., and Tyska, M.J. (2009). Control of cell membrane tension by myosin-I. *Proceedings of the National Academy of Sciences U.S.A* *106*, 11972. 10.1073/pnas.0901641106.

Narayanan, A., Ruyechan, W.T., and Kristie, T.M. (2007). The coactivator host cell factor-1 mediates Set1 and MLL1 H3K4 trimethylation at herpesvirus immediate early promoters for initiation of infection. *Proc Natl Acad Sci U S A* *104*, 10835-10840. 10.1073/pnas.0704351104.

Nelsen, E., Hobson, C.M., Kern, M.E., Hsiao, J.P., O'Brien Iii, E.T., Watanabe, T., Condon, B.M., Boyce, M., Grinstein, S., Hahn, K.M., et al. (2020). Combined Atomic Force Microscope and Volumetric Light Sheet System for Correlative Force and Fluorescence Mechanobiology Studies. *Scientific Reports* *10*, 8133. 10.1038/s41598-020-65205-8.

Newberg, J., Schimpf, J., Woods, K., Loiate, S., Davis, P.H., and Uzer, G. (2020). Isolated nuclei stiffen in response to low intensity vibration. *Journal of Biomechanics* *111*, 110012. <https://doi.org/10.1016/j.jbiomech.2020.110012>.

Nora, E.P., Lajoie, B.R., Schulz, E.G., Giorgetti, L., Okamoto, I., Servant, N., Piolot, T., van Berkum, N.L., Meisig, J., Sedat, J., et al. (2012). Spatial partitioning of the regulatory landscape of the X-inactivation centre. *Nature* *485*, 381-385. 10.1038/nature11049.

Nowak, G., Pestic-Dragovich, L., Hozák, P., Philimonenko, A., Simerly, C., Schatten, G., and de Lanerolle, P. (1997). Evidence for the presence of myosin I in the nucleus. *The Journal of biological chemistry* *272*, 17176-17181. 10.1074/jbc.272.27.17176.

Nozaki, T., Imai, R., Tanbo, M., Nagashima, R., Tamura, S., Tani, T., Joti, Y., Tomita, M., Hibino, K., Kanemaki, M.T., et al. (2017). Dynamic Organization of Chromatin Domains Revealed by Super-Resolution Live-Cell Imaging. *Molecular cell* *67*, 282-293.e287. 10.1016/j.molcel.2017.06.018.

Nthiga, T.M., Kumar Shrestha, B., Sjøttem, E., Bruun, J.A., Bowitz Larsen, K., Bhujabal, Z., Lamark, T., and Johansen, T. (2020). CALCOCO1 acts with VAMP-associated proteins to mediate ER-phagy. *Embo j* *39*, e103649. 10.15252/embj.2019103649.

Nthiga, T.M., Shrestha, B.K., Bruun, J.-A., Larsen, K.B., Lamark, T., and Johansen, T. (2021). Regulation of Golgi turnover by CALCOCO1-mediated selective autophagy. *Journal of Cell Biology* *220*. 10.1083/jcb.202006128.

Nye, A.C., Rajendran, R.R., Stenoien, D.L., Mancini, M.A., Katzenellenbogen, B.S., and Belmont, A.S. (2002). Alteration of large-scale chromatin structure by estrogen receptor. *Molecular and cellular biology* *22*, 3437-3449. 10.1128/mcb.22.10.3437-3449.2002.

Oeckinghaus, A., and Ghosh, S. (2009). The NF-kappaB family of transcription factors and its regulation. *Cold Spring Harbor perspectives in biology* *1*, a000034-a000034. 10.1101/cshperspect.a000034.

Osborne, C.S., Chakalova, L., Brown, K.E., Carter, D., Horton, A., Debrand, E., Goyenechea, B., Mitchell, J.A., Lopes, S., Reik, W., and Fraser, P. (2004). Active genes dynamically colocalize to shared sites of ongoing transcription. *Nature Genetics* *36*, 1065-1071. 10.1038/ng1423.

Oshidari, R., Huang, R., Medghalchi, M., Tse, E.Y.W., Ashgriz, N., Lee, H.O., Wyatt, H., and Mekhail, K. (2020). DNA repair by Rad52 liquid droplets. *Nature Communications* *11*, 695. 10.1038/s41467-020-14546-z.

Osley, M.A., Tsukuda, T., and Nickoloff, J.A. (2007). ATP-dependent chromatin remodeling factors and DNA damage repair. *Mutat Res* *618*, 65-80. 10.1016/j.mrfmmm.2006.07.011.

Osmanagic-Myers, S., and Foisner, R. (2019). The structural and gene expression hypotheses in laminopathic diseases-not so different after all. *Mol Biol Cell* *30*, 1786-1790. 10.1091/mbc.E18-10-0672.

Owen, D.M., Rentero, C., Rossy, J., Magenau, A., Williamson, D., Rodriguez, M., and Gaus, K. (2010). PALM imaging and cluster analysis of protein heterogeneity at the cell surface. *J Biophotonics* *3*, 446-454. 10.1002/jbio.200900089.

Oza, P., Jaspersen, S.L., Miele, A., Dekker, J., and Peterson, C.L. (2009). Mechanisms that regulate localization of a DNA double-strand break to the nuclear periphery. *Genes & Development* *23*, 912-927.

Pageon, S.V., Nicovich, P.R., Mollazade, M., Tabarin, T., and Gaus, K. (2016). Clus-DoC: a combined cluster detection and colocalization analysis for single-molecule localization microscopy data. *Molecular biology of the cell* 27, 3627-3636. 10.1091/mbc.E16-07-0478.

Pai, C.-C., Deegan, R.S., Subramanian, L., Gal, C., Sarkar, S., Blaikley, E.J., Walker, C., Hulme, L., Bernhard, E., Codlin, S., et al. (2014). A histone H3K36 chromatin switch coordinates DNA double-strand break repair pathway choice. *Nature Communications* 5, 4091. 10.1038/ncomms5091.

Pajerowski, J.D., Dahl, K.N., Zhong, F.L., Sammak, P.J., and Discher, D.E. (2007). Physical plasticity of the nucleus in stem cell differentiation. *Proceedings of the National Academy of Sciences U.S.A* 104, 15619. 10.1073/pnas.0702576104.

Palmer, A., Xu, J., and Wirtz, D. (1998). High-frequency viscoelasticity of crosslinked actin filament networks measured by diffusing wave spectroscopy. *Rheologica Acta* 37, 97-106. 10.1007/s003970050095.

Pancholi, A., Klingberg, T., Zhang, W., Prizak, R., Mamontova, I., Noa, A., Sobucki, M., Kobitski, A.Y., Nienhaus, G.U., Zaburdaev, V., and Hilbert, L. (2021). RNA polymerase II clusters form in line with surface condensation on regulatory chromatin. *Molecular Systems Biology* 17, e10272. <https://doi.org/10.15252/msb.202110272>.

Papanicolaou, G.N., and Traut, H.F. (1941). The Diagnostic Value of Vaginal Smears in Carcinoma of the Uterus. *American Journal of Obstetrics and Gynecology* 42, 193-206. [https://doi.org/10.1016/S0002-9378\(16\)40621-6](https://doi.org/10.1016/S0002-9378(16)40621-6).

Park, H., Li, A., Chen, L.-Q., Houdusse, A., Selvin, P.R., and Sweeney, H.L. (2007). The unique insert at the end of the myosin VI motor is the sole determinant of directionality. *Proceedings of the National Academy of Sciences* 104, 778. 10.1073/pnas.0610066104.

Park, H., Ramamurthy, B., Travaglia, M., Safer, D., Chen, L.Q., Franzini-Armstrong, C., Selvin, P.R., and Sweeney, H.L. (2006). Full-length myosin VI dimerizes and moves processively along actin filaments upon monomer clustering. *Molecular cell* 21, 331-336. 10.1016/j.molcel.2005.12.015.

Paull, T.T., Rogakou, E.P., Yamazaki, V., Kirchgessner, C.U., Gellert, M., and Bonner, W.M. (2000). A critical role for histone H2AX in recruitment of repair factors to nuclear foci after DNA damage. *Current Biology* 10, 886-895. [https://doi.org/10.1016/S0960-9822\(00\)00610-2](https://doi.org/10.1016/S0960-9822(00)00610-2).

Pearson, E.L., and Moore, C.L. (2013). Dismantling Promoter-driven RNA Polymerase II Transcription Complexes *in Vitro* by the Termination Factor Rat1 *. *Journal of Biological Chemistry* 288, 19750-19759. 10.1074/jbc.M112.434985.

Percipalle, P., Fomproix, N., Cavellán, E., Voit, R., Reimer, G., Krüger, T., Thyberg, J., Scheer, U., Grummt, I., and Östlund Farrants, A.-K. (2006). The chromatin remodelling complex WSTF-SNF2h interacts with nuclear myosin 1 and has a role in RNA polymerase I transcription. *EMBO reports* 7, 525-530. <https://doi.org/10.1038/sj.embor.7400657>.

Percipalle, P., Fomproix, N., Kylberg, K., Miralles, F., Bjorkroth, B., Daneholt, B., and Visa, N. (2003). An actin-ribonucleoprotein interaction is involved in transcription by RNA polymerase II. *Proc Natl Acad Sci U S A* 100, 6475-6480. 10.1073/pnas.1131933100.

Perry, G.L.W. (2004). SpPack: spatial point pattern analysis in Excel using Visual Basic for Applications (VBA). *Environmental Modelling & Software* 19, 559-569. <https://doi.org/10.1016/j.envsoft.2003.07.004>.

Peterson, T.J., Karmakar, S., Pace, M.C., Gao, T., and Smith, C.L. (2007). The silencing mediator of retinoic acid and thyroid hormone receptor (SMRT) corepressor is required for full estrogen receptor alpha transcriptional activity. *Molecular and cellular biology* 27, 5933-5948. 10.1128/mcb.00237-07.

Pfister, Sophia X., Ahrabi, S., Zalmas, L.-P., Sarkar, S., Aymard, F., Bachrati, Csanád Z., Helleday, T., Legube, G., La Thangue, Nicholas B., Porter, Andrew C.G., and Humphrey, Timothy C. (2014). SETD2-Dependent Histone H3K36 Trimethylation Is Required for Homologous Recombination Repair and Genome Stability. *Cell Reports* 7, 2006-2018. 10.1016/j.celrep.2014.05.026.

Phatnani, H.P., and Greenleaf, A.L. (2006). Phosphorylation and functions of the RNA polymerase II CTD. *Genes Dev* 20, 2922-2936. 10.1101/gad.1477006.

Pichith, D., Travaglia, M., Yang, Z., Liu, X., Zong, A.B., Safer, D., and Sweeney, H.L. (2009). Cargo binding induces dimerization of myosin VI. *Proceedings of the National Academy of Sciences* 106, 17320. 10.1073/pnas.0909748106.

Philimonenko, V.V., Zhao, J., Iben, S., Dingová, H., Kyselá, K., Kahle, M., Zentgraf, H., Hofmann, W.A., de Lanerolle, P., Hozák, P., and Grummt, I. (2004). Nuclear actin and myosin I are required for RNA polymerase I transcription. *Nat Cell Biol* 6, 1165-1172. 10.1038/ncb1190.

Phillips-Cremins, Jennifer E., Sauria, Michael E.G., Sanyal, A., Gerasimova, Tatiana I., Lajoie, Bryan R., Bell, Joshua S.K., Ong, C.-T., Hookway, Tracy A., Guo, C., Sun, Y., et al. (2013). Architectural Protein Subclasses Shape 3D Organization of Genomes during Lineage Commitment. *Cell* 153, 1281-1295. 10.1016/j.cell.2013.04.053.

Pickersgill, H., Kalverda, B., de Wit, E., Talhout, W., Fornerod, M., and van Steensel, B. (2006). Characterization of the *Drosophila melanogaster* genome at the nuclear lamina. *Nature Genetics* 38, 1005-1014. 10.1038/ng1852.

Pincet, F., Adrien, V., Yang, R., Delacotte, J., Rothman, J.E., Urbach, W., and Tareste, D. (2016). FRAP to Characterize Molecular Diffusion and Interaction in Various Membrane Environments. *PLOS ONE* 11, e0158457. 10.1371/journal.pone.0158457.

Plessner, M., and Grosse, R. (2019). Dynamizing nuclear actin filaments. *Current Opinion in Cell Biology* 56, 1-6. <https://doi.org/10.1016/j.ceb.2018.08.005>.

Popp, A.P., Hettich, J., and Gebhardt, J.C.M. (2020). Transcription factor residence time dominates over concentration in transcription activation. *bioRxiv*, 2020.2011.2026.400069. 10.1101/2020.11.26.400069.

Primon, M., Hunter, K.D., Pandha, H.S., and Morgan, R. (2019). Kinase Regulation of HOX Transcription Factors. *Cancers (Basel)* 11. 10.3390/cancers11040508.

Proudfoot, N.J. (2016). Transcriptional termination in mammals: Stopping the RNA polymerase II juggernaut. *Science* 352, aad9926. 10.1126/science.aad9926.

Puleo, J.I., Parker, S.S., Roman, M.R., Watson, A.W., Eliato, K.R., Peng, L., Saboda, K., Roe, D.J., Ros, R., Gertler, F.B., and Mouneimne, G. (2019). Mechanosensing during directed cell migration requires dynamic actin polymerization at focal adhesions. *Journal of Cell Biology* 218, 4215-4235. 10.1083/jcb.201902101.

Puri, C., Chibalina, M.V., Arden, S.D., Kruppa, A.J., Kendrick-Jones, J., and Buss, F. (2010). Overexpression of myosin VI in prostate cancer cells enhances PSA and VEGF secretion, but has no effect on endocytosis. *Oncogene* 29, 188-200. 10.1038/onc.2009.328.

Pyne, A.L., and Hoogenboom, B.W. (2016). Imaging DNA Structure by Atomic Force Microscopy. *Methods in molecular biology (Clifton, N.J.)* 1431, 47-60. 10.1007/978-1-4939-3631-1_5.

Pyne, A.L.B., Noy, A., Main, K.H.S., Velasco-Berrelleza, V., Piperakis, M.M., Mitchenall, L.A., Cugliandolo, F.M., Beton, J.G., Stevenson, C.E.M., Hoogenboom, B.W., et al. (2021). Base-pair resolution analysis of the effect of supercoiling on DNA flexibility and major groove recognition by triplex-forming oligonucleotides. *Nature Communications* 12, 1053. 10.1038/s41467-021-21243-y.

Qi, T., Tang, W., Wang, L., Zhai, L., Guo, L., and Zeng, X. (2011). G-actin participates in RNA polymerase II-dependent transcription elongation by recruiting positive transcription elongation factor b (P-TEFb). *The Journal of biological chemistry* 286, 15171-15181. 10.1074/jbc.M110.184374.

Qualmann, B., Kessels, M.M., and Kelly, R.B. (2000). Molecular links between endocytosis and the actin cytoskeleton. *J Cell Biol* 150, F111-F116. 10.1083/jcb.150.5.f111.

Raab, M., Gentili, M., de Belly, H., Thiam, H.-R., Vargas, P., Jimenez, A.J., Lautenschlaeger, F., Voituriez, R., Lennon-Duménil, A.-M., Manel, N., and Piel, M. (2016). ESCRT III repairs nuclear envelope ruptures during cell migration to limit DNA damage and cell death. *Science* 352, 359. 10.1126/science.aad7611.

Rafique, S., Thomas, J.S., Sproul, D., and Bickmore, W.A. (2015). Estrogen-induced chromatin decondensation and nuclear re-organization linked to regional epigenetic regulation in breast cancer. *Genome Biology* 16, 145. 10.1186/s13059-015-0719-9.

Ranade, D., Pradhan, R., Jayakrishnan, M., Hegde, S., and Sengupta, K. (2019). Lamin A/C and Emerin depletion impacts chromatin organization and dynamics in the interphase nucleus. *BMC Molecular and Cell Biology* 20, 11. 10.1186/s12860-019-0192-5.

Rehfeldt, F., Brown, A.E., Raab, M., Cai, S., Zajac, A.L., Zemel, A., and Discher, D.E. (2012a). Hyaluronic acid matrices show matrix stiffness in 2D and 3D dictates cytoskeletal order and myosin-II phosphorylation within stem cells. *Integr Biol (Camb)* 4, 422-430. 10.1039/c2ib00150k.

Rehfeldt, F., Brown, A.E.X., Raab, M., Cai, S., Zajac, A.L., Zemel, A., and Discher, D.E. (2012b). Hyaluronic acid matrices show matrix stiffness in 2D and 3D dictates cytoskeletal order and myosin-II phosphorylation within stem cells. *Integrative Biology* 4, 422-430. 10.1039/c2ib00150k.

Rehfeldt, F., and Schmidt, C.F. (2017). Physical probing of cells. *Journal of Physics D* 50, 463001.

Richmond, T.J., and Davey, C.A. (2003). The structure of DNA in the nucleosome core. *Nature* 423, 145-150. 10.1038/nature01595.

Ripley, B.D. (1979). Tests of 'Randomness' for Spatial Point Patterns. *Journal of the Royal Statistical Society. Series B (Methodological)* 41, 368-374.

Rober, R.A., Sauter, H., Weber, K., and Osborn, M. (1990). Cells of the cellular immune and hemopoietic system of the mouse lack lamins A/C: distinction versus other somatic cells. *Journal of Cell Science* 95, 587.

Robin, J.D., and Magdinier, F. (2016). Physiological and Pathological Aging Affects Chromatin Dynamics, Structure and Function at the Nuclear Edge. *Frontiers in genetics* 7. 10.3389/fgene.2016.00153.

Rogatsky, I., Zarembek, K.A., and Yamamoto, K.R. (2001). Factor recruitment and TIF2/GRIP1 corepressor activity at a collagenase-3 response element that mediates regulation by phorbol esters and hormones. *Embo j* 20, 6071-6083. 10.1093/emboj/20.21.6071.

Rosin, L.F., Nguyen, S.C., and Joyce, E.F. (2018). Condensin II drives large-scale folding and spatial partitioning of interphase chromosomes in *Drosophila* nuclei. *PLOS Genetics* 14, e1007393. 10.1371/journal.pgen.1007393.

Rother, J., Nöding, H., Mey, I., and Janshoff, A. (2014). Atomic force microscopy-based microrheology reveals significant differences in the viscoelastic response between malignant and benign cell lines. *Open Biology* 4, 140046. 10.1098/rsob.140046.

Rotsch, C., and Radmacher, M. (2000). Drug-Induced Changes of Cytoskeletal Structure and Mechanics in Fibroblasts: An Atomic Force Microscopy Study. *Biophysical Journal* 78, 520-535. 10.1016/S0006-3495(00)76614-8.

Rowat, A.C., Lammerding, J., and Ipsen, J.H. (2006). Mechanical Properties of the Cell Nucleus and the Effect of Emerin Deficiency. *Biophysical Journal* 91, 4649-4664. <https://doi.org/10.1529/biophysj.106.086454>.

Rubbi, C.P., and Milner, J. (2003). p53 is a chromatin accessibility factor for nucleotide excision repair of DNA damage. *Embo j* 22, 975-986. 10.1093/emboj/cdg082.

Ryu, J.-K., Bouchoux, C., Liu Hon, W., Kim, E., Minamino, M., de Groot, R., Katan Allard, J., Bonato, A., Marenduzzo, D., Michieletto, D., et al. (2021). Bridging-induced phase separation induced by cohesin SMC protein complexes. *Science Advances* 7, eabe5905. 10.1126/sciadv.abe5905.

Ryu, T., Spatola, B., Delabaere, L., Bowlin, K., Hopp, H., Kunitake, R., Karpen, G.H., and Chiolo, I. (2015). Heterochromatic breaks move to the nuclear periphery to continue recombinational repair. *Nature Cell Biology* 17, 1401-1411. 10.1038/ncb3258.

Sabari, B.R., Dall'Agnesse, A., Boija, A., Klein, I.A., Coffey, E.L., Shrinivas, K., Abraham, B.J., Hannett, N.M., Zamudio, A.V., Manteiga, J.C., et al. (2018). Coactivator condensation at super-enhancers links phase separation and gene control. *Science* 361, eaar3958. 10.1126/science.aar3958.

Sahlender, D.A., Roberts, R.C., Arden, S.D., Spudich, G., Taylor, M.J., Luzio, J.P., Kendrick-Jones, J., and Buss, F. (2005). Optineurin links myosin VI to the Golgi complex and is involved in Golgi organization and exocytosis. *J Cell Biol* 169, 285-295. 10.1083/jcb.200501162.

Saintillan, D., Shelley, M.J., and Zidovska, A. (2018). Extensile motor activity drives coherent motions in a model of interphase chromatin. *Proceedings of the National Academy of Sciences* *115*, 11442. 10.1073/pnas.1807073115.

Sako, Y., Minoghchi, S., and Yanagida, T. (2000). Single-molecule imaging of EGFR signalling on the surface of living cells. *Nature Cell Biology* *2*, 168-172. 10.1038/35004044.

Saksouk, N., Simboeck, E., and Déjardin, J. (2015). Constitutive heterochromatin formation and transcription in mammals. *Epigenetics & Chromatin* *8*, 3. 10.1186/1756-8935-8-3.

Santos-Rosa, H., Schneider, R., Bannister, A.J., Sherriff, J., Bernstein, B.E., Emre, N.C.T., Schreiber, S.L., Mellor, J., and Kouzarides, T. (2002). Active genes are tri-methylated at K4 of histone H3. *Nature* *419*, 407-411. 10.1038/nature01080.

Sarshad, A., Sadeghifar, F., Louvet, E., Mori, R., Böhm, S., Al-Muzzaini, B., Vintermist, A., Fomproix, N., Östlund, A.-K., and Percipalle, P. (2013). Nuclear Myosin 1c Facilitates the Chromatin Modifications Required to Activate rRNA Gene Transcription and Cell Cycle Progression. *PLOS Genetics* *9*, e1003397. 10.1371/journal.pgen.1003397.

Saxton, M.J. (1994). Single-particle tracking: models of directed transport. *Biophysical Journal* *67*, 2110-2119. 10.1016/S0006-3495(94)80694-0.

Scaffidi, P., and Misteli, T. (2006). Lamin A-dependent nuclear defects in human aging. *Science (New York, N.Y.)* *312*, 1059-1063. 10.1126/science.1127168.

Schrank, B.R., Aparicio, T., Li, Y., Chang, W., Chait, B.T., Gundersen, G.G., Gottesman, M.E., and Gautier, J. (2018). Nuclear ARP2/3 drives DNA break clustering for homology-directed repair. *Nature* *559*, 61-66. 10.1038/s41586-018-0237-5.

Schreiber, K.H., and Kennedy, B.K. (2013). When lamins go bad: nuclear structure and disease. *Cell* *152*, 1365-1375. 10.1016/j.cell.2013.02.015.

Schuller, A.P., Wojtynek, M., Mankus, D., Tatli, M., Kronenberg-Tenga, R., Regmi, S.G., Dip, P.V., Lytton-Jean, A.K.R., Brignole, E.J., Dasso, M., et al. (2021). The cellular environment shapes the nuclear pore complex architecture. *Nature* *598*, 667-671. 10.1038/s41586-021-03985-3.

Schwabish, M.A., and Struhl, K. (2007). The Swi/Snf complex is important for histone eviction during transcriptional activation and RNA polymerase II elongation in vivo. *Molecular and cellular biology* *27*, 6987-6995. 10.1128/mcb.00717-07.

Scully, R., Panday, A., Elango, R., and Willis, N.A. (2019). DNA double-strand break repair-pathway choice in somatic mammalian cells. *Nature reviews. Molecular cell biology* *20*, 698-714. 10.1038/s41580-019-0152-0.

Sedelnikova, O.A., Pilch, D.R., Redon, C., and Bonner, W.M. (2003). Histone H2AX in DNA damage and repair. *Cancer Biol Ther* *2*, 233-235. 10.4161/cbt.2.3.373.

Segal, E., Fondufe-Mittendorf, Y., Chen, L., Thåström, A., Field, Y., Moore, I.K., Wang, J.-P.Z., and Widom, J. (2006). A genomic code for nucleosome positioning. *Nature* *442*, 772-778. 10.1038/nature04979.

Seirin-Lee, S., Osakada, F., Takeda, J., Tashiro, S., Kobayashi, R., Yamamoto, T., and Ochiai, H. (2019). Role of dynamic nuclear deformation on genomic architecture reorganization. *PLOS Computational Biology* *15*, e1007289. 10.1371/journal.pcbi.1007289.

Serebryanny, L.A., Parilla, M., Annibale, P., Cruz, C.M., Laster, K., Gratton, E., Kudryashov, D., Kosak, S.T., Gottardi, C.J., and de Lanerolle, P. (2016). Persistent nuclear actin filaments inhibit transcription by RNA polymerase II. *Journal of Cell Science* *129*, 3412-3425. 10.1242/jcs.195867.

Seto, E., and Yoshida, M. (2014). Erasers of histone acetylation: the histone deacetylase enzymes. *Cold Spring Harbor perspectives in biology* *6*, a018713. 10.1101/cshperspect.a018713.

Sever, R., and Glass, C.K. (2013). Signaling by nuclear receptors. *Cold Spring Harbor perspectives in biology* *5*, a016709-a016709. 10.1101/cshperspect.a016709.

Shah, P., Wolf, K., and Lammerding, J. (2017). Bursting the Bubble – Nuclear Envelope Rupture as a Path to Genomic Instability? *Trends Cell Biol* *27*, 546-555. <https://doi.org/10.1016/j.tcb.2017.02.008>.

Shimamoto, Y., Tamura, S., Masumoto, H., and Maeshima, K. (2017). Nucleosome–nucleosome interactions via histone tails and linker DNA regulate nuclear rigidity. *Molecular Biology of the Cell* *28*, 1580-1589. 10.1091/mbc.e16-11-0783.

Shin, Y., Chang, Y.-C., Lee, D.S.W., Berry, J., Sanders, D.W., Ronceray, P., Wingreen, N.S., Haataja, M., and Brangwynne, C.P. (2018). Liquid Nuclear Condensates Mechanically Sense and Restructure the Genome. *Cell* *175*, 1481-1491.e1413. 10.1016/j.cell.2018.10.057.

Shivashankar, G.V. (2011). Mechanosignaling to the cell nucleus and gene regulation. *Annu Rev Biophys* *40*, 361-378. 10.1146/annurev-biophys-042910-155319.

Sims, R.J., 3rd, Rojas, L.A., Beck, D.B., Bonasio, R., Schüller, R., Drury, W.J., 3rd, Eick, D., and Reinberg, D. (2011). The C-terminal domain of RNA polymerase II is modified by site-specific methylation. *Science* *332*, 99-103. 10.1126/science.1202663.

Sinensky, M., Fantle, K., Trujillo, M., McLain, T., Kupfer, A., and Dalton, M. (1994). The processing pathway of prelamin A. *Journal of Cell Science* *107*, 61.

Smerdon, M.J., and Lieberman, M.W. (1978). Nucleosome rearrangement in human chromatin during UV-induced DNA- reapiir synthesis. *Proceedings of the National Academy of Sciences U.S.A* *75*, 4238. 10.1073/pnas.75.9.4238.

Smith, E.R., Capo-chichi, C.D., and Xu, X.-X. (2018a). Defective Nuclear Lamina in Aneuploidy and Carcinogenesis. *Frontiers in Oncology* *8*. 10.3389/fonc.2018.00529.

Smith, L.R., Cho, S., and Discher, D.E. (2018b). Stem Cell Differentiation is Regulated by Extracellular Matrix Mechanics. *Physiology (Bethesda)* *33*, 16-25. 10.1152/physiol.00026.2017.

Smith, P.R., Morrison, I.E., Wilson, K.M., Fernández, N., and Cherry, R.J. (1999). Anomalous diffusion of major histocompatibility complex class I molecules on HeLa cells determined by single particle tracking. *Biophys J* *76*, 3331-3344. 10.1016/s0006-3495(99)77486-2.

Sobczak, M., Chumak, V., Pomorski, P., Wojtera, E., Majewski, Ł., Nowak, J., Yamauchi, J., and Rędowicz, M.J. (2016). Interaction of myosin VI and its binding partner DOCK7 plays an important role in NGF-stimulated protrusion formation in PC12 cells. *Biochimica et Biophysica Acta (BBA) - Molecular Cell Research* *1863*, 1589-1600. <https://doi.org/10.1016/j.bbamcr.2016.03.020>.

Sofueva, S., Yaffe, E., Chan, W.-C., Georgopoulou, D., Vietri Rudan, M., Mira-Bontenbal, H., Pollard, S.M., Schroth, G.P., Tanay, A., and Hadjur, S. (2013). Cohesin-mediated interactions organize chromosomal domain architecture. *The EMBO Journal* *32*, 3119-3129. <https://doi.org/10.1038/emboj.2013.237>.

Solovei, I., Thanisch, K., and Feodorova, Y. (2016). How to rule the nucleus: divide et impera. *Current Opinion in Cell Biology* *40*, 47-59. <https://doi.org/10.1016/j.ceb.2016.02.014>.

Spichal, M., Brion, A., Herbert, S., Cournac, A., Marbouty, M., Zimmer, C., Koszul, R., and Fabre, E. (2016). Evidence for a dual role of actin in regulating chromosome organization and dynamics in yeast. *J Cell Sci* *129*, 681-692. 10.1242/jcs.175745.

Spink, B.J., Sivaramakrishnan, S., Lipfert, J., Doniach, S., and Spudich, J.A. (2008). Long single α -helical tail domains bridge the gap between structure and function of myosin VI. *Nature Structural & Molecular Biology* *15*, 591-597. 10.1038/nsmb.1429.

Spitz, F., and Furlong, E.E.M. (2012). Transcription factors: from enhancer binding to developmental control. *Nature Reviews Genetics* *13*, 613-626. 10.1038/nrg3207.

Spudich, G., Chibalina, M.V., Au, J.S., Arden, S.D., Buss, F., and Kendrick-Jones, J. (2007). Myosin VI targeting to clathrin-coated structures and dimerization is mediated by binding to Disabled-2 and PtdIns(4,5)P2. *Nat Cell Biol* *9*, 176-183. 10.1038/ncb1531.

Stadhouders, R., Vidal, E., Serra, F., Di Stefano, B., Le Dily, F., Quilez, J., Gomez, A., Collombet, S., Berenguer, C., Cuartero, Y., et al. (2018). Transcription factors orchestrate dynamic interplay between genome topology and gene regulation during cell reprogramming. *Nature Genetics* *50*, 238-249. 10.1038/s41588-017-0030-7.

Stefely, J.A., Zhang, Y., Freiburger, E.C., Kwicien, N.W., Thomas, H.E., Davis, A.M., Lowry, N.D., Vincent, C.E., Shishkova, E., Clark, N.A., et al. (2020). Mass spectrometry proteomics reveals a function

for mammalian CALCOCO1 in MTOR-regulated selective autophagy. *Autophagy* 16, 2219-2237. 10.1080/15548627.2020.1719746.

Stehbens, S., Pemble, H., Murrow, L., and Wittmann, T. (2012). Chapter fifteen - Imaging Intracellular Protein Dynamics by Spinning Disk Confocal Microscopy. In *Methods in Enzymology*, P.M. conn, ed. (Academic Press), pp. 293-313. <https://doi.org/10.1016/B978-0-12-391857-4.00015-X>.

Stein, G.S., Montecino, M., van Wijnen, A.J., Stein, J.L., and Lian, J.B. (2000). Nuclear structure-gene expression interrelationships: implications for aberrant gene expression in cancer. *Cancer Res* 60, 2067-2076.

Stephens, A.D., Banigan, E.J., Adam, S.A., Goldman, R.D., and Marko, J.F. (2017). Chromatin and lamin A determine two different mechanical response regimes of the cell nucleus. *Molecular Biology of the Cell* 28, 1984-1996. 10.1091/mbc.e16-09-0653.

Stephens, A.D., Liu, P.Z., Banigan, E.J., Almassalha, L.M., Backman, V., Adam, S.A., Goldman, R.D., and Marko, J.F. (2018). Chromatin histone modifications and rigidity affect nuclear morphology independent of lamins. *Molecular Biology of the Cell* 29, 220-233. 10.1091/mbc.E17-06-0410.

Sternsdorf, T., Jensen, K., Züchner, D., and Will, H. (1997). Cellular localization, expression, and structure of the nuclear dot protein 52. *J Cell Biol* 138, 435-448. 10.1083/jcb.138.2.435.

Stevens, T.J., Lando, D., Basu, S., Atkinson, L.P., Cao, Y., Lee, S.F., Leeb, M., Wohlfahrt, K.J., Boucher, W., O'Shaughnessy-Kirwan, A., et al. (2017). 3D structures of individual mammalian genomes studied by single-cell Hi-C. *Nature* 544, 59-64. 10.1038/nature21429.

Stock, J.K., Giadrossi, S., Casanova, M., Brookes, E., Vidal, M., Koseki, H., Brockdorff, N., Fisher, A.G., and Pombo, A. (2007). Ring1-mediated ubiquitination of H2A restrains poised RNA polymerase II at bivalent genes in mouse ES cells. *Nature Cell Biology* 9, 1428-1435. 10.1038/ncb1663.

Streppa, L., Ratti, F., Goillot, E., Devin, A., Schaeffer, L., Arneodo, A., and Argoul, F. (2018). Prestressed cells are prone to cytoskeleton failures under localized shear strain: an experimental demonstration on muscle precursor cells. *Scientific Reports* 8, 8602. 10.1038/s41598-018-26797-4.

Strickfaden, H., McDonald, D., Kruhlak, M.J., Haince, J.F., Th'ng, J.P., Rouleau, M., Ishibashi, T., Corry, G.N., Ausio, J., Underhill, D.A., et al. (2016). Poly(ADP-ribosyl)ation-dependent Transient Chromatin Decondensation and Histone Displacement following Laser Microirradiation. *The Journal of biological chemistry* 291, 1789-1802. 10.1074/jbc.M115.694992.

Strickfaden, H., Tolsma, T.O., Sharma, A., Underhill, D.A., Hansen, J.C., and Hendzel, M.J. (2020). Condensed Chromatin Behaves like a Solid on the Mesoscale in Vitro and in Living Cells. *Cell* 183, 1772-1784.e1713. 10.1016/j.cell.2020.11.027.

Strom, A.R., Biggs, R.J., Banigan, E.J., Wang, X., Chiu, K., Herman, C., Collado, J., Yue, F., Politz, J.C.R., Tait, L.J., et al. (2020). HP1 α is a chromatin crosslinker that controls nuclear and mitotic chromosome mechanics. 2020.2010.2009.331900. 10.1101/2020.10.09.331900 %J bioRxiv.

Strom, A.R., Emelyanov, A.V., Mir, M., Fyodorov, D.V., Darzacq, X., and Karpen, G.H. (2017). Phase separation drives heterochromatin domain formation. *Nature* 547, 241-245. 10.1038/nature22989.

Stüven, T., Hartmann, E., and Görlich, D. (2003). Exportin 6: a novel nuclear export receptor that is specific for profilin-actin complexes. *The EMBO Journal* 22, 5928-5940. <https://doi.org/10.1093/emboj/cdg565>.

Sun, X., Phua, D.Y.Z., Axiotakis, L., Smith, M.A., Blankman, E., Gong, R., Cail, R.C., Espinosa de los Reyes, S., Beckerle, M.C., Waterman, C.M., and Alushin, G.M. (2020). Mechanosensing through Direct Binding of Tensed F-Actin by LIM Domains. *Developmental cell* 55, 468-482.e467. <https://doi.org/10.1016/j.devcel.2020.09.022>.

Sun, Y., Jiang, X., Xu, Y., Ayrappetov, M.K., Moreau, L.A., Whetstone, J.R., and Price, B.D. (2009). Histone H3 methylation links DNA damage detection to activation of the tumour suppressor Tip60. *Nat Cell Biol* 11, 1376-1382. 10.1038/ncb1982.

Sutherland, H., and Bickmore, W.A. (2009). Transcription factories: gene expression in unions? *Nature Reviews Genetics* 10, 457-466. 10.1038/nrg2592.

Swift, J., Ivanovska, I.L., Buxboim, A., Harada, T., Dingal, P.C.D.P., Pinter, J., Pajerowski, J.D., Spinler, K.R., Shin, J.-W., Tewari, M., et al. (2013). Nuclear Lamin-A Scales with Tissue Stiffness and Enhances Matrix-Directed Differentiation. *Science* *341*, 1240104. 10.1126/science.1240104.

Szutorisz, H., Dillon, N., and Tora, L. (2005). The role of enhancers as centres for general transcription factor recruitment. *Trends in biochemical sciences* *30*, 593-599. 10.1016/j.tibs.2005.08.006.

Tagami, T., Madison, L.D., Nagaya, T., and Jameson, J.L. (1997). Nuclear receptor corepressors activate rather than suppress basal transcription of genes that are negatively regulated by thyroid hormone. *Molecular and cellular biology* *17*, 2642-2648. 10.1128/mcb.17.5.2642.

Tang, Z., Chen, W.-Y., Shimada, M., Nguyen, Uyen T.T., Kim, J., Sun, X.-J., Sengoku, T., McGinty, Robert K., Fernandez, Joseph P., Muir, Tom W., and Roeder, Robert G. (2013). SET1 and p300 Act Synergistically, through Coupled Histone Modifications, in Transcriptional Activation by p53. *Cell* *154*, 297-310. 10.1016/j.cell.2013.06.027.

Tanigawa, M., Gotoh, M., Machida, M., Okada, T., and Oishi, M. (2000). Detection and mapping of mismatched base pairs in DNA molecules by atomic force microscopy. *Nucleic Acids Research* *28*, e38-e38. 10.1093/nar/28.9.e38.

Tennyson, C.N., Klamut, H.J., and Worton, R.G. (1995). The human dystrophin gene requires 16 hours to be transcribed and is cotranscriptionally spliced. *Nat Genet* *9*, 184-190. 10.1038/ng0295-184.

Théry, M. (2010). Micropatterning as a tool to decipher cell morphogenesis and functions. *Journal of Cell Science* *123*, 4201. 10.1242/jcs.075150.

Théry, M., Racine, V., Pépin, A., Piel, M., Chen, Y., Sibarita, J.B., and Bornens, M. (2005). The extracellular matrix guides the orientation of the cell division axis. *Nat Cell Biol* *7*, 947-953. 10.1038/ncb1307.

Thompson, R.E., Larson, D.R., and Webb, W.W. (2002). Precise Nanometer Localization Analysis for Individual Fluorescent Probes. *Biophysical Journal* *82*, 2775-2783. [https://doi.org/10.1016/S0006-3495\(02\)75618-X](https://doi.org/10.1016/S0006-3495(02)75618-X).

Thomson, I., Gilchrist, S., Bickmore, W.A., and Chubb, J.R. (2004). The radial positioning of chromatin is not inherited through mitosis but is established de novo in early G1. *Current biology : CB* *14*, 166-172. 10.1016/j.cub.2003.12.024.

Thurston, T.L., Ryzhakov, G., Bloor, S., von Muhlinen, N., and Randow, F. (2009). The TBK1 adaptor and autophagy receptor NDP52 restricts the proliferation of ubiquitin-coated bacteria. *Nature immunology* *10*, 1215-1221. 10.1038/ni.1800.

Titus, M.A. (2018). Myosin-Driven Intracellular Transport. *Cold Spring Harbor perspectives in biology* *10*. 10.1101/cshperspect.a021972.

Tompa, P., Schad, E., Tantos, A., and Kalmar, L. (2015). Intrinsically disordered proteins: emerging interaction specialists. *Current Opinion in Structural Biology* *35*, 49-59. <https://doi.org/10.1016/j.sbi.2015.08.009>.

Toomre, D., and Bewersdorf, J. (2010). A New Wave of Cellular Imaging. *Annual Review of Cell and Developmental Biology* *26*, 285-314. 10.1146/annurev-cellbio-100109-104048.

Tosheva, K.L., Yuan, Y., Matos Pereira, P., Culley, S., and Henriques, R. (2020). Between life and death: strategies to reduce phototoxicity in super-resolution microscopy. *J Phys D Appl Phys* *53*, 163001-163001. 10.1088/1361-6463/ab6b95.

Tsompana, M., and Buck, M.J. (2014). Chromatin accessibility: a window into the genome. *Epigenetics & Chromatin* *7*, 33. 10.1186/1756-8935-7-33.

Tsouroula, K., Furst, A., Rogier, M., Heyer, V., Maglott-Roth, A., Ferrand, A., Reina-San-Martin, B., and Soutoglou, E. (2016). Temporal and Spatial Uncoupling of DNA Double Strand Break Repair Pathways within Mammalian Heterochromatin. *Molecular cell* *63*, 293-305. 10.1016/j.molcel.2016.06.002.

Tufegdžić Vidaković, A., Mitter, R., Kelly, G.P., Neumann, M., Harreman, M., Rodríguez-Martínez, M., Herlihy, A., Weems, J.C., Boeing, S., Encheva, V., et al. (2020). Regulation of the RNAPII Pool Is Integral to the DNA Damage Response. *Cell* *180*, 1245-1261.e1221. <https://doi.org/10.1016/j.cell.2020.02.009>.

Tumbarello, D.A., Waxse, B.J., Arden, S.D., Bright, N.A., Kendrick-Jones, J., and Buss, F. (2012). Autophagy receptors link myosin VI to autophagosomes to mediate Tom1-dependent autophagosome maturation and fusion with the lysosome. *Nat Cell Biol* 14, 1024-1035. 10.1038/ncb2589.

van de Linde, S., Heilemann, M., and Sauer, M. (2012). Live-Cell Super-Resolution Imaging with Synthetic Fluorophores. *Annual Review of Physical Chemistry* 63, 519-540. 10.1146/annurev-physchem-032811-112012.

van de Linde, S., Krstić, I., Prisner, T., Doose, S., Heilemann, M., and Sauer, M. (2011a). Photoinduced formation of reversible dye radicals and their impact on super-resolution imaging. *Photochem Photobiol Sci* 10, 499-506. 10.1039/c0pp00317d.

van de Linde, S., Löschberger, A., Klein, T., Heidbreder, M., Wolter, S., Heilemann, M., and Sauer, M. (2011b). Direct stochastic optical reconstruction microscopy with standard fluorescent probes. *Nature Protocols* 6, 991-1009. 10.1038/nprot.2011.336.

van Steensel, B., and Belmont, A.S. (2017). Lamina-Associated Domains: Links with Chromosome Architecture, Heterochromatin, and Gene Repression. *Cell* 169, 780-791. <https://doi.org/10.1016/j.cell.2017.04.022>.

Venit, T., Semesta, K., Farrukh, S., Endara-Coll, M., Havalda, R., Hozak, P., and Percipalle, P. (2020). Nuclear myosin 1 activates p21 gene transcription in response to DNA damage through a chromatin-based mechanism. *Communications Biology* 3, 115. 10.1038/s42003-020-0836-1.

Verlhac, P., Grégoire, I.P., Azocar, O., Petkova, D.S., Baguet, J., Viret, C., and Faure, M. (2015). Autophagy receptor NDP52 regulates pathogen-containing autophagosome maturation. *Cell host & microbe* 17, 515-525. 10.1016/j.chom.2015.02.008.

Vermeulen, M., Mulder, K.W., Denissov, S., Pijnappel, W.W.M.P., van Schaik, F.M.A., Varier, R.A., Baltissen, M.P.A., Stunnenberg, H.G., Mann, M., and Timmers, H.T.M. (2007). Selective Anchoring of TFIID to Nucleosomes by Trimethylation of Histone H3 Lysine 4. *Cell* 131, 58-69. 10.1016/j.cell.2007.08.016.

Vertelov, G., Gutierrez, E., Lee, S.-A., Ronan, E., Groisman, A., and Tkachenko, E. (2016). Rigidity of silicone substrates controls cell spreading and stem cell differentiation. *Scientific Reports* 6, 33411. 10.1038/srep33411.

Vicent, G.P., Nacht, A.S., Font-Mateu, J., Castellano, G., Gaveglia, L., Ballaré, C., and Beato, M. (2011). Four enzymes cooperate to displace histone H1 during the first minute of hormonal gene activation. *Genes Dev* 25, 845-862. 10.1101/gad.621811.

Vicente-Manzanares, M., Ma, X., Adelstein, R.S., and Horwitz, A.R. (2009). Non-muscle myosin II takes centre stage in cell adhesion and migration. *Nature Reviews Molecular Cell Biology* 10, 778-790. 10.1038/nrm2786.

Vietri Rudan, M., and Hadjur, S. (2015). Genetic Tailors: CTCF and Cohesin Shape the Genome During Evolution. *Trends in Genetics* 31, 651-660. 10.1016/j.tig.2015.09.004.

Viguera, E., Canceill, D., and Ehrlich, S.D. (2001). Replication slippage involves DNA polymerase pausing and dissociation. *The EMBO Journal* 20, 2587-2595. <https://doi.org/10.1093/emboj/20.10.2587>.

Viita, T., Kyheröinen, S., Prajapati, B., Virtanen, J., Frilander, M.J., Varjosalo, M., and Vartiainen, M.K. (2019). Nuclear actin interactome analysis links actin to KAT14 histone acetyl transferase and mRNA splicing. *J Cell Sci* 132. 10.1242/jcs.226852.

von Muhlinen, N., Akutsu, M., Ravenhill, B.J., Foeglein, Á., Bloor, S., Rutherford, T.J., Freund, S.M.V., Komander, D., and Randow, F. (2012). LC3C, bound selectively by a noncanonical LIR motif in NDP52, is required for antibacterial autophagy. *Molecular cell* 48, 329-342. 10.1016/j.molcel.2012.08.024.

Vreugde, S., Ferrai, C., Miluzio, A., Hauben, E., Marchisio, P.C., Crippa, M.P., Bussi, M., and Biffo, S. (2006). Nuclear myosin VI enhances RNA polymerase II-dependent transcription. *Molecular cell* 23, 749-755. 10.1016/j.molcel.2006.07.005.

wa Maina, C., Honkela, A., Matarese, F., Grote, K., Stunnenberg, H.G., Reid, G., Lawrence, N.D., and Rattray, M. (2014). Inference of RNA Polymerase II Transcription Dynamics from Chromatin Immunoprecipitation Time Course Data. *PLOS Computational Biology* 10, e1003598. 10.1371/journal.pcbi.1003598.

Wachsmuth, M. (2014). Molecular diffusion and binding analyzed with FRAP. *Protoplasma* 251, 373-382. 10.1007/s00709-013-0604-x.

Wäldchen, S., Lehmann, J., Klein, T., van de Linde, S., and Sauer, M. (2015). Light-induced cell damage in live-cell super-resolution microscopy. *Sci Rep* 5, 15348. 10.1038/srep15348.

Walters, A.D., Bommakanti, A., and Cohen-Fix, O. (2012). Shaping the nucleus: factors and forces. *J Cell Biochem* 113, 2813-2821. 10.1002/jcb.24178.

Wang, A., Kolhe, J.A., Gioacchini, N., Baade, I., Briehner, W.M., Peterson, C.L., and Freeman, B.C. (2020). Mechanism of Long-Range Chromosome Motion Triggered by Gene Activation. *Developmental cell* 52, 309-320.e305. 10.1016/j.devcel.2019.12.007.

Wang, B., Zhang, L., Dai, T., Qin, Z., Lu, H., Zhang, L., and Zhou, F. (2021a). Liquid-liquid phase separation in human health and diseases. *Signal Transduction and Targeted Therapy* 6, 290. 10.1038/s41392-021-00678-1.

Wang, H., Kelley, F.M., Milovanovic, D., Schuster, B.S., and Shi, Z. (2021b). Surface tension and viscosity of protein condensates quantified by micropipette aspiration. *Biophysical Reports* 1, 100011. <https://doi.org/10.1016/j.bpr.2021.100011>.

Wang, H., Wang, B., Zhu, W., and Yang, Z. (2015). Lentivirus-Mediated Knockdown of Myosin VI Inhibits Cell Proliferation of Breast Cancer Cell. *Cancer Biother Radiopharm* 30, 330-335. 10.1089/cbr.2014.1759.

Wang, N., Butler, J.P., and Ingber, D.E. (1993). Mechanotransduction across the cell surface and through the cytoskeleton. *Science* 260, 1124-1127. 10.1126/science.7684161.

Wang, R., Kamgoue, A., Normand, C., Léger-Silvestre, I., Mangeat, T., and Gadai, O. (2016). High resolution microscopy reveals the nuclear shape of budding yeast during cell cycle and in various biological states. *J Cell Sci* 129, 4480-4495. 10.1242/jcs.188250.

Wang, S., Stoops, E., Cp, U., Markus, B., Reuveny, A., Ordan, E., and Volk, T. (2018). Mechanotransduction via the LINC complex regulates DNA replication in myonuclei. *J Cell Biol* 217, 2005-2018. 10.1083/jcb.201708137.

Webster, M., Witkin, K.L., and Cohen-Fix, O. (2009). Sizing up the nucleus: nuclear shape, size and nuclear-envelope assembly. *Journal of Cell Science* 122, 1477-1486. 10.1242/jcs.037333.

Wegel, E., and Shaw, P. (2005). Gene activation and deactivation related changes in the three-dimensional structure of chromatin. *Chromosoma* 114, 331-337. 10.1007/s00412-005-0015-7.

Wei, M., Fan, X., Ding, M., Li, R., Shao, S., Hou, Y., Meng, S., Tang, F., Li, C., and Sun, Y. (2020). Nuclear actin regulates inducible transcription by enhancing RNA polymerase II clustering. *Science Advances* 6, eaay6515. 10.1126/sciadv.aay6515.

Weihhs, D., Mason, T.G., and Teitell, M.A. (2007). Effects of cytoskeletal disruption on transport, structure, and rheology within mammalian cells. *Physics of Fluids* 19, 103102. 10.1063/1.2795130.

Weiss, R.E., Xu, J., Ning, G., Pohlenz, J., O'Malley, B.W., and Refetoff, S. (1999). Mice deficient in the steroid receptor co-activator 1 (SRC-1) are resistant to thyroid hormone. *The EMBO journal* 18, 1900-1904. 10.1093/emboj/18.7.1900.

Weissgerber, T.L., Winham, S.J., Heinzen, E.P., Milin-Lazovic, J.S., Garcia-Valencia, O., Bukumiric, Z., Savic, M.D., Garovic, V.D., and Milic, N.M. (2019). Reveal, Don't Conceal: Transforming Data Visualization to Improve Transparency. *Circulation* 140, 1506-1518. 10.1161/CIRCULATIONAHA.118.037777.

Wells, A.L., Lin, A.W., Chen, L.-Q., Safer, D., Cain, S.M., Hasson, T., Carragher, B.O., Milligan, R.A., and Sweeney, H.L. (1999). Myosin VI is an actin-based motor that moves backwards. *Nature* 401, 505-508. 10.1038/46835.

Welsh, T.J., Shen, Y., Levin, A., and Knowles, T.P.J. (2018). Mechanobiology of Protein Droplets: Force Arises from Disorder. *Cell* 175, 1457-1459. 10.1016/j.cell.2018.11.020.

Wendt, K.S., Yoshida, K., Itoh, T., Bando, M., Koch, B., Schirghuber, E., Tsutsumi, S., Nagae, G., Ishihara, K., Mishiro, T., et al. (2008). Cohesin mediates transcriptional insulation by CCCTC-binding factor. *Nature* 451, 796-801. 10.1038/nature06634.

Wesolowska, N., Avilov, I., Machado, P., Geiss, C., Kondo, H., Mori, M., and Lenart, P. (2020). Actin assembly ruptures the nuclear envelope by prying the lamina away from nuclear pores and nuclear membranes in starfish oocytes. *eLife* 9, e49774. 10.7554/eLife.49774.

West, M.L., and Corden, J.L. (1995). Construction and analysis of yeast RNA polymerase II CTD deletion and substitution mutations. *Genetics* 140, 1223-1233. 10.1093/genetics/140.4.1223.

Whyte, W.A., Orlando, D.A., Hnisz, D., Abraham, B.J., Lin, C.Y., Kagey, M.H., Rahl, P.B., Lee, T.I., and Young, R.A. (2013). Master transcription factors and mediator establish super-enhancers at key cell identity genes. *Cell* 153, 307-319. 10.1016/j.cell.2013.03.035.

Willhoft, O., McCormack, E.A., Aramayo, R.J., Bythell-Douglas, R., Ocloo, L., Zhang, X., and Wigley, D.B. (2017). Crosstalk within a functional INO80 complex dimer regulates nucleosome sliding. *eLife* 6, e25782. 10.7554/eLife.25782.

Wollman, A.J., Shashkova, S., Hedlund, E.G., Friemann, R., Hohmann, S., and Leake, M.C. (2017). Transcription factor clusters regulate genes in eukaryotic cells. *eLife* 6, e27451. 10.7554/eLife.27451.

Wollscheid, H.-P., Biancospino, M., He, F., Magistrati, E., Molteni, E., Lupia, M., Soffientini, P., Rottner, K., Cavallaro, U., Pozzoli, U., et al. (2016). Diverse functions of myosin VI elucidated by an isoform-specific α -helix domain. *Nature Structural & Molecular Biology* 23, 300-308. 10.1038/nsmb.3187.

Würtemberger, J., Tchessalova, D., Regina, C., Bauer, C., Schneider, M., Wagers, A.J., and Hettmer, S. (2020). Growth inhibition associated with disruption of the actin cytoskeleton by Latrunculin A in rhabdomyosarcoma cells. *PLoS One* 15, e0238572. 10.1371/journal.pone.0238572.

Xia, T., Li, N., and Fang, X. (2013). Single-Molecule Fluorescence Imaging in Living Cells. *Annual Review of Physical Chemistry* 64, 459-480. 10.1146/annurev-physchem-040412-110127.

Xie, G., Walker, R.R., 3rd, and Irianto, J. (2020). Nuclear mechanosensing: mechanism and consequences of a nuclear rupture. *Mutat Res* 821, 111717. 10.1016/j.mrfmmm.2020.111717.

Xie, X., Almuzzaini, B., Drou, N., Kremb, S., Yousif, A., Farrants, A., Gunsalus, K., and Percipalle, P. (2018a). β -Actin-dependent global chromatin organization and gene expression programs control cellular identity. *Faseb j* 32, 1296-1314. 10.1096/fj.201700753R.

Xie, X., Jankauskas, R., Mazari, A.M.A., Drou, N., and Percipalle, P. (2018b). β -actin regulates a heterochromatin landscape essential for optimal induction of neuronal programs during direct reprogramming. *PLoS Genet* 14, e1007846. 10.1371/journal.pgen.1007846.

Xie, X., Li, F., Wang, Y., Wang, Y., Lin, Z., Cheng, X., Liu, J., Chen, C., and Pan, L. (2015). Molecular basis of ubiquitin recognition by the autophagy receptor CALCOCO2. *Autophagy* 11, 1775-1789. 10.1080/15548627.2015.1082025.

Xu, J., Ma, H., and Liu, Y. (2017). Stochastic Optical Reconstruction Microscopy (STORM). *Curr Protoc Cytom* 81, 12.46.11-12.46.27. 10.1002/cpcy.23.

Xu, J., Zutter, M.M., Santoro, S.A., and Clark, R.A. (1998). A three-dimensional collagen lattice activates NF-kappaB in human fibroblasts: role in integrin alpha2 gene expression and tissue remodeling. *J Cell Biol* 140, 709-719. 10.1083/jcb.140.3.709.

Yang, C.K., Kim, J.H., Li, H., and Stallcup, M.R. (2006a). Differential Use of Functional Domains by Coiled-coil Coactivator in Its Synergistic Coactivator Function with β -Catenin or GRIP1. *Journal of Biological Chemistry* 281, 3389-3397. 10.1074/jbc.M510403200.

Yang, C.K., Kim, J.H., and Stallcup, M.R. (2006b). Role of the N-Terminal Activation Domain of the Coiled-Coil Coactivator in Mediating Transcriptional Activation by β -Catenin. *Molecular Endocrinology* 20, 3251-3262. 10.1210/me.2006-0200.

Yang, H.-J., Iwamoto, M., Hiraoka, Y., and Haraguchi, T. (2017). Function of nuclear membrane proteins in shaping the nuclear envelope integrity during closed mitosis. *The Journal of Biochemistry* 161, 471-477. 10.1093/jb/mvx020.

Yang, P., Mathieu, C., Kolaitis, R.-M., Zhang, P., Messing, J., Yurtsever, U., Yang, Z., Wu, J., Li, Y., Pan, Q., et al. (2020). G3BP1 Is a Tunable Switch that Triggers Phase Separation to Assemble Stress Granules. *Cell* 181, 325-345.e328. <https://doi.org/10.1016/j.cell.2020.03.046>.

Yang, W., Gelles, J., and Musser Siegfried, M. (2004). Imaging of single-molecule translocation through nuclear pore complexes. *Proceedings of the National Academy of Sciences* *101*, 12887-12892. 10.1073/pnas.0403675101.

Yang, Z., Hong, S.H., and Privalsky, M.L. (1999). Transcriptional anti-repression. Thyroid hormone receptor beta-2 recruits SMRT corepressor but interferes with subsequent assembly of a functional corepressor complex. *The Journal of biological chemistry* *274*, 37131-37138. 10.1074/jbc.274.52.37131.

Yaşar, P., Ayaz, G., User, S.D., Güpür, G., and Muyan, M. (2016). Molecular mechanism of estrogen-estrogen receptor signaling. *Reprod Med Biol* *16*, 4-20. 10.1002/rmb2.12006.

Yildiz, A., Forkey Joseph, N., McKinney Sean, A., Ha, T., Goldman Yale, E., and Selvin Paul, R. (2003). Myosin V Walks Hand-Over-Hand: Single Fluorophore Imaging with 1.5-nm Localization. *Science* *300*, 2061-2065. 10.1126/science.1084398.

Yokoyama, A., Wang, Z., Wysocka, J., Sanyal, M., Aufiero, D.J., Kitabayashi, I., Herr, W., and Cleary, M.L. (2004). Leukemia proto-oncoprotein MLL forms a SET1-like histone methyltransferase complex with menin to regulate Hox gene expression. *Molecular and cellular biology* *24*, 5639-5649. 10.1128/mcb.24.13.5639-5649.2004.

Yoshida, H., Cheng, W., Hung, J., Montell, D., Geisbrecht, E., Rosen, D., Liu, J., and Naora, H. (2004). Lessons from border cell migration in the *Drosophila* ovary: A role for myosin VI in dissemination of human ovarian cancer. *Proc Natl Acad Sci U S A* *101*, 8144-8149. 10.1073/pnas.0400400101.

Yu, C., Feng, W., Wei, Z., Miyanoiri, Y., Wen, W., Zhao, Y., and Zhang, M. (2009). Myosin VI Undergoes Cargo-Mediated Dimerization. *Cell* *138*, 537-548. 10.1016/j.cell.2009.05.030.

Zemel, A., Rehfeldt, F., Brown, A.E., Discher, D.E., and Safran, S.A. (2010). Optimal matrix rigidity for stress fiber polarization in stem cells. *Nat Phys* *6*, 468-473. 10.1038/nphys1613.

Zhang, S., Übelmesser, N., Josipovic, N., Forte, G., Slotman, J.A., Chiang, M., Gothe, H.J., Gusmao, E.G., Becker, C., Altmüller, J., et al. (2021). RNA polymerase II is required for spatial chromatin reorganization following exit from mitosis. *Science advances* *7*, eabg8205-eabg8205. 10.1126/sciadv.abg8205.

Zhao, Z.W., Roy, R., Gebhardt, J.C.M., Suter, D.M., Chapman, A.R., and Xie, X.S. (2014). Spatial organization of RNA polymerase II inside a mammalian cell nucleus revealed by reflected light-sheet superresolution microscopy. *Proceedings of the National Academy of Sciences* *111*, 681. 10.1073/pnas.1318496111.

Zheng, X., Hu, J., Yue, S., Kristiani, L., Kim, M., Sauria, M., Taylor, J., Kim, Y., and Zheng, Y. (2018). Lamins Organize the Global Three-Dimensional Genome from the Nuclear Periphery. *Molecular cell* *71*, 802-815.e807. 10.1016/j.molcel.2018.05.017.

Zhuang, X. (2009). Nano-imaging with STORM. *Nature Photonics* *3*, 365-367. 10.1038/nphoton.2009.101.

Zimmerli, C.E., Allegretti, M., Rantos, V., Goetz Sara, K., Obarska-Kosinska, A., Zagoriy, I., Halavatyi, A., Hummer, G., Mahamid, J., Kosinski, J., and Beck, M. (2021). Nuclear pores dilate and constrict in cellulose. *Science* *0*, eabd9776. 10.1126/science.abd9776.

Ziv, Y., Bielopolski, D., Galanty, Y., Lukas, C., Taya, Y., Schultz, D.C., Lukas, J., Bekker-Jensen, S., Bartek, J., and Shiloh, Y. (2006). Chromatin relaxation in response to DNA double-strand breaks is modulated by a novel ATM- and KAP-1 dependent pathway. *Nat Cell Biol* *8*, 870-876. 10.1038/ncb1446.

Zorca, C.E., Kim, L.K., Kim, Y.J., Krause, M.R., Zenklusen, D., Spilianakis, C.G., and Flavell, R.A. (2015). Myosin VI regulates gene pairing and transcriptional pause release in T cells. *Proceedings of the National Academy of Sciences U.S.A* *112*, E1587. 10.1073/pnas.1502461112.

Zwerger, M., Ho, C.Y., and Lammerding, J. (2011). Nuclear Mechanics in Disease. *Annual Review of Biomedical Engineering* *13*, 397-428. 10.1146/annurev-bioeng-071910-124736.

